Investigation into the Role of the Infectious Bronchitis Virus (IBV) Envelope Protein in Viral Replication and Pathogenicity.

Isobel Sylvia Webb

A dissertation submitted to the University of Bristol in accordance with the requirements for award of the degree of Doctor of Philosophy in the Faculty of Life Sciences

School of Cellular and Molecular Medicine, September 2022

Word Count: 59565

Abstract

Infectious bronchitis virus (IBV) is a highly infectious *Gammacoronavirus*, causing respiratory disease in poultry. The IBV virion consists of four structural proteins: spike (S), membrane (M), nucleocapsid (N) and envelope (E). The E protein has been shown to function in viral assembly, release, and pathogenesis. Two forms of E are found in infected cells: monomeric and a pentameric ion channel. Two mutations, T16A and A26F, select for either the pentameric or monomeric form, respectively. Previous work reports that these two mutations abolish E protein ion channel activity. Using reverse genetics, either the mutation T16A or A26F were incorporated in a non-pathogenic (Beau-R) or pathogenic (M41-K) IBV backbone. The resulting rIBVs were assessed in relation to genetic stability, replication and cytopathogenicity. Characterisation of the Beau-R based rIBVs, BeauR-T16A and BeauR-A26F respectively, identified that the effect of these mutations was dependent on cell-type. Generation of the T16A and A26F mutations in a pathogenic strain, M41-K, aimed to investigate these mutations as vaccine targets. The rIBV M41K-A26F was unable to be rescued suggesting the monomeric form of E is essential for viral replication. Additionally, isolates of rIBV M41K-T16A, unlike BeauR-T16A generated mutations in the S and M proteins, which may have been compensatory and potentially facilitated replication. This indicates that these mutations may have a strain-dependent effect. M41K-T16A retained pathogenicity *in vivo* however the potential role of additional mutations in genome needs to be investigated further. To investigate the role of the E protein in the assembly and release of virus, mass spectrometry, bioimaging techniques and cellular inhibitors were used. This thesis furthers knowledge on the function of the coronavirus E protein during infection and demonstrates that both the cell-type and IBV strain are important considerations for the future study of the E protein in IBV replication.

Acknowledgements

First and foremost, I would like to thank all my supervisors who have been incredibly supportive throughout this project: Dr Erica Bickerton, Dr Helena Maier and Prof. Andrew Davidson. A special thank you to Erica for always finding a way to make me laugh (and not cry) when I made a mistake and for teaching me resilience. A massive thank you to my 'informal' supervisor, Dr Sarah Keep, for being so generous with your time and invaluable advice. Also, for your huge effort in aiding me publishing my first paper and for clothing me! An extra thank you to Erica and Sarah for proof-reading my whole thesis! I would like to thank the British Egg Marketing Board and UKRI for providing the funding for this project. Thank you to everyone who helped with data acquisition and analysis as part of this thesis including Andrew Davidson, Graham Freimanis, Nicole Doyle, Giulia Dowgier, Holly Everest, and Michael Oade.

Many thanks to all the members, past and present, of the Coronavirus and Coronavirus Cellular Biology groups for making this PhD an absolute pleasure. Special mention to my side-kick Phoebe, who made me smile every single day! Also, to Nicole and Katalin, for your foolishness. Thank you to all my great mates, including those from LMS, Leicester and Pirbright, for keeping me busy and boozy in the evenings.

Enormous thanks to my parents who provided me with every opportunity to succeed in life but mostly for donating huge quantities of wine to the cause. Also, a big thank you to my sisters, Madeleine, and Jemima, who are the kindest, smartest, and funniest people I know. Thank you to my pup, Coco, for all your sweetness, you are dearly missed. Thank you to my grandparents and uncles for all their encouragement. The biggest thank you to the illustrator and editor of this thesis, Ben, for everything!

Declaration

I declare that the work in this dissertation was carried out in accordance with the requirements of the University's Regulations and Code of Practice for Research Degree Programmes and that it has not been submitted for any other academic award. Except where indicated by specific reference in the text, the work is the candidate's own work. Work done in collaboration with, or with the assistance of, others, is indicated as such. Any views expressed in the dissertation are those of the author.

SIGNED: 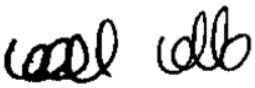 DATE: 8th September 2022

Isobel Webb

Table of Contents

List of Tables and Figures

Abbreviations

aa	Amino acid
ADRP	ADP-ribose-1”-phosphate phosphatase
AID	Auxin-inducible degradation
ANOVA	Analysis of variance
APN	Aminopeptidase N
ARF1	ADP-ribosylation factor
ATP	Adenosine triphosphate
BES	N, N-bis[2-hydroxethy1]-2-aminoethanesulfonic acid
BFA	Brefeldin-A
BME	β-mercaptoethanol
bp	Base pair
BSA	Bovine serum albumin
CAMPSAP2	Calmodulin-regulated spectrin-associated protein 2
cDNA	Complementary DNA
CK	Chick kidney
co-IP	Co-immunoprecipitation
CLEM	Corelative light electron microscopy
COP1	Coat protein complex 1
CoV	Coronavirus

CPE	Cytopathic effect
Ct	Cycle threshold
CT	Cytoplasmic tail
CTD	C-terminal domain
DAPI	4',6-diamidino-2-phenylindole
DMEM	Dulbecco's minimum essential medium
DMSO	Dimethyl sulfoxide
DMV	Double membrane vesicle
DNA	Deoxyribonucleic acid
dNTPs	Deoxynucleotide triphosphates
dpi	Days post infection
dsRNA	Double-stranded RNA
DTT	Dithiothreitol
E	Envelope protein
E. coli	*Escherichia coli*
Ecogpt	*E. coli* guanine phosphoribosyl transferase
EDTA	Ethylenediaminetetraacetic acid
EM	Electron microscopy
EMC	Encephalomyocarditis virus
EMEM	Eagle's minimum essential medium
EPHA2	Ephrin type-A receptor 2

ER	Endoplasmic reticulum
ERES	ER exit sites
ERGIC	ER-Golgi intermediate compartment
ES2	Endosidin-2
EXO70	Exocyst component of 70 kDa
ExoN	Exoribonuclease
FC	Fold change
FCS	Fetal bovine serum
FDR	False discovery rate
FP	Fusion peptide
GBF1	Golgi-specific brefeldin A-resistance guanine nucleotide exchange factor 1
GM130	130 kDa cis-Golgi matrix protein
GMEM	Glasgow minimum essential medium
GPB1	Guanylate Binding Protein 1
h	Hour
H_20	Water
HCD	High energy collision dissociation
HCoV-229E	Human CoV 229E
HE	Haemagglutinin esterase
HeLa	Henrietta Lacks

HIV-1	Human immunodeficiency virus 1
HMA	Hexamethylene amiloride
HMW	High molecular weight
hpi	Hours post infection
HR	Heptad repeats
HRPT1	Hypoxanthine phosphoribosyltransferase 1
HS	Heparan sulphate
HSP70	Heat shock protein 70
HδR	Hepatitis delta antigenome ribozyme
IAV	Influenza A virus
IB	Infectious bronchitis
IBV	Infectious bronchitis virus
IC	Ion channel
ICTV	International Committee on Taxonomy of Viruses
IF	Immunofluorescence
IFN	Interferon
Ig	Immunoglobulin
IL	Interleukin
IRF	IFN regulatory factors
kDa	Kilo Dalton
kb	Kilobase

KIF20	Kinesin Family Member 20A
LAMP1	Lysosomal-associated membrane protein 1
LC3	Microtubule-associated protein 1A/1B-light chain 3
LMAN1	Mannose-binding lectin 1
LMW	Low molecular weight
LONP1	Lon protease homolog
M	Membrane protein
M2	Matrix 2
MAVS	Mitochondrial antiviral-signalling protein
MDA5	Melanoma differentiation associated protein 5
MERS-CoV	Middle East respiratory syndrome coronavirus
Mg	Magnesium
mg	Milligram
$MgCl_2$	Magnesium chloride
MHV	Mouse hepatitis virus
min	Minute
MKLP2	Mitotic kinesin-like proteins 2
ml	Millilitre
mm	Millimetre
MOI	Multiplicity of Infection
MPA	Mycophenolic acid

mRNA	Messenger RNA
N	Nucleocapsid protein
N7-MTase	S-adenosylmethionine (SAM)-dependent (guanine-N7) methyltransferase
NaOH	Sodium hydroxide
NBBS	New-born calf serum
NFκB	Nuclear factor kappa B
NGS	Next generation sequencing
NMR	Nuclear magnetic resonance
NMT	N-myristoyltransferase
ns	Not significant
nsp	Non-structural protein
nt	Nucleotide
NTD	N-terminal domain
OAS*A	2'-5' oligoadenylate synthase
ORF	Open reading frame
OTUD4	OTU domain-containing protein 4
P/S	Penicillin/ Streptomycin
PAGE	Polyacrylamide gel electrophoresis
PAMP	Pathogen-associated molecular patterns
PARP	Poly(ADP-ribose) polymerase family members

PBEF1	Nicotinamide phosphoribosyltransferase
PBS	Phosphate buffered saline
PCR	Polymerase chain reaction
PDB	Protein data bank
PDCoV	Porcine deltacoronavirus
PFA	Paraformaldehyde
PFU	Plaque forming unit
PIC	Protein inhibitor cocktail
pkr	Protein kinase R
pLDDT	Per residue confidence score
PM	Plasma membrane
P-M	Post-mortem
pmol	Picomole
pp	Polyprotein
PRR	Pattern recognition receptors
PSCNV	Planarian secretory cell nidovirus
PTPN1	Protein tyrosine phosphatase non-receptor type 1
qPCR	Quantitative PCR
Rab11	Ras-related protein Rab-11B
Rab1b	Ras-related protein Rab-1b
RdRp	RNA-dependent RNA polymerase

rFPV-T7	Recombinant Fowlpox-T7 virus
RFS	Ribosome frameshift site
rIBV	Recombinant IBV
RIPA	Radioimmunoprecipitation assay
RIR	Rhode Island Red
RNA	Ribonucleic acid
RNaseOUT	Ribonuclease inhibitor
RNP	Ribonucleoprotein
RO	Replication organelle
rpm	Revolutions per minute
RT	Reverse transcription
RTC	Replication-transcription complex
rVV	Recombinant Vaccinia virus
s	Second
S	Spike protein
SARS-CoV	Severe acute respiratory syndrome coronavirus
SARS-CoV-2	Severe acute respiratory syndrome coronavirus 2
SCEL	Sciellin
SD	Standard deviation
SDS	Sodium dodecyl sulphate
SEM	Standard error of the mean

sg	Sub-genomic
sgRNA	Sub-genomic RNA
SPF	Specific pathogen-free
SPS	Synchronous precursor selection
SS	Signal sequence
SSIV	Super Script IV
ST	Swine testicular
TBE	Tris borate EDTA
TCEP	Tris(2-carboxyethyl) phosphine hydrochloride
TDS	Transient dominant selection
TE	Tris/ EDTA
TEM	Transmission EM
TGEV	Transmissible gastroenteritis virus
TGN	*Trans*-Golgi network
TK	Thymidine kinase
TLR	Toll-like receptors
TM	Transmembrane
TMD	Transmembrane domain
TMTpro	Tandem mass tag
TOC	Tracheal organ culture
TPB	Tryptose phosphate broth

TRANK1	TPR and ankyrin repeat-containing protein
TRIM25	Tripartite motif-containing protein 25
TRS	Transcription regulatory sequence
TRS-B	Body transcription regulatory sequence
TRS-L	Leader transcription regulatory sequence
UTR	Untranslated region
V	Volts
VLP	Virus-like particle
Vpu	Viral protein U
WB	Western blot
WT	Wild type
ZNFX1	NFX1-type zinc finger-containing protein 1
µg	Microgram
µl	Microlitre
µm	Micrometre
µM	Micromolar

Publications

Keep S, Stevenson-Leggett P, Steyn A, Oade MS, **Webb I**, Stuart J, Vervelde L, Britton P, Maier HJ, Bickerton E. Temperature Sensitivity: A Potential Method for the Generation of Vaccines against the Avian Coronavirus Infectious Bronchitis Virus. *Viruses.* 2020 Jul 14;12(7):754. doi: 10.3390/v12070754.

Keep S, Carr BV, Lean FZX, Fones A, Newman J, Dowgier G, Freimanis G, Vatzia E, Polo N, Everest H, **Webb I**, Mcnee A, Paudyal B, Thakur N, Nunez A, MacLoughlin R, Maier H, Hammond J, Bailey D, Waters R, Charleston B, Tuthill T, Britton P, Bickerton E, Tchilian E. Porcine Respiratory Coronavirus as a Model for Acute Respiratory Coronavirus Disease. *Front Immunol.* 2022 Mar 28; 13:867707. doi: 10.3389/fimmu.2022.867707.

Webb I, Keep S, Littolff K, Stuart J, Freimanis G, Britton P, Davidson AD, Maier HJ, Bickerton E. The Genetic Stability, Replication Kinetics and Cytopathogenicity of Recombinant Avian Coronaviruses with a T16A or an A26F Mutation within the E Protein is Cell-Type Dependent. Viruses. 2022; 14(8):1784. doi: 10.3390/v1408178

Keep S, Stevenson-Leggett P, Dowgier G, Foldes K, **Webb I**, Fones A, Littolff K, Everest H, Britton P, Bickerton E. A Temperature-Sensitive Recombinant of Avian Coronavirus Infectious Bronchitis Virus Provides Complete Protection against Homologous Challenge. J Virol. 2022 Aug 16:e0110022. doi: 10.1128/jvi.01100-22.

Webb I, Keep S, Everest H, Stuart J, Freimanis G, Britton P, Davidson AD, Maier HJ and Bickerton E. The impact of the T16A and A26F Mutations in the Envelope Protein of an Avian Coronavirus on Viral Replication is Strain Dependent. (In Preparation)

Presentations

Isobel Webb, Sarah Keep, Helena J Maier, Andrew Davidson, and Erica Bickerton. 2022. Characterising the ion channel inactivating mutations in the E protein of Infectious Bronchitis Virus (IBV). Microbiology Society Annual Conference. (Oral presentation)

Isobel Webb, Sarah Keep, Helena J Maier, Andrew Davidson, and Erica Bickerton. 2022. Characterisation of the Infectious Bronchitis Virus E Protein for Rational Vaccine Design. Avian Research Symposium, Microbiology Society. (Oral presentation)

Isobel Webb, Sarah Keep, Helena Maier, Andrew Davidson, and Erica Bickerton. 2021. Characterising the ion channel inactivating mutations in the E protein of Infectious Bronchitis Virus (IBV). Avian Infectious Diseases Conference, The University of Edinburgh. (Oral presentation).

Isobel Webb. 2020. Characterisation of the Infectious Bronchitis Virus E Protein for Rational Vaccine Design. Coronavirus E Protein Interest Group. (Oral Presentation)

Isobel Webb, Sarah Keep, Jamie Stuart, Michael Oade, Paul Britton, Erica Bickerton. 2019. Generation of a recombinant GFP-tagged infectious bronchitis virus (IBV). Microbiology Society Annual Conference. (Poster presentation)

Isobel Webb, Sarah Keep, Paul Britton, Erica Bickerton. 2017. Generation of a recombinant GFP-tagged infectious bronchitis virus (IBV). Microbiology Society Annual Conference. (Poster presentation)

Chapter 1: Introduction

1.1. The *Coronaviridae* Family

1.1.1. *Nidovirales* Order

The *Nidovirales* order is defined by their enveloped virions and positive-sense, single-stranded RNA genomes (1). Although the genomic organisation of the *Nidovirales* order is similar, there is a huge level of variation in genome size. The *Nidovirales* order includes viruses with the largest known RNA genomes, the largest of which being the planarian secretory cell nidovirus (PSCNV) with a genome size of 41 kb (2). Viruses within this order possess proof-reading exoribonuclease (ExoN) activity to prevent the accumulation of sequence error which is hypothesised to restrict the genome size of most other RNA viruses. In contrast, small genomes are found in the *Arteriviridae* sub-order of the *Nidovirales* order contains viruses with a genome length between 12.7 to 15.7 kb. The classification of the viruses found within this order is outlined in Figure 1.1.

1.1.2. Classification of the *Coronaviridae* Family

The *Coronaviridae* (CoV) family were initially classified based on the appearance of the spike protein protruding from the viral envelope which has been compared to the corona of the sun or a crown, giving them the name corona after the Greek κορώνα (3). This family contains the *Orthocoronavirinae* subfamily, which is divided into four genera based on phylogenetic analysis of several viral genes (3) resulting in the genera *Alphacoronavirus, Betacoronavirus* and *Gammacoronavirus,* along with the more recently established *Deltacoronavirus* (4). Subgenera and species within the four genera are detailed in Table 1.1. This table lists examples of *Coronaviridae* virus

species, these viruses infect a wide range of animal hosts, including vertebrate and invertebrate species.

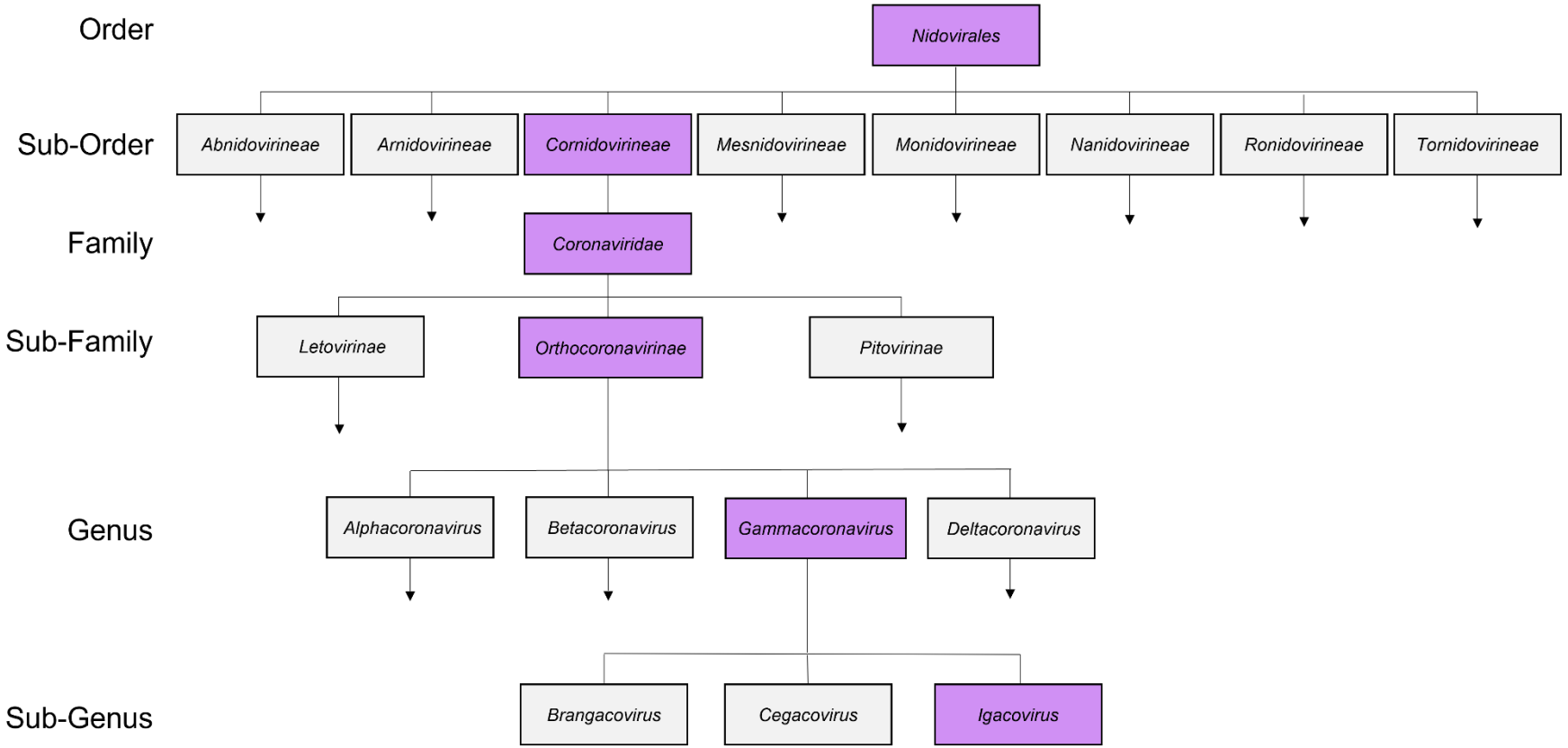

Figure 1.1. Nidovirales Order Classification. Adapted from the International Committee on Taxonomy of Viruses (ICTV) website, as defined in 2022 (ictvonline.org). Purple boxes follow the lineage to infectious bronchitis virus (IBV) which is classified within the subgenus *Igacovirus*. Arrows represent the presence of lineages which have not been detailed within this schematic.

Table 1.1. *Orthocoronavirinae* genera and species.

Genus	Subgenus	Species
Alphacoronavirus	*Amalacovirus*	Alphacoronavirus AMALF
	Colacovirus	Bat coronavirus CDPHE15
	Decacovirus	Alphacoronavirus CHB25
		Alphacoronavirus WA3607
		Bat coronavirus HKU10
		Rhinolophus ferrumequinum alphacoronavirus HuB-2013
	Duvinacovirus	Human coronavirus 229E
	Luchacovirus	Lucheng Rn rat coronavirus
	Minacovirus	Mink coronavirus 1
	Minuacovirus	Miniopterus bat coronavirus 1
		Miniopterus bat coronavirus HKU8
	Myotacovirus	Myotis ricketti alphacoronavirus Sax-2011
	Nyctavocirus	Alphacoronavirus HKU33
		Alphacoronavirus WA2028
		Nyctalus velutinus alphacoronavirus SC-2013
		Pipistrellus kuhlii coronavirus 3398
	Pedacovirus	Alphacoronavirus BT020
		Alphacoronavirus WA1087
		Porcine epidemic diarrhea virus
		Scotophilus bat coronavirus 512
	Rhinacovirus	Rhinolophus bat coronavirus HKU2
	Setracovirus	Human coronavirus NL63
		NL63-related bat coronavirus strain BtKYNL63-9b
	Soracovirus	Sorex araneus coronavirus T14
	Sunacovirus	Suncus murinus coronavirus X74
	Tegacovirus	Alphacoronavirus 1
Betacoronavirus	*Embecovirus*	Betacoronavirus 1
		China Rattus coronavirus HKU24
		Human coronavirus HKU1
		Murine coronavirus
		Myodes coronavirus 2JL14
	Hibecovirus	Bat Hp-betacoronavirus Zhejiang2013
	Merbecovirus	Hedgehog coronavirus 1
		Middle East respiratory syndrome-related coronavirus
		Pipistrellus bat coronavirus HKU5
		Tylonycteris bat coronavirus HKU4
	Nobecovirus	Eidolon bat coronavirus C704
		Rousettus bat coronavirus GCCDC1
		Rousettus bat coronavirus HKU9
	Sarbecovirus	Severe acute respiratory syndrome-related coronavirus
Gammacoronavirus	*Brangacovirus*	Goose coronavirus CB17
	Cegacovirus	Beluga whale coronavirus SW1
	Igacovirus	Avian Coronavirus
		Avian coronavirus 9203,
		Duck coronavirus 2714
Deltacoronavirus	*Andecovirus*	Wigeon coronavirus HKU20
	Buldecovirus	Bulbul coronavirus HKU11
		Common moorhen coronavirus HKU21
		Coronavirus HKU15
		Common moorhen coronavirus HKU21
		Bulbul coronavirus HKU11
	Herdecovirus	Night heron coronavirus HKU19

Notes: IBV is described as Avian Coronavirus. Adapted from International Committee for the Taxonomy of Viruses (ICTV) as in May 2022 (ictvonline.org)

1.2. Infectious Bronchitis Virus (IBV)

IBV is a *Gammacoronavirus* within the subgenus *Igacovirus* (Table 1.1.). IBV was first identified in 1931 (5) and infects the epithelial surfaces of domestic fowl (*Gallus gallus)* causing respiratory disease. IBV is often described as the prototypic *Gammacoronavirus.*

1.2.1. IBV Strain Classification

IBV is unusual amongst the CoVs in that there are many different strains and serotypes, many of which co-circulate (6). IBV strains have been classified using a host of different techniques. Traditionally, IBV strains were serotyped through assessment of neutralisation between strains, i.e., if antiserum generated within chickens infected with a strain cannot neutralise another IBV strain then they are classified as different serotypes (7). To combat the lack of uniformity between serotyping methods, genotyping has been implemented through assessing the phylogeny of the IBV strains in relation to the nucleotide sequence (8).

1.2.2. Clinical Disease

IBV is the causative agent of Infectious Bronchitis (IB) which is a highly infectious disease transmitted by inhalation of aerosolised droplets (9). IB results in the greatest economic losses to the poultry industry in the UK (10) and is present worldwide (6). IB was first identified in the 1930s (11), high mutation rates and genome recombination events have resulted in many serotypes and genotypes emerging since (12). IBV infects the epithelial surfaces of poultry, causing clinical disease ranging from mild respiratory symptoms to severe kidney and oviduct disease (9, 13). Clinical signs include snicking, depression, rales and nasal discharge (6). Different strains of the virus show different tissue tropism profiles, for example M41 infected birds show infection which is predominantly localised to the upper respiratory tract in comparison to strains such as QX which are nephropathogenic (14). Infection of the

oviduct epithelial surfaces results in reduced production and quality of eggs in layers (15). Additionally, infection with IB results in reduced weight gain in broilers and leaves chicks susceptible to secondary bacterial infections (16).

1.2.3. Vaccination Strategies

Vaccination attempts against IBV have been reported since the 1940s (6) with vaccines typically developed through serial passage of pathogenic IBV in embryonated eggs with the aim of attenuating the virulence of the virus. The mechanism of attenuation is not understood (17, 18). Administration of these vaccines is carried out through mass spray of chicks with aerosolised vaccine in the hatchery, but there are questions about the efficiency of this method as there is no way to ensure each chick receives the correct dose (19). These vaccines have several pitfalls as they cannot be administered *in ovo* which would ensure the correct dose is delivered to each individual chick, vaccines are poorly cross protective against different serotypes (20) and additionally vaccination against IBV has been shown to reduce fertility in roosters (21). Whole genome sequencing of *in ovo* passaged virus has shown that only a small number of mutations are able to restore a virulent phenotype (22). Reversion to virulence has previously been demonstrated through vaccine passage in chickens (23). Through enhanced knowledge of the roles of IBV proteins in pathogenicity, there is an increased interest in rationally attenuating IBV to stably alter the pathogenicity; this is being explored using reverse genetics to generate recombinant IBVs (rIBVs) (24). Rationally attenuated rIBV vaccines have been developed against newly emerging serotypes but there are currently no licensed rIBV vaccines commercially used (19). Although, promising candidates are constantly being generated (25).

1.2.4. IBV Structure

IBV virions contain three structural proteins embedded in the virion envelope: spike (S) protein, envelope (E) protein and membrane (M) protein. Within the viral particle, the nucleocapsid (N) protein coats the single-stranded RNA genome in the form of beads-on-a-string (Figure 1.2.A). The S protein is made up of two subunits (S1 and S2), the S1 subunit is the globular head of the protein and the S2 forms a stalk which anchors the protein to the viral envelope. The S protein can be seen in electron micrograph images of IBV (Figure 1.2.B). Some *Betacoronaviruses* including mouse hepatitis virus (MHV), also contain a haemagglutinin esterase (HE) protein which is thought to have been acquired through heterologous recombination with the influenza C virus (26).

1.2.5. IBV Genome Organisation

The IBV RNA genome is 27.5 kb in length with a 5′ cap and a poly-A tail at the 3′ end (9). At the 5′ end of the genome, there is a leader sequence and transcription-regulatory sequence leader (TRS-L) to allow for genome transcription (Introduction Section 1.6.2.). TRS sequences are also present upstream of every open reading frame (ORF). The TRS-L sequence is followed by the replicase gene that consists of two ORFs that constitutes two thirds of the IBV genome. These two ORFs are overlapping but translated via a programmed 'slippery-sequence' resulting in a -1 amino acid (aa) ribosome frameshift site (RFS) to produce two polyproteins denoted pp1a and pp1ab (27) (Figure 1.2.C). The 3′ third of the genome encodes genes for four structural proteins and seven accessory genes. Accessory genes were named in relation to genome location and for IBV, include 3a, 3b, 4b, 4c, 5a and 5b and 7 (28-30). In some strains of IBV, accessory gene 7 is either truncated or missing (28).

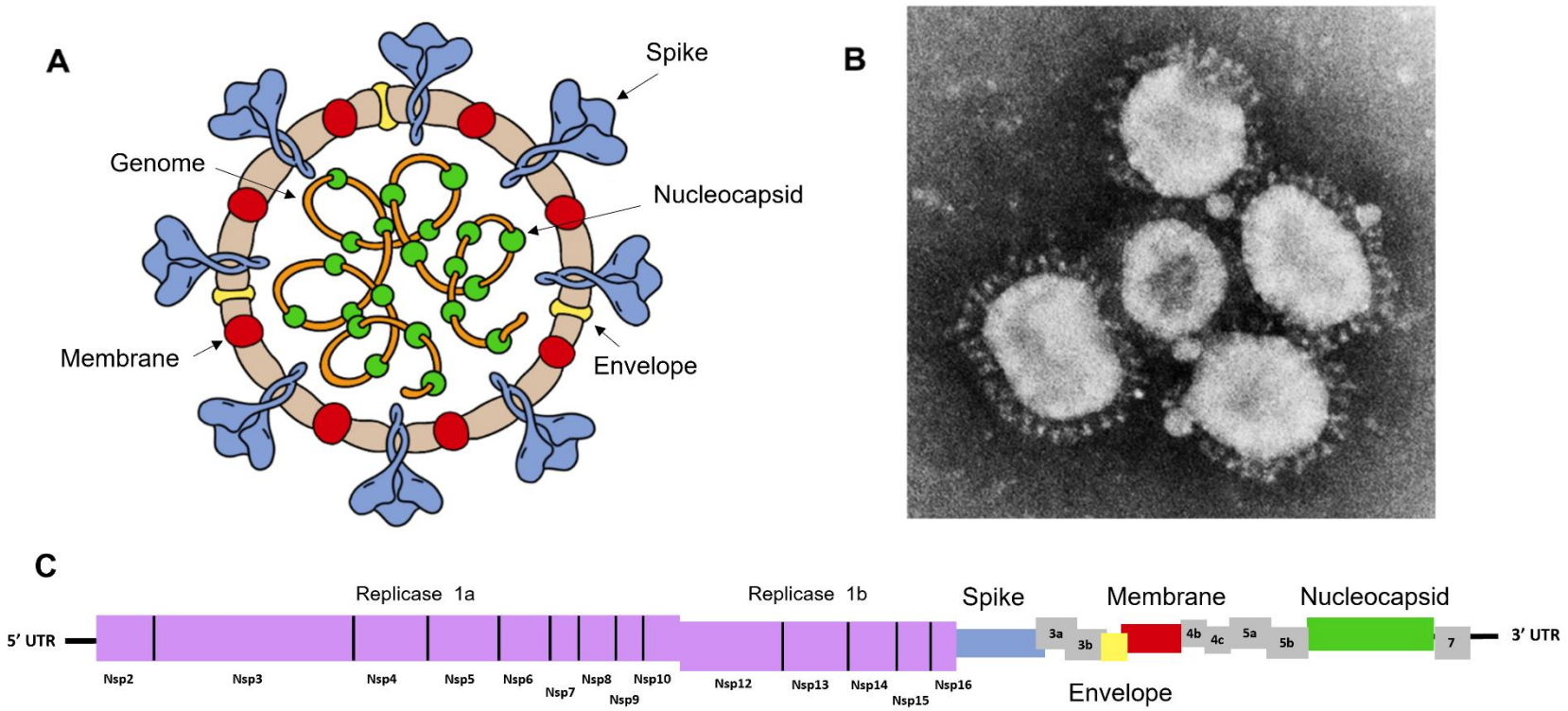

Figure 1.2. Morphological structure and genome organisation of the IBV virion. In the virion and IBV genome, the four structural proteins are represented as follows: spike (S) protein in blue, envelope (E) protein in yellow, membrane (M) protein in red and nucleocapsid (N) protein in green. (A) Schematic representing the structural proteins organisation within the IBV virion. (B) Electron micrograph image of five IBV virions taken from (31). (C) Schematic representing the genome organisation of the IBV genome. The viral replicase gene is displayed in purple, the structural genes are displayed as described above and the accessory genes are shown in grey. Genome schematic is not to scale.

1.2.6. Non-Structural Proteins (nsps)

Polyproteins pp1a and pp1ab are cleaved into fifteen nsps (nsp 2-16) by virus encoded proteinases (32, 33). Nsp 3 contains a papain-like protease domain that cleaves pp1a into its constituent nsps and Nsp 5 contains a 3C-like proteinase which mediates cleavage of pp1ab (34). The genomes of other CoVs also possess nsp 1, but this sequence is not present within the *Gammacoronavirus* genus. The nsps predominantly function in IBV genome replication or the regulation of the innate immune response, reviewed by (35). Many of the functions of the nsps remain unknown.

Nsp 3, 4 and 6 are transmembrane proteins which establish the CoV replication organelles (RO) within infected cells, this was shown as co-expression of these proteins is sufficient for the formation of double membrane vesicles (DMVs) which are the predicted sites of viral replication (36). Nsp 4 is able to induce membrane pairing which is important for the formation of DMVs (37). Autophagosomes possess double membranes and are hypothesised to be modified for the formation of DMVs, the IBV nsp 6 protein can induce the formation of autophagosomes (38).

A group of the nsps assemble into a replication-transcription complex (RTC, Figure 1.3). Nsp 12 is the most conserved CoV protein which is likely due to its role as an RNA-dependent RNA polymerase (RdRp), a nsp 7/nsp 8 complex aids the RNA-binding of nsp 12 (39). Nsp 13 acts as a helicase during IBV replication and additionally has been shown to pause the cell cycle through interaction with host cell DNA polymerases (40). Nsp 14 contains the 3′–5′ ExoN activity which enables proof-reading during RNA synthesis as well as S-adenosylmethionine (SAM)-dependent (guanine-N7) methyltransferase (N7-MTase) activity (41, 42). Further to these functions, nsp 13 and nsp 14 act with nsp 16 to cap the viral RNA genome during replication (39). Nsp 10 acts as a cofactor for nsp 14 and nsp 16 (43). Nsp 9 is an RNA-binding protein which is hypothesised to stabilise nascent RNA (44).

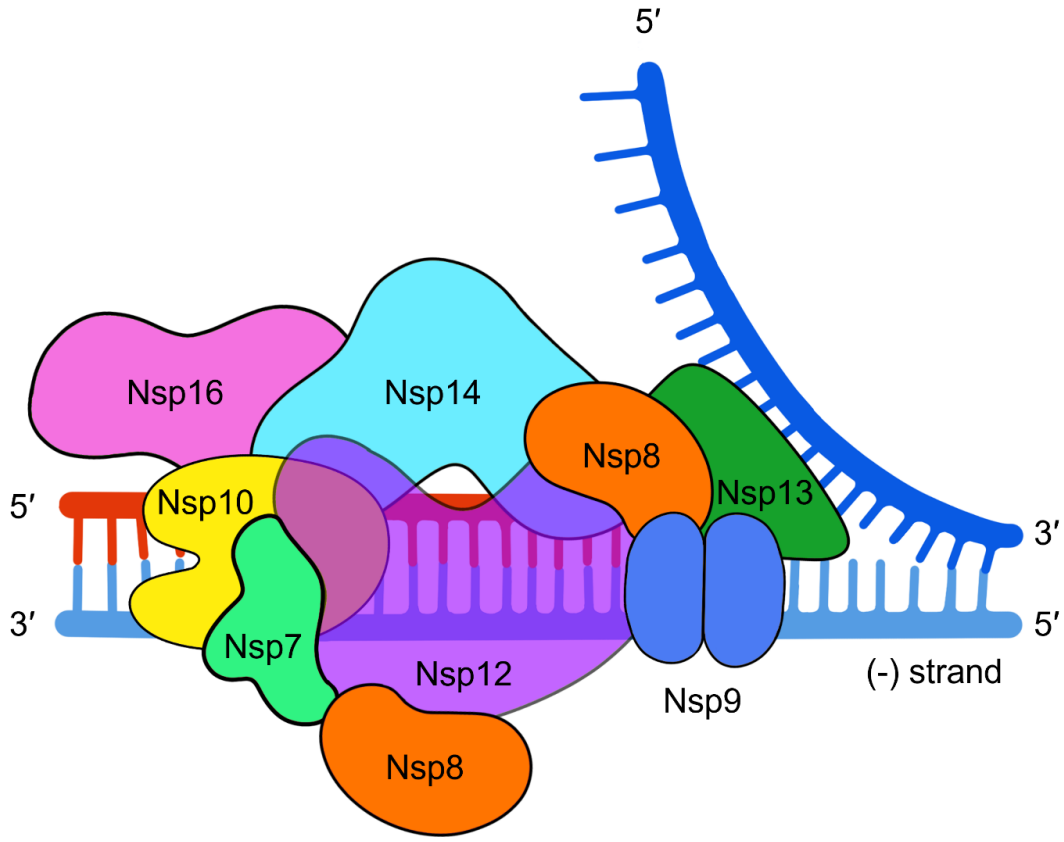

Figure 1.3. Schematic representing nsps within the replication-transcription complex (RTC). Nsp 12 is the replicase enzyme which is attached to two co-factors nsp 7 and nsp 8. Nsp 13 acts as a helicase to separate strands, nsp 9 then acts to protect the single stranded (ss) RNA Nsp 14 is an exonuclease which proofreads nascent RNA. Cap formation is facilitated by nsp 10, 13, 14 and 16. Schematic is not drawn to scale and was adapted from (45).

Nsps are involved in the regulation of the innate immune response. Nsp 2 promotes the replication of IBV by acting as an antagonist of immune factors to maintain protein synthesis activity within infected cells (46). Nsp 3 is a papain-like protease which acts to deubiquitinate innate immune factors and ultimately blocks the synthesis of type 1 interferons (IFNs) (47). Additionally, nsp 3 contains a macro domain, formally referred to as the ADP-ribose-1”-phosphate phosphatase (ADRP) domain, which is hypothesised to act as a pathogenicity factor, as shown in *Betacoronavirus* MHV (48), but not in IBV (49). Nsp 15 is an endonuclease which inhibits the formation of stress granules, which reduces the type 1 IFN response to IBV infection (50). Stress granule inhibition also promotes protein synthesis, demonstrated as nsp 15 knock-out IBV virions had reduced IBV messenger RNA (mRNA) and protein production (51). Nsp 7 and nsp 16 have been shown to inhibit cytokine production and antigen-presentation on the surface of host cells (52). The induction of autophagosomes by nsp 6 may play a role in suppressing the adaptive immune response through degradation of immune factors stimulated by IBV infection (53).

1.3. IBV Life Cycle

The entire life cycle of IBV is detailed in Figure 1.4, the CoV life cycle has recently been reviewed (45)

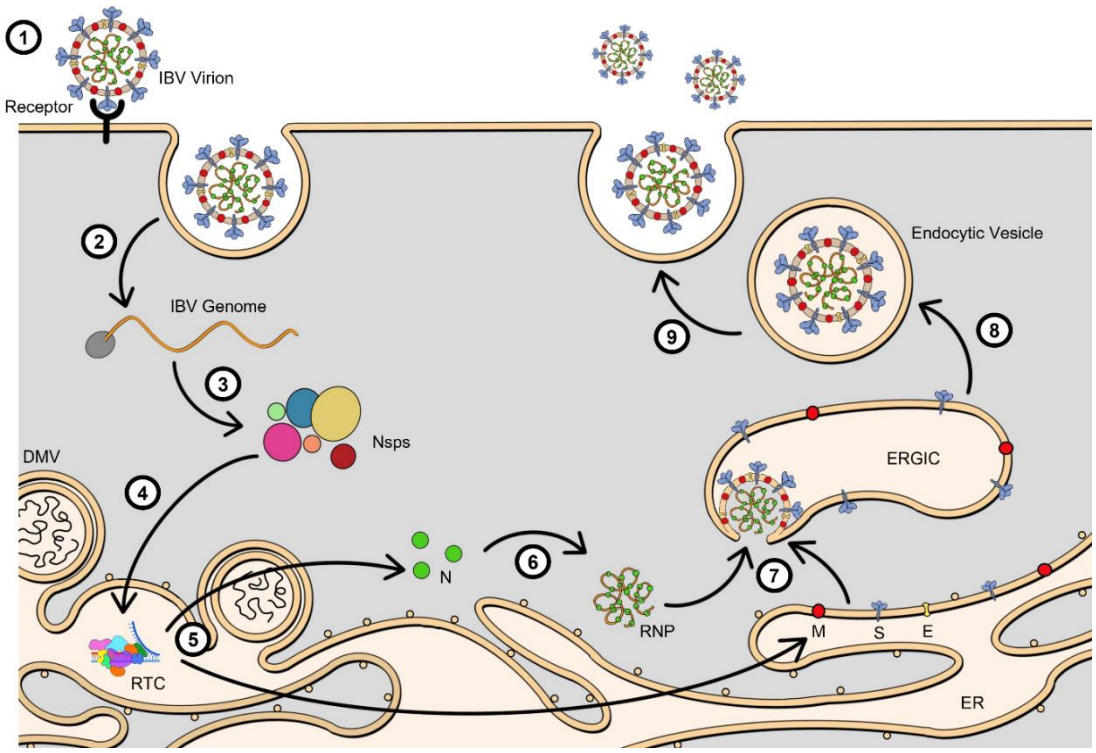

Figure 1.4. IBV Lifecycle. (1) IBV virion enters the cell via endocytosis following attachment and fusion via the spike (S) protein to an unknown receptor. (2) IBV genome is released into the cellular cytoplasm (3) this initiates translation of the non-structural proteins (nsps). (4) The nsps form the replication-transcription complex (RTC) within the endoplasmic reticulum (ER) membranes which generates the sub-genomic (sg) mRNA. Double-membrane vesicles (DMVs) are the site of nascent RNA synthesis. (5) Translation of viral structural proteins on cellular ribosomes. The structural proteins are processed within the ER and Golgi before recycling back to the ER membranes. (6) Association of the nucleocapsid (N) protein with the genome to form the ribonucleoprotein (RNP). (7) Virion assembly takes place within the ERGIC membrane where the RNP is encapsulated within ER-Golgi intermediate compartment (ERGIC) membranes studded with the S, Membrane (M) and Envelope (E) proteins. (8) Progeny viruses are transported to the plasma membrane in vesicles. (9) Viruses are released from cells via exocytosis.

1.3.1. Viral Entry

The receptor for IBV is currently unknown, several receptors have been suggested but disproven, such as Aminopeptidase N (APN, (54, 55)) which acts as a receptor for *Alphacoronaviruses* (56). Attachment factors thought to function in IBV entry include α2,3-linked sialic acid (57, 58), heparan sulphate (HS, (59)) and heat shock protein 70 (HSP70, (60)).The known entry receptors used by CoVs have recently been reviewed (61).

Upon binding to the receptor, the S protein alters its conformation to enable the fusion peptide (FP) to increase membrane permeability and facilitate virus-cell membrane fusion (62). The *Betacoronavirus* HE protein acts to improve viral infectivity by facilitating dissociation from decoy receptors (63). Viruses then enter the cells via endocytosis utilising the endo-lysosomal pathway (64) and the viral genome is released into the cytoplasm of the infected cell.

1.3.2. Genome Replication and Transcription

The released RNA genome is translated into the replicase proteins, pp1a and pp1ab within the cytoplasm. These polyproteins are cleaved to generate fifteen nsps some of which are involved in the assembly of the multimeric enzyme RTC, the roles of the nsps within the RTC are described in Introduction Section 1.2.6.

Replication of the IBV RNA genome requires membrane rearrangements to be formed within infected cells (65). These modifications include DMVs and spherules which are connected to zippered ER (Figure 1.5). DMVs have been identified as the site of RNA synthesis (66) which takes place inside of the membrane (67). This is hypothesised to protect the double-stranded RNA (dsRNA) from detection by the host cell. Autophagosomes possess double membranes and have been hypothesised to be modified for the formation of DMVs (38), although the link between autophagosomes and virus replication has been disproven as dsRNA does not

colocalise with a key autophagosome protein Microtubule-associated protein 1A/1B-light chain 3 (LC3) (53).

The role of the spherules within IBV infection is still debated but they could potentially be instrumental in RNA replication (65). Genome replication is carried out by the RTC following continuous synthesis to generate a negative strand copy of the genomic RNA which can then be used a as template for the synthesis of new IBV genomes.

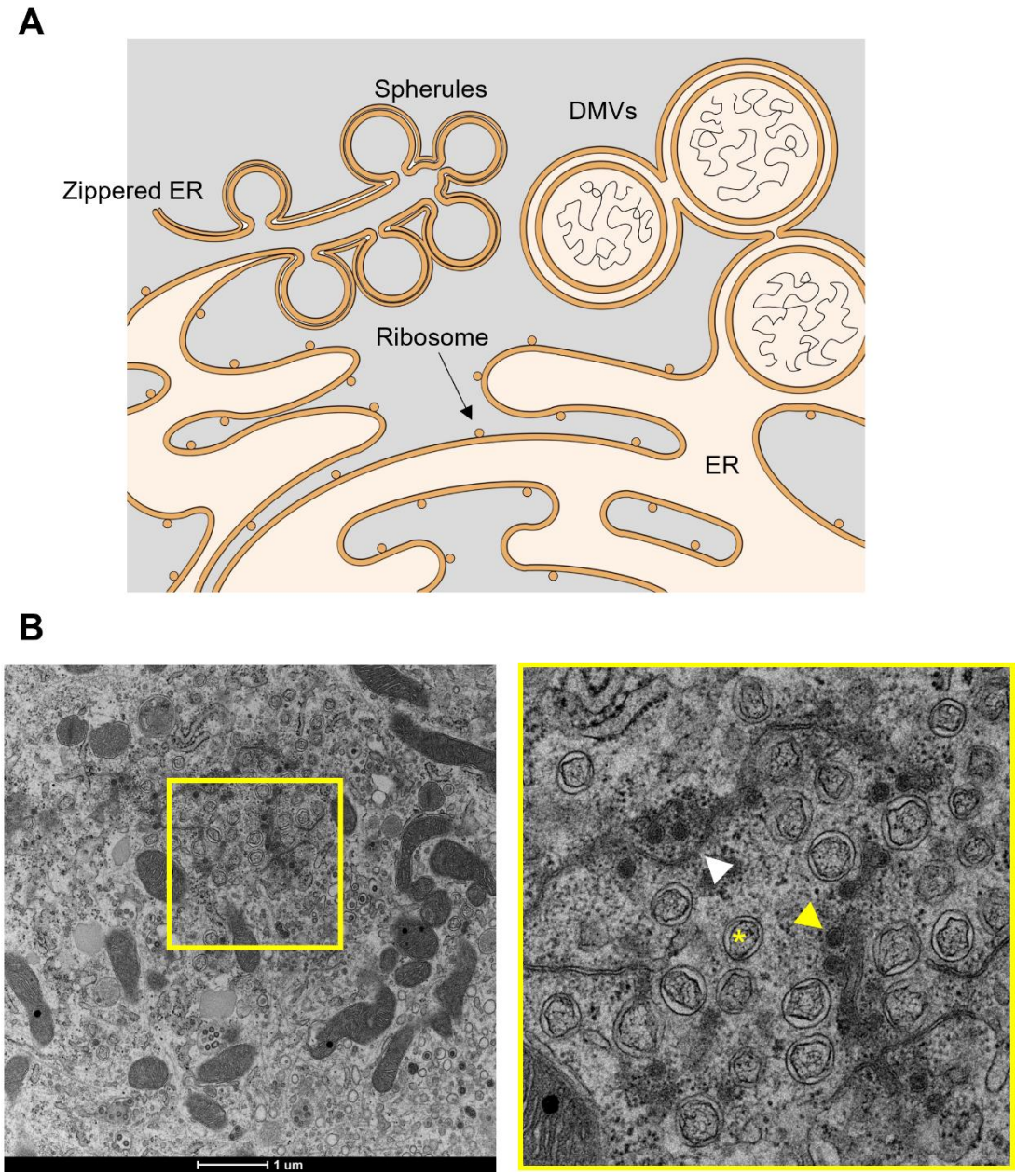

Figure 1.5. Membrane rearrangements formed by IBV for RNA replication. A) Schematic representing structure and components of membrane rearrangements spherules, zippered ER and DMVs. (B) Negative-stain transmission electron microscopy (EM) image of IBV-induced membrane rearrangements within CK cells. A representative double membrane vesicle (*), spherule (yellow arrow) and zippered ER (white arrow) is indicated. EM image was generated from BeauR-A26F infected CK cells during this study.

The accepted model for *Nidovirales* transcription of structural and accessory genes is via discontinuous transcription during negative-strand synthesis (68), this process is outlined in Figure 1.6. TRS sequences are complementary to each other with one located at the 5' end of the genome adjacent to the leader (TRS-L) and the others located upstream of each gene (TRS-B). During negative strand synthesis each TRS-B sequence can stall the RTC, the 5' leader sequence is added through discontinuous synthesis via complementary base pairing interactions (69). This generates a nested set of negative-sense sg RNA, which is then copied into positive-sense sgRNA.

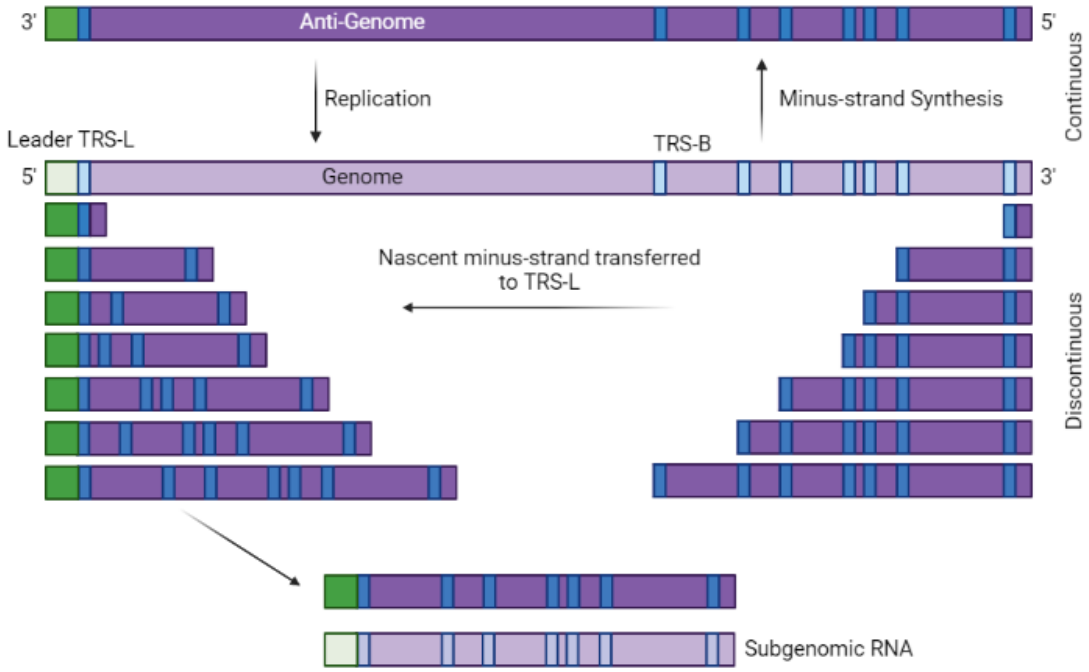

Figure 1.6. Discontinuous Replication for CoV Genome Transcription. A minus-strand copy of the genome is generated to act as a template for RNA synthesis. The replication-transcription complex (RTC) starts at the 3′ end of the positive-strand and synthesis of sg RNA transcripts continues until it is stalled by the presence of a transcriptional regulatory sequence (TRS, shown in blue). At each TRS the RTC either passes through to the next TRS or transfers to the leader TRS located at the 5′ end of the genome, at this point RNA synthesis continues until the end of the leader sequence (shown in green). The minus-sense sg transcripts are transcribed back to positive sense for the translation of viral proteins. This figure was generated using BioRender.

1.3.3. Viral Assembly

The sgRNA generated is translated on ribosomes associated with the ER into the structural and accessory proteins. Following their synthesis, they are packaged in ER exit sites (ERES) transport vesicles for modification and cleavage in the Golgi Apparatus. Any S protein which is not assembled into virions is translocated to the cell surface to facilitate cell-cell fusion to allow for the fusion of infected and uninfected cells, ultimately producing multinucleated cells, termed syncytium (70). The S2 subunit is responsible for the cell-cell fusion via a different mechanism than is used for virus-cell fusion (71).

The structural proteins are folded and post-translationally modified within the ER before transport to the Golgi for further processing. The N protein packages the RNA genome into a helical RNP, the mechanism and location of RNP formation along with targeting of this complex to the budding site is unknown.

The structural proteins then recycle from the Golgi back to the ERES to allow for viral assembly. A Golgi targeting signal has been identified within the cytoplasmic tail of IBV E (72) and the transmembrane domain (TMD) of the M protein (73), and the cytoplasmic tail of the S protein contains an ER retrieval signal (74). These signals ensure the protein's localisation and retention in the ER-Golgi intermediate compartment (ERGIC)/ *cis*-Golgi network for viral budding.

The M protein is hypothesised to act as a scaffold during CoV assembly as it mediates interactions with each of the other structural proteins (75-77) this allows for accumulation of the virion proteins and genomic RNA to a concentrated region, with S, M and E proteins embedded into the ERGIC membranes. Unlike most enveloped viruses, CoVs bud into the lumen of the ERGIC (78), with the RNP encapsulated within the envelope containing the S, M and E structural proteins to form the mature virion.

1.3.4. Viral Egress

The mechanism for CoV egress is poorly understood but several different egress pathways have been suggested, as reviewed (79). A schematic representing these proposed pathways is shown in Figure 1.7. The two proposed routes for CoV egress consist of the classical constitutive pathway through the Golgi Apparatus or the endo-lysosomal recycling circuit.

The dynamics of the Golgi Apparatus is not well defined with several proposed models based on contradicting observations. There are two main proposed mechanisms of cargo transport through the Golgi Apparatus: a dynamic cisternae maturation model and a vesicular transport between stable compartments model, detailed within (80). The first of these routes describes a dynamic model of the Golgi apparatus in which the ERGIC elements mature into *cis*-Golgi and ultimately *trans*-Golgi elements (Figure 1.7). The opposing view is that the Golgi is static with progeny virus in vesicles budding and fusing to the ends of the Golgi Apparatus (Figure 1.7).

In the context of viral egress, both models would require maintenance of Golgi cisternae structure for viral release. Monensin is an ionophore which induces the swelling of the Golgi Apparatus and can therefore be utilised as a Golgi Apparatus inhibitor (81). Evidence supporting the use of the constitutive pathway for viral egress shows that release of the *Alphacoronavirus* transmissible gastroenteritis virus (TGEV) is inhibited by Monensin as a result of viral particle accumulation within the ERGIC (82), although this accumulation was not seen when similar experiments were carried out with IBV (83).

Viruses are much larger cargo than cellular components which would typically pass through the Golgi Apparatus. During IBV infection, neutralisation of the Golgi Apparatus is facilitated by the E protein ion channel (IC) (84), this causes it to dilate which increases the capacity of the secretory elements and house large numbers of

progeny virus, transforming the stacked Golgi Apparatus cisternae into large vacuoles containing viral particles.

Recently, a second mechanism for CoV egress in which the virus progeny bypasses the Golgi Apparatus and is secreted via endosomes directly from the ERGIC (Figure 1.7.3). Evidence for this exit route has been proposed and demonstrated in *Betacoronavirus* MHV due to colocalization of endosomal/lysosomal protein lysosomal-associated membrane protein 1 (LAMP1) with MHV M protein (85). To further validate this hypothesis, recent research carried out within IBV has been shown that the endocytic recycling circuit is utilised within egress, as the M protein was shown to colocalise with the endocytic recycling compartment protein Ras-related protein Rab-11 (Rab11) (86).

Overall, it is unclear which pathway CoV virions follow to allow for efficient release. Potentially it could be a mix of both models as it has been proposed that post-Golgi transport to the plasma membrane (PM) may pass through endosomal compartments (87).

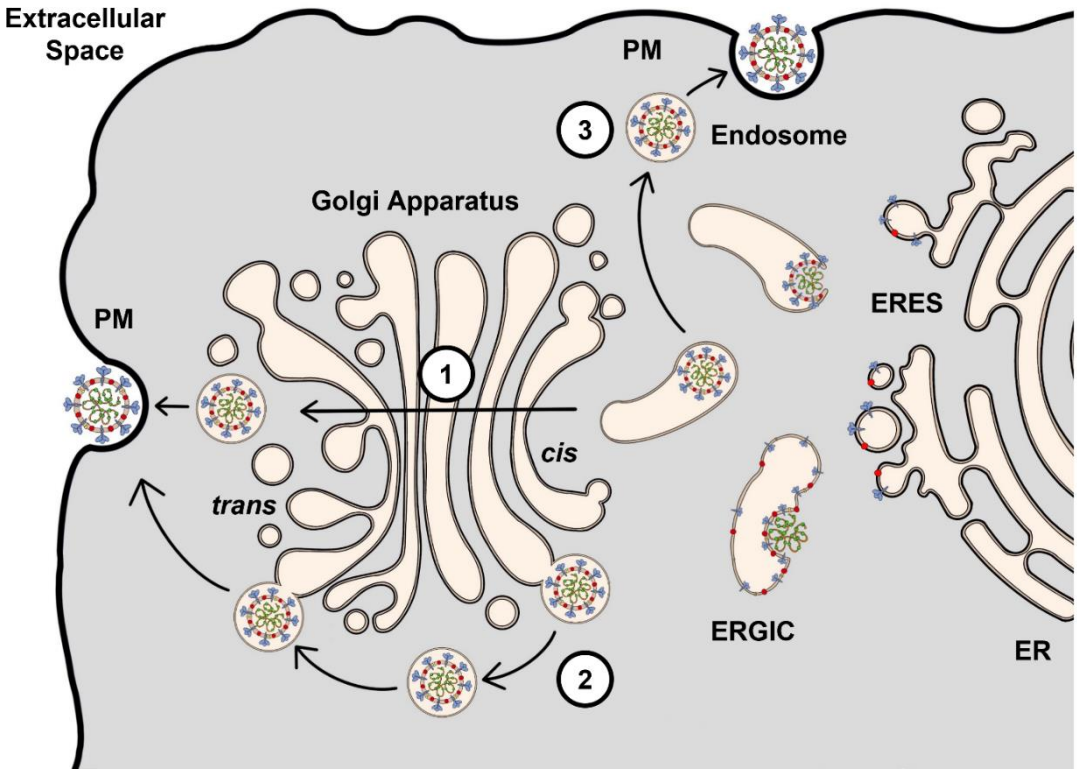

Figure 1.7. Coronavirus (CoV) Assembly and Egress. Translation of structural proteins from sg mRNA takes place at in the endoplasmic reticulum (ER) and then leaves via the ER exit sites (ERES). Viruses obtain their envelope through encapsulation of the nucleocapsid in the ER-Golgi intermediate compartment (ERGIC) membranes studded with S, E and M proteins. Three potential egress routes have been proposed for CoVs. (1) The ERGIC elements containing virus particles mature into cis-Golgi cisternae. The carriers mature through the Golgi in a cis-trans movement. (2) CoVs enter vesicles which bud from and fuse to the ends of the Golgi structure, which is static. Via both these routes, at the trans-Golgi the virus particles are transported to the plasma membrane (PM) and released from the cell. (3) Progeny viruses are transported from the ERGIC carriers directly to endosomes. This route utilises the endocytic recycling circuit to transport virus to the PM. This figure has been adapted from (79).

1.4. Structural Proteins

1.4.1. Spike (S) Protein

The S protein is a ~180 kDa, class 1 virus fusion glycoprotein (88) which oligomerises within the endoplasmic reticulum (ER) of infected cells to form a homotrimer (Figure 1.8.A). The S protein is embedded into the virion envelope and allows for viral attachment to cellular receptors and fusion to cellular membranes (89). The N-linked glycosylation pattern of the S protein is necessary for the binding to host cells (90), this glycosylation pattern differs between strains of IBV (91). The S protein is translated as a single polypeptide which is then cleaved by furin-like proteases within the Golgi apparatus, to form two subunits, S1 and S2 (71), the cleavage site position is displayed in Figure 1.8.B. The S1 forms the globular head of the spike protein and the S2 forms a stalk to form a club-like S protein structure (Figure 1.8.A). An additional cleavage site denoted S2′ exists in the Beaudette strain of IBV and in SARS-CoV-2 which aids viral fusion to cells (92, 93).

The S1 protomer contains two predicted receptor binding domains (denoted as S1 N-terminal domain (S1-NTD) and S1 C-terminal domain (S1-CTD) in Figure 1.8.B). The S1-NTD domain facilitates binding to cellular receptors (94). The binding event results in conformational changes within the protein to allow for the S2 subunit to facilitate fusion to cellular membranes and release of the IBV genome into the cytoplasm of an infected cell (95). The S protein structure displayed in Figure 1.8.A is pre-fusion. The second receptor domain, S1-CTD, is hypothesised to enable chicken-cell tropism as it has a distinct structure from other CoVs (96). The S2 protomer mediates virus-to-cell fusion (88) and consequently, is a determinant of cell tropism (97). Two heptad repeats (HR, denoted HR-N and HR-C, Figure 1.8.B) facilitate the homo-oligomerisation of the S protein (98). The FP (Figure 1.8.B) present within the S2 protomer, has been shown to increase membrane permeability

to facilitate viral entry (62) and cell-cell fusion for the formation of syncytia (97). This cell-cell fusion requires palmitoylation of the S protein (70).

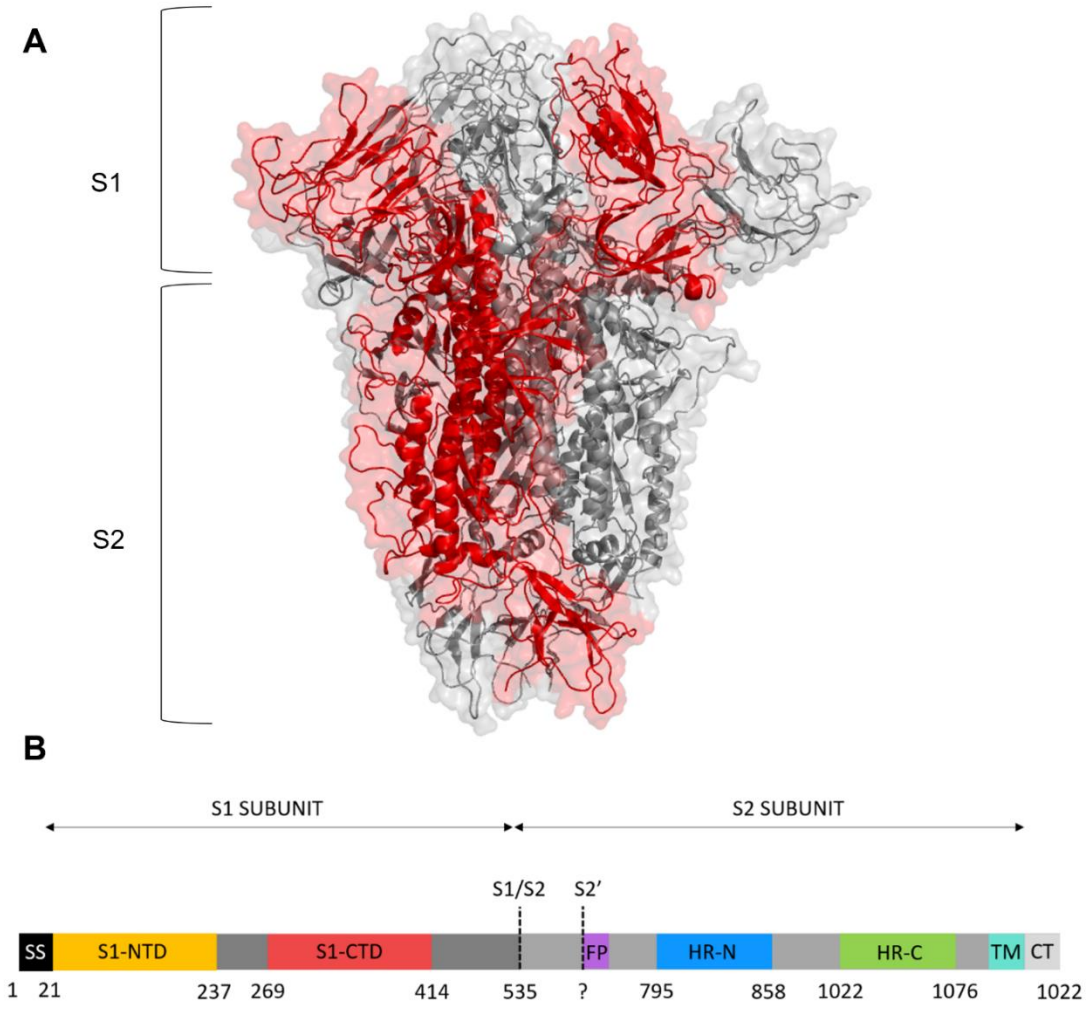

Figure 1.8. Structure of the Spike (S) protein which consists of two subunits (S1 and S2) and forms a homotrimer. (A) Structure of the trimeric IBV M41 Spike Protein. The structure previously solved through cryo-EM (96) was used as a template - RCSB PDB: 6CV0. This structure was rendered using Pymol, with a single spike protomer highlighted in red. (B) Schematic representing the S gene domains, amino acid (aa) locations are taken from (96) except for the location of the S2′ cleavage site, in which the Beaudette sequence location is shown (97). The S gene is flanked by a signal sequence (SS) and a cytoplasmic tail (CT). The S1 subunit contains two domains: NTD = N-terminal domain, CTD = C-terminal domain. The cleavage sites are represented with a dashed line. The S2 subunit contains three domains: FP = fusion peptide, HR = heptad repeat, TM = transmembrane.

1.4.2. Nucleocapsid (N) Protein

The N protein (~45 kDa) and viral RNA genome form a helical filamentous RNP within the virion of IBV (99). N protein monomers self-associate into a dimeric form which interacts with viral RNA (100). Through interaction with viral RNA, the N protein functions as an RNA chaperone to aid RNA folding (101) and enhance transcription efficiency (102).

The N protein is made up of three domains: N-terminal, C-terminal, and a disordered central region (Figure 1.9). The N-terminal domain is involved in RNA interaction and the C-terminal domain acts as a scaffold to aid homo-dimerization and interacts with M protein in the viral envelope (103). The disordered central region of the *Betacoronavirus* MHV N protein has been shown to interact with nsp 3 (104).

Other than RNP formation, the N protein also functions in virion assembly. Interaction between the N and M proteins facilitates genome encapsulation during CoV budding (76). Virus-like-particle (VLP) formation is enhanced in the presence of the N protein (105) so it is thought to promote viral assembly. This improved viral assembly in the presence of the N protein has been implemented in CoV reverse genetics systems, in which transfected N protein is required for the successful recovery of rIBVs (24).

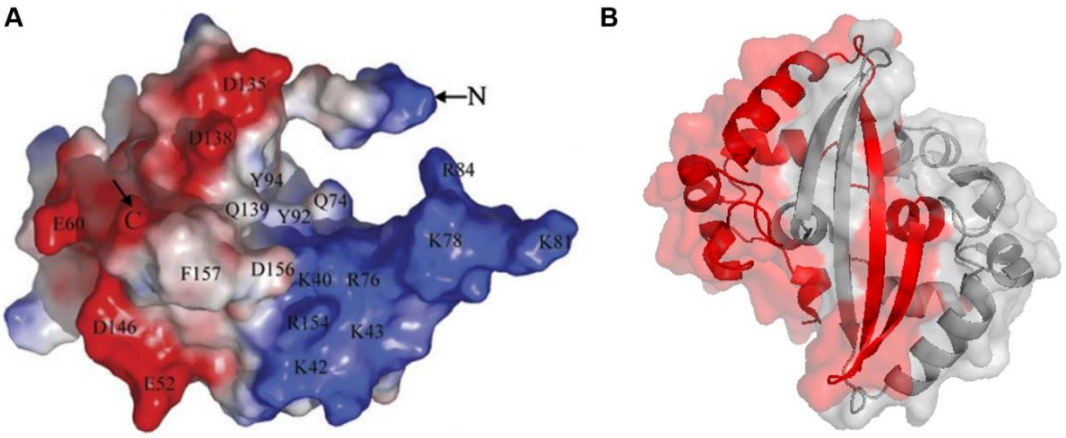

Figure 1.9. Structure of the IBV N protein NTD and CTD. (A) The N-terminal domain (NTD) structure (Figure taken from (100), RSCB-PBD: 2BTL) showing electrostatic charges of the domain: blue (positive) and red (negative). The highlighted residues are hypothesised to facilitate RNA binding. The N- and C-terminal ends of the protein are labelled. (B) Structure of the homodimerised CTDs of the IBV N protein with the two independent domains labelled in different colours. Structure was rendered on PyMOL from a previously solved X-ray crystal structure (RSCB-PBD: 2CA1, (103)).

1.4.3. Membrane (M) Protein

The IBV M protein has three TMDs (106) and is the most abundant protein within the IBV particle. During infection, the M protein functions in virion budding (78) and assembly (75). β-actin filaments are disrupted by the M protein to facilitate this (107). Additionally, M protein self-association is a driver of envelope formation (75).

The CoV M protein ranges in size from 25-30 kDa in its pre-glycosylated form and several glycosylation profiles are observed when the M protein is resolved using a sodium dodecyl sulphate-polyacrylamide gel electrophoresis (SDS-PAGE) gel (108). The IBV M protein glycosylation is exclusively N-linked, inhibition of M protein glycosylation does not inhibit viral assembly but does abolish infectivity of viral particles (109). This difference in infectivity is thought to be caused by a reduced activation of ER stress response, apoptosis and pro-inflammatory cytokines (110).

The M protein is described as the scaffold for virion assembly as it interacts with each of the other structural proteins to allow for virion assembly within the ERGIC membranes (75). The E and M proteins interact via their cytoplasmic tails and have been shown to be necessary and sufficient for VLP formation (75). The E and M proteins can compensate for each other as demonstrated upon passage of *Betacoronavirus* severe acute respiratory syndrome coronavirus (SARS-CoV) with deleted E protein which resulted in a partly duplicated chimeric M protein that could recover virulence (111). Additionally, SARS-CoV M chimera with a growth defect was complemented by the E protein to partially recover growth (112).

1.5. Envelope (E) Protein

The E protein is a small 12 kDa protein which is present in two forms during infection: monomeric and pentameric (113), it has recently been reviewed (114). The E protein is comprised of three domains: NTD, TMD and CTD (Figure 1.10).

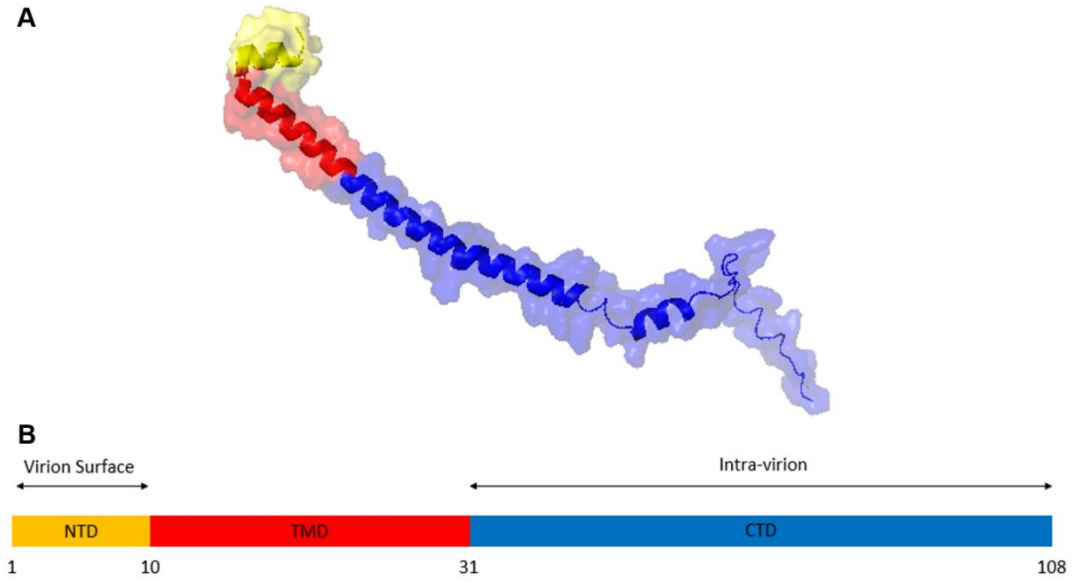

Figure 1.10. Structural domains of the IBV E protein. The domains are coloured as follows: N-terminal domain (NTD) in yellow, transmembrane domain (TMD) in red and the C-terminal domain (CTD) in blue. (A) Predicted E protein structure of the Beau-R E protein, AlphaFold2 prediction software was used to generate the structure which was then rendered within PyMOL. (B) Schematic representing the domains of the E protein, amino acid locations are based on the Beaudette strain of IBV and were sourced from UniProt (https://www.uniprot.org/).

Within IBV, gene 3 sgRNA is tricistronic meaning that it encodes accessory proteins 3a, 3b and structural protein E (also known as 3c). The E protein is translated from this sg mRNA using a ribosomal initiation site (115). The IBV E protein is palmitoylated on one or both cysteine residues within the CTD, the function of which is unknown (72). Within the *Betacoronavirus* MHV, palmitoylation of the E protein has been shown to be important for viral assembly (116) and the stability of the *Betacoronavirus* MHV E protein (117). Other post-translational modifications of the CoV E protein have been identified within SARS-CoV, these include glycosylation (118) and ubiquitination (119).

The IBV E protein spans membranes once with the N-terminus exposed into the Golgi apparatus lumen (or virion surface) and the C-terminus within the cytoplasm (or intra-virion) (118). Conversely, other CoV E proteins are thought to span the membrane twice such as the betacoronaviruses SARS-CoV (118) and MHV (120).

1.5.1. C-terminal domain

The cytoplasmic tail of the E protein has been shown to facilitate viral assembly as it is required for targeting to the Golgi (72) and interaction with the M protein (75). CoVs have a conserved proline reside at aa54 which is within Golgi targeting region aa44-95 (Chapter 8, Section 8.3, Figure 8.7). Within *Betacoronavirus* SARS-CoV, disruption of this proline residue scrambles the Golgi targeting signal (121).

1.5.2. Ion Channel (IC)

Viroporins are viral proteins with at least one TMD which homo-oligomerise to induce membrane permeability by forming an IC within cellular or viral membranes. Viroporins are classified (I, II, III, …) based on the number of TMDs. Induction of membrane permeability was first discovered within encephalomyocarditis (EMC) virus infected cells (122). The first viral protein to be reported with IC activity was the influenza virus A (IAV) Matrix 2 (M2) protein (123). The CoV E protein IC activity was

first identified in the *Betacoronavirus* SARS-CoV (124), this was later shown in IBV (125). A summary of several known viroporins is listed in Table 1.2.

Table 1.2. List of Known Viroporins

Virus Family	Virus	Protein	TMD
Picornaviridae	Poliovirus	3A	1
		2B	2
	Coxsackievirus B3	2B	2
	Enterovirus 71	2B	2
Togaviridae	Semliki forest virus	6K	2
	Sindbis virus	6K	1
	Ross River virus	6K	1
Retroviridae	Human Immunodeficiency Virus Type 1	Vpu	1
Paramyxoviridae	Human Respiratory Syncytial Virus	SH	1
Orthomyxoviridae	Influenza A virus	M2	1
	Influenza B virus	NB	1
		BM2	1
	Influenza C virus	CM2	1
Reoviridae	Avian Reovirus	p10	1
Flaviviridae	Hepatitis C virus	p7	2
Phycodnaviridae	Paramecium bursaria chlorella virus	Kcv	2
	Acanthocystis turfacea chlorella virus	Kcv	2
Rhabdoviridae	Bovine ephemeral fever virus	α-1	1
Coronaviridae	All CoVs	E	*
	Severe Acute Respiratory Syndrome	3a	3
	Severe Acute Respiratory Syndrome	8a	1

Notes: Transmembrane domains (TMDs) are either predicted or known, * signifies that there are either 1 or 2 TMDs in the coronavirus (CoV) E protein. Viroporins are classified (I, II, III) based on the number of TMDs, e.g., 1 TMD is a class I viroporin. Table adapted from (126).

Viroporins have a range of functions in promoting viral infection such as entry, immune evasion, assembly, and egress. The IAV M2 forms a proton channel which has been extensively studied and shown to have roles in virion uncoating post-entry (127) and slowing protein transport through the Golgi to ensure correct viral protein processing (128). Autophagy allows for protein degradation within proteolytic lysosomes. M2 stimulates the formation of autophagosomes but prevents their fusion to lysosomes, this is thought to cause viral antigen retention within autophagosomes to aid immune evasion as it hides viral antigens to prevent their presentation on the cell surface (129). The human immunodeficiency virus 1 (HIV-1) viral protein U (Vpu) protein forms an ion channel which has been shown to promote viral budding and release from cells (130).

Three known viroporins are found within CoV genomes: E, 8a and 3a protein, these proteins have been recently reviewed (131). The 8a ion channel is only present within the genome of *Betacoronavirus* SARS-CoV, whereas 3a is also present within *Betacoronavirus* SARS-CoV-2. The 3a present in SARS-CoV is not the same as the 3a in IBV. The SARS-CoV viroporin 3a is a class III viroporin which transports K^+ ions and acts to promote apoptosis within infected cells (132). Interestingly, the *Alphacoronavirus* Human CoV 229E (HCoV-229E) 4a protein shares sequence homology with the SARS-CoV 3a protein and could potentially act as a K^+ transporter or promote activity of cellular K^+ channels (131). The 8a protein is a class I viroporin which is cation selective (133). Ion channel activity of neither 3a nor 8a are required for the replication or virulence of SARS-CoV, unlike the E protein (134).

The CoV E protein was first identified as an IC in *Betacoronavirus* SARS-CoV (135). The IC activity of the E protein has been demonstrated for each genus of CoV indicating that this activity is conserved within CoVs (125). The IC activity for the IBV E protein has been characterised showing that this channel has a preference for Na^+ ions (125). Within *Betacoronavirus* MHV, an Na^+/H^+ exchanger inhibitor

hexamethylene amiloride (HMA) has been shown to inhibit the ion channel which resulted in inhibition of viral replication (125). This therefore indicates that the CoV E ion channel has a critical role in ensuring productive viral replication.

The monomeric or pentameric structures of the IBV E protein are yet to be solved but several structures exist for the *Betacoronavirus* E protein (136-138), see Figure 1.11.A. These structures may not be representative of the IBV E structure as the primary sequence of IBV E has closer sequence identity to the Uukuniemi virus envelope glycoprotein G1 than other CoV E proteins (72). The pentameric IBV E protein has been evidenced by work using purified E protein which found it can form an oligomer consistent with a homo-pentamer (139). Although, the secondary structure of the CoV E protein is well conserved which suggests it is more important for function than the sequence (140). HMA is unable to block the IBV E protein IC but is able to block the IC of other CoVs, therefore indicating that the structure and topology of the *Gammacoronavirus* E proteins are distinct from the other CoVs (125).

Two individual mutations within the hydrophobic domain of the E protein were shown to inactivate the ion channel activity of *Betacoronavirus* SARS-CoV, these mutations are N15A and V25F (141). The corresponding residues of the IBV E protein (T16 and A26) have been shown to be essential for E protein IC activity (20, 142). The location of these residues are highlighted on the E protein in Figure 1.11.B.

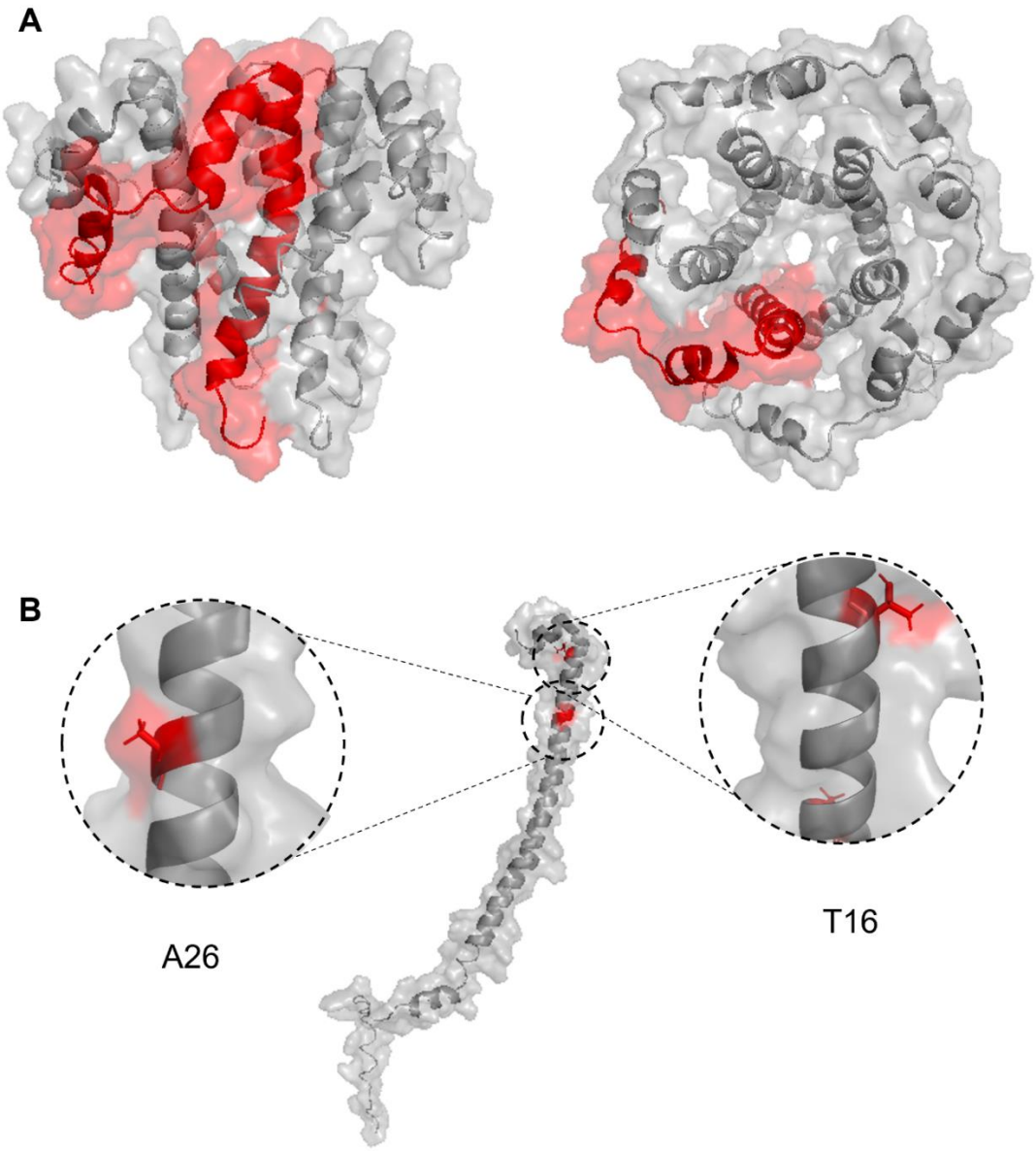

Figure 1.11. Structure of the CoV envelope (E) protein. (A) Structure of the pentameric SARS-CoV E protein. Structure was rendered on PyMOL using RSCB-PBD:5X29. This structure was solved through use of solution nuclear magnetic resonance (NMR) (143). A single monomer of the E protein is highlighted in red. (B) Predicted Beau-R E protein generated using AlphaFold2 and rendered in PyMOL, the T16 and A26 residues are highlighted in red and enhanced.

Mutations at the T16 or A26 residue of the IBV E protein have been shown to impact the fitness and release of infectious virus (20). Sucrose gradients carried out for the E protein have demonstrated two forms of E present: low-molecular weight (LMW, monomeric) or high-molecular weight (HMW, pentameric). Presence of the T16A or A26F mutation selects for either the HMW or LMW pool respectively (113), indicating that the T16 residue is important for the formation of the LMW pool and the A26 residue is required for the homo-oligomerisation. Contradicting evidence has indicated however that these residues have opposite roles (20).

1.5.3. E Protein Role in Viral Assembly and Release

CoVs bud from the ERGIC to obtain the viral envelope (144). The E protein is mainly found embedded into the Golgi membranes of infected cells with only a small number of proteins present in the virion envelope (145). The E protein present in the virion has no known functional so is likely left over from the assembly process. The hydrophobic domain of the E protein has been shown to be essential for the release of viral particles as mutation of this domain results in intracellular accumulation of virus (105). The IBV E protein has a major role in viral assembly, demonstrated as the E and M proteins are sufficient for VLP formation (75). This function has been attributed to the cytoplasmic tail of the E protein (72). The E protein is responsible for membrane curvature (146) and scission (147) during the viral budding. Another proposed role of the E protein is the prevention of M protein aggregation (116)

The CoV E protein neutralises the Golgi during infection causing it to diffuse (84). This Golgi diffusion slows traffic through the complex to allow for correct processing of the structural proteins and potentially to allow for the accumulation of large numbers of viral particles within the Golgi membranes (79). This slowed traffic of cargo alters glycoprotein processing of viral proteins (105). The T16 residue is required for Golgi neutralisation and subsequent diffusion, as shown by the absence of neutralisation and diffusion when the T16A mutation is present (84, 113, 142). The

E protein slows cargo trafficking through the Golgi, presence of the T16A mutation eliminates this effect (142). The IBV S protein is cleaved and glycosylated within the Golgi Apparatus, presence of the T16A mutation within the E protein of IBV results in premature cleavage of the S protein to generate a small c-terminal fragment of the S protein termed the 'stub' (84). Therefore, the E protein mediated disruption of cargo trafficking is thought to ensure correct processing of the S protein.

Presence of the A26F mutation in the IBV E protein results in a lack of VLP production, whereas presence of the T16A mutation results in an increased amount of VLP production generating faulty virions due to the incorrect processing during virion assembly (113, 142).

1.5.4. E protein and Pathogenicity

The CoV E protein has been shown to act as a key virulence factor in SARS-CoV (134, 138, 145, 148, 149). The E protein is critical for SARS-CoV pathogenesis (149, 150) and recombinant viruses lacking the E gene are able to protect mice against challenge (148, 151). Furthermore, the CoV E IC acts as a key virulence factor *in vivo,* shown as recombinant SARS-CoV with an inactivating mutation in the N15 residue caused clinical disease comparable to uninfected mice (138). Additionally, IC inactivated SARS-CoV virions inoculated into mice show decreased levels of Interleukin (IL)-1β and IL-6 indicating that the IC activity may be essential for innate immune activation (138). In IBV, presence of the T16A and A26F mutations reduces the expression of pro-inflammatory cytokines IL-6 and IL-8 *in ovo* (152).

1.6. Accessory Proteins

In addition to the structural proteins, a group of nsps are transcribed by the IBV genome which are designated as accessory proteins. There are seven accessory genes which include 3a, 3b, 4b, 4c, 5a, 5b and 7. Deletion of accessory genes 3a, 3b, 5a and 5b has attenuated the pathogenicity of IBV *in vivo* (153). This attenuation

is a promising vaccine target because IBV lacking either 3a and 3b or 5a and 5b was protective against challenge *in vivo* (154). In addition, a *Betacoronavirus* Middle East respiratory syndrome (MERS-CoV) replicon, with all five accessory genes and the E gene deleted was able to protect against challenge in mice (155). None of the IBV accessory proteins are required for viral replication (28, 29, 156, 157).

1.7. Immune Response to IBV

The immune response to IBV is multi-faceted from innate to adaptive immunity. Adaptive immunity includes cell-mediated, humoral, and maternal immunity. The innate and humoral immune responses are discussed in the sections below.

1.7.1. Innate Immune Response

The innate immune response is known as the first line of defence to viral infections and acts through the production of cytokines and antigen presentation to activate the adaptive immune response (Figure 1.12). The innate immune response activated by IBV infection has been recently reviewed (158).

The innate immune response is initiated by recognition of viral pathogen-associated molecular patterns (PAMPs) by cellular pattern recognition receptors (PRRs). PAMPs represent a wide range of pathogen-associated factors but within CoV infection dsRNA is the predominant marker. CoV virions are internalised by endocytosis via the endosomal compartment (159). PRRs involved in detecting CoV infection include endosomal toll-like receptors (TLRs) which are embedded into endosomal membranes and cytosolic melanoma differentiation associated gene 5 (MDA5) along with adaptor protein mitochondrial antiviral-signalling protein (MAVS) (160). During infection, IBV acts to downregulate both of these factors (161, 162).

The downstream effects of PRRs are signalling pathways which activate transcription regulatory factors such as nuclear factor kappa B (NFκB) and IFN regulatory factors

(IRFs) to induce the production of pro-inflammatory cytokines (163). Pro-inflammatory cytokines produced upon infection with CoV include type 1 IFNs and ILs (164-168). Phagocytosis mechanisms detect foreign particles and form phagolysosomes (which form due to fusion between phagosomes and lysosomes) within the infected cell and present viral antigens on the cell surface (169). SARS-CoV-2 E protein instigates accumulation of autophagosomes to prevent fusion to lysosomes and antigen presentation (170). Ultimately, this activates CD8+ T killer cells which induce apoptosis of the infected cell.

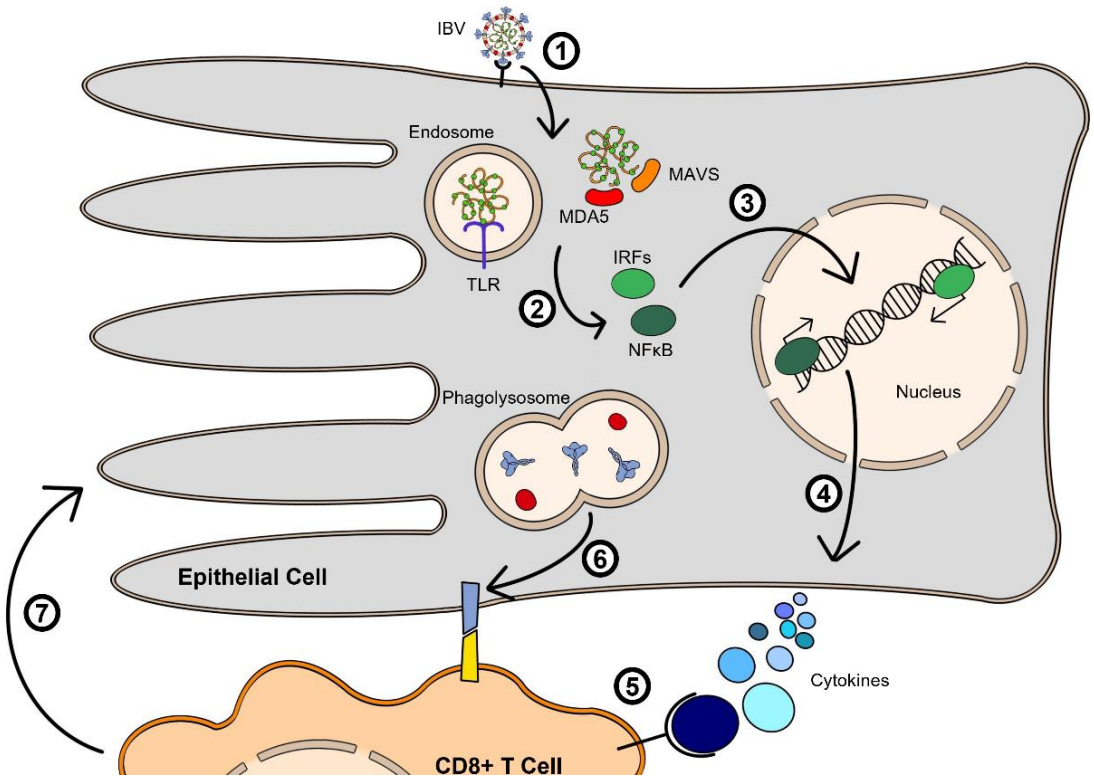

Figure 1.12. Innate Immune Response triggered by IBV infection. (1) IBV enters epithelial cell via endocytosis. (2) IBV pathogen-associated molecular patterns (PAMPs) are recognised by cellular pattern recognition receptors (PRRs). These PRRs include endosomal Toll-like receptors (TLRs), Melanoma differentiation-associated protein 5 (MDA5) and Mitochondrial antiviral-signalling (MAVS). (3) This triggers interferon (IFN) regulatory factor (IRFs) and nuclear factor kappa B (NFκB) (4) to induce expression of inflammatory cytokines. (5) Cytokines are released from the cell are recognised by receptors on CD8+ T cells. (6) Viral antigens are presented on the cell surface via phagolysosomes as part of the phagocytosis mechanism. (7) Apoptosis is induced in the infected epithelial cell by CD8+ T killer cells.

1.7.2. Humoral Immune Response

The humoral immune response is defined by antibody-mediated immunity, with antibodies produced by memory B cells post vaccination or due to prior infection. Antibodies are serotype specific and are a means of classifying different strains of IBV. Level of virus neutralising antibodies present can determine the response to a challenge virus required to establish viral clearance. Presence of high levels of maternal antibodies in young chicks has been shown to be capable of providing partial protection against IBV and reduce the clinical signs caused by the infection (171). During infection, IBV escapes antibody detection through the formation of syncytium which allows for virus to spread between cells without entering the intracellular region.

1.8. Aims and Objectives

1.8.1. Aim One: Generation and characterisation of rIBVs with modified E proteins

Objective 1: Generate rIBVs with mutations in the E gene

Objective 2: Assess the genetic stability of E mutations *in vitro* and *in ovo*

Objective 3: Determine whether E mutations affect replication of the virus *in vitro, in ovo.*

1.8.2. Aim Two: Characterise the role of the E protein during infection

Objective 1: Determine cellular interacting partners with the E protein with T16A or A26F mutations and compare them to parental Beau-R.

Objective 2: Assess the role of the E protein in the manipulation of the cellular machinery *in vitro*

1.8.3. Aim Three: Determine whether IBV with modified E proteins have altered pathogenicity profiles

Objective 1: Assess E protein interactions with immune factors

Objective 2: Assess the effect of E protein mutations in *ex vivo* tracheal organ cultures (TOCs)

Objective 3: Assess the pathogenicity of recombinant virus with a modified E protein *in vivo*.

Chapter 2: Materials and Methods

2.1. Cells, Eggs, and Tracheal Organ Cultures (TOCs)

All cells were provided by the Central Services Unit at The Pirbright Institute. Cell cultures were routinely screened for presence of mycoplasma using the LookOut Mycoplasma PCR Detection Kit (Merck, MP0035). The cell cultures were maintained within incubators set at 37 °C with 5 % carbon dioxide (CO_2). Eggs were maintained at 37 °C, with 30% humidity. TOCs were incubated at 37 °C rotating at a rolling rate of 1 revolution per 7 minutes (min). Medium used to maintain cells and cultures can be found in Table 2.1.

2.1.1. Primary Cells

Chick kidney (CK) cells were prepared at the Central Services Unit department at the Pirbright Institute from 2-3-week-old specific pathogen-free (SPF) Rhode Island Red (RIR) chickens. The cells are obtained from whole kidneys through manual and trypsin disaggregation (172). CK cells were grown within CK growth media and were maintained within either 1 x N, N-bis[2-hydroxethy1]-2-aminoethanesulfonic acid (BES) or 2 x BES (Table 2.1).

2.1.2. Continuous Cell Lines

BHK-21 cells were originally derived from baby hamster kidneys (BHK) of 1-day old Syrian golden hamsters. BHK-21 cells were grown in BHK-21 growth media and were maintained in 1 X Glasgow minimum essential medium (GMEM, Table 2.1).

DF1 cells are an avian cell line of chicken embryo fibroblasts derived from 10-day old East Lansing eggs (173). DF1 cells were grown in DF1 growth media and were maintained in 1 X BES (Table 2.1).

Vero cells are a continuous cell line derived from kidney epithelial cells of the African Green Monkey. Vero cells were grown in Vero growth media and were maintained in 1 X BES or 1 X Eagle's minimum essential medium (EMEM, Table 2.1).

2.1.3. Embryonated Eggs

Embryonated hens' eggs SPF were sourced from VALO BioMedia GmbH. Eggs were set by Animal Services Unit at The Pirbright Institute.

2.1.4. Tracheal Organ Cultures (TOCs)

Trachea was extracted from 19-days-old embryos, from SPF VALO eggs, using a method previously described (174). The trachea was sliced transversely into rings of approximately 1 mm thick to form the TOCs. The TOCs are individually cultured in glass test tubes in TOC growth media (Table 2.1). After 72 hours (h), the percentage of cilia beating for each TOC was quantified using a light microscope. The TOCs with <75% ciliary activity were discarded. TOCs were maintained within TOC infection media (Table 2.1).

2.2. Cell Culture Medium

Details of cell culture media reagents and suppliers can be found in Table 2.1. Tryptose Phosphate Broth (TPB) is composed of four components: Tryptose (20g/L); Dextrose (2g/L); NaCl (5g/L) and Disodium Phosphate (2.5g/L) adjusted to pH 7.3.

Table 2.1. Components of Cell Culture Media used within this Thesis.

	1 x BES	2 x BES	1 x EMEM	2 x EMEM	1 x GMEM	BHK-21 growth	CKC growth	TOC growth	TOC infection	DF1 growth	Supplier and Catalogue Number
10 x EMEM	50 ml	100ml	-	100ml	-	-	-	-	50ml	-	Merck, M0275
GMEM	-	-	-	-	500ml	500ml	-	-	-	-	Merck, G5154
EMEM	-	-	500ml	-	-	-	500ml	500ml	-	-	Merck, M2279
DMEM									-	500ml	Merck, D5796
TPB	50ml	100ml	-	-	55ml	55ml	55ml	-	-	-	Merck, T8159
FCS	-	-	-	50ml	5.5ml	5.5ml	-	-	-	55ml	Fisher Scientific, 10099141
NBBS	-	-	-	-	-	-	55ml	-	-	-	Merck, N4762
10% BSA	10ml	20ml	-	-	-	-	-	-	-	-	Merck, A7906
1M BES pH 7	10ml	20ml	-	-	-	-	-	-	-	-	Merck, B4554
7.5% $NaHCO_3$	14ml	28ml	-	23ml	-	-		-	7.5ml	-	Merck, S8761
L-Glutamine	5ml	10ml	5ml	10ml	5ml	-	5ml	-	-	-	Merck, G7513
1M Hepes, pH 7-7.6	-	-	-	-	-	-	5.5ml	20ml	20ml	-	Merck, H0887
1M methyl-α-D-glucopyranoside	-	-	-	-	-	-	-	-	37.5ml		Merck, M9376
P/S	0.5ml	1ml	-	1ml	0.55ml	-	0.55ml	1ml	0.5ml	-	Fisher Scientific, 11548876
Nystatin	2.5ml	2.5ml	-	2.5ml	2.5ml	-	2.5ml	2.5ml	2.5ml	-	Merck, N1638
H_2O	355ml	218ml	-	311ml	-	-	-	-	382ml	-	Sterile Water

Notes: EMEM: Eagle's minimum essential medium, GMEM: Glasgow minimum essential medium, DMEM: Dulbecco's modified eagle's medium, TPB: tryptose phosphate broth, FCS: fetal bovine serum, NBBS: new-born bovine serum, BSA: bovine serum albumin, BES: N, N-bis[2-hydroxethy1]-2-aminoethanesulfonic acid, P/S: penicillin/streptomycin. FCS was heat inactivated for 1 h at 50 °C before use.

2.3. Viruses

2.3.1. IBV Strains

All IBV viruses were stored at -80 °C. The following virus stocks were grown in embryonated eggs:

Beau-R: A molecular clone of Beau-CK (GenBank Accession number AJ311317) which is a non-pathogenic laboratory strain of IBV (24). Beau-CK was generated through serial passage through embryonated eggs resulting in a non-pathogenic phenotype (25, 175) and an extended cell tropism allowing for replication in CK cells and continuous cell lines DF1 and Vero (97, 176).

M41-CK: Pathogenic laboratory strain of IBV generated through an unknown number of serial passages in CK cells. M41-CK can only replicate in primary CK cells so does not show the extended tropism of Beau-R (176). GenBank Accession number MK728875.1.

M41-K: Pathogenic clone of the M41-CK laboratory strain of IBV, there are several synonymous mutations which differ between M41-CK and M41-K (177).

The following virus stocks were grown in primary CK cells:

BeauR-T16A-E: rIBV based on a Beau-R backbone with a T16A mutation within the E protein. A single nucleotide mutation A24246G, was generated within Beau-R E gene to obtain the T16A mutation. Nucleotide positions listed are in relation to the Beau-CK genome (GenBank accession number AJ311317). This virus was generated prior to the start of this project by Sarah Keep and Jamie Stuart. Isolates of BeauR-T16A-E include: 3.4, 3.6, 4.7 and 4.9.

M41-K-T16A-E: rIBV based on a M41-K backbone with T16A mutation in the E protein. To generate the T16A mutation a single point mutation was made at nucleotide position A24254G in relation to the M41-K genome (NCBI BioSample

database, accession number: SAMN24687558). Isolates of M41K-T16A-E include: 2.3, 2.6 and 8.3.

BeauR-A26F-E: rIBV within a Beau-R backbone with an A26F mutation in the E protein. The A26F mutation was obtained via three point mutations from 24276 to 24278 changing the nucleotide sequence from GCA to TTT, positions are listed in relation to the Beau-CK genome (GenBank accession number AJ311317). Isolates of BeauR-A26F include: 11.2, 11.3 and 12.3.

2.3.2. Fowl pox Virus (FPV)

rFPV-T7: recombinant Fowlpox-T7 virus (rFPV-T7) was required for the rescue system as it expresses the bacteriophage T7 RNA polymerase required to transcribe the rIBV genome and pCi-Nuc-M41-N (178). FPV-T7 was stored at -80 °C.

2.3.3. Vaccinia Viruses

Prior to use all vaccinia viruses were sonicated using a Branson Digital Cup Horn Sonifier 450 with a continuous pulse at 70 % output for 2 min. Vaccinia viruses were stored at -20 °C.

rVV M41-K: Recombinant vaccinia virus (rVV) containing a complementary DNA (cDNA) copy of the M41-K genome.

rVV Beau-R: rVV containing a cDNA copy of the Beau-R genome.

2.4. Buffers and Solutions

Xanthine: 10 mg/ml Xanthine (Merck, X3627) in 0.1N Sodium Hydroxide (NaOH; Merck, S5881); 40 X concentrated

Mycophenolic Acid (MPA): 10 mg/ml MPA (Merck, M3536) in Sodium Hydroxide (NaOH; Merck, S5881); 400 X concentrated

Hypoxanthine: 10 mg/ml hypoxanthine (Merck, H9636) in 0.1M Sodium Hydroxide (NaOH; Merck, S5881); 667 X concentrated

Phosphate Buffered Saline (PBSa) pH 7.2: Prepared by the Central Services Unit at The Pirbright Institute. PBSa powder (Merck, P38135) was reconstituted in type 1 endotoxin-free water and sterilised by autoclaving a 115°C for 20 min.

Tris-EDTA (TE) buffer, pH 9: 10 mM Tris/HCl pH 9.0 (Merck, T2819), 1 mM Ethylenediaminetetraacetic acid pH 9.0 (EDTA; E9884) in Molecular-Grade water (Merck, W4502).

SDS-PAGE Running buffer (10X): 50 ml 20 % SDS (Merck, 05030), 30 g Tris (Merck, M6250), 144 g glycine (VWR, 101194M). Topped up to 1 litre with Molecular-Grade water (Merck, W4502).

DNA loading buffer: 2 ml Glycerol (VWR, 24388.26), 50 mg Ficoll 400 (Merck, F2637), 25 mg Bromophenol blue (Merck, 114391) and 3 ml Molecular-Grade water (Merck, W4502).

3.3 % formaldehyde: 50 ml formaldehyde solution (VWR, 20909.29) made up to 500 ml in PBSa

2 x Proteinase K digestion buffer: 200 mM Tris/HCl pH 7.5 (Merck, T2319) , 10 mM EDTA (Merck, E9884), 0.4 % SDS (Merck, 05030), 400 mM NaCl (S3014)

Proteinase K: 20 mg proteinase K powder (Merck, P2308) in Molecular Grade water (Merck, W4502).

30 % Sucrose solution: 75 g sucrose (Merck, 16104), 250 µl 1M Tris HCl pH 9 (Merck, T2819) and 250 ml of Molecular-Grade water (Merck, W4502).

0.1 % crystal violet: 100ml 1 % crystal violet (Merck, C6158) in 900 ml of Molecular-Grade water (Merck, W4502)

PBS-T: 0.1 % Tween-20 (Merck, T2700) in PBSa

Blocking solution: 0.5 % BSA (Merck, A7906) in sterile PBS

Table 2.2. ERGIC inhibitors used within this project.

Inhibitor	Supplier	Stock concentration	Dilution reagent
BFA	Abcam, ab193369	5.0 mg/ml	DMSO
IMP-1088	Cayman chemical, 25366	50 mM	DMSO
Monensin	Abcam, ab146170	2.0 mM	Ethanol
Paprotrain	Abcam, ab144322	5 mM	DMSO
Blebbistatin	Abcam, ab120425	8 mM	DMSO
Fli-06	Abcam, ab146170	10 mM	DMSO
Exo1	Abcam, ab120292	100 mM	DMSO
ES2	Merck, SML1681	20 mM	DMSO

Notes: Inhibitors were diluted in Dimethyl sulfoxide (DMSO, Merck, D8418) or ethanol (VWR International, 20821.321) either by the manufacturer or from powder to generate a working stock. Further dilutions were made within 1 X BES media. BFA: Brefeldin-A and ES2: Endosidin-2.

2.5. Reverse Genetics

The generation of rIBVs was carried out following the in-house reverse genetic system based on a rVV containing a complementary DNA (cDNA) copy of the complete IBV genome (Figure 2.1) (24, 179, 180). This vaccinia virus based reverse genetics system enables modification of the IBV cDNA through homologous recombination, this therefore requires a plasmid containing the sequence to be modified plus some flanking sequence. The first stage of the system involves inserting the region to be modified into a pGPT-NEB193 plasmid, for use within the second stage which involves modification of the cDNA copy of the IBV genome within the rVV vector. To generate the final rIBV, the modified IBV genome was rescued from the rVV vector to generate infectious virions with the desired mutation.

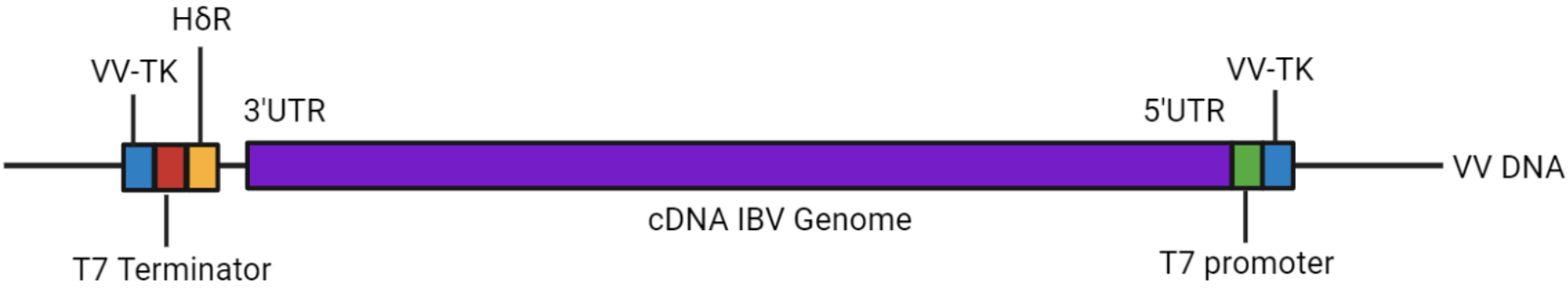

Figure 2.1. cDNA copy of IBV genome within the thymidine kinase (TK) gene of a recombinant vaccinia virus (rVV) vector. The cDNA copy was inserted using *Not I* restriction sites (176). The cDNA copy of the IBV sequence is flanked by a T7 RNA polymerase promoter at the 5′ untranslated region (UTR). To allow for self-cleavage of the subsequent IBV genome RNA, a hepatitis delta antigenome ribozyme (HδR) site was inserted at the 3′ UTR of the IBV genome prior to the T7 RNA polymerase terminator sequence. This schematic has been adapted from (181)

2.5.1. Cloning

pGPT-NEB193 plasmids were cloned to contain the modified E gene flanked by 400 base pairs (bp) of adjacent sequence from the IBV genome. Gene strings were synthesised by GeneArt and were cloned into pGPT-NEB193 plasmids using *Sal I* restriction sites (5′ G$^{\downarrow}$TCGAC 3′) as these sites are not contained within the IBV genome. In this plasmid, the *Escherichia coli* (*E. coli*) guanine phosphoribosyl transferase (*Ecogpt)* gene is required for selection which facilitates purine synthesis via an alternative method in the presence of xanthine and hypoxanthine. A schematic of the plasmid is shown in Figure 2.2.

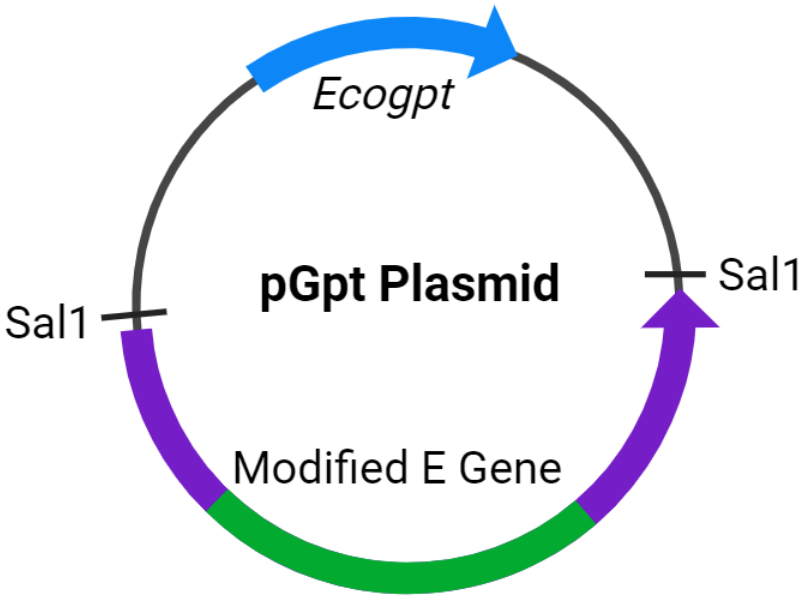

Figure 2.2. pGPTNEB193 plasmid schematic. This plasmid is the recombination vector for manipulation of the rVV genome which possesses a cDNA copy of IBV. The plasmid contains the *Ecogpt* gene under the control of a VV $p_{7.5k}$ promoter. The *Sal I* restriction site was used for cloning because it is not present in the IBV sequence (182).

Each plasmid was transformed in a vial of 50 µl of One-shot MAX efficiency DH5α-T1^{R} competent cells (Thermo Fisher, 12297016) from which a larger stock was grown. DNA was extracted using the QIAGEN Plasmid Maxi kit (Qiagen, 12162) following the manufacturer's protocol and screened to ensure the modification was present using polymerase chain reaction (PCR) over the inserted region and Sanger sequencing (Section 2.8).

2.5.2. Transient Dominant Selection (TDS)

TDS is used to modify the IBV cDNA within the rVV vector, this process is detailed in Figure 2.3.

The first stage of the TDS is homologous recombination between the pGPTNEB193 and the cDNA copy of the IBV genome within the receiver rVV resulting in the entire plasmid inserted within the rVV. MPA shuts off the classical purine biosynthetic pathway. In the presence of the *Ecogpt* gene, xanthine and hypoxanthine an alternate pathway is facilitated. As the pGPTNEB193 contains the *Ecogpt* gene, this allows for selection of rVVs which have undergone the first recombination event and have generated an unstable intermediate which possesses duplicate sequence over the inserted region.

A second recombination event takes place as the selection agents are removed, during three additional rounds of plaque purification. This recombination results in removal of duplicate sequences to produce either the original sequence of the receiver cDNA or the modified sequence. Presence of the modified sequence is established through screening over the *Ecogpt* and E gene.

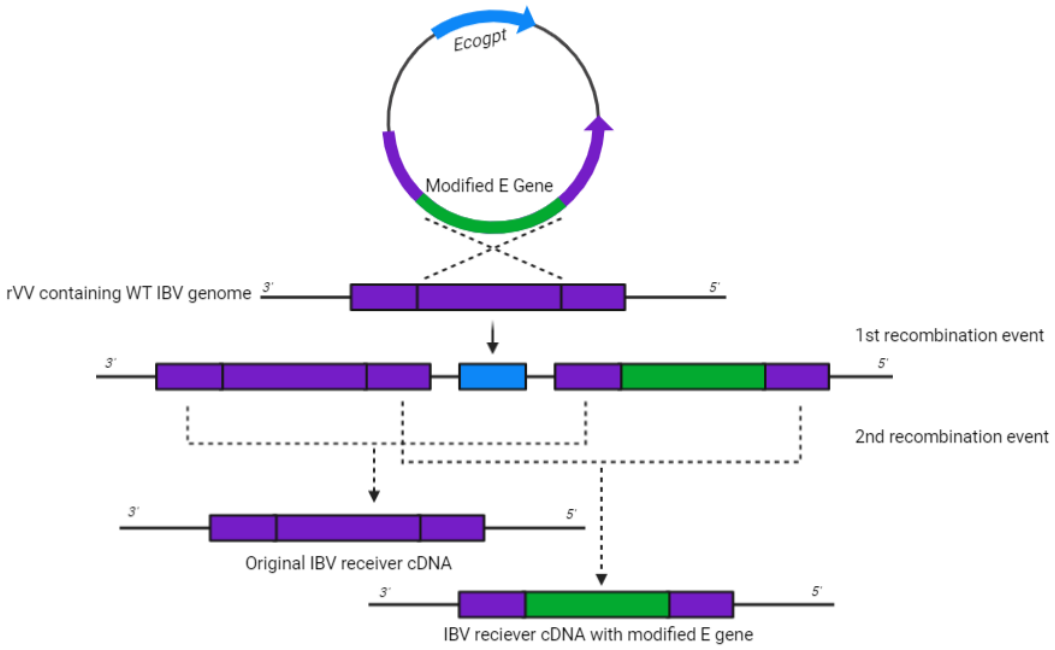

Figure 2.3. Transient dominant selection (TDS) system. TDS system shown for generating IBV cDNA with a modified E protein. Two recombination events were required to insert the desired sequence, the first forms an unstable intermediate with duplicate sequences and the second removes one of the duplicates to either leave the WT sequence or the modified sequence.

The first recombination event used Vero cells seeded in 6 well plates to 50 % confluency, with two independent wells per recombination. Each well was infected with 500 µl rVV at a multiplicity of infection (M.O.I) of approximately 0.2 and incubated for 1 h at 37 °C. Transfection solutions, A and B, were prepared for each recombination. Solution A consists of 5 µg of pGPTNEB193 plasmid-DNA in 1.5 ml of OPTIMEM medium (Fisher Scientific, 11524456). Solution B consists of 12 µl of Lipofectin (Invitrogen, 18292037) in 1.5 ml of OPTIMEM medium (Fisher Scientific, 11524456). Solution A and Solution B were incubated for 30 min at room temperature, then combined and incubated for a further 15 min at room temperature, generating the final transfection mixture. During the incubation, the rVV was removed and cells were washed twice with 2 ml of OPTIMEM medium (Fisher Scientific, 11524456). For each transfection 3 ml of the transfection mixture was added to each well and incubated for 90 min at 37 °C. After the incubation, the transfection mixture removed and replaced with 5 ml of 1 x BES media. Following this, the cells were incubated overnight at 37 °C. Selection agents (12.5 µl MPA, 125 µl of Xanthine and 7.4 µl Hypoxanthine) were added at 24 hpi. Cells were harvested after 2 further days of incubation at 37 °C.

The plaque purification during the TDS protocol was carried out in 6 well plates of confluent Vero cells. Serial dilutions (10^{-1} to 10^{-3}) of the rVV stocks were prepared in 1 X EMEM. Cells were washed once with Phosphate Buffered Saline pH 7.2 (PBSa) and 500 µl of inoculum was added per well, serial dilutions were plated in duplicate wells. Cells were incubated for 2 h at 37 °C after which inoculum was removed.

Post-incubation, the inoculum was removed, and a solid overlay was added which contains equal parts of 2 X EMEM and 2 % agar (Merck, 05040). For the first three rounds of plaque purification, selection agents were added into the overlay media: 30 mM MPA, 66 mM xanthine and 73 mM hypoxanthine. This generates a selection pressure to maintain the rVVs which have successfully carried out the first

recombination stage as they possess the *Ecogpt* selection gene. Plates were incubated for 4 days at 37 °C and then stained with overlay containing equal parts 2 ml of 2 X EMEM, 2 % agar (Merck, 05040) and 0.01% neutral red (Merck, N4638) in Molecular-Grade water (Merck, W4502). Three plaques were picked for each recombinant virus and stored in 400 µl of 1 x EMEM at -20 °C. This was repeated three times to isolate the rVVs which had undergone the initial recombination step. Three more rounds followed in the absence of selection agents to remove the selection pressure and induce the second recombination event.

2.5.3. Growth of Ministocks of rVVs

After the six rounds of plaque purification, ministocks of the rVVs were propagated in six well plates of confluent Vero cells. Cells were washed with PBSa and 150 µl of the sonicated rVV was added to each well in 350 µl of 1 x BES media. Infected cells were incubated at 37 °C for 2 h. Without removing the inoculum, 2.5 ml of 1 x BES media was added to each of the wells and cells were incubated at 37°C until extensive cytopathic effects (CPE) had developed. Vero cells were scraped into the media and harvested into 1.5 ml tubes. Cells were pelleted via low-speed centrifugation. Supernatant was discarded and cells were resuspended in a total of 400 µl of 1 x BES media. Ministocks were stored at -20 °C. Ministocks were numbered based on the well in which they were propagated, these numbers correspond to the first number in the isolate name of the final virus.

rVV DNA was extracted from ministocks using the Qiagen QIAamp DNA mini kit (Qiagen, 51304) following the blood/body fluid spin protocol provided by the manufacturer. rVV DNA was eluted in 200 µl of RNAse free water (provided by manufacturer) and stored at -20 °C. The extracted DNA was analysed by PCR to identify rVVs containing the correct modification which also tested negative for presence of the *Ecogpt* gene (Section 2.8.1). rVV DNA positive for IBV E gene and

negative for *Ecogpt* gene was Sanger sequenced (Section 2.8.3) to determine whether the correct modification in the IBV cDNA sequence was present.

2.5.4. Growth of rVV Maxistocks

Large stocks of rVVs with the correct sequence were generated in 11 x T175 flasks (Greiner Bio-One, 660175) of confluent BHK-21 cells. 2 ml of sonicated rVV was diluted in 18 ml of 1 x GMEM per flask at an MOI of 0.1-1, flasks were then incubated at 37 °C for 2-3 days until cells were completely detached from the surface of the flask. The cells were transferred into 50 ml Falcon tubes (VWR International, 734-0448) and centrifuged for 15 min at 270 x g and 4 °C. The supernatant was discarded, and cells were resuspended in 2 ml Tris-EDTA (TE) buffer pH 9 and stored at -20 °C.

2.5.5. Partial Purification of rVVs

rVVs were detached from BHK-21 cells through sonication using a Branson Digital Cup Horn Sonifier 450 with a continuous pulse at 70 % output for 2 min. To remove the BHK-21 cell nuclei, samples were centrifuged for 10 min at 500 x g. TE buffer was added to the supernatant for a final volume of 13 ml which was layered onto 16 ml of 30 % sucrose in a Beckman Coulter 38.5 ml ultracentrifuge tube (Fisher Scientific, 12706558). Ultracentrifugation was carried out using a Surespin 630 rotor at 36,000 x g for 1 h (4°C). Pellets were resuspended in 5 ml of 1 mM TE buffer and stored at -20 °C.

2.5.6. Phenol-Chloroform DNA Extraction

An equal volume of pre-warmed (50 °C) 2X proteinase K buffer and 200 µl 20 mg/ml solution of proteinase K was added to 10 ml of the partially purified rVV DNA and incubated for 2.5 h at 50 °C.

Phenol-Chloroform (Life Technologies, 17909) was added in equal volume and mixed by inverting the tube 5-10 times before centrifugation at 1,200 x g for 15 min. This

formed two phases within the tube, the upper phase was carefully removed and placed into a 50 ml Falcon tube (VWR International, 734-0448) using a wide-bore pipette tip. The phenol-chloroform step was repeated once and then the process was repeated once with Chloroform (Merck. 32211-M). rVV DNA was then precipitated by adding 2.5 volumes of -20 °C absolute ethanol (VWR International, 20821.321) and 0.1 volumes of 3 M sodium acetate (Fisher Scientific, 11301618). The samples were centrifuged at 3500 revolutions per minute (rpm) for 30 min (Megafuge 16R Heraeus) and the supernatant was removed. 10 ml of -20 °C 70 % ethanol (VWR International, 20821.321) was added to dissolve salts present in the samples, to aid this the 50 ml Falcon tube (VWR International, 734-0448) was placed on ice. Further centrifugation was carried out at 3500 rpm for 30 min (Megafuge 16R Heraeus). Supernatant was removed and pellets left to dry until there most of the ethanol had evaporated. The pellets were resuspended in 300 µl of Molecular-Grade water (Merck, W4502) and stored at 4 °C to avoid shearing the DNA.

2.5.7 Rescue of rIBV

To form a rIBV with the desired mutation, the rIBV genome must be rescued from the rVV vector (Figure 2.4). The N protein is delivered to the reaction via a transfected plasmid: pCi-Nuc (which transcribes the M41-K N protein) or pCi-Neo (which transcribes the Beau-R N protein). The cDNA copy of the IBV genome and the pCi-Nuc and pCi-Neo plasmids are under the control of a T7 promoter in the rVV DNA so this process requires a recombinant Fowl pox virus which encodes the T7 promoter (rFPV-T7) to transcribe the IBV genome.

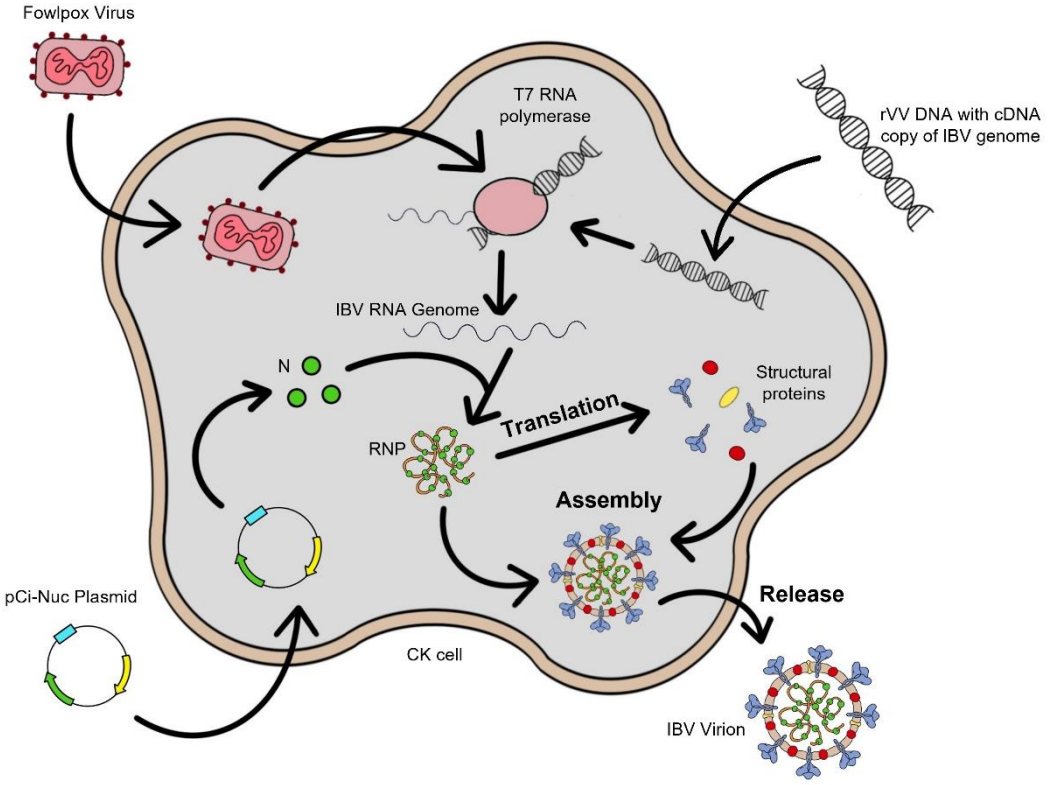

Figure 2.4. Rescue system used to recover rIBV from rVV vector in CK cells. CK cells were infected with rFPV-T7 to provide the T7 RNA polymerase which was required as the cDNA copy of the IBV genome in the rVV genome is controlled by a T7 promoter. The pCi-Nuc/pCi-Neo plasmid and modified IBV genome within rVV derived DNA was transfected into the CK cell. The pCi-Nuc/pCi-Neo plasmid transcribes the IBV N protein which coats the synthesised IBV genomes to form the ribonucleoprotein (RNP). The presence of the IBV genome stimulates normal IBV replication and therefore generates the rIBVs.

Several independent rescue reactions were carried out for each rVV as the rescue process relies on a low probability event. Ideally, at least two independent rVV ministocks (indicated by the first number of the isolate name) are taken forward to the rescue stage. For each virus the rescue attempt was numbered, these numbers correspond to the second number in the isolate name of the final virus. Therefore, the final name of the isolated rIBV details both the rVV stock and rescue attempt from which the virus originated.

CK cells seeded into six well plates to 50 % confluency were used for the rescue process. CK cells were washed with PBSa and inoculated with rFPV-T7 at an MOI of 10 in 1 ml of 1 X BES media. Infected cells were then incubated at 37 °C for 1 h. Transfection solutions, A and B, were prepared for recombination. Solution A consisted of 1.5 ml of OPTIMEM (Fisher Scientific, 11524456), 10 µg of rVV DNA and 5 µg of pCi-Nuc/pCi-Neo per replicate. Solution B consisted of 1.5 ml OPTIMEM (Fisher Scientific, 11524456) and 30 µl of Lipofectin (Invitrogen, 18292037) per replicate. Solution A and Solution B were incubated for 30 min at room temperature, then combined and incubated for a further 15 min to generate the final transfection solution. rFPV-T7 was removed, and cells were washed twice with OPTIMEM (Fisher Scientific, 11524456). 3 ml of the transfection solution was added per well and cells were incubated overnight at 37 °C. The following day, the transfection media was replaced with 1 x BES media and cells were incubated at 37 °C until extensive CPE was seen.

Cell supernatant was harvested, and using a 0.22 µm filter (Merck, SLGP033NS) attached to a 5 ml syringe (Industrial & Scientific, 302187) the rFPV-T7 progeny was removed. Filtered supernatant (passage 0) was stored at -80 °C. To increase the viral titre of the newly propagated rIBV, the supernatant was passaged an additional two times on CK cells. The passage 2 viruses were then screened via RNA extraction,

RT-PCR and Sanger sequencing (Sections 2.6 - 2.8) to ensure the desired sequence was present in the rIBV.

2.6. RNA Extraction

RNeasy Mini Kits (QIAGEN, 74104) were used to extract total RNA from supernatant, allantoic fluid and cell lysates according to the manufacturer's instructions using the RNA clean-up protocol. RNA was eluted from columns in 35µl of RNAse free water (provided by manufacturer) and stored at -20 °C.

To prepare samples for quantitative PCR (qPCR) a DNase treatment (Fisher Scientific, EN0521) was carried out during use of the animal cells spin protocol, following the manufacturer's instructions.

RNA extracted from *in vivo* experiment (Section 2.24) was carried out following the animal tissues spin protocol, following the manufacturer's instructions.

2.7. Reverse Transcription (RT)

RT was carried out as a two-step assay. Denaturation of the RNA strands was achieved through incubation of the mixture from Table 2.2 at 65 °C for 5 min then on ice for 2 min (Table 2.3). Random primer was ordered from Sigma-Aldrich, Merck at a stock concentration of 100 µM and was diluted to 50 µM before use. The sequence for the random primer used was 5′ GTTTCCCAGTCACGATCNNNNNNNNNNNNNN 3′.

Table 2.3. Components of the first RT mixture.

Component	Supplier	Volume	Final Concentration
RNA	-	5 µl	-
Nuclease free H_20	Merck, W4502	6 µl	-
10 mM dNTPs	Life Technologies, R0182	1 µl	0.5 mM of each
50 µM Random Primer	Merck	1 µl	2.5 µM

RNA was transcribed into cDNA using the reverse transcriptase Super Script IV (SSIV). The mixture for the second stage is detailed in Table 2.4 and the thermocycler program is detailed in Table 2.5. Within the reaction, recombinant ribonuclease inhibitor (RNaseOUT) prevents degradation of RNA within the reaction and Dithiothreitol (DTT) is a reducing agent which aids the breakdown of RNA secondary structures.

Table 2.4. Components for the second RT mixture.

Component	Supplier	Volume	Final Concentration
SSIV Buffer	Life Technologies, 18090050	4 µl	1 X
SSIV	Life Technologies, 18090050	1 µl	20 U/µl
RNaseOUT	Life Technologies, 10777019	1 µl	2 U/µl
DTT	Life Technologies, 18090050	1 µl	5 mM

Table 2.5. SuperScript IV thermocycler program

Temperature	Time
23 °C	10 min
55 °C	10 min
80 °C	10 min
18 °C	Hold

2.8. Polymerase Chain Reaction (PCR)

2.8.1. Standard PCR

The DNA polymerase, Taq polymerase, was used to amplify the cDNA according to the manufacturer's instructions. The components required for a standard PCR is detailed in Table 2.6. Magnesium chloride ($MgCl_2$) is required for the reaction as it acts as a cofactor for the Taq polymerase enzyme and aids primer binding. Primer sequences are listed in Table 2.7. The thermocycler program is detailed in Table 2.8, the annealing temperature and extension time varied between primer sets.

Table 2.6. Components required for a standard PCR

Component	Supplier	Volume	Final Concentration
10X PCR Rxn Buffer	Life Technologies, 10342046	5 µl	1 X
$MgCl_2$	Life Technologies, 10342046	2 µl	2 mM
dNTPs	Life Technologies, R0182	1 µl	0.2 mM
Forward Primer	See Table 2.7	1 µl	0.2 pmol
Reverse Primer	See Table 2.7	1 µl	0.2 pmol
Taq DNA Polymerase	Life Technologies, 10342046	0.5 µl	2.5 U
Template DNA	-	5 µl	-
Nuclease free H_20	Merck, W4502	34.5 µl	-

Primers used throughout this project are listed below. Primers were synthesised by Sigma-Aldrich, Merck. Stocks are at 100 mM and are diluted in Molecular-Grade water (Merck, W4502) to 10 mM before use.

Table 2.7. Oligonucleotide sequences and targets for RT and standard PCR.

Primer	Sequence	Target
BG50	5′ TAGCGCTCCAACAACTAA 3′	E
BG144	5′ CAGTGTTTGCGTGTCTGTCT 3′	E
M Forward	5′ AAATCCAGCAAATTTTCAAG 3′	M
M Reverse	5′ TACTCTCTACACACACACAT 3′	M
E Forward	5′ GCTGAAGATTGTTCAGGTGA 3′	E
E Reverse	5′ GCTGAACTGACTGTTCAAAG 3′	E
Ecogpt forward	5′ ATGAGCGAAAAATACATCGTC 3′	GPT selection marker
Ecogpt reverse	5′ TTAGCGACCGGAGATTGGC 3′	GPT selection marker

Table 2.8. Standard PCR thermocycler program

Temperature	Time	Number of Cycles
95°C	3 min	1
95°C	45 seconds (sec)	25
Annealing Temp. (~60 °C)	30 sec	
72°C	Extension Time (sec per bp)	
72°C	5 min	1
18°C	Hold	1

2.8.2. Gel Electrophoresis

Gel electrophoresis was used to visualise amount and size of PCR product using 1 kb DNA ladder (NEB, N3232L). 5 µl of each sample was diluted in 2 µl of DNA loading buffer.

Gels were assembled in 9 x 11 horizontal submarine gel apparatus (Galileo Bioscience, 80-0911). The gel comprised of 1 % agarose (Merck, A9539) in 0.5 X Tris Borate EDTA (TBE) buffer (Life Technologies, 15581044) containing SYBR™ Safe DNA Gel Stain (Invitrogen, S33102). Gels were run at 150 V for 1 h.

2.8.3. Sanger Sequencing

PCR products were sent for sequencing by Eurofins GATC. Each sequencing reaction contained 5 µl of PCR product (20-80 ng/µl) and 5 µl or primer (5 µM) within Molecular-Grade water (Merck, W4502). Results were analysed using Staden sequence analysis software.

Plasmids were diluted to 100 ng/µl in 10 µl of Molecular-Grade water (Merck, W4502).

2.9. Quantitative Polymerase Chain Reaction (qPCR)

TaqMan qPCR was performed using TaqMan ® Fast Advance Master Mix (Life Technologies, 4444557) or TaqMan™ Multiplex Master Mix (Life Technologies, 4486295) depending on the reporter sequence of the probes. For probes which use an ABY/JUN reporter (Table 2.10) TaqMan ® FastAdvance Mastermix (Life Technologies, 4444557) cannot be used as the ROX passive reference creates the same signal as the reporter. qPCRs were run on a 7500 Fast Real Time System (Applied Biosystems) within MicroAmp™ Fast Optical 96-Well Reaction Plates (Life Technologies, 4346907). The cycle for all qPCRs carried out within this project is detailed in Table 2.9.

Table 2.9. Fast qPCR thermocycler program

Temperature	Time	Number of Cycles
95°C	20 sec	1
95°C	1 sec	40
60°C	20 sec	

Details of the RNA extraction and RT methods used prior to qPCR can be found in Sections 2.6 and 2.7. Post-extraction, the RNA was normalised to ensure that there are comparable quantities of RNA input into the cDNA reaction. This normalisation was also carried out before the cDNA was inputted into the qPCR reaction to ensure that all the samples contained approximately 50 ng/µl of cDNA.

Two different methods of qPCR were carried out within the project. The first assessed the level of viral RNA present. The second assessed the upregulation of cellular genes upon viral infection. The primer and probe sets used within qPCR are listed in Table 2.10, reagents contained within each qPCR reaction are listed in Table 2.11.

Table 2.10. Primer and Probes used within qPCR.

Gene	Forward Primer (5′ to 3′)	Reverse Primer (5′ to 3′)	Probe Sequence	Reporter	Quencher
E gene	GGTAGAGCACTTCAAGCATTT	CCGGATTGTTAAGTTTTCTACC	CCAGGAGCTAAGGGTACAGCCT	FAM	TAMRA
Sg3	CTAGCCTTGCGCTAGATTTTTAACT	CCGGATTGTTAAGTTTTCTACC	CCAGGAGCTAAGGGTACAGCCT	FAM	TAMRA
IBV 5′	GCTTTTGAGCCTAGCGTT	GCCATGTTGTCACTGTCTATTG	CACCACCAGAACCTGTCACCTC	FAM	TAMRA
β-Actin	GCATACAGATCCTTACGGATATCCA	CAGGTCATCACCATTGGCAAT	CACAGGACTCCATACCCAAGAAAGATGGC	FAM	TAMRA
HPRT1	TGTAATCGAGGGCGTATCCAA	TGGTCAAAAGAACTCCTCGAAGT	TCCAACAAAGTCTGGCCGATATCCCA	FAM	TAMRA
IL-6	GCTCGCCGGCTTCGA	GGTAGGTCTGAAAGGCGAACAG	AGGAGAAATGCCTGACGAAGCTCTCCA	FAM	TAMRA
IL-1B	GCTCTACATGTCGTGTGTGATGAG	TGTCGATGTCCCGCATGA	CCACACTGCAGCTGGAGGAAGCC	FAM	TAMRA
IFNα	GACAGCCAACGCCAAAGC	GTCGCTGCTGTCCAAGCATT	CTCAACCGGATCCACCGCTACACC	ABY	QSY
IFNβ	CCTCCAACACCTCTTCAACATG	TGGCGTGTGCGGTCAAT	TTAGCAGCCCACACACTCCAAAACACTG	JUN	QSY

Notes: Before use, the primers were diluted to 10 μM and probes were diluted to 5 μM. The sg3 forward primer covers a sequence present in Leader 1 and the reverse primer is the E qPCR reverse primer. The same probe sequence for the E gene and sg3 was used.

Table 2.11. Components required for qPCR.

Component	Supplier	Volume	Final Concentration
TaqMan Fast Advance Master Mix/ TaqMan Multiplex Master Mix	Life Technologies, 4444557/ Life Technologies, 4486295	5 µl	1 X
Forward Primer	See Table 2.10	0.5 µl	0.1 µM
Reverse Primer	See Table 2.10	0.5 µl	0.1 µM
Probe	See Table 2.10	0.25 µl	0.1 µM
Nuclease free H_20	Merck, W4502	1.75 µl	-
cDNA	-	2 µl	-

2.9.1. Assessing Viral Load Using qPCR

Primers and Probes for the E gene qPCR were designed using Snapgene and were synthesised by Sigma-Aldrich (Merck). The qPCR standards were generated through standard PCR (Section 2.8.1) using the qPCR primers. The PCR products generated were quantified and diluted to $0.5x10^9$ molecules/µl in Molecular Grade water (Merck, W4502).

The components required for the reaction are listed in Table 2.11.

Standards were serially diluted from 10^9 copies/µl to generate a standard curve. The output of the experiment was represented in Ct values. The Ct values of the diluted standards are plotted as a semi-log line to allow for interpolation of the sample values to determine a value for viral copies present within each sample.

2.9.2. Assessing Upregulation of Host Factors Using qPCR

The Ct value of each potential reference gene was analysed across a variety of samples, the genes selected have been shown to be appropriate for cellular gene expression in CK cells (183).

The raw data was exported as a .csv file and imported into Excel. Using the GeNorm add-on, the GeNorm M value which represents the stability of each reference gene and the GeNorm V value which represents the optimal reference gene number was determined (184).

Once an appropriate cellular control was selected, four innate immune response factors were investigated: IL-6, IL-1B, IFNα and IFNβ. The primer and probe sequences for each of the housekeeping genes and experimental genes can be found in Table 2.10.

The qPCR reactions were carried out in duplicate, the components required are listed in Table 2.11. Individual master mixes were required for the experimental and housekeeping genes. The Ct Mean data generated for each sample against the experimental gene is assessed in comparison to the housekeeping gene using the following calculation:

ΔΔCt = (Ct Mean experimental gene - Ct Mean housekeeping gene) - (Ct Mean experimental gene reference sample - Ct Mean housekeeping gene reference sample)

The ΔΔCt calculation takes the reference sample as mock infected samples. The ΔΔCt for the mock group is generally 0 as that gives a fold change (FC) of 1. The $2^{-\Delta\Delta Ct}$ calculation is used to determine the relative FC of the experimental gene in comparison to the housekeeping gene for each sample.

2.10. NGS Sequencing

2.10.1. Virus Purification

Partial purification for the isolation of viral RNA was carried out following previously described protocol (185). To purify virus in preparation for NGS sequencing analysis, ultracentrifugation was carried out using 5 ml Beckman Coulter tubes (Fisher

Scientific, 10601651). The solution was incubated with continuous mixing and heat to melt the sugar and was filtered using a 0.2 µM Nalgene™ vacuum filter (Fisher Scientific, 10421791). 1 ml of the 30 % sucrose solution was added to the ultracentrifugation tube and 4 ml of viral solution was overlayed. The tubes were added into the ultracentrifugation buckets and each bucket was balanced to ensure the weight was within 0.01 g through addition of PBSa.

The buckets were added to a Beckman Coulter SW-55-Ti rotor and the samples were centrifuged for 1 h at 223,600 x g as previously described (185). After centrifugation the liquid was removed from the ultracentrifugation tube and discarded into a beaker. The pellet was resuspended in 350 µl of RLT buffer which was provided within the Qiagen RNeasy kit (QIAGEN, 74104). The viral RNA was extracted from this sample following the method described in Section 2.6.

The RNA concentration was measured using the Qubit fluorometer RNA Assay HS kit (Fisher Scientific, Q32852). The Qubit HS kit was equilibrated to room temperature before use. Assay tubes were set up for the standards and the samples. The Qubit working solution was prepared by diluting the Qubit RNA Reagent 1:200 in Qubit RNA buffer. The assay tubes were prepared as listed in Table 2.12.

Table 2.12. Components required for Standard and Sample Assay tubes for use within the Qubit RNA Assay kit.

	Standards	**Samples**
Working Solution	190 µl	198 µl
Standard (from kit)	10 µl	-
User Sample	-	2 µl
Total volume in each tube	200 µl	200 µl

Standards and samples were vortexed for 2-3 sec and incubated at room temperature for 2 min. The Qubit 2.0 Fluorometer was set to the RNA assay and was calibrated

with the standards before analysis of the samples. Concentrated viral RNA was stored at -80 °C.

2.10.2. NGS Sequencing

The NGS sequencing was carried out by the Sequencing Unit at The Pirbright Institute, following the method detailed within (186). Data analysis was carried out by Graham Freimanis, The Pirbright Institute.

2.11. *In silico* Modelling Methods

In silico modelling methods were carried out by Holly Everest, The Pirbright Institute. Rendering of the models within PyMol software was carried out by the author.

2.11.1. Spike Models

Predicted structures of the trimeric IBV S protein within WT M41-K, M41K-T16A-2.6 and M41K-T16A-8.3 were generated using SWISS-MODEL (187). Amino acid sequences containing the M41K-T16A-2.6 F36L mutation or the M41K-T16A-8.3 I637T mutation were inputted into SWISS-MODEL using an existing IBV M41 cryo-EM structure [53] as a template - RCSB PDB: 6CV0. The PDB structures were then exported and rendered using PyMol [6l1]. Rendered predicted structures of the S proteins possessed by the M41K-T16A isolates were overlayed with the solved WT M41K structure. The point mutations F36L and I637T were isolated and enhanced.

2.11.2. E and M Models

As there are currently no structures solved for the IBV E protein, predicted structures of the WT virus with or without mutations at the T16A or A26F residues within the E protein were generated using AlphaFold2 Colab (188, 189). The predicted structure for the M protein was also carried out using AlphaFold2. The sequences were sourced from UniProt (https://www.uniprot.org) with the mutations being inserted into the desired residues. The resulting sequences were imported into AlphaFold2 and

PDB files were exported. Predicted models of each of these proteins were rendered using PyMol. As previously, predicted structures were overlayed and point mutations isolated and enhanced.

2.12. Replication Kinetics of Viruses *In Vitro*

2.12.1. Replication Kinetics

Replication kinetics of the recombinant viruses were assessed in three different cell types: Vero cells, DF1 cells or CK cells. Cells were seeded into six well plates to confluency. Cells were washed once with PBSa. Each well was infected with 500 µl of virus which had been diluted to a set titre in 1 x BES media. After a 1 h incubation at 37 °C, cells were washed with PBSa and 3 ml of 1 x BES media was added. Further incubation was carried out at 37 °C. Supernatant was harvested at 1-, 24-, 48-, 72- and 96-hours post infection (hpi) or 1-, 2-, 4-, 6-, 8-, 10- and 11-hpi. Viral titre for each timepoint was determined by plaque assay using CK cells (Section 2.13). Samples from the 96 hpi timepoint were Sanger sequenced over the E gene (Method Sections 2.6-2.8).

2.12.2. Viral Release Assay

Viral release was assessed in three different cell types: Vero cells, DF1 cells or CK cells. Cells were seeded into 6 well plates to confluency. Cells were infected with virus at a set titre and incubated for 1 h at 37 °C. After the incubation the inoculum was removed, and the cells were washed twice with PBSa. The cells were topped up with 3 ml of 1 x BES media. After 24 hpi, the supernatant was removed from the cells and stored at -80 °C. Plates were washed once with PBSa and 1 ml of 1 x BES media was added to cells before the plates were freeze-thawed to extract the cell lysate. The harvested supernatant and cell lysate were titrated on CK cells to assess the amount of virus present, as detailed in Section 2.13.

2.13. Viral Titration by Plaque Assay

CK cells were seeded into 12 well plates and virus preparations were serially diluted (tenfold) in 1 x BES media. Cells were washed once with PBSa and infected with 250 µl of diluted virus per well for 1 h at 37 °C, each dilution was plated in triplicate. After this incubation, the inoculum was removed, and a solid overlay made up of 2 ml of equal parts 1 x BES and 1 % agar (Merck, 05040) was added per well. Three days after infection cells were fixed with 3.3 % formaldehyde and stained with 0.1 % crystal violet.

The number of plaques at each dilution were counted in triplicate and the average determines the plaque forming units (PFU) per 250 µl. To convert this into PFU/ml, the average number of plaques was multiplied by four and the titre was calculated from the dilution.

2.14. Genetic Stability of Viruses *In Vitro*

To evaluate genetic stability, viruses were passaged fifteen times in CK cells. CK cells were seeded into 6 well plates and washed once with PBSa before infecting with 500 µl of passaged virus per well, diluted 1 in 10 in 1 x BES media. Plates were incubated for 1 h at 37 °C. Following this, the inoculum was removed from each well and 3 ml of 1 x BES was added. Four replicates of each isolate were passaged, each replicate was sequenced at passage 5, 10 and 15.

2.15. *In Ovo* Characterisation of Recombinant Viruses

2.15.1. Infecting Eggs with IBV

Embryonated SPF eggs were candled at 10 days incubation to ensure that the embryos were viable. The air sac and a position 1 cm from sac membrane was marked and a hole was drilled without breaking the shell using a Dremel Electric

Engraver. Virus was diluted to a set titre in PBSa and 0.1 ml of inoculum per egg was injected into the allantoic cavity using a 25-gauge Microlance™ 3 Needle (BD, 300300) and a BD Plastipak™ syringe (BD, 303172). Eggs were then incubated rocking in an egg incubator at 37 °C for 24 hpi to allow viral replication. To cull the embryos, the eggs were placed at 4 °C for at least four h (Schedule 1 method).

2.15.2. Harvesting Allantoic Fluid from Embryonated Eggs

Eggshell was removed using forceps which were inserted into the engraved hole used to infect the eggs. The eggshell was cut away ensuring that the air sac membrane was left intact. Using 3 ml pipettes the allantoic fluid was removed, yolk and blood vessels were avoided. The allantoic fluid collected from eggs inoculated with the same virus was pooled into a 50 ml Falcon tube (VWR International, 734-0448), allantoic fluid from eggs inoculated with different viruses were harvested individually. The allantoic fluid was clarified by low-speed centrifugation at 4 °C to remove debris. The supernatant was then aliquoted into 1.5 ml tubes and stored at -80 °C. To screen allantoic fluid, RNA was extracted and then screened by RT-PCR. To determine whether any mutations were generated, the virus genomes were Sanger sequenced over the E gene.

2.16. *Ex Vivo* Characterisation of Recombinant Viruses

2.16.1. Replication Kinetics of Viruses in TOCs

To carry out a multi-step replication kinetics experiment, TOCs prepared from embryos were used. Five TOCs were infected per virus in the same tube. TOCs were washed with PBSa and infected with 1 ml of virus diluted to a set titre within TOC infection media. After a 1 h incubation at 37 °C, with tubes upright, TOCs were washed twice in PBSa before topping up with 1 ml of TOC infection media. Further

incubation was carried out in tissue culture rollers at 37 °C with a rolling rate of 1 revolution per 7 min. Supernatant was harvested from 2 tubes per timepoint at 1-, 24-, 48-, 72- and 96-hpi. Viral titre for each timepoint was determined by plaque assay using CK cells (Section 2.13). Samples from the 96 hpi timepoint were Sanger sequenced over the E gene (Methods Section 2.6-2.8).

2.16.2. Ciliary Activity Assay in TOCs

Before infection, TOCs were washed twice with PBSa. TOCs were infected at a set titre of virus which was diluted in TOC infection media. Ten replicates were carried out per virus. Tubes were incubated upright for 1 h at 37 °C and then washed twice with PBSa before topping up with 1 ml of TOC media. Further incubation was carried out at 37 °C with a rolling rate of 1 revolution per 7 min. Ciliary activity of TOCs was observed at 24 h intervals using a light microscope, where the proportion of cilia beating is represented with a score of 0, 25, 50 or 100 %.

2.17. ERGIC Inhibitors

2.17.1. Preliminary Inhibitor Screen

CK cells were seeded into 6 well plates to confluency. Cells were infected with 10^4 PFU of Beau-R or BeauR-T16A-3.4. CK cells were incubated with diluted virus for 1 h at 37 °C. After the incubation, the inoculum was removed, and the cells were washed once with PBSa. The cells were topped up with media containing ERGIC inhibitors (Table 2.2) at a concentration which has previously been shown to be effective for inhibition. Control wells with either no treatment (media only) or Dimethyl sulfoxide (DMSO, Merck, D8418) were included. The concentration of DMSO used was the highest volume present in the inhibitor stocks. At 24 hpi, the supernatant and cell lysate were harvested from the cells and stored at -80 °C. The amount of virus present was assessed through titration on CK cells, see Method Section 2.13.

2.17.2. Dose Response Assay

CK cells were seeded into 6 well plates to confluency. Cells were infected with 500 µl of virus at a titre of 10^4 PFU and incubated for 1 h at 37 °C. The cells were then washed once with PBSa and a range of concentrations of the ERGIC inhibitors were added to each well diluted within 3 ml of 1xBES. Control wells were included which either contained no treatment or DMSO (Merck, D8418) The inhibitors selected were Monensin, Exo1, Brefeldin-A (BFA) and Fli-06, sources can be found in Table 2.2. The supernatant and cell lysate for each concentration was harvested and stored at -80 °C. The titre was assessed through titration on CK cells (Method Section 2.13).

2.17.3. BFA Time-Course

CK cells were seeded into 6 well plates to confluency. Cells were infected with 500 µl of virus at a titre of 10^4 PFU. Cells were incubated with inoculum for 1 h at 37 °C. After the incubation, the cells were treated with 3ml of either untreated 1 x BES media or 1 x BES media containing 1 µg/µl of BFA. At 2-, 4-, 6-, 8-, and 10-hpi media was replaced in one of the plates to include media with 1 µg/µl of BFA. At 24 hpi the supernatant and cell lysate were harvested from each of the wells and was stored at -80 °C. Cell lysate was harvested through removal of the supernatant by washing once with PBSa. The supernatant was replaced with 1 ml of 1 x BES media, and the plate was freeze-thawed to generate the cell lysate. The titre was assessed through titration on CK cells, see Method Section 2.9.

2.18. Cell Titer-Glo Cell Viability Assay

2.18.1. Cell Viability in Presence of Varying Inhibitor Concentrations

CK cells were seeded to confluency within a 96 well plate (Fisher Scientific, 167008). Cells were washed once in PBSa and inoculated with ERGIC inhibitors. The amount

of ERGIC inhibitor present was serially diluted (1:2) down the plate. Cells were incubated at 37 °C for 24 h. Following incubation, the cells were transferred to an opaque 96 well plate white opaque 96-well plate (OptiPlate-96, PerkinElmer, 6007290). CellTiter-Glo® (Promega, G7571) reagents were added to each well as per the manufacturer's instructions. The level of luminescence was read using the Promega GloMax plate reader (Promega, GM3000).

2.18.2. Cell Viability in Presence of Varying Viral Titre

CK, DF1 or Vero cells were seeded to confluency within a 96 well plate (Fisher Scientific, 167008). Cells were washed once in PBS and infected with virus. The virus was serially diluted two-fold down the plate. Cells were incubated for 96 h and the CellTiter Glo® (Promega, G7571) reagents were added every 24 h. Prior to reading the level of luminescence the cells were transferred to a white opaque 96 well plate (OptiPlate-96, PerkinElmer, 6007290). The level of luminescence was read using the Promega GloMax plate reader (Promega, GM3000).

2.19. Viral Protein Analysis by Immunoprecipitation

2.19.1. Generating Cell Lysates

To generate cell lysates, six well plates of confluent CK cells were infected with equal titres of virus and incubated at 37 °C. Cells were washed with cold PBSa prior to lysis using 350 µl of radioimmunoprecipitation assay (RIPA) lysis buffer (Fisher Scientific, 10017003) containing 1X Protein Inhibitor Cocktail (PIC, Fisher Scientific, 78442) at 24- or 48-hpi. Plates were incubated on ice for 20 min and then cells were scraped into the buffer. To remove the cell debris, tubes were centrifuged at 10,000 rpm (Biofuge Pico, Heraeus) for 3 min. The supernatant generated was then stored at -20 °C.

2.19.2. SDS-PAGE Electrophoresis

Cell lysates were resolved using SDS-PAGE. Samples were diluted in Laemmeli sample buffer (4X) (Biorad, 1610747) containing β-mercaptoethanol (BME, Merck, M6250) and were incubated at 80 °C for 10 min. Cell lysates were run for 1 h at 150 V alongside molecular weight ladder (Precision Plus Protein™ Dual Color Standards, Biorad, 1610374) on Mini TGX Protean 4-15 % gel (Biorad, 4561085). SDS-PAGE running buffer used is detailed below.

Proteins were transferred onto a nitrocellulose membrane, all reagents were provided within the Trans-Blot Turbo Nitrocellulose kit (Biorad, 1704270). Transfer was carried out using TransBlot® Turbo™ Transfer System (Biorad, 1704150EDU) program 1X Mini TGX gel – 3 min. Transfer buffer was prepared as per the manufacturer's instructions.

2.19.3. Western Blot (WB)

Nonspecific binding sites were blocked with 5 % milk solution in PBS-tween (PBS-T) for 1 h.

Primary antibody dilutions were prepared in 5 % milk solution and 3 ml was added per membrane. Antibody dilutions are detailed in Table 2.13. Membranes were incubated overnight on an orbital shaker at 4 °C. Primary antibody was removed by washing three times in PBS-T for 5 min per wash.

Table 2.13. Primary antibody concentrations and sources

Antibody Name	Supplier	Dilution	Reactivity
Anti-E IE7	Generated in-house	1:100	Mouse IgG
Anti-E AF12	Generated in-house	1:100	Mouse IgG2b
Anti-S2 26.1	Wageningen, 7500892	1:500	Mouse IgG2a
Anti-Beta-actin	Abcam, ab8227	1:2000	Rabbit IgG
Anti-IBV	Abcam, ab ab31671	1:1000	Chicken IgG

Secondary antibody dilutions were prepared in blocking solution and 15 ml was added per membrane, Table 2.14. Membranes were incubated for 1 h at room temperature with constant agitation. Secondary antibody was removed from the membrane by washing three times in PBS-T for 5 min per wash. Membranes were washed once in Molecular-Grade water (Merck, W4502) before visualisation using the LICOR Odyssey CLx Imaging System.

Table 2.14. Secondary antibody concentrations and sources

Antibody Name	Supplier	Dilution	IR Dye
Goat Anti-Rabbit	Abcam, ab216777	1:15,000	680 RD
Donkey Anti-Mouse	Abcam, ab216774	1:15,000	800 CW
Donkey Anti-Chicken	LI-COR, 926-32218	1:15,000	800 CW

2.20. Visualisation of Viral Proteins Using Immunofluorescence (IF)

CK or Vero cells were seeded to 80 % confluency in a 24 well plate (Scientific Laboratory, 353047) containing glass coverslips (TAAB, M160/1.0) which were

sterilised using absolute ethanol (VWR International, 20821.321). These cells were infected with 200 µl of diluted virus per well and incubated for 1 h at 37 °C before adding 1 ml of 1 x BES. At 24 hpi, cells were washed with PBSa and fixed with 4 % paraformaldehyde (PFA, Agar Scientific, AGR1026) in PBSa for 20 min at room temperature. PFA was washed from coverslips using PBSa and the cells were then permeabilised with 0.1 % Triton (Merck, X100) in PBSa for 10 min.

Coverslips were washed with PBSa and 200 µl of 0.5 % BSA (bovine serum albumin, blocking solution) was added for 1 h at room temperature to prevent non-specific binding. Blocking solution was removed, cells were then incubated for 1 h at room temperature with 200 µl of primary antibody diluted in the blocking solution, see Table 2.15 for antibody dilutions.

Table 2.15. Primary antibody concentrations and sources

Antibody Name	Supplier	Dilution	Reactivity
AF12 anti-E	Generated in-house	1:100	Mouse IgG2b
Anti-LC3B	Abcam, ab48394	1:200	Rabbit IgG
Anti-GM130	Abcam, ab52649	1:250	Rabbit IgG
Anti-LMANT1	Cell Signalling Technology, E2B6H	1:100	Rabbit IgG
Anti-ERGIC-53/p58	Sigma-Aldrich, E1031	1:100	Rabbit IgG

Cells were then washed three times with PBS before incubation for 1 h with 200 µl secondary antibodies diluted in the blocking solution. Secondary antibodies are listed in Table 2.16.

Table 2.16. Secondary Antibody concentrations and sources

Antibody Name	Supplier	Dilution	Signal
Donkey Anti-Mouse IgG	Fisher Scientific, A21202	1:500	AlexaFluor 488
Goat Anti-Chicken IgY	Fisher Scientific, A11039	1:500	AlexaFluor 488
Goat Anti-Rabbit IgG	Fisher Scientific, A11011	1:500	AlexaFluor 568
Goat anti-Mouse IgM	Fisher Scientific, A21042	1:500	AlexaFluor 488
Goat anti-Mouse IgG1	Fisher Scientific, A21121	1:500	AlexaFluor 488
Goat anti-Mouse IgG2a	Fisher Scientific, A21131	1:500	AlexaFluor 488
Goat anti-Mouse IgG2b	Fisher Scientific, A21141	1:500	AlexaFluor 488

The coverslips were then washed three times with PBSa and 200 µl 4',6-diamidino-2-phenylindole (DAPI, Merck, D9542) diluted 1 in 10,000 in Molecular-Grade water (Merck, W4502) was added for 4 min to stain the nuclei. Coverslips were then washed with Molecular-Grade water and removed from the cell culture plate and mounted onto glass slides using Vectashield® Antifade Mounting Medium (Vector Laboratories, H-1000-10). Coverslips were sealed with nail varnish and stored in fridge until visualisation using a Leica SP5 confocal microscope. Single-plane images were generated using the Leica LAS Software.

2.21. Electron Microscopy (EM)

EM analysis was performed by Nicole Doyle, The Pirbright Institute. The method used has been detailed previously (190).

CK cells were seeded onto round plastic coverslips in a 24-well plate (Scientific Laboratory, 353047). Cells were mock infected or infected with IBV, at various timepoints post infection the media was removed from cells and 1 ml of fixature was added to the cell.

Cells were fixed with 2 % glutaraldehyde for 1 h at 8-, 16- and 24-hpi. The fixative solution was provided by the Bioimaging Service, The Pirbright Institute.

2.22. Immunoprecipitation for Mass Spectrometry

2.22.1. Immunoprecipitation

PureProteome Protein A/G magnetic beads (Merck, LSKMAGAG) were added to a 1.5 ml tube washed in 500 µl PBSa for 10 sec. One tube was prepared per immunoprecipitation sample and 35 µl of magnetic beads were added per tube. The tubes were placed into a magnetic stand to capture the beads allowing for the removal of the PBSa. This wash step was repeated once before 2 µl of capture antibody (Anti-E, AF12, Table 2.13/ 2.15) was added. The beads were incubated with the antibody for 30 min at room temperature with continuous mixing. The tube was returned to the magnetic stand and the unattached antibody was removed. The beads were washed three times using 500 µl PBSa to facilitate removal of the unbound antibody, wash step detailed above. The cell lysate sample (50 µl) was added to the magnetic beads with immobilised antibody. The tubes were incubated at 4 °C overnight with continuous mixing. The magnet was re-engaged, and the sample was removed. The beads were washed three times in PBSa for 10 sec per wash, as detailed above.

To carry out denaturing elution, 60 µl of Laemmeli sample buffer (4X) (Biorad, 1610747) containing BME (Merck, M6250) was added to the beads. Tubes were heated at 70 °C for 10 min. The magnet was re-engaged to allow for the supernatant which contains the eluted beads to be transferred to a new tube.

For mass spectrometry analysis the beads were left in a small volume of the final PBSa wash to be eluted during the mass spectrometry technique.

2.22.2. Western Blot (WB)

Immunoprecipitated samples were eluted using the denaturing elution buffer. To ensure that the E antibody immunoprecipitation had been successful a WB was carried out using the protocol listed in Section 2.19.3.

2.22.3. Silver Stain

Silver stain was carried out to assess the amount of protein obtained from the co-immunoprecipitation (co-IP). This assay was performed with the Pierce Silver Stain Kit (Fisher Scientific, 24612), following the manufacturer's protocol.

The denatured pull-down samples were run on an SDS-PAGE gel (Section 2.19.2). Upon resolution the gels were washed twice in Molecular-Grade water (Merck, W4502) with constant agitation for 5 min per wash. A fixing solution containing 30 % ethanol (VWR International, 20821.321) and 10 % acetic acid (Merck, 33209-M) was prepared. The gel was fixed through two incubations with the fixing solution for 15 min per incubation. The fixing solution was removed from the gels through washing twice in 10 % ethanol (VWR International, 20821.321) for 4 min per wash and then twice in Molecular-Grade water (Merck, W4502) for 5 min per wash. The sensitizer solution was prepared from 50 µl of the sensitizer working solution provided in the Pierce Silver Stain Kit (Fisher Scientific, 24612) with 25 ml of Molecular-Grade water (Merck, W4502). The gel was sensitised for 1 min using the prepared sensitizer solution which was then removed through two wash steps with Molecular-Grade water (Merck, W4502) for 1 min per wash. The stain working solution was prepared from 0.5 ml Enhancer solution and 25 ml stain which were both provided within the Pierce Silver Stain Kit (Fisher Scientific, 24612). The stain solution was added to the gel for 30 min to stain the gel. The developer working solution was prepared using 0.5 ml enhancer solution and 25 ml of developer solution, both solutions were provided within the Pierce Silver Stain Kit (Fisher Scientific, 24612). The gel was

washed twice in Molecular-Grade water (Merck, W4502) for 20 sec per wash and then the gel was developed for 2-3 min until the bands appeared. The stop solution which contained 5 % acetic acid (Merck, 33209-M) in ultrapure water (Merck, W4502) was added for 10 min to prevent the further exposure of the bands. Gels were imaged using a digital camera.

2.23. Mass Spectrometry

The mass spectrometry analysis was carried out by the Proteomic Department at the University of Bristol, following the provided protocol detailed below. The below protocol was written by Kate Heesom, University of Bristol.

2.23.1. TMT Labelling and High pH Reversed-Phase Chromatography

Immunoprecipitated samples generated following the protocol in Section 2.21.1 were reduced through incubation with 10 mM Tris(2-carboxyethyl) phosphine hydrochloride (TCEP) for 1 h at 55 °C. The beads were then alkylated using 18.75 mM iodoacetamide at room temperature for 30min. The peptides were digested from the beads through overnight incubation with trypsin at 37 °C.

Digested peptides were then labelled with Tandem Mass Tag (TMTpro) sixteen plex reagents according to the manufacturer's protocol (Thermo Fisher Scientific). The labelled samples were pooled and desalted using a SepPak cartridge according to the manufacturer's instructions (Waters, Milford). Eluted samples from the SepPak cartridge were evaporated to dryness and resuspended in Buffer A (20 mM ammonium hydroxide, pH 10) prior to fractionation by high pH reversed-phase chromatography using an Ultimate 3000 liquid chromatography system (Thermo Scientific). Each of the samples were loaded onto an XBridge BEH C18 Column (130Å, 3.5 µm, 2.1 mm X 150 mm, Waters, UK) in buffer A and peptides were eluted

with an increasing gradient of buffer B (20 mM Ammonium Hydroxide in acetonitrile, pH 10) from 0-95 % over 60 min. The resulting fractions (6 in total) were evaporated to dryness and resuspended in 1 % formic acid prior to analysis by nano-LC MSMS using an Orbitrap Fusion Lumos mass spectrometer (Thermo Scientific).

2.23.2. Nano-LC Mass Spectrometry

High pH RP fractions were further fractionated using an Ultimate 3000 nano-LC system in line with an Orbitrap Fusion Lumos mass spectrometer (Thermo Scientific). Peptides in 1 % (vol/vol) formic acid were injected onto an Acclaim PepMap C18 nano-trap column (Thermo Scientific). After washing with 0.5 % (vol/vol) acetonitrile 0.1 % (vol/vol) formic acid peptides were resolved on a 250 mm × 75 μm Acclaim PepMap C18 reverse phase analytical column (Thermo Scientific) over a 150 min organic gradient, using 7 gradient segments (1-6 % solvent B over 1 min., 6-15 % B over 58min., 15-32 % B over 58 min., 32-40 % B over 5 min., 40-90 % B over 1 min., held at 90 % B for 6 min and then reduced to 1 % B over 1 min.) with a flow rate of 300 nl min−1. Solvent A was 0.1 % formic acid and Solvent B was aqueous 80 % acetonitrile in 0.1 % formic acid. Peptides were ionized by nano-electrospray ionization at 2.0 kV using a stainless-steel emitter with an internal diameter of 30 μm (Thermo Scientific) and a capillary temperature of 300 °C.

All spectra were acquired using an Orbitrap Fusion Lumos mass spectrometer controlled by Xcalibur 3.0 software (Thermo Scientific) and operated in data-dependent acquisition mode using an SPS-MS3 workflow. FTMS1 spectra were collected at a resolution of 120 000, with an automatic gain control (AGC) target of 200 000 and a max injection time of 50 ms. Precursors were filtered with an intensity threshold of 5000, according to charge state (to include charge states 2-7) and with monoisotopic peak determination set to Peptide. Previously interrogated precursors were excluded using a dynamic window (60s +/-10 ppm). The MS2 precursors were isolated with a quadrupole isolation window of 0.7 m/z. ITMS2 spectra were collected

with an AGC target of 10 000, max injection time of 70 ms and CID collision energy of 35 %.

For FTMS3 analysis, the Orbitrap was operated at 50,000 resolution with an AGC target of 50 000 and a max injection time of 105 ms. Precursors were fragmented by high energy collision dissociation (HCD) at a normalised collision energy of 60 % to ensure maximal TMT reporter ion yield. Synchronous Precursor Selection (SPS) was enabled to include up to 10 MS2 fragment ions in the FTMS3 scan.

2.23.3. Data Analysis

The raw data files were processed and quantified using Proteome Discoverer software v2.4 (Thermo Scientific) and searched against the UniProt *Gallus gallus* database (downloaded February 2022: 34751 entries) and a list of the IBV proteins using the SEQUEST HT algorithm. Peptide precursor mass tolerance was set at 10 ppm, and MS/MS tolerance was set at 0.6 Da. Search criteria included oxidation of methionine (+15.995 Da), acetylation of the protein N-terminus (+42.011 Da) and Methionine loss plus acetylation of the protein N-terminus (-89.03 Da) as variable modifications and carbamidomethylation of cysteine (+57.0214) and the addition of the TMTpro mass tag (+304.207) to peptide N-termini and lysine as fixed modifications. Searches were performed with full tryptic digestion and a maximum of 2 missed cleavages were allowed. The reverse database search option was enabled, and all data was filtered to satisfy false discovery rate (FDR) of 5 %.

Data analysis was carried out using the Perseus software and figures were generated using Cytoscape Software.

2.24. Pathogenicity Trial *In Vivo*

To assess whether M41K-T16A-2.6 was pathogenic within 8-day old SPF RIR chickens, 15 chickens were randomly assigned (indiscriminate of sex) to each group.

Groups B and D were assigned to different viruses. The groups included were as follows:

- Group A: Mock infected with PBS
- Group C: M41K-T16A-2.6 infected
- Group E: M41-K infected

Birds were housed in raised floor pens, with effective enrichment and each group housed in individual rooms. Husbandry was carried out by the Animal Services department at The Pirbright Institute. An overview of the experiment timeline is detailed in Chapter 6, Figure 6.5.

2.24.1. Serum Collection from Chickens

Serum was collected via wing prick from birds one day prior to inoculation. During post-mortem (P-M), blood was collected from each bird. Serum was collected from birds at 14 days post infection (dpi). To obtain the serum, blood was allowed to clot through storage at 4 °C for 1 h. Centrifugation at 270 x g for 5 minutes was utilised to clarify the red blood cells from the serum. Serum was transferred to a new tube and stored at -20 °C.

2.24.2. Inoculation of Chickens

At seven days of age SPF RIR chickens were inoculated via the intraocular and intranasal route with 0.1 ml of PBS (mock), M41-K or M41K-T16A-E-2.6 at a titre of 10^4 PFU. Virus was diluted in PBS.

2.24.3. Clinical Signs

Clinical signs were evaluated from 3-, 7- and 14-dpi by at least two individual assessors. The clinical signs which were assessed included snicking, wheezing, rales, watery eyes, and nasal discharge. To assess the amount of snicking, birds

were observed for 2 min and the number of snicks were counted by each person, from which an average was calculated.

2.24.4. Post-Mortem (P-M) of Chickens

On days 4-, 6- and 14-dpi 5 birds were culled at random, and seven tissues were extracted at P-M. These tissues include trachea, eyelid, beak, lung, bursa, spleen, and kidney. Tissues were stored at -80 °C in either PBS or RNAlater (Life Technologies, AM7021).

TOCs were generated from the trachea collected during the P-M and were sliced into ten 1 mm rings. Three rings from the upper, four from the middle and three from the lower section of the trachea were analysed using a light microscope to assess the level of ciliary activity. The scoring system used was as described in Section 2.16.2.

The ten rings of trachea used for ciliary activity, eyelids and beak were homogenised via six min at 27 Hz in 500 µl in PBS containing antibiotics (P/S, Fisher Scientific, 11548876) and fungicide (Nystatin, Merck, N1638). The total RNA was extracted (Section 2.6) and viral presence was determined via RT-PCR and sequencing over the E gene to ensure the correct sequence was present (Sections 2.7 and 2.8).

Chapter 3: The Genetic Stability, Replication Kinetics and Cytopathogenicity of Recombinant Avian Coronaviruses with a T16A or an A26F Mutation within the E Protein Is Cell-Type Dependent

3.1. Declaration

The results for this chapter consist of a research article (191). My contribution to this article consisted of experimental planning, generation of experimental data as detailed below, data analysis and preparation of the original manuscript. I also submitted the research article and aided in replying to the reviewers' comments. To clarify my contribution in terms of data generation, I generated the rIBV BeauR-A26F isolates using the reverse genetics system. The rIBV BeauR-T16A was generated prior to the start date of this project by Sarah Keep and Jamie Stuart. I performed all characterisation of the rIBVs, aside from the following exceptions. The NGS data was obtained and analysed by Graham Freimanis and some of the qPCR reactions were performed by Kieran Littolff. The resulting data from the qPCR was analysed by

myself. Copyright information can be found in the Appendix (Appendix 8.1, Figure 8.1).

3.2. Introduction

The E protein of IBV has pleiotropic roles during IBV infection. Mutation at either the T16A or A26F residues in the TMD has been shown to alter the function of the E protein (84, 113, 142) and abolish IC activity (20, 152). To further characterise the effect of these mutations in a range of cell systems, rIBVs were generated in a Beau-R backbone which possess either a T16A or A26F mutation, denoted BeauR-T16A and BeauR-A26F. The viruses were generated using a vaccinia virus based reverse genetics system (24, 179, 180). The inserted sequences for the BeauR-T16A and BeauR-A26F rIBVs can be found in Chapter 8, Section 8.2, Figures 8.3 and 8.5.

Four isolates were rescued for BeauR-T16A and three isolates were rescued for BeauR-A26F. Post-rescue, these viruses were coded with two numbers representing the rVV stock and rescue attempt. In the research article included as the results section of this chapter, these names were altered for clarity. There are four isolates of BeauR-T16A, 3.4 (1), 3.6 (2), 4.7 and 4.9 (3). BeauR-T16A-4.7 was not included in the publication as there was no available NGS data to confirm that there were no mutations present in other regions of the genome. There are three BeauR-A26F isolates, 11.2 (1), 11.3 (2) and 12.3 (3).

3.3. Results

The results section of this chapter is contained within the following research article:

Webb I, Keep S, Littolff K, Stuart J, Freimanis G, Britton P, Davidson AD, Maier HJ, Bickerton E. The Genetic Stability, Replication Kinetics and Cytopathogenicity of Recombinant Avian Coronaviruses with a T16A or an A26F Mutation within the E Protein is Cell-Type Dependent. Viruses. 2022; 14(8):1784. doi: 10.3390/v1408178.

viruses

MDPI

Article

The Genetic Stability, Replication Kinetics and Cytopathogenicity of Recombinant Avian Coronaviruses with a T16A or an A26F Mutation within the E Protein Is Cell-Type Dependent

Isobel Webb [1,2], Sarah Keep [1], Kieran Littolff [1], Jamie Stuart [1], Graham Freimanis [1], Paul Britton [1], Andrew D. Davidson [2], Helena J. Maier [1] and Erica Bickerton [1,*]

[1] The Pirbright Institute, Woking GU24 0NF, UK
[2] School of Cellular and Molecular Medicine, Faculty of Life Sciences, The University of Bristol, Bristol BS8 1TH, UK
* Correspondence: erica.bickerton@pirbright.ac.uk

Abstract: The envelope (E) protein of the avian coronavirus infectious bronchitis virus (IBV) is a small-membrane protein present in two forms during infection: a monomer and a pentameric ion channel. Each form has an independent role during replication; the monomer disrupts the secretory pathway, and the pentamer facilitates virion production. The presence of a T16A or A26F mutation within E exclusively generates the pentameric or monomeric form, respectively. We generated two recombinant IBVs (rIBVs) based on the apathogenic molecular clone Beau-R, containing either a T16A or A26F mutation, denoted as BeauR-T16A and BeauR-A26F. The replication and genetic stability of the rIBVs were assessed in several different cell types, including primary and continuous cells, ex vivo tracheal organ cultures (TOCs) and in ovo. Different replication profiles were observed between cell cultures of different origins. BeauR-A26F replicated to a lower level than Beau-R in Vero cells and in ovo but not in DF1, primary chicken kidney (CK) cells or TOCs. Genetic stability and cytopathic effects were found to differ depending on the cell system. The effect of the T16A and A26F mutations appear to be cell-type dependent, which, therefore, highlights the importance of cell type in the investigation of the IBV E protein.

Keywords: avian coronavirus; cell type; envelope protein; chicken; viroporin

Citation: Webb, I.; Keep, S.; Littolff, K.; Stuart, J.; Freimanis, G.; Britton, P.; Davidson, A.D.; Maier, H.J.; Bickerton, E. The Genetic Stability, Replication Kinetics and Cytopathogenicity of Recombinant Avian Coronaviruses with a T16A or an A26F Mutation within the E Protein Is Cell-Type Dependent. *Viruses* **2022**, *14*, 1784. https://doi.org/10.3390/v14081784

Academic Editors: Shengwang Liu, Huixin Li and Xin Zhang

Received: 20 July 2022
Accepted: 11 August 2022
Published: 15 August 2022

1. Introduction

Coronaviruses (CoVs) are a highly diverse family of enveloped viruses with large positive-sense single-stranded RNA genomes that belong to the order *Nidovirales*, suborder *Coronavirinae*, family *Coronaviridae*, subfamily *Orthocoronavirinae*. Within the subfamily, there are four genera, *Alphacoronavirus*, *Betacoronavirus*, *Gammacoronavirus* and *Deltacoronavirus*. In humans, the *Alphacoronavirus* human coronavirus (HCoV) 229E and related coronaviruses are responsible for 18% of common cold cases [1]; however, infection with the *Betacoronaviruses* severe acute respiratory syndrome CoV (SARS-CoV), severe acute respiratory syndrome CoV-2 (SARS-CoV-2) and Middle East respiratory syndrome coronavirus (MERS-CoV) can lead to more serious respiratory disease that can result in mortality [2–4]. In animals, the *Deltacoronavirus* porcine deltacoronavirus (PDCoV), which was first identified in 2012 [5], causes enteric disease within pigs [6]. Infectious bronchitis virus (IBV) is the prototype *Gammacoronavirus* and causes the highest direct disease costs to the poultry industry within the UK and across the globe [7]. IBV infects the epithelial surfaces within the trachea, oviduct and kidney of poultry and can cause clinical signs ranging from mild respiratory signs, including snicking and tracheal rales, to severe kidney and oviduct disease [8]. As a result, it reduces egg production and quality in layers, causes reduced

weight gain in broilers and leaves chickens vulnerable to secondary bacterial infections which may be fatal [9].

The IBV genome, similarly to all other CoVs, encodes four structural proteins: Spike (S), Nucleocapsid (N), Membrane (M) and Envelope (E) [10]. The CoV E protein is a small ~12 kDa protein, present in low quantities in the viral envelope [11]. The IBV E protein is present in two distinct forms during infection: monomeric and pentameric [12]. These two separate forms are thought to have different roles during infection. The monomer interacts with cellular proteins to alter the secretory pathway, and the pentamer forms an ion channel (IC) in planar lipid bilayers with low or poor selectivity [13]; viral proteins, which act as ICs, are described as viroporins. Prior studies have proposed roles for CoV E proteins in assembly [12,14,15], viral release [16–18] and pathogenesis [19–21]. CoVs assemble and bud intracellularly at the ER-Golgi intermediate compartment (ERGIC), and it has been reported during IBV infection that the majority of E remains localised in the membranes of the Golgi complexes [22]. Research suggests that both M and E proteins of IBV are required for viral budding and the formation of the viral envelope, as both E and M are reported to be necessary for the formation of virus-like particles (VLPs) [23]. Additionally, the E protein is thought to facilitate scission, as mutations introduced into the E protein of the *Betacoronavirus* mouse hepatitis virus (MHV) resulted in elongated virions [14]. The role of the E protein in pathogenesis is thought to be facilitated by the C-terminal domain, which has been shown in SARS-CoV to cause the overexpression of inflammatory cytokines [21].

The first discovered viroporin was found within the encephalomyocarditis (EMC) virus, as it was able to induce membrane permeability within infected cells [24], an activity identified for the SARS-CoV E protein [25]. Mutations generated either at residue N15 or V25 within the transmembrane domain of the SARS-CoV E protein abolish IC activity [26]. Mutation of equivalent residues in IBV, T16 and A26 reportedly caused the same effect [16], and the effect of these mutations has been predominantly characterised within continuous cell lines that are not relevant to IBV natural infection. The V25 residue of the SARS-CoV E protein is located between the monomer–monomer interface of the E homo-pentamer [20]. Mutation of the corresponding A26 residue in the IBV E protein prevents homodimerisation [12], this residue is required for the formation of VLPs [12]. The T16 residue forms the monomeric IBV E protein [12], a T16A mutation at this residue has been shown to prevent the disassembly of the Golgi [12,27] and cause premature cleavage of the S protein [28]. A separate study, however, proposed that it is the T16 residue and not A26 which is essential for homodimerisation [16]. Regardless, recombinant SARS-CoV containing the N15A mutation resulted in reduced clinical signs in mice, indicating that the E protein is a virulence factor and a target for vaccine development [20].

In this study, we characterised the effect of the two mutations, T16A and A26F, on the replication of IBV in cell systems relevant to IBV natural infection, including primary chicken kidney (CK) cells and ex vivo tracheal organ cultures, with the aim of determining whether the T16 and A26 residues were vital for IBV replication. Using a vaccinia virus-based reverse genetics system [29], we generated recombinant IBVs (rIBVs) based on the apathogenic molecular clone, Beau-R, that contained either the mutation T16A or A26F within the E protein. The replication of the rIBVs was assessed in continuous cell lines Vero and DF1, primary CK cells, and in ovo and in ex vivo tracheal organ cultures (TOCs). Different replication profiles were observed between cell cultures of different origins. The genetic stability of the mutations was also assessed in CK cells and in ovo and was also found to differ depending on the cell system. This report furthers previous research and the current understanding of E protein in IBV replication through the characterisation of the rIBVs in relevant cell systems to IBV natural infection and highlights the cell-dependent effect of the T16A and A26F mutations.

2. Materials and Methods

2.1. Cells and Viruses

All cells were provided by the Central Services Unit at the Pirbright Institute. The cell cultures were maintained within incubators set at 37 °C with 5% carbon dioxide (CO_2). Primary CK cells were extracted from 2–3 week old specific pathogen-free (SPF) Rhode Island Red (RIR) chickens following a previously described protocol [30]. DF1 cells are a continuous avian cell line of chicken embryo fibroblasts derived from 10-day-old East Lansing eggs [31]. Vero cells are a continuous cell line derived from kidney epithelial cells of the African green monkey. Embryonated VALO hens' eggs were sourced from VALO BioMedia GmbH. TOCs were generated from trachea extracted from 19-day-old SPF embryos using a method previously described [32].

The rIBV Beau-R has been described previously [29]. Beau-R is a molecular clone of the non-pathogenic IBV strain Beau-CK (GenBank Accession number AJ311317). Beau-R was propagated in 10-day-old SPF embryonated hens' eggs, and allantoic fluid was harvested 24 hours (h) post infection (hpi) and clarified using low-speed centrifugation. All genome positions are in relation to GenBank accession number AJ311317.

2.2. Construction of rIBVs Containing the T16A and A26F Mutations

Two individual point mutations were generated within rIBV Beau-R using an established vaccinia-virus-based reverse genetics system [29,33]. The T16A mutation was created via a single nucleotide mutation A24246G and A26F was generated through three-point mutations from 24276 to 24278, changing the nucleotide sequence from GCA to TTT. These mutations are identical to those generated within a Beaudette backbone, which were described as IC inactive, but the conductivity data was not shown [16]. Three isolates, denoted as 1, 2 or 3, of each rIBV were successfully rescued and were passaged in primary CK cells. Viral stocks were propagated within primary CK cells with the supernatant harvested at 24 hpi.

2.3. Full Genome Sequencing of Viral Stocks

BeauR-T16A and BeauR-A26F, 4 mL of each isolate, were concentrated using a 30% sucrose cushion and ultracentrifugation for 1 h at 223,600× *g*—as described [34]. RNA was extracted from the resulting pellet using a Qiagen RNeasy mini kit following the manufacturer's protocol. The RNA concentration was quantified using the Qubit fluorometer RNA Assay HS kit. Next Generation Sequencing (NGS) was carried out by the Sequencing Unit at The Pirbright Institute, following a method detailed previously [35].

2.4. Titration of IBV via Plaque Assay and Quantification of Plaque Size

Plaque assays were carried out using CK cells as previously described [36]. All samples were titrated in triplicate. Plaque sizes were measured from ten plaques per biological repeat using NIH ImageJ software [37], totalling 30 plaques per virus.

2.5. Assessment of Viral Release

CK or Vero cells were seeded into 6-well plates to confluency. Cells were infected with 500 µL of Beau-R, BeauR-T16A or BeauR-A26F isolates at a titre of 1×10^4 plaque forming units (PFU) and incubated for 1 h at 37 °C with 5% CO_2. After incubation, the inoculum was removed, and the cells were washed twice with PBS, followed by the addition of 3 mL of N, N-bis [2-hydroxethy1]-2-aminoethanesulfonic acid (BES) media [33]. At 24 hpi, the supernatant was removed from the cells and stored at −80 °C. The plates were washed once with PBS, and 1 mL of BES media was added to the cells before the plates were freeze-thawed to release the virus (cell lysate). The quantity of infectious progeny in both the harvested supernatant and cell lysate was determined in triplicate via plaque assay in CK cells.

2.6. Viral Replication Kinetics Assessment In Vitro

Confluent CK, DF1 or Vero cells, seeded in 6-well plates were infected with 500 µL of Beau-R, BeauR-T16A or BeauR-A26F isolates at a titre of either 1×10^4 or 1×10^5 PFU and incubated at 37 °C for 1 h with 5% CO_2. The virus was removed, and the cells were washed twice with PBS followed by the addition of 3 mL BES media. The supernatant containing the infectious progeny was harvested at either 1, 24, 48, 72 and 96 hpi, to establish replication over multiple rounds of viral replication, or at 1, 2, 4, 6, 8, 10 and 11 hpi, to assess replication over the first round of viral replication. The quantity of infectious progeny was quantified in triplicate via plaque assay in CK cells.

2.7. Ciliary Activity Assessment in Ex Vivo TOCs

TOCs, singly plated in glass tubes, were washed twice with PBS. In replicates of ten, each TOC was inoculated with 500 µL TOC infection medium [30], containing 1×10^4 PFU of Beau-R, BeauR-T16A or BeauR-A26F isolates. Mock infected TOCs were inoculated with 500 µL TOC medium. Tubes were incubated upright for 1 h at 37 °C, after which the inoculum was removed and the TOCs washed twice with PBS. 1ml of TOC infection media was added per tube, and the TOCs were incubated at 37 °C, 1 revolution per 7 min. The ciliary activity of each TOC was assessed at 24 h intervals using a light microscope, and the percentage of cilia beating was calculated as described [38,39].

2.8. Viral Replication Kinetics Assessment in Ex Vivo TOCs

Six TOCs were plated per glass tube and were washed twice in PBS. Each tube was inoculated with 500 µL TOC infection medium containing 1×10^4 PFU of Beau-R, BeauR-T16A-1, or BeauR-A26F-3. Tubes were incubated upright for 1 h at 37 °C after which the inoculum was removed and the TOCs washed twice with PBS. 1 mL of TOC infection media was added per tube, and the TOCs were incubated at 37 °C, 1 revolution per 7 min. The supernatant from each tube was harvested at 1, 24, 48, 72 and 96 hpi, and the quantity of infectious progeny was quantified in triplicate via plaque assay in CK cells.

2.9. Virus Replication Kinetics In Ovo

A protocol for propagation of IBV in eggs has been described [40]. In replicates of three, 10-day-old SPF embryonated hens' eggs were inoculated via the allantoic cavity with either 1×10^4 or 1×10^5 PFU of either Beau-R, BeauR-T16A or BeauR-A26F isolates. After 24 h, embryos were culled by refrigeration for a minimum of 4 h, and the allantoic fluid from each egg was harvested. The allantoic fluid was clarified using low-speed centrifugation. The quantity of infectious progeny was determined via plaque assay in triplicate in CK cells. The sequence of the E gene was determined as described in Section 2.11.

2.10. Serial Passaging of rIBVs in CK Cells

Confluent CK cells seeded into 6-well plates were washed once with PBS. In replicates of four, 500 µL of BES medium containing neat rIBV was added per well and incubated for 1 h at 37 °C. The inoculum was removed and replaced with 3 mL BES media and incubated for a further 23 h. The supernatant was harvested and diluted 1 in 10 for subsequent inoculation of the CK cells. The E gene of the resulting passaged isolates was Sanger sequenced at passage 5, 10 and 15 as described in Section 2.11.

2.11. Sequencing the E Gene

RNA was extracted from either the cell supernatant or allantoic fluid using the Qiagen RNeasy kit following the manufacturer's protocol for RNA clean up. RNA was reverse transcribed using random primer, 5′ GTTTCCCAGTCACGATCNNNNNNNNNNNNNN 3′ and a SuperScript IV reverse transcription kit following the manufacturer's protocol (Life Technologies). The E gene was amplified using recombinant Taq Polymerase (Life Technologies) using primers 5′-GCTGAAGATTGTTCAGGTGA-3′ and 5′-GCTGAACTGACT

GTTCAAAG-3′. The PCR products were Sanger sequenced by Eurofins, and the resulting sequencing data was analysed using the Staden Package 2.0.0b11.

2.12. Imaging of Cytopathic Effects (CPE)

CK cells seeded into 6-well plates were inoculated with 1×10^5 PFU of Beau-R, BeauR-T16A or BeauR-A26F isolates or mock infected with BES media. At 24 hpi, the inoculated CK cells were imaged with an AMG EVOS^{TM} XL Core microscope.

2.13. Cell Viability Assay

Cells were seeded to confluency in 96-well plates and washed once with PBS prior to inoculation with a two-fold serial dilution, in BES medium, of Beau-R, BeauR-T16A or BeauR-A26F isolates starting at 1×10^5 PFU. Mock infected cells were inoculated with the BES medium. At 24 h intervals, the viability of the cells was assessed using the luciferase assay CellTiter-Glo® kit (Promega), which measures the quantity of ATP present to quantify the number of viable cells following the manufacturer's instructions, detailed in [41]. The percentage of cell viability determined by the level of luminescence was calculated in comparison to the mock infected cells.

2.14. Assessment of Innate Immune Response by Real Time Quantitative PCR (qRT-PCR)

CK cells were seeded to confluency in 6-well plates and were washed once with PBS. Cells were mock infected with BES media or inoculated with 500 µL of Beau-R, BeauR-T16A or BeauR-A26F isolates at a titre of 1×10^5 PFU in BES medium. At 6 and 24 hpi, the cells were harvested, and RNA extracted using the Qiagen RNeasy kit including an on-column DNAse treatment, following the manufacturer's (Qiagen) instructions. Reverse transcription was carried out using 1.25 µg of total RNA using Superscript IV reverse transcription kit according to the manufacturer's protocol using random primer (5′ GTTTCCCAGTCACGATCNNNNNNNNNNNNNN 3′). The resulting cDNA was diluted to ensure 100 µg was added per qRT-PCR reaction. TaqMan qPCR reagents were used to perform qPCR, using either TaqMan ® Fast Advance Master Mix or TaqMan ® Multiplex Mastermix (Life Technologies). Primers were used at 10 µM, and hydrolysis probes were diluted to 5 µM. A GeNorm was carried out and Beta-Actin was selected as an endogenous control; this control has been used in CK cells previously [42]. Sequences for the primers and probes used are listed in Table 1. The qPCR reaction was run on a 7500 Fast Real-Time System following the cycle: 95 °C for 20 s and 40 cycles of 95 °C for 1 s at 60 °C for 20 s.

Table 1. Sequences of primers and probes used within qPCR.

Gene		Sequence (5′ to 3′)
E gene	Forward	GGTAGAGCACTTCAAGCATTT
	Reverse	CCGGATTGTTAAGTTTTCTACC
	Probe	CCAGGAGCTAAGGGTACAGCCT
β-Actin	Forward	GCATACAGATCCTTACGGATATCCA
	Reverse	CAGGTCATCACCATTGGCAAT
	Probe	CACAGGACTCCATACCCAAGAAAGATGGC
IL-6	Forward	GCTCGCCGGCTTCGA
	Reverse	GGTAGGTCTGAAAGGCGAACAG
	Probe	AGGAGAAATGCCTGACGAAGCTCTCCA
IL-1B	Forward	GCTCTACATGTCGTGTGTGATGAG
	Reverse	TGTCGATGTCCCGCATGA
	Probe	CCACACTGCAGCTGGAGGAAGCC
IFN-A	Forward	GACAGCCAACGCCAAAGC
	Reverse	GTCGCTGCTGTCCAAGCATT
	Probe	CTCAACCGGATCCACCGCTACACC
IFN-B	Forward	CCTCCAACACCTCTTCAACATG
	Reverse	TGGCGTGTGCGGTCAAT
	Probe	TTAGCAGCCCACACACTCCAAAACACTG

2.15. Statistical Analysis

The statistical analysis was assessed using GraphPad Prism 8.0. The standard deviation and normality were assessed prior to any statistical analysis.

3. Results

3.1. The Generation of rIBVs Containing Either the T16A or A26F Mutation within the E Protein

The E protein is divided into three domains; a short hydrophilic N terminal domain, a transmembrane domain, which is the focus of this study, and a long hydrophilic C terminal domain [43]. A comparison of the amino acid sequence between a range of IBV strains, representing diverse serotypes as well as genotypes, identified that the sequence of the transmembrane domain of the E is relatively conserved (Figure 1). All IBV strains analysed possessed the residue threonine (T) at amino acid position 16 and alanine (A) at amino acid position 26. The conservation of the amino acid sequence particularly surrounding the T16 and A26 residues highlights that the non-pathogenic laboratory strain, Beau-CK, is a representative IBV strain with regards to the E protein. Therefore, using a vaccinia-virus-based reverse genetics system based on Beau-CK [29], two rIBVs were generated containing individual amino acid changes in the E protein that have been reported to abolish IC activity [16]. The first, denoted by BeauR-T16A, contained a single-point mutation A24246G resulting in the amino acid change T16A. The second rIBV, denoted by BeauR-A26F, contains three-point mutations, GCA to TTT at positions 24276 to 24278, generating the single amino acid change A26F. Both BeauR-T16A and BeauR-A26F were successfully rescued and propagated in primary CK cells. Three isolates of each, from independent rescues, were generated, denoted by BeauR-T16A 1, 2 or 3 and BeauR-A26F 1, 2 or 3. Viral stocks were generated via passaging three times in CK cells for BeauR-A26F and four times in CK cells for BeauR-T16A. The ability to successfully rescue rIBVs with mutations T16A or A26F within the E protein suggests that these residues are not required for viral replication in vitro. This is in line with earlier reports [16,18].

Figure 1. Alignment showing the amino acid sequence similarity between IBV strains over the transmembrane domain of the E protein, highlighted in red. Amino acid sequence alignment over the E protein of different strains of IBV, showing the T16 and A26 residue present in each strain highlighted in yellow. The accession number of strains included were Beau-CK (CAC39117.1), M41-CK (QCE31536.1), QX (ARI46255.1), H120 (UQM93960.1), CR88 (QKV27915.1), UK/68/84 (P30247.1), UK/183/66 (P30248.1), Portugal/322/82 (P30246.1), KB8523 (P19744.1), Italy02 (QKV27954.1), Ind/TN92/03 (YP_009825001), D1466 (QKV27928.1), California/99 (AAS00083), B1648 (ALH21114) and Ark99 (AAX39774). The alignment was assembled on Mega11 using the MUSCLE alignment tool, * represents conserved amino acid.

3.2. Next-Generation Sequencing Identified an Additional Mutation in One Isolate of BeauR-T16A and One Isolate of BeauR-A26F

Complete genome sequences of the three isolates representing rIBVs BeauR-T16A and BeauR-A26F were assembled using NGS technologies. Consensus genomic sequences generated from stock viruses of all three isolates of both BeauR-T16A and BeauR-A26F were assembled and compared to the Beau-CK reference sequence (GenBank Accession number AJ311317). The stocks of BeauR-T16A and BeauR-A26F were generated at passages 4 and 3 in CK cells, respectively. In all isolates of both BeauR-T16A and BeauR-A26F, the

consensus sequences generated confirmed the presence of the mutations T16A and A26F, respectively (Table 2). In BeauR-T16A-2, a synonymous mutation, T13658C, was identified in nsp12. One synonymous mutation in BeauR-A26F-2, T2628C, was identified within nsp3. As the NGS analysis was carried out on viruses that had been passaged, it cannot be determined whether the additional mutations identified arose during the rescue process or the passaging for viral stock generation.

Table 2. NGS sequence data showed either T16A or A26F mutations were present at consensus level within rIBVs.

rIBV	Isolate	Position	Ref. nt	Alt. nt	Depth	Freq. (%)	Aa	Gene
BeauR-T16A	1	24246	A	G	22067	87.3023	T16A	E
	2	**13658**	**T**	**C**	**528**	**92.803**	**Y451Y**	**Nsp12**
		24246	A	G	16849	93.0382	T16A	E
	3	24246	A	G	18270	94.4773	T16A	E
BeauR-A26F	1	24276	G	T	8184	99.6823	A26F	E
		24277	C	T	8052	99.6398	A26F	E
		24278	A	T	8071	99.5787	A26F	E
	2	**2628**	**T**	**C**	**464**	**54.9569**	**C29C**	**Nsp3**
		24276	G	T	20386	99.6566	A26F	E
		24277	C	T	20457	99.6432	A26F	E
		24278	A	T	20603	99.6408	A26F	E
	3	24276	G	T	18670	99.6358	A26F	E
		24277	C	T	18857	99.6288	A26F	E
		24278	A	T	18639	99.6083	A26F	E

Notes: BeauR-T16A and BeauR-A26F stocks used to generate this sequence data were at passages 4 and 3 in CK cells, respectively. Nucleotide positions listed are in relation to the Beau-CK genome (GenBank accession number AJ311317). The "Ref. nt" column shows the nucleotide present at that position within Beau-R, and the "Alt. nt" column represents the different nucleotide present within the isolate. The depth shows the number of reads over the position of the mutation, and the allele frequency is the percentage of reads which contained the altered nucleotide. Consensus-level mutations listed were determined by a percentage within the population (% population) of above 50%. Mutations present in other regions of the genome are shown in bold.

3.3. T16 and A26 Residues within the E Protein Are Not Essential for Virus Replication In Vitro

The replication of all isolates of BeauR-T16A and BeauR-A26F were investigated in primary CK cells (Figure 2A,B). All the rIBVs exhibited largely comparable replication to the parental Beau-R from 8–11 hpi and from 24–96 hpi, although some minor differences were observed. The titres of Beau-R were higher than all isolates of BeauR-A26F at 72 hpi (Figure 2B), and, interestingly, BeauR-T16A-3 exhibited lower titres than both the other BeauR-T16A isolates and Beau-R (Figure 2).

The Beaudette strain of IBV has extended cell tropism [44,45]. The replication of the rIBVs was, therefore, also assessed in DF1 cells, an avian cell line derived from chicken embryo fibroblasts [31] and in Vero cells. Vero cells are a mammalian cell line derived from an African green monkey, and, although not directly relatable to natural infection of chickens, they are used for IBV research due to the easier availability of reagents and additionally are of interest as they are licenced for vaccine manufacturing [46,47]. Replication of all three isolates of BeauR-T16A was found to be comparable to Beau-R in both Vero and DF1 cells (Figure 2). Isolates of BeauR-A26F showed comparable replication to Beau-R in DF1 cells (Figure 2C) but not within Vero cells (Figure 2D). In this experiment it must be noted that the replication of the Beau-R control reached almost 10^9 PFU, which, although unusual, has previously been observed [45]. The reduced replication of BeauR-A26F in Vero cells but not DF1 or CK cells, may suggest that the effect of the A26F mutation is dependent on cell type.

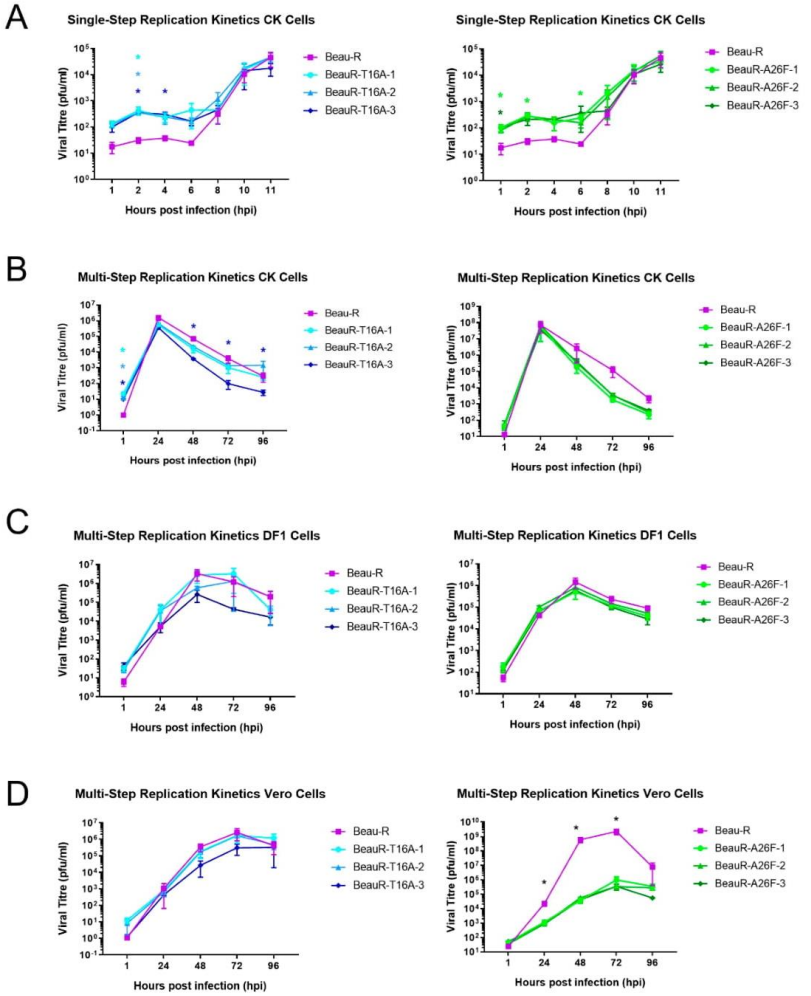

Figure 2. Replication kinetics of rIBVs differ between cell type. (**A**) Single-step replication kinetics of rIBVs in CK cells. (**B**) Multi-step replication of rIBVs in CK cells. (**C**) Multi-step replication kinetics of rIBVs in DF1 cells. (**D**) Multi-step replication kinetics of rIBVs in Vero cells. CK, Vero or DF1 cells were infected at a titre of 1×10^4 PFU (MOI~0.008) for isolates of BeauR-T16A and 1×10^5 (MOI~0.08) for isolates of BeauR-A26F. For multi-step replication kinetics, the supernatant was harvested at 1, 24, 48, 72 and 96 hpi. For single-step replication kinetics, the supernatant was harvested at 1, 2, 4, 6, 8, 10 and 11 hpi. Supernatant was titrated in triplicate on CK cells to determine the quantity of progeny virus. Error bars represent ± standard error of the mean (SEM) of three independent experiments. Statistical analysis was carried out using a two-way analysis of variance (ANOVA), with significance taken at p-value of <0.05, significance is represented with a * in relation to Beau-R and for (**A**,**B**) significance is represented with a * with different colours corresponding to the different isolates.

3.4. BeauR-T16A and BeauR-A26F Exhibit Reduced Plaque Size in CK Cells

Beaudette rIBVs containing either the T16A or A26F mutations showed reduced plaque size in comparison to WT in Vero cells [18]. Conversely, earlier work by the same

group, also in Vero cells, found that the plaque size for the rIBVs containing either the T16A or A26F mutations was comparable to WT [16]. The plaque morphology and size exhibited by all isolates of BeauR-T16A and BeauR-A26F were therefore assessed in chicken cells, specifically primary CK cells and compared to Beau-R (Figure 3). Whilst the plaque morphology appeared comparable, the diameters of the plaques generated by all isolates of BeauR-T16A and BeauR-A26F were smaller than that of Beau-R. This reduction in plaque size may suggest impaired viral spread for viruses with T16A or A26F mutations, as previously hypothesised [18].

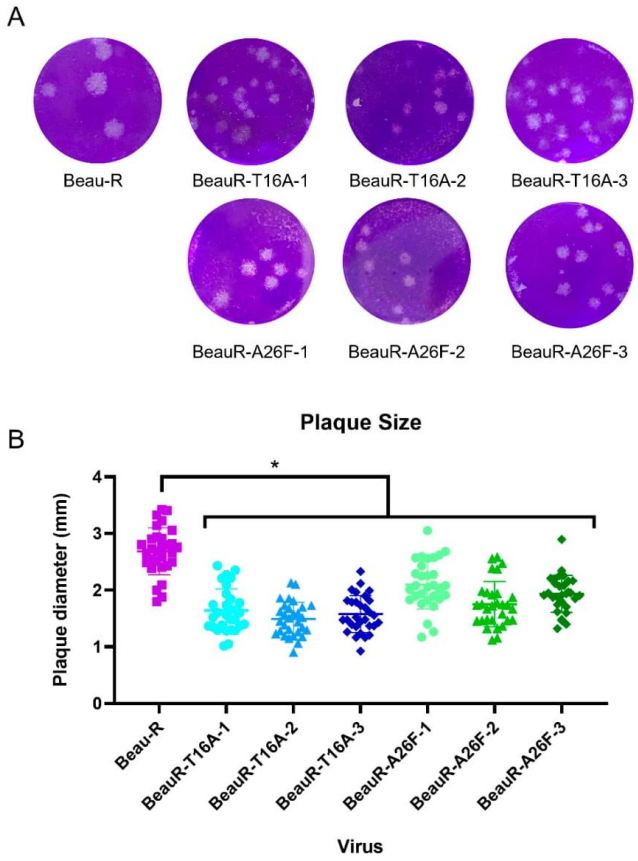

Figure 3. BeauR-T16A and BeauR-A26F exhibit smaller plaque size than parental Beau-R. (**A**) Representative images of plaques formed by each of the rIBVs. (**B**) Plaque diameter measured using ImageJ software with 30 plaques counted per virus, 10 plaques were counted per biological repeat. Error bars represent the standard deviation (SD) of the 30 different plaque sizes. Statistical analysis was carried out using a one-way ANOVA with significance taken as p-value < 0.05, represented as *. Significance shown is in relation to Beau-R.

3.5. BeauR-A26F May Exhibit Impaired Viral Release within Continuous Cell Lines but Not within CK Cells

To et al. indicated that, in Vero cells, the T16A and A26F mutations impede viral release [16]. Research using HeLa cells also showed that the presence of the A26F mutation results in reduced VLP production [12]. To establish whether the T16A and A26F mutations

impede viral release, and therefore spread, in biologically relevant cells, the cell lysate and supernatant were harvested from virus-infected CK cells at the peak of viral infection, as determined by the peak in titre as observed in Figure 2. The quantities of infectious progeny in the cell lysate and supernatant were assessed (Figure 4A). An increase in the viral titre of the cell lysate in comparison to the supernatant suggests that the infectious progeny is not effectively being released from the cell, therefore implying a deficiency in the release stage of the replication cycle. Vero cells were also investigated to assess whether any cell-type-dependent differences in results occurred (Figure 4B). It must be noted that the peak titres of IBV replication differ between CK and Vero cells with the peaks observed at 24 and 72 hpi, respectively (Figure 2). Supernatant and cell lysate were therefore harvested at 24 hpi for CK cells and 72 hpi for Vero cells. Cells were inoculated with either Beau-R, BeauR-T16A-1 or BeauR-A26F-3. The latter two isolates were chosen, as no differences were observed between the replications of these isolates and the other isolates of either BeauR-T16A or BeauR-A26F, respectively, as shown in Figure 2. Progeny viruses present within the supernatant and cell lysate were quantified by plaque assay. For CK cells, there was no difference in viral titres between the harvested cell lysates or supernatants, suggesting that neither the T16A nor the A26F mutation were impeding viral release (Figure 4A). For Vero cells, however, higher titres of BeauR-A26F were detected in the cell lysate in comparison to the supernatant (Figure 4B). The reduction observed may suggest that, in this cell type, the A26F mutation is affecting viral release and, therefore, may impede viral spread.

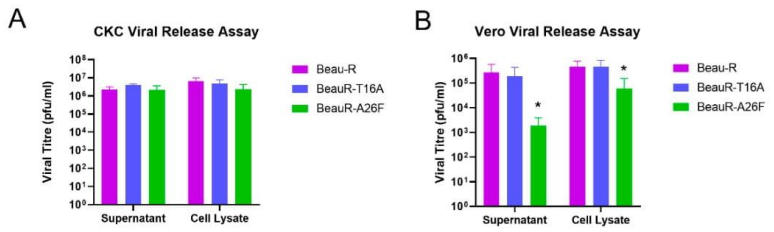

Figure 4. BeauR-A26F exhibits reduced cell release during infection of Vero cells. Confluent (**A**) CK cells and (**B**) Vero cells seeded in 6 well plates were infected at 1×10^4 PFU (MOI~0.008) of either Beau-R, BeauR-T16A-1 or BeauR-A26F-3. Supernatant and cell lysates were harvested at either (**A**) 24 hpi or (**B**) 72 hpi and the quantity of infectious progeny determined via plaque assay in CK cells. Error bars represent ± SEM of three independent experiments. Statistical analysis was carried out using a one-way ANOVA, significance was taken as p-value < 0.05, represented as *. Significance shown in relation to Beau-R.

3.6. Amino Acid Residues T16 and A26 Are Not Essential for Virus Replication in Ex Vivo TOCs

In vivo, IBV replication primarily occurs in ciliated tracheal epithelial cells [8]. TOCs are an ex vivo culture system consisting of sliced tracheal rings prepared from 19-day-old embryos that offer a more representative model for natural infection than traditional cell cultures. Ciliary activity is reduced in the ciliated tracheal cells of the TOCs following infection with IBV, with the complete cessation termed ciliostasis; this reduction occurs during a natural IBV infection [48]. The reduction in ciliary activity caused by IBV in infected chickens is commonly used in both research and industry to determine the presence of pathogenic IBV [32,48] and can be subsequently used as an indicator of the amount of replicating virus. To investigate the effect of the T16A and A26F mutations on IBV induced reduction in ciliary activity, replicates of 10 ex vivo TOCs were inoculated with either BeauR-T16A, BeauR-A26F, Beau-R or mock infected with media only (Figure 5A). The ciliary activity was observed at 24 h intervals and was comparable between both rIBVs and Beau-R, suggesting comparable replication kinetics. To confirm this, one isolate of each rIBV was selected for a replication assay in which the quantity of infectious progeny generated

during the infection of ex vivo TOCs was quantified via titration in CK cells. Although BeauR-A26F appears to have a slightly reduced titre at 96 hpi, statistical significance was not reached (Figure 5B). Replication in ex vivo TOCs is not, therefore, affected by the presence of either the T16A or A26F mutations, suggesting these residues are not required for viral replication in trachea, the site of natural IBV infection.

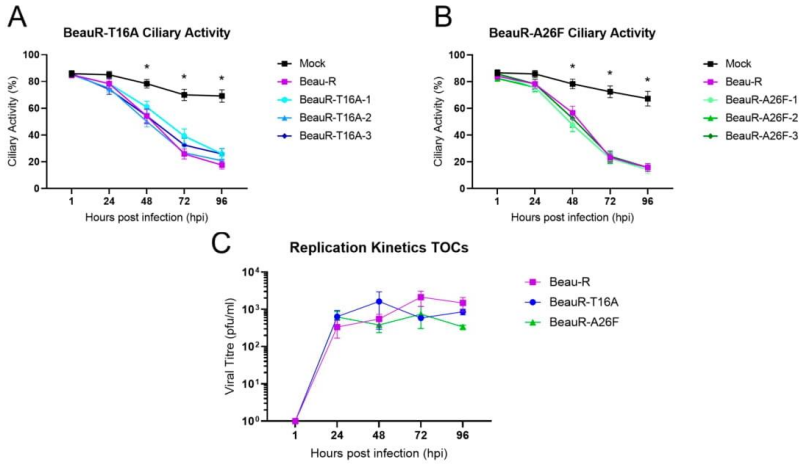

Figure 5. Comparable replication of rIBVs and parental Beau-R in TOCs. (**A**) Ten TOCs were infected with each virus at a titre of 1×10^4 PFU. The ciliary activity was assessed every 24 h from 1 hpi. Each TOC ring was given a score of either 0, 25, 50, 75 or 100% to reflect the proportion of cilia beating at each timepoint. Error bars represent ± SD of three independent experiments. Statistical analysis was carried out using a Friedman test, *p*-value of <0.05 is shown in comparison to mock and indicated by * to represent all viruses. No differences were observed between the rIBVs. (**B**) Six TOCs were infected with viruses at a titre of 1×10^4 PFU. Isolates BeauR-T16A-1 and BeauR-A26F-3 were used for this experiment. Supernatant was harvested over a 96 h time-course every 24 hpi. Virus titre within the supernatant was quantified by titration on CK cells. Error bars represent the ±SEM of three independent experiments. Statistical analysis was carried out using a two-way ANOVA with significance taken as *p*-value of <0.05, no significance was found.

3.7. Both BeauR-T16A and BeauR-A26F Generate Revertant Mutations upon Passage in CK Cells Suggesting a Preference to Retain the T16 and A26 Residues In Vitro

To investigate the genetic stability of both the T16A and A26F mutations, four replicates of Beau-R and the three independent isolates of BeauR-T16A and BeauR-A26F were serially passaged 15 times in CK cells. The E gene of progeny viruses was Sanger sequenced at passages 5, 10 and 15 (Figure 6).

All isolates of BeauR-T16A maintained the T16A mutation at passage 5 and generated no other mutations within the E gene; however, mutations were observed at passage 10 (Figure 6A). A single nucleotide change, G24246A, was observed in all four replicates of BeauR-T16A-1, leading to the reversion of the T16A mutation. In all four replicates of BeauR-T16A-2, the T16A mutation was retained but a C24277T mutation (GCA → GTA) was observed resulting in the amino acid change A26V. One replicate of BeauR-T16A-3 also generated this mutation. The A26V mutation was identified in Vero and DF1 passaged isolates and has been shown to recover IC activity [16]. At passage 15, the BeauR-T16A-1 and BeauR-T16A-2 isolates exhibited the same sequence as at passage 10. Interestingly, the BeauR-T16A-3 isolate showed a different profile in two of the replicates. The replicate which contained the A26V mutation reverted, therefore restoring the original T16A sequence. The replicate which stably maintained the T16A mutation at passage 10 maintained the T16A

but generated an A17V mutation, which has not been described. The pattern of mutations suggests that, although IC activity was observed to not be required for in vitro replication, there may be a preference to retain it.

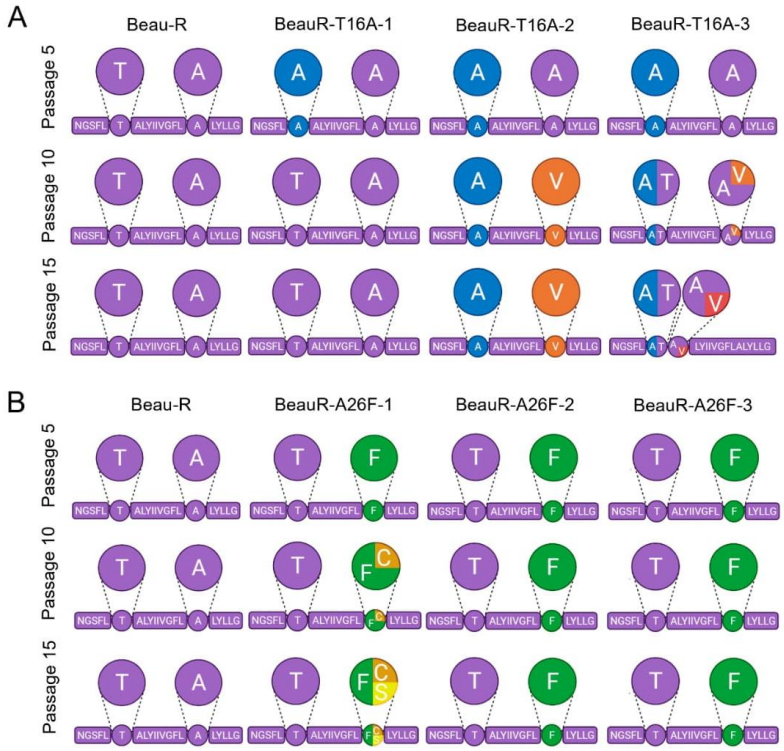

Figure 6. Selective pressure exists to maintain T16 and A26 residues upon passage in CK cells. The transmembrane domain of the E gene is shown, as that is where all mutations were found. The circles highlight the T16 and A26 residues, except in the case of BeauR-T16A-3 at passage 15 in which A17 is highlighted. Larger circles represent a pie chart of the four replicates of each isolate at each passage showing the sequences present. Every 5 passages, the supernatant was harvested, and Sanger sequenced over the E gene to detect any mutations generated. Mock wells did not contain any virus at each round of screening through RT-PCR. (**A**) Four replicates of each isolate of BeauR-T16A virus were passaged alongside Beau-R and media mock wells for 15 passages, diluted 1 in 10 at each round. The Beau-R sequence is shown in purple, T16A mutation is shown in blue, A26V is shown in orange, and A17V is shown in red. (**B**) Four replicates of each isolate of BeauR-A26F were passaged 15 times alongside Beau-R and mock infected wells. Beau-R sequence is shown in purple, the A26F mutation is shown in green, F26C is shown in orange, and F26S is shown in yellow.

The BeauR-A26F isolates showed greater genetic stability than BeauR-T16A. Isolates BeauR-A26F-2 and BeauR-A26F-3 maintained the A26F mutation over all 15 passages and generated no compensatory mutations within the E gene (Figure 6B). BeauR-A26F-1 generated a point mutation at position T24277G to create a F26C mutation in one replicate at passage 10, which has been shown to restore IC activity [16]. At passage 15, the BeauR-A26F-1 replicate with the F26C mutation remained stable, but, additionally, a different replicate generated a point mutation at position T24277C to generate an amino acid change F26S mutation, which has not been described previously.

3.8. High Selection Pressure to Maintain E Protein Activity to Facilitate Replication In Ovo

The IBV strain Beaudette exhibits a non-pathogenic phenotype in birds [49]. This is likely the result of serial passage both in vitro and in ovo; the passaging history of the Beaudette strain is unknown, but reports suggest it has been serially passaged 100–300 times [50]. The Beaudette strain has, however, retained pathogenicity in ovo [18]. Previous research suggested that the IC contributes to the pathogenesis of IBV in embryonated eggs, as the recombinant virus expressing the T16A mutation exhibited a lower 50% embryonic lethal dose (ELD_{50}) [18]. To investigate this further, in replicates of three, 10^4 or 10^5 PFU of either Beau-R, BeauR-T16A or BeauR-A26F were inoculated into allantoic cavities of 10-day-old SPF embryonated hen's eggs. The quantity of infectious progeny present, within the allantoic fluid at 24 hpi was determined via titration in CK cells. Additionally, the sequence of the E gene of the isolated passaged viruses was determined via Sanger sequencing.

In contradiction to previous research [18], all isolates of BeauR-T16A exhibited comparable titres to Beau-R (Figure 7A), suggesting comparable replication kinetics. Sequence analysis identified that all replicates of the BeauR-T16A isolates had generated compensatory or revertant mutations, with each isolate generating the same mutation in each replicate. Isolate 1 reverted the T16A mutation, while isolates 2 and 3 generated the compensatory A26V mutation. All isolates of BeauR-A26F displayed statistically lower titres of infectious progeny in comparison to the parental Beau-R (Figure 7A), and, unlike BeauR-T16A, the BeauR-A26F isolates showed stability over the E gene after passage in ovo (Figure 7B). The reduced replication paired with the maintenance of the A26F mutation may therefore suggest that the A26 residue within the E protein is advantageous for in ovo replication. The rapid acquisition of revertant or compensatory mutations observed in the BeauR-T16A isolates, which likely restored replication to a level comparable to Beau-R, may also suggest the T16 residue is advantageous for in ovo replication.

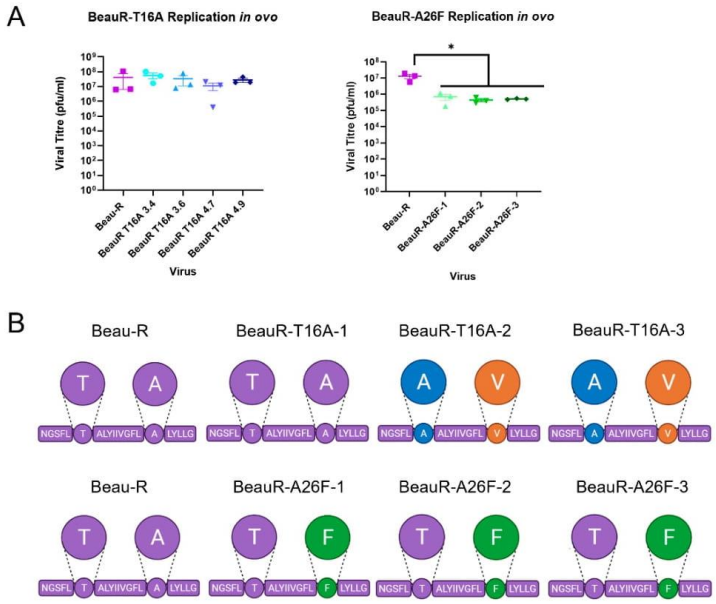

Figure 7. Reduced replication or genetic stability of rIBVs in ovo. Eggs were infected at a titre of 1×10^5 PFU (MOI~0.08) for Beau-R and all isolates of BeauR-T16A and BeauR-A26F. (**A**) The allantoic fluid from the eggs was harvested at 24 hpi and titrated on CK cells to determine the quantity of virus

present. Error bars represent ± SEM of three independent experiments. Statistical analysis was carried out using a one-way ANOVA with significance taken as p-value < 0.05 in comparison to Beau-R and is indicated by *. (**B**) The schematic represents the transmembrane domain of the E protein with the T16 and A26 residues highlighted with circles. Three replicates of each virus were harvested, and Sanger sequenced over the E gene. Beau-R sequence is shown in purple, T16A is shown in green, A26V is shown in orange, and A26F is shown in green.

3.9. Infection with BeauR-T16A Results in Reduced CPE in Primary CK Cells

To further examine the effect of the T16A and A26F mutations in a relevant cell type, CK cells were inoculated with 10^5 PFU of either Beau-R, BeauR-T16A or BeauR-A26F, and the CPE was observed. CK cells infected with the IBV show a prominent CPE, including syncytium formation (the fusion of virus infected cells with neighbouring cells resulting in a multinucleated cell) [51], cell rounding, and detaching from the cell culture dish [52]. Syncytia formation is not observed during the infection of cell cultures with all strains of IBV; however, Beau-R does cause extensive syncytia [52]. In CK cells, there was no observed difference in the CPE induced by Beau-R or BeauR-A26F. However, there was a reduction in the level of syncytia formation in BeauR-T16A infected cells in comparison to either Beau-R or BeauR-A26F (Figure 8), suggesting the T16A mutation may have affected the host response to viral infection or viral protein processing, resulting in less fusogenicity.

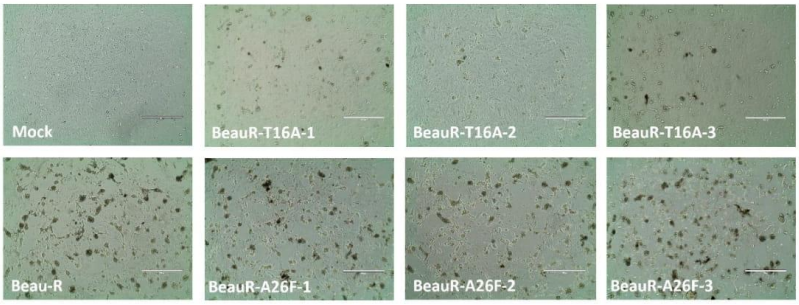

Figure 8. CPE caused by rIBVs. Representative CPE images were taken at 24 hpi on a light microscope for each rIBV. The CK cells were infected with 500 µL of diluted virus at a titre of 1×10^5 PFU (MOI~0.08). Scale bars represent 400 µm.

3.10. Neither Infection with BeauR-T16A or BeauR-A26F Impacts CK Cell Viability

The reduced CPE induced by BeauR-T16A was further investigated using a luciferase assay, CellTiter-Glo®, which measures ATP levels to quantify the number of metabolically active, and therefore viable, cells [41]. CK cells were inoculated with BeauR-T16A, BeauR-A26F or Beau-R at 1×10^5 PFU and serially diluted twofold. Cell viability was measured at 24 h intervals. At all the time points assessed, the cell viability was observed to be comparable between both rIBVs and the parental Beau-R, indicating infection results in equivalent cell cytotoxicity (Figure 9A).

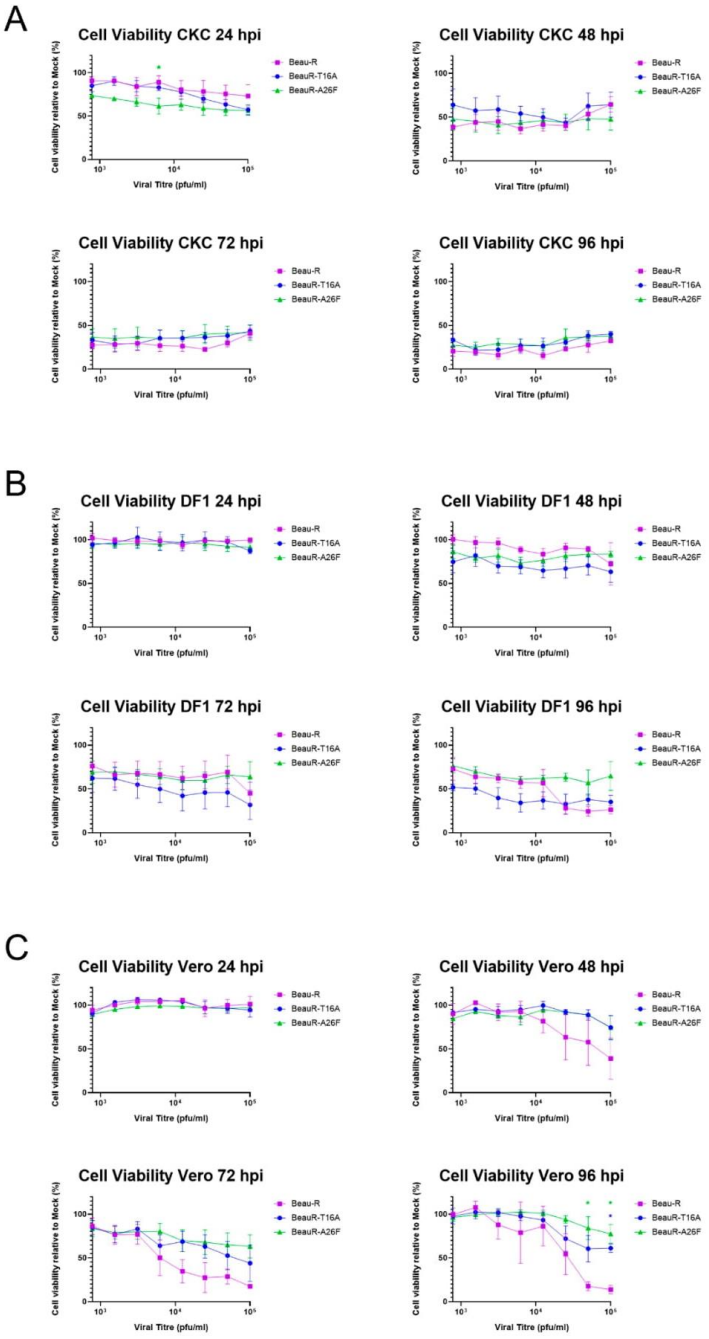

Figure 9. Cell viability reduction differs between cell type. CellTiter-Glo® reagent was used to quantify cell viability within CK (**A**), DF1 (**B**) and Vero (**C**) cells over a 96 h time-course of infection

at a range of viral titres. Cell viability was assessed every 24 h. Beau-R, BeauR-T16A-1 and BeauR-A26F-3 were used in this experiment, as well as a cell and media control to account for excess signal. The data is represented as percentage viability in relation to mock-infected cells. Error bars represent ± SEM of three independent experiments. Statistical analysis was carried out using a two-way ANOVA with significance taken as p-value < 0.05, significance is shown with an *. Green * and blue * represent A26F and T16A in comparison to Beau-R, respectively.

The same set-up was repeated in DF1 and Vero cells. Interestingly, differences were observed within these continuous cell lines (Figure 9B,C). DF1 cells (Figure 9B) infected with BeauR-T16A exhibited lower cell viability over all titres at 48 and 72 hpi than either BeauR-A26F or Beau-R; however, statistical significance was not reached. At 96 hpi, Beau-R showed lower cell viability when infected with higher titres (ns). Vero cells (Figure 9C) infected with $>10^4$ PFU of both BeauR-T16A and BeauR-A26F did not exhibit a reduction in cell viability comparable to Beau-R at 48–96 hpi, with statistical significance reached at 96 hpi. This indicates that the cytotoxic effects of both BeauR-T16A and BeauR-A26F are, therefore, not only dependent on cell type, but may also be dependent on the quantity of virus. This result may also have been influenced by the level of virus production present in Beau-R infected Vero cells in comparison to BeauR-A26F (Figure 2D).

3.11. rIBVs Upregulate Innate Immune Factors Comparably to Parental Beau-R

The E protein IC has been shown to be a pathogenicity factor in *Betacoronavirus* SARS-CoV, and mice inoculated with IC inactivated SARS-CoV exhibited decreased levels of Interleukin (IL)-1B and IL-6 [20]. In IBV, IC inactive viruses showed decreased upregulation of IL-6 in Vero cells and 10-day old embryonated eggs, indicating to the authors a role for the IC in the host's innate immune response to IBV infection [18]. The upregulation of four innate immune factors, Interferon (IFN)-α, IFN-β, IL-6 and IL-1B, within the cell lysate of CK cells infected with either BeauR-T16A, BeauR-A26F or Beau-R (Figure 10) was examined. These factors were selected as they have previously been shown to be upregulated during IBV infection [53–56]. qRT-PCRs determined comparable levels of IBV-derived RNA between samples, suggesting comparable replication kinetics (Figure 10A). Comparable levels of IFN-α IFN-β, IL-6 and IL-1B upregulation within cells infected with rIBVs containing either a T16A or A26F mutation and Beau-R were also observed (Figure 10B). Whilst it may appear that the rIBVs with a T16A or A26F mutation show slightly higher levels of upregulation of IFN-α and IFN-β than parental Beau-R, statistical significance was not reached.

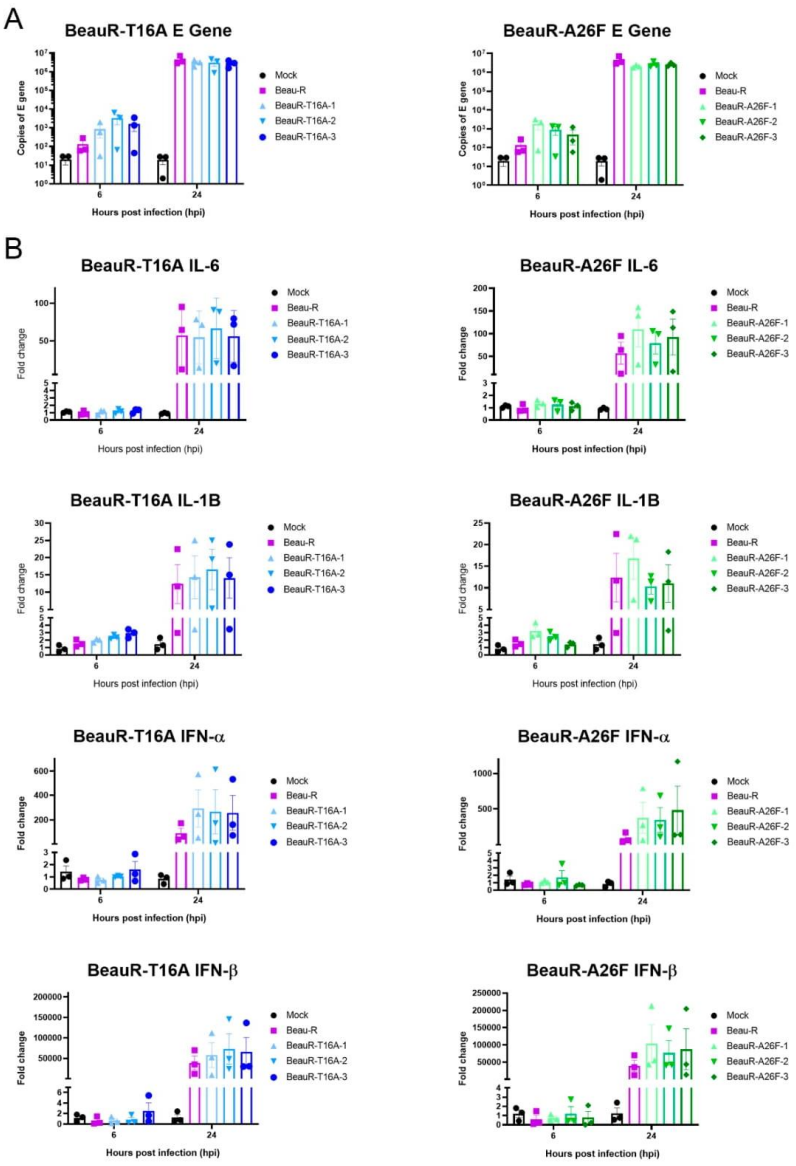

Figure 10. Upregulation of IL-6, IL-1B, IFN-α and IFN-β expression is comparable between parental Beau-R and rIBVs. CK cells were infected with 1×10^5 PFU (MOI~0.08) virus. At 6 and 24 hpi, cells were harvested, and RNA extracted. Error bars represent ± SEM of three independent experiments. (**A**) qPCR representing E transcript present within each sample indicating comparable levels of viral load. (**B**) qPCR investigating upregulation of a range of innate immune factors. Statistical analysis was carried out using a two-way ANOVA and statistical significance was taken as p-value < 0.05, no significance was identified.

4. Discussion

The ability to successfully rescue rIBVs with either the mutation T16A or A26F within the E protein suggests that these residues are not required for viral replication in vitro, in line with earlier reports [16,18]. It must be noted that work by To et al., also introduced the T16A or A26F mutation into a Beaudette-based backbone [16]. Replication was largely comparable between the two rIBVs and the WT virus in the mammalian cell line, Vero, although the plaque size was reduced [18]. In this study, we generated comparable rIBVs within Beau-R using our independently generated reverse genetics system [29], denoted by BeauR-T16A and BeauR-A26F. The rIBVs in this study were, unlike those generated by To et al. [16], recovered and passaged in chicken cells and the replication kinetics assessed in primary chicken cells and chicken-derived ex vivo cultures. The replication of both BeauR-T16A and BeauR-A26F was comparable to that in the parent virus, Beau-R, in primary CK cells (Figure 2A,B), DF1 cells, a continuous chicken cell line (Figure 2C), and in ex vivo TOCs (Figure 5B), suggesting that these residues are not required for the replication of IBV. This is in line with previous reports not only of IBV [16], but also of other coronaviruses, including SARS-CoV [20].

The replication of BeauR-A26F was reduced in Vero cells in comparison to unmodified Beau-R (Figures 2D and 4C). This is in contradiction with research by To et al., which identified comparable growth kinetics in the rIBVs containing the A26F mutations and WT virus [16]. The differences in findings between the studies may be the consequence of sequence differences between the Beaudette isolates used, in which the rIBVs are based and/or may be the result of difference in batches or lineage of Vero cells. In this study, in Vero cells, a subsequent analysis demonstrated that a higher quantity of infectious progeny was detected in cell lysate rather than supernatant (Figure 4B). Previous research has shown that the hydrophobic domain, in which the T16A and A26F mutations are present, is required for the efficient release of virions [17]. Additionally, the reduced release of infectious virus from Vero cells showed that this reduction in released virus was associated with the IC-inactivating mutations [17]. This, however, was not observed in CK cells, suggesting that, along with the differences in replication kinetics (Figure 4A), the phenotypic effect of either the T16A or A26F mutation may be dependent on cell type. Additionally, in this study, the effect was also not observed with BeauR-T16A, suggesting that the two mutations have differential phenotypic effects and may exert such effects through different mechanistic actions.

The potential for the different mechanistic actions of either the T16A or A26F mutations is further illustrated, as BeauR-A26F exhibited reduced replication in ovo in comparison to both BeauR-T16A and Beau-R (Figure 7A). Sequencing of the E gene of the in ovo passaged viruses, however, identified that all isolates of BeauR-T16A either contained the revertant mutation, A16T, or the compensatory mutation, A26V (Figure 7B). In contrast, no reversion or compensatory mutations were identified in the sequence of all isolates of BeauR-A26F. Rather than differences in mechanistic action, this may simply be the result of the fact that only one nucleotide change is required for the reversion of the T16A mutation (G24246A), but three-point mutations are required to revert the A26F (TTT 24276-8 GCA). Previous research identified that both the T16A and A26F mutations were unstable after five passages in either DF1 or Vero cells, not only highlighting a preference to retain these residues, but also highlighting the mutagenesis ability of the T16A and A26F residues [16]. Conversely, in this study, the passaging of BeauR-A26F isolates 2 and 3 in CK cells identified that the A26F mutation was stably maintained at passage 15, and only two replicates of BeauR-A26F isolate 1 had a mutation at residue 26, T24277G and T24277C, resulting in the amino acid change of F26C and F26S, respectively (Figure 6B). Passage 10 of BeauR-T16A identified either compensatory or revertant mutations in all isolates (Figure 6A). This data (Figure 6) in partnership with the assessment of replication kinetics (Figure 2) and alongside previous research [16] suggest that, while the T16 and A26 residues may not be required for viral replication, there is a selection pressure to retain it. The data also suggests that there is a different selection pressure exerted by the differing cell culture systems, including in

ovo. This not only highlights the cell-dependent effect of the T16A and A26F mutations, but may also suggest a cell-dependent role of the E protein itself. Additionally, work on SARS-CoV-2 has also shown cell-type-dependent selection pressure. This work found that a deletion of the cleavage site within the S gene arose upon passage in Vero-E6 cells, which is not dominant in clinical samples [57].

The E protein is thought to play a key role in the assembly [12,14,15] and release [16–18] of infectious virions. The E protein IC neutralises and subsequently dissociates the Golgi to ensure the correct processing of viral proteins [17]. The T16 residue has been demonstrated to be required for this dissociation; however, this research was completed in HeLa cells, a human cell line [12]. The cleavage and processing of the S2 subunit take place within the Golgi apparatus, and it been shown that the presence of the T16A mutation subsequently results in the incorrect processing of the S2 subunit [28]. Syncytia formation (which allows for humoral immune evasion, as it enables viruses to spread between cells without having to enter the extracellular environment, therefore shielding progeny virions from neutralising antibodies [58] is facilitated by the S2 subunit of the S protein of IBV [45]. Lower levels of syncytium were observed during BeauR-T16A and BeauR-A26F infection of CK cells (Figure 9), which may suggest that the mutations have resulted in the incorrect processing of the S2 subunit. Furthermore, both BeauR-T16A and BeauR-A26F exhibit smaller plaque phenotypes than Beau-R (Figure 3), as demonstrated in Vero cells [18]. This may be the result of reduced syncytium formation negatively impacting the viral spread between cells.

A classical characteristic of viroporin activity is the modulation of the host response to infection. It has been shown that IC inactive mutants of both SARS-CoV [20] and IBV [18] exhibit differential upregulation of the expression of innate immune genes in comparison to WT. In this study, the upregulation of four innate immune factors was shown to be comparable between both BeauR-T16A and BeauR-A26F, as well as the parental Beau-R (Figure 10) in CK cells. This is contrary to research in ovo and in Vero cells, which showed a reduction in innate immune upregulation when IC inactivating mutations were present [18]. The differing results obtained from this work are likely due to the use of primary CK cells in comparison to other culture systems. It must be noted that Vero cells have a restricted innate immune response [59], and chick embryos at 10 days have a limited innate immune response, which is not fully established until day 18 of embryonic development [60,61]. The differing results observed, therefore, may suggest further that both the T16A and A26F mutations have a cell-dependent effect. Interestingly in this study, different cytotoxicity effects were observed in Vero cells infected with either BeauR-T16A or BeauR-A26F, with a significantly lower level of cytotoxicity observed compared to Beau-R. This effect was not observed with either CK cells or DF1 cells, further indicating the cell-dependent effect of the T16A or A26F mutations and, therefore, possibly the E protein itself. This is not the first study to indicate cell-type-dependent results. Cell-type-dependent virus–host interactions have been identified in the study of autophagy, with IBV inducing autophagy in Vero cells but not within avian cell lines, DF1 and CK cells [62].

5. Conclusions

In conclusion, we have generated and characterised the T16A and A26F mutations within the hydrophobic domain of the E gene in the rIBV Beau-R. The rIBVs BeauR-T16A and BeauR-A26F are replication-competent, demonstrating that these residues are not essential for viral replication. The genetic stability of the T16A and A26F mutations, the replication of the rIBVs and the cytopathogenicity induced were assessed in a variety of systems, ranging from avian primary cell lines, continuous cell lines of both avian and mammalian origin, and in ovo and avian ex vivo TOCs. Differing results were observed through the assessment of the same parameter within different systems, highlighting the importance of cell-type or cell-system selection during IBV E protein research. Further studies in biologically relevant systems are therefore required to further elucidate the role of the IBV E protein during infection.

Author Contributions: Conceptualization, E.B. and P.B.; methodology, S.K., I.W., H.J.M., A.D.D. and E.B.; formal analysis, I.W., G.F., H.J.M., E.B., A.D.D. and S.K.; investigation, I.W., S.K., G.F., J.S. and K.L.; writing—original draft preparation, I.W. and S.K.; writing—review and editing, S.K., E.B., H.J.M., A.D.D. and P.B.; visualization, I.W. and S.K.; supervision, E.B., H.J.M., S.K. and A.D.D.; funding acquisition, E.B. All authors have read and agreed to the published version of the manuscript.

Funding: This research was funded by The British Egg Marketing Board Trust PhD scholarship to Isobel Webb and the Pirbright Institute. This work was additionally supported by the Institute Strategic Programme Grant funding from BBSRC to The Pirbright Institute with grant numbers BBS/E/I/00007030, BBS/E/I/00007031, BBS/E/I/00007034, BBS/E/I/00007035, BBS/E/I/00007037, BBS/E/I/00007038 and BBS/E/I/00007039.

Institutional Review Board Statement: No ethical approval was required for this study. This is not applicable.

Informed Consent Statement: No human studies were included.

Data Availability Statement: The sequence of Beau-CK has been deposited in GenBank under the accession number AJ311317.

Acknowledgments: The authors wish to acknowledge the help and support provided by the Cell Culture team and Bioinformatics, Sequencing and Proteomics (BSP) team at The Pirbright Institute.

Conflicts of Interest: The authors declare no conflict of interest.

References

1. Larson, H.; Reed, S.E.; Tyrrell, D. Isolation of rhinoviruses and coronaviruses from 38 colds in adults. *J. Med. Virol.* **1980**, *5*, 221–229. [CrossRef] [PubMed]
2. Halim, A.A.; Alsayed, B.; Embarak, S.; Yaseen, T.; Dabbous, S. Clinical characteristics and outcome of ICU admitted MERS corona virus infected patients. *Egypt. J. Chest Dis. Tuberc.* **2015**, *65*, 81–87. [CrossRef] [PubMed]
3. Lee, N.; Hui, D.; Wu, A.; Chan, P.; Cameron, P.; Joynt, G.M.; Ahuja, A.; Yung, M.Y.; Leung, C.; To, K.; et al. A Major Outbreak of Severe Acute Respiratory Syndrome in Hong Kong. *N. Engl. J. Med.* **2003**, *348*, 1986–1994. [CrossRef] [PubMed]
4. Wu, P.; Hao, X.; Lau, E.H.Y.; Wong, J.Y.; Leung, K.S.M.; Wu, J.T.; Cowling, B.J.; Leung, G.M. Real-time tentative assessment of the epidemiological characteristics of novel coronavirus infections in Wuhan, China, as at 22 January 2020. *Eurosurveillance* **2020**, *25*, 2000044. [CrossRef] [PubMed]
5. Woo, P.C.Y.; Lau, S.K.P.; Lam, C.S.F.; Lau, C.C.Y.; Tsang, A.K.L.; Lau, J.H.N.; Bai, R.; Teng, J.L.L.; Tsang, C.C.C.; Wang, M.; et al. Discovery of Seven Novel Mammalian and Avian Coronaviruses in the Genus Deltacoronavirus Supports Bat Coronaviruses as the Gene Source of Alphacoronavirus and Betacoronavirus and Avian Coronaviruses as the Gene Source of Gammacoronavirus and Deltacoronavirus. *J. Virol.* **2012**, *86*, 3995–4008. [CrossRef]
6. Chen, Q.; Gauger, P.; Stafne, M.; Thomas, J.; Arruda, P.; Burrough, E.; Madson, D.; Brodie, J.; Magstadt, D.; Derscheid, R.; et al. Pathogenicity and pathogenesis of a United States porcine deltacoronavirus cell culture isolate in 5-day-old neonatal piglets. *Virology* **2015**, *482*, 51–59. [CrossRef]
7. Bennett, R.; Ijpelaar, J. Updated Estimates of the Costs Associated with Thirty Four Endemic Livestock Diseases in Great Britain: A Note. *J. Agric. Econ.* **2005**, *56*, 135–144. [CrossRef]
8. Cavanagh, D. Coronavirus avian infectious bronchitis virus. *Vet. Res.* **2007**, *38*, 281–297. [CrossRef]
9. Matthijs, M.G.R.; Van Eck, J.H.H.; Landman, W.J.M.; Stegeman, J.A. Ability of Massachusetts-type infectious bronchitis virus to increase colibacillosis susceptibility incommercial broilers: A comparison between vaccine and virulent field virus. *Avian Pathol.* **2003**, *32*, 473–481. [CrossRef]
10. Boursnell, M.E.G.; Brown, T.D.K.; Foulds, I.J.; Green, P.F.; Tomley, F.M.; Binns, M.M. Completion of the Sequence of the Genome of the Coronavirus Avian Infectious Bronchitis Virus. *J. Gen. Virol.* **1987**, *68*, 57–77. [CrossRef]
11. Liu, D.; Inglis, S. Association of the infectious bronchitis virus 3c protein with the virion envelope. *Virology* **1991**, *185*, 911–917. [CrossRef]
12. Westerbeck, J.W.; Machamer, C.E. A Coronavirus E Protein Is Present in Two Distinct Pools with Different Effects on Assembly and the Secretory Pathway. *J. Virol.* **2015**, *89*, 9313–9323. [CrossRef] [PubMed]
13. Wilson, L.; Gage, P.; Ewart, G. Hexamethylene amiloride blocks E protein ion channels and inhibits coronavirus replication. *Virology* **2006**, *353*, 294–306. [CrossRef]
14. Fischer, F.; Stegen, C.F.; Masters, P.S.; Samsonoff, W.A. Analysis of Constructed E Gene Mutants of Mouse Hepatitis Virus Confirms a Pivotal Role for E Protein in Coronavirus Assembly. *J. Virol.* **1998**, *72*, 7885–7894. [CrossRef] [PubMed]
15. Ye, Y.; Hogue, B.G. Role of the Coronavirus E Viroporin Protein Transmembrane Domain in Virus Assembly. *J. Virol.* **2007**, *81*, 3597–3607. [CrossRef] [PubMed]
16. To, J.; Surya, W.; Fung, T.S.; Li, Y.; Verdià-Bàguena, C.; Queralt-Martín, M.; Aguilella, V.; Liu, D.X.; Torres, J. Channel-Inactivating Mutations and Their Revertant Mutants in the Envelope Protein of Infectious Bronchitis Virus. *J. Virol.* **2017**, *91*. [CrossRef]

17. Ruch, T.R.; Machamer, C.E. The Hydrophobic Domain of Infectious Bronchitis Virus E Protein Alters the Host Secretory Pathway and Is Important for Release of Infectious Virus. *J. Virol.* **2011**, *85*, 675–685. [CrossRef]
18. Li, S.; Yuan, L.; Dai, G.; Chen, R.A.; Liu, D.X.; Fung, T.S. Regulation of the ER Stress Response by the Ion Channel Activity of the Infectious Bronchitis Coronavirus Envelope Protein Modulates Virion Release, Apoptosis, Viral Fitness, and Pathogenesis. *Front. Microbiol.* **2020**, *10*, 3022. [CrossRef]
19. Stodola, J.K.; Dubois, G.; Le Coupanec, A.; Desforges, M.; Talbot, P.J. The OC43 human coronavirus envelope protein is critical for infectious virus production and propagation in neuronal cells and is a determinant of neurovirulence and CNS pathology. *Virology* **2017**, *515*, 134–149. [CrossRef]
20. Nieto-Torres, J.L.; DeDiego, M.L.; Verdiá-Báguena, C.; Guardeno, J.M.J.; Regla-Nava, J.A.; Fernandez-Delgado, R.; Castaño-Rodriguez, C.; Alcaraz, A.; Torres, J.; Aguilella, V.; et al. Severe Acute Respiratory Syndrome Coronavirus Envelope Protein Ion Channel Activity Promotes Virus Fitness and Pathogenesis. *PLoS Pathog.* **2014**, *10*, e1004077. [CrossRef]
21. Jimenez-Guardeño, J.M.; Nieto-Torres, J.L.; DeDiego, M.L.; Regla-Nava, J.A.; Fernandez-Delgado, R.; Castaño-Rodriguez, C.; Enjuanes, L. The PDZ-Binding Motif of Severe Acute Respiratory Syndrome Coronavirus Envelope Protein Is a Determinant of Viral Pathogenesis. *PLoS Pathog.* **2014**, *10*, e1004320. [CrossRef] [PubMed]
22. Cohen, J.R.; Lin, L.D.; Machamer, C.E. Identification of a Golgi Complex-Targeting Signal in the Cytoplasmic Tail of the Severe Acute Respiratory Syndrome Coronavirus Envelope Protein. *J. Virol.* **2011**, *85*, 5794–5803. [CrossRef] [PubMed]
23. Corse, E.; Machamer, C.E. The cytoplasmic tails of infectious bronchitis virus E and M proteins mediate their interaction. *Virology* **2003**, *312*, 25–34. [CrossRef]
24. Carrasco, L. Modification of membrane permeability induced by animal viruses early in infection. *Virology* **1981**, *113*, 623–629. [CrossRef]
25. Liao, Y.; Lescar, J.; Tam, J.P.; Liu, D. Expression of SARS-coronavirus envelope protein in Escherichia coli cells alters membrane permeability. *Biochem. Biophys. Res. Commun.* **2004**, *325*, 374–380. [CrossRef]
26. Torres, J.; Maheswari, U.; Parthasarathy, K.; Ng, L.; Liu, D.X.; Gong, X. Conductance and amantadine binding of a pore formed by a lysine-flanked transmembrane domain of SARS coronavirus envelope protein. *Protein Sci.* **2007**, *16*, 2065–2071. [CrossRef] [PubMed]
27. Ruch, T.R.; Machamer, C.E. A Single Polar Residue and Distinct Membrane Topologies Impact the Function of the Infectious Bronchitis Coronavirus E Protein. *PLoS Pathog.* **2012**, *8*, e1002674. [CrossRef]
28. Westerbeck, J.W.; Machamer, C.E. The Infectious Bronchitis Coronavirus Envelope Protein Alters Golgi pH To Protect the Spike Protein and Promote the Release of Infectious Virus. *J. Virol.* **2019**, *93*, e00015-19. [CrossRef]
29. Casais, R.; Thiel, V.; Siddell, S.G.; Cavanagh, D.; Britton, P. Reverse Genetics System for the Avian Coronavirus Infectious Bronchitis Virus. *J. Virol.* **2001**, *75*, 12359–12369. [CrossRef]
30. Hennion, R.M.; Hill, G. *The Preparation of Chicken Kidney Cell Cultures for Virus Propagation*; Springer: Berlin/Heidelberg, Germany, 2014; Volume 1282, pp. 57–62.
31. Himly, M.; Foster, D.N.; Bottoli, I.; Iacovoni, J.S.; Vogt, P.K. The DF-1 Chicken Fibroblast Cell Line: Transformation Induced by Diverse Oncogenes and Cell Death Resulting from Infection by Avian Leukosis Viruses. *Virology* **1998**, *248*, 295–304. [CrossRef]
32. Hennion, R.M. The Preparation of Chicken Tracheal Organ Cultures for Virus Isolation, Propagation, and Titration. *Coronaviruses* **2015**, *1282*, 51–56. [CrossRef]
33. Keep, S.; Britton, P.; Bickerton, E. Transient Dominant Selection for the Modification and Generation of Recombinant Infectious Bronchitis. *Coronaviruses* **2020**, *2203*, 147–165. [CrossRef]
34. Keep, S.M.; Bickerton, E.; Britton, P. Partial Purification of IBV and Subsequent Isolation of Viral RNA for Next-Generation Sequencing. In *Coronaviruses*; Humana Press: New York, NY, USA, 2015; Volume 1282, pp. 109–112. [CrossRef]
35. Freimanis, G.L.; Oade, M.S. Whole-Genome Sequencing Protocols for IBV and Other Coronaviruses Using High-Throughput Sequencing. In *Coronaviruses*; Humana Press: New York, NY, USA, 2020; Volume 2203, pp. 67–74. [CrossRef]
36. Kint, J.; Maier, H.J.; Jagt, E. Quantification of Infectious Bronchitis Coronavirus by Titration In Vitro and In Ovo. In *Coronaviruses*; Humana Press: New York, NY, USA, 2015; Volume 1282, pp. 89–98. [CrossRef]
37. Schneider, C.A.; Rasband, W.S.; Eliceiri, K.W. NIH Image to ImageJ: 25 Years of image analysis. *Nat. Methods* **2012**, *9*, 671–675. [CrossRef] [PubMed]
38. Cavanagh, D.; Elus, M.M.; Cook, J.K.A. Relationship between sequence variation in the S1 spike protein of infectious bronchitis virus and the extent of cross-protection in vivo. *Avian Pathol.* **1997**, *26*, 63–74. [CrossRef] [PubMed]
39. Cook, J.K.A.; Huggins, M.B.; Orbell, S.J.; Mawditt, K.; Cavanagh, D. Infectious bronchitis virus vaccine interferes with the replication of avian pneumovirus vaccine in domestic fowl. *Avian Pathol.* **2001**, *30*, 233–242. [CrossRef]
40. Guy, J.S. Isolation and Propagation of Coronaviruses in Embryonated Eggs. *Coronaviruses* **2020**, *2203*, 107–117. [CrossRef]
41. Riss, T.; Niles, A.; Moravec, R.; Karassina, N.; Vidugiriene, J. Cytotoxicity Assays: In Vitro Methods to Measure Dead Cells. In *Assay Guidance Manual [Internet]*; Markossian, S., Grossman, A., Brimacombe, K., Arkin, M., Auld, D., Austin, C., Baell, J., Chung, T.D.Y., Coussens, N.P., Dahlin, J.L., et al., Eds.; Eli Lilly & Company and the National Center for Advancing Translational Sciences: Bethesda, MD, USA, 2004.
42. Batra, A.; Maier, H.J.; Fife, M.S. Selection of reference genes for gene expression analysis by real-time qPCR in avian cells infected with infectious bronchitis virus. *Avian Pathol.* **2016**, *46*, 173–180. [CrossRef]
43. Ruch, T.R.; Machamer, C.E. The Coronavirus E Protein: Assembly and Beyond. *Viruses* **2012**, *4*, 363–382. [CrossRef]

44. Casais, R.; Dove, B.; Cavanagh, D.; Britton, P. Recombinant Avian Infectious Bronchitis Virus Expressing a Heterologous Spike Gene Demonstrates that the Spike Protein Is a Determinant of Cell Tropism. *J. Virol.* **2003**, *77*, 9084–9089. [CrossRef]
45. Bickerton, E.; Maier, H.J.; Stevenson-Leggett, P.; Armesto, M.; Britton, P. The S2 Subunit of Infectious Bronchitis Virus Beaudette Is a Determinant of Cellular Tropism. *J. Virol.* **2018**, *92*, e01044-18. [CrossRef]
46. Montagnon, B.J.; Fanget, B.; Nicolas, A.J. The large-scale cultivation of VERO cells in micro-carrier culture for virus vaccine production. Preliminary results for killed poliovirus vaccine. *Dev. Biol. Stand.* **1981**, *47*, 55–64. [PubMed]
47. Frazatti-Gallina, N.M.; Mourão-Fuches, R.M.; Paoli, R.L.; Silva, M.L.; Miyaki, C.; Valentini, E.J.; Raw, I.; Higashi, H.G. Vero-cell rabies vaccine produced using serum-free medium. *Vaccine* **2004**, *23*, 511–517. [CrossRef] [PubMed]
48. Cook, J.K.A.; Darbyshire, J.H.; Peters, R.W. The use of chicken tracheal organ cultures for the isolation and assay of avian infectious bronchitis virus. *Arch. Virol.* **1976**, *50*, 109–118. [CrossRef]
49. Keep, S.; Stevenson-Leggett, P.; Steyn, A.; Oade, M.; Webb, I.; Stuart, J.; Vervelde, L.; Britton, P.; Maier, H.; Bickerton, E. Temperature Sensitivity: A Potential Method for the Generation of Vaccines against the Avian Coronavirus Infectious Bronchitis Virus. *Viruses* **2020**, *12*, 754. [CrossRef] [PubMed]
50. Hodgson, T.; Casais, R.; Dove, B.; Britton, P.; Cavanagh, D. Recombinant Infectious Bronchitis Coronavirus Beaudette with the Spike Protein Gene of the Pathogenic M41 Strain Remains Attenuated but Induces Protective Immunity. *J. Virol.* **2004**, *78*, 13804–13811. [CrossRef] [PubMed]
51. Daubenmire, R.F. The use of the terms coenocyte and syncytium in biology. *Science* **1936**, *84*, 533. [CrossRef]
52. Churchill, A.E. The use of chicken kidney tissue culture in the study of the avian viruses of newcastle disease, infectious laryngo tracheitis and infectious bronchitis. *Res. Vet. Sci.* **1965**, *6*, 162–171. [CrossRef]
53. Amarasinghe, A.; Abdul-Cader, M.S.; Almatrouk, Z.; van der Meer, F.; Cork, S.C.; Gomis, S.; Abdul-Careem, M.F. Induction of innate host responses characterized by production of interleukin (IL)-1β and recruitment of macrophages to the respiratory tract of chickens following infection with infectious bronchitis virus (IBV). *Vet. Microbiol.* **2018**, *215*, 1–10. [CrossRef]
54. Asif, M.; Lowenthal, J.W.; Ford, M.E.; Schat, K.A.; Kimpton, W.; Bean, A.G. Interleukin-6 Expression after Infectious Bronchitis Virus Infection in Chickens. *Viral Immunol.* **2007**, *20*, 479–486. [CrossRef]
55. Kint, J.; Fernandez-Gutierrez, M.M.; Maier, H.J.; Britton, P.; Langereis, M.A.; Koumans, J.; Wiegertjes, G.F.; Forlenza, M. Activation of the Chicken Type I Interferon Response by Infectious Bronchitis Coronavirus. *J. Virol.* **2015**, *89*, 1156–1167. [CrossRef]
56. Yang, X.; Li, J.; Liu, H.; Zhang, P.; Chen, D.; Men, S.; Li, X.; Wang, H. Induction of innate immune response following introduction of infectious bronchitis virus (IBV) in the trachea and renal tissues of chickens. *Microb. Pathog.* **2018**, *116*, 54–61. [CrossRef] [PubMed]
57. Davidson, A.D.; Williamson, M.K.; Lewis, S.; Shoemark, D.; Carroll, M.W.; Heesom, K.J.; Zambon, M.; Ellis, J.; Lewis, P.A.; Hiscox, J.A.; et al. Characterisation of the transcriptome and proteome of SARS-CoV-2 reveals a cell passage induced in-frame deletion of the furin-like cleavage site from the spike glycoprotein. *Genome Med.* **2020**, *12*, 1–15. [CrossRef] [PubMed]
58. Cifuentes-Muñoz, N.; Dutch, R.E.; Cattaneo, R. Direct cell-to-cell transmission of respiratory viruses: The fast lanes. *PLoS Pathog.* **2018**, *14*, e1007015. [CrossRef]
59. Desmyter, J.; Melnick, J.L.; Rawls, W.E. Defectiveness of Interferon Production and of Rubella Virus Interference in a Line of African Green Monkey Kidney Cells (Vero). *J. Virol.* **1968**, *2*, 955–961. [CrossRef]
60. Schilling, M.A.; Katani, R.; Memari, S.; Cavanaugh, M.; Buza, J.; Radzio-Basu, J.; Mpenda, F.N.; Deist, M.S.; Lamont, S.J.; Kapur, V. Transcriptional Innate Immune Response of the Developing Chicken Embryo to Newcastle Disease Virus Infection. *Front. Genet.* **2018**, *9*, 61. [CrossRef] [PubMed]
61. Davison, T. The immunologists' debt to the chicken. *Br. Poult. Sci.* **2003**, *44*, 6–21. [CrossRef] [PubMed]
62. Maier, H.J.; Cottam, E.M.; Stevenson-Leggett, P.; Wilkinson, J.A.; Harte, C.J.; Wileman, T.; Britton, P. Visualizing the autophagy pathway in avian cells and its application to studying infectious bronchitis virus. *Autophagy* **2013**, *9*, 496–509. [CrossRef]

3.4. Discussion

A previous study, from another research group also introduced the T16A or A26F mutation into a Beaudette based backbone (16). The study presented in this Chapter (191), found many contradicting results to the previous research. One of the possible reasons for this is the difference in origin of the Beaudette backbone in which the mutations were made. Although Beau-R is a molecular clone of Beau-CK, which is a Beaudette strain, the sequence of each laboratory isolate of Beaudette varies, which is magnified by the unknown passaging history of the Beaudette strain which was first isolated in 1937 (44). Additionally, Beau-CK has been adapted to replicate in primary CK cells through additional serial passaging (46). Consequently, each distinct isolate of Beaudette contains differences in sequence (29) and as a result whilst the individual mutations T16A and A26F are comparable, the origin of the virus is different and therefore it is likely to contain sequence differences elsewhere in the genome. These sequence differences may be the cause of the differing results, which may indicate that the strain of IBV plays an additional role in the effect of the T16A and A26F mutations.

As mentioned above the Beaudette strain is heavily lab adapted and additionally is non-pathogenic in chickens (25). This attenuated phenotype is an important caveat to consider as these viruses are not representative of natural IBV infection. The exact mechanism of this attenuation is unknown and therefore the proteins and cell interactions which are different during infection with a Beaudette strain to facilitate this attenuation could result in phenotypic differences from pathogenic strains. These viruses are still powerful tools for virus characterisation due to the extended cell tropism of Beau-R which has enabled characterisation of the rIBVs in a wide range of cellular systems, ranging from cell lines to *ex vivo* cultures (192).

The factors present within different cell systems varies largely. Recent research has implicated the CoV E protein in the modulation of the host response (138, 148, 150, 152) and both Vero and DF1 cells have notable deficiencies in the host response. Vero cells do not secrete IFN-α or lFN-β (193) and DF1s have a weakened IFN I response (194). Even within an *in ovo* model which contains an entire chick, the innate immune response is not representative of natural infection (195, 196). Additionally, mammalian cellular proteins are not always representative of those found within an avian cell. These differences may impact viral replication in different ways resulting in mutations that are not comparable between cell type. Differing mutations arose when rIBVs with T16A and A26F mutations were passaged in Vero and DF1 cells (20), in comparison to the passaging data obtained using primary CK cells within this study (Figure 6).

Characterisation of the ion channel activity of these rIBVs was not possible as part of this work. Previously, it was reported that either the T16A or A26F mutation abolishes ion channel activity (20). To gain insight into the effect of the T16A and A26F mutations in the rIBVs generated as part of this project, the hydrophobicity of the transmembrane domain was predicted using the HeliQuest online tool (https://heliquest.ipmc.cnrs.fr/cgi-bin/ComputParams.py). This found that the hydrophobicity moment of the Beau-R E protein was 0.284. The T16A mutation had a minimal effect and changed the hydrophobicity moment to 0.281, unlike the A26F mutation which was 0.268. The presence of the A26V mutation which was found during passaging of the BeauR-T16A isolates (Figure 6 and 7) has previously been shown to recover ion channel activity (20). E proteins which contained both the T16A and A26V mutation had a hydrophobic moment of 0.268, which was the same value as the A26F mutation. This indicates that modification of the A26 residue alters the hydrophobicity of the E protein transmembrane domain, but this is not necessarily a determinant of ion channel activity.

In conclusion, this chapter builds upon previous research by characterising the role of the T16A and A26F mutations in a range of cell systems. This study not only highlighted the cell-type dependency of the effect of these mutations but furthered the characterisation of these residues through a range of different assays. The overall conclusion demonstrated within the research article highlights the key role cell type selection plays and therefore cell type should be a major consideration in experimental design.

Chapter 4: Modification of the IBV E Protein within the Pathogenic Strain, M41-K, for Rational Vaccine Design.

4.1. Declaration

The work presented here is the author's sole effort except for the following exceptions. Reverse genetics to generate M41K-T16A isolates, excluding rescue of M41K-T16A-2.3 and M41K-T16A-2.6, was performed by Sarah Keep and Jamie Stuart. Predicted structural models were generated but not rendered by Holly Everest. NGS sequencing analysis was carried out by Graham Freimanis and Michael Oade, The Pirbright Institute. At the time of writing, data contained within this chapter is in preparation for publication under the title, "The impact of the T16A and A26F Mutations in the Envelope Protein of an Avian Coronavirus on Viral Replication is Strain Dependent." The authors for the publication are as follows: Isobel Webb, Sarah Keep, Holly Everest, Jamie Stuart, Graham Freimanis, Paul Britton, Andrew D. Davidson, Helena J. Maier and Erica Bickerton.

4.2. Introduction

As discussed in the previous chapter (Chapter 3) recombinant CoVs with a modified E protein have previously been generated with the aim of assessing the role of the E protein during infection (20, 148, 149). These include the recombinant *Betacoronavirus* SARS-CoV with an E protein deletion which were successfully rescued and were able to protect mice against challenge with WT virus (148, 197). IBV virions have been generated with a deletion of the hydrophobic domain of the E protein in the non-pathogenic Beaudette strain, the resulting rIBVs were deficient in viral release (105). IBV with a total deletion of the E protein has been reported to be irrecoverable (198).

In the *Betacoronavirus* SARS-CoV E protein, mutations of either N15A or V25F eliminated the IC activity (136). Sequence alignment of the SARS-CoV and IBV E proteins found that the equivalent mutations in IBV are T16 and A26 (Chapter 8, Section 8.3.1, Figure 8.7). Presence of either a T16A or A26F mutation within the hydrophobic domain of the IBV E protein was reported to cause the same IC inactivation (20). These mutations have exclusively been characterised in the non-pathogenic Beaudette strain of IBV (20, 84, 113, 152).

The T16A and A26F mutations, as discussed in the previous chapter, select for the two forms of E present during infection: pentameric IC and monomeric, respectively (113). The data presented in Chapter 3 indicates that when these mutations are generated within the non-pathogenic strain of IBV, Beau-R, these two residues have distinct impacts on viral replication. Prior to the work presented in this chapter, there has been no investigation into the role of the E protein in pathogenic strains of IBV.

Previous work on the SARS-CoV and the IBV E proteins has highlighted a role within pathogenesis of the virus (138, 148, 152). Notably, for SARS-CoV, viruses lacking the E protein can protect against challenge in mice (148, 151) and viruses with the

N15A mutation were non-pathogenic in mice (138). Within this chapter, rIBVs have been generated in a pathogenic IBV backbone, denoted M41-K (177) to allow for investigation of the role of the E protein in IBV pathogenicity. These rIBVs have been designed to alter either the expression level or the activity of the E protein.

This chapter aims to investigate whether the E protein has comparable roles within a pathogenic strain as a non-pathogenic strain. Ultimately, these rIBVs were designed with the aim of assessing their viability as vaccine candidates.

4.3. Results

4.3.1. Comparison between the Beau-R and M41-CK E proteins

The T16A and A26F mutations have been reported to alter the activity of the E protein when assessed in a non-pathogenic strain, Beaudette (20, 84, 113, 152). To allow for comparison of the role of these mutations in different strains of IBV, they have been generated both in a non-pathogenic (Chapter 3) and, in this chapter, a pathogenic strain. This was important to assess, as there appeared to be key differences between the E protein within the two strains. Both viruses, M41-CK and Beau-CK, belong to the same serotype and genome classification with the key difference being the pathogenicity phenotypes. Two molecular clones exist for these viruses in which the modifications were generated. M41-K is the pathogenic clone of M41-CK and Beau-R is a clone of the non-pathogenic Beau-CK.

Despite amino acid conservation of 97%, three amino acid differences were identified between Beau-CK and M41-CK (Figure 4.1). The M41 sequence has an additional methionine residue at the start of the E protein, along with different amino acids at positions I22F and A102V. These positions refer to the M41-CK sequence in relation to the Beau-CK.

```
         1           11          21          31          41          51
Beau-CK -MNLLNKSLE ENGSFLTALY IIVGFLALYL LGRALQAFVQ AADACCLFWY TWVVI
M41-CK  MMNLLNKSLE ENGSFLTALY IFVGFLALYL LGRALQAFVQ AADACCLFWY TWVVI

               61          71          81          91          101
Beau-CK PGAKG TAFVYKYTYG RKLNNPELEA VIVNEFPKNG WNNKNPANFQ DAQRDKLYS
M41-CK  PGAKG TAFVYKYTYG RKLNNPELEA VIVNEFPKNG WNNKNPANFQ DVQRDKLYS
```

Figure 4.1. IBV E gene sequence alignment showing Beau-CK and M41-CK strains. The differing residues between the strains are highlighted in yellow. The accession numbers for the strains compared are as follows: Beau-CK (CAC39117.1) and M41-CK (QCE31536.1). An alignment showing a more extensive range of IBV strains can be found in Appendix Section 8.2.2, Figure 8.8.

CK cells were infected with Beau-R or M41-CK to allow for investigation of the expression of E protein during *in vitro* replication; higher expression was observed in M41-CK infected cells, in comparison to Beau-R at 24 hpi (Figure 4.2). To control for virus present, the expression of the N protein was also assessed. This showed that although the E expression was higher in M41-CK, this pattern was not observed in the N protein.

.

A

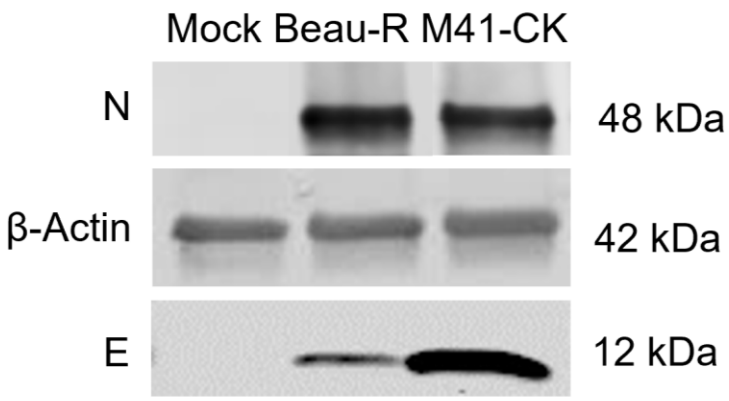
Mock Beau-R M41-CK
N
48 kDa
β-Actin
42 kDa
E
12 kDa

B

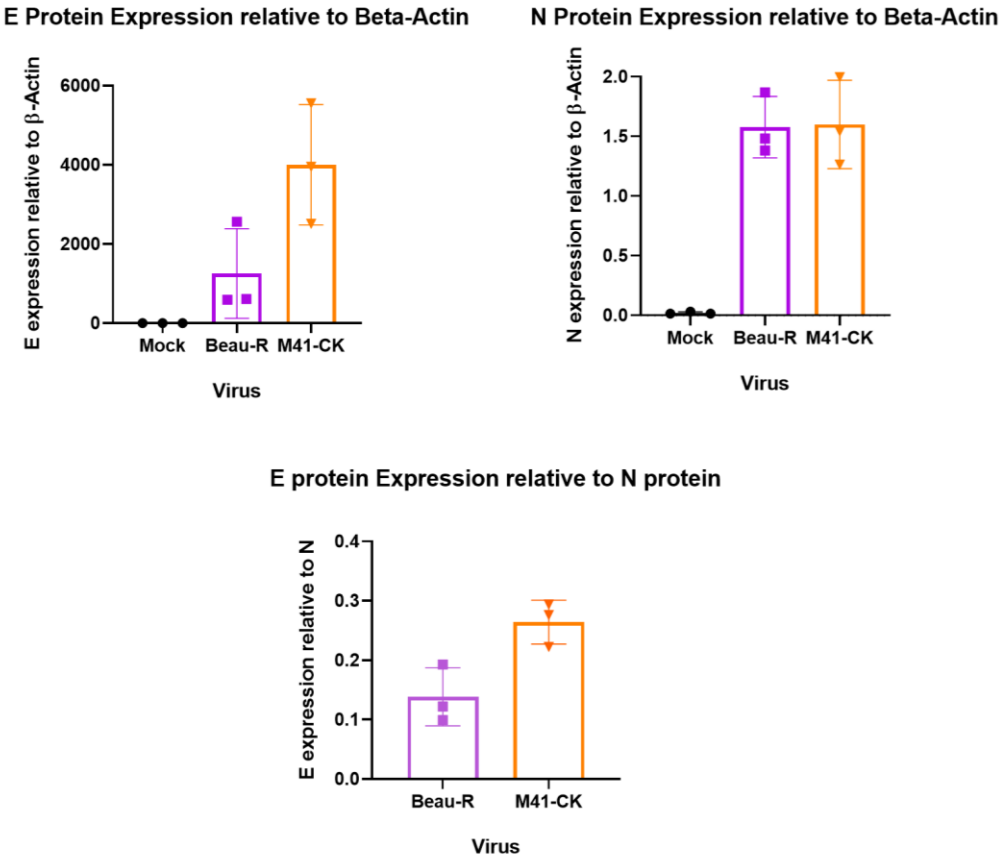
E Protein Expression relative to Beta-Actin
E expression relative to β-Actin
6000
4000
2000
0
Mock
Beau-R
M41-CK
Virus
N Protein Expression relative to Beta-Actin
N expression relative to β-Actin
2.0
1.5
1.0
0.5
0.0
Mock
Beau-R
M41-CK
Virus
E protein Expression relative to N protein
E expression relative to N
0.4
0.3
0.2
0.1
0.0
Beau-R
M41-CK
Virus

Figure 4.2. Differences between the Beau-R and M41-CK E protein expression. CK cells were infected with $1x10^6$ PFU of either Beau-R or M41-CK with cell lysate harvested at 24 hpi. (A) Bands were resolved using SDS-PAGE and a western blot (WB) was carried out using primary antibodies AF12 (anti-E) and endogenous control (anti-β-actin). Secondary antibodies used were IRDye® donkey anti-mouse IgG 800CW and IRDye® goat anti-rabbit IgG 680RD. The bands representing the E (~12kDa), β-actin (~42kDa) and N (~48kDa) proteins are indicated. (B) Quantification of protein expression was carried out using the densitometry of the respective bands from three independent experiments. The plotted values were normalised to levels of anti-β-actin or anti-N. Statistical analysis was carried out using one-way analysis of variance (ANOVA), significance was taken as p-value < 0.05 and is represented with * relative to Beau-R. Error bars represent ± standard deviation (SD) of three independent experiments.

The structure of the pentameric CoV E protein has been solved for *Betacoronaviruses* SARS-CoV and SARS-CoV-2 (138, 199). No structural data is available for the IBV E protein. Any structure predicted could only be described as a model, as there is low sequence identity between *Betacoronaviruses* and IBV E proteins (Chapter 8, Section 8.3.1, Figure 8.7). To combat this, Beau-R and M41-CK E protein structures were predicted using AlphaFold2 software, which generates highly accurate monomeric protein structures based on amino acid sequence alone (188).

In silico modelling using AlphaFold2 predicted that the c-terminal domains of Beau-R and M41-CK structures differ, as there are additional alpha helices in M41-CK which are not present in Beau-R. Although, the two extra helices are within a region of “very low” per residue confidence score (pLDDT < 50 %). Overall, the predicted structural analysis of the E proteins showed drastic differences between M41-CK and Beau-R, despite high sequence similarity between these strains (Figure 4.3). These structural predictions however need to be confirmed with experimental data. Potentially these structural differences are the result of the Beau-R E protein being misfolded. This may have impacted the expression level of the Beau-R E protein (Figure 4.2) as it may be more prone to proteasomal degradation.

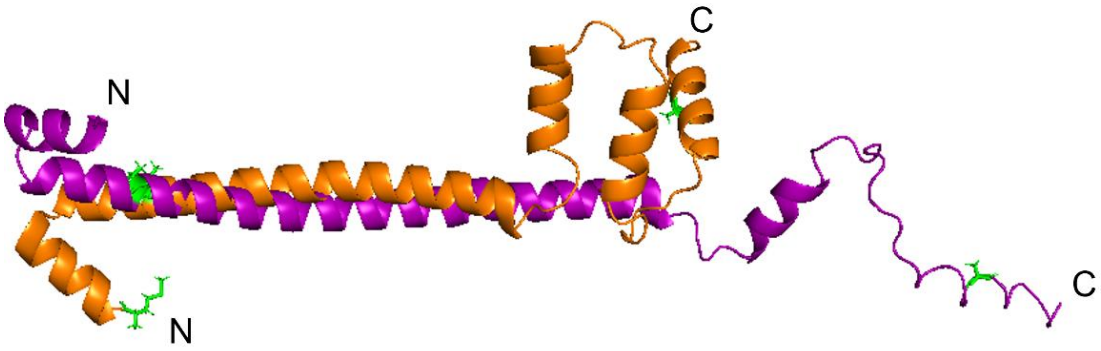

Figure 4.3. Predicted E protein structures of Beau-R and M41-CK were generated using AlphaFold2. The relevant sequences were imported and PDB files exported. Rendered structures were overlayed and amino acid sequence differences between the two proteins were highlighted in green. Image was rendered within PyMOL. Beau-R is shown in purple and M41-CK in orange.

4.3.2. Generating rIBVs which alter expression of the E protein.

An rIBV was designed with the aim of reducing the expression of the E protein in a pathogenic M41-K backbone. This rIBV was designed using a technique termed codon reshuffling (200) instead of an E deletion as it has been reported that IBV lacking the E protein cannot be recovered (198).

RNA viruses have a high mutation rate, consequently, these viruses are not strictly a clonal group but instead a population of closely related variant viruses (201), described as a 'viral swarm' (202). Reshuffling the codons aims to redirect virus evolution into 'risky' sequence space within its population through the generation of stop codons within a target gene. This method has previously been shown to attenuate RNA viruses (200). To re-shuffle the codons, synonymous changes were made in the E gene so that mutation of only one nucleotide results in the generation of a stop codon. This has only been carried out for serine and leucine residues as they have the highest redundancy, following a method detailed previously (200). The sequence of the inserted region can be found in Chapter 8, Section 8.2, Figure 8.2. This rIBV was designed within an M41-K background and is named M41K-Cdn-Sh. The cDNA encoding for the full-length genome of the designed rIBVs was assembled using a VV based reverse genetics system detailed in Chapter 2, Section 2.5.

The modified E gene sequences were inserted into receiver rVV containing a cDNA copy of M41-K. rVV isolates were deemed successful if the E gene was present and the selection gene (*Ecogpt*) had been lost. Correct insertions were verified using Sanger sequencing over the E gene. Ministocks with the correct sequence were 1, 6 and 12 for M41K-Cdn-Sh (Figure 4.4). Several rescue attempts were carried out for the generation of M41K-Cdn-Sh, but none were successful. This may have been due to the success rate of the rescue system or have been caused by disruption of RNA structure in the regions where the codons were reshuffled.

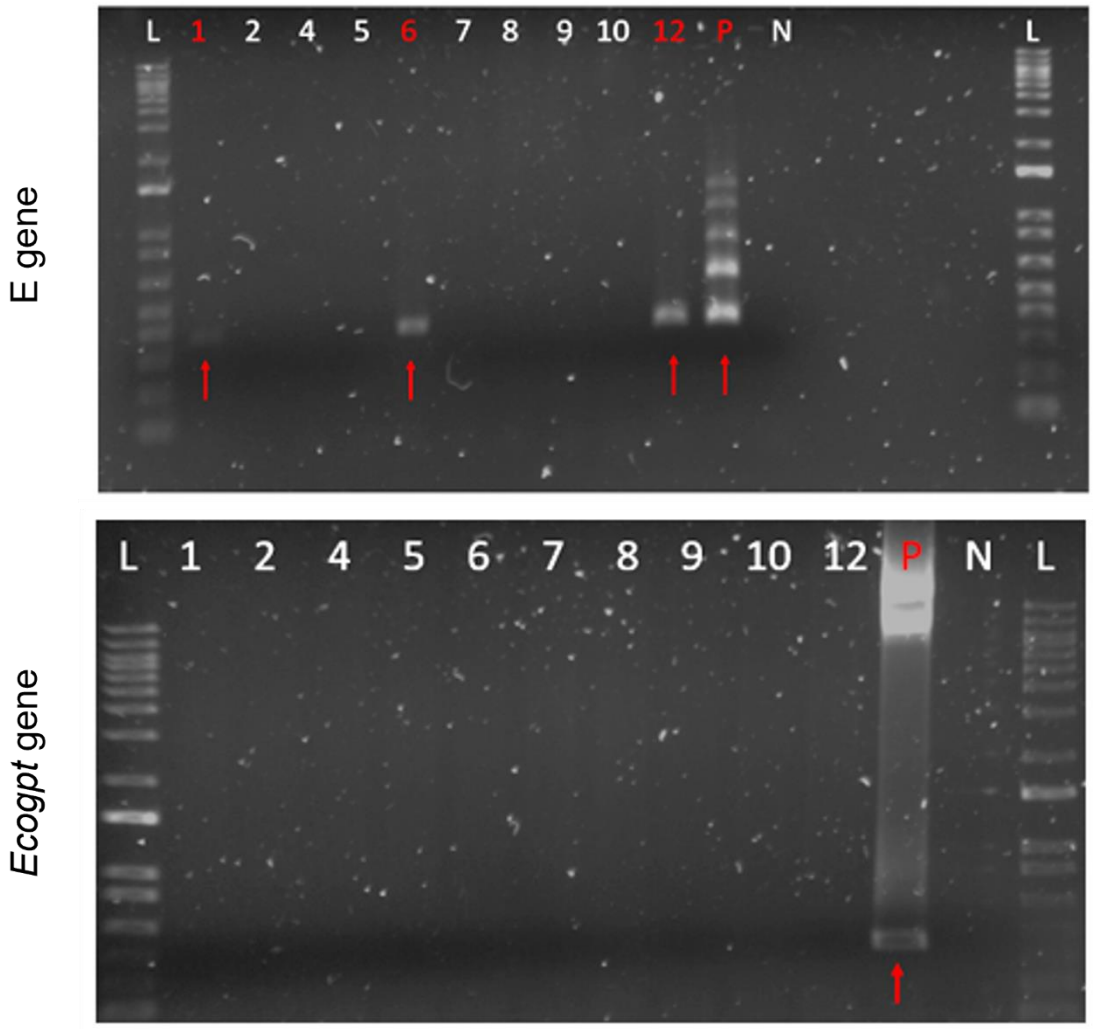

Figure 4.4. rVV ministocks screened for M41K-Cdn-Sh over the E and *Ecogpt* gene. Red arrows and labels indicate wells containing rVVs, which are positive for the E gene or *Ecogpt* gene. Numbers indicate different replicates of each rVV. P = positive control and N = negative control, H_2O. Samples were run alongside 1kb+ DNA Ladder (Invitrogen). Primers used were Ecogpt forward, Ecogpt reverse, E forward and E reverse; primer sequences can be found in Methods Section 2.7.1.

4.3.3. Generating rIBVs with either a T16A or A26F mutation in the E protein

Two rIBVs were generated in an M41-K backbone, with either a T16A or A26F mutation in the E gene, denoted M41K-T16A and M41K-A26F respectively. These viruses altered the same nucleotides as described previously for Beaudette (20) and those generated in Chapter 3. The first mutation, T16A, contained a single point mutation, A24246G, resulting in the amino acid change T16A. To generate the second mutation, A26F, three point mutations GCA → TTT were made at positions 24276 – 24278 within the E gene. These nucleotide locations are given in reference to the M41-K genome (GenBank Accession number SAMN24687558). The sequences of the inserted region can be found in Chapter 8, Section 8.2, Figures 8.4 and 8.6.

The rIBVs were generated using an in-house reverse genetics system following the protocol described in Chapter 2, Section 2.5. Following assembly of the full-length cDNA within the VV genome, two independent rVV isolates were chosen for the generation of each rIBV, to be carried forward for the recovery of rIBV (Chapter 2, Section 2.5.7). The rVV isolates were selected based on PCR verification of the lack of the *Ecogpt* selection gene and Sanger sequencing over the E gene to ensure the presence of the correct modification. Several rescue attempts were required for each rIBV, with differing success rates (Table 4.1).

Table 4.1. Rescue success rate calculated for each rIBV showing that the Beau-R rIBVs required fewer rescue attempts and had higher percentage success in comparison to those based on M41-K.

Virus	Rescue Attempts	Percentage Success
BeauR-T16A	17	52.94%
BeauR-A26F	7	42.86%
M41K-T16A	39	33.3%
M41K-A26F	20	0%

Notes: Rescue attempts have been classified as number of wells in which a rescue was attempted. Successful rescues were identified by a positive PCR band E forward and E reverse primers; primer sequences can be found in Methods Section 2.7.1. Sanger sequencing was used to ensure the correct sequence was present over the inserted region. Unlike the other rIBVs, success of BeauR-T16A isolates was assessed by the presence of visible CPE in passage 2 of the rescued virus.

Three isolates were generated for M41K-T16A denoted 2.3, 2.6 and 8.3. A standard nomenclature for each of the viruses was used in which the first number represents the rVV ministock and the second number represents the rescue attempt. This means that 2.3 and 2.6 are derived from the same rVV ministock and therefore the same IBV cDNA assembly; 8.3 was derived independently. No successful rescues were achieved for M41K-A26F. To confirm the mutation was the limiting factor and not the rescue system, a rescue attempt with M41-K was carried out concurrently with M41K-A26F. The controlled rescue resulted in the successful rescue of M41-K but not M41K-A26F. This demonstrated that the rescue system was not the issue with generating M41K-A26F, but instead indicated that this virus was replication incompetent. This is in contradiction to the BeauR-A26F isolates that rescued successfully, requiring only a small number of attempts (Table 4.1). This suggests that the A26 residue has a more critical role within viral replication of the M41 strain of IBV.

Stocks of M41K-T16A isolates were generated at passage 3 within CK cells due to the lack of genetic stability observed within BeauR-T16A *in ovo* (Chapter 3, Figure 7B). Initial stocks were harvested at 24 hpi and the M41K-T16A-2.3 stock contained only 10^2 PFU of virus. The M41K-T16A-2.6 and M41K-T16A-8.3 stocks were initially at 10^3 and 10^4 PFU, respectively. A later stock at passage 4 was harvested at 48 hpi in which the M41K-T16A-2.3 stock reached 10^3 PFU of virus. Within the later stock the other two isolates of M41K-T16A were at 10^5 PFU. Consequently, experiments detailed within this chapter were carried out with very low quantities of virus to allow for inclusion of this isolate. Throughout this thesis, parental M41-K will be shown in orange, M41K-T16A isolates will be shown in red and M41K-A26F will be shown in yellow.

4.3.4. Generating whole genome sequences of rIBVs using Next Generation Sequencing (NGS)

Whole genome sequences of M41K-T16A isolates were assembled using NGS, to obtain a consensus sequence of each. These sequences were compared to the parental M41-K sequence (GenBank Accession number SAMN24687558). Due to financial limitations of this project, only one replicate was performed. Accordingly, no variant calling could be performed on the resulting data and artifacts of the sequencing reaction could not be established.

The M41K-T16A isolates required many rescue attempts, and the rescued viruses generated several mutations in other regions of the genome which may have facilitated the success of the rescue. The T16A mutation is a single nucleotide change at position 24254 from **A**CA → **G**CA. This mutation was detected at consensus level and high frequency for each isolate of M41K-T16A. Non-synonymous mutations in other regions of the genome were detected at consensus level, including several within the S and M genes (Table 4.2).

Table 4.2. Whole genome sequencing to assess mutations present at consensus level within M14K-T16A isolates.

rIBV	Isolate	Position	Reference nt	Altered nt	Depth	Allele freq. in population (%)	aa change	Gene
M41K-T16A	2.3	13926	G	T	10	60.00	S538I	Nsp12
		13930	A	G	10	60.00	T539T	Nsp12
		23843	T	TAAA	574	78.92	1158+K	S2
		24254	A	G	1474	98.71	T16A	E
	2.6	20469	T	C	702	86.04	F36L	S1
		24254	A	G	3353	96.18	T16A	E
		25319	TA	T	2750	73.09	*	4b
	8.3	22273	T	C	2731	70.49	I637T	S2
		24254	A	G	8245	99.96	T16A	E
		25051	G	A	17159	99.86	R182H	M
		25458	T	TA	14427	92.35	*	4b

Notes: M41K-T16A stocks used to generate this sequence data was at passage 4 in CK cells. The “Reference nt” column shows the nucleotide present at that position in parental M41-K (GenBank Accession number SAMN24687558) and the “Altered nt” column represents the different nucleotide present in the isolate. The depth shows the number of reads over the nucleotide position of interest and the allele frequency is the percentage of reads which contained the altered nucleotide. Mutations listed were determined to be consensus level if the percentage within the population was above 50 %. Rows highlighted in purple indicate the T16A mutation. * indicates a mutation within a string of adenosine nucleotides, these were previously observed in populations of IBV (203).

In M41K-T16A-2.3, two mutations G13926T and A13930G were identified in the RdRp nsp12 which correspond to the amino acid changes S538I and T539T. The depth over this region is extremely low so these mutations are likely artifacts caused by the lack of reads. Additionally, three adenosine residues were inserted near the end of the S gene in the M41K-T16A-2.3 isolate, resulting in a codon (AAA) insertion. This inserts a lysine residue into the S2 subunit and therefore does not cause a frameshift in the sequence. These mutations are present within a string of adenosine nucleotides in the M41-K sequence and could be a result of sequencing error, as it is a low complexity region.

Mutations were observed in accessory protein ORF 4b of the M41K-T16A-2.6 and M41K-T16A-8.3 isolates. These mutations are present in a region of 4b which has a high level of sequence variation (203), so are unlikely to have functional roles.

Several mutations were detected which are hypothesised to implement functional changes within the virion. In M41K-T16A-2.6, a T20469C substitution within the S gene was identified which resulted in the amino acid change F36L in the S1 subunit. A T22273C mutation was discovered in M41K-T16A-8.3 which resulted in the amino acid change I637T in the S2 subunit. An additional mutation in M41K-T16A-8.3, G25051A within the M gene, was found which caused the amino acid change R182H.

Different mutations are present within isolates which originated from the same original rVV stock (i.e., 2.3 v. 2.6). This suggests that the mutations identified within the M41K-T16A isolates were acquired from the rescue and therefore may have been selected for to facilitate successful viral replication.

4.3.5. Computational modelling of the S and M protein mutations uncovered by NGS sequencing

Two independent non-synonymous mutations were discovered within the S gene of the M41K-T16A isolates. The F36L mutation in the M41K-T16A-2.6 isolate is present within the S1 receptor binding domain, which is predicted to be within the region aa19-69 (204). Consequently, this work aimed to predict whether this mutation imposed structural changes to the receptor binding pocket. Notably, the receptor for IBV is still unknown and therefore the receptor binding domain is not confirmed. Several potential receptors for IBV have recently been reviewed (61).

The predicted models found no differences in S structure caused by the F36L mutation (Figure 4.5.A). Additionally, no differences in electrostatic charge of the S protein were detected for the whole protein, or over the predicted receptor binding domain (Figure 4.5.B). This suggests the F36L mutation in M41K-T16A-2.6 did not alter the structure, or charge of the predicted receptor binding pocket in the S1 protein.

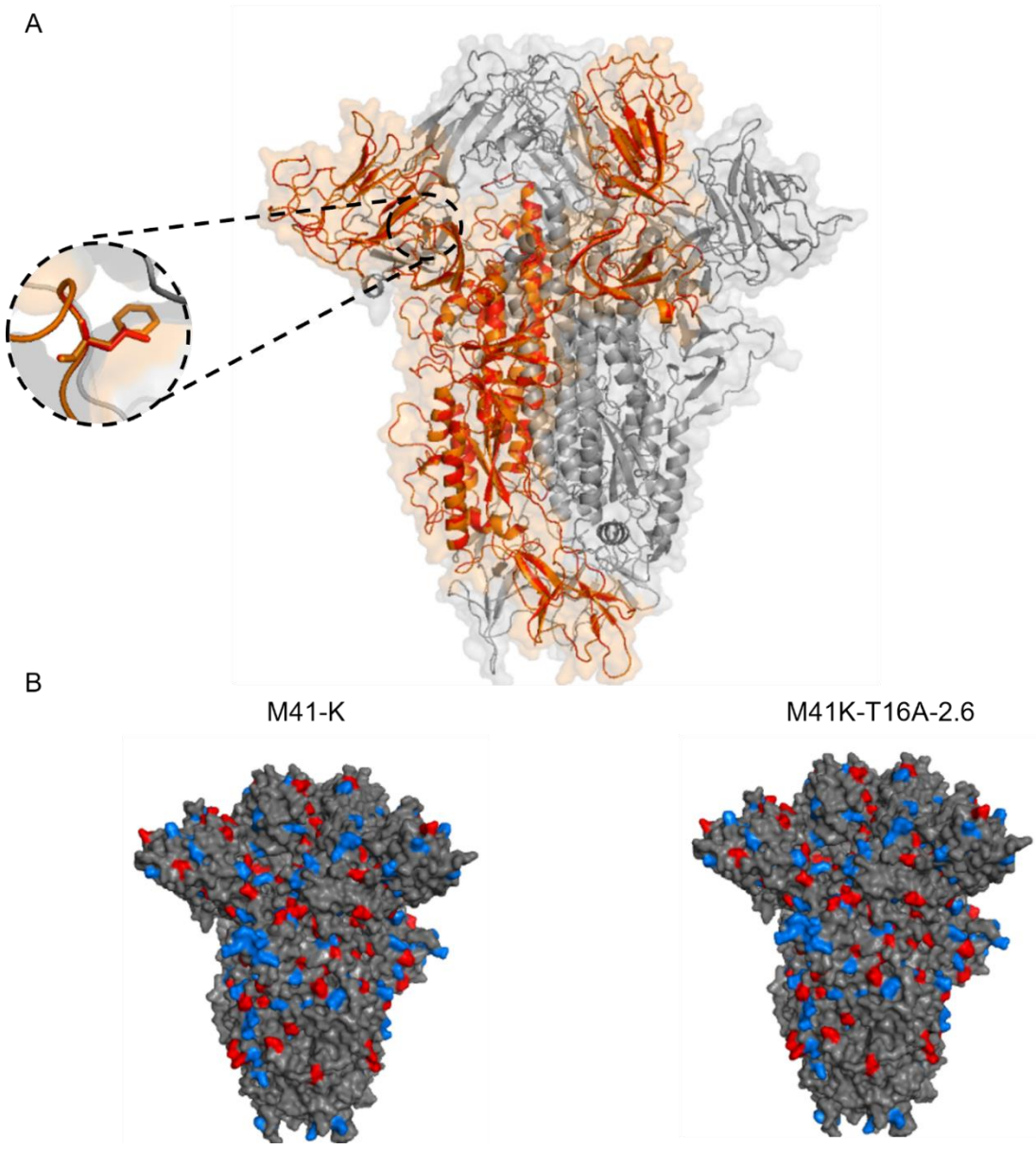

Figure 4.5. Structural changes within the S protein resulting from the F36L mutation present in M41K-T16A-2.6. Predicted trimeric S structures of the M41-K and M41K-T16A-2.6 isolates were generated using SWISS-MODEL. The relevant sequences were inputted and used an existing IBV M41 cryo-EM structure was used as a template - RCSB PDB: 6CV0. The PDB structures were then exported and rendered using PyMol. (A) Rendered structures were overlayed and the F36L point mutation was isolated and enhanced. A single S protomer is highlighted in orange for M41-K and red for M41K-T16A-2.6. (B) Electrostatic charges of trimeric S protein in M41-K and M41K-T16A-2.6.

FPs are essential for the fusion of viral envelopes with cellular membranes. The I637T mutation present in the M41K-T16A-8.3 isolate (Figure 4.6) is located near the region (aa?-795), predicted to act as a FP within the S2 protein (96, 97). This mutation may not be within the FP, as the position of the starting amino acid residue of the FP is unknown for IBV. The exact aa sequence of the FP has been identified within the *Betacoronavirus* S2 proteins (205). The predicted structure of the IBV S protein with the I637T mutation was modelled. No differences in structure were observed (Figure 4.6).

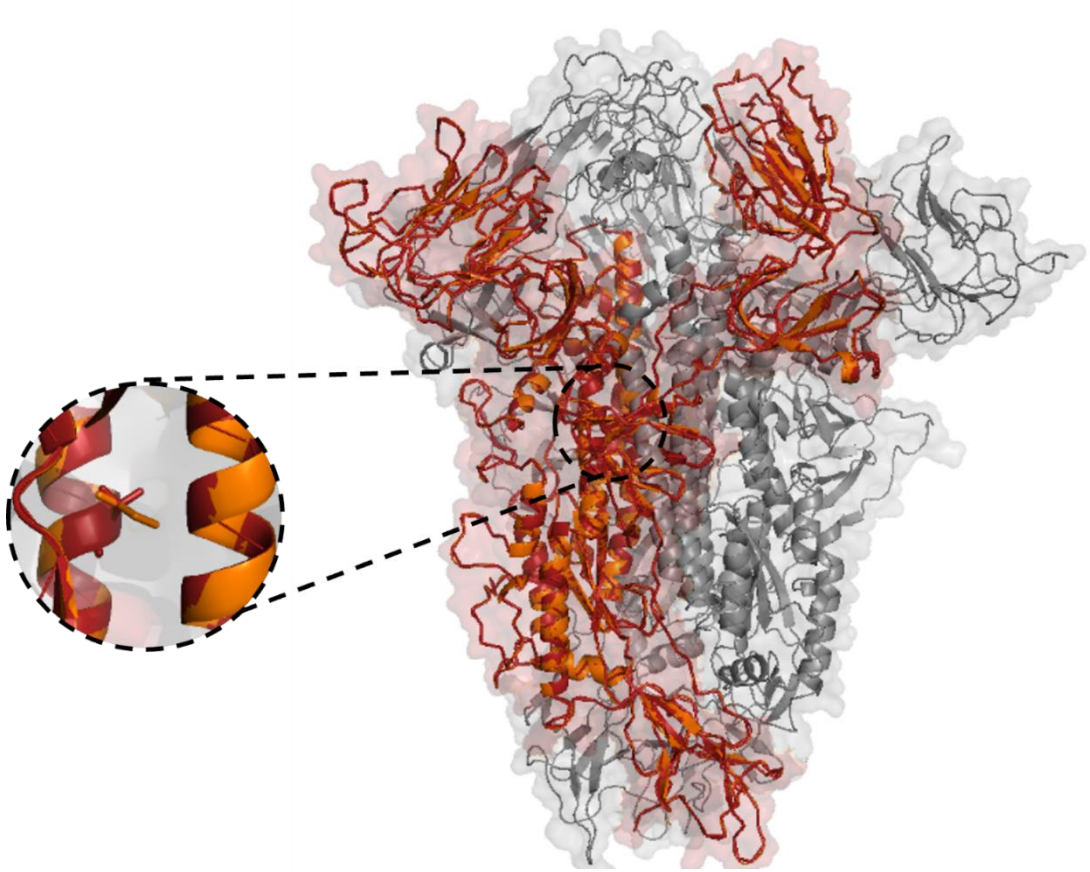

Figure 4.6. Predicted structural changes in the S protein when the 1637T mutation is present in M41K-T16A-8.3. Predicted structures of the M41-K and M41K-T16A-8.3 isolate trimeric S structures were generated using SWISS-MODEL. The relevant sequences were inputted and used an existing IBV M41 cryo-EM structure as a template - RCSB PDB: 6CV0. The PDB structures were then exported and rendered using PyMol. A single S protomer is highlighted in orange for M41-K and red for M41K-T16A-8.3. Rendered structures were overlayed and the I637T point mutation was isolated and enhanced.

The G25051A mutation found within the M41K-T16A-8.3 isolate resulted in the amino acid change R182H. This mutation is present within the aa119-203 region of the M protein, which is required for interaction between the E and M proteins (75). The structure of the IBV M protein has not yet been solved, so a predicted model of the M41-K M protein was obtained using AlphaFold2 (Figure 4.7). No differences in structure were found in the region around the R182H residue other than the altered amino acid. Although, a structural change resulting in the formation of an alpha helix was detected at positions aa163-165, which have the amino acid sequence PDH. The amino acid sequence is comparable between M41-K and M41K-T16A-8.3 over this region. This indicates that the R182H mutation may have caused this subsequent twist in the structure. As this aa163-165 structural change is located within the region aa119-203, required for E and M protein interaction (75), it may result in differing binding affinity between these proteins.

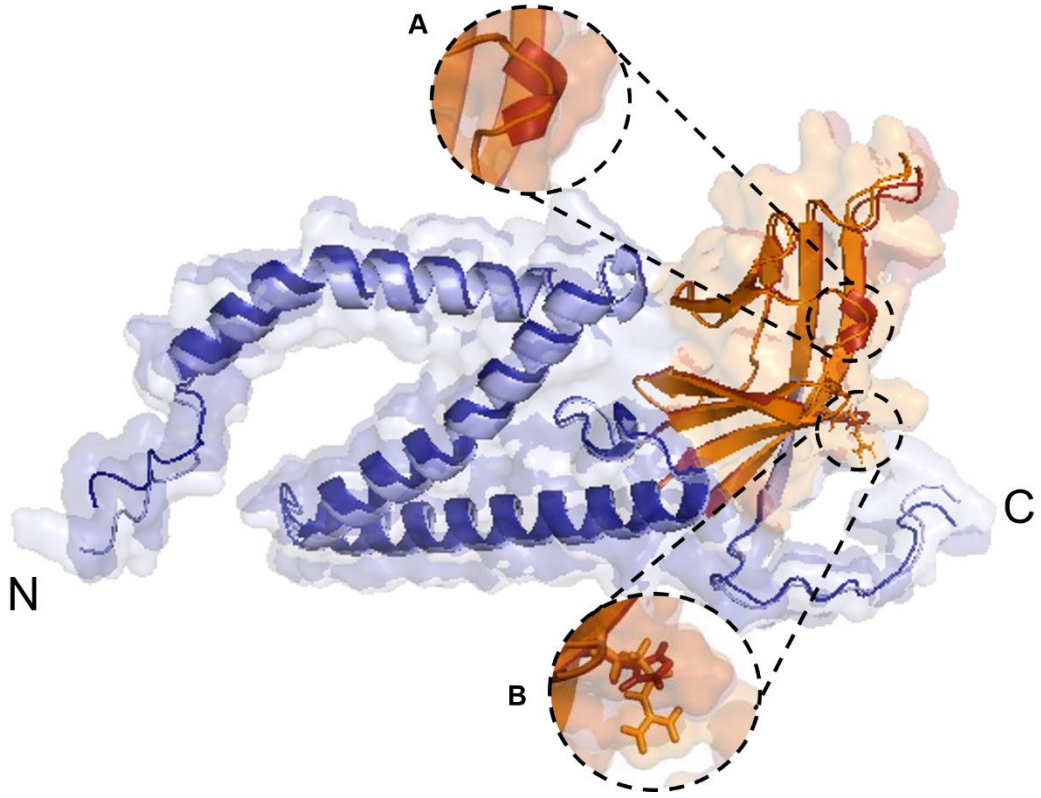

Figure 4.7. Predicted structural changes generated within the M41K-T16A-8.3 M protein with the R182H mutation. Predicted structures of the M41-K M protein (light blue/orange) overlayed with the M41K-T16A-8.3 M protein (dark blue/ red). Region predicted to be responsible for E and M interaction (aa119-203) is highlighted in orange/red. Predicted models of each M protein were generated using AlphaFold2. The relevant sequences were imported and PDB files exported. Rendered structures were overlayed and areas of interest were isolated and enhanced. (A) aa163-165 within the M protein sequence. (B) Location and structural changes resulting from the R182 mutation.

4.3.6. Investigating the genetic stability of the T16A mutation *in vitro.*

Previous research within the Beaudette strain of IBV with a T16A mutation showed that there is a selective pressure to maintain the IC activity of these residues in Vero and DF1 cells (20). This was also seen in this thesis during investigation of genetic stability of the BeauR-T16A isolates *in ovo* and in CK cells (Chapter 3, Figures 6 and 7).

The M41K-T16A isolates have been passaged in CK cells and *in ovo* to assess whether the same selection is present when this mutation is generated within a pathogenic strain (Figure 4.8). No mutations were detected outside of the TMD detailed in Figure 4.8. The M41K-T16A-8.3 isolate was stable after one passage *in ovo* and 10 passages *in vitro*. *In vitro,* the M41K-T16A-2.6 isolate generated a A16T mutation in half the passaged replicates. When passaged *in ovo,* M41K-T16A-2.6 generated a A16S mutation in all three replicates. The M41K-T16A-2.3 passaging information is not detailed in Figure 4.8 because it was not detected at passage 5 in CK cells. The sequence for this virus was stable after one passage *in ovo.*

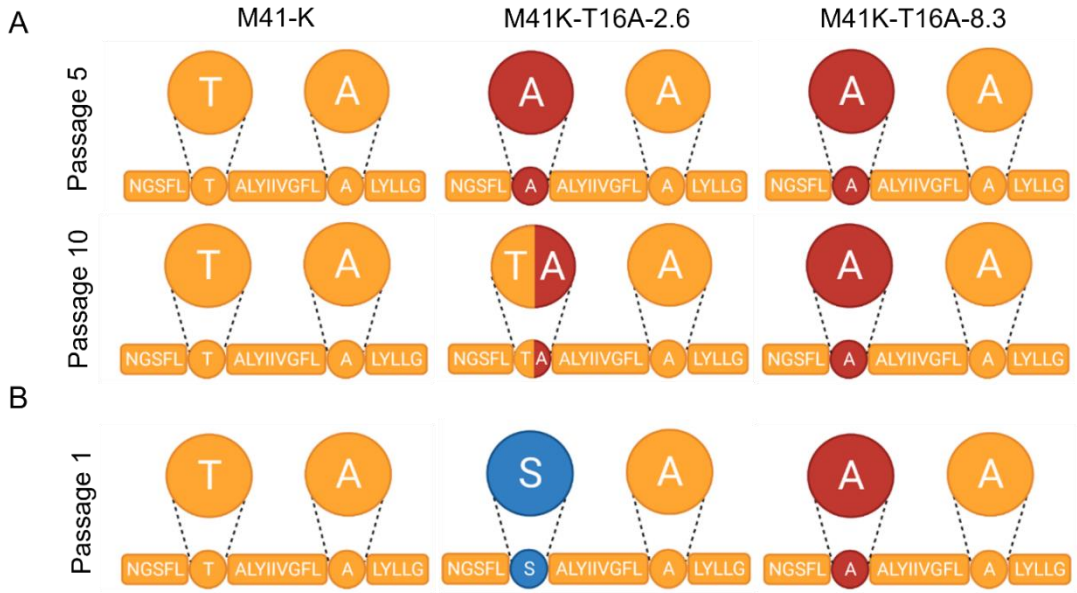

Figure 4.8. Assessing the genetic stability of M41K-T16A in CK cells and *in ovo*. The schematic represents the transmembrane domain (TMD) of the E gene with the T16 and A26 residues highlighted with circles. M41-K sequence is shown in orange, the T16A mutation in red and the A16S mutation in blue. (A) Four replicates of each virus were passaged 10 times alongside parental Beau-R and mock wells. At passage 5 and 10, supernatant was harvested, and Sanger sequenced over the E gene. (B) In replicates of three, embryonated eggs were infected with each virus. Allantoic fluid was harvested 24 hpi and Sanger sequenced over the E gene.

4.3.7. M41K-T16A-2.3 produces smaller plaques in CK cells than M41-K.

Research carried out within the Beaudette strain of IBV containing the T16A mutation observed reduced plaque size in comparison to WT in Vero cells (152). In this thesis, BeauR-T16A also exhibited reduced plaque size compared to parental Beau-R, upon infection in primary CK cells (Chapter 3, Figure 3).

To determine whether this same reduction would be observed in pathogenic strains, the plaque morphology and size observed by all M41K-T16A isolates were investigated in primary CK cells and compared to M41-K (Figure 4.9). This work found that the M41K-T16A-2.3 isolate displayed differing plaque morphology to the other isolates of M41K-T16A and M41-K (Figure 4.9.A). Additionally, the plaque size of M41K-T16A-2.3 was significantly smaller than those generated by M41-K (Figure 4.9.B). The other two isolates of M41K-T16A showed comparable plaque morphology and size to M41-K.

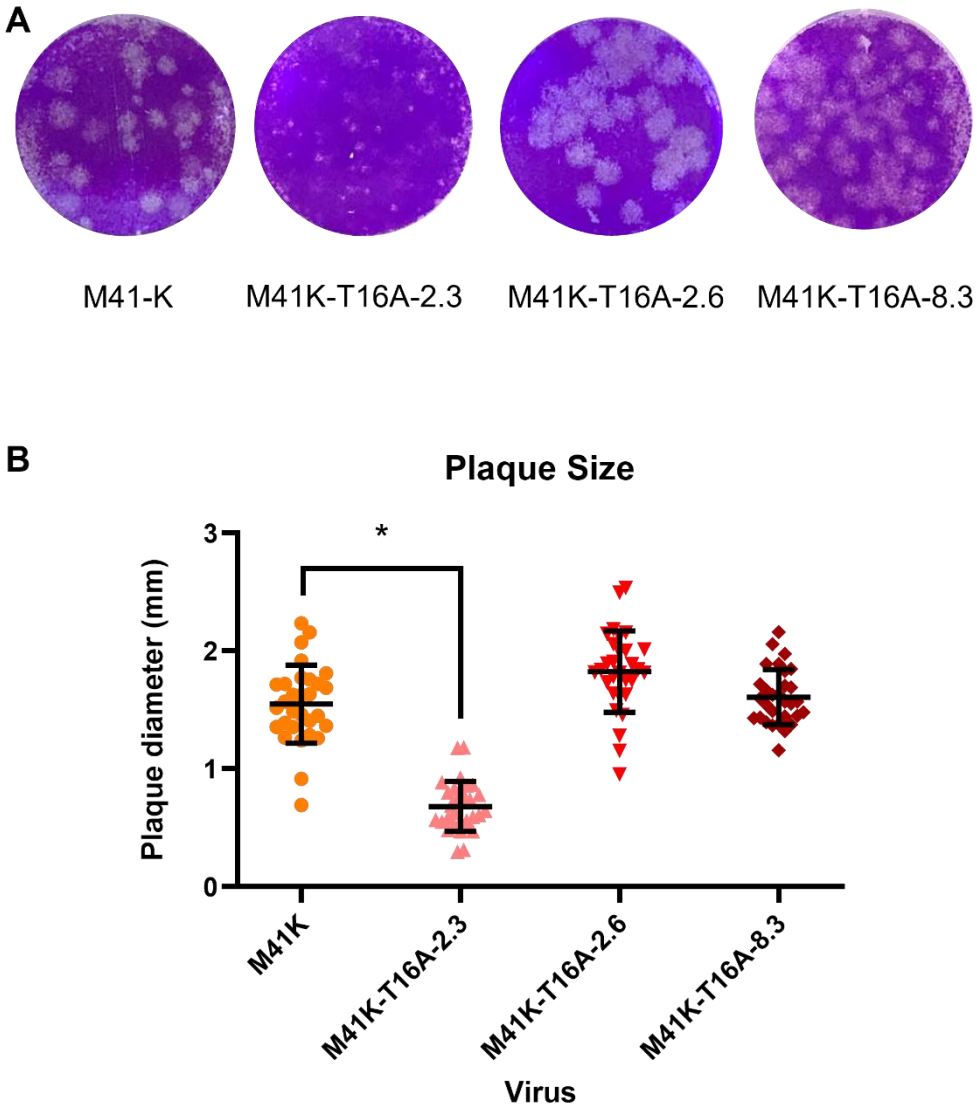

Figure 4.9. M41K-T16A-2.3 exhibits smaller plaque size than parental M41-K. (A) Representative images of plaques formed by each of the rIBVs. (B) Plaque diameter was measured using ImageJ software with 10 plaques counted per virus for each of the three biological repeats. Error bars represent standard deviation (SD). Statistical analysis was carried out using a one-way analysis of variance (ANOVA) with significance taken as p-value <0.05, represented with *.

4.3.8. Assessment of the replication kinetics of rIBVs *in vitro*

Previously, Beaudette containing a T16A mutation was shown to replicate comparably to parental Beaudette within Vero cells (20). This same result was observed within this thesis when the replication kinetics of BeauR-T16A was assessed in CK, DF1 and Vero cells (Chapter 3, Figure 2). This work aimed to assess whether the T16A mutation would affect the replication kinetics of a pathogenic strain of IBV *in vitro* (Figure 4.10).

The M41K-T16A-2.6 and M41K-T16A-8.3 isolates replicated comparably to the parental M41-K (Figure 4.10). Conversely, M41K-T16A-2.3 replicated to a significantly lower titre than M41-K at 48 hpi. This suggests that the consensus level mutations present in S and M genes in M41K-T16A-2.6 and M41K-T16A-8.3 may be capable of compensating for the T16A mutation. This result substantiated the difference in plaque size observed in Figure 4.9. The supernatant from the 96 hpi was Sanger sequenced over the E gene and each isolate had the expected sequence. Additionally, single-step replication kinetics were also assessed for the M41K-T16A isolates but no virus could be detected over the course of the experiment, due to the initial infection being carried out at a low titre.

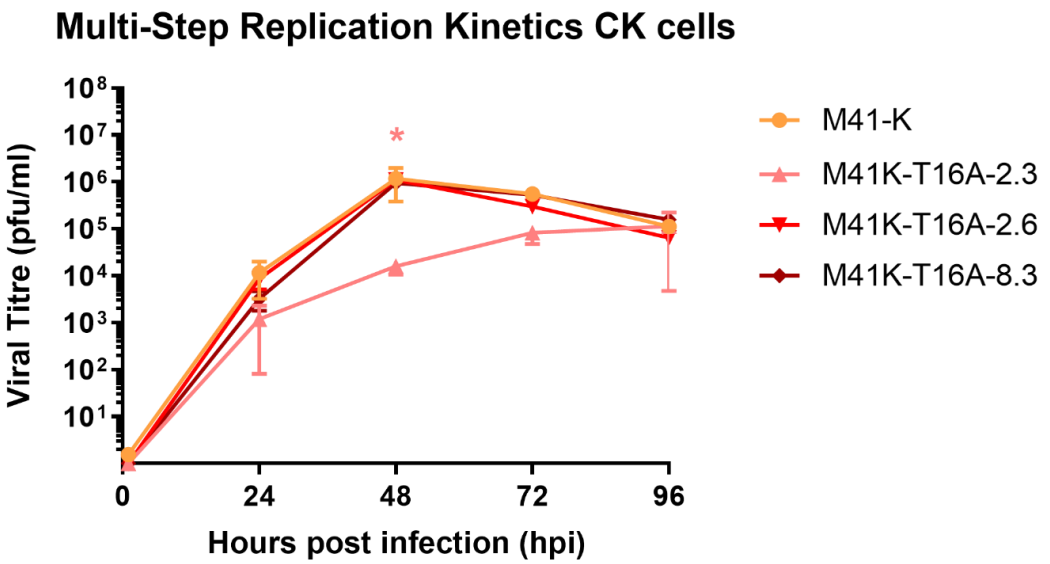

Figure 4.10. Replication kinetics of M41K-T16A isolates in chick kidney (CK) cells. All isolates of M41K-T16A were assessed in CK cells and compared to M41-K, infected at a titre of $1x10^2$ PFU. The supernatant was harvested at 1-, 24-, 48-, 72- and 96-hpi and titrated on CK cells to determine the quantity of virus present. Error bars represent ± standard error of the mean (SEM) of three independent experiments. Statistical analysis was carried out using a two-way analysis of variance (ANOVA), p-value of <0.05 (*) is indicated in relation to M41-K.

4.3.9. Replication of the M41K-T16A isolates is not comparable to parental M41-K *in ovo*.

Previous work investigating the T16A mutation in the non-pathogenic strain, Beaudette, found that this rIBV had a marginally lower embryonic lethal dose *in ovo,* which may indicate that the T16 residue aids replication of IBV *in ovo* (152). This was also investigated using the BeauR-T16A isolates which found comparable growth of the isolates to Beau-R *in ovo* but each isolate generated compensatory or revertant mutations thought to facilitate this (Chapter 3, Figure 7). To further investigate the replication of the M41K-T16A isolates, viruses were inoculated into the allantoic cavities of 10-day-old SPF embryonated VALO eggs (Figure 4.11). In replicates of three, isolates of M41K-T16A were inoculated at a titre of $1x10^2$ PFU, and the allantoic fluid was harvested at 24 hpi (Figure 4.11).

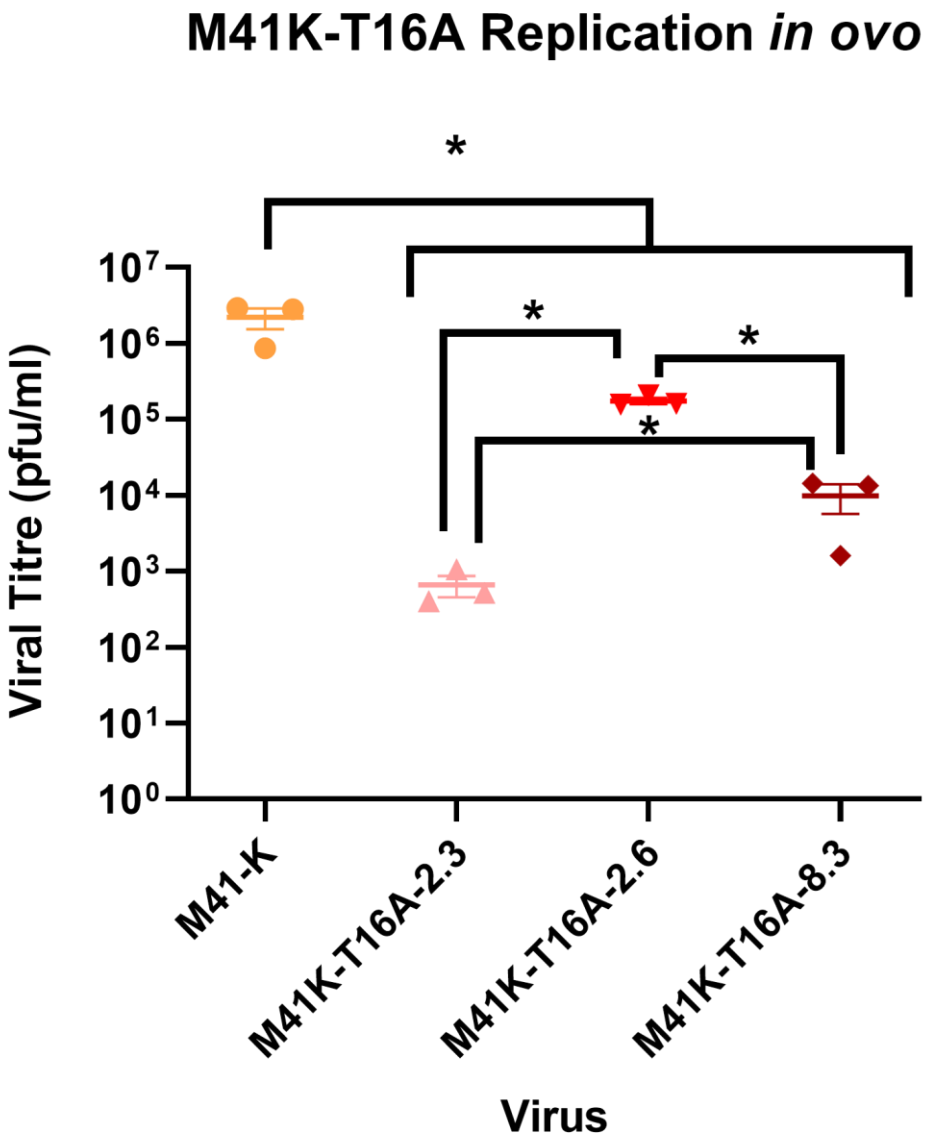

Figure 4.11. Assessment of replication of M41K-T16A isolates *in ovo.* Embryonated VALO eggs were infected with M41-K or the M41K-T16A isolates at a titre of $1x10^2$ PFU. The allantoic fluid from the eggs was harvested at 24 hpi and titrated on CK cells to determine the quantity of virus present. Error bars represent ± standard error of the mean (SEM) of three independent experiments. A one-way analysis of variance (ANOVA) test was performed, p-value of <0.05 is indicated by *.

The genetic stability of the isolates during this experiment are detailed in Figure 4.8.B, except M41K-T16A-2.3 which is not shown but had a stable sequence over the E gene. These results showed that in all three independent replicates of the M41K-T16A-2.6 isolate, a G24254T mutation (**G**CA → **T**CA) was generated, resulting in amino acid change A16S (Figure 4.8). This mutation may be compensatory, as the M41K-T16A-2.6 isolate grows at a higher titre than the other two isolates.

This result, along with the *in ovo* replication of BeauR-T16A, suggests that the T16 residue is advantageous for *in ovo* replication. M41K-T16A isolates all replicated to significantly different titres. The differences between M41K-T16A-2.3 and M41K-T16A-8.3 may be due to mutations present in other regions of the genome (Table 4.2), which could partially compensate for the T16A mutation. Notably, as in the replication kinetics assessed in the CK cells, M41K-T16A-2.3 replicated to the lowest titre.

4.3.10. Infection with M41K-T16A-2.3 isolate displayed reduced CPE in primary CK cells.

CPE associated with CK cells infected with IBV include syncytial formation, cell rounding and detaching from the cell culture dish (206). During investigation into the BeauR-T16A isolates, reduced CPE was observed within CK cells in comparison to Beau-R and BeauR-A26F isolates (Chapter 3, Figure 8). It was unknown whether a T16A mutation generated in the pathogenic M41-K strain would cause the same lack of CPE. To investigate this, CK cells were infected with the M41K-T16A isolates along with control virus M41-K, which showed that the M41K-T16A-2.3 caused marginally reduced CPE, including fewer rounding cells, in comparison to parental M41-K (Figure 4.12).

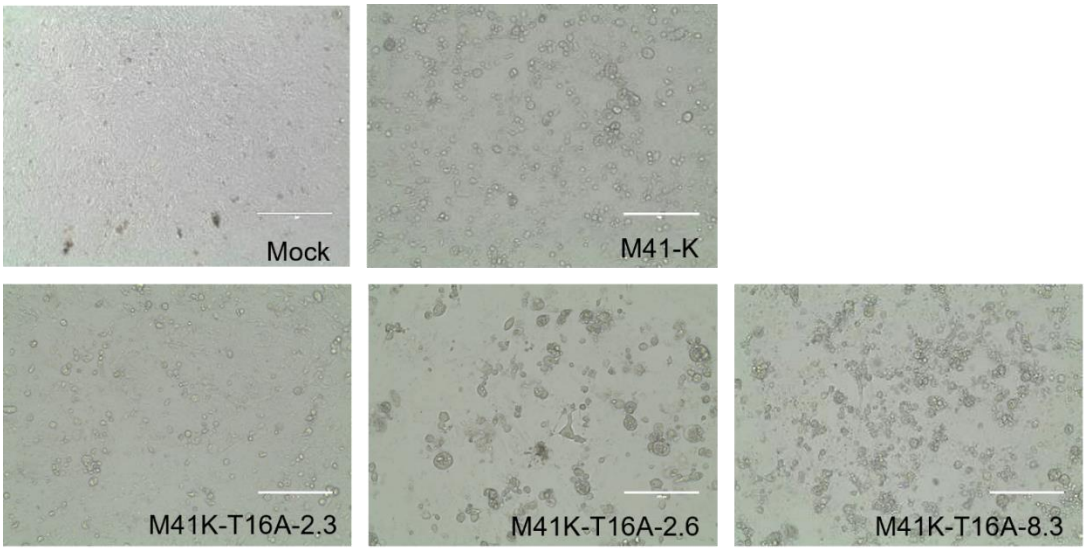

Figure 4.12. CPE observed in rIBV infected CK cells. CK cells uninfected and infected with M41-K or M41K-T16A isolates at a titre $1x10^2$ PFU. Mock cells were inoculated with media. Images were taken on a light microscope at 48 hpi. Scale bar represents 200 µM.

CellTiter Glo® reagent quantifies the number of metabolically active cells present through the level of ATP present (207). This assay was used to assess the cell viability of cells infected with M41K-T16A isolates in comparison to M41-K. Overall, the M41K-T16A caused a comparable reduction in cell viability to M41-K, but it does appear that the M41K-T16A-2.6 isolate shows the greatest reduction in viability and M41K-T16A-2.3 shows the lowest reduction (Figure 4.13).

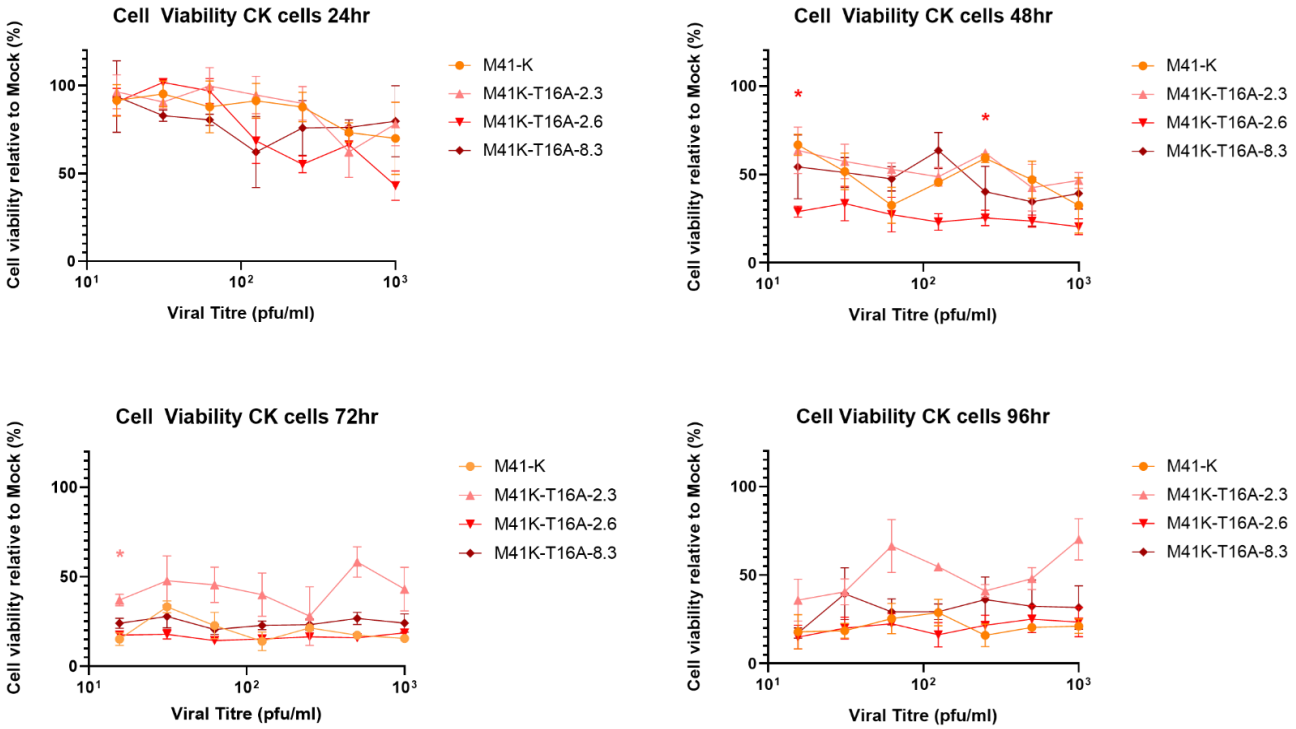

Figure 4.13. Reduction in cell viability observed in CK cells upon infection with the M41K-T16A isolates or M41-K. CellTiter Glo® reagent was used to quantify cell viability in CK cells at a range of viral titres. Cell viability was assessed every 24 hpi. Cell and media only controls were included to account for background signal. Data is represented as percentage cell viability relative to mock infected cells. Error bars represent ± standard error of the mean (SEM) of three independent experiments. Statistical analysis was carried out using a two-way analysis of variance (ANOVA) with significance taken as p-value <0.05, significance represented in relation to M41-K with a *, in a colour corresponding to the isolate.

4.3.11. M41K-T16A-2.6 expresses higher levels of E protein

Syncytial formation is attributed to the S2 protomer during CoV infection and the presence of the T16A mutation has been demonstrated to result in the incorrect processing of the S2 protein (84). To investigate whether the observed differences in CPE are the consequence of the T16A mutation, an immunoblot was carried out to determine whether the level of S2 protein differed between the viruses (Figure 4.14.A). The level of protein expression was quantified and is displayed relative to β-actin (Figure 4.14.B). It appears M41K-T16A-2.3 and M41K-T16A-8.3 showed slightly lower levels of S2 than M41-K however the measure of expression suggests that overall, the S2 protein expression was comparable for each of the viruses. Unexpectedly, this work found that the level of E protein expression differed between the viruses with the M41K-T16A-2.6 isolate expressing significantly more E protein than the other isolates or M41-K (Figure 4.14).

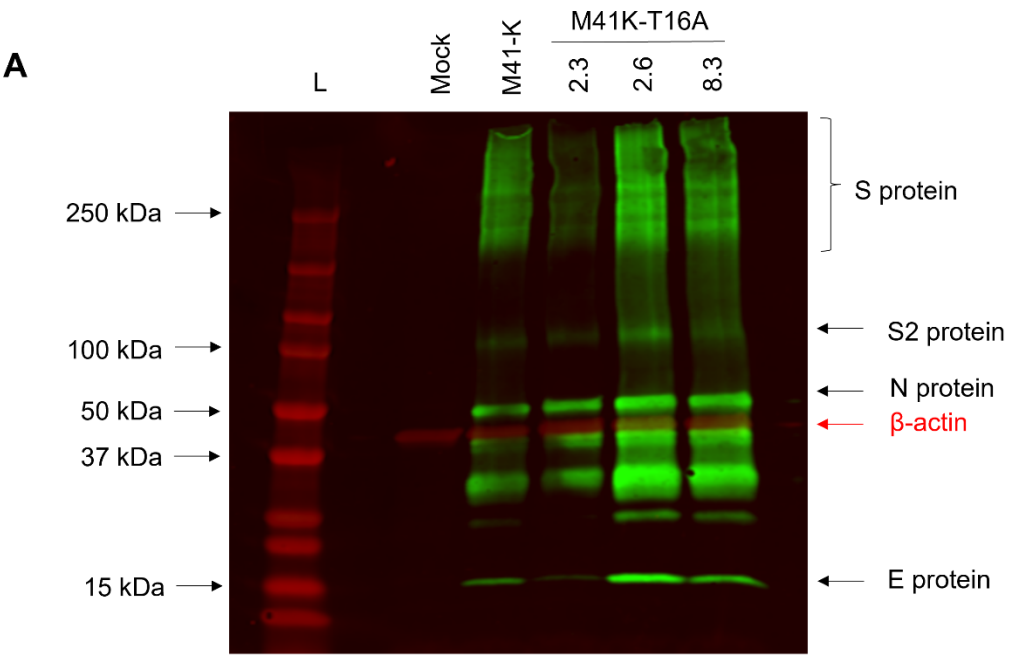
A
L
Mock
M41-K
M41K-T16A
2.3
2.6
8.3
250 kDa
100 kDa
50 kDa
37 kDa
15 kDa
S protein
S2 protein
N protein
β-actin
E protein

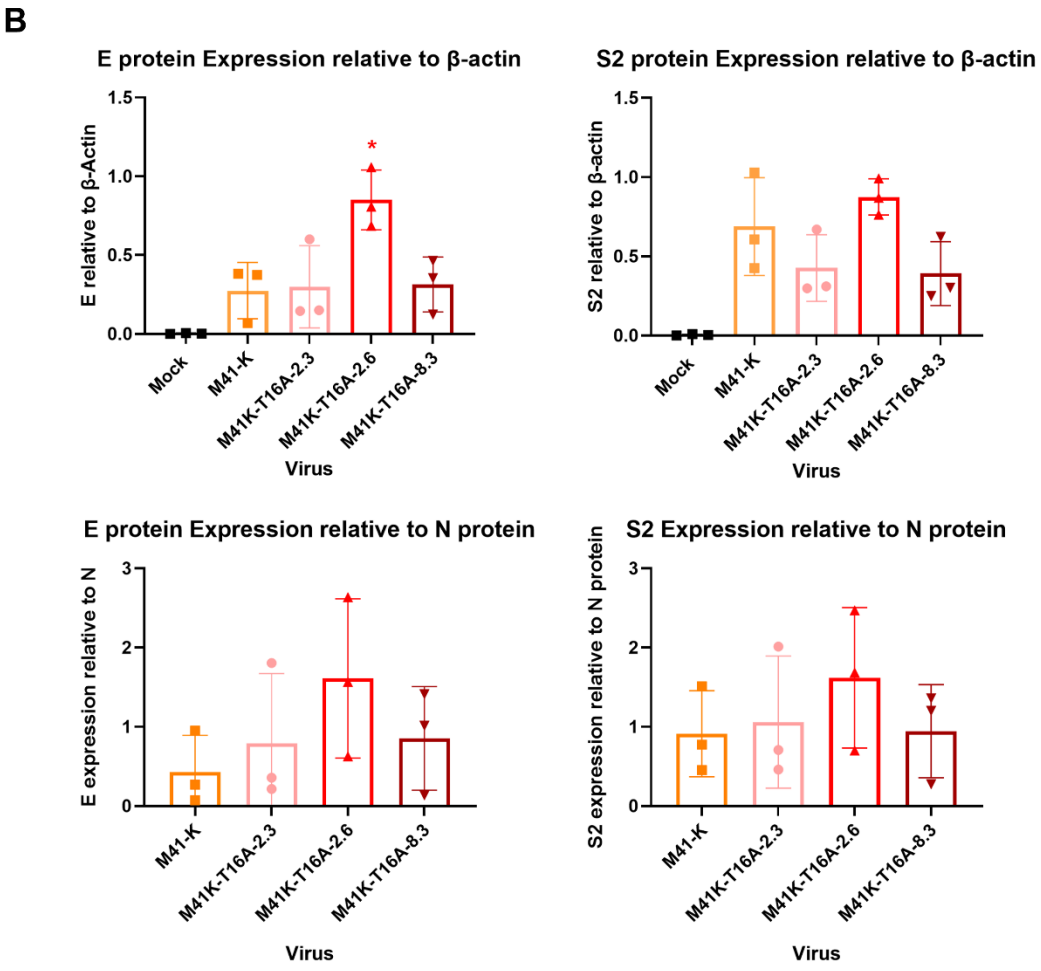
B
E protein Expression relative to β-actin
E relative to β-Actin
Mock
M41-K
M41K-T16A-2.3
M41K-T16A-2.6
M41K-T16A-8.3
Virus
S2 protein Expression relative to β-actin
S2 relative to β-actin
E protein Expression relative to N protein
E expression relative to N
S2 Expression relative to N protein
S2 expression relative to N protein

Figure 4.14. E protein expression is higher within M41K-T16A-2.6 infected cells. CK cells were mock infected or infected with $1x10^2$ PFU with M41-K or M41K-T16A isolates. Cell lysates were harvested at 24 hpi. (A) Samples were separated by SDS-PAGE followed by western blot (WB) using anti-IBV (anti-S2), AF12 (anti-E) and anti-β-actin antibodies. (B) Quantification of western blot (WB) using ImageStudio software. Protein expression displayed has been calculated relative to β-actin or the N protein. Error bars represent ± standard deviation (SD). Statistical analysis was carried out using a one-way analysis of variance (ANOVA), significance is taken as p-value < 0.05 and * indicates significance relative to M41-K.

4.3.12. M41K-T16A isolates display comparable thermal stability to parental M41-K.

The CoV E protein has been hypothesised to play a role in viral stability through interaction with the viral envelope (208). The thermostability of the M41K-T16A isolates was assessed to ensure that the T16A mutation does not affect the stability of the virion envelope.

An initial experiment was performed in which viruses were incubated for 1 h at a wide range of temperatures to determine which should be investigated. The temperatures included in the initial experiment were 4 °C, 21 °C, 37 °C, 41 °C and 56 °C. The 4 °C temperature was selected to determine whether there was a decrease in viral titre at lower temperatures. 21 °C was selected to represent room temperature. The 37 °C was selected to represent the temperature at which the virus is incubated during cell culture and the temperature of the respiratory tract which is where IBV replicates in the bird. 41 °C was selected as it is the internal body temperature of a chicken (209). Finally, 56 °C was selected as it has previously been shown that incubating IBV for 1 h at 56 °C inactivates the virus (210).

This preliminary experiment showed that the virus was inactivated at 47 °C, data not shown. Additionally, there was no decrease in viral titre at 37 °C. As a result, the viruses were then assessed between 37 °C and 47 °C with increments of 2 °C.

For all isolates of M41K-T16A, the thermal stability was comparable to M41-K, indicating that the T16A mutation did not affect the overall stability of the virus (Figure 4.15). Only two replicates were performed due to the large volumes of M41K-T16A-2.3 required for each replicate.

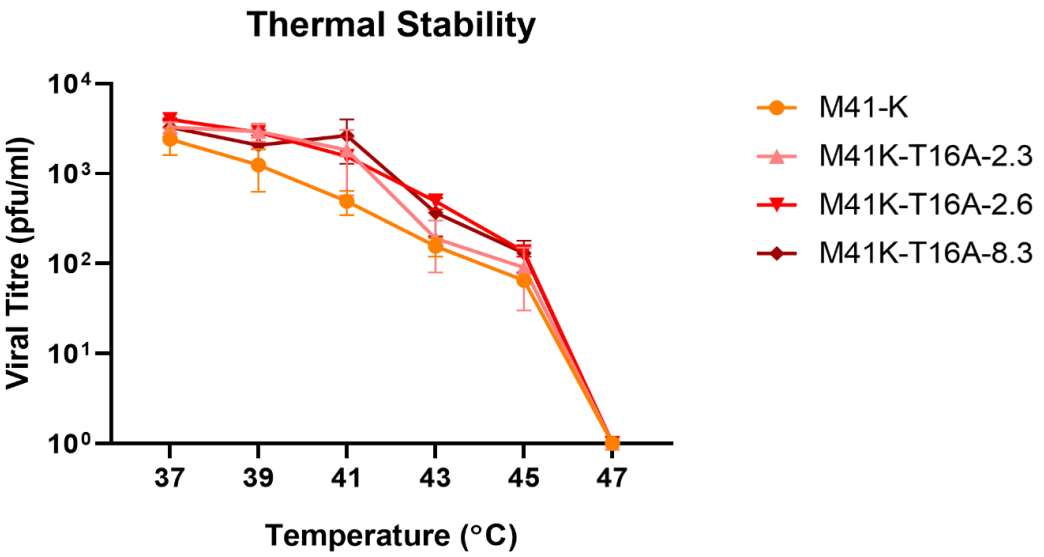

Figure 4.15. Thermal stability of the M41K-T16A isolates is comparable to M41-K. All isolates of M41K-T16A and M41-K were diluted in 1 x BES media to a titre of 1x10^3 PFU. rIBVs were incubated for 1 h over a range of 37 °C – 47 °C, in 2 °C increments. Quantification of virus present was assessed through titration on CK cells. Error bars represent ± standard error of the mean (SEM) of two independent experiments.

4.4. Discussion

For *Betacoronavirus* SARS-CoV, several studies have proposed eliminating E protein expression to generate vaccine candidates (148, 149, 197). Deletion of the E protein attenuates CoVs SARS-CoV and MHV, but these virions are replication-competent (149, 211). Conversely, for some CoVs such as TGEV, MERS-CoV and IBV loss of the E protein results in virions which are not viable. TGEV virions with a deleted E protein are not infectious (212) and MERS-CoV with an E protein deletion is propagation defective (213). The E protein is reported to be essential for recovery of IBV virions (198). To establish whether rIBVs with an altered E protein expression level had altered pathogenicity, rIBVs were designed in a pathogenic backbone, M41-K.

The M41K-Cdn-Sh rIBV could not be rescued indicating that it was replication incompetent. To characterise the role of the E protein in the future, E deletion viruses could be designed within non-pathogenic Beau-R. However, this wouldn't allow for assessment of pathogenicity. Alternatively, a partial deletion of the E protein over a region such as the hydrophobic domain could be generated. The hydrophobic domain of the E protein was deleted in Beaudette (105). These viruses were replication competent but replicated to a lower titre than WT Beaudette and were deficient in release (105).

The auxin-dependent degradation (AID) system uses a degron tag attached to the target protein. In the presence of auxin, the tagged protein is targeted for rapid degradation via the proteosome (214), which allows for controlled degradation of a protein *in vitro*. This system could be used in future work to facilitate the characterisation of pathogenic IBV lacking the E protein. Although, tagging the E protein within the virus would be difficult as it overlaps with adjacent genes at each

end. Furthermore, tagging the E protein has previously been shown to alter the membrane topology and could therefore alter functionality (142, 215).

Another method of virus attenuation targeting the E protein is altering the IC activity. The E protein IC activity was first identified in SARS-CoV (135) and was consequently shown in IBV (125). Mutations N15A and V25F in SARS-CoV have been shown to inactivate the E protein IC (136). The N15 residue is a key virulence factor *in vivo* (138), indicating that the IC activity of the E protein is a virulence determinant. The corresponding mutations in IBV are T16A and A26F, which are reported to have the same IC inactivating effect (20). These mutations were integrated in a pathogenic M41-K backbone with the aim of generating potential vaccine targets.

Three isolates of M41K-T16A were successfully rescued however the consensus sequences of the rescued viruses revealed several mutations in other regions of the genome (Table 4.2). Of note, an F36L mutation in S1 was found in M41K-T16A-2.6. Mutations in S2 (I637T) and M (R182H) were also found in M41K-T16A-8.3. Interestingly, the M41-K backbone was more sensitive to the A26F mutation than the non-pathogenic Beau-R equivalent. Twenty rescue attempts were carried out, but none were successful, whereas BeauR-A26F rescued readily. This indicates that the A26 residue plays a more critical role in viral replication in M41-K than in Beau-R. Beaudette strains of IBV are heavily lab adapted and may have lost some E functionality in the process. This work highlights the importance of characterising the E protein in a more relevant strain of IBV to those present within the field. Furthermore, it could be hypothesised that this residue is a pathogenicity determinant, as mutation of this residue in pathogenic M41-K is not viable.

The A26F mutation selects for the monomeric pool of the E protein during infection (113). The inability of M41K-A26F isolates to replicate indicates that this form of the E protein, hypothesised to alter the secretory pathway, may be essential for replication of M41-K but not Beau-R. The effect of these mutations in different strains

and assays has been summarised in a table to highlight the strain dependent effect of these mutations (Table 4.3).

Table 4.3. Summary of rIBVs generated as part of this project.

rIBV	Rescue success (%)	Isolate	Average titre (pfu/ml)	NS mutations	Genetic Stability in CK cells	Genetic Stability in ovo	Replication kinetics
Beau-R	-	-	$4.5x10^6$	-	Stable	Stable	-
BeauR-T16A	52.94	-	$5.6x10^6$	N/A	Mutations in all isolates at p10	Mutation in all isolates at p1	Comparable in CK cells and in ovo
BeauR-A26F	42.86	-	$3.7x10^6$	N/A	Mutations in one isolate at p10	Stable	Comparable in CK cells not in ovo
M41-K	-	-	$4.5x10^6$	-	Stable	Stable	-
M41K-T16A	33.33	2.3	$2.5x10^3$	N/A	N/A	Stable	Not comparable
		2.6	$1.0x10^4$	F36L (S1)	Mutation at p10	Mutation at p1	Comparable in CK cells not in ovo
		8.3	$2.3x10^4$	I637T (S2) R182H (M)	Stable	Stable	Comparable in CK cells not in ovo
M41K-A26F	0	-	-	-	-	-	-

Notes: Beau-R and M41-K were generated prior to start of this project and coincidentally the stocks used were at the same titre. NS: non-synonymous, p: passage.

In M41K-T16A-2.6 and M41K-T16A-8.3 the two independent mutations identified, F36L and I637T, respectively, in the S gene were both in predicted functional domains of the S protein. The F36L mutation was present in the predicted receptor binding domain and I637T in the FP. Exact locations of both the receptor binding domain (204) and the FP are unknown for IBV, so it is unclear whether these mutations are within these regions. In silico modelling predicted that neither of these mutations altered the structure of the S protein. Reverse genetics would need to be

carried out incorporating the mutations into M41-K to see if the binding to permissive cells had been altered. Alternatively, S protein expression plasmids with these mutations could be generated for use within binding assays.

An R182H mutation, present in M41K-T16A 8.3, was identified in the E-M binding site, aa 119-203, in the M protein (75). Predicted structure modelling found this residue did not alter the structure around this residue. The single amino acid point mutation in R182H does however cause the loss of an extended loop which is replaced with an α-helix at residues aa163-165. This change would have altered the flexibility of the M protein. Although loops do not have regular, periodic structures they can still be rigid and well defined and drastically affect the protein secondary structure. Loops on a protein surface usually mediate interactions with other molecules and the aa163-165 structural change is located within the region aa119-203, required for E and M protein interaction (75). This suggests that presence of the α-helix could change the binding affinity of this interaction. Changes in the M protein have been identified previously. A chimeric M protein was generated upon passage of the SARS-CoV-ΔE viruses, which could recover activity of the E protein to increase viral replication (111). This shows that altering the M protein could compensate for lack of E protein functionality. It would be interesting to continue this work to establish experimentally through co-IP whether the R182H mutation alters the binding affinity between these proteins.

No mutations of functional concern were detected in M41K-T16A-2.3. Throughout characterisation of these viruses, this isolate appeared the most attenuated regarding plaque size (Figure 4.9) and replication (Figure 4.10 and 4.11). It is therefore theorised that M41K-T16A-2.3 is the ‘true’ M41K-T16A isolate. If this is correct, the T16A mutation does impact viral replication and therefore the monomeric form of the E protein is important for M41-K replication. Interestingly as observed for BeauRT16A, the M41K-T16A-2.3 isolate caused less CPE than parental M41-K. The

M41KT16A-2.6 and M41K-T16A-8.3 isolates caused an increased CPE profile, including the induction of syncytium. The S protein mutations present in these isolates could be capable of inducing this increased CPE. The corresponding cytotoxicity found that although the M41K-T16A isolates caused a comparable reduction in cell viability overall, the M41K-T16A-2.3 did appear to be slightly less cytotoxic at later timepoints.

The S2 protein expression displayed within M41K-T16A isolates was comparable to parental M41-K, although this was slightly lower for M41K-T16A-2.3 and M41K-T16A8.3 (Figure 4.14). Unexpectedly, the M41K-T16A-2.6 isolate showed significantly higher E expression than the other isolates of M41K-T16A and M41-K. It would be valuable to follow this work up with qPCR assessing levels of sub-genomic (sg) mRNA 3, to establish whether this increase is also seen at transcript level.

Thermal stability is an important consideration for implementation of a vaccine in the field. This has been a critical limiting factor for many manufactured vaccines, which rapidly lose viral titre due to the lack of reliability of the cold chain required to transport the vaccine (216). The requirement for thermostable vaccines for use in the veterinary field has recently been reviewed (217). Betacoronavirus SARS-CoV with an E protein deletion has been shown to have comparable thermostability to WT virus (149). The M41K-T16A isolates showed comparable thermal stability to M41-K, which follows from the previous finding that modification or deletion of the E protein does not affect thermal stability of virions. It would however be interesting to assess the thermal stability of these isolates over longer periods.

In conclusion, this chapter found that the pathogenic M41-K strain of IBV is less tolerant to E mutations than Beau-R, with M41K-A26F unable to rescue. This indicates that T16 and A26 residues may be more vital, and with regards to latter, essential for replication of M41-K. This follows on from previous research, which found that an equivalent V25F mutation in SARS-CoV genetically unstable (138).

Chapter 5: Manipulation of the Host Cell Machinery During IBV Infection

5.1. Declaration

The work included within this study is the authors sole effort apart from the following exceptions. The mass spectrometry was carried out by Kate Heesom at the Proteomics Department at the University of Bristol. Mass spectrometry analysis was carried out by Andrew Davidson, The University of Bristol. EM was performed by Nicole Doyle, The Pirbright Institute.

5.2. Introduction

The IBV E protein has many proposed roles during infection, including manipulation of the secretory pathway (84, 113), which facilitates viral assembly and release (75, 105, 152, 218). Reports investigating these roles have predominantly been carried out using transfection systems which masks the effect of other viral proteins within these processes (84, 113, 218, 219). To remedy this, this study investigates the role of the E protein in the context of recombinant viruses.

In infected cells, the E protein is predominantly embedded into the Golgi Apparatus membranes (220), with only a small amount present within the virion envelope (221). During IBV infection, the Golgi Apparatus swells and disassembles (105). This is thought to aid the transport of viral components through the constitutive secretory

pathway by two mechanisms. The first is the slowing of the transport through the Golgi Apparatus, which facilitates correct post-translational modification of viral proteins (84). Secondly, this swelling is thought to facilitate enclosure of whole viral particles within Golgi compartments, as virions are larger than typical Golgi cargo (105).

Viroporins have been demonstrated to be responsible for this diffusion. The IAV M2 protein equilibrates the pH between the Golgi and cytoplasm resulting in cisternae dilution and slow transport through the organelle (222). The hydrophobic domain of the IBV E protein facilitates this Golgi diffusion (105), through neutralisation of the Golgi compartment (84) . Specifically, the T16 residue which is in the hydrophobic domain, has been shown to be required for this manipulation (113). Presence of the T16A mutation has been shown to result in premature cleavage of the S2 protein, due to lack of Golgi neutralisation and diffusion (84).

The role of the secretory pathway in CoV assembly and release has been investigated using cellular inhibitors. Addition of Monensin to TGEV infected cells has demonstrated that successful maturation of the virions relies on progression through the Golgi cisternae (82). Similar effects have been observed with IBV, as Monensin inhibits the assembly and release of virions (83).

The work detailed within this chapter builds on characterisation of the BeauR-T16A and BeauR-A26F viruses from Chapter 3. The exact mechanisms used by the E protein to alter the cellular machinery remain elusive, therefore, this chapter aims to investigate the manipulation of cellular machinery using rIBVs possessing either the T16A or A26F mutations. Additionally, a wide range of inhibitors which target different components of the secretory system have been used to interrogate the role of the T16A and A26F mutations in assembly and release of virions.

5.3. Results

5.3.1. E antibody optimisation

An optimised E protein antibody was required to facilitate interrogation of the E protein using immunoassays. Currently, there are no commercially available antibodies against the IBV E protein. The antibodies assessed were obtained from the laboratory archives of the Coronavirus Group, The Pirbright Institute.

Two antibodies, IE7 and AF12 were assessed using a WB. Both antibodies generated a band at the expected size (~ 12 kDa) for the IBV E protein in Beau-R or M41-CK infected cells (Figure 5.1). Additionally non-specific bands were not identified. The AF12 E antibody was carried forward within this work as there was a larger volume of antibody available. The expression of the E protein in M41-CK is higher than in Beau-R, this is discussed in Chapter 4, Figure 4.2.

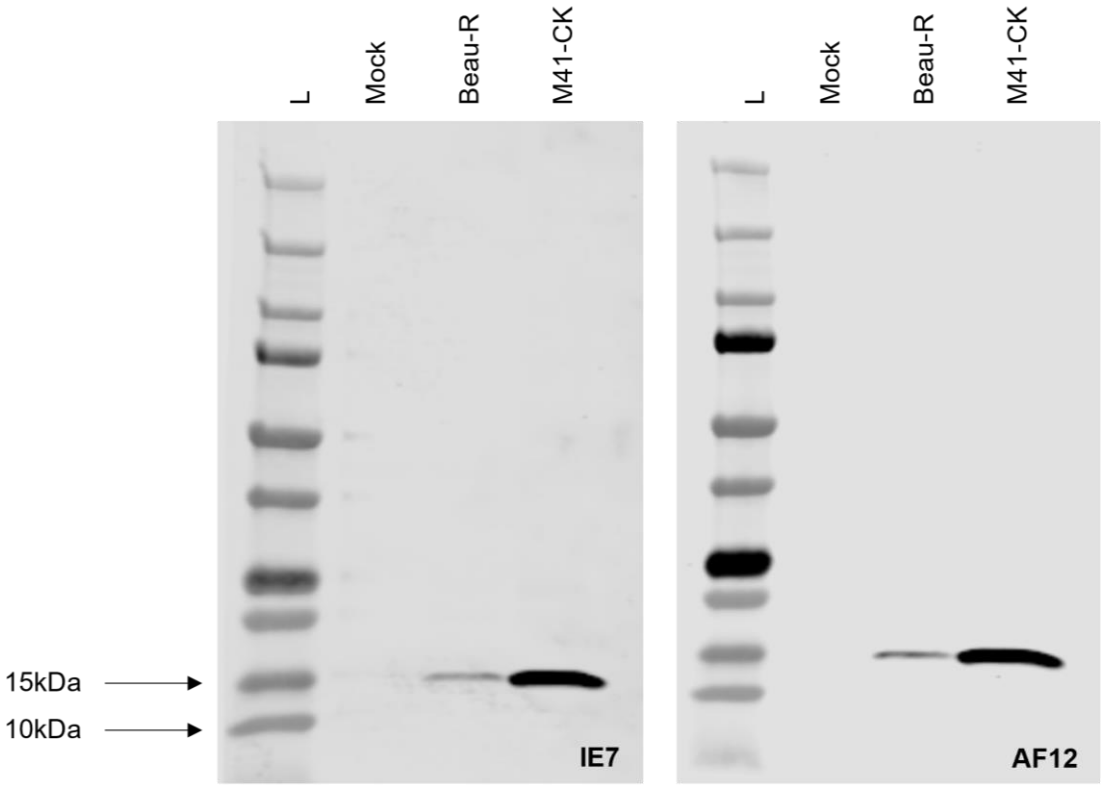

Figure 5.1. Assessment of potential E antibodies for use in this project. CK cells were infected with virus at 1x10^6 PFU of either Beau-R or M41-CK. Cell lysate was harvested at 24 hpi. A western blot (WB) was carried out to assess prospective primary antibodies IE7 and AF12 which were diluted 1/100 within 5 % milk. The secondary antibody used was IRDye® donkey anti-mouse IgG 800CW. Band shown represents the E protein which is ~ 12 kDa in size.

The AF12 E antibody was carried forward to determine whether it could be used in IF. This aimed to establish whether a clear signal was generated in infected cells without background signal in mock infected, this validation is shown in Figure 5.2.

Antibodies are classed into isotypes based on the variable region at the tip of the heavy chain. The AF12 E antibody was known to be an anti-mouse IgG, but there was no record of the reactive isotype. To establish this, Vero cells were uninfected or infected with Beau-R and probed using a range of anti-mouse secondary antibodies. IgG was included as a positive control. Vero cells were used in this experiment as CK cells were unavailable, M41-CK is not able to replicate in Vero cells so was not included in this experiment. The secondary antibodies included were IgG, IgM, IgG1, IgG2a and IgG2b. This characterisation found that the AF12 anti-E antibody is reactive to the IgG2b isotype (Figure 5.2).

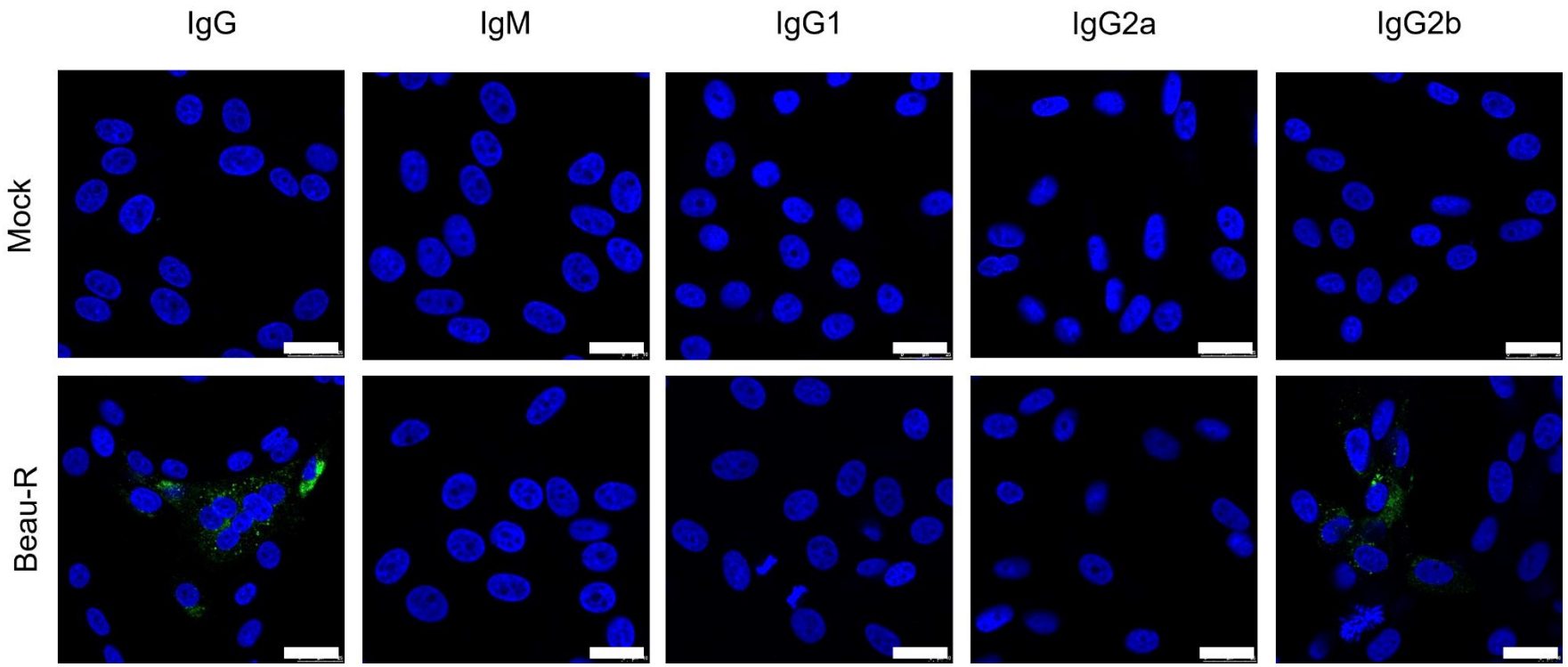

Figure 5.2. Immunofluorescence (IF) to assess the isotype of the AF12 E antibody. Vero cells were mock infected or infected with $1x10^5$ PFU of Beau-R. Cells were fixed at 24 hpi with 4 % PFA in PBS. Cells were permeabilised with 0.1 % Triton X-100 in PBS and blocked in 0.5 % BSA in PBS. IF was carried out using the primary AF12 E antibody with a range of anti-mouse secondary antibodies. The secondary antibodies used were AlexaFluor donkey anti-mouse 488 IgG, AlexaFluor goat anti-mouse 488 IgM, AlexaFluor goat anti-mouse 488 IgG1, AlexaFluor goat anti-mouse 488 IgG2a and AlexaFluor goat anti-mouse 488 IgG2b. Nuclei were counterstained with DAPI (blue). Scale bars represent 25 µm.

The AF12 E antibody was assessed to establish whether it could facilitate proteomic analysis of the IBV E protein. Co-IP was optimised using A/G magnetic beads with immobilised AF12 E antibody. Beau-R, BeauR-T16A and BeauR-A26F infected CK cells were lysed at 24 hpi and cell lysate was harvested. This cell lysate was incubated with the magnetic beads conjugated to the AF12 E capture antibody overnight. To assess the success of the co-IP, a denaturing elution was performed using Laemmli buffer containing BME. The resulting solution was resolved using SDS-PAGE and visualised using a WB and silver stain.

WBs were performed using the AF12 E protein antibody, which found that the E protein was successfully immunoprecipitated within Beau-R infected cells (Figure 5.3.A), demonstrating that the AF12 E antibody was capable for use within co-IP. The light and heavy chains of the AF12 E protein antibody can be seen in both the mock and Beau-R wells indicating that along with the E protein, some of the antibody has also detached from the magnetic beads.

A silver stain is the most sensitive method for detecting the total protein present within a sample. The silver stain found many proteins in Beau-R infected cells after co-IP. Many proteins were also pulled down in the mock infected cells, but these appeared to have a slightly different profile to the Beau-R infected cells (Figure 5.3.B). As a result of this preliminary experiment, the AF12 E antibody was carried forward for use in co-IP for mass spectrometry.

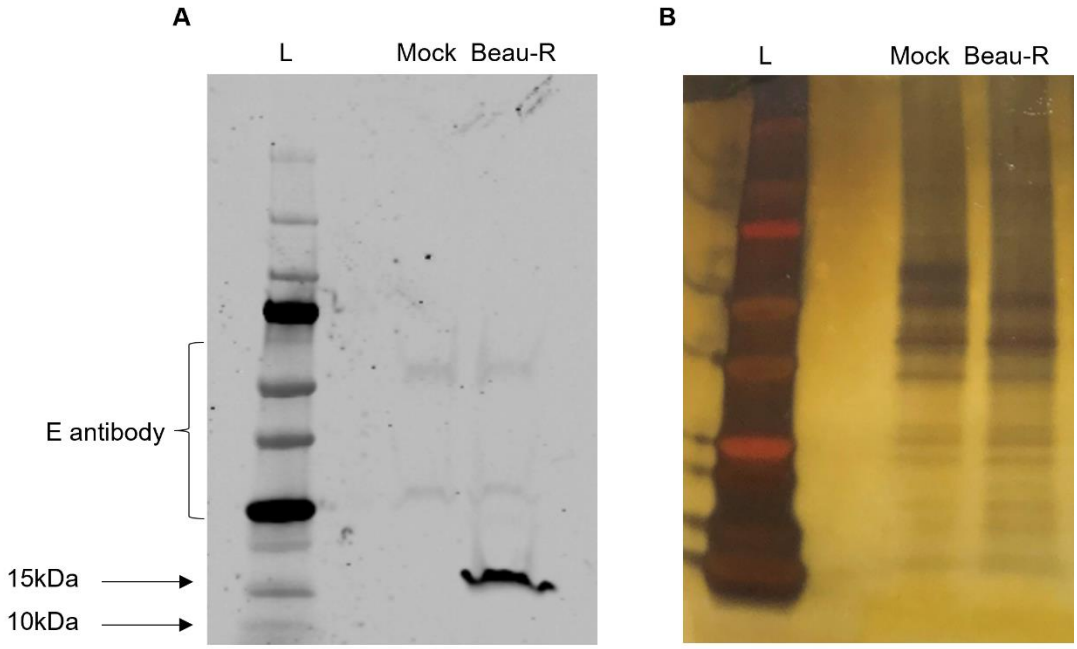

Figure 5.3. The AF12 E antibody can be used within co-immunoprecipitation (co-IP) experiments. CK cells were mock infected or infected with $1x10^5$ PFU of Beau-R. Cell lysates were harvested at 24 hpi and co-IP with the AF12 E antibody conjugated to A/G magnetic beads. Resulting eluate was separated using a 4-15 % SDS-PAGE gel. (A) Western blot (WB) probed using the AF12 E protein to determine the success of the co-IP. (B) Silver stain showing the total proteins obtained via co-IP using the AF12 E antibody.

5.3.2. Interactome of rIBVs containing either a T16A or A26F mutation

The monomeric form of the E protein is hypothesised to interact with cellular proteins to manipulate the cellular secretory system, and the pentameric IC is thought to facilitate viral assembly via IC activity (113). The specific targets of these forms are still unknown. The monomeric and pentameric pools of the E protein can be selected for with a A26F or T16A mutation, respectively (113). Building on establishing the role of the T16 and A26 residues during IBV infection, mass spectrometry was performed to generate interactomes for Beau-R, BeauR-T16A-3.4 and BeauR-A26F-12.3 E proteins. Representative isolates of BeauR-T16A and BeauR-A26F were selected for use in this study due to sequence similarity between the isolates and comparable replication kinetics (Chapter 3, Table 2, and Figure 2).

The proteomics data has allowed for specific interacting partners to be uncovered, which potentially could facilitate some of the predicted roles of the E protein. To obtain results which most accurately mimic interactions which take place during IBV infection, primary CK cells were infected with a representative isolate of each rIBV. This ensures that all the viral components are present to take part in the interactions and that the cell type used is relevant to infection within the bird. In Chapter 3, the importance of cell type selection for characterisation of the T16A and A26F mutations was highlighted (191).

When investigating interacting partners, a FC threshold must be established. Initially, statistical analysis was performed from the three independent experiments to determine proteins which are significantly different from those found in mock infected cells. Significance was assessed using a t-test and was defined by a p-value of < 0.05. A method to assess the distribution of proteins identified is a volcano plot. Volcano plots display the entire dataset for each virus in a graph showing the

significance plotted against the FC. A negative FC in comparison to mock has been discredited, as when carrying out interatomic analysis, negative values are likely non-specific interactors from the pull down. From the volcano plots, interacting partners were defined by statistical significance and a FC greater than 1.3 in comparison to mock infected (Figure 5.4).

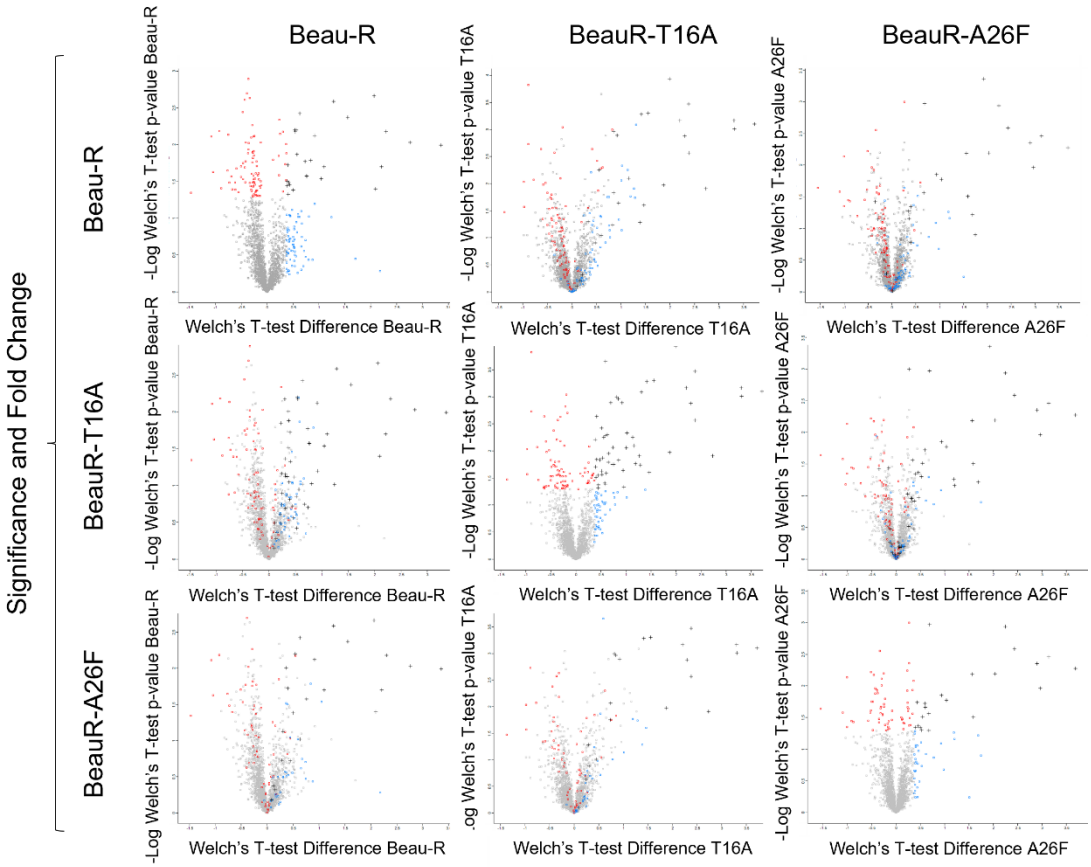

Figure 5.4. Volcano plots were used to establish an appropriate fold change (FC) threshold. Volcano plots representing data sets generated from mass spectrometry analysis of Beau-R, BeauR-T16A-3.4 or BeauR-A26F-12.3 infected CK cells. Graphs were assembled with data sets from each virus with the significance (red) and FC (blue) shown. Proteins which are both significant and over the FC threshold are shown as black crosses. Proteins meeting these criteria were transposed onto the datasets of other the viruses.

The data sets shown in the Volcano plots demonstrate that proteins which were significant and over the FC threshold for each virus were not comparable. This is demonstrated as the Beau-R colour-coding transposed onto the BeauR-T16A or BeauR-A26F datasets, did not exhibit the same pattern. This is interesting as it appears that there was a high level of diversity in the interactomes between the E proteins of the three viruses.

To further illustrate this phenomenon, Venn diagrams were assembled to assess the distribution of interacting proteins obtained from this analysis. Only a few proteins identified as significant were associated with all three forms of the E protein. This was further reduced in the number of proteins which were defined as interacting (Figure 5.5). This implies that the T16A and A26F mutations drastically alter the interactomes of the Beau-R E protein.

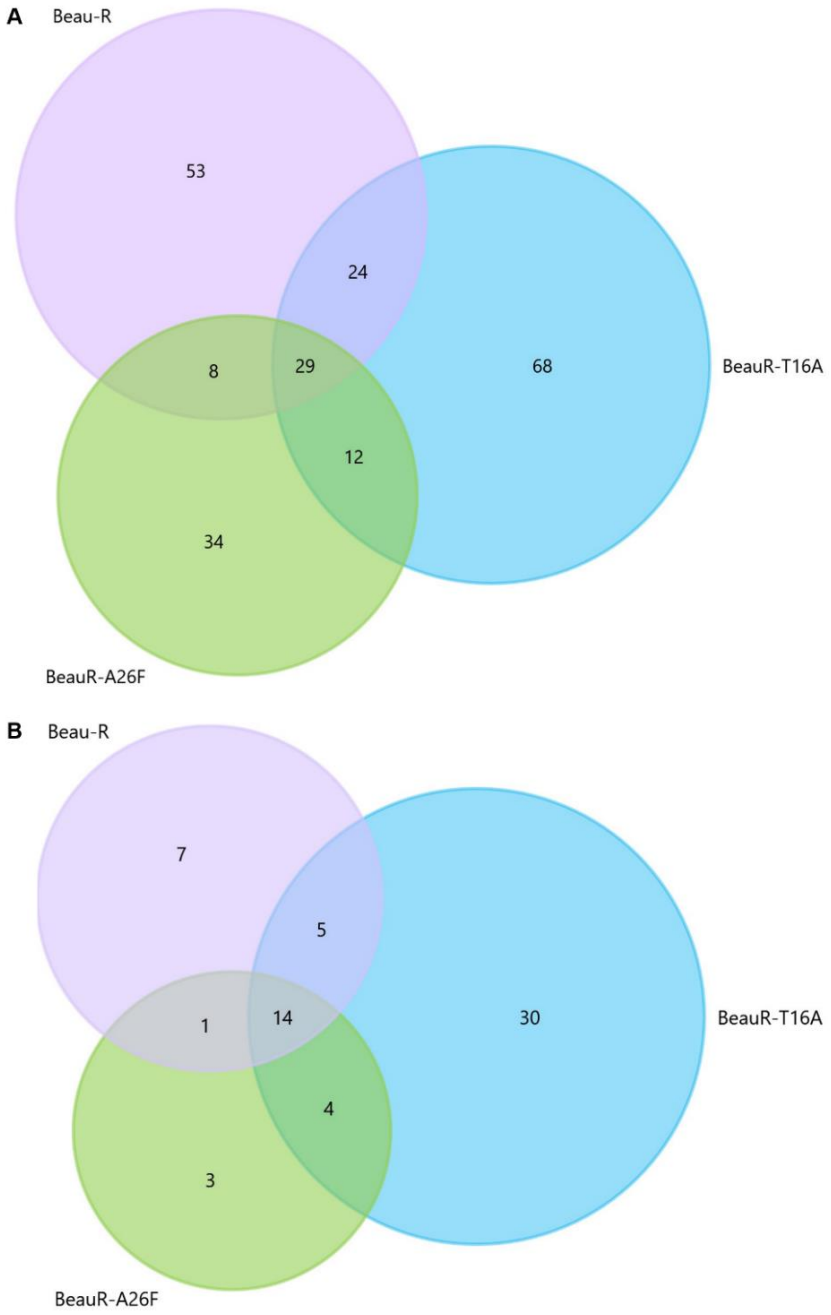

Figure 5.5. The number of proteins which interact with Beau-R, BeauR-T16A or BeauR-A26F E proteins varies between viruses. (A) Venn diagram representing proteins which interact with either the Beau-R, BeauR-T16A-3.4 or BeauR-A26F-12.3 E proteins which were significantly different from mock infected cells. (B) Venn diagram representing proteins which were found to be interacting partners. This was defined by a significant difference and a fold change (FC) equal to or greater than 1.3 for each virus in comparison to mock infected cells.

The interacting partners of the Beau-R, BeauR-T16A-3.4 or BeauR-A26F-12.3 E proteins were plotted within a Cytoscape network (Figure 5.6). The proteins found to interact with each E protein were broadly grouped by function. These groups include secretory pathway, transcription, and translation, IBV proteins, IC, immune factor, receptor, cytoskeleton, metabolism and unknown.

The Cytoscape network further demonstrates that only a few proteins were associated with all three forms of the E protein. The proteins which were found to interact included all the detected IBV proteins. The E protein was shown to interact with the other three structural proteins and the replicase pp1ab. The interaction with accessory protein 5a was not previously described and the impact of this interaction on viral assembly and replication could be an interesting avenue to follow up.

Several proteins had an unknown function in the context of IBV infection and were grouped together. RCJMB04_23i8 is an uncharacterised protein. Sciellin (SCEL) is known to be the precursor of the cornified envelope of keratinocyte cells (223), but it is unclear how it would impact viral replication. The function of TPR and ankyrin repeat-containing protein (TRANK1) is unknown, but it has been reported to be a risk factor for bipolar disorder (224).

The immune factors which interact with the E proteins include those involved in the cytokine response and pathogen sensors. Transcription and translation contain a broad group of proteins including helicases, DNA damage response, splicing factors, heat shock proteins and stress granule components. Lon protease homolog (LONP1) is included in this group and acts to regulate mitochondrial gene expression.

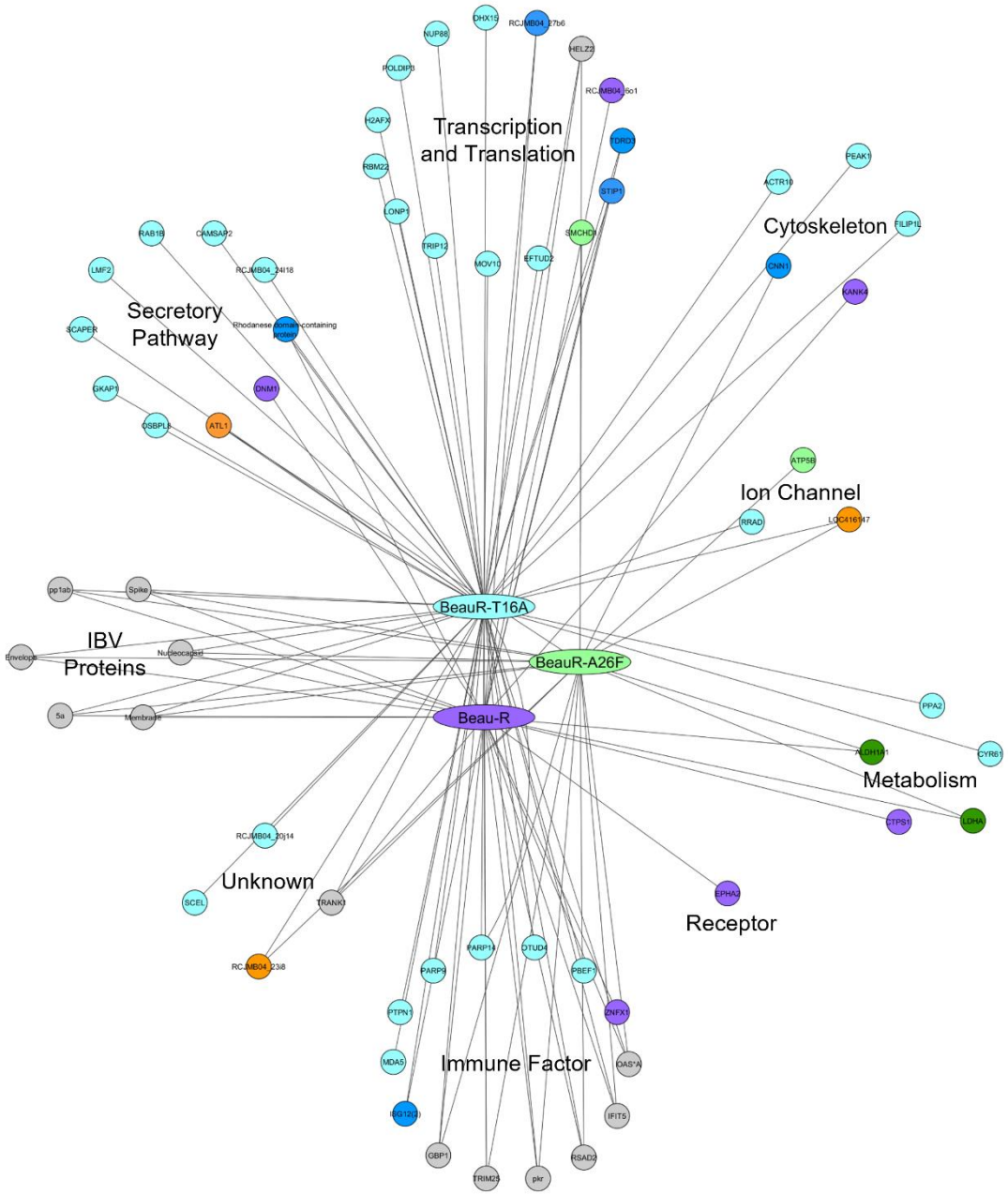
Transcription and Translation
Cytoskeleton
Secretory Pathway
Ion Channel
IBV Proteins
Metabolism
Unknown
Receptor
Immune Factor
BeauR-T16A
BeauR-A26F
Beau-R
DHX15
NUP88
HELZ2
H2AFX
TDRD3
RBM22
STIP1
LDNP1
SMCHD1
TRIP12
MOV10
EFTUD2
PEAK1
ACTR1B
FILIP1L
CNN1
KANK4
RAB1B
CAMSAP2
LMF2
SCAPER
GKAP1
DNM1
OSBPL8
ATL1
ATP5B
RRAD
pp1ab
Spike
Envelope
Nucleocapsid
5a
Membrane
PPA2
CYR61
CTPS1
LDHA
SCEL
TRANK1
EPHA2
PARP9
PARP14
OTUD4
PBEF1
PTPN1
ZNFX1
MDA5
OAS*A
IFIT5
GBP1
TRIM25
RSAD2

Figure 5.6. Cytoscape network representing the interactomes of Beau-R, BeauR-T16A and BeauR-A26F E proteins. CK cells were infected with $1x10^5$ PFU of Beau-R, BeauR-T16A-3.4 or BeauR-A26F-12.3. Cell lysate was harvested at 24 hpi and co-immunoprecipitated using the AF12 (anti-E) antibody conjugated to magnetic beads. Mass spectrometry was performed. A t-test was performed against mock infected sample for each virus treated sample. Interacting partners are defined by statistical significance and a fold change (FC) greater than 1.3 in comparison to mock infected. Interacting proteins were broadly grouped based on their function and nested into nodes. Proteins found to interact with all the tested viruses are shown in grey. Proteins which were only found to interact with Beau-R are shown in purple, BeauR-T16A in light blue and BeauR-A26F in light green. Proteins which are interacting partners of both Beau-R and BeauR-T16A or BeauR-A26F are shown in dark blue and dark green, respectively. Proteins which interact with BeauR-T16A and BeauR-A26F are shown in orange.

Secretory pathway proteins include those which are components of the membrane, involved in transport or biogenesis of Golgi, ER or endosomes. The rhodanese domain-containing protein detected is an endosomal component. The Ephrin receptor A2 (EPHA2) protein was found to interact with Beau-R and is epithelial receptor (225).

The cytoskeleton group includes proteins which are components of the cytoskeleton or regulate the structure of these components. Calmodulin regulated spectrin associated protein family member 2 (CAMPSAP2) has been grouped with the secretory pathway due to its association with the Golgi, but it is also a regulator of the cellular cytoskeleton. The IC group contains proteins which have been shown to act as transporters within the cell. The metabolism group contains proteins which are involved in metabolic processes.

The proteomic data was generated from the cell lysates of primary CK cells. Although these act as a valuable tool as they are biologically relevant to IBV infection, they are not a homogenous culture. There is a large amount of variation between each preparation of the culture and therefore this has generated variability within these results. Investigation into these results found that the samples clustered based on the replicate of the experiment (i.e., the preparation of CK cells) rather than the virus (Figure 5.7).

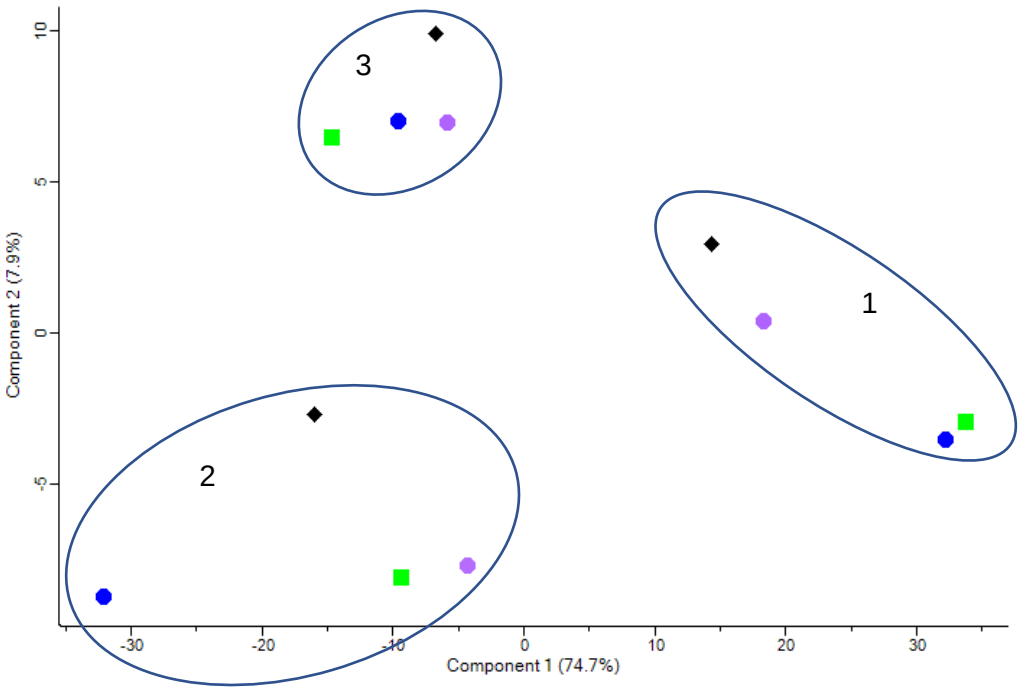

Figure 5.7. Principal component analysis (PCA) scatter plot showing the samples cluster by replicate rather than by virus. CK cells were mock infected or infected with $1x10^5$ PFU of Beau-R, BeauR-T16A-3.4 or BeauR-A26F-12.3. Cell lysates were harvested at 24 hpi and co-immunoprecipitated using magnetic beads conjugated with the AF12 (anti-E) antibody. Circles represent samples which were carried out within the same biological repeat. Mock is shown in black, Beau-R is shown in purple, BeauR-T16A-3.4 is shown in blue and BeauR-A26F-12.3 is shown in green.

5.3.3. Golgi diffusion observed in avian and mammalian cell lines

The IBV E protein implements Golgi Apparatus diffusion during IBV infection, which has been attributed to the T16 residue (105, 113). Previous work investigating the effect of the T16A and A26F mutations on this diffusion has been carried out within mammalian Henrietta Lacks (HeLa) cells using expression plasmids (113). HeLa cells are human epithelial cells and are therefore not representative of natural IBV infection within the chicken. Additionally, effects observed within expression plasmids are not always replicated when research is conducted in the presence of the whole virus.

In Chapter 3, the importance of cell type selection when characterising the T16A and A26F mutations has been highlighted. This study builds on previous characterisation of Golgi diffusion by establishing whether the same effects would be observed in primary CK cells infected with recombinant viruses with the T16A or A26F mutations (Figure 5.8). Representative isolates of BeauR-T16A and BeauR-A26F were selected due to sequence similarity between the isolates and comparable replication kinetics (Chapter 3, Table 2, and Figure 2).

IF was performed using an antibody against the Golgi protein 130 kDa cis-Golgi matrix protein (GM130) as it is part of the Golgi matrix and is regularly used as a Golgi marker (226). Additionally, this marker was used in previous research characterising the IBV E protein (105, 113). The GM130 signal is more dispersed in virus infected cells. This dispersion is comparable between Beau-R, BeauR-T16A and BeauR-A26F, indicating that when assessed using IF, Golgi diffusion is not present in avian cells (Figure 5.8).

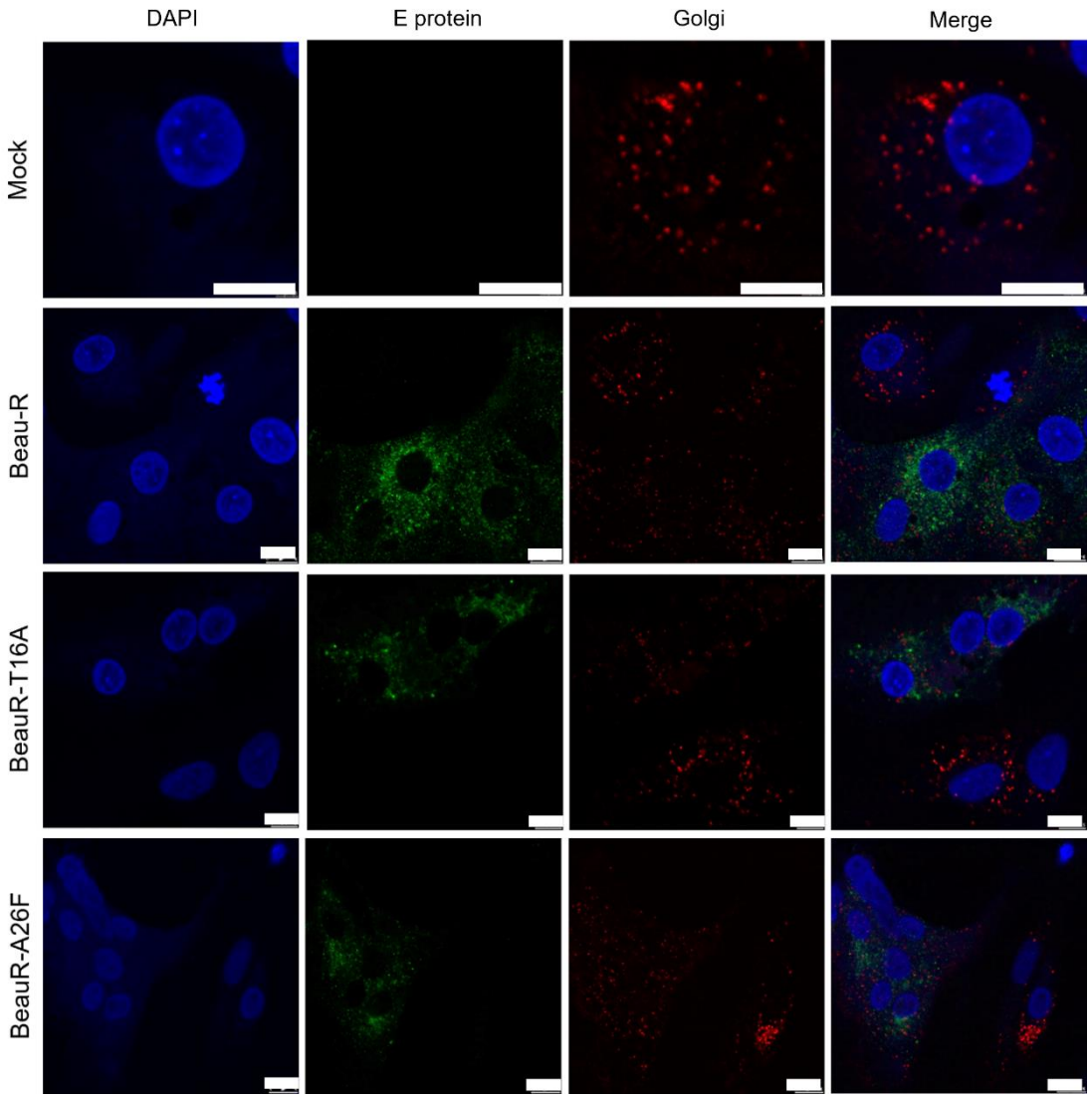

Figure 5.8. BeauR-T16A and BeauR-A26F appear to cause comparable Golgi diffusion to Beau-R in primary CK cells. CK cells were mock infected or infected with Beau-R, BeauR-T16A-3.4 or BeauR-A26F-11.2 at ~ 10^5 PFU. Cells were fixed at 24 hpi with 4 % PFA in PBS. Cells were permeabilised with 0.1 % Triton X-100 in PBS and blocked in 0.5 % BSA in PBS. Primary antibodies used were AF12 (anti-E) and GM130 (anti-Golgi). The secondary antibodies used were AlexaFluor donkey anti-mouse 488 IgG (AF12, green) and AlexaFluor goat anti-rabbit 568 IgG (GM130, red). Nuclei were counterstained with DAPI (blue). Scale bars represent 10 µm, images taken at x40 magnification.

The Golgi Apparatus in the primary CK cells displayed a diffuse profile (Figure 5.8, mock) when probed with the anti-GM130 antibody. This inherent diffusion has hindered the determination of the effect of each rIBV on the Golgi diffusion.

The GM130 antibody used in this study has not been validated to react with avian cells. It was unclear whether the cause of this diffusion was due to non-specific binding of the antibody or morphological differences between the mammalian and avian Golgi Apparatus. To combat this, other antibodies which target the ERGIC/ Golgi compartments were used to determine whether the same diffusion would be present.

Two antibodies which target ERGIC-53, also known as Mannose-binding lectin 1 (LMAN1), were used to assess this. ERGIC-53 is present within the ERGIC and is involved in transport between the ER and Golgi (227). This found that the same diffuse signal was present when assessed with each of the antibodies, indicating that it wasn't due to lack of reactivity of the GM130 antibody (Figure 5.9). Therefore, this confirmed the cellular secretory system present in avian cells is diffuse.

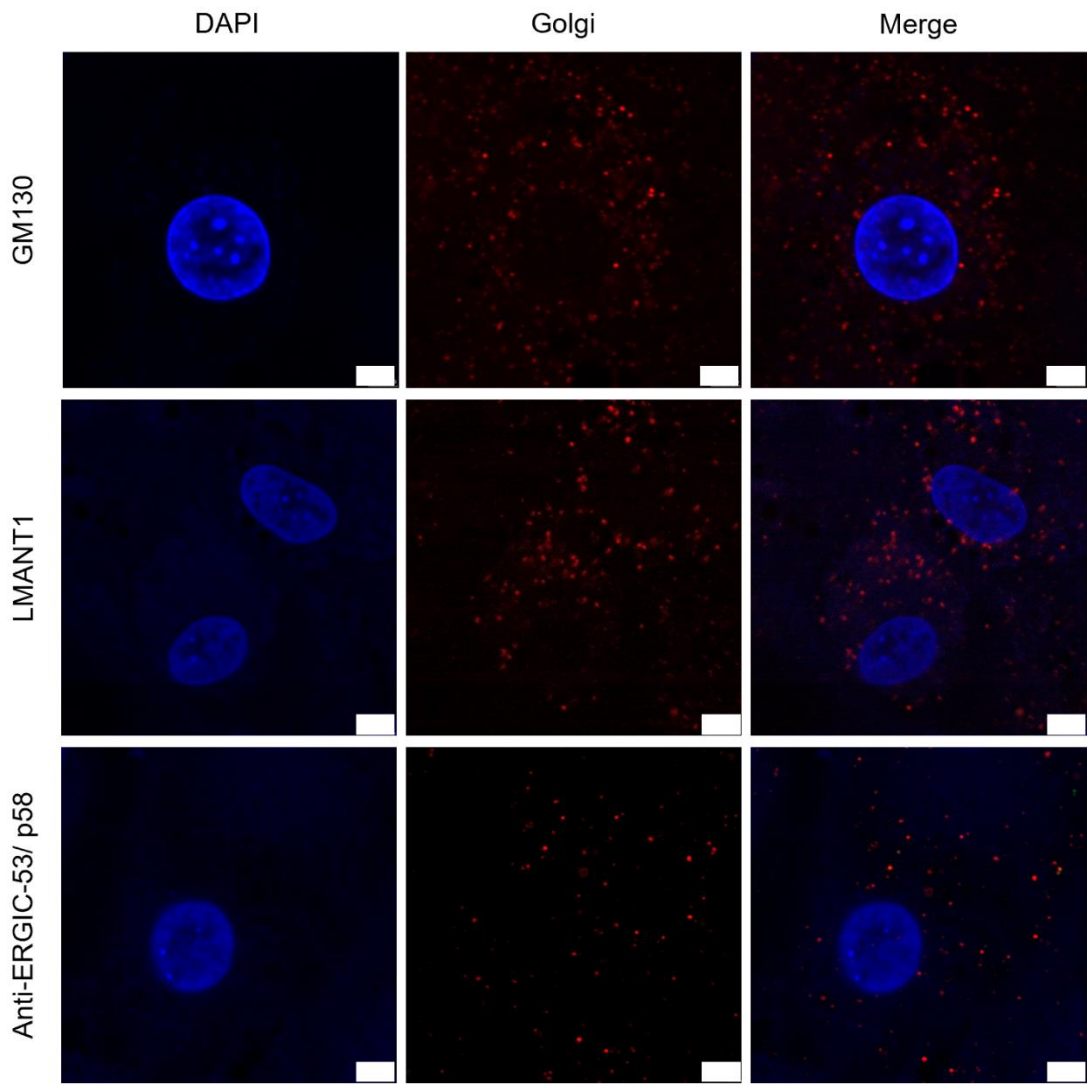

Figure 5.9. The ERGIC/ Golgi Apparatus is dispersed in primary CK cells when probed with a variety of antibodies. CK cells were mock infected and fixed at 24 hpi with 4 % PFA in PBS. Cells were permeabilised with 0.1 % Triton X-100 in PBS and blocked in 0.5 % BSA in PBS. Primary antibodies used were GM130, LMANT1 and Anti-ERGIC-53/ p58. The secondary antibody used was AlexaFluor goat anti-rabbit 568 IgG (red). Nuclei were counterstained with DAPI (blue). Scale bars represent 5 µm, images taken at x40 magnification.

The diffusion of the Golgi Apparatus was validated within avian cells, but this diffusion made it very difficult to establish changes to Golgi morphology elicited by the rIBVs. In previous work using mammalian HeLa cells, the GM130 marker generated a compact Golgi signal and therefore the effect of the T16A mutation was clearly observed (113). This result could have been due to the use of mammalian cells or an artifact due to the E proteins being delivered to cells via an expression plasmid.

To establish whether this effect was cell-type dependent, this study was replicated within mammalian Vero cells. Vero cells were used instead of HeLa, as the Beau-R strain can replicate in Vero cells (97). Within Vero cells the effect of the Golgi diffusion was more apparent due to the compact appearance of the GM130 signal. In the BeauR-T16A infected cells, the Golgi did not appear to be diffuse, unlike in Beau-R and BeauR-A26F infected cells (Figure 5.10).

To confirm this result, IF images were quantified using ImageJ software which determined that the size of the Golgi present in BeauR-T16A infected cells is comparable to mock infected and therefore significantly smaller than in Beau-R or BeauR-A26F infected cells (Figure 5.11). This result mirrors what was previously observed in HeLa cells using transfected plasmids (113). As in Chapter 3, the effect of the T16A and A26F mutation has differed between cell systems. This result therefore indicates that the lack of Golgi diffusion in BeauR-T16A infected cells may be a consequence of using mammalian cells to investigate an avian virus.

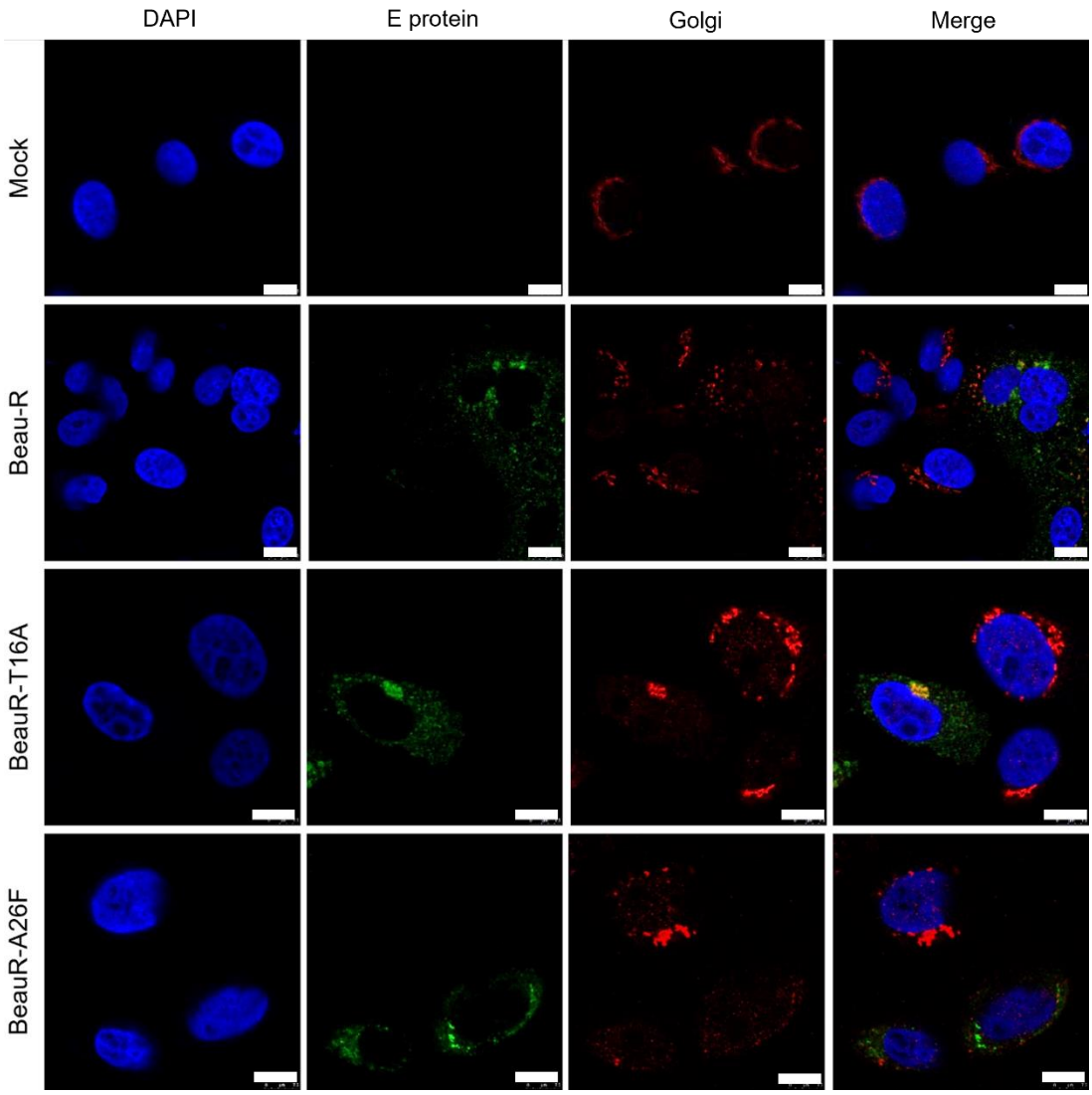

Figure 5.10. BeauR-T16A does not cause Golgi diffusion within mammalian Vero cells. Vero cells were mock infected or infected with Beau-R, BeauR-T16A-3.4 or BeauR-A26F-11.2 at an MOI of 0.4. Cells were fixed at 24 hpi with 4 % PFA in PBS. Cells were permeabilised with 0.1 % Triton X-100 in PBS and blocked in 0.5 % BSA in PBS. Primary antibodies used were AF12 (anti-E) and GM130 (anti-Golgi). The secondary antibodies used were AlexaFluor donkey anti-mouse 488 IgG (AF12, green) and AlexaFluor goat anti-rabbit 568 IgG (GM130, red). Nuclei were counterstained with DAPI (blue). Scale bars represent 10 µm, images taken at x40 magnification.

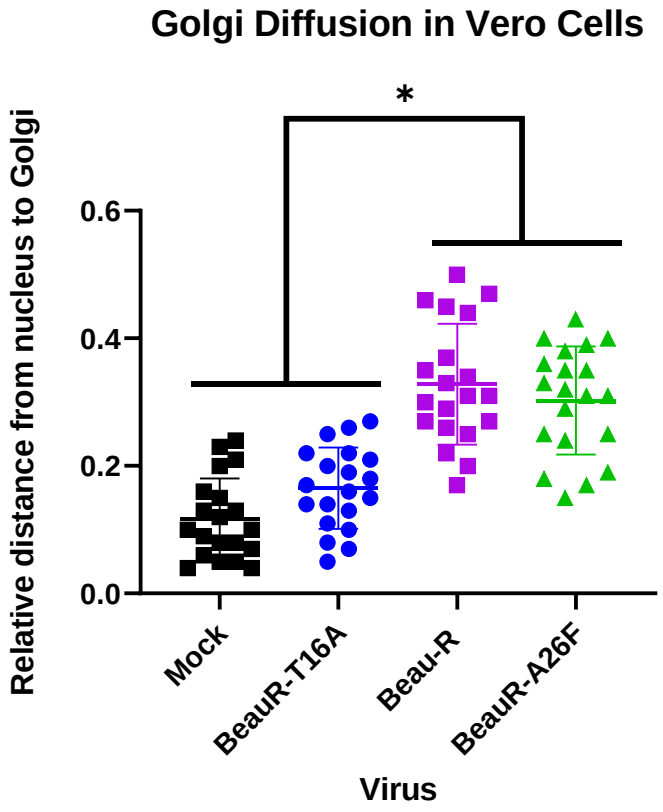

Figure 5.11. BeauR-T16A infected Vero cells do not exhibit comparable Golgi diffusion to Beau-R or BeauR-A26F. Vero cells were mock infected or infected with Beau-R, BeauR-T16A-3.4 or BeauR-A26F-11.2 at an MOI of 0.4. Cells were fixed at 24 hpi with 4 % PFA in PBS. Immunofluorescence images were obtained using AF12 (anti-E) and GM130 (anti-Golgi) antibodies. The distance between the nucleus and the edge of the Golgi was measured using ImageJ for 20 cells from three independent experiments. Statistical analysis was undertaken using a one-way analysis of variance (ANOVA), significance was taken as p-value < 0.05. Error bars represent ± standard deviation (SD) of three independent experiments.

5.3.4. EM images showing differences in Golgi morphology in CK cells infected with Beau-R, BeauR-T16A and BeauR-A26F

In Chapter 3, the effect of the T16A and A26F mutations was shown to be cell type dependent. This study displays different Golgi diffusion results within avian and mammalian cells. Confirmation was required to ensure that the result obtained from Vero cells was not an artifact caused by use of a mammalian cell line, which are not biologically relevant. To gain a higher resolution view into the morphology of the Golgi in primary CK cells infected with the rIBVs, EM was carried out. Membrane rearrangements induced by IBV infection are associated with the ROs, these membrane rearrangements include zippered ER, spherules, and DMVs (65). CK cells infected with Beau-R, BeauR-T16A and BeauR-A26F were chemically fixed at either 16- or 24-hpi and observed using EM for presence of intact Golgi Apparatus. Membrane re-arrangements including zippered ER, spherules and DMVs were observed (Figure 5.12). Intact Golgi was only observed in CK cells infected with BeauR-T16A but not with Beau-R or BeauR-A26F (Figure 5.13). No structures resembling the Golgi apparatus were observed in Beau-R or BeauR-A26F infected cells at either 16 or 24 hpi. This suggests that the pattern of Golgi diffusion observed in mammalian cells may be representative of natural IBV infection.

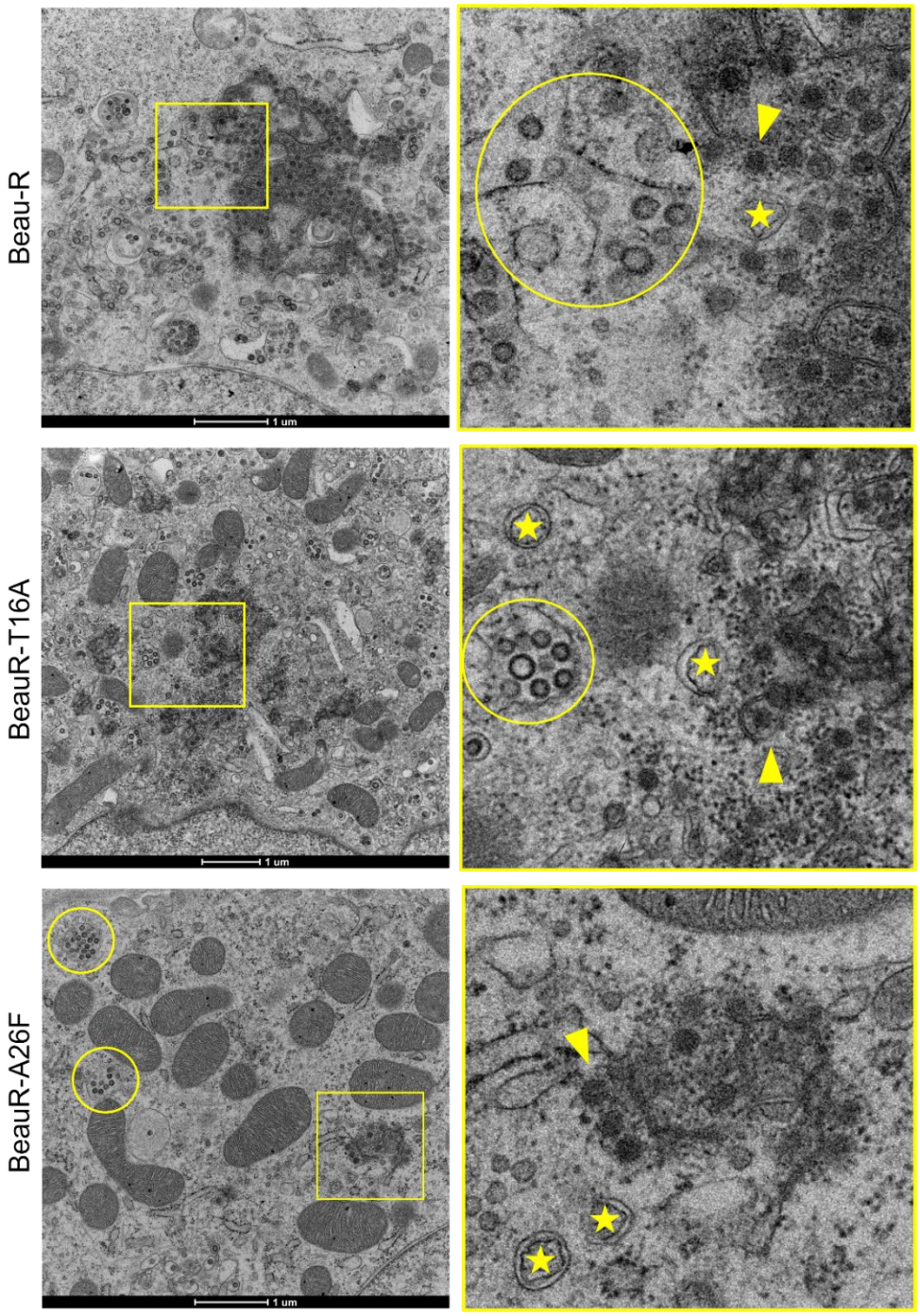

Figure 5.12. CK cells infected with Beau-R, BeauR-T16A and BeauR-A26F show replication organelle. CK cells were infected with Beau-R, BeauR-T16A-3.4 or BeauR-A26F-12.3 at a titre of $1x10^6$ PFU. At 24 hpi cells were fixed by chemical fixation using 2 % glutaraldehyde. The right panels represent enlarged sections of negative-stain transmission electron microscopy (EM) images, the region is indicated with a box. Stars highlight double-membrane vesicles, triangles show zippered ER and spherules, virus particles within vesicles are circled.

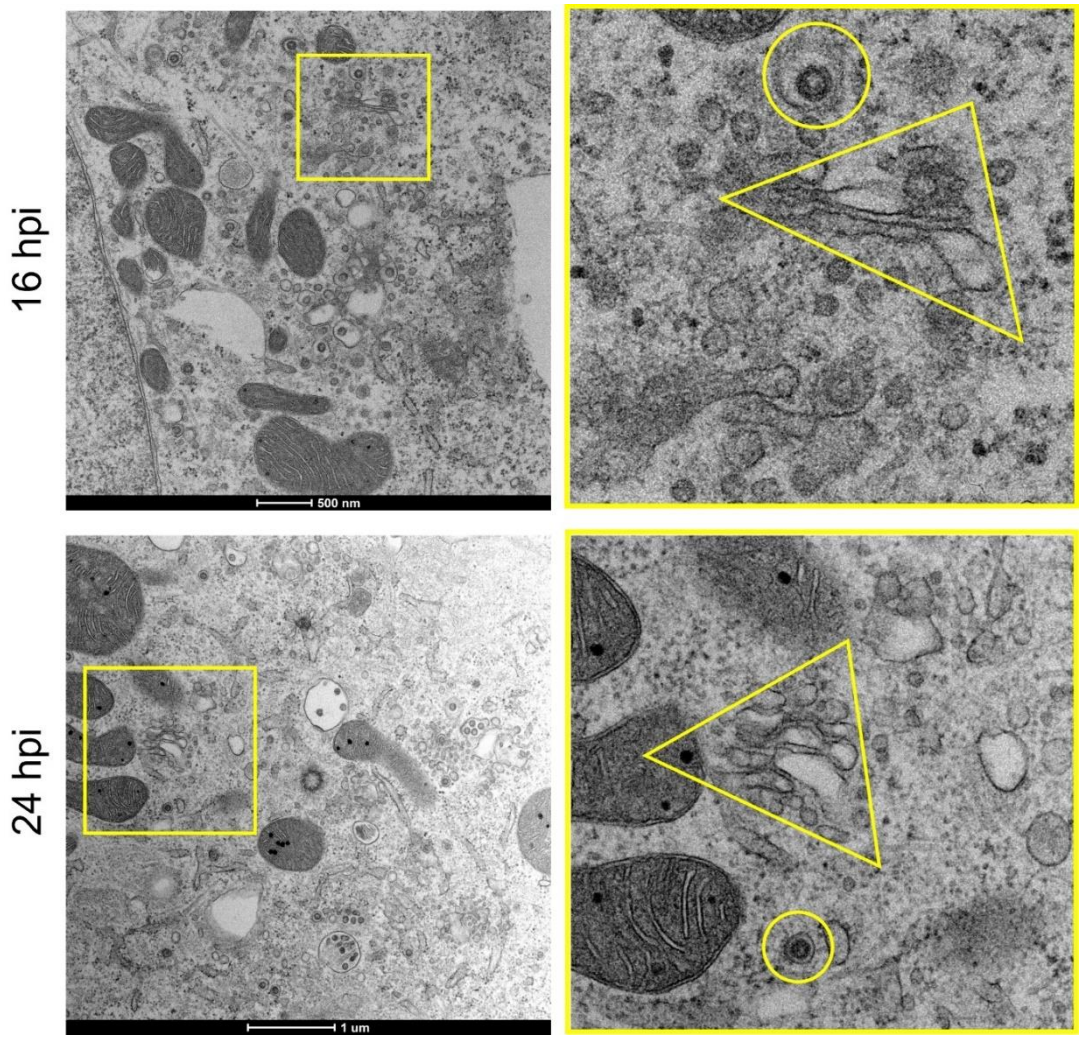

Figure 5.13. BeauR-T16A has intact Golgi and when investigated using negative stain transmission electron microscopy (EM). CK cells were infected with BeauR-T16A-3.4 at a titre of $1x10^6$ PFU. At 16- or 24-hpi, cells were fixed by chemical fixation using 2 % glutaraldehyde. Circles highlight virus particles within vesicles and triangles indicate the Golgi Apparatus. Images of Beau-R and BeauR-A26F could not be included as no structures resembling the Golgi Apparatus were observed.

5.3.5. BeauR-A26F infected cells possess abnormal structures.

The IBV E protein plays a major role in viral assembly, evidenced as presence of only the E and M proteins is sufficient to produce VLPs (75). Presence of an A26F mutation in transfected E protein has been shown to prevent this VLP production (113). In this thesis, it was shown that BeauR-A26F infected Vero cells were deficient in virus release (Chapter 3, Figure 4).

An observation of abnormal structures outside the PM was found in the BeauR-A26F infected cells (Figure 5.14). These structures were observed in several cells and appear to be released virions. The structures are empty and are a similar size to virions. Although empty virions are often observed in Beau-R infected cells, typically only a small proportion of these virions are released, as demonstrated in virions released from the Beau-R and BeauR-T16A infected cell shown in Figure 5.14. Potentially, these structures could be faulty virions generated because of unregulated assembly in the presence of an A26F mutation.

To confirm that these released structures are not microvesicles, corelative light electron microscopy (CLEM) could be performed using a viral antibody to determine whether these particles contain viral components.

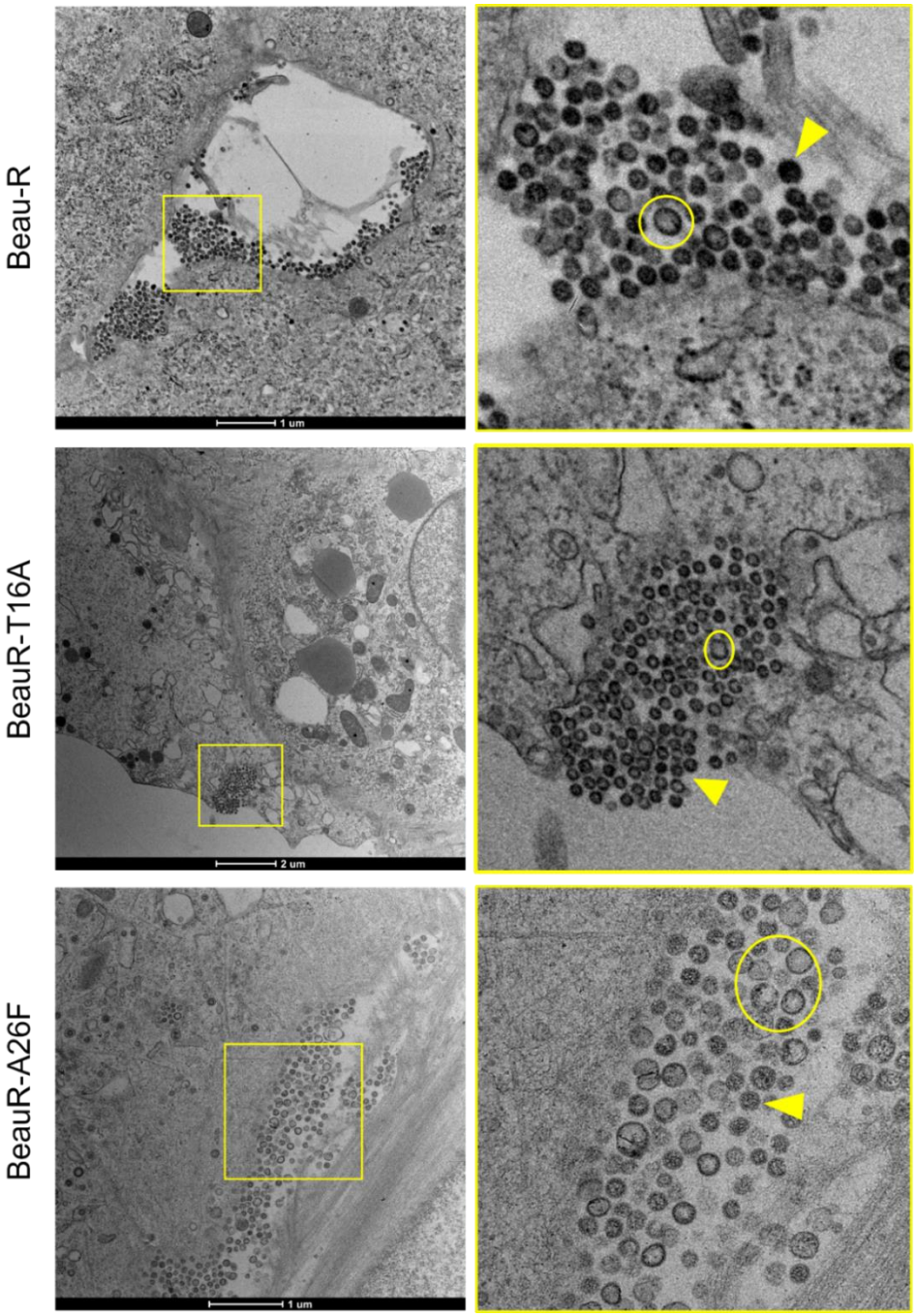

Figure 5.14: BeauR-A26F infected CK cells contained abnormal empty structures at the plasma membrane (PM). CK cells were infected with Beau-R, BeauR-T16A-3.4 or BeauR-A26F-12.3 at a titre of $1x10^6$ PFU. At 24 hpi cells were fixed by chemical fixation using 2 % glutaraldehyde. The right panels represent enlarged sections of negative-stain transmission electron microscopy (EM) images, the region is indicated with a box. Circles highlight empty virions and triangles show normal virus particles.

5.3.6. The effect of Golgi diffusion on S protein processing

During IBV virus assembly, the S protein is cleaved within the Golgi Apparatus to generate the S1 and S2 subunits as well as a Beaudette specific S2′ site, which is required for fusion with the cell (93). Neutralisation and consequent diffusion of the Golgi within IBV infected cells ensures the correct cleavage of the S2 protein (84). As shown previously (113) and within this study, the T16 residue is required for this dissociation within both mammalian and avian cell lines. Previous studies which established incorrect cleavage in the presence of the T16A mutation was carried out using expression plasmids in mammalian HeLa cells. This study aims to validate this result using rIBV possessing the T16A residue within primary CK cells.

The incorrect cleavage product generated in the presence of the T16A mutation is a short 10 kb c-terminal fragment of the S2 protomer and has been termed a 'stub' (84). Unfortunately, the 26.1 anti-S2 antibody commercially available was unable to detect the 'stub' in IBV infected CK cells (Figure 5.15.A).

Although the 'stub' was not detected by the antibody, the level of S2 and E protein expression was quantified to establish whether there were differences in overall protein between the viruses (Figure 5.15.B). This found that the level of E protein present in Beau-R, BeauR-T16A and BeauR-A26F infected cells was comparable. The level of S2 expression in BeauR-T16A infected cells was comparable to WT Beau-R, but not comparable to BeauR-A26F infected cells.

As seen in the mass spectrometry analysis, there is variation between the biological replicates of this experiment. This is likely because CK cells are not a homogenous culture and therefore the amount of each type of cells present cannot be controlled per repeat.

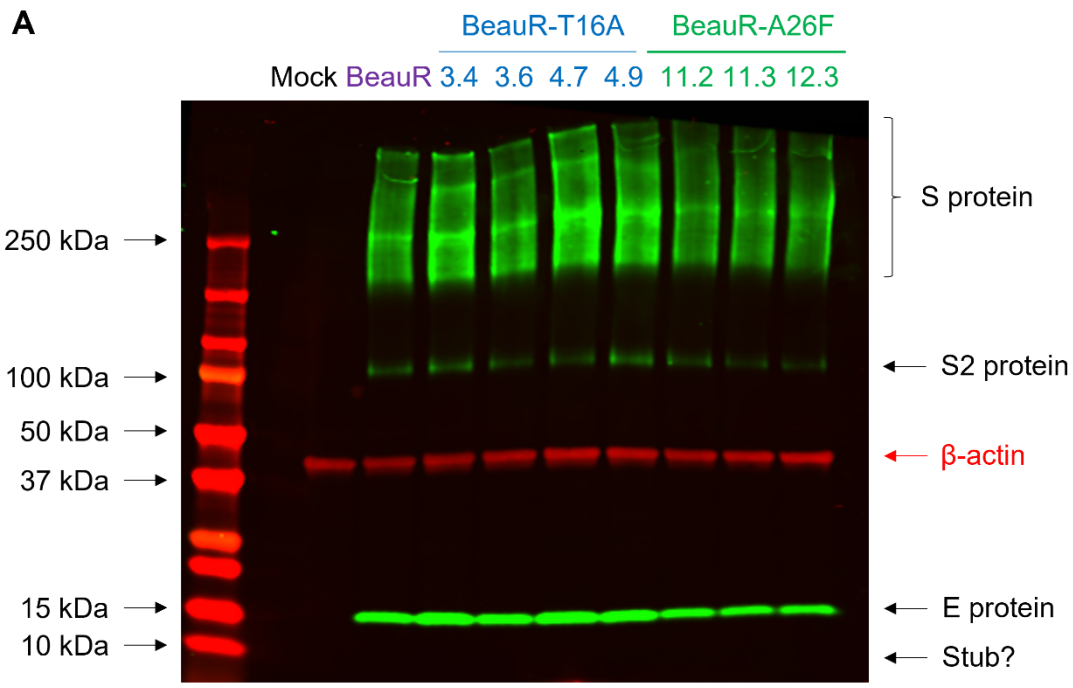
A
BeauR-T16A
BeauR-A26F
Mock BeauR 3.4 3.6 4.7 4.9 11.2 11.3 12.3
250 kDa
100 kDa
50 kDa
37 kDa
15 kDa
10 kDa
S protein
S2 protein
β-actin
E protein
Stub?

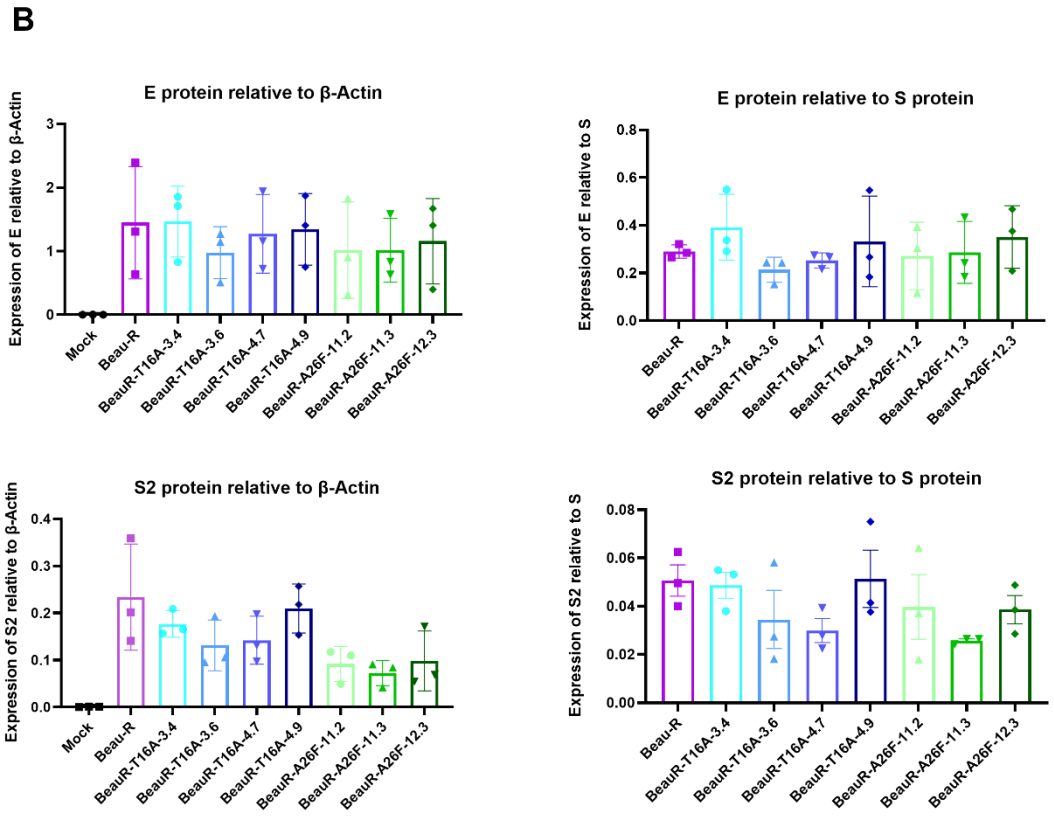
B
E protein relative to β-Actin
Expression of E relative to β-Actin
E protein relative to S protein
Expression of E relative to S
S2 protein relative to β-Actin
Expression of S2 relative to β-Actin
S2 protein relative to S protein
Expression of S2 relative to S
Mock
Beau-R
BeauR-T16A-3.4
BeauR-T16A-3.6
BeauR-T16A-4.7
BeauR-T16A-4.9
BeauR-A26F-11.2
BeauR-A26F-11.3
BeauR-A26F-12.3

Figure 5.15: Representative western blot (WB) showing that S2 expression differs between Beau-R, BeauR-T16A and BeauR-A26F, but E expression is comparable. (A) CK cells were mock infected or infected with $1x10^5$ PFU of Beau-R, BeauR-T16A isolates or BeauR-A26F isolates. Cell lysates were harvested at 24 hpi and separated using a 4-15 % SDS-PAGE gel. WB was performed with the AF12 (anti-E), 26.1 (anti-S) and β-actin primary antibodies. The secondary antibodies used were IRDye® goat anti-rabbit IgG 680 RD and IRDye® donkey anti-mouse IgG 800 CW. The bands representing the S, E and β-actin proteins are indicated. The size of the 'stub' product is highlighted. (B) Densitometry of WB showing that the S2 protein expression differs between Beau-R and BeauR-A26F isolates. Quantification of protein expression was carried out using the densitometry of the respective bands from three independent experiments. The plotted values were normalised to levels of anti-β-actin. Statistical analysis was carried out using one-way analysis of variance (ANOVA), significance was taken as p-value < 0.05 and is represented with * relative to Beau-R. Error bars represent ± standard deviation (SD) of three independent experiments.

5.3.7. ERGIC inhibitors

CoVs bud from the ERGIC compartment and manipulation of the cellular secretory pathway is thought to facilitate this. This activity has been attributed to the E protein (105, 113). This study has found that presence of the T16A or A26F mutation alters this manipulation. To gain a better understanding of the mechanisms behind this manipulation, several inhibitors of the constitutive secretory pathway were used in a broad screen.

The inhibitors selected inhibit transport between secretory pathway elements, alter the morphology of the Golgi Apparatus, or alter post-translational modification of proteins. A schematic has been assembled in which the inhibitor activities are transposed on to potential routes for CoV egress (Figure 5.16). The inhibitor IMP-1088 is not shown in the schematic as it does not directly impact the secretory pathway.

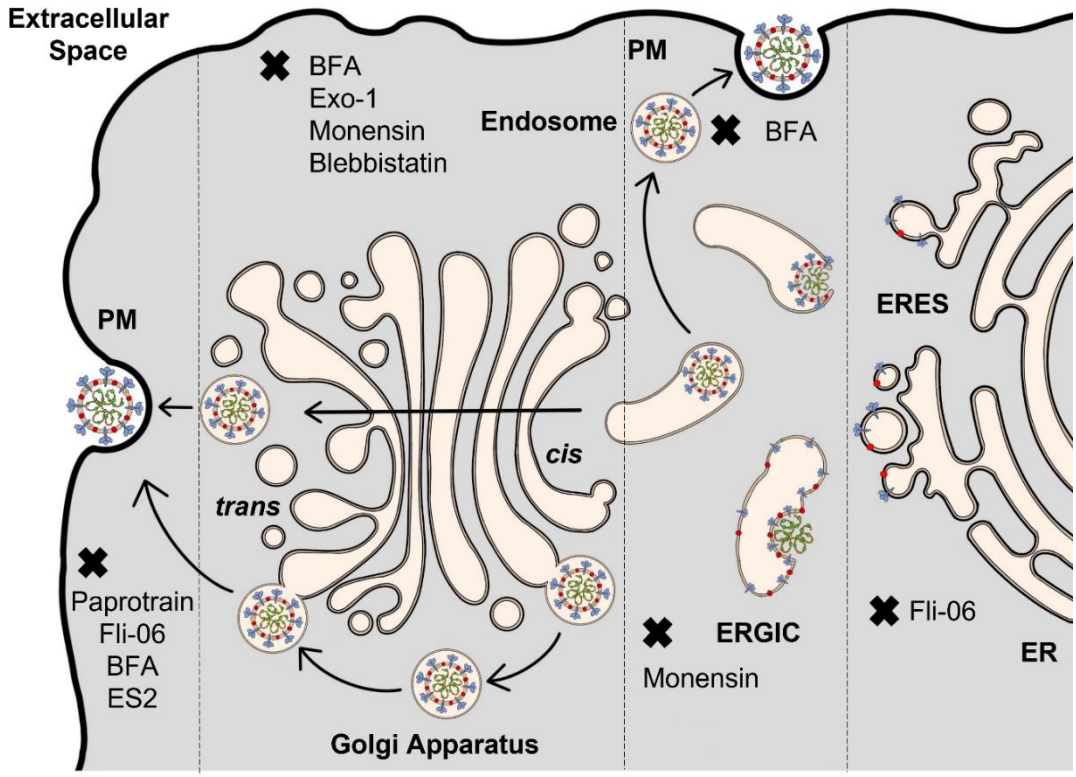

Figure 5.16. Schematic representing the assembly and egress of CoV particles with areas each inhibitor targets indicated. Fli-06 inhibits transport from endoplasmic reticulum (ER) exit sites (ERES). Monensin causes swelling of the ER-Golgi intermediate compartment (ERGIC) and Golgi. Brefeldin-A (BFA) inhibits endosomes. BFA, Exo-1, Monensin and Blebbistatin alter the morphology of the Golgi. Paprotrain, Fli-06, BFA and Endosidin-2 (ES2) inhibit transport from the *trans*-Golgi to the plasma membrane (PM).

BFA is a fungal compound which causes the redistribution of proteins from the Golgi Apparatus to the ER and its consequent disassembly (228). Exo1 also induces this dissociation of the Golgi. It is hypothesised that these inhibitors use different mechanisms, but both factors ultimately facilitate this dissociation through releasing the ADP-ribosylation factor (ARF1) from Golgi membranes, preventing formation of the Coat protein complex 1 (COP1 coat) (229, 230). A schematic of the process for COP1 coat formation is shown in Figure 5.17.

Notably, one of the interacting factors of the BeauR-T16A E protein uncovered by the proteomic analysis was Ras-related protein Rab-1b (Rab1b) (Figure 5.6). Rab1b modulates ER-Golgi transport (231) by activating the COP1 coat (232, 233). This interaction has functional implications related to the E protein, as Rab1b depletion induces swelling of the Golgi (234). Rab1b dependent activation of the COP1 coat is inhibited by BFA (Figure 5.17).

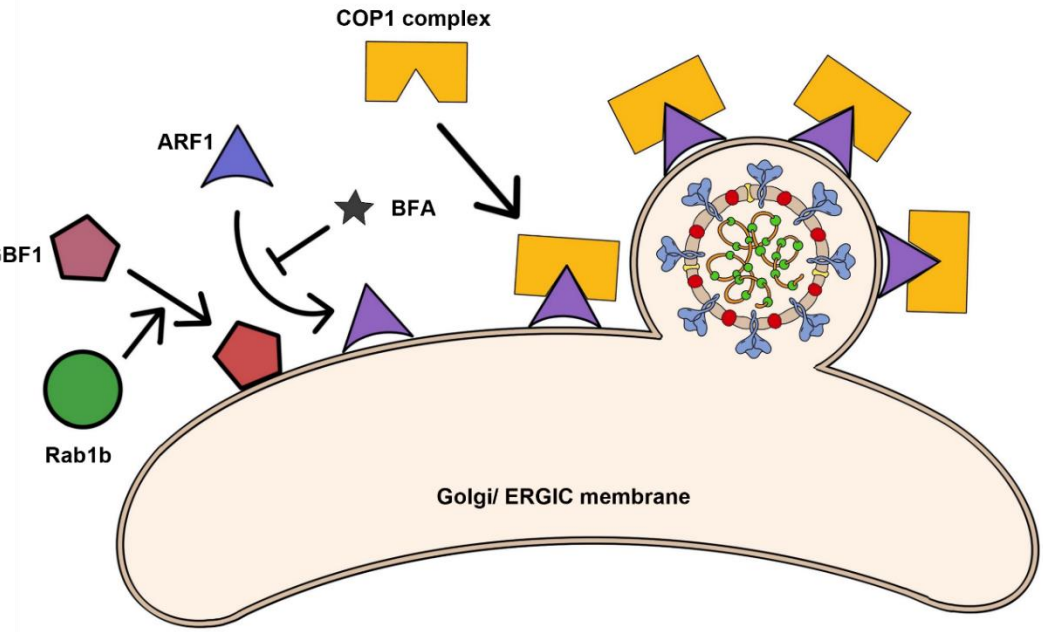

Figure 5.17. Rab1b is an interacting partner of the IBV E protein and is essential for the formation of the COP1 coat. Rab1b activates Golgi-specific brefeldin A-resistance guanine nucleotide exchange factor 1 (GBF1), which catalyses the hydrolysis (GDP/GTP exchange) of the GTPase ADP-ribosylation factor (ARF1). Activated ARF1 recruits Coat protein complex 1 (COP1) complexes to the Golgi/ ERGIC membranes. COP1 complexes allow for cargo encapsulation and induction of membrane curvature, facilitating retrograde transport from the Golgi compartment to the ER. BFA inhibits the ARF1 hydrolysis which ultimately prevents formation of the COP1 coat. This schematic has been adapted from (235).

As well as combining of the Golgi components within the ER, BFA induces mixing of the trans-Golgi network (TGN) and endosomes, resulting in the formation of an extended tubular network (236). Exo1 has no effect on the TGN or endosomes (230). This distinguishes the two functions of these inhibitors. Fli-06 is a compound that inhibits transport from the TGN using an independent method used by BFA (237). Fli-06 is a valuable tool as it is the only molecule known to impact the transport before or at the ERES (238).

Paprotrain and ES2 inhibit cargo transport from the Golgi Apparatus to the PM. Paprotrain inhibits the family of mitotic kinesin-like proteins 2 (MKLP2), which interact with microtubules to affect Golgi Apparatus dynamics and cell cycle regulation (239). Kinesin Family Member 20A (KIF20) belongs to the MKLP2 family and alters Golgi Apparatus dynamics by activating Rab6 (240). This activation anchors Rab6 on the TGN membranes, which is required to allow Rab6 to regulate transport from Golgi and PM (241). ES2 is a compound which binds to and inhibits the exocyst component of 70 kDa (EXO70). The exocyst complex regulates protein trafficking between the endosome and PM (242).

Monensin and Blebbistatin alter the morphology of the Golgi Apparatus. Monensin is a sodium ionophore which neutralises the IC and Golgi lumen, causing fragmentation and dispersion of the Golgi stacks (243). Presence of Monensin inhibits transport from the ER to the Golgi (83, 243). Blebbistatin inhibits the assembly of cytoskeletal protein Myosin II (244), which is required for membrane blebbing in the Golgi Apparatus (245).

IMP-1088 inhibits N-myristoyltransferase (NMT) enzymes, consequently preventing myristoylation of proteins, which is the co-translational addition of a myrisoyl group to a protein (246). This inhibitor has been shown to prevent rhinovirus replication and is a promising potential treatment for the common cold (246, 247). This inhibitor was

included in the screen to determine whether it would influence any IBV viral proteins and potentially inhibit replication.

Due to the number of inhibitors being assessed and time constraints imposed on the project, a preliminary screen was carried out using concentrations of inhibitors which have previously been used in the literature. Previous literature has used BFA at 1-5 μg/μl (72, 248), Exo1 at 100 μM (230), IMP-1088 at 1-2 μM (246), Paprotrain at 10 μM (249, 250), Endosidin 2 (ES2) at 40 μM (242), Monensin at 1-6 μM (83, 243, 248, 251), Blebbistatin at 150 μM (252) and Fli-06 at 10 μM (237).

To ensure that the inhibitors were not cytotoxic over the selected concentration, primary CK cells were inoculated with a range of concentrations of each inhibitor and cytotoxicity was measured at 24 h. This cell viability assay found that cell viability was not reduced lower than 50% for any inhibitor over any of the concentrations investigated (Figure 5.18). Several of the inhibitors, such as BFA and monensin, were found to be cytotoxic, which was unsurprising as they significantly alter the cellular environment.

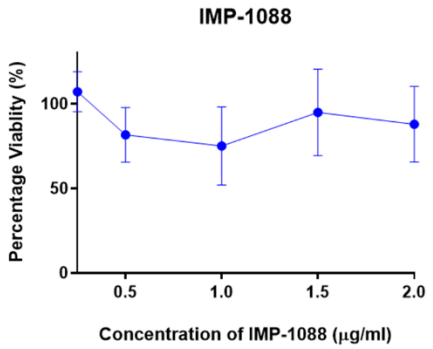
IMP-1088
Percentage Viability (%)
100
50
0
0.5
1.0
1.5
2.0
Concentration of IMP-1088 (µg/ml)

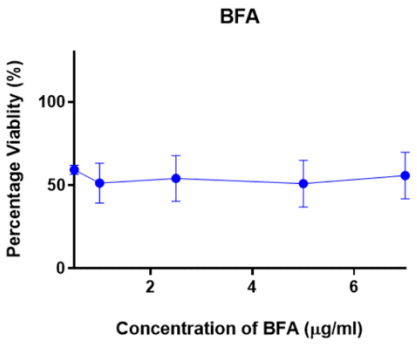
BFA
Percentage Viability (%)
100
50
0
2
4
6
Concentration of BFA (µg/ml)

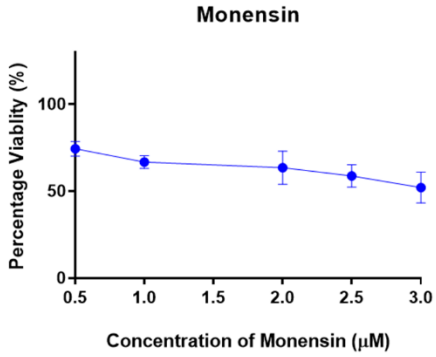
Monensin
Percentage Viability (%)
100
50
0
0.5
1.0
1.5
2.0
2.5
3.0
Concentration of Monensin (µM)

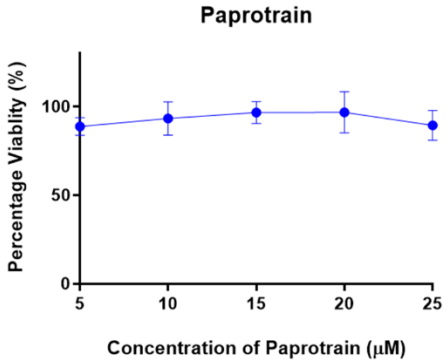
Paprotrain
Percentage Viability (%)
100
50
0
5
10
15
20
25
Concentration of Paprotrain (µM)

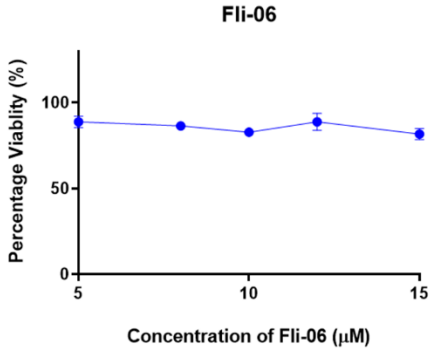
Fli-06
Percentage Viability (%)
100
50
0
5
10
15
Concentration of Fli-06 (µM)

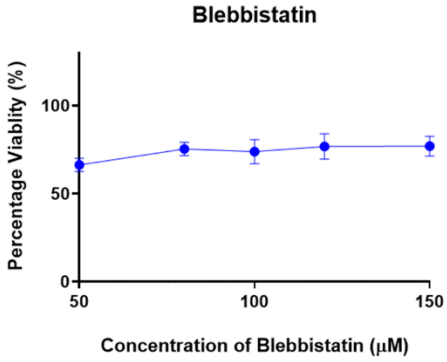
Blebbistatin
Percentage Viability (%)
100
50
0
50
100
150
Concentration of Blebbistatin (µM)

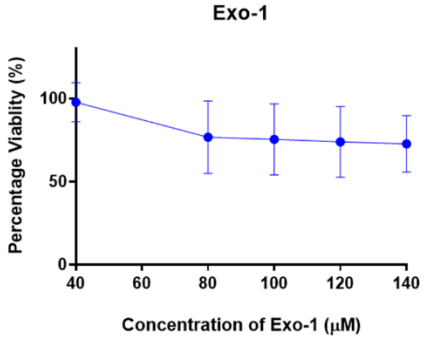
Exo-1
Percentage Viability (%)
100
50
0
40
60
80
100
120
140
Concentration of Exo-1 (µM)

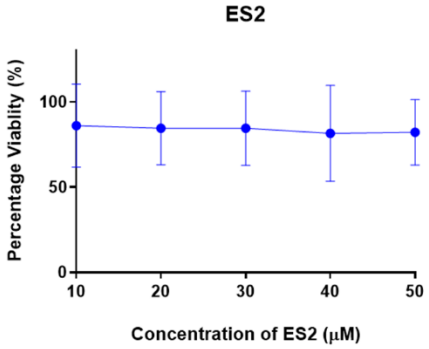
ES2
Percentage Viability (%)
100
50
0
10
20
30
40
50
Concentration of ES2 (µM)

Figure 5.18. Cytotoxicity caused by ERGIC inhibitors within CK cells over a range of concentrations. Inhibitors IMP-1088, Brefeldin-A (BFA), Monensin, Paprotrain, Fli-06, Blebbistatin, Exo-1 and Endosidin-2 (ES2) were added to CK cells over a range of concentrations, based on concentrations used in the literature. CellTiter Glo® reagent was used to assess cytotoxicity at 24 hpi with each inhibitor. Percentage viability is shown relative to mock. Error bars represent ± standard deviation (SD) of three independent experiments

The inhibitors were carried forward to a broad screen in which inhibitor concentrations were used to assess their effect on viral assembly and release. Cell lysate and supernatant was harvested from CK cells infected with either Beau-R or BeauR-T16A with or without ERGIC inhibitors at 24 hpi. The 24 hpi timepoint was selected as this timepoint had the peak titre in the multi-step replication assay in CK cells (Chapter 3, Figure 2B). BeauR-A26F was not included in this screen as it had not been rescued when this experiment was carried out. The harvested cell lysate and supernatant was titrated on CK cells to assess whether presence of the inhibitors resulted in a reduction in viral production (Figure 5.19).

The preliminary screen found that only BFA and Fli-06 inhibited viral production (Figure 5.19.A). This reduction in titre was significantly different to mock treated cells in both supernatant and cell lysate (Figure 5.19.B).

Beau-R infected cells treated with BFA had significantly higher titres of virus present in the cell lysate in comparison to the supernatant, which suggests this inhibitor impacted viral release of Beau-R. This significance was not found in BeauR-T16A infected cells treated with BFA (Figure 5.19.C). Beau-R and BeauR-T16A infected cells treated with Fli-06 showed comparable viral titre in the supernatant and cell lysate (Figure 5.19.C).

A

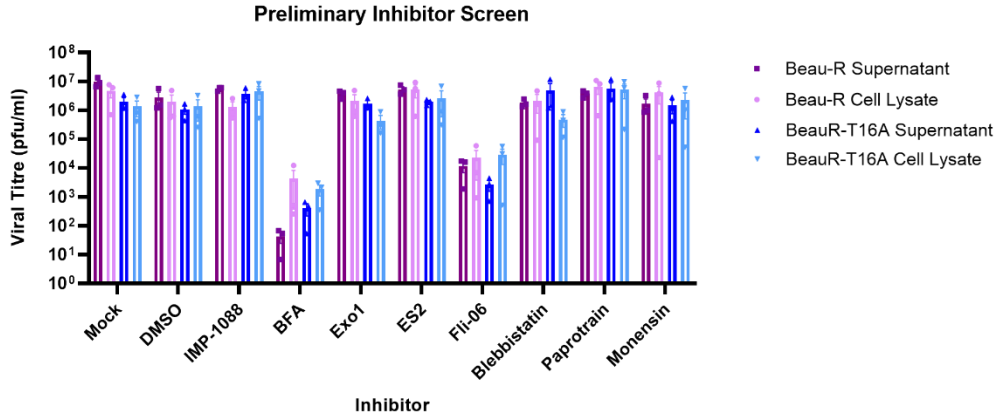
Preliminary Inhibitor Screen
Viral Titre (pfu/ml)
Inhibitor
Mock
DMSO
IMP-1088
BFA
Exo1
ES2
Fli-06
Blebbistatin
Paprotrain
Monensin
Beau-R Supernatant
Beau-R Cell Lysate
BeauR-T16A Supernatant
BeauR-T16A Cell Lysate

B

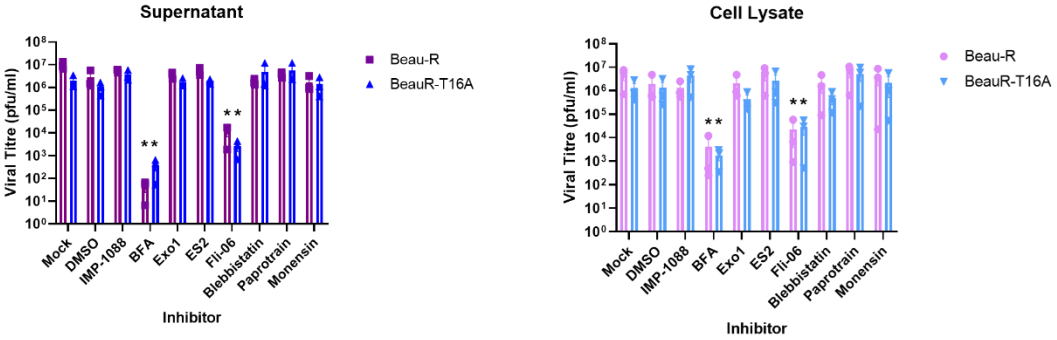
Supernatant
Cell Lysate
Viral Titre (pfu/ml)
Inhibitor
Beau-R
BeauR-T16A

C

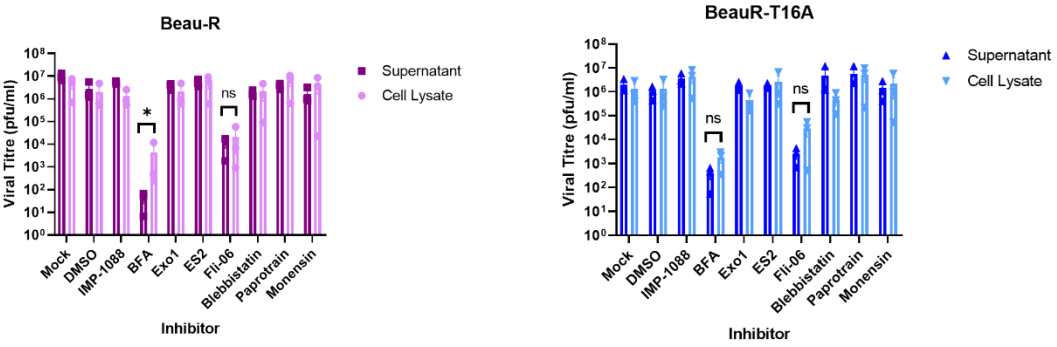
Beau-R
BeauR-T16A
Viral Titre (pfu/ml)
Inhibitor
Supernatant
Cell Lysate
ns

Figure 5.19: Brefeldin-A (BFA) and Fli-06 inhibit viral replication in both BeauR and BeauR-T16A infected CK cells. (A) CK cells were infected with BeauR or BeauR-T16A-3.4 at a titre of 1 x 10^5 PFU. At 1 hpi, the cell media was replaced with media containing an ERGIC inhibitor at a concentration previously cited in the literature. DMSO was included to ensure that this buffer would not impact the viral titre. DMSO was diluted 1 in 20 as this is the maximum amount used in any of the inhibitor treatments The inhibitors assessed were used at the following concentrations: IMP-1088 (1 µg/µl), BFA (1 µg/µl), Exo-1 (100 µM), ES2 (40 µM), Fli-06 (10 µM), Blebbistatin (100 µM), Paprotrain (10 µM) and Monensin (1 µM). At 24 hpi, cell lysate and supernatant were harvested and titrated on CK cells. Error bars represent ± standard error of the mean (SEM) of three independent experiments (B) Supernatant and cell lysate values for Beau-R and BeauR-T16A-3.4 infected samples. Statistical analysis was carried out using a two-way analysis of variance (ANOVA). Significance was taken as p-value < 0.05 and is represented with * in relation to mock treated. (C) Beau-R and BeauR-T16A-3.4 values highlighting differences between supernatant and cell lysate. Statistical analysis was carried out using a two-way analysis of variance (ANOVA), significance was taken as p-value < 0.05 and was assessed in relation to supernatant v. cell lysate values for each virus and inhibitor treatment, significance is represented with *.

Typically, assessing the effect of an inhibitor is preceded by a dose response assay to determine which concentration causes the optimum impact with the minimum loss of cell viability. Due to the number of inhibitors used in this screen, dose response assays were only carried out for a select group of inhibitors which produced interesting results in the initial screen.

As BFA reduced the viral titre of both Beau-R and BeauR-T16A, it was followed up by a dose response assay over a range of concentrations from 0, 0.1, 0.5, 1, 1.5 and 2 µg/µl (Figure 5.20.A). As was observed in the preliminary screen, the titre of virus in BFA treated cells at all concentrations was significantly lower than mock treated (Figure 5.20.B). A dose dependent response was not observed in the cell lysate, the viral titre was comparable between each dose. Conversely, an increased dose of BFA reduced the viral titre within the supernatant but there was no significance found between the doses of the inhibitor.

Beau-R and BeauR-T16A infected cells treated with BFA had significantly higher titres of virus present in the cell lysate, in comparison to the supernatant, except at the 0.1 µg/µl concentration of BFA. This suggests that BFA is impacting the release of virions in a dose dependent manner. BeauR-A26F infected cells treated with all concentrations of BFA had significantly higher titres in the cell lysate than in the supernatant. As this significance was reached at a lower dose of BFA, it could be that BeauR-A26F is more sensitive to BFA treatment than the other viruses.

A

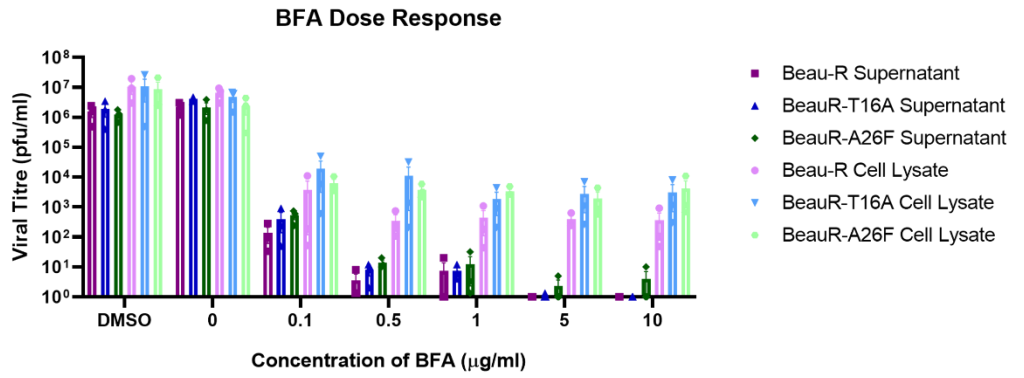
BFA Dose Response
Viral Titre (pfu/ml)
DMSO
0
0.1
0.5
1
5
10
Concentration of BFA (µg/ml)
Beau-R Supernatant
BeauR-T16A Supernatant
BeauR-A26F Supernatant
Beau-R Cell Lysate
BeauR-T16A Cell Lysate
BeauR-A26F Cell Lysate

B

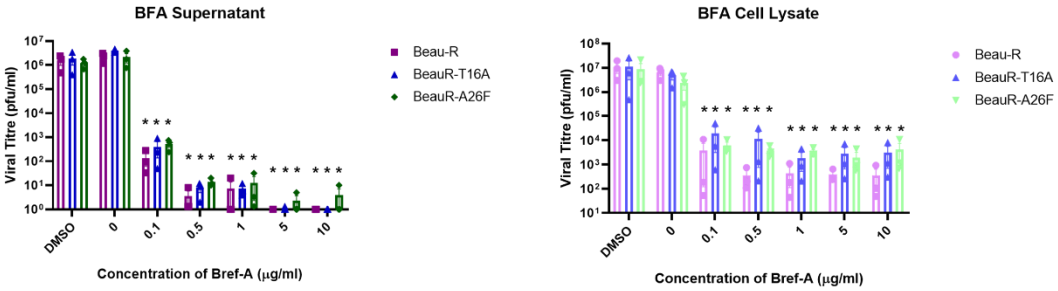
BFA Supernatant
Viral Titre (pfu/ml)
Concentration of Bref-A (µg/ml)
Beau-R
BeauR-T16A
BeauR-A26F
BFA Cell Lysate
Viral Titre (pfu/ml)
Concentration of Bref-A (µg/ml)
Beau-R
BeauR-T16A
BeauR-A26F

C

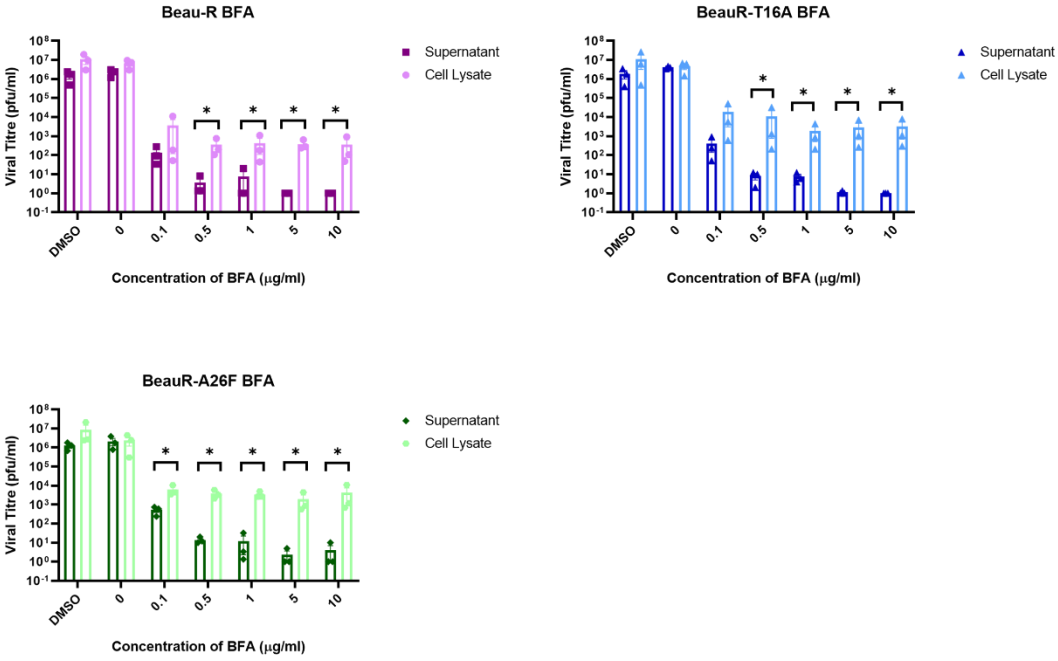
Beau-R BFA
Viral Titre (pfu/ml)
Concentration of BFA (µg/ml)
Supernatant
Cell Lysate
BeauR-T16A BFA
Viral Titre (pfu/ml)
Concentration of BFA (µg/ml)
Supernatant
Cell Lysate
BeauR-A26F BFA
Viral Titre (pfu/ml)
Concentration of BFA (µg/ml)
Supernatant
Cell Lysate

Figure 5.20. Dose response assay showing BFA inhibits viral replication over a range of concentrations. (A) BFA dose response assay. CK cells were infected with $1x10^5$ PFU of BeauR, BeauR-T16A-3.4 or BeauR-A26F-12.3. At 1 hpi, BFA was added to the cells over a range of concentrations (0, 0.1, 0.5, 1, 5, 10 µg/µl). DMSO was included to ensure that this buffer would not impact the viral titre. At 24 hpi, supernatant and cell lysate were harvested and quantified through titration on CK cells. (B) Supernatant and cell lysate values for Beau-R, BeauR-T16A-3.4 and BeauR-A26F-12.3 infected samples. Statistical analysis was carried out using a two-way analysis of variance (ANOVA). Significance was taken as p-value < 0.05 and is represented with * in relation to mock treated. No significance (ns) found between Beau-R, BeauR-T16A3.4 and BeauR-A26F-12.3. (C) Beau-R, BeauR-T16A-3.4 and BeauR-A26F-12.3 values highlighting differences between supernatant and cell lysate. Statistical analysis was carried out using a two-way analysis of variance (ANOVA), significance was taken as p-value < 0.05 and was assessed in relation to supernatant v. cell lysate values for each virus and inhibitor treatment, significance is represented with *.

Treatment with BFA inhibited release of infectious progeny (Figure 5.19 and 5.20). To establish which stage of the replication cycle BFA was impacting, BFA was added at several points over the course of the first round of viral replication (1, 4, 6, 8 and 10 hpi). The start of infection is represented by samples treated at 1 hpi, 4-8 hpi represent the start of viral assembly and at 10 hpi the initial progeny virions are released from the cell. Therefore, a reduction in titre earlier than 10 hpi indicates that BFA is also impacting the assembly of virions.

The supernatant and cell lysate were harvested from cells at 24 hpi to increase the titre present and therefore the ability to distinguish differences between the timepoints/ viruses. Ideally, the supernatant and cell lysate would have been harvested at 12 hpi after the first round of replication. This was not performed as the titre of virus present at 11 hpi is very low (Chapter 3, Figure 2A) so it would be difficult to distinguish inhibition of viral production. Additionally, any effect observed would unlikely reach significance. The titre of virus generated is significantly lower when treated with BFA at 1-8 hpi in comparison to when it is treated at 10 hpi for each virus (Figure 5.21). Therefore, this treatment has inhibited viral production from the early stages of viral assembly as well as inhibiting release.

M41-CK infected cells generated a significantly lower titre of virus in both the supernatant and cell lysate (Figure 5.21.B). Interestingly, the difference between the supernatant and cell lysate for M41-CK infected cells was not significantly different. Indicating that BFA does not impact the release of M41-CK. This follows from work in the previous chapter showing different effects of the Beau-R and M41-CK strains of IBV (Chapter 4, Figures 4.2 and 4.3).

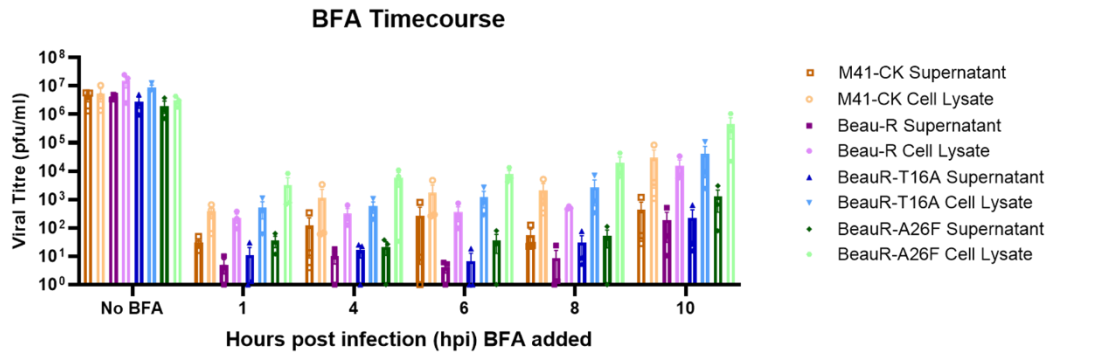
BFA Timecourse
Viral Titre (pfu/ml)
No BFA
1
4
6
8
10
Hours post infection (hpi) BFA added
M41-CK Supernatant
M41-CK Cell Lysate
Beau-R Supernatant
Beau-R Cell Lysate
BeauR-T16A Supernatant
BeauR-T16A Cell Lysate
BeauR-A26F Supernatant
BeauR-A26F Cell Lysate

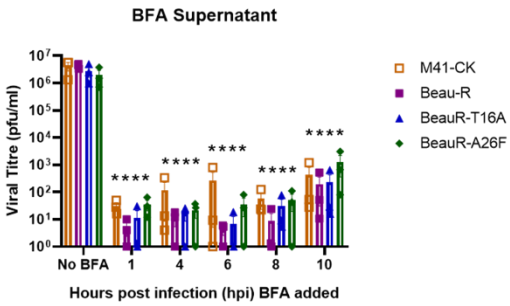
BFA Supernatant
Viral Titre (pfu/ml)
No BFA
Hours post infection (hpi) BFA added
M41-CK
Beau-R
BeauR-T16A
BeauR-A26F

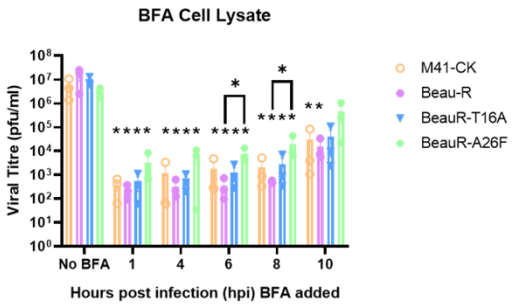
BFA Cell Lysate
Viral Titre (pfu/ml)
No BFA
Hours post infection (hpi) BFA added
M41-CK
Beau-R
BeauR-T16A
BeauR-A26F

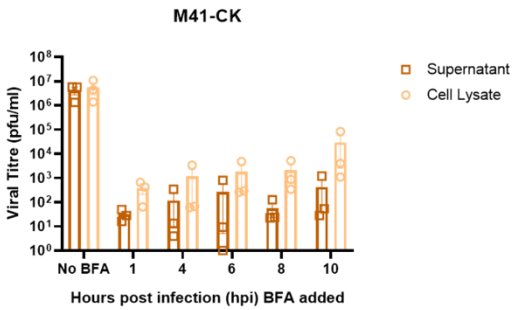
M41-CK
Viral Titre (pfu/ml)
No BFA
Hours post infection (hpi) BFA added
Supernatant
Cell Lysate

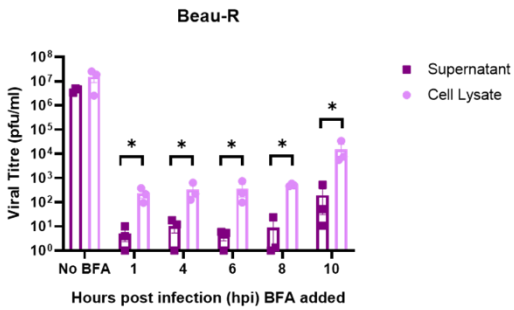
Beau-R
Viral Titre (pfu/ml)
No BFA
Hours post infection (hpi) BFA added
Supernatant
Cell Lysate

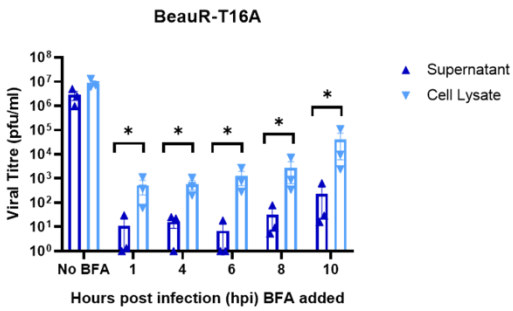
BeauR-T16A
Viral Titre (pfu/ml)
No BFA
Hours post infection (hpi) BFA added
Supernatant
Cell Lysate

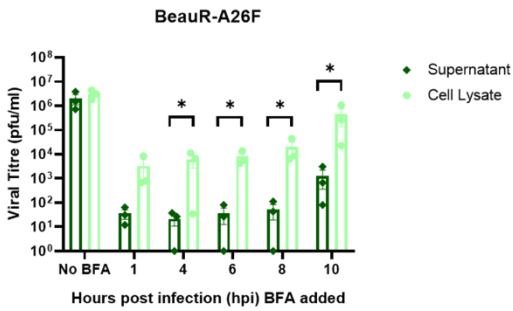
BeauR-A26F
Viral Titre (pfu/ml)
No BFA
Hours post infection (hpi) BFA added
Supernatant
Cell Lysate

Figure 5.21. Time-course assessing the effect of BFA inhibition at different stages during viral assembly and release. (A) BFA time-course. CK cells were infected with M41-CK, Beau-R, BeauR-T16A and BeauR-A26F at a titre of $1x10^5$ PFU. At 1, 4, 6, 8 and 10 hpi 1 µg/µl of BFA was added to the cells. At 24 hpi, supernatant and cell lysate were harvested and quantified through titration on CK cells. (B) Supernatant and cell lysate values for M41-CK, Beau-R, BeauR-T16A and BeauR-A26F infected samples, statistical analysis was carried out using a two-way analysis of variance (ANOVA). Significance was taken as p-value < 0.05 and is represented with * relative to mock treated. (C) M41-CK, Beau-R, BeauR-T16A and BeauR-A26F values highlighting differences between supernatant and cell lysate. Statistical analysis was carried out using a two-way analysis of variance (ANOVA), significance was taken as p-value < 0.05 and was assessed in comparison to supernatant against cell lysate values for each virus and inhibitor treatment. Significance is indicated with *.

The Fli-06 inhibitor was also followed up with a dose response assay as it caused a reduction in viral titre in the initial inhibitor screen (Figure 5.19). The concentrations investigated were 1, 5, 10, 50 and 100 μM. CK cells were infected with Beau-R, BeauR-T16A and BeauR-A26F and treated with Fli-06 at 1 hpi. Cell lysate and supernatant was harvested at 24 hpi and titrated on CK cells to quantify virus present (Figure 5.22).

In both the supernatant and cell lysate samples the titre of virus in cells treated with 5 - 100 μM of Fli-06 was significantly lower than the titre in untreated cells (Figure 5.22.A). The titre at 1 μM was not significantly different to untreated cells, showing that this effect was dose dependent. For each of the viruses, the titre of virus present in the supernatant and cell lysate was comparable (Figure 5.22.B). This suggests that this inhibitor is impacting the assembly of virions and not the release.

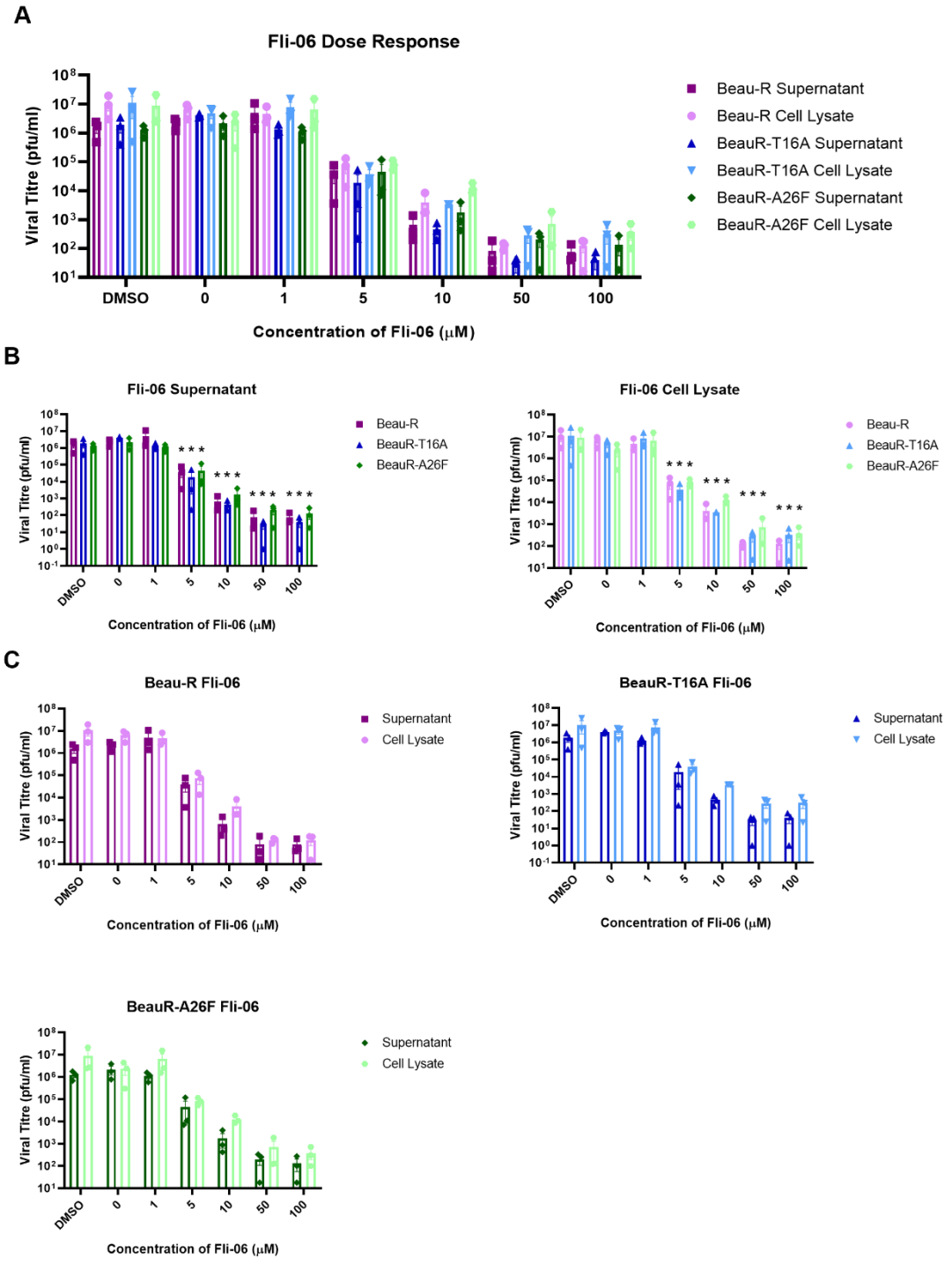
A
Fli-06 Dose Response
Viral Titre (pfu/ml)
Concentration of Fli-06 (μM)
DMSO
0
1
5
10
50
100
Beau-R Supernatant
Beau-R Cell Lysate
BeauR-T16A Supernatant
BeauR-T16A Cell Lysate
BeauR-A26F Supernatant
BeauR-A26F Cell Lysate
B
Fli-06 Supernatant
Fli-06 Cell Lysate
Beau-R
BeauR-T16A
BeauR-A26F
C
Beau-R Fli-06
BeauR-T16A Fli-06
BeauR-A26F Fli-06
Supernatant
Cell Lysate

Figure 5.22. Fli-06 does not impact release of infectious virions. (A) Fli-06 dose response assay. CK cells were infected with $1x10^5$ PFU of Beau-R, BeauR-T16A or BeauR-A26F. Fli-06 was added to cells at 1 hpi at a range of concentrations (0, 1, 5, 10, 50 and 100 µM). DMSO was included to ensure that this buffer would not impact the viral titre. At 24 hpi, supernatant and cell lysate were harvested and quantified through titration on CK cells. (B) Supernatant and cell lysate values for Beau-R, BeauR-T16A and BeauR-A26F infected samples, statistical analysis was carried out using a two-way analysis of variance (ANOVA). Significance was taken as p-value < 0.05 and is represented with * relative to mock treated. No significance (ns) found between Beau-R, BeauR-T16A and BeauR-A26F. (C) Beau-R, BeauR-T16A and BeauR-A26F values highlighting differences between supernatant and cell lysate. Statistical analysis was carried out using a two-way analysis of variance (ANOVA), no significance was found between supernatant and cell lysate.

Exo1 has a similar mode of action to BFA, as both inhibitors cause the collapse of the Golgi Apparatus into the ER (230). It was surprising that the reduction in viral titre seen in BFA was not mirrored in Exo1 treated cells. To ensure that the cause of this discrepancy was not due to use of the wrong dose, a dose response assay was also carried out for Exo1.

CK cells were infected with Beau-R, BeauR-T16A or BeauR-A26F and treated with a range of concentrations of Exo1 (10, 50, 100, 500 and 1000 µM). DMSO treated cells were included as a control as Exo1 was reconstituted in DMSO. Supernatant from cells was harvested at 24 hpi and titrated on primary CK cells. This found that the viral titre obtained from Exo1 treated cells was comparable to mock treated over all concentrations (Figure 5.23). Cell lysate harvested was not titrated as no difference was seen in viral titre in the supernatant, indicating that this inhibitor has not impacted viral assembly or release.

An important caveat to this work is that treatment with Exo1 at higher concentrations found that it precipitated from solution at 500 and 1000 µM. This does not necessarily invalidate the conclusion as it has previously shown that Exo1 functions at 100 µM (230).

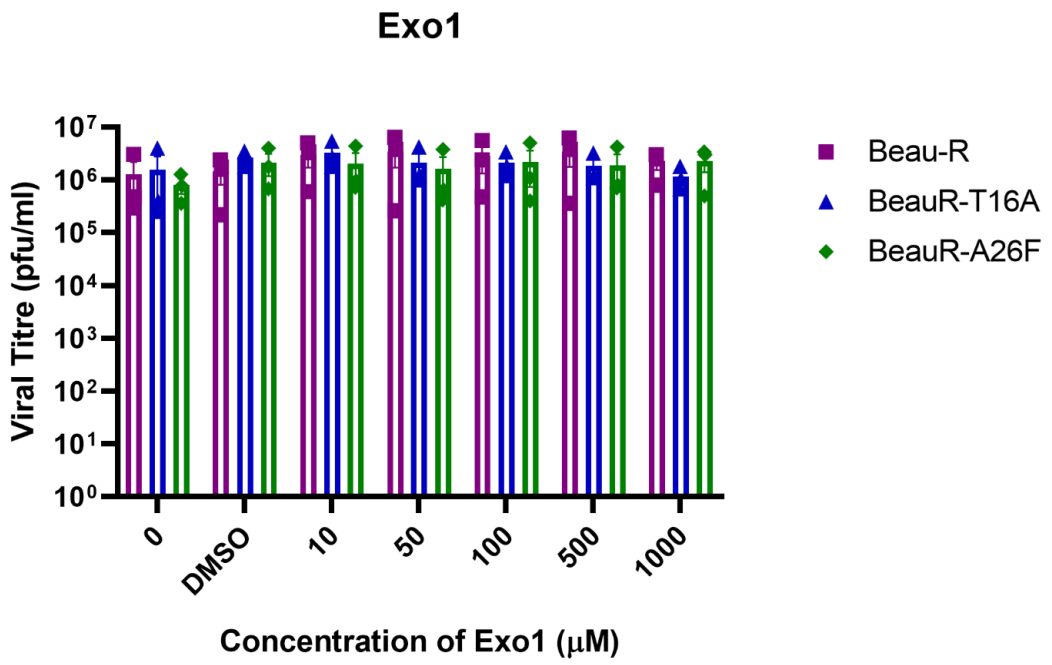

Figure 5.23. Exo1 does not inhibit viral production. CK cells were infected with 1x10^5 PFU of Beau-R, BeauR-T16A-3.4 and BeauR-A26F-12.3. At 1 hpi, Exo1 was added to the cells at a range of concentrations (0, 10, 50, 100, 500, 1000 μM). DMSO was included to ensure that this buffer would not impact the viral titre. Supernatant was harvested at 24 hpi and titrated on CK cells to quantify the virus present. Statistical analysis was carried out using a two-way analysis of variance (ANOVA), no significance was found.

Monensin impacts CoV assembly and release. Monensin has also been shown to inhibit viral release from Vero cells in IBV (83), from 17-Cl1 cells in MHV (253) and from swine testicular (ST) cells in TGEV (243) infections. It is a useful tool as it has been shown to alter the pH of the Golgi Apparatus in a similar mechanism to that used by other viroporins, such as the IAV M2 (222). The preliminary inhibitor screen found that there was no reduction in viral titre in either the cell lysate or supernatant of Monensin treated cells in comparison to mock (Figure 5.19). The inhibition of viral release was previously observed using the Beaudette strain of IBV treated with 1-10 μM of Monensin (83). The preliminary inhibitor screen used Monensin at 1 μM. To determine whether the dose was too low to observe the effect of the inhibitor, a dose response assay was performed for the Monensin inhibitor.

CK cells were infected with Beau-R, BeauR-T16A or BeauR-A26F and treated with a range of concentrations of Monensin (5, 10 and 50 μM) at 1 hpi. Supernatant and cell lysate was harvested at 24 hpi and titrated on CK cells to quantify the virus present (Figure 5.24.A). Upon treatment with 50 μM of Monensin, the virus titre was significantly reduced in comparison to mock treated in both supernatant and cell lysate samples (Figure 5.24.B). Although there appears to be a lower titre present in the supernatant of BeauR-T16A and BeauR-A26F infected cells, this did not reach significance. This ultimately indicates that Monensin is impacting virus assembly and not release.

A

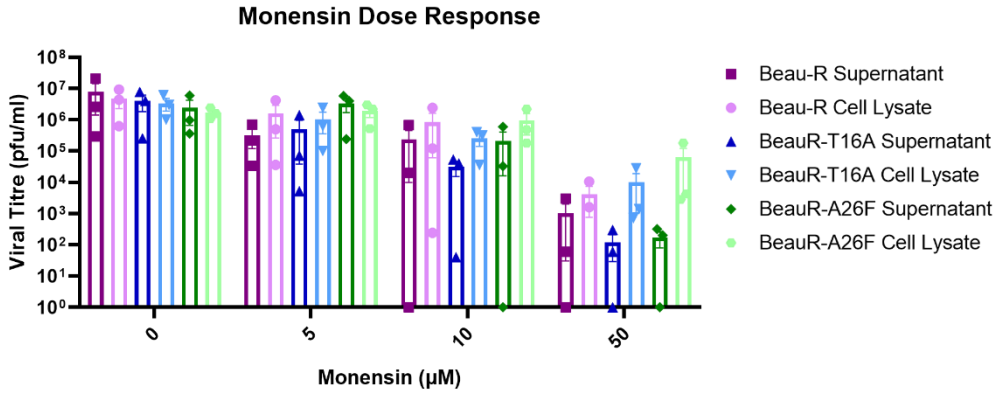
Monensin Dose Response
Viral Titre (pfu/ml)
Monensin (μM)
Beau-R Supernatant
Beau-R Cell Lysate
BeauR-T16A Supernatant
BeauR-T16A Cell Lysate
BeauR-A26F Supernatant
BeauR-A26F Cell Lysate

B

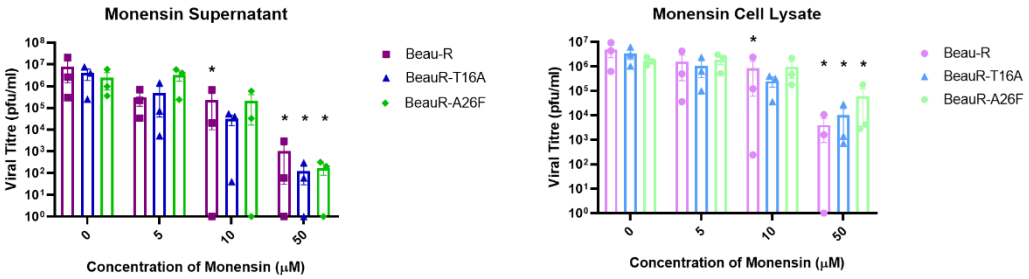
Monensin Supernatant
Monensin Cell Lysate
Viral Titre (pfu/ml)
Concentration of Monensin (μM)
Beau-R
BeauR-T16A
BeauR-A26F

C

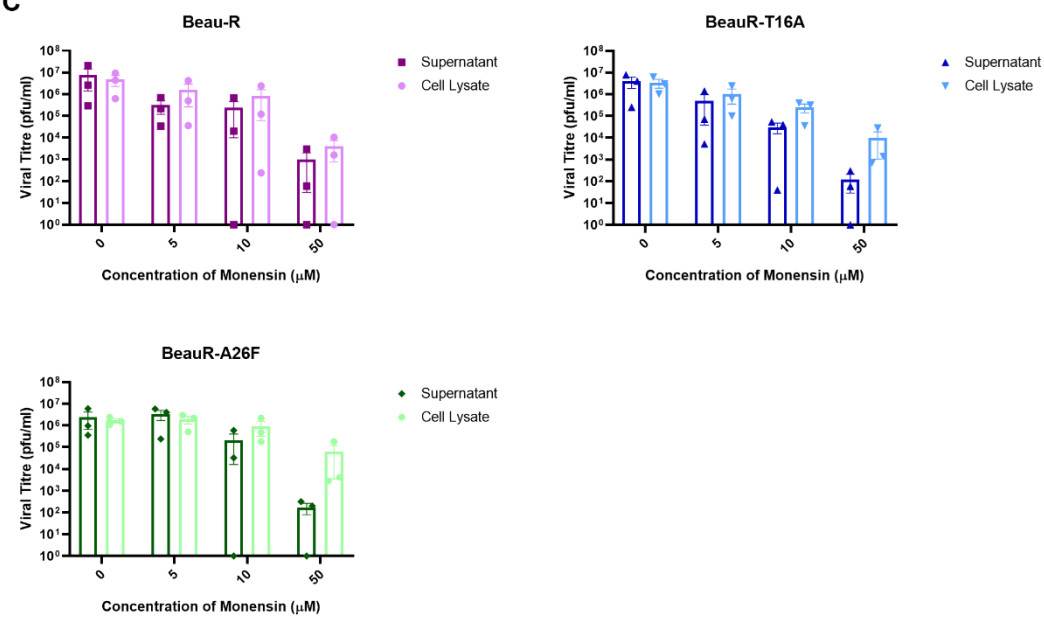
Beau-R
BeauR-T16A
BeauR-A26F
Viral Titre (pfu/ml)
Concentration of Monensin (μM)
Supernatant
Cell Lysate

Figure 5.24. Monensin inhibits viral production at high concentrations. (A) Monensin dose response assay. CK cells were infected with $1x10^5$ PFU of Beau-R, BeauR-T16A-3.4 or BeauR-A26F-12.3. Monensin was added to cells at 1 hpi at a range of concentrations (0, 5, 10 and 50 μM). At 24 hpi, supernatant and cell lysate were harvested and quantified through titration on CK cells. (B) Supernatant and cell lysate values for Beau-R, BeauR-T16A-3.4 and BeauR-A26F-12.3 infected samples. Statistical analysis was carried out using a two-way analysis of variance (ANOVA). Significance was taken as p-value < 0.05 and is represented with * relative to mock treated. No significance (ns) was found between Beau-R, BeauR-T16A-3.4 and BeauR-A26F-12.3. (C) Beau-R, BeauR-T16A-3.4 and BeauR-A26F-12.3 values, highlighting differences between supernatant and cell lysate. Statistical analysis was carried out using a two-way analysis of variance (ANOVA), no significance was found between supernatant and cell lysate.

The reduction in viral titre upon monensin treatment was found at 50 μM (Figure 5.24). At this concentration, it was observed that the monensin precipitated from solution (Figure 5.25).

Monensin disrupts the structure of the Golgi (222). Golgi disruption mediated by the E protein has previously been shown to be important for the correct cleavage of the S2 protein (84). The S2 protein generates syncytium during infection (97). Cells treated with monensin exhibited a reduction in syncytium in virus infected cells (Figure 5.25). This indicates that monensin-induced disruption of the Golgi Apparatus is distinct from that implemented by the E protein, to allow for correct processing of the S2 protein and suggests that this disruption results in incorrect processing of the S2 protein.

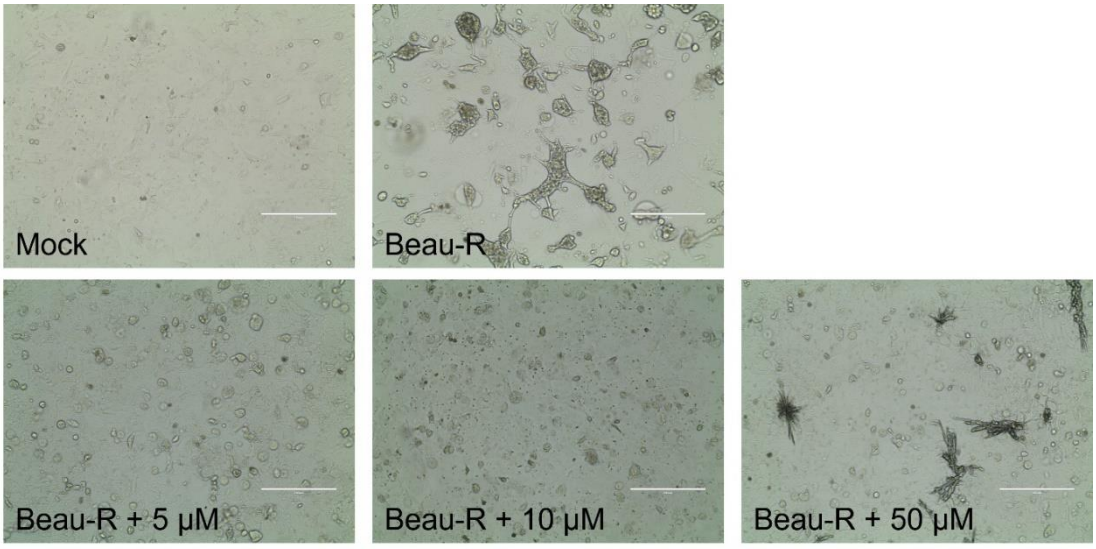

Figure 5.25. Beau-R infected cells treated with Monensin exhibit no syncytium formation. CK cells were mock infected or infected with Beau-R at $1x10^5$ PFU. Cells were treated with either 5, 10 or 50 µM of monensin at 1 hpi. Representative images were taken on a light microscope at 24 hpi. At 50 µM, Monensin has started to precipitate from solution. Scale bars represent 200 µm.

5.4. Discussion

Due to the lack of availability of avian or IBV specific reagents, work in this field often requires assay optimisation. There are no commercially available antibodies for the IBV E protein, but antibodies IE7 and AF12 were in the lab archives. The exact targets of these antibodies are unknown, but both were found to be effective probes for the E protein. The AF12 antibody has been a valuable tool in this project and has facilitated use of many immunoassays.

Co-IP is often performed using epitope tags on the target protein. The rIBVs generated as part of this project do not have a tagged E protein. This is because the IBV E protein cannot be tagged in a recombinant virus with an epitope tag (such as FLAG), as the gene overlaps at both the 5' and 3' end with adjacent genes. Additionally, tagging the E protein is hypothesised to alter the protein's membrane topology (215).

The interactomes of the different E proteins differed greatly, as shown in the Volcano plots and Venn diagrams (Figure 5.4 and 5.5). This indicates that the T16A and A26F mutations have a large effect on the interactions made during infection. The BeauR-T16A virus had the highest number of interacting proteins. The T16 residue is thought to promote the action of the monomeric form in interacting with cellular proteins (113). Therefore, the increased number of interacting partners may be required to compensate for the loss of the T16 residue activity. Alternatively, this result could be the product of the use of primary CK cells which generate highly variable results, as regularly discussed in this thesis.

The use of primary CK cells is effective for this analysis, as these cells have the same factors present as those found during natural IBV infection. The caveats of this, however, are that it reduces the number of characterised proteins which will be detected due to the lack of avian cell characterisation in comparison to mammalian

cells. Additionally, as these cells are not a homogenous culture there is variability in the results, as demonstrated in Figure 5.7. To combat this problem, a paired t-test could be performed to account for this variation.

Many immune factors were found to be interacting partners of the E protein. One which all E proteins interacted with was Tripartite motif-containing protein 25 (TRIM25), a ubiquitin E3 ligase which has been shown to have a crucial role in the innate immune response against viral infection (254). Initiation of the innate immune response is instigated by PRRs in the cell (Chapter 1, Section 1.7.1). Several PRRs were detected as interacting partners of the E protein. PAMPs for IBV are predominantly dsRNA, several factors detected are dsRNA sensors: 2'-5' oligoadenylate synthase (OAS*A), NFX1-type zinc finger-containing protein 1 (ZNFX1) and protein kinase R (pkr). Other PRRs shown to be involved in detecting IBV infection include MDA5 and MAVS. BeauR-T16A E protein was shown to interact with MDA5 and OTU domain-containing protein 4 (OTUD4). OTUD4 stabilises MAVS and promotes its antiviral activity (255). IBV has been shown to downregulate expression of MDA5 and MAVS via unknown mechanisms (161, 162).

Several factors detected were involved in the cytokine response. IFIT5, ISG12(2) and RSAD2 are induced by the type 1 IFN response. Guanylate binding protein 1 (GPB1) and Protein tyrosine phosphatase non-receptor type 1 (PTPN1) are regulators of the IFN-γ and IL-10, respectively. Nicotinamide phosphoribosyltransferase (PBEF1) acts as a cytokine. Poly(ADP-ribose) polymerase family members 9 and 14 (PARP9 and PARP14) were found as interacting partners. The PARP family of proteins inhibit CoV replication and enhance IFN production (256). Although interesting, interrogation of the innate immune response using a non-pathogenic strain must be caveated with the knowledge that it does not cause disease in the bird. It would be valuable to investigate whether these factors also interact with the E proteins of pathogenic strains of IBV, such as M41-CK or D388(QX).

The receptor for IBV is currently unknown. Within the proteomic screen, an epithelial cell receptor EPHA2 was found to interact with the E protein. This receptor has previously been shown to facilitate viral entry (225, 257). As the primary site of IBV infection is within epithelial cells, this receptor should be investigated as a potential entry receptor for IBV. Additionally, the role of these receptors in immunity and pathogenesis has recently been reviewed (258).

Proteins which are involved in the secretory pathway were found to interact with the IBV E protein. Most of these interactions were with the BeauR-T16A E protein. This is important as the T16A mutation has appeared to alter the manipulation of the cellular environment in comparison to the Beau-R E protein. CAMPSAP2 and Rab1b interact with the BeauR-T16A E protein but not Beau-R or BeauR-A26F E proteins. CAMPSAP2 is required for organisation and stabilisation of several organelles including the Golgi Apparatus (259). Interrogation using IF of the Golgi and autophagosomes found that BeauR-T16A infected cells had morphological differences in these organelles in comparison to Beau-R or BeauR-A26F. Potentially, interaction with CAMPSAP2 is facilitating these differences.

The altered Golgi morphology in BeauR-T16A infected cells in comparison to Beau-R or BeauR-A26F, may be corroborated by proteomic data. An interacting protein of only the BeauR-T16A E protein was CAMPSAP2 (Figure 5.6). CAMPSAP2 regulates Golgi morphology and organization through mediating interaction between the microtubules and the Golgi stacks (260).

The absence of Golgi diffusion was validated in BeauR-T16A infected primary CK cells using EM. This was required as the Golgi present in avian cells is diffuse (Figure 5.9), so it is difficult to observe using a low-resolution technique such as IF. Intact Golgi was only observed in BeauR-T16A infected cells which validates the work performed in mammalian cells (Figure 5.13).

This diffusion of the Golgi ensures the correct processing of the S2 protein (84). In the presence of a T16A mutation, a c-terminal fragment of the S2 protein is generated through incorrect cleavage, termed a 'stub' (84). The 'stub' product was undetectable when probed with the 26.1 anti-S2 antibody. Again, the previous work which demonstrated this incorrect cleavage was carried out in mammalian cells, so this may have been a cell-type dependent effect.

Processing of a glycoprotein, such as S, is influenced by whether the protein is glycosylated within mammalian or avian cells (261). This study found a reduction in S2 expressed in BeauR-A26F infected cells, but not in BeauR-T16A infected cells in comparison to Beau-R (Figure 5.15). The pattern of S2 protein expression was not corroborated by previous work using expression plasmids in mammalian HeLa cells (84). This work found that the Beau-R and BeauR-A26F showed comparable levels of S2 with an increase in BeauR-T16A (84). This further highlighted that there may be a cell-type dependent effect of the processing of the S protein.

The S2 protein is required for syncytium formation (97). In this thesis, it was demonstrated that the BeauR-T16A infected cells did not cause syncytium formation (Chapter 3, Figure 8). Therefore, it does appear as though the S2 protein is impacted by the presence of the T16A mutation. The problem likely lies with the sensitivity of the 26.1 anti-S2 antibody. To establish this in the future, purified virus at a higher concentration could be used to determine if this was able to detect the 'stub.' This was used previously to allow for alternate cleavage products of the S2 protein to be detected (97). There was no syncytium observed in CK cells infected with Beau-R and treated with monensin (Figure 5.25). This indicates that the mechanism monensin uses to dissociate the Golgi is discrete from that implemented by the E protein during infection.

The viral egress mechanism for CoVs is highly debated, with three overarching routes proposed (Chapter 1, Section 1.3.4, Figure 1.7). A new theory has recently emerged

in which the recycling endosomal pathway, rather than the TGN, is responsible for the delivery of CoV particles to the cell surface (85). This route has recently been demonstrated for IBV virions (262).

The use of inhibitors had two distinct aims. The first was to interrogate the role of the T16 and A26 residues in assembly and release. The second was to use these tools to gain insight into the egress pathways used by IBV.

The results obtained investigating the first aim found that the T16A and A26F viruses showed comparable reduction in titre in the presence of inhibitors as Beau-R. Significant difference between the supernatant and cell lysate in BFA treated BeauR-A26F infected cells was observed at a lower titre than the other viruses. Additionally, the time at which this effect was identified was earlier. This suggests that this virus is more sensitive to the effect of BFA. Potentially, this result relates to defective viral assembly/ release of BeauR-A26F observed in earlier work (Chapter 3, Figure 4).

During the EM analysis, BeauR-A26F infected cells had abnormal empty structures present at the PM (Figure 5.14). The IBV E and M proteins are sufficient to produce VLPs (75), an A26F mutation in transfected E protein has been shown to prevent this VLP production (113). Potentially, this reduction in VLP production is caused by the build-up of aberrant particles. This would be interesting to follow up, to identify these structures. This follows from earlier data in this thesis, which found that the BeauR-A26F viruses exhibited reduced release of infectious virions in Vero but not in CK cells (Chapter 3, Figure 4). Potentially, this cell-type dependent effect is due to increased efficiency of assembly in avian cells, so effects are more obvious in mammalian cells. Therefore, although there are potential aberrant particles observed in CK cells, this is possibly compensated for by the number of particles generated.

Ideally, this study would include the viruses generated in a M41-K background, but Chapter 4 demonstrated the difficulty of generating and characterising T16A and

A26F mutations in this backbone. The M41K-T16A isolates could have been included, but due to the mutations present in other regions of the genome, characterisation of the T16A mutation alone was not feasible. Beau-R rIBVs were used instead as it allowed for full characterisation of both the T16A and A26F mutations. Throughout this chapter it is important to consider that this work has been carried out in a heavily lab adapted strain of IBV, and the effects may be different in a pathogenic strain. This was highlighted in Figure 5.21 in which M41-CK infected cells showed no difference in viral titre between that in the supernatant and cell lysate, unlike the Beau-R based viruses.

To address this second aim, the inhibitors selected abolished transport between different stages of the secretory pathway. The initial screen found that Fli-06 and BFA were able to inhibit viral titre present in released virus. This was followed up by assessing the effect of these inhibitors over a range of concentrations. The inhibitor Exo1 was also included, although it had no effect in the initial screen, as it impacts similar regions of the secretory pathway to BFA (230).

The dose response assay further showed that there was no inhibition upon use with Exo1 over a range of concentrations. This result, however, must be caveated by some Exo1 precipitating out of solution at higher concentrations. Several techniques, such as sonication, were implemented to try to increase the solubility of Exo1. Unfortunately, none were successful. Regardless, Exo1 has been shown to be effective at 100 μM (230) so any effect should be observed at this concentration.

Referring to the potential egress pathways (Chapter 1, Section 1.3.4, Figure 1.7) and the action of the inhibitors (Figure 5.19), the inhibitor data has been evaluated in relation to the effect each action has on the secretory pathway. Both Fli-06 and monensin were shown to inhibit the released viral titre in infected cells, but the titre present in the supernatant and cell lysate was comparable, indicating that these inhibitors were impacting assembly and not release (Figures 5.22 and 5.24).

Monensin impacts function of the ERGIC and Golgi compartments, therefore it follows that this inhibitor impacts the assembly of virions.

Fli-06 prevents exit from the ERES and transport from the *trans*-Golgi network to the PM (237). It is likely that the inhibition implemented by Fli-06 which causes the reduced titre is due to its action at the ERES, as this inhibitor did not affect release of virus. Therefore, this supports the idea that IBV particles do not use the *trans*-Golgi for release of virions. Furthermore, BFA inhibits the *trans*-Golgi and the endosomes (236). This inhibitor was found to cause a reduction in released virus. Therefore, this indicates that IBV virions could use the endosomal compartment for viral egress. Additionally, a Rhodanese domain-containing protein was identified as an interacting partner. This protein has not been well characterised, likely due to it being avian specific, but it has been reported on UniProt to be an extrinsic component of endosomes. This work corroborates the new theory that CoVs use the endosomal recycling circuit for egress (262).

A time-course was performed to assess whether BFA also inhibited viral assembly (Figure 5.21). There is a greater reduction in titre when the inhibitor is added during assembly than when it is added at the point of release (Figure 5.20), confirming this.

In conclusion, this chapter corroborates research showing that the T16A mutation prevents Golgi diffusion in infected cells (105, 113, 142). It also furthers the previous conclusions that the effect of the T16A and A26F mutations is cell-type dependent. Furthermore, this study suggests that the recent hypothesis that IBV egress bypasses the Golgi Apparatus is correct.

Chapter 6: The pathogenicity of the M41K-T16A isolates.

6.1. Declaration

The work included within this study is the author's sole effort, except from the following exceptions. qPCR primers and probes were designed by Giulia Dowgier, The Pirbright Institute.

6.2. Introduction

The CoV E protein is a key virulence factor (134, 149). In SARS-CoV, viruses with a deleted E protein can protect mice against challenge with WT virus (197). In SARS-CoV the IC activity of the E protein influences viral pathogenesis *in vivo* (138). This activity is inactivated by the N15A or V25F mutations (136), which aligns to T16A or A26F in IBV respectively (Chapter 8, Section 8.3.1, Figure 8.7). Presence of the N15A mutation in SARS-CoV caused comparable clinical signs in uninfected mice (138). Viruses with the V25F mutation in the E gene rapidly generated mutations to recover IC activity, which recovered the pathogenicity of the virus (138).

In IBV, the pathogenicity of viruses containing either a T16A or A26F mutation in the E protein has not been assessed as the equivalent mutations have been generated in the attenuated IBV, Beaudette (20, 152, 191). This chapter follows on from work within Chapter 4, which described the generation of rIBV containing the T16A mutation in a pathogenic IBV backbone; the resulting virus was denoted M41K-T16A. Presence of an A26F mutation prevented the generation of viable virus (Chapter 4,

Table 4.1). This chapter therefore aims to characterise the role of the T16 residue in the pathogenesis of IBV.

6.3. Results

6.3.1. qPCR assessment of innate immune response factors after rIBV infection of CK cells.

Previous research with SARS-CoV found that the N15A mutation causes reduced upregulation of IL-6 and IL-1B *in vivo* (138). Insertion of a T16A mutation in the Beaudette strain of IBV has been shown to alter the upregulation of pro-inflammatory cytokines in 10-day old embryonated eggs (152). There are caveats to this work however, as it was carried out using a non-pathogenic strain, Beaudette, which is attenuated *in vivo* but is pathogenic to embryos. Additionally, the innate immune response is not fully established in chick embryos until 18-days (195, 196). In Chapter 3, the innate immune response was characterised in BeauR-T16A and BeauR-A26F infected CK cells (Chapter 3, Figure 10). This found there was no difference in cytokine upregulation in the rIBVs in comparison to Beau-R. In this study, primary CK cells were infected with the M41K-T16A isolates (2.3, 2.6 and 8.3), or M41-K. RNA from these cell lysates was extracted to analyse innate immune factor upregulation via qPCR. mRNA levels are not necessarily indicative of protein expression; therefore, it would have been ideal to also assess the amount of protein produced. Potentially, this could be performed via an ELISA.

Primary CK cells were infected at a set titre for each of the viruses and cell lysate was harvested at 6 and 48 hpi. as these times indicate the start of viral replication and the peak viral titre, respectively (Chapter 4, Figure 4.10).

To establish the viral load present in each of the cell lysate samples, an experimental procedure was designed to target the E transcript. The qPCR reagents for the E

transcript were designed for use with multiple strains of IBV, including Beau-R and M41-K, using Snapgene. To ensure that the qPCR primers (Chapter 2, Section 2.9, Table 2.10) were covering the correct region, a standard PCR was carried out using these primers and the PCR product was sent for Sanger sequencing. The Sanger sequencing results confirmed primers amplified the expected sequence over the E gene.

Generation of standards for evaluating levels of E transcript was carried out via standard RT-PCR using M41-K RNA amplified by the designed qPCR E primers. The molecular weight and quantity of the PCR product was used to calculate and standardise the number of copies of the standard qPCR product. To validate their use within qPCR, the generated standard was assessed and interpolated (Figure 6.1.A). This found that the qPCR was sensitive down to 100 copies of the E gene (Figure 6.1.A). A Beau-R standard was also successfully generated via the same method, which was used for qPCR analysis of the BeauR-T16A and BeauR-A26F rIBVs (Chapter 3, Figure 10). The qPCR over the E gene showed that the number of copies of genomic RNA present was comparable to the parent virus (Figure 6.1.B). This was not expected as the M41K-T16A-2.3 isolate replicated to a significantly lower titre at 48 hpi than the other M41K-T16A isolates and M41-K (Chapter 4, Figure 4.10)

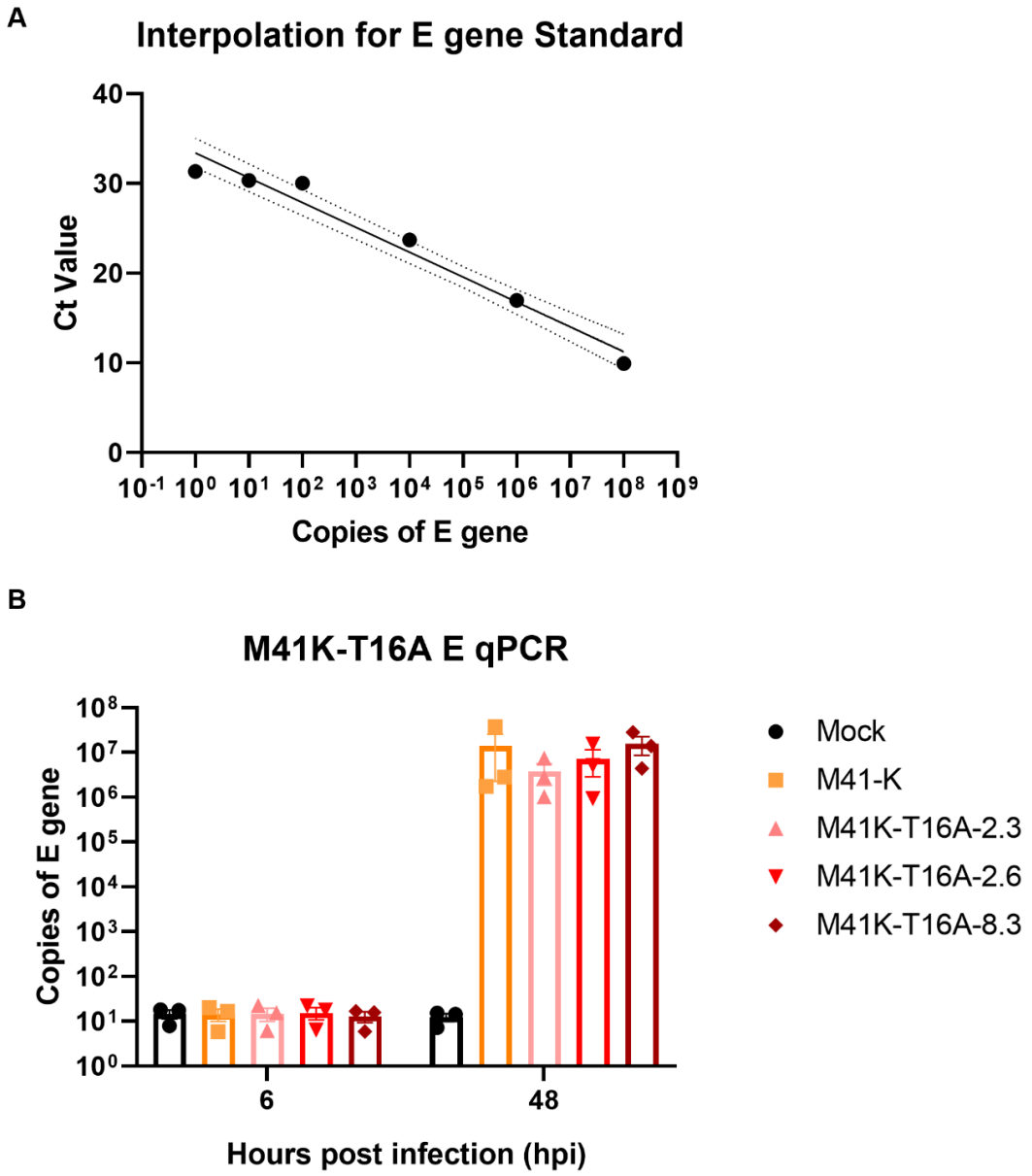

Figure 6.1. E transcript expression is comparable between isolates of M41K-T16A and M41-K. (A) Standard curve of E gene standard. (B) CK cells were infected with rIBVs at a titre of $1x10^2$ PFU for M41K-T16A. At 6 and 48 hpi, cells were extracted, and RNA harvested. qPCR was carried out using the E qPCR primers. The number of copies of the E gene was calculated through interpolation against the standard to establish the viral load.

The same samples were carried forward to assess the upregulation of innate immune factors in cells infected with each virus. This was determined by comparison of the innate immune factor expression relative to a constitutively expressed cellular gene, which is unaltered by viral infection. Previously, several endogenous genes have been proposed for innate immune response quantification in primary CK cells (183). Two of these factors, hypoxanthine phosphoribosyltransferase 1 (HPRT1) and β-actin were tested using GeNorm to validate which would be the best for use within this study (Figure 6.2).

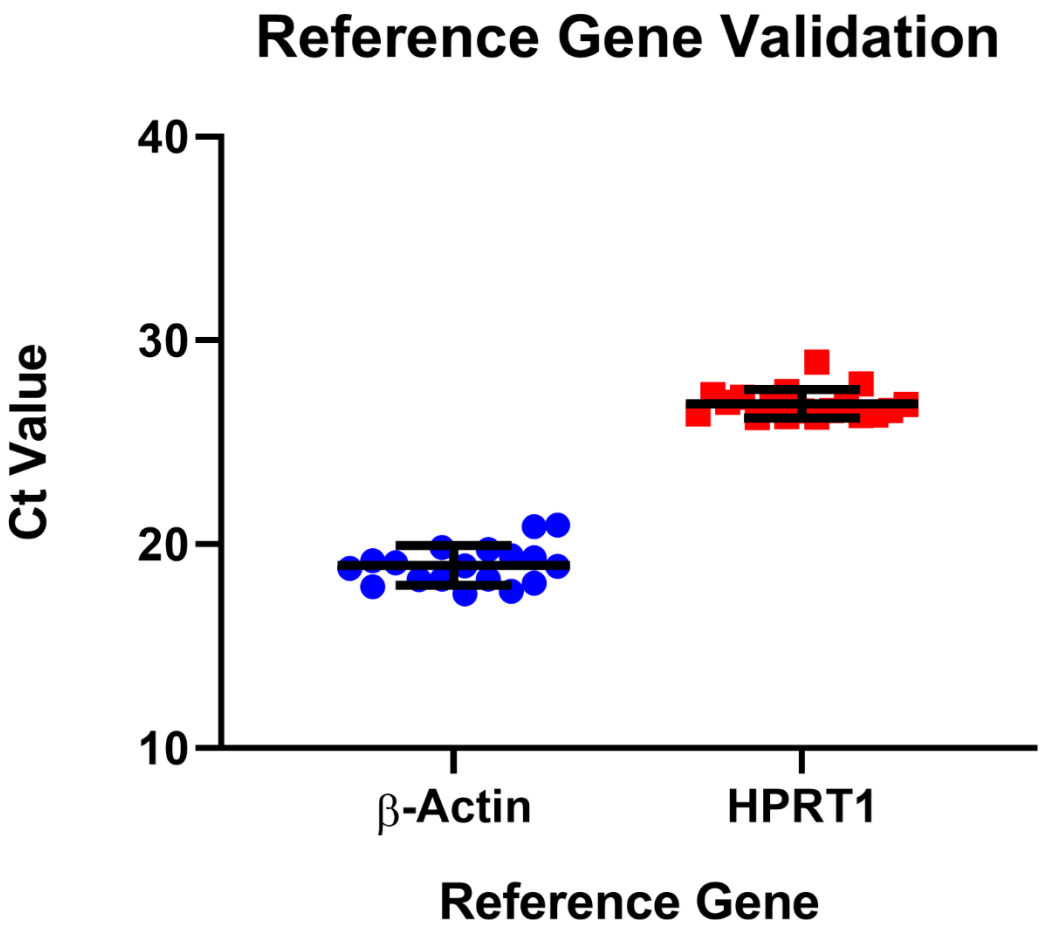

Figure 6.2. Transcriptional stability and expression of candidate reference genes β-Actin and HPRT1. CK cells were mock-infected, infected with Beau-R, or BeauR-T16A isolates at $1x10^5$ PFU. Cells were harvested at 6 and 24 hpi and RNA extracted. Reference gene mRNA was amplified using TaqMan qPCR. The error bars represent the ± standard deviation (SD) of the Ct values.

When determining the optimum reference gene for endogenous control, variation (standard deviation, SD) and expression level (Cycle threshold (Ct) values) of β-Actin and HPRT1 were compared. Variation is important to consider, to ensure comparable expression of the endogenous control between samples. High expression of the control gene is desirable to increase reliability of expression. Analysis using the Excel Add-in GeNorm showed that the SD of HPRT1 was lower than β-Actin, though both were comparable. Ct values for β-Actin were lower, indicating that the expression level is greater than that of HPRT1. From this analysis, β-Actin was selected for use as the reference.

Several immune factors were investigated; IL-6, IL-1β, IFN-α and IFN-β. These factors have previously been shown to exhibit upregulation during IBV infection (164-166, 263, 264). The upregulation of the cytokines has been investigated for M41-K and M41K-T16A isolates and has been determined in comparison to the endogenous control β-Actin (Figure 6.3).

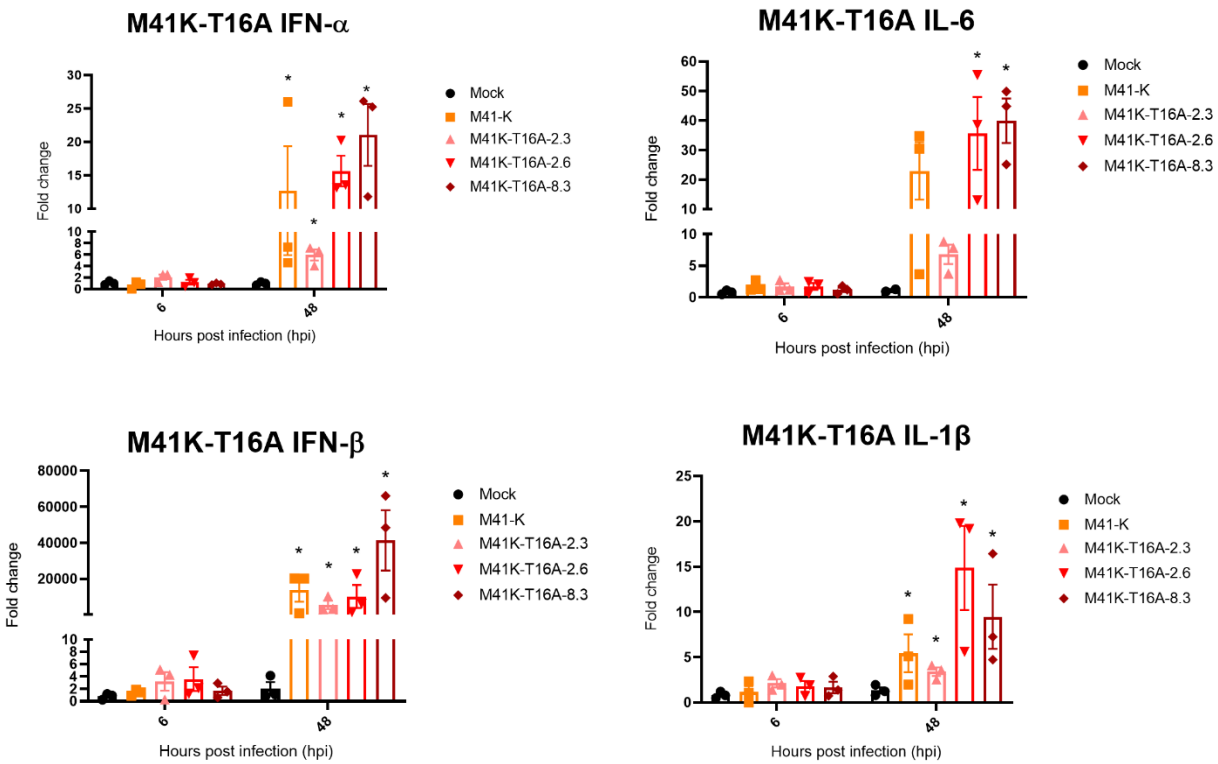

Figure 6.3. Assessment of IL-6, IL-1β, IFN-α and IFN-β upregulation post infection with M41K-T16A isolates. CK cells were infected with $1x10^2$ PFU of virus. At 6 and 48 hpi, cells were harvested, and RNA extracted. Error bars represent ± standard error of the mean (SEM) of three independent experiments. Statistical analysis was carried out using a two-way analysis of variance (ANOVA) and significance was taken as p-value < 0.05 and represented with * relative to mock infected.

For each IFN-α, IFN-β and IL-1β, the upregulation of immune factors was significantly higher in all virus-infected cells than in uninfected cells at 48 hpi, but not at 6 hpi. No upregulation of innate immune factors was detected in mock infected cells. For IL-6, the upregulation caused by M41-K and M41K-T16A-2.3 was comparable to mock infected cells. For M41K-T16A-2.3 this result appears to be decisive due to the low standard error of the mean (SEM) between the replicates of the experiment. There is a wide range of variation in the upregulation of IL-6 between each repeat of the M41-K infected cells.

There was increased variability between each replicate of the experiment, which was considered likely due to the non-homogenous nature of primary CK cell cultures. Because primary CK cells are not a homogeneous culture, there is variation in the amount and type of cell present between different batches. These cells were used as M41-K is replication incompetent within continuous cell lines (97).

For the M41K-T16A-2.3 isolate, the upregulation of IFN-α, IL-6 and IL-1β was lower than the expression of the other M41K-T16A isolates and M41-K (ns). This suggests M41K-T16A-2.3 induces a reduced immune response, which may be indicative of a reduction in pathogenicity. The M41K-T16A-2.6 isolate showed increased upregulation of IL-6 and IL-1β, but not in the type 1 IFNs: IFN-α and IFN-β in comparison to M41-K.

Remarkably, the M41K-T16A-8.3 shows greater upregulation of each cytokine than M41-K. It is important to note that the isolates of M41K-T16A are not clonal, as there are several other mutations present in the genome (Chapter 4, Table 4.2). These mutations could affect the upregulation of the innate immune response independently to the effect of the T16A mutation.

6.3.2. Viral replication within *ex vivo* TOCs

During IBV infection *in vivo*, the ciliated epithelial cells in the trachea are the primary site of viral replication (13). These cells are an early barrier against viral infection, as the beating cilia act as a mucociliary escalator which clears particles from the airways. Loss of this beating contributes to pathogenesis of respiratory diseases (265). During infection with IBV, the beating of the cilia is diminished which ultimately results in complete lack of movement, termed ciliostasis (24, 266). Ciliostasis caused by IBV is used as a marker of pathogenicity and viral replication within research and industry (174).

To determine the loss of ciliary activity caused by the M41K-T16A isolates, embryonic TOCs were infected, and the ciliary activity was assessed at 24 h intervals (Figure 6.4). M41K-T16A-2.3 infected TOCs had significantly higher ciliary activity in comparison to M41-K infected TOCs at 48 – 96 hpi (Figure 6.4). TOCs infected with the other M41K-T16A isolates also retained higher ciliary activity than M41-K at these timepoints, but this did not reach significance.

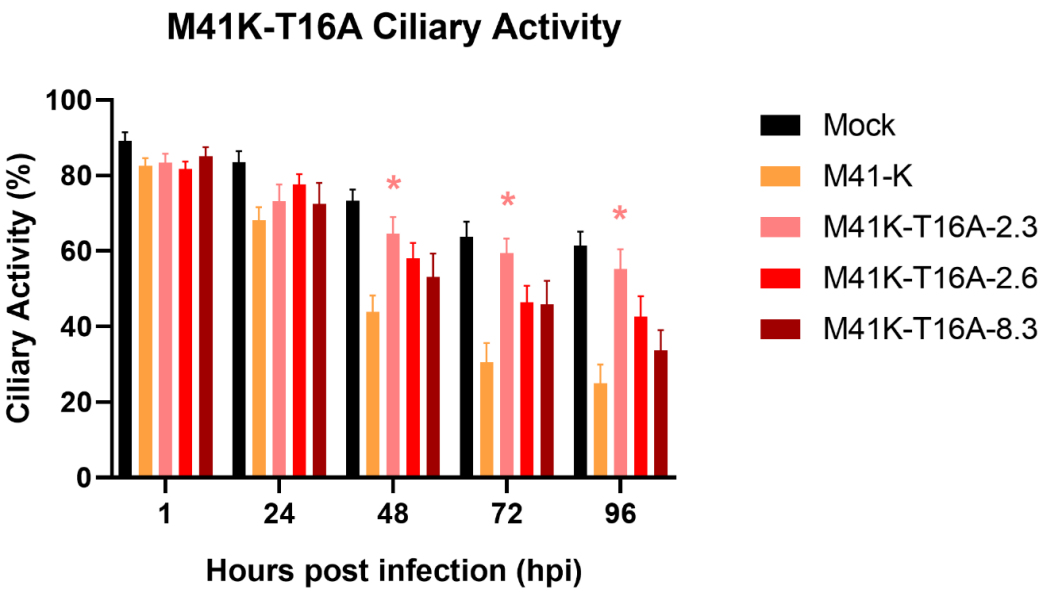

Figure 6.4. The ciliary activity of M41K-T16A infected embryonic *ex vivo* TOCs was different to M41-K. Ten TOCs were mock infected or infected with $1x10^2$ PFU of either M41-K, or the M41K-T16A isolates. Ciliary activity was assessed and scored under a light microscope every 24 hpi from 1 – 96 hpi. The data shown represents the average values of the 10 TOCs from three independent experiments, totalling 30 TOCs. Ciliary activity is displayed as a percentage, error bars represent ± standard deviation (SD). Statistical analysis was carried out via a Friedman test, statistical significance was taken as p-value < 0.05, is represented with * and is shown in comparison to M41-K.

6.3.3. Experimental plan for the M41K-T16A-2.6 pathogenicity experiment

Previous work on the N15A mutation in SARS-CoV showed that infection with this recombinant SARS-CoV induced no clinical signs in mice (138). Accordingly, it was hypothesised that the IBV equivalent mutation of T16A would attenuate virulence *in vivo*.

Pathogenicity trials typically use virus at an amount of 10^5 PFU (177) however, the stocks of M41K-T16A were insufficient, so the experiment was carried out at 10^4 PFU, which has previously generated reliable data (25, 49). Only the M41K-T16A-2.6 and M41K-T16A-8.3 isolates were at a titre suitable for a pathogenicity trial. These isolates of M41K-T16A have mutations in other regions of the genome. M41K-T16A-2.6 has an F36L mutation within the S1 protein (Chapter 4, Table 4.2). M41K-T16A-8.3 has a I637T in the S2 protein and R182H mutation in the M protein (Chapter 4, Table 4.2). M41K-T16A-2.6 was selected for the pathogenicity trial as it had the least consensus level mutations.

To assess the pathogenicity of M41K-T16A-2.6 in comparison to M41-K, groups of 15 8-day old SPF RIR chickens were mock infected with PBS or infected with M41-K or M41K-T16A-2.6. The inoculation was performed via the intra-ocular and intra-nasal route. This route was selected as it replicates natural transmission of IBV, as it typically spreads as an aerosol (13). Clinical signs, including snicking and rales were observed from 3 – 7 and at 14 dpi to determine the severity of disease in each group. Post-mortem (P-M) tissues were extracted from five randomly selected birds from each group on 4, 6 and 14 dpi. The trachea taken from 4 and 6 dpi were assessed for ciliary activity. The experimental plan is detailed in Figure 6.5.

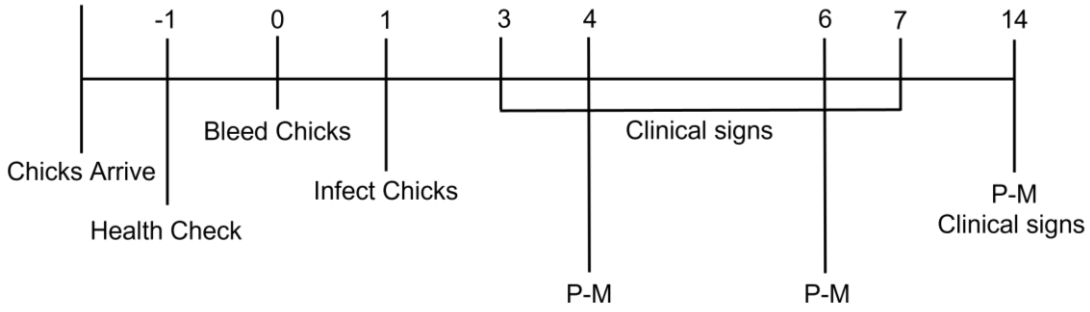

Figure 6.5. Experimental plan for the pathogenicity trial. Days are listed in relation to the date of infection. On day 1, chickens were mock infected or infected with 10^4 PFU of IBV diluted in PBS. Clinical signs were assessed from 3 – 7 dpi and on the final day of the trial (14 dpi). Post-mortem (P-M) of chickens was carried out at 4, 6 and 14 dpi.

6.3.4. Clinical signs observed during *in vivo* experiment

Clinical signs observed during IBV infection are associated with the respiratory tract and include snicking, nasal discharge, tracheal rales, and watery eyes (13). Snicking is the chicken equivalent of a sneeze. To assess the severity of disease, snicking and tracheal rales were evaluated over the course of the pathogenicity trial. The number of snicks for each group were counted for 2 min by two or three persons and were subsequently calculated as an average number of snicks per minute per bird, results are shown in Figure 6.6.A. Tracheal rales were assessed for each individual bird and are characterised by a vibration within the chest of the bird The percentage of birds with rales is shown in Figure 6.6.B.

No clinical signs were observed in mock infected birds, as no rales and a negligible amount of snicking were seen (Figure 6.6). M41-K infected birds showed typical signs of IBV infection (177). The peak number of snicks was observed at 6 dpi and the number of rales detected increased from 3 – 7 dpi.

The M41K-T16A-2.6 infected birds showed a similar pattern of clinical signs to M41-K infected birds (Figure 6.6). The level of snicking similarly peaked at 6 dpi however the number of snicks counted in M41K-T16A-2.6 group was lower. Additionally, despite a similar pattern of rales, increasing from 3 to 7 dpi, at 3 – 5 dpi the percentage observed was lower than in M41-K. This suggests that although the M41K-T16A-2.6 isolate has retained pathogenicity, the respiratory disease is slightly reduced in comparison to M41-K. At 14 dpi, no clear clinical signs were observed in birds in either the M41K-T16A-2.6 or M41-K groups, indicating the birds had recovered from infection.

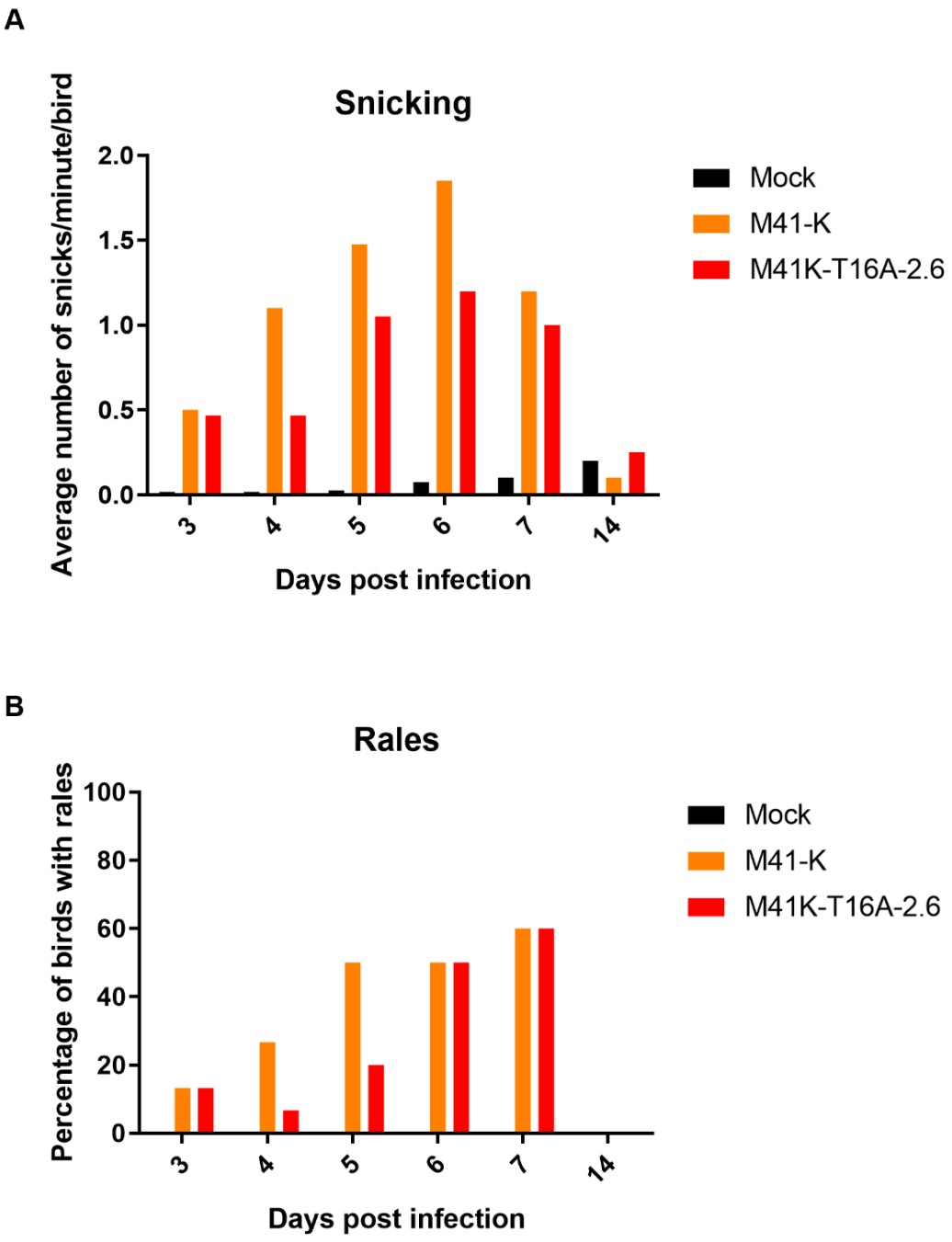

Figure 6.6. M41K-T16A-2.6 caused delayed clinical signs *in vivo* in comparison to M41-K. From 3-7 dpi, the birds were assessed daily for clinical signs associated with IBV infection. (A) The number of snicks per bird per minute was assessed for all birds. (B) The presence of rales was assessed for each individual bird. The number of rales is shown as a percentage of the total number of birds present.

6.3.5. Ciliary activity assessed during *in vivo* pathogenicity experiment

As aforementioned, ciliated tracheal cells infected with IBV have impaired ciliary activity. The presence of pathogenicity in a viral isolate is defined by at least a 50 % reduction in ciliary activity (267). The trachea was extracted from five randomly chosen birds at 4 and 6 dpi and sectioned into rings. Three sections were selected from each end of the trachea and four sections were selected from the centre. The ciliary activity was measured using light microscopy and the mean ciliary activity of the ten rings was calculated per trachea (Figure 6.7).

As mentioned above, the marker for pathogenicity is a reduction in ciliary activity greater than 50 %. At 4 dpi, the ciliary activity observed in the trachea of all five birds infected with M41K-T16A-2.6 was equal to or greater than 50 %. In M41-K infected trachea, three of the five birds had a reduction in ciliary activity greater than 50 %. This indicates that the M41K-T16A-2.6 infected birds had reduced clinical disease. It would be expected that all the mock infected birds would have ciliary activity above 50 %. Unexpectedly, in one of the mock infected birds, there was a large reduction in ciliary activity (Figure 6.7). This bird was assessed for viral presence via RT-PCR, but none was detected. The lack of ciliary activity present in this mock bird is likely due to damage caused during extraction of the trachea.

At 6 dpi, the M41K-T16A-2.6 isolate caused comparable ciliary activity to M41-K and was significantly lower than in mock infected birds. Three birds infected with M41K-T16A-2.6 and two birds infected with M41-K presented ciliary activity lower than 50 %. This correlates with the clinical signs observed at this timepoint (Figure 6.7). The comparable ciliary activity to M41-K at 6 dpi and the presence of clinical signs demonstrates that the M41K-T16A-2.6 isolate has retained pathogenicity. At 6 dpi, all mock infected birds displayed ciliary activity equal to or greater than 75 %.

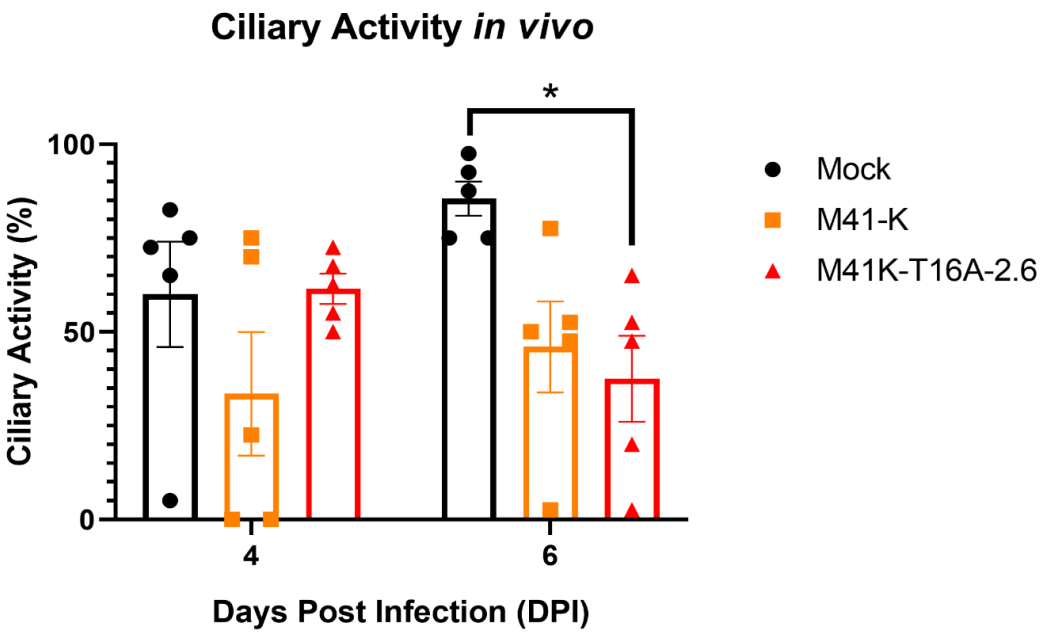

Figure 6.7. M41K-T16A-2.6 has a delayed reduction in ciliary activity in comparison to M41-K. Trachea from five birds culled on 4 and 6 dpi were sliced into 10 x 1 mm sections. Ten sections were analysed per trachea, three from the dorsal and terminal sections and four from the medial section. Ciliary activity was measured using a light microscope. Points represent the average of ten rings from individual birds, error bars are represented as ± standard error of the mean (SEM). Statistical analysis was carried out using a two-way analysis of variance (ANOVA), significance is taken as $p < 0.05$ and is represented with a *.

6.4. Discussion

The pathogenicity of SARS-CoV is reduced in the presence of the N15A mutation *in vivo* (138). The equivalent mutation in IBV, T16A, was inserted into a pathogenic strain of IBV, M41-K, to allow for investigation into the role of the T16A residue in pathogenicity (Chapter 4). This chapter characterises the pathogenicity of the resulting viruses using *in vitro*, *ex vivo* and *in vivo* systems.

The M41K-T16A isolates were difficult to rescue, requiring multiple rescue attempts and resulting in the generation of mutations in other regions of the genome. The isolates are not clonal due to these unexpected mutations at consensus level which are present in two of the isolates, M41K-T16A-2.6 and M41K-T16A-8.3, including those within the S gene (Chapter 4, Table 4.2).

A rIBV generated within a M41-K backbone containing the Beau-R S gene was found to be non-pathogenic, indicating that the S protein plays a key role in viral pathogenicity (268). Additionally, mutations in the S gene of IBV have been shown to act as pathogenicity determinants (269). It is therefore important to consider the impact of the F36L and I637T mutations in the S gene when assessing the pathogenicity of the M41K-T16A isolates.

The innate immune response is the initial response to infection. The increased immune response induced by a viral infection causes inflammation which is associated with severity of clinical disease (264). The cytokines investigated in this work were IL-6, IL-1B, IFN-α and IFN-β, these factors were selected as they have been shown to be impacted by IBV infection (164-166, 263, 264).

This investigation found a high level of variation in the amount of upregulation observed between the isolates of M41K-T16A. Overall, the M41K-T16A-2.3 isolate showed lower levels of cytokine upregulation than M41-K. This lower expression of cytokines was found previously within the Beaudette strain of IBV possessing a T16A

mutation (152), but not in work carried out with BeauR-T16A isolates within this thesis (Chapter 3, Figure 10). The T16A mutation has previously been shown to cause a reduction in cytokine upregulation (152). This corroborates a previous hypothesis that M41K-T16A-2.3 is the 'true' isolate of M41K-T16A (Chapter 4). Although, M41K-T16A-2.3 replicates to a lower titre than the other isolates, in CK cells at 48 hpi (Chapter 4, Figure 4.10). Therefore, this reduction in innate immune factor upregulation may be due to the lower level of virus present.

The upregulation of IFN-β was comparable for M41K, M41K-T16A-2.3 and M41K-T16A-2.6 but not M41K-T16A-8.3. It would be interesting to determine whether the innate immune upregulation found in primary CK cells was comparable to the clinical samples from the *in vivo* trial. Unfortunately, due to time constraints of the project this could not be completed, but it would be valuable to carry out in the future.

The ideal choice for this pathogenicity trial was the M41K-T16A-2.3 isolate. This isolate had the fewest mutations present at consensus levels in other regions of the genome (Chapter 4, Table 4.2) and it replicated to lower levels *in vitro* and *in ovo* (Chapter 4, Figure 4.10 and 4.11). Additionally, it appears have lower pathogenicity, as indicated by reduced upregulation of innate immune factors and higher ciliary activity. Unfortunately, this isolate could not be carried forward to an *in vivo* experiment as it could only replicate to a very low level, so a high titre stock required for inoculation was not available for use.

As a result, the pathogenicity of the T16A mutation *in vivo* was assessed using the M41K-T16A-2.6 isolate. This isolate was selected as it had fewer mutations in other regions of the IBV genome than M41K-T16A-8.3 at consensus level. One of the mutations present in M41K-T16A-8.3, G25051A, resulted in a R182H mutation in the M protein. Previous work in *Betacoronavirus* SARS-CoV showed that a chimeric M protein can recover replication of viruses with a deletion of the E gene (111). This

work ultimately showed that this mutation was able to recover virulence of the recombinant SARS-CoV.

Two receptor binding domains are present within the IBV S protein, S1-NTD and S1-CTD (Chapter 1, Section 1.4.1, Figure 1.8.B). The M41K-T16A-2.6 isolate possesses a T20469C nucleotide mutation resulting in the non-synonymous F36L amino acid change in the S1 protein at consensus level. This mutation is present in a predicted receptor binding domain of the S1 protein (S1-NTD, aa 19-69) (204). The study which predicted the location of the S1-NTD receptor binding domain has several significant caveats. One major caveat is that the binding of the S protein was assessed in relation to α-2,3-sialic acid (204) but the receptor for IBV infection is currently unknown. Additionally, this research used fragments of the S protein to investigate this and therefore the fragments were not in the native form (204).

Regardless of whether the mutation is present in a receptor binding domain, a selective pressure to maintain the T16A mutation in M41K-T16A-2.6 was observed *in vitro* and *in ovo* (Chapter 4, Figure 4.8). This suggests that the S1 mutation was unable to compensate for mutation of the T16 residue. Furthermore, predicted structural data indicated that this mutation does not alter the structure of the S protein and therefore the binding pocket (Chapter 4, Figure 4.5). Additionally, this virus elicited higher ciliary activity *ex vivo* and a different innate immune upregulation profile *in vitro* in comparison to M41-K.

Ciliostasis of ciliated epithelial cells is a characteristic of IBV infection and can be used as a pathogenicity determinant (174). TOCs are an *ex vivo* culture which are a powerful tool to assess IBV at the natural site of infection. In *ex vivo* TOCs, the M41K-T16A-2.3 isolate elicited a comparable reduction in ciliary activity to mock infection of TOCs and the ciliary activity of these TOCs was significantly higher than M41-K. TOCs infected with the other two M41K-T16A isolates displayed higher ciliary activity than M41-K (ns). Additionally, the ciliary activity of the M41K-T16A-2.3 isolate

assessed in embryonated TOCs follows the same replication kinetics profile as seen in both primary CK cells (Chapter 4, Figure 4.10) and *in ovo* (Chapter 4, Figure 4.11). This demonstrates that the M41K-T16A-2.3 is unable to replicate to the same titre as the other isolates and M41-K.

In *ex vivo* TOCs, the ciliary activity of M41K-T16A-2.6 infected TOCs was less than M41-K but this did not reach significance. During the pathogenicity trial, the ciliary activity of M41K-T16A-2.6 infected TOCs was above 50 % in all birds at 4 dpi, indicating a lack of clinical disease. Although at 6 dpi, the ciliary activity of M41K-T16A-2.6 infected TOCs was comparable to M41-K, as several birds had a reduction in ciliary activity equal to or greater than 50 %. This pattern was also observed in clinical signs. Potentially, M41K-T16A-2.6 shows a delayed disease profile, or the virus generated mutations which reverted to virulence between day 4 and day 6. Sanger sequencing over the E and S gene to establish the stability of the T16A and F36L mutations would be valuable to establish potential revertant or compensatory mutations. Due to time constraints on this project, downstream analysis of the pathogenicity trial could not be completed.

The clinical signs data supports the pathogenicity of M41-K and M41K-T16A, but the ciliary activity data is less convincing. A limitation of this study is the amount of virus with which the birds were infected. If an increased titre of virus could have been inoculated into the birds, more classical ciliary activity data may have been obtained. Potentially, a higher titre would also have allowed for the differences between the viruses to be distinguished.

Ideally, this pathogenicity trail would have been completed with an isolate of M41K-T16A without any other mutations in the genome. As the M41K-T16A-2.6 isolate has a F36L within the S1 gene, the effect of these two mutations individually cannot be distinguished. It would be interesting to generate the F36L mutation in a rIBV to characterise its effect.

Chapter 7: Final Discussion

The aim of this thesis was to characterise E protein activity in a range of cellular systems in the context of different IBV backbones. Three overarching themes were investigated in this body of work. The first is that the effect of the T16A and A26F mutations is cell-type dependent. The second found that these effects were further impacted by the viral background in which the mutations were generated. Finally, characterisation of the T16 and A26 residue's role in replication and pathogenesis was performed. Potential roles of these residues during IBV infection have been discussed.

7.1. Cell-Type Dependency

The T16A and A26F mutations were generated in a non-pathogenic backbone, Beau-R, for several reasons. Beau-R is a molecular clone of the Beaudette strain of IBV which has exclusively been used for the characterisation of the E protein in IBV replication (20, 84, 105, 113, 142, 152). Consequently, generating the T16A and A26F mutations in this backbone allowed for direct comparison to previous studies which have assessed these mutations. Previously, the T16A and A26F mutations have been assessed in Beaudette based expression plasmids (84, 113) or Beaudette based rIBVs (20). Additionally, the Beaudette strain, including the molecular clone Beau-R, is heavily lab adapted and consequently has an extended cell tropism (97, 176). Accordingly, the rIBVs BeauR-T16A and BeauR-A26F were assessed in a wide range of cell systems. These include avian cell types primary CK and continuous DF1 cells, along with the continuous mammalian cell line, Vero cells. Further to this, *ex vivo* TOCs and embryonated eggs were also used for investigation (Chapter 3, (191)).

Previously, T16A and A26F mutations were introduced into a Beaudette backbone and displayed genetic instability in DF1 and Vero cells (20). The genetic stability of

Beaudette containing the T16A and A26F mutations upon passage in CK cells and *in ovo* differed (Chapter 3, Figure 6 and 7B). The selective pressure to maintain the T16 and A26 mutations therefore differs between cell systems. The replication of BeauR-A26F isolates displayed different profiles in different cellular systems (Chapter 3, Figure 2), demonstrated by the amount of virus released from infected CK or Vero cells (Chapter 3, Figure 4). Further evidence was provided as the cytotoxicity induced by the rIBVs differed between CK, Vero and DF1 cells (Chapter 3, Figure 9).

In mammalian HeLa cells, the IBV E protein has been shown to diffuse the Golgi which is important for the correct cleavage of the S2 protein. Presence of a T16A mutation results in incorrect S2 protein cleavage (84). This study, performed within avian CK cells, did not observe the 'incorrect' cleavage product in BeauR-T16A infected cells and additionally observed a reduction in S2 expression in BeauR-A26F infected cells (Chapter 5, Figure 5.15). This discrepancy highlighted a potential cell-type dependent effect of the processing of the S protein in the presence of the T16A and A26F mutations. Consequently, this work demonstrates that the effect of the T16A and A26F mutations is cell-type dependent.

Cell type dependency has previously been observed in IBV, as autophagy induction was only be observed in mammalian Vero cells but not avian DF1 or CK cells (38). In wider coronaviruses, cell type dependent selection pressure was detected in the *Betacoronavirus* SARS-CoV-2. Passaging in Vero-E6 cells resulted in a deletion of the cleavage site in the S gene, which is not dominant in clinical samples (270).

7.2. Strain Dependency

The most striking result of this work was the differing tolerance of the T16A and A26F mutations in either a Beau-R (Chapter 3) or M41-K (Chapter 4) backbone. M41-K is a pathogenic molecular clone of M41-CK, a virus that belongs to the same serotype

and genotype as Beaudette (8). The BeauR-T16A and BeauR-A26F isolates rescued with relative ease, unlike the M41-K equivalents, M41K-T16A and M41K-A26F.

The BeauR-T16A was rescued prior to the start of this project, these viruses replicated comparably to Beau-R (Chapter 3, Figure 2). M41K-T16A viruses had a rescue success rate of 33.3% (Chapter 4, Table 4.1) which ultimately led to the successful stock generation of three rIBV isolates. NGS sequencing was performed to generate whole genome sequences of each isolate generated from these viruses. The BeauR-T16A and M41K-T16A viruses all possessed the T16A mutation at consensus level (Chapter 3, Table 2 and Chapter 4, Table 4.2). The BeauR-T16A sequences were as expected other than a synonymous mutation, T13658C, identified in the BeauR-T16A-3.6 in the nsp12 gene (Chapter 3, Table 2). The M41K-T16A isolates all contained additional mutations. Mutations were generated in the S and M genes of isolates, M41K-T16A-2.6 and M41K-T16A-8.3, which potentially facilitated their replication. The M41K-T16A-2.3 isolate displayed attenuated replication in comparison to M41-K (Chapter 4, Figure 4.10 and 4.11) and contained no mutations thought to be capable of compensating for the T16A mutation (Chapter 4, Table 4.2). The acquisition of several possible compensatory mutations in M41K-T16A isolates, not observed in BeauR-T16A isolates indicates that the Beau-R backbone and hence the Beaudette strain of IBV was more tolerant of the T16A mutation.

BeauR-A26F required only seven rescue attempts and NGS sequencing data showed that this mutation was present at consensus level in each isolate of this rIBV and no non-synonymous mutations in other regions of the genome were identified (Chapter 3, Table 2). Twenty rescue attempts were performed for the M41K-A26F rIBV, including a controlled rescue with M41-K, none of which were successful (Chapter 4, Table 4.1). This shows that this virus is replication-incompetent. Although there was a reduction titre found in the replication kinetics assessed for BeauR-A26F (Chapter 3, Figure 2), these viruses were replication competent. This highlights a

significant difference between the role of the A26 residue in the two strains, as it is not necessary for replication in Beau-R but is essential in M41-K. Also indicating that the monomeric form, selected for by the A26F mutation, is essential for replication in M41-K.

The strain-dependent effect of the E protein role was also seen during the assessment of the BFA inhibitor. This result found that in Beau-R infected cells, significantly higher titres of virus were observed in the supernatant in comparison to the cell lysate indicating that the inhibitor was affecting viral release (Chapter 5, Figure 5.20 and 5.21). This significance was not found in M41-CK infected cells (Chapter 5, Figure 5.21), which may indicate that different strains of IBV may cause different disruptions of the secretory pathway and/or use differing egress pathways. This is a result that should be followed up in future work.

In conclusion, the effect of the T16A and A26F mutations is distinct between the two strains, potentially indicating that these residues, and potentially the whole E protein, play different roles of varying prominence in different IBV strains. The Beau-R strain does not cause clinical disease in the bird and is therefore not representative of wild type IBV strains that infect chickens (25, 175). This study ultimately highlights the importance of using IBV strains which are relevant to natural infection for the characterisation of the role of the E protein in viral infection.

7.3. The T16A and A26F mutations alter virus-cell interactions

The T16A and A26F mutations have both been reported to inactivate the IC activity of the IBV E protein (20). These residues, and consequently their potential effect on IC activity, have differing effects on viral replication. This is demonstrated as the replication kinetics of the BeauR-T16A and BeauR-A26F isolates in the same cell

type differs (Chapter 3, Figure 2). Additionally, the diverse interactomes of the Beau-R, BeauR-T16A and BeauR-A26F demonstrate the scale of the impact these mutations impose on the Beau-R E protein (Chapter 5, Figure 5.5).

In mammalian HeLa cells, it has been observed that the IBV E protein diffuses the Golgi during infection and that presence of the T16A mutation prevents this diffusion (113, 142). In this thesis, this effect was not observed upon IF performed in avian CK cells but could be clearly observed in mammalian Vero cells (Chapter 5, Figures 5.8 and 5.10). Preliminary higher resolution analysis using EM later identified this effect in avian CK cells, as the intact Golgi Apparatus was only observed in BeauR-T16A infected cells (Chapter 5, Figure 5.13). The cellular proteins CAMPSAP2 and Rab1b were found to interact with BeauR-T16A but not the other viruses (Chapter 5, Figure 5.6). Both proteins are involved in Golgi maintenance (234, 260). This is interesting as the BeauR-T16A infected cells exhibited differing morphology in this organelle than Beau-R or BeauR-A26F. Potentially, the interaction with these proteins has facilitated this differing morphology.

Golgi diffusion is thought to slow traffic through the Golgi to facilitate correct cleavage of the S2 protein during infection (84). Delayed trafficking of glycoproteins through the secretory pathway has been demonstrated as a function of other viroporins, such as the IAV M2 protein (271). The S2 incorrect cleavage product shown to be produced in the presence of transfected E protein with a T16A mutation (84) was not observed in this study (Chapter 5, Figure 5.15). This result could be due to the S2 antibody used as it may not be able to detect this incorrect cleavage product. The S2 protein is required for syncytium formation (192) and a reduced amount of syncytium was observed in BeauR-T16A infected CK cells (Chapter 3, Figure 8). This indicates that although the incorrect cleavage product wasn't observed, it is likely that the S2 has been incorrectly processed in the presence of the T16A mutation.

The A26F mutation has been shown to reduce the formation of VLPs (113). The BeauR-A26F virus exhibited impaired replication and release in Vero cells (Chapter 3, Figure 2 and Figure 4). Additionally, the M41K-A26F virus was not replication competent (Chapter 4, Table 2.1). EM was performed on BeauR-A26F infected cells, and this led to the observation of unknown structures which were potentially empty virus particles (Chapter 5, Figure 5.14). Therefore, this thesis further indicates that the A26F mutation has a role in viral assembly.

7.4. The M41K-T16A-2.6 isolate retained pathogenicity *in vivo*

In SARS-CoV, the equivalent mutation to T16A, N15A, has been shown to be a pathogenicity determinant (138). Recombinant SARS-CoV with N15A mutation infected into mice caused no clinical signs which resembled the condition of uninfected mice (138). Consequently, the role of the T16A mutation in pathogenicity was evaluated in this work aiming to validate this result in IBV.

Pathogenicity in the presence of a T16A or an A26F mutation could only be assessed using the pathogenic, M41-K strain of IBV as Beau-R does not cause clinical disease in the bird (25, 175). One of the main drawbacks of this work was the lack of tolerance for the T16A and A26F mutations in the M41-K strain. Consequently, the pathogenicity elicited by viruses possessing the A26F mutation could not be assessed within this study, as the M41K-A26F rIBV was not replication competent (Chapter 4, Table 4.1). It would be interesting to confirm whether this was specific to M41 or whether other strains of IBV, such as D388, could be rescued with the A26F mutation.

Upon characterisation of the M41K-T16A isolates, it was apparent that they were not clonal. This was likely due to mutations present in other regions of the genome

(Chapter 4, Table 2.2). The M41K-T16A-2.3 isolate displayed an attenuated replication phenotype (Chapter, Figure 4.10), a reduced innate immune factor upregulation (Chapter 6, Figure 6.3) and possessed no obvious compensatory mutations in other regions of the genome (Chapter 4, Table 2.2). Ideally, this isolate would have been carried forward to the *in vivo* pathogenicity trial, but unfortunately the titre of the stock virus was too low to facilitate this.

The other two isolates possess mutations in the S and M genes. The M41K-T16A-2.6 isolate has a F36L mutation in the S1-NTD (Chapter 4, Table 2.2), which is in one of the predicted receptor binding domains of IBV S protein (204). M41K-T16A-8.3 has an I637T mutation in the FP of the S2 protein and a R182H mutation in the M protein (Chapter 4, Table 2.2).

The M41K-T16A-2.6 isolate was selected for pathogenicity assessment as it had fewer mutations in other regions of the genome. Ultimately, the pathogenicity trial found that the M41K-T16A-2.6 isolate retained pathogenicity but it displayed a delayed disease profile (Chapter 6, Figure 6.6 and 6.7). The T16A mutation in this isolate was unstable when investigated both *in vitro* (Chapter 4, Figure 4.10) and *in ovo* (Chapter 4, Figure 4.11). Potentially, the cause of the delayed onset of clinical signs was due to reversion which took place between 4 and 6 dpi (Chapter 6, Figure 6.6). Regardless, this retained pathogenicity cannot be entirely attributed to the T16A mutation as it is unclear what role the F36L mutation played.

7.5. Future Work

The IC inactivation of the IBV E protein in the presence of a T16A or A26F mutation has previously been stated but the data was not shown (20). It would be useful to assess this inactivation again to confirm this result. Furthermore, it would be valuable to assess this inactivation in the E proteins of other IBV strains to ensure that these mutations exhibit the same effects in other pathogenic strains of IBV.

A vital piece of work would be continuing the comparison between the Beau-R and M41-K E proteins. To further establish potential differing roles, the interactomes of these E proteins during infection could be assessed using mass spectrometry. Additionally, the characterisation of the effect of these mutations in manipulating the cellular machinery should be investigated in other strains of IBV to establish whether the results obtained using the Beau-R strain are indicative of natural infection. A key piece of work would be investigating the tolerance of the T16A and A26F mutations in other strains of IBV. This would establish whether the low tolerance for these mutations was M41-K specific or whether this effect is extended to other pathogenic strains. Therefore, this could allow for investigation into whether these mutations are virulence factors.

There has been limited characterisation into the phenotypic effect of the A26F mutation. Investigation into the role this residue plays on the assembly of IBV virions could potentially further knowledge on the mechanism behind this stage of replication.

Currently, the entry receptor used for IBV is unknown. One of the most exciting avenues to follow up would be establishing whether the EPHA2 receptor identified as an interacting partner of the Beau-R E protein (Chapter 5, Figure 5.6) is the entry receptor used by IBV. This receptor is found on epithelial cells, which are the main site of IBV replication, and has been shown to act as an entry receptor for other viruses (225).

Limited investigation was performed into the mutations uncovered in the M41K-T16A isolates (Chapter 4, Table 2.2). The mutation found in the S1 protein of M41K-T16A-2.6, F36L, is in one of the two predicted receptor binding domains. It would be valuable to investigate the functional role of this mutation. The M41K-T16A-2.6 isolate retained pathogenicity *in* vivo, it would be valuable to assess whether this was the result of the T16A or F36L mutation. Potentially, a rIBV with the F36L mutation alone

could be generated by reverse genetics and assessed *in vitro* to assess the resulting phenotype.

The M41K-T16A-8.3 isolate generated an I637T mutation in a region predicted to act as a fusion peptide in the S2 (Chapter 4, Table 2.2). The effect of this mutation could also be assessed to determine the role of this residue during infection. The other mutation in M41K-T16A-8.3, R182H, in the M protein (Chapter 4, Table 2.2) is in the region responsible for interaction between the E and M proteins, aa119-203 (75). It would be valuable to assess whether this mutation alters the interaction between E and M. Additionally, a structural change was observed in the M protein aa163-165 (Chapter 4, Figure 4.7), this change could potentially have further altered the binding affinity between these two proteins.

Recently, the endosomal recycling circuit has been suggested as the egress route used by CoVs (79, 85, 86). In this thesis, use of cellular inhibitors which target the secretory pathway added further evidence to this hypothesis (Chapter 5). It would be valuable to further analyse this potential route to establish potential mechanisms. Additionally, it would be interesting to establish whether this is used in each strain of IBV or whether this effect is only observed in Beau-R.

7.6. Limitations

One of the limitations of this thesis is associated with the cells and cell systems which are available for use with IBV. The use of primary cells was required for assessment of M41-K based viruses and is a valuable tool as it is biologically relevant. The use of these cells has impacted the consistency of results, however, as data obtained from the mass spectrometry analysis clustered by preparation of CK cells rather than by virus (Chapter 5, Figure 5.7). Additionally, it would have been valuable to assess the interacting partners of the M41-K E protein to establish mechanistic differences between the protein in the two strains.

The use of inhibitors to assess effects on viral egress is a powerful tool but many inhibitors have a broad range of actions, some of which are unknown. Additionally, the mechanisms behind how many of the inhibitor's act is elusive. Potentially there could be a lack of inhibition in chicken cells as the cellular factors and processes differ between mammalian and avian cells. Therefore, further investigation into the E protein interacting partners would be valuable to validate the results obtained using the inhibitors. Furthermore, the inhibitor assessment was only performed with the Beau-R based viruses and it would be informative to assess whether disruptions of the secretory pathway and egress differed between strains of IBV.

A limitation of this study was the single repeat of whole genome sequencing over the viral stocks. Only one repeat was performed due to financial constraints of the project. Due to this, variants could not be called, and mutations present in regions of low depth could not be validated.

The M41K-T16A-2.3 appeared to be the 'true' M41K-T16A isolate, therefore it would have been the best choice to carry forward to the *in vivo* trial. Due to the additional mutations in the other M41K-T16A isolates it was not possible to attribute the retained pathogenicity to the T16A mutation alone. Ideally, it would have been valuable to assess the pathogenicity in the presence of the T16A mutation alone. Since this is not possible, all three isolates could have been included in the pathogenicity trial to determine the impact of the different mutations. The data from the *in vivo* trial produced some variation in the clinical signs and ciliary activity. To combat this the titre at which the experiment was performed could be increased. Potentially, the viruses could be concentrated before use in any future experiments. A lack of genetic stability of the M41K-T16A-2.6 isolate was found both *in vitro* and *in ovo* (Chapter 4, Figure 4.8). Potentially, this impacted the results of the pathogenicity trial. Due to time limitations, sequencing analysis to assess this could not be performed.

7.7. Overall Conclusion

In conclusion, this thesis has built upon previous research to establish roles of the E protein during infection and more specifically to interrogate the effects of the T16A and A26F mutations. The phenotypic effects of these mutations have been shown to be both cell-type and strain dependent. This ultimately highlights the importance of using biologically relevant systems when investigating the IBV E protein. The manipulation of the cell environment has been assessed to establish effects observed within primary CK cells. Additionally, I have demonstrated the effects of the T16A and A26F mutations and how they alter viral replication. Finally, M41-K with T16A in the E protein and F36L in the S protein was not attenuated *in vivo*. Although, to confirm, the virus would need to be sequenced to establish that there was no reversion over the course of the experiment.

Chapter 8: Appendix

8.1. MDPI Viruses Copyright Information

Figure 8.1. Copyright permission for Webb *et al.*, 2022.

8.2. Sequences inserted into GPT-NEB-193 plasmids

Gene strings were ordered from GeneArt. Sequences were designed with 400 nucleotides of excess IBV sequence either side of the modified region.

In all below sequences the same colour-coding has been implemented. *Sal I* restriction site is underlined. Light blue indicates the included S gene sequence, orange sequence is ORF3a, yellow is ORF3b. Overlap between ORF3b and the E gene is shown in green, the E gene is shown in dark blue. Overlap between the E and M genes are shown in purple. The M gene is shown in red. Start and stop codons are highlighted in green and yellow, respectively. Mutations inserted into the E gene are highlighted in blue.

8.2.1 M41K-Cdn-Sh nucleotide and amino acid sequence

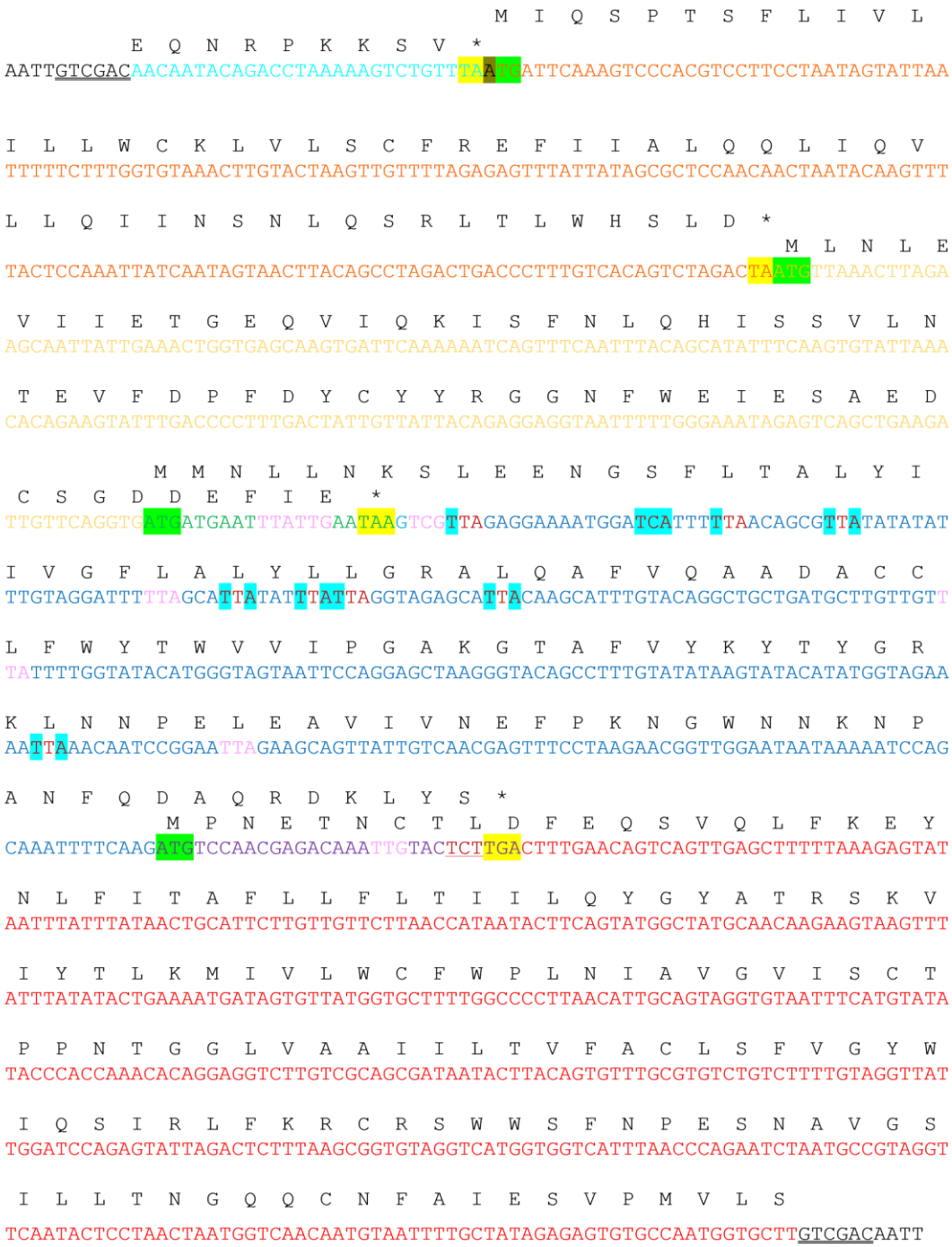

Figure 8.2. Nucleotide and amino acid sequence of M41K-Scr-AUG cloned into pGPT-NEB-193 plasmid. The amino acid sequence is shown above the nucleotide sequence. The sequence over the E gene is shown in dark blue. Leucine and serine residues are shown in pink and dark red, respectively, nucleotide mutations created to generate 1-to-Stop mutations are highlighted in blue

8.2.2. BeauR-T16A nucleotide and amino acid sequence

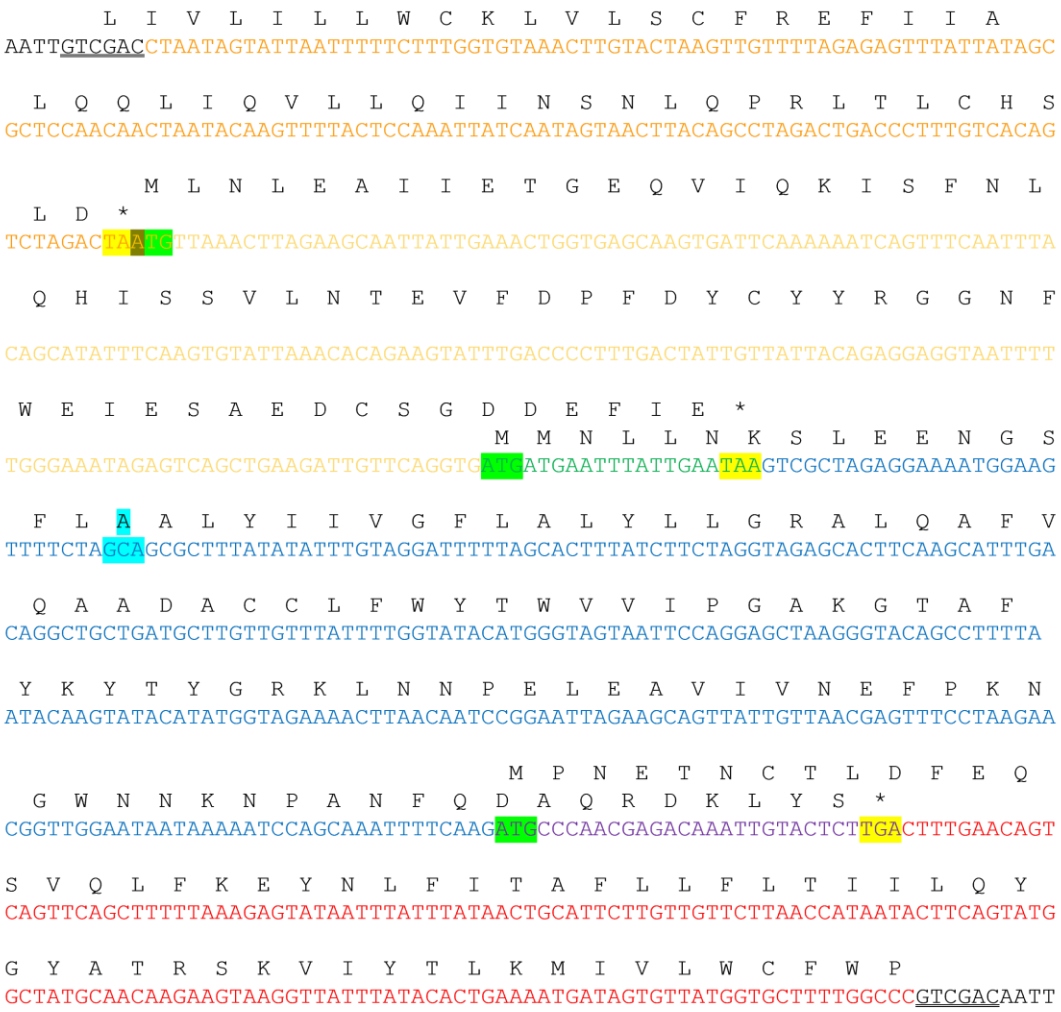

Figure 8.3. Nucleotide and amino acid sequence of BeauR-T16A cloned into pGPT-NEB-193 plasmid. The amino acid sequence is shown above the nucleotide sequence. The sequence over the E gene is shown in dark blue, modified nucleotides to generate the T16A mutation are highlighted in blue.

8.2.3. M41K-T16A nucleotide and amino acid sequence

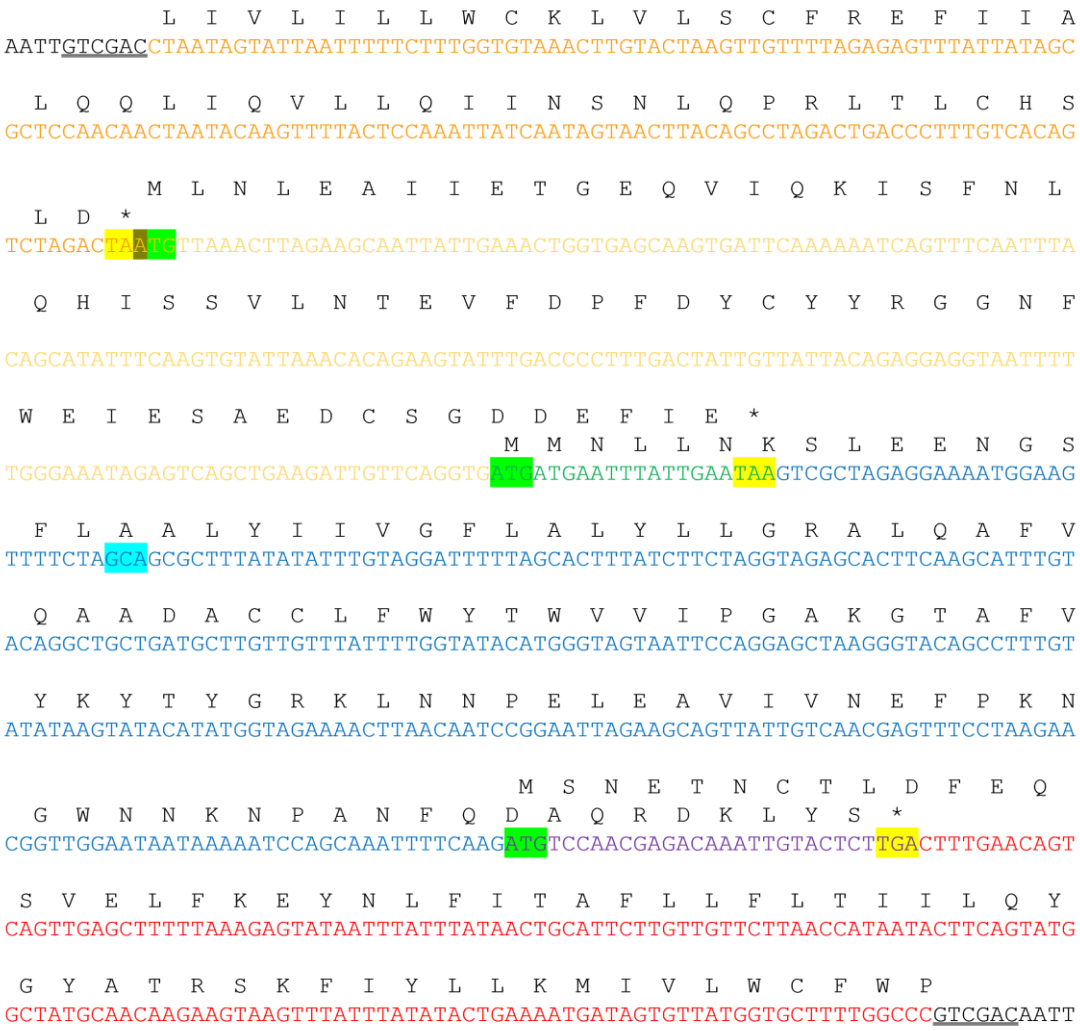

Figure 8.4. Nucleotide and amino acid sequence of M41K-T16A cloned into pGPT-NEB-193 plasmid. The amino acid sequence is shown above the nucleotide sequence. The sequence over the E gene is shown in dark blue, modified nucleotides to generate the T16A mutation are highlighted in blue.

8.2.4. BeauR-A26F nucleotide and amino acid sequence.

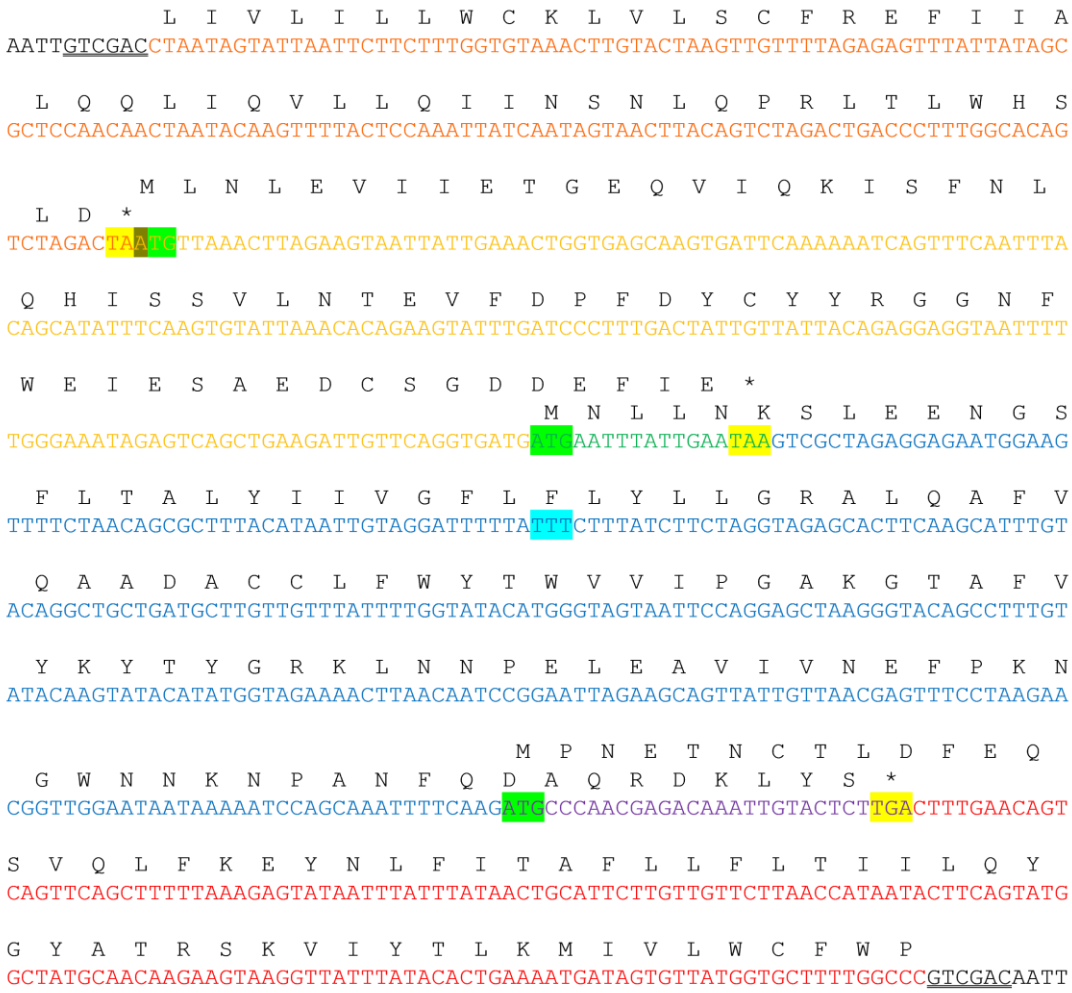

Figure 8.5. Nucleotide and amino acid sequence of BeauR-A26F cloned into pGPT-NEB-193 plasmid. The amino acid sequence is shown above the nucleotide sequence. The sequence over the E gene is shown in dark blue, modified nucleotides to generate the A26F mutation are highlighted in blue.

8.2.5. M41K-A26F nucleotide and amino acid sequence

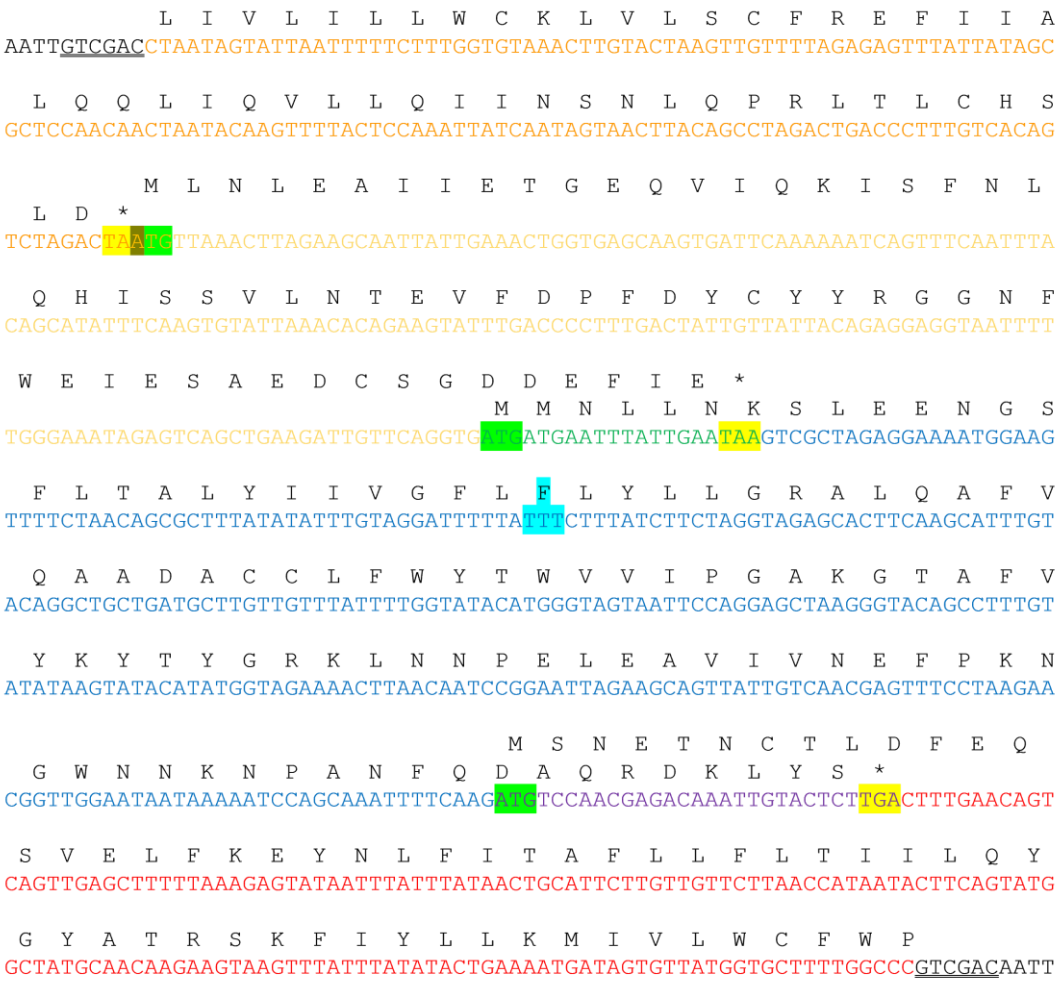

Figure 8.6. Nucleotide and amino acid sequence of M41K-A26F cloned into pGPT-NEB-193 plasmid. The amino acid sequence is shown above the nucleotide sequence. The sequence over the E gene is shown in dark blue, modified nucleotides to generate the A26F mutation are highlighted in blue.

8.3. Amino Acid Alignments of the E protein

8.3.1. Amino acid alignment of the E protein of CoVs.

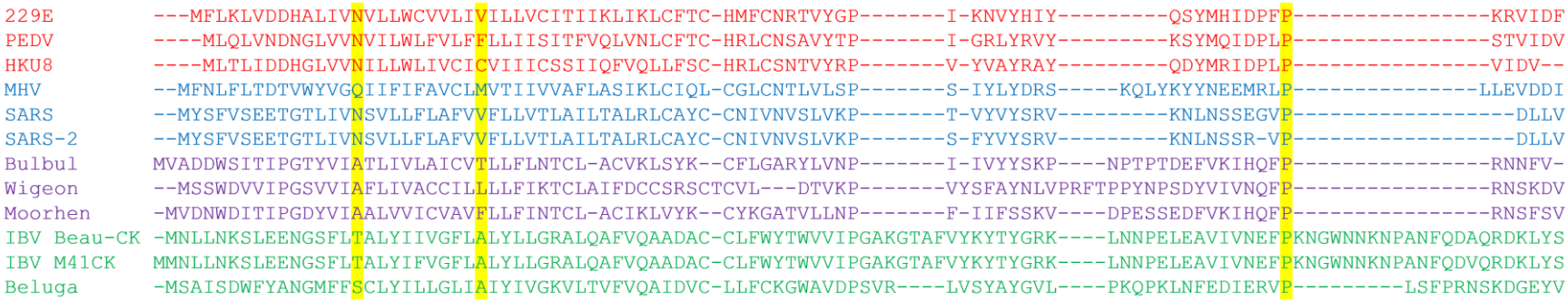

Figure 8.7. CoV E protein amino acid sequence alignment. The conserved proline residues along with the position of the T16 and A26 residues are highlighted in yellow. The genus of each virus is displayed within the figure: *alphacoronavirus* (red), *betacoronavirus* (blue), *deltacoronavirus* (purple) and *gammacoronavirus* (green). The accession numbers for the strains compared are as follows: human coronavirus 229E (QNT54757.1), porcine epidemic diarrhoea virus (QER78629.1), miniopterus bat coronavirus HKU8 (YP_001718614.1), murine hepatitis virus A59 (ACO72886.1), severe acute respiratory syndrome (AYV99820.1), severe acute respiratory syndrome coronavirus 2 (QJQ84090.1), bulbul coronavirus HKU11-934 (YP_002308480.1), wigeon coronavirus HKU20 (YP_005352872.1), common moorhen coronavirus HKU21 (AFD29245.1), IBV Beau-CK (CAC39117.1), IBV M41-CK (QCE31536.1) and beluga whale coronavirus SW1 (ABW87821.1). The alignment was assembled on Mega11 software, alignment was performed using the MUSCLE alignment tool.

8.3.2. Amino acid alignment of the E protein of IBV strains

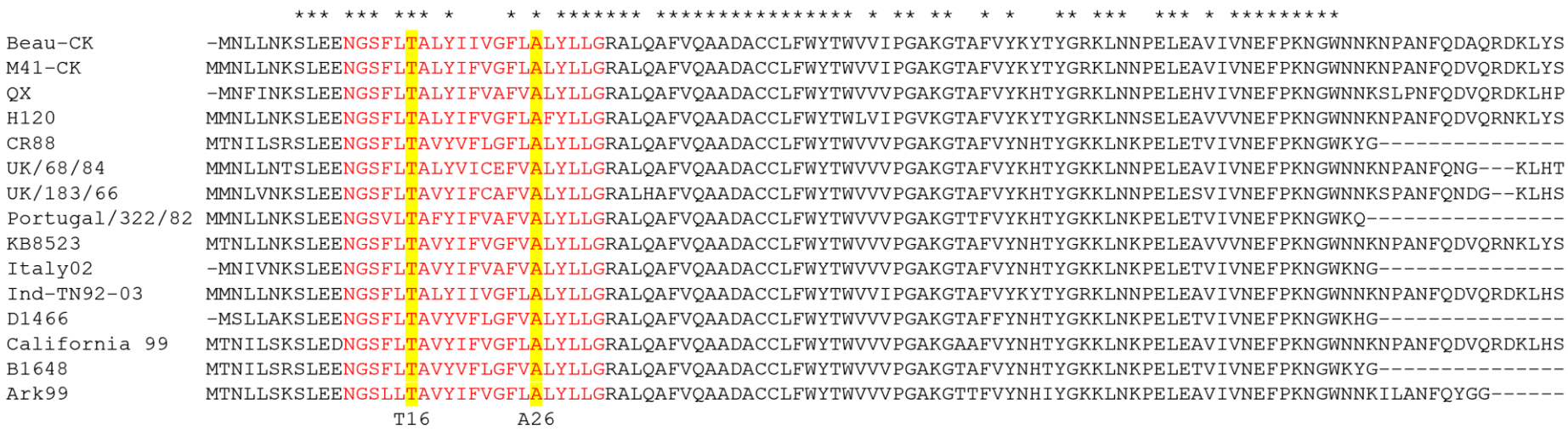

Figure 8.8. IBV E protein amino acid sequence alignment. The transmembrane domain (TMD) of the E protein is indicated in red. T16 and A26 residues are highlighted in yellow and * indicates that the residue is conserved between every strain aligned. The accession numbers for the strains compared are as follows: Beau-CK (CAC39117.1), CR88 (QKV27915.1), D1466 (QKV27928.1), H120 (UQM93960.1), Italy02 (QKV27954.1), QX (ARI46255.1), M41-CK (QCE31536.1), UK/183/66 (P30248.1), UK/68/84 (P30247.1), Portugal/322/82 (P30246.1), KB8523 (P19744.1), Ind/TN92/03 (YP_009825001), Ark99 (AAX39774), California/99 (AAS00083) and B1648 (ALH21114). The alignment was assembled on Mega11 software, alignment was performed using the MUSCLE alignment tool.

8.4. Mass Spectrometry Datasets

Only the proteins which were found to be significant to mock are displayed in these tables. The complete dataset can be provided upon request.

8.4.1. Mass spectrometry data for Beau-R infected CK cells.

Table 8.1. Beau-R mass spectrometry dataset

Accession	Description	-Log Welch's T-test p-value BeauR_Mock	Welch's T-test q-value BeauR_Mock	log2 FC_BeauR_Mock
nucleocapsid	nucleocapsid nucleocapsid	1.993138054	0.3164	3.357065837
membrane	membrane membrane	2.031127843	0.320769	2.762232304
5a	5a 5a	2.181140596	0.364	2.300138156
O13255	2'-5' oligoadenylate synthase (Fragment) OS=Gallus gallus OX=9031 GN=OAS*A PE=2 SV=1	1.699139385	0.414491	2.209358533
envelope	envelope envelope	1.397589789	0.551319	2.096845945
pp1ab	pp1ab pp1ab	2.662353534	0.704	2.064800262
spike	spike spike	2.36968289	0.430667	1.558053096
A0A125RM76	Interferon-induced protein with tetratricopeptide repeats 5 OS=Gallus gallus OX=9031 GN=IFIT5 PE=2 SV=1	2.584400075	0.390667	1.282459736
A0A3Q3AUC8	UvrD-like helicase ATP-binding domain-containing protein OS=Gallus gallus OX=9031 GN=TRANK1 PE=4 SV=1	1.701668276	0.422462	1.101292292
Q6IEC5	Putative ISG12(2) protein OS=Gallus gallus OX=9031 GN=ISG12(2) PE=2 SV=1	1.538116854	0.542882	1.04602019
F1NLJ6	Viperin OS=Gallus gallus OX=9031 GN=RSAD2 PE=2 SV=2	2.121069048	0.3386	0.914958636
F1NFA4	Uncharacterized protein OS=Gallus gallus OX=9031 GN=ZNFX1 PE=4 SV=2	1.784835539	0.419048	0.839039485
A0A3Q2TXL9	Uncharacterized protein OS=Gallus gallus OX=9031 GN=STIP1 PE=4 SV=1	1.570965803	0.5176	0.766482512
A0A3Q3AR57	C3H1-type domain-containing protein OS=Gallus gallus OX=9031 GN=HELZ2 PE=4 SV=1	1.57590095	0.519746	0.757453283
E1BXW9	Tudor domain-containing protein 3 OS=Gallus gallus OX=9031 GN=TDRD3 PE=4 SV=2	1.772009575	0.416727	0.730490843
Q75UT8	Double-stranded RNA-activated protein kinase OS=Gallus gallus OX=9031 GN=pkr PE=2 SV=1	2.423029721	0.4195	0.633821487
Q5ZLB3	Helix-destabilizing protein OS=Gallus gallus OX=9031 GN=HNRNPA1 PE=2 SV=1	1.86828089	0.356973	0.577999751
E1BXY4	Dynamin GTPase OS=Gallus gallus OX=9031 GN=DNM1 PE=3 SV=4	2.197583242	0.42	0.560214202
A0A3Q2U1Z7	Rhodanese domain-containing protein OS=Gallus gallus OX=9031 PE=4 SV=1	2.1762851	0.34725	0.544178327
A0A0B5H7I8	Tripartite motif containing 25 OS=Gallus gallus OX=9031 GN=TRIM25 PE=2 SV=1	2.200574235	0.444667	0.537347158
E1BTT8	L-lactate dehydrogenase OS=Gallus gallus OX=9031 GN=LDHA PE=3 SV=2	1.384471806	0.54751	0.498942852
A0A1D5PSR2	CTP synthase OS=Gallus gallus OX=9031 GN=CTPS1 PE=3 SV=1	1.456555396	0.526571	0.430226008
A0A1D5PXE5	Receptor protein-tyrosine kinase OS=Gallus gallus OX=9031 GN=EPHA2 PE=4 SV=3	1.48221746	0.512927	0.421106497
Q5ZIF6	U1-type domain-containing protein OS=Gallus gallus OX=9031 GN=ZMAT2 PE=2 SV=1	1.326893868	0.602692	0.405928771
A0A3Q2TTG8	GB1/RHD3-type G domain-containing protein OS=Gallus gallus OX=9031 GN=GBP1 PE=3 SV=1	1.72228369	0.433714	0.397137483
P27463	Aldehyde dehydrogenase 1A1 OS=Gallus gallus OX=9031 GN=ALDH1A1 PE=2 SV=1	1.502096749	0.53072	0.38588953
A0A3Q2U9Y8	Ankyrin_rpt-contain_dom domain-containing protein OS=Gallus gallus OX=9031 GN=KANK4 PE=4 SV=1	1.440348315	0.533931	0.382490635
F1NC46	U1-type domain-containing protein OS=Gallus gallus OX=9031 GN=SCAPER PE=4 SV=5	1.881453016	0.357	0.374895414
A0A1D5PE33	Uncharacterized protein OS=Gallus gallus OX=9031 GN=RAB1B PE=4 SV=2	1.517800878	0.527671	0.368424733

A0A3Q2U6B2	Uncharacterized protein OS=Gallus gallus OX=9031 GN=LOC416147 PE=4 SV=1	2.006870617	0.310345	0.364752134
F1NTA4	Uncharacterized protein OS=Gallus gallus OX=9031 GN=ABCB5 PE=4 SV=2	1.735885163	0.425083	0.349895795
Q5F4B6	RRM domain-containing protein OS=Gallus gallus OX=9031 GN=POLDIP3 PE=2 SV=1	1.362439025	0.559612	0.306022008
F1N891	Protein kinase domain-containing protein OS=Gallus gallus OX=9031 GN=PEAK1 PE=4 SV=2	2.173065556	0.326824	0.301463127
Q5ZM75	Seryl-tRNA synthetase OS=Gallus gallus OX=9031 GN=RCJMB04_2o24 PE=2 SV=1	2.147018538	0.350444	0.252373536
F1P2M3	IF3_N domain-containing protein OS=Gallus gallus OX=9031 GN=MTIF3 PE=3 SV=3	2.337239054	0.4248	0.235136191
A0A1D5P2N4	GTP-binding protein 1 OS=Gallus gallus OX=9031 GN=GTPBP1 PE=4 SV=1	1.582710474	0.515484	0.229272842
A0A1D5P275	Poly [ADP-ribose] polymerase OS=Gallus gallus OX=9031 GN=PARP14 PE=3 SV=1	1.848124387	0.366564	0.223765532
F1P593	Heat shock 27 kDa protein OS=Gallus gallus OX=9031 GN=HSPB1 PE=3 SV=2	1.798162757	0.407122	0.116283576
Q5ZLA7	Dolichyl-diphosphooligosaccharide--protein glycotransferase OS=Gallus gallus OX=9031 GN=STT3A PE=2 SV=1	1.453269977	0.519395	-0.112854958
F1P3X1	Uncharacterized protein OS=Gallus gallus OX=9031 GN=MYH1G PE=3 SV=4	2.028741948	0.308889	-0.122898738
E1BYH2	Protein kinase domain-containing protein OS=Gallus gallus OX=9031 GN=TAOK1 PE=4 SV=1	1.505102847	0.534486	-0.123299281
Q7SX63	Heat shock protein 70 OS=Gallus gallus OX=9031 GN=HSP70 PE=3 SV=1	1.418931555	0.535652	-0.133468946
Q90828	Cytoplasmic dynein 1 light intermediate chain 1 OS=Gallus gallus OX=9031 GN=DYNC1LI1 PE=1 SV=1	1.303561781	0.602549	-0.140693188
E1C3T2	Uncharacterized protein OS=Gallus gallus OX=9031 GN=NCOR2 PE=3 SV=5	1.438926385	0.527864	-0.142305374
F1NCX7	Serine/threonine-protein kinase PLK OS=Gallus gallus OX=9031 GN=PLK1 PE=3 SV=3	1.303703765	0.607929	-0.153402646
B6V3H8	Calcium-activated neutral proteinase 2 OS=Gallus gallus OX=9031 GN=CAPN2 PE=2 SV=1	1.527816052	0.524389	-0.156613032
E1BT66	Uncharacterized protein OS=Gallus gallus OX=9031 GN=TAF15 PE=3 SV=2	1.607931359	0.506441	-0.163022836
E1BSJ3	Uncharacterized protein OS=Gallus gallus OX=9031 GN=RBSN PE=4 SV=3	1.306849121	0.615127	-0.181317329
A0A1D5PNS1	HOOK_N domain-containing protein OS=Gallus gallus OX=9031 GN=CCDC88B PE=4 SV=1	1.585628784	0.523934	-0.181976
E1BSR5	PWI domain-containing protein OS=Gallus gallus OX=9031 PE=4 SV=3	1.380597906	0.54008	-0.193160693
A0A1D5PFM2	I-kappa-B kinase OS=Gallus gallus OX=9031 GN=CWF19L1 PE=4 SV=2	1.709037637	0.42944	-0.199818452
E1BYZ3	Uncharacterized protein OS=Gallus gallus OX=9031 GN=MICALL2 PE=4 SV=3	1.380613285	0.545535	-0.205684344
A0A3Q2UM43	Uncharacterized protein OS=Gallus gallus OX=9031 GN=AKAP13 PE=4 SV=1	1.772844053	0.424186	-0.207664967
A0A3Q2U5W6	SH3 domain-containing protein OS=Gallus gallus OX=9031 GN=LOC107050955 PE=4 SV=1	1.367252616	0.556235	-0.213275909
F1NCY5	E3 UFM1-protein ligase 1 OS=Gallus gallus OX=9031 GN=UFL1 PE=3 SV=1	1.314623774	0.608477	-0.217428366
A0A1D5PVC4	CCR4-NOT transcription complex subunit 9 OS=Gallus gallus OX=9031 GN=CNOT9 PE=3 SV=1	1.302906831	0.599158	-0.219943364
A0A1D5PYP1	CRAL-TRIO domain-containing protein OS=Gallus gallus OX=9031 GN=PRUNE2 PE=3 SV=2	1.610875883	0.515172	-0.223367373
Q5F4A2	Phosphatidylinositol-4,5-bisphosphate 3-kinase OS=Gallus gallus OX=9031 GN=PIK3CB PE=2 SV=1	1.354963981	0.563048	-0.225412051
A0A3Q2TXR3	Rho guanine nucleotide exchange factor 6 OS=Gallus gallus OX=9031 GN=ARHGEF6 PE=4 SV=1	1.535544353	0.538609	-0.232438723
F1N8K3	Arf-GAP domain-containing protein OS=Gallus gallus OX=9031 GN=ARFGAP1 PE=4 SV=2	1.455206129	0.520376	-0.243321419
A0A3Q2U9T1	SH3 domain-containing protein OS=Gallus gallus OX=9031 GN=PPP1R13B PE=4 SV=1	2.118903232	0.327048	-0.248488426
A0A1D5PPI2	Endoribonuclease Dicer OS=Gallus gallus OX=9031 GN=DICER1 PE=3 SV=2	1.484858914	0.533077	-0.250689824
Q5ZM53	ENTH domain-containing protein OS=Gallus gallus OX=9031 GN=RCJMB04_3c5 PE=2 SV=1	1.325118438	0.597111	-0.254659335
E1BX23	Uncharacterized protein OS=Gallus gallus OX=9031 GN=GLT8D1 PE=4 SV=2	1.852010491	0.367263	-0.257124901
A0A1D5PYW8	Transcription and mRNA export factor ENY2 OS=Gallus gallus OX=9031 GN=ENY2 PE=3 SV=1	1.494049358	0.532947	-0.261082331
E1BTW4	Phosphoinositide 5-phosphatase OS=Gallus gallus OX=9031 GN=SYNJ2 PE=3 SV=5	2.114316848	0.312182	-0.261144638
A0A1D5P5B6	Uncharacterized protein OS=Gallus gallus OX=9031 GN=KIF13B PE=3 SV=2	1.909601925	0.367625	-0.264330069
E1BUJ1	Splicing factor 45 OS=Gallus gallus OX=9031 GN=RBM17 PE=4 SV=4	1.57433848	0.513313	-0.266959031
A0A1D5PZQ9	Uncharacterized protein OS=Gallus gallus OX=9031 GN=GAS7 PE=4 SV=2	1.429780474	0.526857	-0.26891311
A0A1D5PZK5	Uncharacterized protein OS=Gallus gallus OX=9031 GN=ARHGAP12 PE=4 SV=2	1.532491321	0.531775	-0.270422777
A0A3Q3B0A5	IRF-2BP1_2 domain-containing protein OS=Gallus gallus OX=9031 GN=IRF2BP2 PE=4 SV=1	1.306210681	0.609586	-0.272993882
F1NYI3	RNA-splicing ligase RtcB homolog OS=Gallus gallus OX=9031 GN=RTCB PE=3 SV=2	1.483751761	0.529468	-0.274483681
A0A1D5PMR8	RRM domain-containing protein OS=Gallus gallus OX=9031 GN=CPSF7 PE=3 SV=2	1.430672027	0.531333	-0.276679834
A0A1D5PB68	Uncharacterized protein OS=Gallus gallus OX=9031 GN=RBMS2 PE=4 SV=2	1.890438092	0.364824	-0.277096113
F1N8G6	SMB domain-containing protein OS=Gallus gallus OX=9031 GN=TINAGL1 PE=3 SV=4	1.821631223	0.3872	-0.277404626

F1P1C3	SEC7 domain-containing protein OS=Gallus gallus OX=9031 GN=IQSEC1 PE=3 SV=4	1.894879474	0.372606	-0.28352054
A0A1D5PGI9	BUD13 homolog OS=Gallus gallus OX=9031 GN=BUD13 PE=3 SV=2	1.757383762	0.409826	-0.285601219
A0A1D5PGX3	Uncharacterized protein OS=Gallus gallus OX=9031 GN=ANK3 PE=4 SV=2	2.265201587	0.456364	-0.287687302
A0A3Q3A7W7	Uncharacterized protein OS=Gallus gallus OX=9031 GN=LOC107050990 PE=4 SV=1	1.606336972	0.498	-0.294510206
A0A3Q3AH06	DNA ligase (ATP) OS=Gallus gallus OX=9031 GN=LIG1 PE=3 SV=1	1.369972395	0.556198	-0.305034637
F1N9S3	Uncharacterized protein OS=Gallus gallus OX=9031 GN=FAM98A PE=3 SV=1	2.09807398	0.295333	-0.308108966
A0A3Q2U797	TFIIS N-terminal domain-containing protein OS=Gallus gallus OX=9031 GN=LOC100859302 PE=4 SV=1	1.389152591	0.543711	-0.30817318
Q5ZLC8	Serine/threonine-protein phosphatase 6 regulatory ankyrin repeat subunit C OS=Gallus gallus OX=9031 GN=ANKRD52 PE=2 SV=1	1.436922236	0.527011	-0.322557131
H9L0N7	CID domain-containing protein OS=Gallus gallus OX=9031 GN=RPRD2 PE=4 SV=4	2.632399114	0.559	-0.333123207
F1NPA4	Integrator complex subunit 7 OS=Gallus gallus OX=9031 GN=INTS7 PE=3 SV=4	1.478309248	0.510651	-0.339125792
Q9DE64	p95-APP2 OS=Gallus gallus OX=9031 GN=p95-APP2 PE=2 SV=1	2.021603835	0.305714	-0.359817187
E1C6R7	Uncharacterized protein OS=Gallus gallus OX=9031 GN=RAI14 PE=4 SV=3	1.935641446	0.351742	-0.359970729
F1NY56	Diacylglycerol kinase OS=Gallus gallus OX=9031 GN=DGKQ PE=3 SV=2	2.892190678	1	-0.3613801
E1BXF4	Uncharacterized protein OS=Gallus gallus OX=9031 GN=RCN1 PE=4 SV=3	1.882093028	0.3672	-0.369143804
O93419	Collagen XVIII OS=Gallus gallus OX=9031 PE=2 SV=2	2.696121974	1	-0.388115565
Q9DGN8	Actin-associated protein palladin (Fragment) OS=Gallus gallus OX=9031 PE=4 SV=1	2.032229962	0.32976	-0.412486871
A0A1D5PRA2	Coiled-coil domain-containing protein 128 OS=Gallus gallus OX=9031 GN=PPP1R21 PE=4 SV=1	1.769950807	0.407467	-0.41487662
F1NAP9	RRM domain-containing protein OS=Gallus gallus OX=9031 GN=RBPMS PE=4 SV=3	1.489241231	0.533974	-0.424363931
E1C123	Aha1_N domain-containing protein OS=Gallus gallus OX=9031 GN=AHSA1 PE=3 SV=1	2.60932562	0.4688	-0.431246201
A0A3Q2UG82	Uncharacterized protein OS=Gallus gallus OX=9031 GN=BCAR3 PE=4 SV=1	1.692326942	0.420963	-0.433695793
Q5F449	HTH La-type RNA-binding domain-containing protein OS=Gallus gallus OX=9031 GN=RCJMB04_3f2 PE=2 SV=1	1.746366839	0.415745	-0.46237278
A0A3Q2TYV2	Uncharacterized protein OS=Gallus gallus OX=9031 GN=SRGAP2 PE=4 SV=1	1.532632656	0.539371	-0.466037114
F1NNP2	Transforming growth factor beta OS=Gallus gallus OX=9031 GN=TGFB2 PE=3 SV=2	2.441218287	0.479429	-0.470909278
A0A1D5PJ02	C2H2-type domain-containing protein OS=Gallus gallus OX=9031 GN=ZNF609 PE=4 SV=2	1.705942013	0.42102	-0.50599432
E1BSS2	Ubiquitin specific peptidase 53 OS=Gallus gallus OX=9031 PE=4 SV=2	1.56165966	0.515821	-0.509503047
F1NRM5	Actin-related protein 2 OS=Gallus gallus OX=9031 GN=ACTR2 PE=3 SV=3	1.356467781	0.561731	-0.552205086
Q5F3U8	Aldolase_II domain-containing protein OS=Gallus gallus OX=9031 GN=RCJMB04_6m11 PE=2 SV=1	1.677933709	0.433309	-0.593217373
E1C4L8	Uncharacterized protein OS=Gallus gallus OX=9031 GN=ARHGEF28 PE=4 SV=3	1.389229444	0.549375	-0.612064997
A0A1D5PL17	Poly [ADP-ribose] polymerase OS=Gallus gallus OX=9031 GN=PARP4 PE=3 SV=1	1.482261974	0.519259	-0.622484287
Q9W770	Spondin-1 OS=Gallus gallus OX=9031 GN=SPON1 PE=2 SV=1	1.394698828	0.550232	-0.676825205
D6PZR1	PRNP OS=Gallus gallus OX=9031 PE=3 SV=1	1.567932074	0.51703	-0.692880392
Q9PWM9	Tyrosine-protein kinase OS=Gallus gallus OX=9031 GN=JAK1 PE=2 SV=1	1.482853972	0.5244	-0.732612769
Q98TQ8	Connective tissue growth factor OS=Gallus gallus OX=9031 GN=NOV PE=2 SV=1	2.138189359	0.349895	-0.747988701
E1C172	Eukaryotic elongation factor 2 kinase OS=Gallus gallus OX=9031 GN=EEF2K PE=3 SV=3	1.647531096	0.477	-0.764276505
F1NKH3	Calponin-homology (CH) domain-containing protein OS=Gallus gallus OX=9031 GN=HOOK3 PE=3 SV=4	1.408024234	0.546151	-0.885549784
A0A3Q3AKA0	Uncharacterized protein OS=Gallus gallus OX=9031 GN=LTBP1 PE=4 SV=1	2.183262838	0.39	-0.921954473
F1NGT3	92 kDa gelatinase OS=Gallus gallus OX=9031 GN=MMP9 PE=3 SV=3	1.629983943	0.487368	-1.042433739
A0A3Q2UBC9	Uncharacterized protein OS=Gallus gallus OX=9031 GN=LTBP2 PE=4 SV=1	2.112833521	0.304	-1.075757027
A0A1L1S0I3	Uncharacterized protein OS=Gallus gallus OX=9031 GN=CHGB PE=3 SV=2	1.344771094	0.573208	-1.469719887

8.4.2. Mass Spectrometry data for BeauR-T16A

Table 8.2. BeauR-T16A mass spectrometry dataset

Accession	Description	-Log Welch's T-test p-value T16A_Mock	Welch's T-test q-value T16A_Mock	log2 FC_T16A_Mock
nucleocapsid	nucleocapsid nucleocapsid	3.101114462	0.075555556	3.720647335
membrane	membrane membrane	3.008477876	0.067	3.314131101
O13255	2'-5' oligoadenylate synthase (Fragment) OS=Gallus gallus OX=9031 GN=OAS*A PE=2 SV=1	3.163560587	0.097142857	3.308157285
envelope	envelope envelope	1.911450267	0.254083333	2.734827201
5a	5a 5a	2.568983892	0.10688	2.384850025
A0A125RM76	Interferon-induced protein with tetratricopeptide repeats 5 OS=Gallus gallus OX=9031 GN=IFIT5 PE=2 SV=1	3.47445488	0.085	2.383724372
pp1ab	pp1ab pp1ab	2.876793268	0.073176471	2.297831694
spike	spike spike	3.163501936	0.085	2.203772386
F1NLJ6	Viperin OS=Gallus gallus OX=9031 GN=RSAD2 PE=2 SV=2	3.934640291	0	1.995915572
A0A3Q3AUC8	UvrD-like helicase ATP-binding domain-containing protein OS=Gallus gallus OX=9031 GN=TRANK1 PE=4 SV=1	1.97590337	0.221130435	1.872107029
Q75UT8	Double-stranded RNA-activated protein kinase OS=Gallus gallus OX=9031 GN=pkr PE=2 SV=1	3.301764268	0.136	1.557053248
Q6IEC5	Putative ISG12(2) protein OS=Gallus gallus OX=9031 GN=ISG12(2) PE=2 SV=1	1.60315875	0.374105263	1.469245672
A0A3Q3AR57	C3H1-type domain-containing protein OS=Gallus gallus OX=9031 GN=HELZ2 PE=4 SV=1	3.286514693	0.113333333	1.416068554
F1N9F3	Oxysterol-binding protein OS=Gallus gallus OX=9031 GN=OSBPL8 PE=3 SV=3	3.087482199	0.068	1.310903231
A0A2I4SJU8	RNA helicase OS=Gallus gallus OX=9031 GN=MDA5 PE=2 SV=1	1.742300409	0.290967742	1.289288441
A0A1L1RNY8	Histone H2A OS=Gallus gallus OX=9031 GN=H2AFX PE=3 SV=2	1.909014675	0.251102041	1.266355356
F1NW22	Uncharacterized protein OS=Gallus gallus OX=9031 GN=RRAD PE=3 SV=2	1.764838797	0.292813559	1.194163958
E1BXW9	Tudor domain-containing protein 3 OS=Gallus gallus OX=9031 GN=TDRD3 PE=4 SV=2	2.098905361	0.199675676	1.160797755
A0A3Q3AWY5	Tyrosine-protein phosphatase non-receptor type OS=Gallus gallus OX=9031 GN=PTPN1 PE=3 SV=1	2.252064266	0.171875	1.135232766
F1NG10	Uncharacterized protein OS=Gallus gallus OX=9031 GN=ACTR10 PE=3 SV=1	2.33494038	0.152857143	1.021475315
A0A1L1RXY9	116 kDa U5 small nuclear ribonucleoprotein component OS=Gallus gallus OX=9031 GN=EFTUD2 PE=3 SV=2	2.055459103	0.186285714	1.005096912
A0A1D5PUD5	Uncharacterized protein OS=Gallus gallus OX=9031 GN=NUP88 PE=4 SV=2	1.33823004	0.526096774	0.95950079
A0A3Q2TXL9	Uncharacterized protein OS=Gallus gallus OX=9031 GN=STIP1 PE=4 SV=1	1.638877928	0.352	0.947217782
A0A3Q2TTG8	GB1/RHD3-type G domain-containing protein OS=Gallus gallus OX=9031 GN=GBP1 PE=3 SV=1	2.892768096	0.0744	0.92343839
A0A3Q2U1Z7	Rhodanese domain-containing protein OS=Gallus gallus OX=9031 PE=4 SV=1	1.831250945	0.28	0.849497159
A0A0B5H7I8	Tripartite motif containing 25 OS=Gallus gallus OX=9031 GN=TRIM25 PE=2 SV=1	2.967159409	0.064	0.847978751
A0A3Q2U6B2	Uncharacterized protein OS=Gallus gallus OX=9031 GN=LOC416147 PE=4 SV=1	2.997774254	0.061846154	0.81942145
F1NHI3	RNA helicase OS=Gallus gallus OX=9031 GN=DHX15 PE=3 SV=3	1.751496521	0.291672131	0.753100554
Q5F3B3	Uncharacterized protein OS=Gallus gallus OX=9031 GN=RCJMB04_23i8 PE=2 SV=1	2.063481755	0.190829268	0.741000811
A0A1L1RNI5	GB1/RHD3-type G domain-containing protein OS=Gallus gallus OX=9031 GN=ATL1 PE=3 SV=2	1.75235739	0.296533333	0.730028152
R4GG61	LIM zinc-binding domain-containing protein OS=Gallus gallus OX=9031 GN=SCEL PE=4 SV=3	2.889834519	0.06975	0.694823424
A0A1L1RMP5	Uncharacterized protein OS=Gallus gallus OX=9031 GN=PARP9 PE=3 SV=2	1.952264877	0.228680851	0.656763554
E1BQC5	Poly [ADP-ribose] polymerase OS=Gallus gallus OX=9031 GN=PARP14 PE=3 SV=5	1.792445625	0.288350877	0.648150444
A0A1D5P275	Poly [ADP-ribose] polymerase OS=Gallus gallus OX=9031 GN=PARP14 PE=3 SV=1	2.300088073	0.166482759	0.630108833
Q5ZKD7	Putative helicase MOV-10 OS=Gallus gallus OX=9031 GN=MOV10 PE=2 SV=1	1.590285084	0.384051282	0.608604272
A0A1D5PY43	Uncharacterized protein OS=Gallus gallus OX=9031 GN=GKAP1 PE=3 SV=3	3.652979574	0.041333333	0.595343749
Q5ZJ59	Uncharacterized protein OS=Gallus gallus OX=9031 GN=RCJMB04_20j14 PE=2 SV=1	1.389836131	0.493928571	0.594530423
F1NC46	U1-type domain-containing protein OS=Gallus gallus OX=9031 GN=SCAPER PE=4 SV=5	2.280507722	0.168266667	0.588376363
Q5ZKZ9	Lipase maturation factor 2 OS=Gallus gallus OX=9031 GN=LMF2 PE=2 SV=2	1.409629906	0.485137615	0.578381538

Q5ZIF6	U1-type domain-containing protein OS=Gallus gallus OX=9031 GN=ZMAT2 PE=2 SV=1	2.255463763	0.173419355	0.554834366
A0A1D5PE33	Uncharacterized protein OS=Gallus gallus OX=9031 GN=RAB1B PE=4 SV=2	1.872141173	0.268	0.534443061
A0A1D5NYJ2	Lon protease homolog, mitochondrial OS=Gallus gallus OX=9031 GN=LONP1 PE=3 SV=1	1.565289736	0.385238095	0.517999013
A0A1D5PFX4	Ubiquitinyl hydrolase 1 OS=Gallus gallus OX=9031 GN=OTUD4 PE=4 SV=2	1.626597186	0.358465753	0.516142686
Q5F4B6	RRM domain-containing protein OS=Gallus gallus OX=9031 GN=POLDIP3 PE=2 SV=1	2.42227821	0.141846154	0.514969508
E1C0V8	Uncharacterized protein OS=Gallus gallus OX=9031 PE=4 SV=5	1.837104739	0.281153846	0.479849974
Q58I02	Nicotinamide phosphoribosyltransferase OS=Gallus gallus OX=9031 GN=PBEF1 PE=2 SV=1	1.377339344	0.51380531	0.449221452
E1BY04	Uncharacterized protein OS=Gallus gallus OX=9031 GN=CAMSAP2 PE=3 SV=3	1.552658641	0.394117647	0.446984291
A0A1L1RIY7	Pre-mRNA-splicing factor RBM22 OS=Gallus gallus OX=9031 GN=RBM22 PE=3 SV=2	1.315286976	0.554299213	0.442540805
A0A1D5PM39	Inorganic diphosphatase OS=Gallus gallus OX=9031 GN=PPA2 PE=3 SV=2	1.842755426	0.282117647	0.414942106
F1N891	Protein kinase domain-containing protein OS=Gallus gallus OX=9031 GN=PEAK1 PE=4 SV=2	2.639420467	0.090909091	0.413390001
Q5F3A5	AAA domain-containing protein OS=Gallus gallus OX=9031 GN=RCJMB04_24l18 PE=2 SV=1	1.509347021	0.3915	0.400064071
A0A1D5PFC0	E3 ubiquitin-protein ligase TRIP12 OS=Gallus gallus OX=9031 GN=TRIP12 PE=3 SV=1	1.70721996	0.310787879	0.392741362
P19336	CCN family member 1 OS=Gallus gallus OX=9031 GN=CCN1 PE=2 SV=1	2.207688596	0.180705882	0.387497902
F2Z4K6	KOW domain-containing protein OS=Gallus gallus OX=9031 GN=RPL26L1 PE=3 SV=1	1.454646707	0.450823529	0.362963359
A0A3Q2UAA1	J domain-containing protein OS=Gallus gallus OX=9031 GN=LOC107049075 PE=4 SV=1	1.58104886	0.38565	0.346392949
F1P2M3	IF3_N domain-containing protein OS=Gallus gallus OX=9031 GN=MTIF3 PE=3 SV=3	1.551126574	0.383136364	0.332950115
Q8UWG7	60S ribosomal protein L6 OS=Gallus gallus OX=9031 GN=RPL6 PE=2 SV=1	1.544604756	0.387910112	0.32350715
E1C0J4	Uncharacterized protein OS=Gallus gallus OX=9031 GN=UPF1 PE=3 SV=3	1.502260867	0.396082474	0.310668151
A0A1L1RVH4	PH domain-containing protein OS=Gallus gallus OX=9031 GN=NIPSNAP1 PE=3 SV=2	1.410295977	0.48962963	0.268024604
A4F5B2	TAP binding protein OS=Gallus gallus OX=9031 GN=TPN PE=2 SV=1	2.086034486	0.192205128	0.267955939
E1C2U4	DNA replication licensing factor MCM4 OS=Gallus gallus OX=9031 GN=MCM4 PE=3 SV=3	1.455386348	0.452990099	0.254930337
P53478	Actin, cytoplasmic type 5 OS=Gallus gallus OX=9031 PE=3 SV=1	1.787228234	0.285517241	0.250814279
A0A1D5NXR2	Endoplasmic reticulum transmembrane protein OS=Gallus gallus OX=9031 GN=BCAP31 PE=3 SV=1	1.413723905	0.489570093	0.244682789
A0A3Q2UET9	LsmAD domain-containing protein OS=Gallus gallus OX=9031 GN=ATXN2L PE=3 SV=1	1.607170864	0.377653333	0.242127577
Q98TF7	60S ribosomal protein L35 OS=Gallus gallus OX=9031 GN=RPL35 PE=2 SV=3	1.407191506	0.482378378	0.224908034
Q5F443	Uncharacterized protein OS=Gallus gallus OX=9031 GN=RCJMB04_3i14 PE=2 SV=1	1.677847888	0.325705882	0.182536761
F1NXH1	MOSC domain-containing protein OS=Gallus gallus OX=9031 GN=MARC1 PE=4 SV=2	1.599454736	0.376935065	0.175428867
A0A1D5NVY0	Uncharacterized protein OS=Gallus gallus OX=9031 GN=USMG5 PE=4 SV=1	1.530558133	0.391333333	0.136579355
D2Z1L9	LIM and SH3 domain protein 1 OS=Gallus gallus OX=9031 GN=LASP1 PE=2 SV=1	1.584098121	0.387746835	0.089808623
E1C453	Heterogeneous nuclear ribonucleoprotein K OS=Gallus gallus OX=9031 GN=HNRNPK PE=4 SV=3	NaN	1	0
E1BQU4	Vesicle-fusing ATPase OS=Gallus gallus OX=9031 GN=NSF PE=3 SV=2	1.445677068	0.455378641	-0.073258877
E1BYH2	Protein kinase domain-containing protein OS=Gallus gallus OX=9031 GN=TAOK1 PE=4 SV=1	1.58051775	0.380888889	-0.12820816
E1BW94	RRM domain-containing protein OS=Gallus gallus OX=9031 GN=SF3B6 PE=4 SV=2	1.374911915	0.505947826	-0.156696955
F1NY56	Diacylglycerol kinase OS=Gallus gallus OX=9031 GN=DGKQ PE=3 SV=2	1.344018183	0.523180328	-0.168522199
F1NQR2	Na(+)/H(+) exchange regulatory cofactor NHE-RF OS=Gallus gallus OX=9031 GN=SLC9A3R2 PE=4 SV=4	2.705806458	0.089	-0.169583797
A0A1D5NWU3	Active breakpoint cluster region-related protein OS=Gallus gallus OX=9031 GN=ABR PE=4 SV=3	1.360307412	0.530862069	-0.185777823
F1P3X1	Uncharacterized protein OS=Gallus gallus OX=9031 GN=MYH1G PE=3 SV=4	3.041688505	0.073090909	-0.19070673
Q90593	Endoplasmic reticulum chaperone BiP OS=Gallus gallus OX=9031 GN=HSPA5 PE=1 SV=1	1.529548573	0.378709677	-0.20209837
R4GH36	Uncharacterized protein OS=Gallus gallus OX=9031 GN=SNRPB2 PE=4 SV=1	1.348376652	0.526733333	-0.207492669
E1BWW2	Uncharacterized protein OS=Gallus gallus OX=9031 GN=TSG101 PE=3 SV=2	1.437213673	0.454438095	-0.208321889
A0A1D5PRJ2	HECT-type E3 ubiquitin transferase OS=Gallus gallus OX=9031 GN=NEDD4L PE=4 SV=2	2.818342997	0.076	-0.213844776
A0A1D5P3E5	NUC153 domain-containing protein OS=Gallus gallus OX=9031 GN=ESF1 PE=3 SV=1	1.30061311	0.561090909	-0.217584769

A0A1D5PFM2	I-kappa-B kinase OS=Gallus gallus OX=9031 GN=CWF19L1 PE=4 SV=2	2.097663784	0.194421053	-0.233711878
A0A1D5P8T2	Uncharacterized protein OS=Gallus gallus OX=9031 GN=SPAG9 PE=3 SV=2	1.618383632	0.362648649	-0.24288861
Q5F449	HTH La-type RNA-binding domain-containing protein OS=Gallus gallus OX=9031 GN=RCJMB04_3f2 PE=2 SV=1	1.35260907	0.529966102	-0.246694565
F1NAZ3	Kinesin-like protein OS=Gallus gallus OX=9031 GN=KIF2A PE=3 SV=2	1.441694796	0.453269231	-0.254247506
A0A3Q3A7W7	Uncharacterized protein OS=Gallus gallus OX=9031 GN=LOC107050990 PE=4 SV=1	1.376930631	0.509298246	-0.26070563
Q5ZJ00	55 kDa erythrocyte membrane protein OS=Gallus gallus OX=9031 GN=MPP1 PE=2 SV=1	1.530178599	0.387032967	-0.265137355
A0A3Q3AEI2	Capsid protein p27, alternate cleaved 1 OS=Gallus gallus OX=9031 GN=LOC107053122 PE=4 SV=1	1.312427248	0.549085271	-0.265622854
R4GHM9	Uncharacterized protein OS=Gallus gallus OX=9031 GN=NDUFAF2 PE=3 SV=1	1.309973194	0.550953846	-0.273884614
Q5ZI99	Actin-related protein 2/3 complex subunit OS=Gallus gallus OX=9031 GN=ARPC1B PE=2 SV=1	1.658564253	0.33884058	-0.292101701
E1C6R7	Uncharacterized protein OS=Gallus gallus OX=9031 GN=RAI14 PE=4 SV=3	1.417114394	0.486150943	-0.293090661
F1ND55	Aldolase_II domain-containing protein OS=Gallus gallus OX=9031 GN=ADD1 PE=3 SV=2	2.180729961	0.187314286	-0.308720271
E1C8M6	Uncharacterized protein OS=Gallus gallus OX=9031 GN=PIK3R3 PE=3 SV=3	2.631248055	0.086956522	-0.309350967
A0A3Q3AN84	Mothers against decapentaplegic homolog OS=Gallus gallus OX=9031 GN=SMAD2Z PE=3 SV=1	1.528670555	0.374680851	-0.310547829
A0A1D5PYW8	Transcription and mRNA export factor ENY2 OS=Gallus gallus OX=9031 GN=ENY2 PE=3 SV=1	1.551270534	0.38754023	-0.323536555
A0A1D5P4K8	Uncharacterized protein OS=Gallus gallus OX=9031 GN=SASH1 PE=4 SV=1	1.628846466	0.361944444	-0.32925415
Q5ZMU5	HECT-type E3 ubiquitin transferase OS=Gallus gallus OX=9031 GN=RCJMB04_1c11 PE=2 SV=1	1.806370842	0.284290909	-0.33709844
Q8UWG6	Mitogen-activated protein kinase OS=Gallus gallus OX=9031 PE=2 SV=1	1.56775423	0.387421687	-0.343477249
O93419	Collagen XVIII OS=Gallus gallus OX=9031 PE=2 SV=2	2.570711884	0.111333333	-0.357241154
A0A1D5PZF2	Vacuolar protein sorting-associated protein 41 homolog OS=Gallus gallus OX=9031 GN=VPS41 PE=3 SV=1	1.641340518	0.357028571	-0.361706893
Q9I9B8	Non-Canonical UBiquitin Conjugating Enzyme 1 (NCUBE1) OS=Gallus gallus OX=9031 GN=ncube1 PE=2 SV=1	1.313205142	0.55253125	-0.365344206
A0A3Q2U6D5	NifU_N domain-containing protein OS=Gallus gallus OX=9031 GN=ISCU PE=3 SV=1	1.408181106	0.484654545	-0.377173583
A0A1D5PZ86	RING finger protein 10 OS=Gallus gallus OX=9031 GN=RNF10 PE=3 SV=2	2.21146446	0.186181818	-0.38327376
A0A3Q2UG82	Uncharacterized protein OS=Gallus gallus OX=9031 GN=BCAR3 PE=4 SV=1	1.55237487	0.390604651	-0.389331023
R4GLV4	FHA domain-containing protein OS=Gallus gallus OX=9031 GN=MKI67 PE=4 SV=4	1.712053416	0.307446154	-0.392483393
E1BX23	Uncharacterized protein OS=Gallus gallus OX=9031 GN=GLT8D1 PE=4 SV=2	1.325469155	0.543136	-0.406663736
A0A1D5PPI2	Endoribonuclease Dicer OS=Gallus gallus OX=9031 GN=DICER1 PE=3 SV=2	1.358550562	0.527247863	-0.413227876
A0A1D5PRA2	Coiled-coil domain-containing protein 128 OS=Gallus gallus OX=9031 GN=PPP1R21 PE=4 SV=1	1.799735306	0.287642857	-0.417585373
Q9DE64	p95-APP2 OS=Gallus gallus OX=9031 GN=p95-APP2 PE=2 SV=1	1.720063116	0.3035	-0.420061111
F1NAP9	RRM domain-containing protein OS=Gallus gallus OX=9031 GN=RBPMS PE=4 SV=3	1.739494066	0.291809524	-0.442050298
A0A1D5P1L0	SH3 domain-containing protein OS=Gallus gallus OX=9031 GN=BCAR1 PE=3 SV=2	2.37632717	0.145777778	-0.443976879
F1N8G6	SMB domain-containing protein OS=Gallus gallus OX=9031 GN=TINAGL1 PE=3 SV=4	1.527877457	0.370736842	-0.468199571
A0A1L1RPU6	Uncharacterized protein OS=Gallus gallus OX=9031 GN=TMEM53 PE=3 SV=2	1.703520661	0.30961194	-0.493448416
E1BTP9	DUF3504 domain-containing protein OS=Gallus gallus OX=9031 GN=QRICH1 PE=4 SV=3	1.457617865	0.45428	-0.498112996
F1NNP2	Transforming growth factor beta OS=Gallus gallus OX=9031 GN=TGFB2 PE=3 SV=2	1.829813804	0.274814815	-0.5031449
E1C7S5	Uncharacterized protein OS=Gallus gallus OX=9031 GN=PLEKHG1 PE=4 SV=4	1.529938361	0.382826087	-0.508063873
E1C4L8	Uncharacterized protein OS=Gallus gallus OX=9031 GN=ARHGEF28 PE=4 SV=3	2.014030051	0.212727273	-0.537553151
Q9W6V0	Hyperion protein, 419 kD isoform OS=Gallus gallus OX=9031 GN=hyperion PE=2 SV=1	1.351994164	0.526554622	-0.542941332
F1NKH3	Calponin-homology (CH) domain-containing protein OS=Gallus gallus OX=9031 GN=HOOK3 PE=3 SV=4	1.977333961	0.223911111	-0.584522565
E1C172	Eukaryotic elongation factor 2 kinase OS=Gallus gallus OX=9031 GN=EEF2K PE=3 SV=3	1.345768096	0.525454545	-0.59475557
A0A3Q2U0I8	Uncharacterized protein OS=Gallus gallus OX=9031 GN=RBMS3 PE=4 SV=1	2.175646662	0.182111111	-0.599504471
Q98TQ8	Connective tissue growth factor OS=Gallus gallus OX=9031 GN=NOV PE=2 SV=1	2.641561767	0.095238095	-0.63257122
A0A0A0MQ32	Lysyl oxidase homolog OS=Gallus gallus OX=9031 GN=LOXL2 PE=3 SV=1	1.308692496	0.54821374	-0.636476676
A0A3Q2U1W2	Uncharacterized protein OS=Gallus gallus OX=9031 PE=4 SV=1	1.338530894	0.530373984	-0.636590878
Q5ZIP6	Deubiquitinase OTUD6B OS=Gallus gallus OX=9031 GN=OTUD6B PE=2 SV=1	1.320474403	0.54831746	-0.642895063

E1C947	Golgin subfamily A member 5 OS=Gallus gallus OX=9031 GN=GOLGA5 PE=4 SV=3	1.463168947	0.448606061	-0.748106559
Q9PWM9	Tyrosine-protein kinase OS=Gallus gallus OX=9031 GN=JAK1 PE=2 SV=1	2.07470897	0.1905	-0.779001554
F1NGT3	92 kDa gelatinase OS=Gallus gallus OX=9031 GN=MMP9 PE=3 SV=3	3.827510534	0.062	-0.886952877
A0A3Q3AKA0	Uncharacterized protein OS=Gallus gallus OX=9031 GN=LTBP1 PE=4 SV=1	2.730760113	0.088631579	-0.890786966
Q9W770	Spondin-1 OS=Gallus gallus OX=9031 GN=SPON1 PE=2 SV=1	1.572582718	0.386682927	-0.973212242
A0A3Q2UBC9	Uncharacterized protein OS=Gallus gallus OX=9031 GN=LTBP2 PE=4 SV=1	2.029737369	0.195348837	-0.979249795
A0A1L1S0I3	Uncharacterized protein OS=Gallus gallus OX=9031 GN=CHGB PE=3 SV=2	1.469819753	0.443183673	-1.373869419

8.4.3. Mass Spectrometry data for BeauR-A26F

Table 8.3. BeauR-A26F mass spectrometry dataset

Accession	Description	Log T-test p-value A26F_Mock	Welch's T-test q-value A26F_Mock	log2 FC_A26F_Mock
nucleocapsid	nucleocapsid nucleocapsid	2.274569712	0.4664	3.686522961
membrane	membrane membrane	2.457706805	0.448	3.137411435
O13255	2'-5' oligoadenylate synthase (Fragment) OS=Gallus gallus OX=9031 GN=OAS*A PE=2 SV=1	1.965290035	0.486363636	2.966278712
5a	5a 5a	2.353186556	0.429777778	2.897422155
envelope	envelope envelope	2.584440132	0.3832	2.433044593
pp1ab	pp1ab pp1ab	2.9370527	0.116	2.243480206
spike	spike spike	2.189628067	0.421428571	2.035666704
A0A125RM76	Interferon-induced protein with tetratricopeptide repeats 5 OS=Gallus gallus OX=9031 GN=IFIT5 PE=2 SV=1	3.359566394	0.216	1.926018556
A0A3Q3AUC8	UvrD-like helicase ATP-binding domain-containing protein OS=Gallus gallus OX=9031 GN=TRANK1 PE=4 SV=1	1.505190334	0.698714286	1.589276473
F1NLJ6	Viperin OS=Gallus gallus OX=9031 GN=RSAD2 PE=2 SV=2	2.186615233	0.393333333	1.565274874
A0A3Q3AR57	C3H1-type domain-containing protein OS=Gallus gallus OX=9031 GN=HELZ2 PE=4 SV=1	1.775217839	0.599354839	1.037437439
Q75UT8	Double-stranded RNA-activated protein kinase OS=Gallus gallus OX=9031 GN=pkr PE=2 SV=1	1.84983351	0.514068966	0.936810493
A0A0B5H7I8	Tripartite motif containing 25 OS=Gallus gallus OX=9031 GN=TRIM25 PE=2 SV=1	2.972221289	0.154666667	0.684399128
E1BTT8	L-lactate dehydrogenase OS=Gallus gallus OX=9031 GN=LDHA PE=3 SV=2	1.563593313	0.637803922	0.671858788
A0A1L1RY04	ATP synthase subunit beta OS=Gallus gallus OX=9031 GN=ATP5B PE=3 SV=2	1.663782064	0.6257	0.597863992
A0A3Q2U6B2	Uncharacterized protein OS=Gallus gallus OX=9031 GN=LOC416147 PE=4 SV=1	1.725268531	0.578888889	0.59316047
P19336	CCN family member 1 OS=Gallus gallus OX=9031 GN=CCN1 PE=2 SV=1	1.513232369	0.686254545	0.543795745
Q5F3B3	Uncharacterized protein OS=Gallus gallus OX=9031 GN=RCJMB04_23i8 PE=2 SV=1	1.302041508	0.885204819	0.522220612
E1C832	SMC hinge domain-containing protein OS=Gallus gallus OX=9031 GN=SMCHD1 PE=4 SV=3	1.341612313	0.825282051	0.49669377
A0A1L1RNI5	GB1/RHD3-type G domain-containing protein OS=Gallus gallus OX=9031 GN=ATL1 PE=3 SV=2	1.365815824	0.815837838	0.453949928
A0A1D5PXI1	Multifunctional fusion protein OS=Gallus gallus OX=9031 GN=ALDH4A1 PE=3 SV=1	1.738558101	0.593176471	0.435593128
A0A3Q2TTG8	GB1/RHD3-type G domain-containing protein OS=Gallus gallus OX=9031 GN=GBP1 PE=3 SV=1	1.345362151	0.825506494	0.394691626
P53478	Actin, cytoplasmic type 5 OS=Gallus gallus OX=9031 PE=3 SV=1	2.07988013	0.426526316	0.360679468
A0A1D5PM39	Inorganic diphosphatase OS=Gallus gallus OX=9031 GN=PPA2 PE=3 SV=2	1.562761387	0.625538462	0.337971846
F1NVJ2	PKS_ER domain-containing protein OS=Gallus gallus OX=9031 GN=LOC424430 PE=4 SV=4	1.938427077	0.49	0.337301731
A0A1D5P407	Uncharacterized protein OS=Gallus gallus OX=9031 GN=SRSF5A PE=3 SV=1	1.37980071	0.805388889	0.295624097
A0A1D6UPU6	Dolichyl-diphosphooligosaccharide--protein glycosyltransferase subunit 2 OS=Gallus gallus OX=9031 GN=RPN2 PE=3 SV=2	1.491630098	0.703793103	0.279592991
A0A3Q2U7V0	Uncharacterized protein OS=Gallus gallus OX=9031 GN=DHRS7 PE=3 SV=1	1.376544759	0.797369863	0.265697638
A0A1D5P275	Poly [ADP-ribose] polymerase OS=Gallus gallus OX=9031 GN=PARP14 PE=3 SV=1	3.000031085	0.232	0.265464942

Q90WR6	Sulfotransferase OS=Gallus gallus OX=9031 GN=SULT1C PE=2 SV=1	2.359376124	0.468	0.264865239
A0A1D5PBY1	Uncharacterized protein OS=Gallus gallus OX=9031 GN=ACSM4 PE=3 SV=1	1.642467415	0.601818182	0.254763285
Q5ZLA7	Dolichyl-diphosphooligosaccharide--protein glycotransferase OS=Gallus gallus OX=9031 GN=STT3A PE=2 SV=1	1.600782842	0.626638298	0.243881385
D0VX32	Complex III subunit 8 OS=Gallus gallus OX=9031 PE=1 SV=1	1.663181828	0.613073171	0.235644817
R4GLG2	Uncharacterized protein OS=Gallus gallus OX=9031 GN=SLC25A20 PE=3 SV=1	1.735407755	0.5888	0.235309442
F1P5U3	Arylamine N-acetyltransferase OS=Gallus gallus OX=9031 GN=PNAT10 PE=3 SV=1	2.240873677	0.464727273	0.234320958
A0A1D5NVY0	Uncharacterized protein OS=Gallus gallus OX=9031 GN=USMG5 PE=4 SV=1	1.922456702	0.478615385	0.231336912
E1C0F1	Dolichyl-diphosphooligosaccharide--protein glycosyltransferase subunit 1 OS=Gallus gallus OX=9031 GN=RPN1 PE=3 SV=3	1.404656761	0.786898551	0.168583393
F1N9I5	ELAV-like protein OS=Gallus gallus OX=9031 GN=ELAVL1 PE=3 SV=1	1.420446269	0.750058824	0.153344313
F1NBN1	Plug_translocon domain-containing protein OS=Gallus gallus OX=9031 GN=SEC61A1 PE=3 SV=2	1.320473466	0.8625	0.152172565
A0A1D5PIF0	Succinate dehydrogenase [ubiquinone] iron-sulfur subunit, mitochondrial OS=Gallus gallus OX=9031 GN=SDHB PE=3 SV=1	1.478070855	0.716610169	0.13102897
E1BX02	26S proteasome non-ATPase regulatory subunit 2 OS=Gallus gallus OX=9031 GN=PSMD2 PE=3 SV=2	1.468015755	0.730032787	0.119236151
A0A1D5P2W2	Uncharacterized protein OS=Gallus gallus OX=9031 GN=ESYT2 PE=3 SV=1	1.500548146	0.690035088	0.109645367
E1BYQ6	Nucleoprotein TPR OS=Gallus gallus OX=9031 GN=TPR PE=3 SV=3	1.605489433	0.637913043	-0.07934618
E1BYN9	Pribosyltran_N domain-containing protein OS=Gallus gallus OX=9031 GN=PRPSAP1 PE=3 SV=1	1.462643286	0.727096774	-0.086934884
A0A1D5PGX3	Uncharacterized protein OS=Gallus gallus OX=9031 GN=ANK3 PE=4 SV=2	1.321739228	0.873417722	-0.14233319
F1NHI3	RNA helicase OS=Gallus gallus OX=9031 GN=DHX15 PE=3 SV=3	1.438602033	0.736307692	-0.151311874
F1NLL5	AHD domain-containing protein OS=Gallus gallus OX=9031 GN=MLLT1 PE=4 SV=3	1.350760793	0.832746667	-0.160081704
E1BT38	Uncharacterized protein OS=Gallus gallus OX=9031 GN=DLG1 PE=3 SV=2	1.310260388	0.880148148	-0.166838169
A0A1D5P467	Uncharacterized protein OS=Gallus gallus OX=9031 GN=ITSN1 PE=4 SV=2	1.399485471	0.782628571	-0.172544003
F1NCB0	DNA-directed RNA polymerase subunit beta OS=Gallus gallus OX=9031 GN=POLR2B PE=3 SV=1	1.385564116	0.807492958	-0.226500034
F1P4F1	Uncharacterized protein OS=Gallus gallus OX=9031 GN=SH3BP4 PE=4 SV=3	1.798699213	0.578533333	-0.228429794
A0A1D5PV58	Arf-GAP domain-containing protein OS=Gallus gallus OX=9031 GN=ARFGAP3 PE=4 SV=2	1.713605134	0.574810811	-0.246395588
F1N8G6	SMB domain-containing protein OS=Gallus gallus OX=9031 GN=TINAGL1 PE=3 SV=4	1.676261421	0.628421053	-0.249062538
F1ND55	Aldolase_II domain-containing protein OS=Gallus gallus OX=9031 GN=ADD1 PE=3 SV=2	2.19578876	0.453846154	-0.257481734
A0A1D5PJ02	C2H2-type domain-containing protein OS=Gallus gallus OX=9031 GN=ZNF609 PE=4 SV=2	1.538725362	0.650962963	-0.273762544
Q9DE64	p95-APP2 OS=Gallus gallus OX=9031 GN=p95-APP2 PE=2 SV=1	1.554653205	0.626264151	-0.27824529
Q5ZJH3	RING-type E3 ubiquitin transferase OS=Gallus gallus OX=9031 GN=RCJMB04_18c10 PE=2 SV=1	2.11430861	0.425777778	-0.298120181
E1C8M6	Uncharacterized protein OS=Gallus gallus OX=9031 GN=PIK3R3 PE=3 SV=3	2.008353142	0.4928	-0.301641464
A0A3Q2U211	Uncharacterized protein OS=Gallus gallus OX=9031 GN=TNFRSF11B PE=4 SV=1	1.667854821	0.636205128	-0.311912855
A0A1D5PZQ9	Uncharacterized protein OS=Gallus gallus OX=9031 GN=GAS7 PE=4 SV=2	1.649294528	0.617047619	-0.319233259
A0A1D5PGI9	BUD13 homolog OS=Gallus gallus OX=9031 GN=BUD13 PE=3 SV=2	1.56780156	0.64304	-0.320312897
A0A3Q2UM43	Uncharacterized protein OS=Gallus gallus OX=9031 GN=AKAP13 PE=4 SV=1	2.551040253	0.319333333	-0.335731506
A0A1D5P1L0	SH3 domain-containing protein OS=Gallus gallus OX=9031 GN=BCAR1 PE=3 SV=2	1.477839865	0.704666667	-0.348863443
A0A3Q2U1Z7	Rhodanese domain-containing protein OS=Gallus gallus OX=9031 PE=4 SV=1	1.423559647	0.75641791	-0.35188961
F1NMK5	Fmp27_GFWDK domain-containing protein OS=Gallus gallus OX=9031 GN=KIAA0100 PE=4 SV=3	1.884593013	0.519407407	-0.379410267
A0A1D5PRA2	Coiled-coil domain-containing protein 128 OS=Gallus gallus OX=9031 GN=PPP1R21 PE=4 SV=1	1.92284375	0.49776	-0.383018653
F1P356	Protein kinase domain-containing protein OS=Gallus gallus OX=9031 GN=NUAK1 PE=4 SV=2	1.938844957	0.511304348	-0.406327724
A0A1D5PPI2	Endoribonuclease Dicer OS=Gallus gallus OX=9031 GN=DICER1 PE=3 SV=2	1.96561152	0.50952381	-0.42503341
A0A1D5PAT5	Uncharacterized protein OS=Gallus gallus OX=9031 GN=SMARCC1 PE=4 SV=2	1.878615144	0.504142857	-0.427459319
A0A3Q2U1W2	Uncharacterized protein OS=Gallus gallus OX=9031 PE=4 SV=1	2.174990061	0.39775	-0.454154968
A0A1D5PUM9	FAM83 domain-containing protein OS=Gallus gallus OX=9031 GN=FAM83H PE=3 SV=3	1.754830229	0.611875	-0.473562082
P33145	B-cadherin (Fragment) OS=Gallus gallus OX=9031 GN=K-CAM PE=2 SV=1	1.302294019	0.893170732	-0.480429967
A0A3Q3AMA4	Uncharacterized protein OS=Gallus gallus OX=9031 GN=PPFIBP1 PE=3 SV=1	1.750119143	0.593333333	-0.498063564
E1C172	Eukaryotic elongation factor 2 kinase OS=Gallus gallus OX=9031 GN=EEF2K PE=3 SV=3	2.221970371	0.463333333	-0.513819933
A0A3Q2TYV2	Uncharacterized protein OS=Gallus gallus OX=9031 GN=SRGAP2 PE=4 SV=1	1.612843319	0.6424	-0.518563906

A0A1D5P4K8	Uncharacterized protein OS=Gallus gallus OX=9031 GN=SASH1 PE=4 SV=1	1.581102773	0.6395	-0.527484894
O93419	Collagen XVIII OS=Gallus gallus OX=9031 PE=2 SV=2	1.454127912	0.727619048	-0.574007829
Q9W770	Spondin-1 OS=Gallus gallus OX=9031 GN=SPON1 PE=2 SV=1	1.430395805	0.749636364	-0.880779584
Q9PWM9	Tyrosine-protein kinase OS=Gallus gallus OX=9031 GN=JAK1 PE=2 SV=1	1.446114849	0.7269375	-0.916995684
F1NGT3	92 kDa gelatinase OS=Gallus gallus OX=9031 GN=MMP9 PE=3 SV=3	2.136355863	0.420235294	-1.00635004
A0A3Q3AKA0	Uncharacterized protein OS=Gallus gallus OX=9031 GN=LTBP1 PE=4 SV=1	1.350072843	0.824842105	-1.011052926
A0A3Q2UBC9	Uncharacterized protein OS=Gallus gallus OX=9031 GN=LTBP2 PE=4 SV=1	1.577650105	0.630857143	-1.093609174
A0A1L1S0I3	Uncharacterized protein OS=Gallus gallus OX=9031 GN=CHGB PE=3 SV=2	1.643704117	0.60744186	-1.550846418

8.5. Statistical Analysis

8.5.1. Chapter 3

Table 8.4. Figure 2A, **BeauR-T16A Single-Step Replication Kinetics CK cells**

Tukey's multiple comparisons test	Summary	Adjusted P Value
1		
Beau-R vs. BeauR-T16A-1	ns	0.3291
Beau-R vs. BeauR-T16A-2	ns	0.3481
Beau-R vs. BeauR T16A 4.7	ns	0.3385
Beau-R vs. BeauR-T16A-3	ns	0.4654
BeauR-T16A-1 vs. BeauR-T16A-2	ns	0.9991
BeauR-T16A-1 vs. BeauR T16A 4.7	ns	>0.9999
BeauR-T16A-1 vs. BeauR-T16A-3	ns	0.9221
BeauR-T16A-2 vs. BeauR T16A 4.7	ns	>0.9999
BeauR-T16A-2 vs. BeauR-T16A-3	ns	0.9653
BeauR T16A 4.7 vs. BeauR-T16A-3	ns	0.9432
2		
Beau-R vs. BeauR-T16A-1	*	0.0266
Beau-R vs. BeauR-T16A-2	*	0.0366
Beau-R vs. BeauR T16A 4.7	ns	0.0702
Beau-R vs. BeauR-T16A-3	*	0.0214
BeauR-T16A-1 vs. BeauR-T16A-2	ns	0.9998
BeauR-T16A-1 vs. BeauR T16A 4.7	ns	0.9998
BeauR-T16A-1 vs. BeauR-T16A-3	ns	0.9998
BeauR-T16A-2 vs. BeauR T16A 4.7	ns	0.9974
BeauR-T16A-2 vs. BeauR-T16A-3	ns	>0.9999
BeauR T16A 4.7 vs. BeauR-T16A-3	ns	0.9974
4		
Beau-R vs. BeauR-T16A-1	ns	0.1616
Beau-R vs. BeauR-T16A-2	ns	0.4847
Beau-R vs. BeauR T16A 4.7	ns	0.1388
Beau-R vs. BeauR-T16A-3	*	0.0176
BeauR-T16A-1 vs. BeauR-T16A-2	ns	0.9990
BeauR-T16A-1 vs. BeauR T16A 4.7	ns	0.8778
BeauR-T16A-1 vs. BeauR-T16A-3	ns	0.9211
BeauR-T16A-2 vs. BeauR T16A 4.7	ns	0.8718
BeauR-T16A-2 vs. BeauR-T16A-3	ns	0.9223
BeauR T16A 4.7 vs. BeauR-T16A-3	ns	0.9859
6		
Beau-R vs. BeauR-T16A-1	ns	0.3611
Beau-R vs. BeauR-T16A-2	ns	0.0625
Beau-R vs. BeauR T16A 4.7	ns	0.1774
Beau-R vs. BeauR-T16A-3	ns	0.0605
BeauR-T16A-1 vs. BeauR-T16A-2	ns	0.9947
BeauR-T16A-1 vs. BeauR T16A 4.7	ns	0.9793
BeauR-T16A-1 vs. BeauR-T16A-3	ns	0.9967
BeauR-T16A-2 vs. BeauR T16A 4.7	ns	0.9964
BeauR-T16A-2 vs. BeauR-T16A-3	ns	>0.9999

BeauR T16A 4.7 vs. BeauR-T16A-3	ns	0.9927
8		
Beau-R vs. BeauR-T16A-1	ns	0.9980
Beau-R vs. BeauR-T16A-2	ns	0.8139
Beau-R vs. BeauR T16A 4.7	ns	0.9991
Beau-R vs. BeauR-T16A-3	ns	0.9383
BeauR-T16A-1 vs. BeauR-T16A-2	ns	0.9094
BeauR-T16A-1 vs. BeauR T16A 4.7	ns	>0.9999
BeauR-T16A-1 vs. BeauR-T16A-3	ns	0.9913
BeauR-T16A-2 vs. BeauR T16A 4.7	ns	0.7956
BeauR-T16A-2 vs. BeauR-T16A-3	ns	0.9680
BeauR T16A 4.7 vs. BeauR-T16A-3	ns	0.9359
10		
Beau-R vs. BeauR-T16A-1	ns	>0.9999
Beau-R vs. BeauR-T16A-2	ns	0.9390
Beau-R vs. BeauR T16A 4.7	ns	0.9964
Beau-R vs. BeauR-T16A-3	ns	0.9994
BeauR-T16A-1 vs. BeauR-T16A-2	ns	0.9800
BeauR-T16A-1 vs. BeauR T16A 4.7	ns	0.9989
BeauR-T16A-1 vs. BeauR-T16A-3	ns	0.9993
BeauR-T16A-2 vs. BeauR T16A 4.7	ns	0.9996
BeauR-T16A-2 vs. BeauR-T16A-3	ns	0.9364
BeauR T16A 4.7 vs. BeauR-T16A-3	ns	0.9903
11		
Beau-R vs. BeauR-T16A-1	ns	0.9989
Beau-R vs. BeauR-T16A-2	ns	>0.9999
Beau-R vs. BeauR T16A 4.7	ns	0.9983
Beau-R vs. BeauR-T16A-3	ns	0.7668
BeauR-T16A-1 vs. BeauR-T16A-2	ns	>0.9999
BeauR-T16A-1 vs. BeauR T16A 4.7	ns	>0.9999
BeauR-T16A-1 vs. BeauR-T16A-3	ns	0.5715
BeauR-T16A-2 vs. BeauR T16A 4.7	ns	0.9998
BeauR-T16A-2 vs. BeauR-T16A-3	ns	0.7392
BeauR T16A 4.7 vs. BeauR-T16A-3	ns	0.7140

Table 8.5: Figure 2B, BeauR-T16A Multi-Step Replication Kinetics CK cells

Tukey's multiple comparisons test	Summary	Adjusted P Value
1		
BeauR vs. BeauR T16A 3.4	*	0.0185
BeauR vs. BeauR T16A 3.6	*	0.0122
BeauR vs. BeauR T16A 4.7	**	0.0095
BeauR vs. BeauR T16A 4.9	**	0.0089
BeauR T16A 3.4 vs. BeauR T16A 3.6	ns	0.4153
BeauR T16A 3.4 vs. BeauR T16A 4.7	ns	0.5947
BeauR T16A 3.4 vs. BeauR T16A 4.9	ns	0.2313
BeauR T16A 3.6 vs. BeauR T16A 4.7	ns	0.9572
BeauR T16A 3.6 vs. BeauR T16A 4.9	ns	0.8651
BeauR T16A 4.7 vs. BeauR T16A 4.9	ns	0.5045
24		

BeauR vs. BeauR T16A 3.4	ns	0.4684
BeauR vs. BeauR T16A 3.6	ns	0.6224
BeauR vs. BeauR T16A 4.7	ns	0.7106
BeauR vs. BeauR T16A 4.9	ns	0.2566
BeauR T16A 3.4 vs. BeauR T16A 3.6	ns	0.5309
BeauR T16A 3.4 vs. BeauR T16A 4.7	ns	0.9225
BeauR T16A 3.4 vs. BeauR T16A 4.9	ns	0.4267
BeauR T16A 3.6 vs. BeauR T16A 4.7	ns	>0.9999
BeauR T16A 3.6 vs. BeauR T16A 4.9	ns	0.2035
BeauR T16A 4.7 vs. BeauR T16A 4.9	ns	0.4227
48		
BeauR vs. BeauR T16A 3.4	ns	0.2082
BeauR vs. BeauR T16A 3.6	ns	0.1578
BeauR vs. BeauR T16A 4.7	ns	0.1895
BeauR vs. BeauR T16A 4.9	*	0.0175
BeauR T16A 3.4 vs. BeauR T16A 3.6	ns	0.7914
BeauR T16A 3.4 vs. BeauR T16A 4.7	ns	0.9675
BeauR T16A 3.4 vs. BeauR T16A 4.9	ns	0.3339
BeauR T16A 3.6 vs. BeauR T16A 4.7	ns	0.9715
BeauR T16A 3.6 vs. BeauR T16A 4.9	***	0.0007
BeauR T16A 4.7 vs. BeauR T16A 4.9	ns	0.1149
72		
BeauR vs. BeauR T16A 3.4	ns	0.4499
BeauR vs. BeauR T16A 3.6	ns	0.6166
BeauR vs. BeauR T16A 4.7	ns	0.7193
BeauR vs. BeauR T16A 4.9	*	0.0316
BeauR T16A 3.4 vs. BeauR T16A 3.6	ns	0.9507
BeauR T16A 3.4 vs. BeauR T16A 4.7	ns	0.9608
BeauR T16A 3.4 vs. BeauR T16A 4.9	ns	0.1719
BeauR T16A 3.6 vs. BeauR T16A 4.7	ns	>0.9999
BeauR T16A 3.6 vs. BeauR T16A 4.9	ns	0.0697
BeauR T16A 4.7 vs. BeauR T16A 4.9	ns	0.0874
96		
BeauR vs. BeauR T16A 3.4	ns	>0.9999
BeauR vs. BeauR T16A 3.6	ns	0.9271
BeauR vs. BeauR T16A 4.7	ns	0.5404
BeauR vs. BeauR T16A 4.9	ns	0.3244
BeauR T16A 3.4 vs. BeauR T16A 3.6	ns	0.9327
BeauR T16A 3.4 vs. BeauR T16A 4.7	ns	0.2964
BeauR T16A 3.4 vs. BeauR T16A 4.9	ns	0.1670
BeauR T16A 3.6 vs. BeauR T16A 4.7	ns	0.4242
BeauR T16A 3.6 vs. BeauR T16A 4.9	ns	0.2844
BeauR T16A 4.7 vs. BeauR T16A 4.9	ns	0.7244

Table 8.6. Figure 2C: BeauR-T16A Multi-Step Replication Kinetics DF1 cells

Tukey's multiple comparisons test	Summary	Adjusted P Value
1		
BeauR vs. BeauR-T16A-1	ns	0.3152
BeauR vs. BeauR-T16A-2	ns	0.3920

BeauR vs. BeauR T16A 4.7	ns	0.1737
BeauR vs. BeauR-T16A-3	ns	0.4000
BeauR-T16A-1 vs. BeauR-T16A-2	ns	0.9830
BeauR-T16A-1 vs. BeauR T16A 4.7	ns	0.5776
BeauR-T16A-1 vs. BeauR-T16A-3	ns	>0.9999
BeauR-T16A-2 vs. BeauR T16A 4.7	ns	0.3427
BeauR-T16A-2 vs. BeauR-T16A-3	ns	0.9940
BeauR T16A 4.7 vs. BeauR-T16A-3	ns	0.8758
24		
BeauR vs. BeauR-T16A-1	ns	0.9951
BeauR vs. BeauR-T16A-2	ns	0.9843
BeauR vs. BeauR T16A 4.7	ns	0.9794
BeauR vs. BeauR-T16A-3	ns	0.9668
BeauR-T16A-1 vs. BeauR-T16A-2	ns	>0.9999
BeauR-T16A-1 vs. BeauR T16A 4.7	ns	0.9999
BeauR-T16A-1 vs. BeauR-T16A-3	ns	0.9665
BeauR-T16A-2 vs. BeauR T16A 4.7	ns	0.9992
BeauR-T16A-2 vs. BeauR-T16A-3	ns	0.9389
BeauR T16A 4.7 vs. BeauR-T16A-3	ns	0.9217
48		
BeauR vs. BeauR-T16A-1	ns	0.9959
BeauR vs. BeauR-T16A-2	ns	0.5158
BeauR vs. BeauR T16A 4.7	ns	0.9327
BeauR vs. BeauR-T16A-3	ns	0.2728
BeauR-T16A-1 vs. BeauR-T16A-2	ns	0.8525
BeauR-T16A-1 vs. BeauR T16A 4.7	ns	0.9963
BeauR-T16A-1 vs. BeauR-T16A-3	ns	0.4766
BeauR-T16A-2 vs. BeauR T16A 4.7	ns	0.9597
BeauR-T16A-2 vs. BeauR-T16A-3	ns	0.6155
BeauR T16A 4.7 vs. BeauR-T16A-3	ns	0.5700
72		
BeauR vs. BeauR-T16A-1	ns	0.9971
BeauR vs. BeauR-T16A-2	ns	0.9742
BeauR vs. BeauR T16A 4.7	ns	0.9872
BeauR vs. BeauR-T16A-3	ns	0.3854
BeauR-T16A-1 vs. BeauR-T16A-2	ns	0.9309
BeauR-T16A-1 vs. BeauR T16A 4.7	ns	0.9495
BeauR-T16A-1 vs. BeauR-T16A-3	ns	0.4257
BeauR-T16A-2 vs. BeauR T16A 4.7	ns	0.9999
BeauR-T16A-2 vs. BeauR-T16A-3	ns	0.9024
BeauR T16A 4.7 vs. BeauR-T16A-3	ns	0.7497
96		
BeauR vs. BeauR-T16A-1	ns	0.9584
BeauR vs. BeauR-T16A-2	ns	0.9879
BeauR vs. BeauR T16A 4.7	ns	0.7774
BeauR vs. BeauR-T16A-3	ns	0.6881
BeauR-T16A-1 vs. BeauR-T16A-2	ns	>0.9999
BeauR-T16A-1 vs. BeauR T16A 4.7	ns	0.9413
BeauR-T16A-1 vs. BeauR-T16A-3	ns	0.8595
BeauR-T16A-2 vs. BeauR T16A 4.7	ns	0.9885
BeauR-T16A-2 vs. BeauR-T16A-3	ns	0.9786
BeauR T16A 4.7 vs. BeauR-T16A-3	ns	>0.9999

Table 8.7. Figure 2D: BeauR-T16A Multi-Step Replication Kinetics Vero cells

Tukey's multiple comparisons test	Summary	Adjusted P Value
1		
BeauR vs. BeauR T16A 3.4	ns	0.0535
BeauR vs. BeauR T16A 3.6	ns	0.6897
BeauR vs. BeauR T16A 4.7	ns	0.5215
BeauR vs. BeauR T16A 4.9	ns	0.9444
BeauR T16A 3.4 vs. BeauR T16A 3.6	ns	0.8067
BeauR T16A 3.4 vs. BeauR T16A 4.7	ns	0.8274
BeauR T16A 3.4 vs. BeauR T16A 4.9	ns	0.0586
BeauR T16A 3.6 vs. BeauR T16A 4.7	ns	0.9998
BeauR T16A 3.6 vs. BeauR T16A 4.9	ns	0.7318
BeauR T16A 4.7 vs. BeauR T16A 4.9	ns	0.5625
24		
BeauR vs. BeauR T16A 3.4	ns	0.9325
BeauR vs. BeauR T16A 3.6	ns	0.9814
BeauR vs. BeauR T16A 4.7	ns	0.9990
BeauR vs. BeauR T16A 4.9	ns	0.9816
BeauR T16A 3.4 vs. BeauR T16A 3.6	ns	0.9937
BeauR T16A 3.4 vs. BeauR T16A 4.7	ns	0.7522
BeauR T16A 3.4 vs. BeauR T16A 4.9	ns	0.9296
BeauR T16A 3.6 vs. BeauR T16A 4.7	ns	0.8786
BeauR T16A 3.6 vs. BeauR T16A 4.9	ns	0.9999
BeauR T16A 4.7 vs. BeauR T16A 4.9	ns	0.8551
48		
BeauR vs. BeauR T16A 3.4	ns	0.9998
BeauR vs. BeauR T16A 3.6	ns	>0.9999
BeauR vs. BeauR T16A 4.7	ns	0.9972
BeauR vs. BeauR T16A 4.9	ns	0.8047
BeauR T16A 3.4 vs. BeauR T16A 3.6	ns	0.9997
BeauR T16A 3.4 vs. BeauR T16A 4.7	ns	0.9514
BeauR T16A 3.4 vs. BeauR T16A 4.9	ns	0.3555
BeauR T16A 3.6 vs. BeauR T16A 4.7	ns	0.9829
BeauR T16A 3.6 vs. BeauR T16A 4.9	ns	0.4767
BeauR T16A 4.7 vs. BeauR T16A 4.9	ns	0.8552
72		
BeauR vs. BeauR T16A 3.4	ns	>0.9999
BeauR vs. BeauR T16A 3.6	ns	>0.9999
BeauR vs. BeauR T16A 4.7	ns	0.9988
BeauR vs. BeauR T16A 4.9	ns	0.9814
BeauR T16A 3.4 vs. BeauR T16A 3.6	ns	0.9995
BeauR T16A 3.4 vs. BeauR T16A 4.7	ns	0.9909
BeauR T16A 3.4 vs. BeauR T16A 4.9	ns	0.9190
BeauR T16A 3.6 vs. BeauR T16A 4.7	ns	>0.9999
BeauR T16A 3.6 vs. BeauR T16A 4.9	ns	0.9931
BeauR T16A 4.7 vs. BeauR T16A 4.9	ns	0.9930
96		
BeauR vs. BeauR T16A 3.4	ns	0.8621

BeauR vs. BeauR T16A 3.6	ns	0.9471
BeauR vs. BeauR T16A 4.7	ns	0.9783
BeauR vs. BeauR T16A 4.9	ns	0.9834
BeauR T16A 3.4 vs. BeauR T16A 3.6	ns	0.9711
BeauR T16A 3.4 vs. BeauR T16A 4.7	ns	0.5749
BeauR T16A 3.4 vs. BeauR T16A 4.9	ns	0.7959
BeauR T16A 3.6 vs. BeauR T16A 4.7	ns	0.9701
BeauR T16A 3.6 vs. BeauR T16A 4.9	ns	0.9890
BeauR T16A 4.7 vs. BeauR T16A 4.9	ns	>0.9999

Table 8.8: Figure 2A, BeauR-A26FSingle-Step Replication Kinetics CK cells

Tukey's multiple comparisons test	Summary	Adjusted P Value
1		
Beau-R vs. BeauR-A26F-1	ns	0.3350
Beau-R vs. BeauR-A26F-2	ns	0.3762
Beau-R vs. BeauR-A26F-3	ns	0.3152
BeauR-A26F-1 vs. BeauR-A26F-2	ns	0.9567
BeauR-A26F-1 vs. BeauR-A26F-3	ns	0.9796
BeauR-A26F-2 vs. BeauR-A26F-3	ns	0.5389
2		
Beau-R vs. BeauR-A26F-1	*	0.0255
Beau-R vs. BeauR-A26F-2	ns	0.1024
Beau-R vs. BeauR-A26F-3	ns	0.0833
BeauR-A26F-1 vs. BeauR-A26F-2	ns	0.9495
BeauR-A26F-1 vs. BeauR-A26F-3	ns	0.7011
BeauR-A26F-2 vs. BeauR-A26F-3	ns	0.9839
4		
Beau-R vs. BeauR-A26F-1	ns	0.4963
Beau-R vs. BeauR-A26F-2	*	0.0284
Beau-R vs. BeauR-A26F-3	*	0.0286
BeauR-A26F-1 vs. BeauR-A26F-2	ns	0.8364
BeauR-A26F-1 vs. BeauR-A26F-3	ns	0.8303
BeauR-A26F-2 vs. BeauR-A26F-3	ns	>0.9999
6		
Beau-R vs. BeauR-A26F-1	*	0.0226
Beau-R vs. BeauR-A26F-2	ns	0.1735
Beau-R vs. BeauR-A26F-3	ns	0.3664
BeauR-A26F-1 vs. BeauR-A26F-2	ns	0.7999
BeauR-A26F-1 vs. BeauR-A26F-3	ns	0.9864
BeauR-A26F-2 vs. BeauR-A26F-3	ns	0.9946
8		
Beau-R vs. BeauR-A26F-1	ns	0.8385
Beau-R vs. BeauR-A26F-2	ns	0.7994
Beau-R vs. BeauR-A26F-3	ns	0.8572
BeauR-A26F-1 vs. BeauR-A26F-2	ns	>0.9999
BeauR-A26F-1 vs. BeauR-A26F-3	ns	0.9761
BeauR-A26F-2 vs. BeauR-A26F-3	ns	0.9680
10		
Beau-R vs. BeauR-A26F-1	ns	0.9831

Beau-R vs. BeauR-A26F-2	ns	0.9979
Beau-R vs. BeauR-A26F-3	ns	0.9998
BeauR-A26F-1 vs. BeauR-A26F-2	ns	0.9988
BeauR-A26F-1 vs. BeauR-A26F-3	ns	0.9776
BeauR-A26F-2 vs. BeauR-A26F-3	ns	0.9953
11		
Beau-R vs. BeauR-A26F-1	ns	0.9942
Beau-R vs. BeauR-A26F-2	ns	0.9995
Beau-R vs. BeauR-A26F-3	ns	0.9000
BeauR-A26F-1 vs. BeauR-A26F-2	ns	0.9887
BeauR-A26F-1 vs. BeauR-A26F-3	ns	0.9521
BeauR-A26F-2 vs. BeauR-A26F-3	ns	0.9059

Table 8.9: Figure 2B, BeauR-A26F Multi-Step Replication Kinetics CK cells

Tukey's multiple comparisons test	Summary	Adjusted P Value
1		
Beau-R vs. BeauR-A26F-1	ns	0.2237
Beau-R vs. BeauR-A26F-2	ns	0.3552
Beau-R vs. BeauR-A26F-3	ns	0.0962
BeauR-A26F-1 vs. BeauR-A26F-2	ns	0.9964
BeauR-A26F-1 vs. BeauR-A26F-3	ns	0.9991
BeauR-A26F-2 vs. BeauR-A26F-3	ns	0.9991
24		
Beau-R vs. BeauR-A26F-1	ns	0.9610
Beau-R vs. BeauR-A26F-2	ns	0.9995
Beau-R vs. BeauR-A26F-3	ns	0.9046
BeauR-A26F-1 vs. BeauR-A26F-2	ns	0.9874
BeauR-A26F-1 vs. BeauR-A26F-3	ns	0.9980
BeauR-A26F-2 vs. BeauR-A26F-3	ns	0.9594
48		
Beau-R vs. BeauR-A26F-1	ns	0.5667
Beau-R vs. BeauR-A26F-2	ns	0.8024
Beau-R vs. BeauR-A26F-3	ns	0.8364
BeauR-A26F-1 vs. BeauR-A26F-2	ns	0.8858
BeauR-A26F-1 vs. BeauR-A26F-3	ns	0.9269
BeauR-A26F-2 vs. BeauR-A26F-3	ns	>0.9999
72		
Beau-R vs. BeauR-A26F-1	ns	0.0786
Beau-R vs. BeauR-A26F-2	ns	0.1078
Beau-R vs. BeauR-A26F-3	ns	0.0954
BeauR-A26F-1 vs. BeauR-A26F-2	ns	0.5626
BeauR-A26F-1 vs. BeauR-A26F-3	ns	0.7642
BeauR-A26F-2 vs. BeauR-A26F-3	ns	0.9982
96		
Beau-R vs. BeauR-A26F-1	ns	0.0681
Beau-R vs. BeauR-A26F-2	ns	0.1013
Beau-R vs. BeauR-A26F-3	ns	0.1615
BeauR-A26F-1 vs. BeauR-A26F-2	ns	0.9174
BeauR-A26F-1 vs. BeauR-A26F-3	ns	0.4969

BeauR-A26F-2 vs. BeauR-A26F-3	ns	0.8069

Table 8.10: Figure 2C, BeauR-A26F Multi-Step Replication Kinetics DF1 cells

Tukey's multiple comparisons test	Summary	Adjusted P Value
1		
Beau-R vs. BeauR-A26F-1	ns	0.3970
Beau-R vs. BeauR-A26F-2	ns	0.2871
Beau-R vs. BeauR-A26F-3	ns	0.3802
BeauR-A26F-1 vs. BeauR-A26F-2	ns	0.9998
BeauR-A26F-1 vs. BeauR-A26F-3	ns	0.9762
BeauR-A26F-2 vs. BeauR-A26F-3	ns	0.9576
24		
Beau-R vs. BeauR-A26F-1	ns	0.3191
Beau-R vs. BeauR-A26F-2	ns	0.1093
Beau-R vs. BeauR-A26F-3	ns	0.4406
BeauR-A26F-1 vs. BeauR-A26F-2	ns	0.2837
BeauR-A26F-1 vs. BeauR-A26F-3	ns	0.8982
BeauR-A26F-2 vs. BeauR-A26F-3	ns	0.2249
48		
Beau-R vs. BeauR-A26F-1	ns	0.5883
Beau-R vs. BeauR-A26F-2	ns	0.8917
Beau-R vs. BeauR-A26F-3	ns	0.6702
BeauR-A26F-1 vs. BeauR-A26F-2	ns	0.7986
BeauR-A26F-1 vs. BeauR-A26F-3	ns	0.8854
BeauR-A26F-2 vs. BeauR-A26F-3	ns	0.9607
72		
Beau-R vs. BeauR-A26F-1	ns	0.5730
Beau-R vs. BeauR-A26F-2	ns	0.7920
Beau-R vs. BeauR-A26F-3	ns	0.4254
BeauR-A26F-1 vs. BeauR-A26F-2	ns	0.9985
BeauR-A26F-1 vs. BeauR-A26F-3	ns	0.8570
BeauR-A26F-2 vs. BeauR-A26F-3	ns	0.9257
96		
Beau-R vs. BeauR-A26F-1	ns	0.3201
Beau-R vs. BeauR-A26F-2	ns	0.4855
Beau-R vs. BeauR-A26F-3	ns	0.2096
BeauR-A26F-1 vs. BeauR-A26F-2	ns	0.6700
BeauR-A26F-1 vs. BeauR-A26F-3	ns	0.9271
BeauR-A26F-2 vs. BeauR-A26F-3	ns	0.4327

Table 8.11: Figure 2D, BeauR-A26F Multi-Step Replication Kinetics Vero cells

Tukey's multiple comparisons test	Summary	Adjusted P Value
1		
Beau-R vs. BeauR-A26F-1	ns	0.4017
Beau-R vs. BeauR-A26F-2	ns	0.8493
Beau-R vs. BeauR-A26F-3	ns	0.0907

BeauR-A26F-1 vs. BeauR-A26F-2	ns	0.9146
BeauR-A26F-1 vs. BeauR-A26F-3	ns	0.9189
BeauR-A26F-2 vs. BeauR-A26F-3	ns	0.6385
24		
Beau-R vs. BeauR-A26F-1	*	0.0265
Beau-R vs. BeauR-A26F-2	*	0.0405
Beau-R vs. BeauR-A26F-3	*	0.0273
BeauR-A26F-1 vs. BeauR-A26F-2	ns	0.9683
BeauR-A26F-1 vs. BeauR-A26F-3	ns	0.9571
BeauR-A26F-2 vs. BeauR-A26F-3	ns	0.9981
48		
Beau-R vs. BeauR-A26F-1	**	0.0023
Beau-R vs. BeauR-A26F-2	*	0.0103
Beau-R vs. BeauR-A26F-3	**	0.0029
BeauR-A26F-1 vs. BeauR-A26F-2	ns	0.5970
BeauR-A26F-1 vs. BeauR-A26F-3	ns	0.9936
BeauR-A26F-2 vs. BeauR-A26F-3	ns	0.6951
72		
Beau-R vs. BeauR-A26F-1	*	0.0147
Beau-R vs. BeauR-A26F-2	**	0.0023
Beau-R vs. BeauR-A26F-3	**	0.0029
BeauR-A26F-1 vs. BeauR-A26F-2	ns	0.9282
BeauR-A26F-1 vs. BeauR-A26F-3	ns	0.9235
BeauR-A26F-2 vs. BeauR-A26F-3	ns	>0.9999
96		
Beau-R vs. BeauR-A26F-1	ns	0.6715
Beau-R vs. BeauR-A26F-2	ns	0.6272
Beau-R vs. BeauR-A26F-3	ns	0.3022
BeauR-A26F-1 vs. BeauR-A26F-2	ns	0.9998
BeauR-A26F-1 vs. BeauR-A26F-3	ns	0.3084
BeauR-A26F-2 vs. BeauR-A26F-3	ns	0.1157

Table 8.12: Figure 3B, Plaque Size

Tukey's multiple comparisons test	Summary	Adjusted P Value
Beau-R vs. BeauR-T16A-1	****	<0.0001
Beau-R vs. BeauR-T16A-2	****	<0.0001
Beau-R vs. BeauR-T16A-3	****	<0.0001
Beau-R vs. BeauR-A26F-1	****	<0.0001
Beau-R vs. BeauR-A26F-2	****	<0.0001
Beau-R vs. BeauR-A26F-3	****	<0.0001
BeauR-T16A-1 vs. BeauR-T16A-2	ns	0.5916
BeauR-T16A-1 vs. BeauR-T16A-3	ns	0.9948
BeauR-T16A-1 vs. BeauR-A26F-1	****	<0001
BeauR-T16A-1 vs. BeauR-A26F-2	ns	0.8648
BeauR-T16A-1 vs. BeauR-A26F-3	*	0.0165
BeauR-T16A-2 vs. BeauR-T16A-3	ns	0.9324
BeauR-T16A-2 vs. BeauR-A26F-1	****	<0.0001
BeauR-T16A-2 vs. BeauR-A26F-2	*	0.0460
BeauR-T16A-2 vs. BeauR-A26F-3	****	<0.0001

BeauR-T16A-3 vs. BeauR-A26F-1	****	<0.0001
BeauR-T16A-3 vs. BeauR-A26F-2	ns	0.4667
BeauR-T16A-3 vs. BeauR-A26F-3	**	0.0017
BeauR-A26F-1 vs. BeauR-A26F-2	*	0.0109
BeauR-A26F-1 vs. BeauR-A26F-3	ns	0.8027
BeauR-A26F-2 vs. BeauR-A26F-3	ns	0.3682

Table 8.13: Figure 4A, Viral Release CK cells

Tukey's multiple comparisons test	Summary	Adjusted P Value
Supernatant		
Beau-R vs. BeauR-T16A	ns	0.5899
Beau-R vs. BeauR-A26F	ns	0.9664
BeauR-T16A vs. BeauR-A26F	ns	0.4477
Cell Lysate		
Beau-R vs. BeauR-T16A	ns	0.8184
Beau-R vs. BeauR-A26F	ns	0.1328
BeauR-T16A vs. BeauR-A26F	ns	0.3316

Table 8.14: Figure 4B, Viral Release Vero cells

Tukey's multiple comparisons test	Summary	Adjusted P Value
Supernatant		
Beau-R vs. BeauR-T16A	ns	0.9156
Beau-R vs. BeauR-A26F	**	0.0014
BeauR-T16A vs. BeauR-A26F	**	0.0027
Cell Lysate		
Beau-R vs. BeauR-T16A	ns	0.9728
Beau-R vs. BeauR-A26F	*	0.0272
BeauR-T16A vs. BeauR-A26F	*	0.0406

Table 8.15: Figure 5A, BeauR-T16A Ciliary Activity

Tukey's multiple comparisons test	Summary	Adjusted P Value
1		
Mock vs. Beau-R	ns	0.9998
Mock vs. BeauR-T16A-1	ns	0.9998
Mock vs. BeauR-T16A-2	ns	0.9998
Mock vs. BeauR-T16A-3	ns	>0.9999
Beau-R vs. BeauR-T16A-1	ns	>0.9999
Beau-R vs. BeauR-T16A-2	ns	>0.9999
Beau-R vs. BeauR-T16A-3	ns	0.9998
BeauR-T16A-1 vs. BeauR-T16A-2	ns	>0.9999
BeauR-T16A-1 vs. BeauR-T16A-3	ns	0.9998

BeauR-T16A-2 vs. BeauR-T16A-3	ns	0.9998
24		
Mock vs. Beau-R	ns	0.5200
Mock vs. BeauR-T16A-1	ns	0.5200
Mock vs. BeauR-T16A-2	ns	0.1148
Mock vs. BeauR-T16A-3	ns	0.1440
Beau-R vs. BeauR-T16A-1	ns	>0.9999
Beau-R vs. BeauR-T16A-2	ns	0.9942
Beau-R vs. BeauR-T16A-3	ns	0.9536
BeauR-T16A-1 vs. BeauR-T16A-2	ns	0.9942
BeauR-T16A-1 vs. BeauR-T16A-3	ns	0.9536
BeauR-T16A-2 vs. BeauR-T16A-3	ns	0.9979
48		
Mock vs. Beau-R	**	0.0087
Mock vs. BeauR-T16A-1	*	0.0179
Mock vs. BeauR-T16A-2	****	<0.0001
Mock vs. BeauR-T16A-3	**	0.0022
Beau-R vs. BeauR-T16A-1	ns	0.9938
Beau-R vs. BeauR-T16A-2	ns	0.9211
Beau-R vs. BeauR-T16A-3	ns	>0.9999
BeauR-T16A-1 vs. BeauR-T16A-2	ns	0.5603
BeauR-T16A-1 vs. BeauR-T16A-3	ns	0.9667
BeauR-T16A-2 vs. BeauR-T16A-3	ns	0.9696
72		
Mock vs. Beau-R	****	<0.0001
Mock vs. BeauR-T16A-1	*	0.0205
Mock vs. BeauR-T16A-2	***	0.0003
Mock vs. BeauR-T16A-3	*	0.0107
Beau-R vs. BeauR-T16A-1	ns	0.3107
Beau-R vs. BeauR-T16A-2	ns	0.9652
Beau-R vs. BeauR-T16A-3	ns	0.4596
BeauR-T16A-1 vs. BeauR-T16A-2	ns	0.8318
BeauR-T16A-1 vs. BeauR-T16A-3	ns	0.9999
BeauR-T16A-2 vs. BeauR-T16A-3	ns	0.9262
96		
Mock vs. Beau-R	****	<0.0001
Mock vs. BeauR-T16A-1	****	<0.0001
Mock vs. BeauR-T16A-2	****	<0.0001
Mock vs. BeauR-T16A-3	***	0.0003
Beau-R vs. BeauR-T16A-1	ns	0.5337
Beau-R vs. BeauR-T16A-2	ns	0.8973
Beau-R vs. BeauR-T16A-3	ns	0.2014
BeauR-T16A-1 vs. BeauR-T16A-2	ns	0.9791
BeauR-T16A-1 vs. BeauR-T16A-3	ns	0.9953
BeauR-T16A-2 vs. BeauR-T16A-3	ns	0.7906

Table 8.16: Figure 5B, BeauR-A26F Ciliary Activity

Tukey's multiple comparisons test	Summary	Adjusted P Value
1		

Mock vs. Beau-R	ns	0.9364
Mock vs. BeauR-A26F-1	ns	0.9857
Mock vs. BeauR-A26F-2	ns	0.6770
Mock vs. BeauR-A26F-3	ns	0.9990
Beau-R vs. BeauR-A26F-1	ns	0.9989
Beau-R vs. BeauR-A26F-2	ns	0.9827
Beau-R vs. BeauR-A26F-3	ns	0.9851
BeauR-A26F-1 vs. BeauR-A26F-2	ns	0.9287
BeauR-A26F-1 vs. BeauR-A26F-3	ns	0.9990
BeauR-A26F-2 vs. BeauR-A26F-3	ns	0.8241
24		
Mock vs. Beau-R	ns	0.3282
Mock vs. BeauR-A26F-1	ns	0.1625
Mock vs. BeauR-A26F-2	ns	0.1078
Mock vs. BeauR-A26F-3	ns	0.3854
Beau-R vs. BeauR-A26F-1	ns	0.9700
Beau-R vs. BeauR-A26F-2	ns	0.9863
Beau-R vs. BeauR-A26F-3	ns	0.9997
BeauR-A26F-1 vs. BeauR-A26F-2	ns	0.9997
BeauR-A26F-1 vs. BeauR-A26F-3	ns	0.9945
BeauR-A26F-2 vs. BeauR-A26F-3	ns	0.9990
48		
Mock vs. Beau-R	*	0.0258
Mock vs. BeauR-A26F-1	***	0.0001
Mock vs. BeauR-A26F-2	**	0.0015
Mock vs. BeauR-A26F-3	***	0.0008
Beau-R vs. BeauR-A26F-1	ns	0.6018
Beau-R vs. BeauR-A26F-2	ns	0.5325
Beau-R vs. BeauR-A26F-3	ns	0.8821
BeauR-A26F-1 vs. BeauR-A26F-2	ns	0.9965
BeauR-A26F-1 vs. BeauR-A26F-3	ns	0.9852
BeauR-A26F-2 vs. BeauR-A26F-3	ns	0.9340
72		
Mock vs. Beau-R	****	<0.0001
Mock vs. BeauR-A26F-1	****	<0.0001
Mock vs. BeauR-A26F-2	****	<0.0001
Mock vs. BeauR-A26F-3	****	<0.0001
Beau-R vs. BeauR-A26F-1	ns	>0.9999
Beau-R vs. BeauR-A26F-2	ns	0.9998
Beau-R vs. BeauR-A26F-3	ns	0.9993
BeauR-A26F-1 vs. BeauR-A26F-2	ns	0.9998
BeauR-A26F-1 vs. BeauR-A26F-3	ns	0.9993
BeauR-A26F-2 vs. BeauR-A26F-3	ns	>0.9999
96		
Mock vs. Beau-R	****	<0.0001
Mock vs. BeauR-A26F-1	****	<0.0001
Mock vs. BeauR-A26F-2	****	<0.0001
Mock vs. BeauR-A26F-3	****	<0.0001
Beau-R vs. BeauR-A26F-1	ns	0.9943
Beau-R vs. BeauR-A26F-2	ns	0.9821
Beau-R vs. BeauR-A26F-3	ns	>0.9999
BeauR-A26F-1 vs. BeauR-A26F-2	ns	>0.9999

BeauR-A26F-1 vs. BeauR-A26F-3	ns	0.9943
BeauR-A26F-2 vs. BeauR-A26F-3	ns	0.9821

Table 8.17: Figure 5C, Replication Kinetics TOCs

Tukey's multiple comparisons test	Summary	Adjusted P Value
1		
BeauR vs. BeauR-T16A		
BeauR vs. BeauR-A26F		
BeauR-T16A vs. BeauR-A26F		
24		
BeauR vs. BeauR-T16A	ns	0.6232
BeauR vs. BeauR-A26F	ns	0.5941
BeauR-T16A vs. BeauR-A26F	ns	0.9988
48		
BeauR vs. BeauR-T16A	ns	0.9966
BeauR vs. BeauR-A26F	ns	0.7987
BeauR-T16A vs. BeauR-A26F	ns	0.9744
72		
BeauR vs. BeauR-T16A	ns	0.1981
BeauR vs. BeauR-A26F	ns	0.3601
BeauR-T16A vs. BeauR-A26F	ns	0.9600
96		
BeauR vs. BeauR-T16A	ns	0.6083
BeauR vs. BeauR-A26F	ns	0.1042
BeauR-T16A vs. BeauR-A26F	*	0.0497

Table 8.18: Figure 7A, BeauR-T16A Replication *in ovo*

Tukey's multiple comparisons test	Summary	Adjusted P Value
Beau-R vs. BeauR T16A 3.4	ns	0.9012
Beau-R vs. BeauR T16A 3.6	ns	0.9997
Beau-R vs. BeauR T16A 4.7	ns	0.8033
Beau-R vs. BeauR T16A 4.9	ns	0.9953
BeauR T16A 3.4 vs. BeauR T16A 3.6	ns	0.9534
BeauR T16A 3.4 vs. BeauR T16A 4.7	ns	0.3445
BeauR T16A 3.4 vs. BeauR T16A 4.9	ns	0.9856
BeauR T16A 3.6 vs. BeauR T16A 4.7	ns	0.7102
BeauR T16A 3.6 vs. BeauR T16A 4.9	ns	0.9996
BeauR T16A 4.7 vs. BeauR T16A 4.9	ns	0.6010

Table 8.19: Figure 7A, BeauR-A26F Replication *in ovo*

Tukey's multiple comparisons test	Summary	Adjusted P Value
Beau-R vs. BeauR-A26F-1	**	0.0013
Beau-R vs. BeauR-A26F-2	***	0.0008

Beau-R vs. BeauR-A26F-3	**	0.0012
BeauR-A26F-1 vs. BeauR-A26F-2	ns	0.9495
BeauR-A26F-1 vs. BeauR-A26F-3	ns	0.9991
BeauR-A26F-2 vs. BeauR-A26F-3	ns	0.9776

Table 8.20: Figure 9A, Cell viability CK cell 24 hpi

Tukey's multiple comparisons test	Summary	Adjusted P Value
Row 1		
Beau-R vs. BeauR-T16A	ns	0.5420
Beau-R vs. BeauR-A26F	ns	0.5000
BeauR-T16A vs. BeauR-A26F	ns	0.9927
Row 2		
Beau-R vs. BeauR-T16A	ns	0.5822
Beau-R vs. BeauR-A26F	ns	0.3301
BeauR-T16A vs. BeauR-A26F	ns	0.7402
Row 3		
Beau-R vs. BeauR-T16A	ns	0.8598
Beau-R vs. BeauR-A26F	ns	0.4634
BeauR-T16A vs. BeauR-A26F	ns	0.5357
Row 4		
Beau-R vs. BeauR-T16A	ns	0.9938
Beau-R vs. BeauR-A26F	ns	0.4419
BeauR-T16A vs. BeauR-A26F	ns	0.3083
Row 5		
Beau-R vs. BeauR-T16A	ns	0.7512
Beau-R vs. BeauR-A26F	ns	0.2244
BeauR-T16A vs. BeauR-A26F	ns	0.3081
Row 6		
Beau-R vs. BeauR-T16A	ns	0.9940
Beau-R vs. BeauR-A26F	ns	0.3918
BeauR-T16A vs. BeauR-A26F	ns	0.1872
Row 7		
Beau-R vs. BeauR-T16A	ns	0.9931
Beau-R vs. BeauR-A26F	**	0.0049
BeauR-T16A vs. BeauR-A26F	ns	0.0582
Row 8		
Beau-R vs. BeauR-T16A	ns	0.7834
Beau-R vs. BeauR-A26F	ns	0.1076
BeauR-T16A vs. BeauR-A26F	ns	0.3910

Table 8.21: Figure 9A, Cell Viability CK cell 48 hpi

Tukey's multiple comparisons test	Summary	Adjusted P Value
Row 1		
Beau-R vs. BeauR-T16A	ns	0.9918
Beau-R vs. BeauR-A26F	ns	0.5470
BeauR-T16A vs. BeauR-A26F	ns	0.6499

Row 2		
Beau-R vs. BeauR-T16A	ns	0.9003
Beau-R vs. BeauR-A26F	ns	0.8740
BeauR-T16A vs. BeauR-A26F	ns	0.7261
Row 3		
Beau-R vs. BeauR-T16A	ns	0.9037
Beau-R vs. BeauR-A26F	ns	0.9688
BeauR-T16A vs. BeauR-A26F	ns	0.9966
Row 4		
Beau-R vs. BeauR-T16A	ns	0.8045
Beau-R vs. BeauR-A26F	ns	0.9243
BeauR-T16A vs. BeauR-A26F	ns	0.9606
Row 5		
Beau-R vs. BeauR-T16A	ns	0.2936
Beau-R vs. BeauR-A26F	ns	0.8412
BeauR-T16A vs. BeauR-A26F	ns	0.6509
Row 6		
Beau-R vs. BeauR-T16A	ns	0.7604
Beau-R vs. BeauR-A26F	ns	0.9652
BeauR-T16A vs. BeauR-A26F	ns	0.5970
Row 7		
Beau-R vs. BeauR-T16A	ns	0.7626
Beau-R vs. BeauR-A26F	ns	0.9990
BeauR-T16A vs. BeauR-A26F	ns	0.7955
Row 8		
Beau-R vs. BeauR-T16A	ns	0.3896
Beau-R vs. BeauR-A26F	ns	0.8340
BeauR-T16A vs. BeauR-A26F	ns	0.7232

Table 8.22: Figure 9A, Cell Viability CK cell 72 hpi

Tukey's multiple comparisons test	Summary	Adjusted P Value
Row 1		
Beau-R vs. BeauR-T16A	ns	0.9667
Beau-R vs. BeauR-A26F	ns	0.9996
BeauR-T16A vs. BeauR-A26F	ns	0.9736
Row 2		
Beau-R vs. BeauR-T16A	ns	0.6521
Beau-R vs. BeauR-A26F	ns	0.5911
BeauR-T16A vs. BeauR-A26F	ns	0.9815
Row 3		
Beau-R vs. BeauR-T16A	ns	0.2102
Beau-R vs. BeauR-A26F	ns	0.4325
BeauR-T16A vs. BeauR-A26F	ns	0.9946
Row 4		
Beau-R vs. BeauR-T16A	ns	0.7066
Beau-R vs. BeauR-A26F	ns	0.7249
BeauR-T16A vs. BeauR-A26F	ns	>0.9999

Row 5		
Beau-R vs. BeauR-T16A	ns	0.8183
Beau-R vs. BeauR-A26F	ns	0.8247
BeauR-T16A vs. BeauR-A26F	ns	>0.9999
Row 6		
Beau-R vs. BeauR-T16A	ns	0.9988
Beau-R vs. BeauR-A26F	ns	0.9054
BeauR-T16A vs. BeauR-A26F	ns	0.9077
Row 7		
Beau-R vs. BeauR-T16A	ns	0.9986
Beau-R vs. BeauR-A26F	ns	0.9068
BeauR-T16A vs. BeauR-A26F	ns	0.9179
Row 8		
Beau-R vs. BeauR-T16A	ns	0.8967
Beau-R vs. BeauR-A26F	ns	0.7982
BeauR-T16A vs. BeauR-A26F	ns	0.9735

Table 8.23: Figure 9A, Cell Viability CK cell 96 hpi

Tukey's multiple comparisons test	Summary	Adjusted P Value
Row 1		
Beau-R vs. BeauR-T16A	ns	0.2981
Beau-R vs. BeauR-A26F	ns	0.6250
BeauR-T16A vs. BeauR-A26F	ns	0.8930
Row 2		
Beau-R vs. BeauR-T16A	ns	0.6184
Beau-R vs. BeauR-A26F	ns	0.6706
BeauR-T16A vs. BeauR-A26F	ns	0.9801
Row 3		
Beau-R vs. BeauR-T16A	ns	0.1139
Beau-R vs. BeauR-A26F	ns	0.4613
BeauR-T16A vs. BeauR-A26F	ns	0.9375
Row 4		
Beau-R vs. BeauR-T16A	ns	0.6438
Beau-R vs. BeauR-A26F	ns	0.3461
BeauR-T16A vs. BeauR-A26F	ns	0.9730
Row 5		
Beau-R vs. BeauR-T16A	ns	0.9351
Beau-R vs. BeauR-A26F	ns	0.7648
BeauR-T16A vs. BeauR-A26F	ns	0.9637
Row 6		
Beau-R vs. BeauR-T16A	ns	0.8898
Beau-R vs. BeauR-A26F	ns	0.3502
BeauR-T16A vs. BeauR-A26F	ns	0.7060
Row 7		
Beau-R vs. BeauR-T16A	ns	0.9949
Beau-R vs. BeauR-A26F	ns	0.6796
BeauR-T16A vs. BeauR-A26F	ns	0.8736
Row 8		
Beau-R vs. BeauR-T16A	ns	0.4584

Beau-R vs. BeauR-A26F	ns	0.6166
BeauR-T16A vs. BeauR-A26F	ns	0.8290

Table 8.24: Figure 9B, Cell Viability DF1 cell 24 hpi

Tukey's multiple comparisons test	Summary	Adjusted P Value
Row 1		
Beau-R vs. BeauR-T16A	ns	0.0903
Beau-R vs. BeauR-A26F	ns	0.3922
BeauR-T16A vs. BeauR-A26F	ns	0.7743
Row 2		
Beau-R vs. BeauR-T16A	ns	0.9751
Beau-R vs. BeauR-A26F	ns	0.6418
BeauR-T16A vs. BeauR-A26F	ns	0.8389
Row 3		
Beau-R vs. BeauR-T16A	ns	>0.9999
Beau-R vs. BeauR-A26F	ns	0.8656
BeauR-T16A vs. BeauR-A26F	ns	0.9321
Row 4		
Beau-R vs. BeauR-T16A	ns	0.9860
Beau-R vs. BeauR-A26F	ns	0.9603
BeauR-T16A vs. BeauR-A26F	ns	0.9990
Row 5		
Beau-R vs. BeauR-T16A	ns	0.9946
Beau-R vs. BeauR-A26F	ns	0.8812
BeauR-T16A vs. BeauR-A26F	ns	0.9738
Row 6		
Beau-R vs. BeauR-T16A	ns	0.9627
Beau-R vs. BeauR-A26F	ns	0.9247
BeauR-T16A vs. BeauR-A26F	ns	0.8972
Row 7		
Beau-R vs. BeauR-T16A	ns	0.8945
Beau-R vs. BeauR-A26F	ns	0.6679
BeauR-T16A vs. BeauR-A26F	ns	0.9787
Row 8		
Beau-R vs. BeauR-T16A	ns	0.5018
Beau-R vs. BeauR-A26F	ns	0.7325
BeauR-T16A vs. BeauR-A26F	ns	0.9820

Table 8.25: Figure 9B, Cell Viability DF1 cell 48 hpi

Tukey's multiple comparisons test	Summary	Adjusted P Value
Row 1		
Beau-R vs. BeauR-T16A	ns	0.9997
Beau-R vs. BeauR-A26F	ns	0.7959
BeauR-T16A vs. BeauR-A26F	ns	0.3756
Row 2		
Beau-R vs. BeauR-T16A	ns	0.3624

Beau-R vs. BeauR-A26F	ns	0.4440
BeauR-T16A vs. BeauR-A26F	ns	0.5246
Row 3		
Beau-R vs. BeauR-T16A	ns	0.2836
Beau-R vs. BeauR-A26F	ns	0.5903
BeauR-T16A vs. BeauR-A26F	ns	0.5127
Row 4		
Beau-R vs. BeauR-T16A	ns	0.2986
Beau-R vs. BeauR-A26F	ns	0.7595
BeauR-T16A vs. BeauR-A26F	ns	0.5510
Row 5		
Beau-R vs. BeauR-T16A	ns	0.2690
Beau-R vs. BeauR-A26F	ns	0.3120
BeauR-T16A vs. BeauR-A26F	ns	0.9024
Row 6		
Beau-R vs. BeauR-T16A	ns	0.1685
Beau-R vs. BeauR-A26F	ns	0.3839
BeauR-T16A vs. BeauR-A26F	ns	0.5704
Row 7		
Beau-R vs. BeauR-T16A	ns	0.5891
Beau-R vs. BeauR-A26F	ns	0.1606
BeauR-T16A vs. BeauR-A26F	ns	0.9944
Row 8		
Beau-R vs. BeauR-T16A	ns	0.3728
Beau-R vs. BeauR-A26F	ns	0.4026
BeauR-T16A vs. BeauR-A26F	ns	0.7290

Table 8.26: Figure 9B, Cell Viability DF1 cell 72 hpi

Tukey's multiple comparisons test	Summary	Adjusted P Value
Row 1		
Beau-R vs. BeauR-T16A	ns	0.7032
Beau-R vs. BeauR-A26F	ns	0.7298
BeauR-T16A vs. BeauR-A26F	ns	0.4225
Row 2		
Beau-R vs. BeauR-T16A	ns	0.6165
Beau-R vs. BeauR-A26F	ns	0.9990
BeauR-T16A vs. BeauR-A26F	ns	0.5168
Row 3		
Beau-R vs. BeauR-T16A	ns	0.7120
Beau-R vs. BeauR-A26F	ns	0.9993
BeauR-T16A vs. BeauR-A26F	ns	0.6511
Row 4		
Beau-R vs. BeauR-T16A	ns	0.5807
Beau-R vs. BeauR-A26F	ns	0.9987
BeauR-T16A vs. BeauR-A26F	ns	0.5603
Row 5		
Beau-R vs. BeauR-T16A	ns	0.6793
Beau-R vs. BeauR-A26F	ns	0.9990
BeauR-T16A vs. BeauR-A26F	ns	0.6592

Row 6		
Beau-R vs. BeauR-T16A	ns	0.7597
Beau-R vs. BeauR-A26F	ns	0.9965
BeauR-T16A vs. BeauR-A26F	ns	0.6773
Row 7		
Beau-R vs. BeauR-T16A	ns	0.9698
Beau-R vs. BeauR-A26F	ns	0.9133
BeauR-T16A vs. BeauR-A26F	ns	0.7829
Row 8		
Beau-R vs. BeauR-T16A	ns	0.6363
Beau-R vs. BeauR-A26F	ns	0.8212
BeauR-T16A vs. BeauR-A26F	ns	0.9090

Table 8.27: Figure 9B, Cell Viability DF1 cell 96 hpi

Tukey's multiple comparisons test	Summary	Adjusted P Value
Row 1		
Beau-R vs. BeauR-T16A	ns	0.6981
Beau-R vs. BeauR-A26F	ns	0.1995
BeauR-T16A vs. BeauR-A26F	ns	0.3881
Row 2		
Beau-R vs. BeauR-T16A	ns	0.4266
Beau-R vs. BeauR-A26F	ns	0.2604
BeauR-T16A vs. BeauR-A26F	ns	0.6459
Row 3		
Beau-R vs. BeauR-T16A	ns	0.9828
Beau-R vs. BeauR-A26F	ns	0.2488
BeauR-T16A vs. BeauR-A26F	ns	0.2373
Row 4		
Beau-R vs. BeauR-T16A	ns	0.5638
Beau-R vs. BeauR-A26F	ns	0.8329
BeauR-T16A vs. BeauR-A26F	ns	0.3069
Row 5		
Beau-R vs. BeauR-T16A	ns	0.3440
Beau-R vs. BeauR-A26F	ns	0.8446
BeauR-T16A vs. BeauR-A26F	ns	0.2936
Row 6		
Beau-R vs. BeauR-T16A	ns	0.3766
Beau-R vs. BeauR-A26F	ns	0.9388
BeauR-T16A vs. BeauR-A26F	ns	0.3496
Row 7		
Beau-R vs. BeauR-T16A	ns	0.4673
Beau-R vs. BeauR-A26F	ns	0.8074
BeauR-T16A vs. BeauR-A26F	ns	0.1755
Row 8		
Beau-R vs. BeauR-T16A	ns	0.3444
Beau-R vs. BeauR-A26F	ns	0.9413
BeauR-T16A vs. BeauR-A26F	ns	0.1037

Table 8.28: Figure 9C, Cell Viability Vero cell 24 hpi

Tukey's multiple comparisons test	Summary	Adjusted P Value
Row 1		
Beau-R vs. BeauR-T16A	ns	0.8654
Beau-R vs. BeauR-A26F	ns	0.9378
BeauR-T16A vs. BeauR-A26F	ns	0.9294
Row 2		
Beau-R vs. BeauR-T16A	ns	0.9435
Beau-R vs. BeauR-A26F	ns	0.9214
BeauR-T16A vs. BeauR-A26F	ns	>0.9999
Row 3		
Beau-R vs. BeauR-T16A	ns	0.9960
Beau-R vs. BeauR-A26F	ns	0.9942
BeauR-T16A vs. BeauR-A26F	ns	>0.9999
Row 4		
Beau-R vs. BeauR-T16A	ns	0.8678
Beau-R vs. BeauR-A26F	ns	0.1619
BeauR-T16A vs. BeauR-A26F	ns	0.2054
Row 5		
Beau-R vs. BeauR-T16A	ns	0.8851
Beau-R vs. BeauR-A26F	ns	0.3911
BeauR-T16A vs. BeauR-A26F	ns	0.1136
Row 6		
Beau-R vs. BeauR-T16A	ns	0.8915
Beau-R vs. BeauR-A26F	ns	0.3942
BeauR-T16A vs. BeauR-A26F	ns	0.1548
Row 7		
Beau-R vs. BeauR-T16A	ns	0.5778
Beau-R vs. BeauR-A26F	ns	0.1857
BeauR-T16A vs. BeauR-A26F	ns	0.0792
Row 8		
Beau-R vs. BeauR-T16A	ns	0.8743
Beau-R vs. BeauR-A26F	ns	0.7328
BeauR-T16A vs. BeauR-A26F	ns	0.9322

Table 8.29: Figure 9C, Cell Viability Vero cell 48 hpi

Tukey's multiple comparisons test	Summary	Adjusted P Value
Row 1		
Beau-R vs. BeauR-T16A	ns	0.3964
Beau-R vs. BeauR-A26F	ns	0.4005
BeauR-T16A vs. BeauR-A26F	ns	0.9998
Row 2		
Beau-R vs. BeauR-T16A	ns	0.5656
Beau-R vs. BeauR-A26F	ns	0.5607
BeauR-T16A vs. BeauR-A26F	ns	0.9963
Row 3		
Beau-R vs. BeauR-T16A	ns	0.5967

Beau-R vs. BeauR-A26F	ns	0.5985
BeauR-T16A vs. BeauR-A26F	ns	0.9975
Row 4		
Beau-R vs. BeauR-T16A	ns	0.5406
Beau-R vs. BeauR-A26F	ns	0.6553
BeauR-T16A vs. BeauR-A26F	ns	0.7027
Row 5		
Beau-R vs. BeauR-T16A	ns	0.9601
Beau-R vs. BeauR-A26F	ns	0.9362
BeauR-T16A vs. BeauR-A26F	ns	0.7195
Row 6		
Beau-R vs. BeauR-T16A	ns	0.9850
Beau-R vs. BeauR-A26F	ns	0.9606
BeauR-T16A vs. BeauR-A26F	ns	0.7583
Row 7		
Beau-R vs. BeauR-T16A	ns	0.1763
Beau-R vs. BeauR-A26F	ns	0.0561
BeauR-T16A vs. BeauR-A26F	ns	0.6470
Row 8		
Beau-R vs. BeauR-T16A	ns	0.9697
Beau-R vs. BeauR-A26F	ns	0.9539
BeauR-T16A vs. BeauR-A26F	ns	0.1406

Table 8.30: Figure 9C, Cell Viability Vero cell 72 hpi

Tukey's multiple comparisons test	Summary	Adjusted P Value
Row 1		
Beau-R vs. BeauR-T16A	ns	0.5997
Beau-R vs. BeauR-A26F	*	0.0437
BeauR-T16A vs. BeauR-A26F	ns	0.6337
Row 2		
Beau-R vs. BeauR-T16A	ns	0.4525
Beau-R vs. BeauR-A26F	ns	0.2385
BeauR-T16A vs. BeauR-A26F	ns	0.7640
Row 3		
Beau-R vs. BeauR-T16A	ns	0.3196
Beau-R vs. BeauR-A26F	ns	0.2905
BeauR-T16A vs. BeauR-A26F	ns	0.9608
Row 4		
Beau-R vs. BeauR-T16A	ns	0.3749
Beau-R vs. BeauR-A26F	ns	0.3694
BeauR-T16A vs. BeauR-A26F	ns	0.9990
Row 5		
Beau-R vs. BeauR-T16A	ns	0.7551
Beau-R vs. BeauR-A26F	ns	0.5722
BeauR-T16A vs. BeauR-A26F	ns	0.5875
Row 6		
Beau-R vs. BeauR-T16A	ns	0.8738
Beau-R vs. BeauR-A26F	ns	0.9645
BeauR-T16A vs. BeauR-A26F	ns	0.9611

Row 7		
Beau-R vs. BeauR-T16A	ns	0.9986
Beau-R vs. BeauR-A26F	ns	0.9624
BeauR-T16A vs. BeauR-A26F	ns	0.9714
Row 8		
Beau-R vs. BeauR-T16A	ns	0.9957
Beau-R vs. BeauR-A26F	ns	0.9785
BeauR-T16A vs. BeauR-A26F	ns	0.9914

Table 8.31: Figure 9C, Cell Viability Vero cell 96 hpi

Tukey's multiple comparisons test	Summary	Adjusted P Value
Row 1		
Beau-R vs. BeauR-T16A	**	0.0051
Beau-R vs. BeauR-A26F	*	0.0271
BeauR-T16A vs. BeauR-A26F	ns	0.4418
Row 2		
Beau-R vs. BeauR-T16A	ns	0.1701
Beau-R vs. BeauR-A26F	*	0.0481
BeauR-T16A vs. BeauR-A26F	ns	0.5264
Row 3		
Beau-R vs. BeauR-T16A	ns	0.8099
Beau-R vs. BeauR-A26F	ns	0.3890
BeauR-T16A vs. BeauR-A26F	ns	0.4462
Row 4		
Beau-R vs. BeauR-T16A	ns	0.9562
Beau-R vs. BeauR-A26F	ns	0.8119
BeauR-T16A vs. BeauR-A26F	ns	0.7354
Row 5		
Beau-R vs. BeauR-T16A	ns	0.8667
Beau-R vs. BeauR-A26F	ns	0.8023
BeauR-T16A vs. BeauR-A26F	ns	0.6920
Row 6		
Beau-R vs. BeauR-T16A	ns	0.7242
Beau-R vs. BeauR-A26F	ns	0.7352
BeauR-T16A vs. BeauR-A26F	ns	0.9961
Row 7		
Beau-R vs. BeauR-T16A	ns	0.8639
Beau-R vs. BeauR-A26F	ns	0.5783
BeauR-T16A vs. BeauR-A26F	ns	0.9262
Row 8		
Beau-R vs. BeauR-T16A	ns	0.9816
Beau-R vs. BeauR-A26F	ns	0.8322
BeauR-T16A vs. BeauR-A26F	ns	0.9891

Table 8.32: Figure 10A, BeauR-T16A qPCR E Gene

Tukey's multiple comparisons test	Summary	Adjusted P Value
6		
Mock vs. Beau-R	ns	0.3320
Mock vs. BeauR-T16A-1	ns	0.0715
Mock vs. BeauR-T16A-2	**	0.0094
Mock vs. BeauR-T16A-3	*	0.0273
Beau-R vs. BeauR-T16A-1	ns	0.9011
Beau-R vs. BeauR-T16A-2	ns	0.3811
Beau-R vs. BeauR-T16A-3	ns	0.6663
BeauR-T16A-1 vs. BeauR-T16A-2	ns	0.8705
BeauR-T16A-1 vs. BeauR-T16A-3	ns	0.9894
BeauR-T16A-2 vs. BeauR-T16A-3	ns	0.9874
24		
Mock vs. Beau-R	****	<0.0001
Mock vs. BeauR-T16A-1	****	<0.0001
Mock vs. BeauR-T16A-2	****	<0.0001
Mock vs. BeauR-T16A-3	****	<0.0001
Beau-R vs. BeauR-T16A-1	ns	0.9988
Beau-R vs. BeauR-T16A-2	ns	0.9938
Beau-R vs. BeauR-T16A-3	ns	0.9963
BeauR-T16A-1 vs. BeauR-T16A-2	ns	>0.9999
BeauR-T16A-1 vs. BeauR-T16A-3	ns	>0.9999
BeauR-T16A-2 vs. BeauR-T16A-3	ns	>0.9999

Table 8.33: Figure 10A, BeauR-A26F qPCR E Gene

Tukey's multiple comparisons test	Summary	Adjusted P Value
6		
Mock vs. Beau-R	ns	0.2169
Mock vs. BeauR-A26F-1	**	0.0059
Mock vs. BeauR-A26F-2	*	0.0229
Mock vs. BeauR-A26F-3	*	0.0497
Beau-R vs. BeauR-A26F-1	ns	0.4176
Beau-R vs. BeauR-A26F-2	ns	0.7754
Beau-R vs. BeauR-A26F-3	ns	0.9314
BeauR-A26F-1 vs. BeauR-A26F-2	ns	0.9713
BeauR-A26F-1 vs. BeauR-A26F-3	ns	0.8602
BeauR-A26F-2 vs. BeauR-A26F-3	ns	0.9957
24		
Mock vs. Beau-R	****	<0.0001
Mock vs. BeauR-A26F-1	****	<0.0001
Mock vs. BeauR-A26F-2	****	<0.0001
Mock vs. BeauR-A26F-3	****	<0.0001

Beau-R vs. BeauR-A26F-1	ns	0.9710
Beau-R vs. BeauR-A26F-2	ns	0.9936
Beau-R vs. BeauR-A26F-3	ns	0.9917
BeauR-A26F-1 vs. BeauR-A26F-2	ns	0.9996
BeauR-A26F-1 vs. BeauR-A26F-3	ns	0.9998
BeauR-A26F-2 vs. BeauR-A26F-3	ns	>0.9999

Table 8.34: Figure 10B, BeauR-T16A qPCR IL-6

Tukey's multiple comparisons test	Summary	Adjusted P Value
6		
Mock vs. Beau-R	ns	0.9961
Mock vs. BeauR-T16A-1	ns	>0.9999
Mock vs. BeauR-T16A-2	ns	>0.9999
Mock vs. BeauR-T16A-3	ns	0.9996
Beau-R vs. BeauR-T16A-1	ns	0.9991
Beau-R vs. BeauR-T16A-2	ns	0.9886
Beau-R vs. BeauR-T16A-3	ns	0.9785
BeauR-T16A-1 vs. BeauR-T16A-2	ns	0.9993
BeauR-T16A-1 vs. BeauR-T16A-3	ns	0.9976
BeauR-T16A-2 vs. BeauR-T16A-3	ns	>0.9999
24		
Mock vs. Beau-R	****	<0.0001
Mock vs. BeauR-T16A-1	****	<0.0001
Mock vs. BeauR-T16A-2	****	<0.0001
Mock vs. BeauR-T16A-3	****	<0.0001
Beau-R vs. BeauR-T16A-1	ns	>0.9999
Beau-R vs. BeauR-T16A-2	ns	0.9853
Beau-R vs. BeauR-T16A-3	ns	0.9998
BeauR-T16A-1 vs. BeauR-T16A-2	ns	0.9894
BeauR-T16A-1 vs. BeauR-T16A-3	ns	>0.9999
BeauR-T16A-2 vs. BeauR-T16A-3	ns	0.9969

Table 8.35: Figure 10B, BeauR-A26F qPCR IL-6

Tukey's multiple comparisons test	Summary	Adjusted P Value
6		
Mock vs. Beau-R	ns	0.9967
Mock vs. BeauR-A26F-1	ns	0.9969
Mock vs. BeauR-A26F-2	ns	>0.9999
Mock vs. BeauR-A26F-3	ns	>0.9999
Beau-R vs. BeauR-A26F-1	ns	0.9580
Beau-R vs. BeauR-A26F-2	ns	0.9910
Beau-R vs. BeauR-A26F-3	ns	0.9974
BeauR-A26F-1 vs. BeauR-A26F-2	ns	0.9993
BeauR-A26F-1 vs. BeauR-A26F-3	ns	0.9962
BeauR-A26F-2 vs. BeauR-A26F-3	ns	>0.9999
24		

Mock vs. Beau-R	****	<0.0001
Mock vs. BeauR-A26F-1	****	<0.0001
Mock vs. BeauR-A26F-2	****	<0.0001
Mock vs. BeauR-A26F-3	****	<0.0001
Beau-R vs. BeauR-A26F-1	ns	0.6298
Beau-R vs. BeauR-A26F-2	ns	0.8778
Beau-R vs. BeauR-A26F-3	ns	0.9171
BeauR-A26F-1 vs. BeauR-A26F-2	ns	0.9894
BeauR-A26F-1 vs. BeauR-A26F-3	ns	0.9773
BeauR-A26F-2 vs. BeauR-A26F-3	ns	>0.9999

Table 8.36: Figure 10B, BeauR-T16A qPCR IL-1β

Tukey's multiple comparisons test	Summary	Adjusted P Value
6		
Mock vs. Beau-R	ns	0.7271
Mock vs. BeauR-T16A-1	ns	0.4676
Mock vs. BeauR-T16A-2	ns	0.2624
Mock vs. BeauR-T16A-3	ns	0.1551
Beau-R vs. BeauR-T16A-1	ns	0.9918
Beau-R vs. BeauR-T16A-2	ns	0.9123
Beau-R vs. BeauR-T16A-3	ns	0.7729
BeauR-T16A-1 vs. BeauR-T16A-2	ns	0.9935
BeauR-T16A-1 vs. BeauR-T16A-3	ns	0.9485
BeauR-T16A-2 vs. BeauR-T16A-3	ns	0.9977
24		
Mock vs. Beau-R	*	0.0172
Mock vs. BeauR-T16A-1	**	0.0093
Mock vs. BeauR-T16A-2	**	0.0035
Mock vs. BeauR-T16A-3	**	0.0092
Beau-R vs. BeauR-T16A-1	ns	0.9985
Beau-R vs. BeauR-T16A-2	ns	0.9498
Beau-R vs. BeauR-T16A-3	ns	0.9985
BeauR-T16A-1 vs. BeauR-T16A-2	ns	0.9918
BeauR-T16A-1 vs. BeauR-T16A-3	ns	>0.9999
BeauR-T16A-2 vs. BeauR-T16A-3	ns	0.9920

Table 8.37: Figure 10B, BeauR-A26F qPCR IL-1β

Tukey's multiple comparisons test	Summary	Adjusted P Value
6		
Mock vs. Beau-R	ns	0.5937
Mock vs. BeauR-A26F-1	*	0.0483
Mock vs. BeauR-A26F-2	ns	0.1357
Mock vs. BeauR-A26F-3	ns	0.7041
Beau-R vs. BeauR-A26F-1	ns	0.5494
Beau-R vs. BeauR-A26F-2	ns	0.8476
Beau-R vs. BeauR-A26F-3	ns	0.9997

BeauR-A26F-1 vs. BeauR-A26F-2	ns	0.9831
BeauR-A26F-1 vs. BeauR-A26F-3	ns	0.4416
BeauR-A26F-2 vs. BeauR-A26F-3	ns	0.7541
24		
Mock vs. Beau-R	**	0.0042
Mock vs. BeauR-A26F-1	***	0.0004
Mock vs. BeauR-A26F-2	**	0.0029
Mock vs. BeauR-A26F-3	**	0.0051
Beau-R vs. BeauR-A26F-1	ns	0.8350
Beau-R vs. BeauR-A26F-2	ns	0.9998
Beau-R vs. BeauR-A26F-3	ns	>0.9999
BeauR-A26F-1 vs. BeauR-A26F-2	ns	0.9073
BeauR-A26F-1 vs. BeauR-A26F-3	ns	0.7925
BeauR-A26F-2 vs. BeauR-A26F-3	ns	0.9989

Table 8.38: Figure 10B, BeauR-T16A qPCR IFN-α

Tukey's multiple comparisons test	Summary	Adjusted P Value
6		
Mock vs. Beau-R	ns	0.9640
Mock vs. BeauR-T16A-1	ns	0.9282
Mock vs. BeauR-T16A-2	ns	0.9983
Mock vs. BeauR-T16A-3	ns	>0.9999
Beau-R vs. BeauR-T16A-1	ns	0.9999
Beau-R vs. BeauR-T16A-2	ns	0.9960
Beau-R vs. BeauR-T16A-3	ns	0.9530
BeauR-T16A-1 vs. BeauR-T16A-2	ns	0.9856
BeauR-T16A-1 vs. BeauR-T16A-3	ns	0.9118
BeauR-T16A-2 vs. BeauR-T16A-3	ns	0.9968
24		
Mock vs. Beau-R	****	<0.0001
Mock vs. BeauR-T16A-1	****	<0.0001
Mock vs. BeauR-T16A-2	****	<0.0001
Mock vs. BeauR-T16A-3	****	<0.0001
Beau-R vs. BeauR-T16A-1	ns	0.7018
Beau-R vs. BeauR-T16A-2	ns	0.9871
Beau-R vs. BeauR-T16A-3	ns	0.7561
BeauR-T16A-1 vs. BeauR-T16A-2	ns	0.9294
BeauR-T16A-1 vs. BeauR-T16A-3	ns	>0.9999
BeauR-T16A-2 vs. BeauR-T16A-3	ns	0.9545

Table 8.39: Figure 10B, BeauR-A26F qPCR IFN-α

Tukey's multiple comparisons test	Summary	Adjusted P Value
6		
Mock vs. Beau-R	ns	0.9353
Mock vs. BeauR-A26F-1	ns	0.9994
Mock vs. BeauR-A26F-2	ns	>0.9999

Mock vs. BeauR-A26F-3	ns	0.8245
Beau-R vs. BeauR-A26F-1	ns	0.9810
Beau-R vs. BeauR-A26F-2	ns	0.9179
Beau-R vs. BeauR-A26F-3	ns	0.9984
BeauR-A26F-1 vs. BeauR-A26F-2	ns	0.9985
BeauR-A26F-1 vs. BeauR-A26F-3	ns	0.9171
BeauR-A26F-2 vs. BeauR-A26F-3	ns	0.7959
24		
Mock vs. Beau-R	****	<0.0001
Mock vs. BeauR-A26F-1	****	<0.0001
Mock vs. BeauR-A26F-2	****	<0.0001
Mock vs. BeauR-A26F-3	****	<0.0001
Beau-R vs. BeauR-A26F-1	ns	0.3741
Beau-R vs. BeauR-A26F-2	ns	0.3000
Beau-R vs. BeauR-A26F-3	ns	0.2609
BeauR-A26F-1 vs. BeauR-A26F-2	ns	0.9999
BeauR-A26F-1 vs. BeauR-A26F-3	ns	0.9992
BeauR-A26F-2 vs. BeauR-A26F-3	ns	>0.9999

Table 8.40: Figure 10B, BeauR-T16A qPCR IFN-β

Tukey's multiple comparisons test	Summary	Adjusted P Value
6		
Mock vs. Beau-R	ns	0.7064
Mock vs. BeauR-T16A-1	ns	0.8931
Mock vs. BeauR-T16A-2	ns	0.9659
Mock vs. BeauR-T16A-3	ns	0.9720
Beau-R vs. BeauR-T16A-1	ns	0.9953
Beau-R vs. BeauR-T16A-2	ns	0.9673
Beau-R vs. BeauR-T16A-3	ns	0.3550
BeauR-T16A-1 vs. BeauR-T16A-2	ns	0.9989
BeauR-T16A-1 vs. BeauR-T16A-3	ns	0.5681
BeauR-T16A-2 vs. BeauR-T16A-3	ns	0.7219
24		
Mock vs. Beau-R	****	<0.0001
Mock vs. BeauR-T16A-1	****	<0.0001
Mock vs. BeauR-T16A-2	****	<0.0001
Mock vs. BeauR-T16A-3	****	<0.0001
Beau-R vs. BeauR-T16A-1	ns	0.9993
Beau-R vs. BeauR-T16A-2	ns	0.9536
Beau-R vs. BeauR-T16A-3	ns	0.9766
BeauR-T16A-1 vs. BeauR-T16A-2	ns	0.9894
BeauR-T16A-1 vs. BeauR-T16A-3	ns	0.9967
BeauR-T16A-2 vs. BeauR-T16A-3	ns	>0.9999

Table 8.41: Figure 10B, BeauR-A26F qPCR IFN-β

Tukey's multiple comparisons test	Summary	Adjusted P Value

6		
Mock vs. Beau-R	ns	0.7013
Mock vs. BeauR-A26F-1	ns	0.9896
Mock vs. BeauR-A26F-2	ns	0.9986
Mock vs. BeauR-A26F-3	ns	0.9164
Beau-R vs. BeauR-A26F-1	ns	0.9201
Beau-R vs. BeauR-A26F-2	ns	0.8474
Beau-R vs. BeauR-A26F-3	ns	0.9963
BeauR-A26F-1 vs. BeauR-A26F-2	ns	0.9997
BeauR-A26F-1 vs. BeauR-A26F-3	ns	0.9938
BeauR-A26F-2 vs. BeauR-A26F-3	ns	0.9767
24		
Mock vs. Beau-R	****	<0.0001
Mock vs. BeauR-A26F-1	****	<0.0001
Mock vs. BeauR-A26F-2	****	<0.0001
Mock vs. BeauR-A26F-3	****	<0.0001
Beau-R vs. BeauR-A26F-1	ns	0.7793
Beau-R vs. BeauR-A26F-2	ns	0.9022
Beau-R vs. BeauR-A26F-3	ns	0.9790
BeauR-A26F-1 vs. BeauR-A26F-2	ns	0.9987
BeauR-A26F-1 vs. BeauR-A26F-3	ns	0.9755
BeauR-A26F-2 vs. BeauR-A26F-3	ns	0.9977

8.5.2. Chapter 4

Table 8.42: Figure 4.2.A, E Protein Expression

Tukey's multiple comparisons test	Summary	Adjusted P Value
Mock vs. Beau-R	***	0.0006
Mock vs. M41-CK	***	0.0002
Beau-R vs. M41-CK	ns	0.1402

Table 8.43: Figure 4.2.B, N Protein Expression

Tukey's multiple comparisons test	Summary	Adjusted P Value
Mock vs. Beau-R	****	<0.0001
Mock vs. M41-CK	****	<0.0001
Beau-R vs. M41-CK	ns	0.9998

Table 8.44: Figure 4.9.B, M41K-T16A Plaque Size

Tukey's multiple comparisons test	Summary	Adjusted P Value
M41K vs. M41K-T16A-2.3	****	<0.0001
M41K vs. M41K-T16A-2.6	ns	0.0555

M41K vs. M41K-T16A-8.3	ns	0.8145
M41K-T16A-2.3 vs. M41K-T16A-2.6	****	<0.0001
M41K-T16A-2.3 vs. M41K-T16A-8.3	****	<0.0001
M41K-T16A-2.6 vs. M41K-T16A-8.3	ns	0.1590

Table 8.45: Figure 4.10, M41K-T16A Multi-Step Replication Kinetics CK cells

Tukey's multiple comparisons test	Summary	Adjusted P Value
Row 1		
M41K vs. M41K T16A 2.3	ns	0.7683
M41K vs. M41K T16A 2.6	ns	0.7683
M41K vs. M41K T16A 8.3	ns	0.7683
M41K T16A 2.3 vs. M41K T16A 2.6		
M41K T16A 2.3 vs. M41K T16A 8.3		
M41K T16A 2.6 vs. M41K T16A 8.3		
Row 2		
M41K vs. M41K T16A 2.3	ns	0.6673
M41K vs. M41K T16A 2.6	ns	0.9705
M41K vs. M41K T16A 8.3	ns	>0.9999
M41K T16A 2.3 vs. M41K T16A 2.6	ns	0.1432
M41K T16A 2.3 vs. M41K T16A 8.3	ns	0.2598
M41K T16A 2.6 vs. M41K T16A 8.3	ns	0.7430
Row 3		
M41K vs. M41K T16A 2.3	*	0.0102
M41K vs. M41K T16A 2.6	ns	0.9991
M41K vs. M41K T16A 8.3	ns	0.9740
M41K T16A 2.3 vs. M41K T16A 2.6	***	0.0004
M41K T16A 2.3 vs. M41K T16A 8.3	***	0.0007
M41K T16A 2.6 vs. M41K T16A 8.3	ns	0.9830
Row 4		
M41K vs. M41K T16A 2.3	ns	0.0670
M41K vs. M41K T16A 2.6	ns	0.1960
M41K vs. M41K T16A 8.3	ns	0.9991
M41K T16A 2.3 vs. M41K T16A 2.6	ns	0.1602
M41K T16A 2.3 vs. M41K T16A 8.3	ns	0.0754
M41K T16A 2.6 vs. M41K T16A 8.3	ns	0.1184
Row 5		
M41K vs. M41K T16A 2.3	ns	0.4274
M41K vs. M41K T16A 2.6	ns	0.1013
M41K vs. M41K T16A 8.3	ns	0.6553
M41K T16A 2.3 vs. M41K T16A 2.6	ns	0.6867
M41K T16A 2.3 vs. M41K T16A 8.3	ns	0.3476
M41K T16A 2.6 vs. M41K T16A 8.3	ns	0.0521

Table 8.46: Figure 4.11, M41K-T16A Replication *in ovo*

Tukey's multiple comparisons test	Summary	Adjusted P Value
M41-K-T16A-2.6 vs. M41-K-T16A-2.3	****	<0.0001

M41-K-T16A-2.6 vs. M41-K-T16A-8.3	**	0.0035
M41-K-T16A-2.6 vs. M41-K	*	0.0197
M41-K-T16A-2.3 vs. M41-K-T16A-8.3	*	0.0194
M41-K-T16A-2.3 vs. M41-K	****	<0.0001
M41-K-T16A-8.3 vs. M41-K	****	<0.0001

Table 8.47: Figure 4.13, M41K-T16A Cell Viability 24 hr

Tukey's multiple comparisons test	Summary	Adjusted P Value
Row 1		
M41K vs. M41K-T16A-2.3	ns	0.9838
M41K vs. M41K-T16A-2.6	ns	0.6678
M41K vs. M41K-T16A-8.3	ns	0.9846
M41K-T16A-2.3 vs. M41K-T16A-2.6	ns	0.2493
M41K-T16A-2.3 vs. M41K-T16A-8.3	ns	0.9999
M41K-T16A-2.6 vs. M41K-T16A-8.3	ns	0.4728
Row 2		
M41K vs. M41K-T16A-2.3	ns	0.8869
M41K vs. M41K-T16A-2.6	ns	0.8438
M41K vs. M41K-T16A-8.3	ns	0.9718
M41K-T16A-2.3 vs. M41K-T16A-2.6	ns	0.9927
M41K-T16A-2.3 vs. M41K-T16A-8.3	ns	0.7995
M41K-T16A-2.6 vs. M41K-T16A-8.3	ns	0.6250
Row 3		
M41K vs. M41K-T16A-2.3	ns	0.9980
M41K vs. M41K-T16A-2.6	ns	0.1177
M41K vs. M41K-T16A-8.3	ns	0.9023
M41K-T16A-2.3 vs. M41K-T16A-2.6	ns	0.1389
M41K-T16A-2.3 vs. M41K-T16A-8.3	ns	0.8653
M41K-T16A-2.6 vs. M41K-T16A-8.3	ns	0.6431
Row 4		
M41K vs. M41K-T16A-2.3	ns	0.9954
M41K vs. M41K-T16A-2.6	ns	0.5606
M41K vs. M41K-T16A-8.3	ns	0.6227
M41K-T16A-2.3 vs. M41K-T16A-2.6	ns	0.4884
M41K-T16A-2.3 vs. M41K-T16A-8.3	ns	0.5650
M41K-T16A-2.6 vs. M41K-T16A-8.3	ns	0.9922
Row 5		
M41K vs. M41K-T16A-2.3	ns	0.9072
M41K vs. M41K-T16A-2.6	ns	0.9383
M41K vs. M41K-T16A-8.3	ns	0.9561
M41K-T16A-2.3 vs. M41K-T16A-2.6	ns	0.9956
M41K-T16A-2.3 vs. M41K-T16A-8.3	ns	0.4533
M41K-T16A-2.6 vs. M41K-T16A-8.3	ns	0.3284
Row 6		
M41K vs. M41K-T16A-2.3	ns	0.9410
M41K vs. M41K-T16A-2.6	ns	0.8265
M41K vs. M41K-T16A-8.3	ns	0.5261
M41K-T16A-2.3 vs. M41K-T16A-2.6	ns	0.2231
M41K-T16A-2.3 vs. M41K-T16A-8.3	ns	0.4914

M41K-T16A-2.6 vs. M41K-T16A-8.3	*	0.0380
Row 7		
M41K vs. M41K-T16A-2.3	ns	0.9803
M41K vs. M41K-T16A-2.6	ns	0.9998
M41K vs. M41K-T16A-8.3	ns	0.9996
M41K-T16A-2.3 vs. M41K-T16A-2.6	ns	0.9630
M41K-T16A-2.3 vs. M41K-T16A-8.3	ns	0.9992
M41K-T16A-2.6 vs. M41K-T16A-8.3	ns	0.9988

Table 8.48: Figure 4.13, M41K-T16A Cell Viability 48 hr

Tukey's multiple comparisons test	Summary	Adjusted P Value
Row 1		
M41K vs. M41K-T16A-2.3	ns	0.8225
M41K vs. M41K-T16A-2.6	ns	0.8754
M41K vs. M41K-T16A-8.3	ns	0.9789
M41K-T16A-2.3 vs. M41K-T16A-2.6	*	0.0480
M41K-T16A-2.3 vs. M41K-T16A-8.3	ns	0.8753
M41K-T16A-2.6 vs. M41K-T16A-8.3	ns	0.3886
Row 2		
M41K vs. M41K-T16A-2.3	ns	0.9925
M41K vs. M41K-T16A-2.6	ns	0.3478
M41K vs. M41K-T16A-8.3	ns	0.8853
M41K-T16A-2.3 vs. M41K-T16A-2.6	ns	0.5991
M41K-T16A-2.3 vs. M41K-T16A-8.3	ns	0.9728
M41K-T16A-2.6 vs. M41K-T16A-8.3	ns	0.8623
Row 3		
M41K vs. M41K-T16A-2.3	ns	0.7271
M41K vs. M41K-T16A-2.6	*	0.0187
M41K vs. M41K-T16A-8.3	ns	0.6364
M41K-T16A-2.3 vs. M41K-T16A-2.6	*	0.0245
M41K-T16A-2.3 vs. M41K-T16A-8.3	ns	0.5524
M41K-T16A-2.6 vs. M41K-T16A-8.3	ns	0.7689
Row 4		
M41K vs. M41K-T16A-2.3	ns	0.9415
M41K vs. M41K-T16A-2.6	ns	0.0717
M41K vs. M41K-T16A-8.3	ns	0.4768
M41K-T16A-2.3 vs. M41K-T16A-2.6	ns	0.0743
M41K-T16A-2.3 vs. M41K-T16A-8.3	ns	0.6243
M41K-T16A-2.6 vs. M41K-T16A-8.3	ns	0.1144
Row 5		
M41K vs. M41K-T16A-2.3	ns	0.4100
M41K vs. M41K-T16A-2.6	ns	0.9794
M41K vs. M41K-T16A-8.3	ns	0.6579
M41K-T16A-2.3 vs. M41K-T16A-2.6	ns	0.2702
M41K-T16A-2.3 vs. M41K-T16A-8.3	ns	0.8919
M41K-T16A-2.6 vs. M41K-T16A-8.3	ns	0.4455
Row 6		
M41K vs. M41K-T16A-2.3	ns	0.9765
M41K vs. M41K-T16A-2.6	ns	0.6215

M41K vs. M41K-T16A-8.3	ns	>0.9999
M41K-T16A-2.3 vs. M41K-T16A-2.6	ns	0.4210
M41K-T16A-2.3 vs. M41K-T16A-8.3	ns	0.9592
M41K-T16A-2.6 vs. M41K-T16A-8.3	ns	0.5809
Row 7		
M41K vs. M41K-T16A-2.3	ns	0.9959
M41K vs. M41K-T16A-2.6	*	0.0339
M41K vs. M41K-T16A-8.3	ns	0.9077
M41K-T16A-2.3 vs. M41K-T16A-2.6	ns	0.2690
M41K-T16A-2.3 vs. M41K-T16A-8.3	ns	0.9721
M41K-T16A-2.6 vs. M41K-T16A-8.3	ns	0.6032

Table 8.49: Figure 4.13, M41K-T16A Cell Viability 72 hr

Tukey's multiple comparisons test	Summary	Adjusted P Value
Row 1		
M41K vs. M41K-T16A-2.3	ns	0.3419
M41K vs. M41K-T16A-2.6	ns	0.5734
M41K vs. M41K-T16A-8.3	ns	0.5116
M41K-T16A-2.3 vs. M41K-T16A-2.6	ns	0.4030
M41K-T16A-2.3 vs. M41K-T16A-8.3	ns	0.5636
M41K-T16A-2.6 vs. M41K-T16A-8.3	ns	0.7493
Row 2		
M41K vs. M41K-T16A-2.3	ns	0.0870
M41K vs. M41K-T16A-2.6	ns	0.9408
M41K vs. M41K-T16A-8.3	ns	0.2611
M41K-T16A-2.3 vs. M41K-T16A-2.6	ns	0.0930
M41K-T16A-2.3 vs. M41K-T16A-8.3	ns	0.1377
M41K-T16A-2.6 vs. M41K-T16A-8.3	ns	0.2014
Row 3		
M41K vs. M41K-T16A-2.3	ns	0.9747
M41K vs. M41K-T16A-2.6	ns	0.2558
M41K vs. M41K-T16A-8.3	ns	0.9558
M41K-T16A-2.3 vs. M41K-T16A-2.6	ns	0.8910
M41K-T16A-2.3 vs. M41K-T16A-8.3	ns	0.9898
M41K-T16A-2.6 vs. M41K-T16A-8.3	ns	0.3811
Row 4		
M41K vs. M41K-T16A-2.3	ns	0.3752
M41K vs. M41K-T16A-2.6	ns	0.9950
M41K vs. M41K-T16A-8.3	ns	0.5281
M41K-T16A-2.3 vs. M41K-T16A-2.6	ns	0.3957
M41K-T16A-2.3 vs. M41K-T16A-8.3	ns	0.6005
M41K-T16A-2.6 vs. M41K-T16A-8.3	ns	0.2207
Row 5		
M41K vs. M41K-T16A-2.3	ns	0.3824
M41K vs. M41K-T16A-2.6	ns	0.7066
M41K vs. M41K-T16A-8.3	ns	0.9908
M41K-T16A-2.3 vs. M41K-T16A-2.6	ns	0.2062
M41K-T16A-2.3 vs. M41K-T16A-8.3	ns	0.2884
M41K-T16A-2.6 vs. M41K-T16A-8.3	ns	0.3446

Row 6		
M41K vs. M41K-T16A-2.3	ns	0.7573
M41K vs. M41K-T16A-2.6	ns	0.0724
M41K vs. M41K-T16A-8.3	ns	0.8712
M41K-T16A-2.3 vs. M41K-T16A-2.6	ns	0.3677
M41K-T16A-2.3 vs. M41K-T16A-8.3	ns	0.6210
M41K-T16A-2.6 vs. M41K-T16A-8.3	ns	0.5628
Row 7		
M41K vs. M41K-T16A-2.3	*	0.0341
M41K vs. M41K-T16A-2.6	ns	0.9252
M41K vs. M41K-T16A-8.3	ns	0.3283
M41K-T16A-2.3 vs. M41K-T16A-2.6	*	0.0384
M41K-T16A-2.3 vs. M41K-T16A-8.3	ns	0.1258
M41K-T16A-2.6 vs. M41K-T16A-8.3	ns	0.3368

Table 8.50: Figure 4.13, M41K-T16A Cell Viability 96 hr

Tukey's multiple comparisons test	Summary	Adjusted P Value
Row 1		
M41K vs. M41K-T16A-2.3	ns	0.1068
M41K vs. M41K-T16A-2.6	ns	0.9933
M41K vs. M41K-T16A-8.3	ns	0.8462
M41K-T16A-2.3 vs. M41K-T16A-2.6	ns	0.1096
M41K-T16A-2.3 vs. M41K-T16A-8.3	ns	0.2468
M41K-T16A-2.6 vs. M41K-T16A-8.3	ns	0.9406
Row 2		
M41K vs. M41K-T16A-2.3	ns	0.0955
M41K vs. M41K-T16A-2.6	ns	0.9272
M41K vs. M41K-T16A-8.3	ns	0.8545
M41K-T16A-2.3 vs. M41K-T16A-2.6	ns	0.2380
M41K-T16A-2.3 vs. M41K-T16A-8.3	ns	0.7757
M41K-T16A-2.6 vs. M41K-T16A-8.3	ns	0.9686
Row 3		
M41K vs. M41K-T16A-2.3	ns	0.1123
M41K vs. M41K-T16A-2.6	ns	0.9058
M41K vs. M41K-T16A-8.3	ns	0.5679
M41K-T16A-2.3 vs. M41K-T16A-2.6	ns	0.1595
M41K-T16A-2.3 vs. M41K-T16A-8.3	ns	0.9789
M41K-T16A-2.6 vs. M41K-T16A-8.3	ns	0.7437
Row 4		
M41K vs. M41K-T16A-2.3	ns	0.1779
M41K vs. M41K-T16A-2.6	ns	0.6476
M41K vs. M41K-T16A-8.3	ns	0.9999
M41K-T16A-2.3 vs. M41K-T16A-2.6	ns	0.0726
M41K-T16A-2.3 vs. M41K-T16A-8.3	ns	0.0632
M41K-T16A-2.6 vs. M41K-T16A-8.3	ns	0.4815
Row 5		
M41K vs. M41K-T16A-2.3	ns	0.2519
M41K vs. M41K-T16A-2.6	ns	0.9906
M41K vs. M41K-T16A-8.3	ns	0.9858

M41K-T16A-2.3 vs. M41K-T16A-2.6	ns	0.2175
M41K-T16A-2.3 vs. M41K-T16A-8.3	ns	0.2958
M41K-T16A-2.6 vs. M41K-T16A-8.3	ns	0.8844
Row 6		
M41K vs. M41K-T16A-2.3	ns	0.2078
M41K vs. M41K-T16A-2.6	ns	0.9973
M41K vs. M41K-T16A-8.3	ns	0.6052
M41K-T16A-2.3 vs. M41K-T16A-2.6	ns	0.2817
M41K-T16A-2.3 vs. M41K-T16A-8.3	ns	0.9999
M41K-T16A-2.6 vs. M41K-T16A-8.3	ns	0.6610
Row 7		
M41K vs. M41K-T16A-2.3	ns	0.6769
M41K vs. M41K-T16A-2.6	ns	0.9933
M41K vs. M41K-T16A-8.3	ns	0.9998
M41K-T16A-2.3 vs. M41K-T16A-2.6	ns	0.5178
M41K-T16A-2.3 vs. M41K-T16A-8.3	ns	0.5476
M41K-T16A-2.6 vs. M41K-T16A-8.3	ns	0.9876

Table 8.51: Figure 4.14.B, M41K-T16A E protein

Tukey's multiple comparisons test	Summary	Adjusted P Value
Mock vs. M41-K	ns	0.4114
Mock vs. M41K-T16A-2.3	ns	0.3370
Mock vs. M41K-T16A-2.6	**	0.0015
Mock vs. M41K-T16A-8.3	ns	0.2959
M41-K vs. M41K-T16A-2.3	ns	0.9998
M41-K vs. M41K-T16A-2.6	*	0.0207
M41-K vs. M41K-T16A-8.3	ns	0.9988
M41K-T16A-2.3 vs. M41K-T16A-2.6	*	0.0266
M41K-T16A-2.3 vs. M41K-T16A-8.3	ns	>0.9999
M41K-T16A-2.6 vs. M41K-T16A-8.3	*	0.0311

Table 8.52: Figure 4.14.B, M41K-T16A S2 protein

Tukey's multiple comparisons test	Summary	Adjusted P Value
Mock vs. M41-K	****	<0.0001
Mock vs. M41K-T16A-2.3	***	0.0001
Mock vs. M41K-T16A-2.6	****	<0.0001
Mock vs. M41K-T16A-8.3	***	0.0001
M41-K vs. M41K-T16A-2.3	ns	0.9461
M41-K vs. M41K-T16A-2.6	ns	0.9902
M41-K vs. M41K-T16A-8.3	ns	0.9038
M41K-T16A-2.3 vs. M41K-T16A-2.6	ns	0.7656
M41K-T16A-2.3 vs. M41K-T16A-8.3	ns	0.9999
M41K-T16A-2.6 vs. M41K-T16A-8.3	ns	0.6897

Table 8.53: Figure 4.15, M41K-T16A Thermal Stability

Tukey's multiple comparisons test	Summary	Adjusted P Value
37		
M41K vs. M41K-T16A-2.3	ns	0.7964
M41K vs. M41K-T16A-2.6	ns	0.5919
M41K vs. M41K-T16A-8.3	ns	0.8436
M41K-T16A-2.3 vs. M41K-T16A-2.6	ns	0.6373
M41K-T16A-2.3 vs. M41K-T16A-8.3	ns	>0.9999
M41K-T16A-2.6 vs. M41K-T16A-8.3	ns	0.7897
39		
M41K vs. M41K-T16A-2.3	ns	0.5573
M41K vs. M41K-T16A-2.6	ns	0.5577
M41K vs. M41K-T16A-8.3	ns	0.7291
M41K-T16A-2.3 vs. M41K-T16A-2.6	ns	>0.9999
M41K-T16A-2.3 vs. M41K-T16A-8.3	ns	0.6630
M41K-T16A-2.6 vs. M41K-T16A-8.3	ns	0.2745
41		
M41K vs. M41K-T16A-2.3	ns	0.7201
M41K vs. M41K-T16A-2.6	ns	0.7139
M41K vs. M41K-T16A-8.3	ns	0.3575
M41K-T16A-2.3 vs. M41K-T16A-2.6	ns	0.9997
M41K-T16A-2.3 vs. M41K-T16A-8.3	ns	0.9443
M41K-T16A-2.6 vs. M41K-T16A-8.3	ns	0.8995
43		
M41K vs. M41K-T16A-2.3	ns	>0.9999
M41K vs. M41K-T16A-2.6	ns	0.1501
M41K vs. M41K-T16A-8.3	ns	0.6190
M41K-T16A-2.3 vs. M41K-T16A-2.6	ns	0.5694
M41K-T16A-2.3 vs. M41K-T16A-8.3	ns	0.8092
M41K-T16A-2.6 vs. M41K-T16A-8.3	ns	0.8723
45		
M41K vs. M41K-T16A-2.3	ns	>0.9999
M41K vs. M41K-T16A-2.6	ns	0.0983
M41K vs. M41K-T16A-8.3	ns	0.6244
M41K-T16A-2.3 vs. M41K-T16A-2.6	ns	0.8370
M41K-T16A-2.3 vs. M41K-T16A-8.3	ns	0.9080
M41K-T16A-2.6 vs. M41K-T16A-8.3	ns	0.9906

8.5.3. Chapter 5

Table 8.54: Figure 5.11, Golgi Diffusion in Vero cells

Tukey's multiple comparisons test	Summary		Adjusted P Value
Mock vs. BeauR-T16A	ns		0.2081
Mock vs. Beau-R	****		<0.0001
Mock vs. BeauR-A26F	****		<0.0001
BeauR-T16A vs. Beau-R	****		<0.0001

BeauR-T16A vs. BeauR-A26F	****		<0.0001
Beau-R vs. BeauR-A26F	ns		0.7288

Table 8.55: Figure 5.15B, E Expression relative to β-actin

Tukey's multiple comparisons test	Summary	Adjusted P Value
Mock vs. Beau-R	ns	0.4214
Mock vs. BeauR-T16A-3.4	ns	0.1998
Mock vs. BeauR-T16A-3.6	ns	0.2375
Mock vs. BeauR-T16A-4.7	ns	0.2988
Mock vs. BeauR-T16A-4.9	ns	0.2360
Mock vs. BeauR-A26F-11.2	ns	0.5466
Mock vs. BeauR-A26F-11.3	ns	0.3059
Mock vs. BeauR-A26F-12.3	ns	0.3918
Beau-R vs. BeauR-T16A-3.4	ns	>0.9999
Beau-R vs. BeauR-T16A-3.6	ns	0.8241
Beau-R vs. BeauR-T16A-4.7	ns	0.9229
Beau-R vs. BeauR-T16A-4.9	ns	0.9988
Beau-R vs. BeauR-A26F-11.2	ns	0.9881
Beau-R vs. BeauR-A26F-11.3	ns	0.9866
Beau-R vs. BeauR-A26F-12.3	ns	0.8983
BeauR-T16A-3.4 vs. BeauR-T16A-3.6	ns	0.2272
BeauR-T16A-3.4 vs. BeauR-T16A-4.7	ns	0.9910
BeauR-T16A-3.4 vs. BeauR-T16A-4.9	ns	0.9921
BeauR-T16A-3.4 vs. BeauR-A26F-11.2	ns	0.6420
BeauR-T16A-3.4 vs. BeauR-A26F-11.3	ns	0.6085
BeauR-T16A-3.4 vs. BeauR-A26F-12.3	ns	0.5499
BeauR-T16A-3.6 vs. BeauR-T16A-4.7	ns	0.7977
BeauR-T16A-3.6 vs. BeauR-T16A-4.9	ns	0.3556
BeauR-T16A-3.6 vs. BeauR-A26F-11.2	ns	>0.9999
BeauR-T16A-3.6 vs. BeauR-A26F-11.3	ns	>0.9999
BeauR-T16A-3.6 vs. BeauR-A26F-12.3	ns	0.9027
BeauR-T16A-4.7 vs. BeauR-T16A-4.9	ns	0.9888
BeauR-T16A-4.7 vs. BeauR-A26F-11.2	ns	0.9985
BeauR-T16A-4.7 vs. BeauR-A26F-11.3	ns	0.9972
BeauR-T16A-4.7 vs. BeauR-A26F-12.3	ns	0.9951
BeauR-T16A-4.9 vs. BeauR-A26F-11.2	ns	0.9811
BeauR-T16A-4.9 vs. BeauR-A26F-11.3	ns	0.9694
BeauR-T16A-4.9 vs. BeauR-A26F-12.3	ns	0.6978
BeauR-A26F-11.2 vs. BeauR-A26F-11.3	ns	>0.9999
BeauR-A26F-11.2 vs. BeauR-A26F-12.3	ns	0.9997
BeauR-A26F-11.3 vs. BeauR-A26F-12.3	ns	0.9997

Table 8.56: Figure 5.15.B, S2 Expression relative to β-actin

Tukey's multiple comparisons test	Summary	Adjusted P Value
Mock vs. Beau-R	**	0.0018
Mock vs. BeauR-T16A-3.4	*	0.0236

Mock vs. BeauR-T16A-3.6	ns	0.1592
Mock vs. BeauR-T16A-4.7	ns	0.1052
Mock vs. BeauR-T16A-4.9	**	0.0054
Mock vs. BeauR-A26F-11.2	ns	0.5568
Mock vs. BeauR-A26F-11.3	ns	0.8074
Mock vs. BeauR-A26F-12.3	ns	0.4772
Beau-R vs. BeauR-T16A-3.4	ns	0.9327
Beau-R vs. BeauR-T16A-3.6	ns	0.4148
Beau-R vs. BeauR-T16A-4.7	ns	0.5488
Beau-R vs. BeauR-T16A-4.9	ns	0.9997
Beau-R vs. BeauR-A26F-11.2	ns	0.1026
Beau-R vs. BeauR-A26F-11.3	*	0.0447
Beau-R vs. BeauR-A26F-12.3	ns	0.1309
BeauR-T16A-3.4 vs. BeauR-T16A-3.6	ns	0.9808
BeauR-T16A-3.4 vs. BeauR-T16A-4.7	ns	0.9965
BeauR-T16A-3.4 vs. BeauR-T16A-4.9	ns	0.9978
BeauR-T16A-3.4 vs. BeauR-A26F-11.2	ns	0.6387
BeauR-T16A-3.4 vs. BeauR-A26F-11.3	ns	0.3860
BeauR-T16A-3.4 vs. BeauR-A26F-12.3	ns	0.7181
BeauR-T16A-3.6 vs. BeauR-T16A-4.7	ns	>0.9999
BeauR-T16A-3.6 vs. BeauR-T16A-4.9	ns	0.7292
BeauR-T16A-3.6 vs. BeauR-A26F-11.2	ns	0.9920
BeauR-T16A-3.6 vs. BeauR-A26F-11.3	ns	0.9166
BeauR-T16A-3.6 vs. BeauR-A26F-12.3	ns	0.9974
BeauR-T16A-4.7 vs. BeauR-T16A-4.9	ns	0.8484
BeauR-T16A-4.7 vs. BeauR-A26F-11.2	ns	0.9662
BeauR-T16A-4.7 vs. BeauR-A26F-11.3	ns	0.8231
BeauR-T16A-4.7 vs. BeauR-A26F-12.3	ns	0.9843
BeauR-T16A-4.9 vs. BeauR-A26F-11.2	ns	0.2566
BeauR-T16A-4.9 vs. BeauR-A26F-11.3	ns	0.1231
BeauR-T16A-4.9 vs. BeauR-A26F-12.3	ns	0.3146
BeauR-A26F-11.2 vs. BeauR-A26F-11.3	ns	>0.9999
BeauR-A26F-11.2 vs. BeauR-A26F-12.3	ns	>0.9999
BeauR-A26F-11.3 vs. BeauR-A26F-12.3	ns	0.9996

Table 8.57: Figure 5.15.B, E expression relative to S

Tukey's multiple comparisons test	Summary	Adjusted P Value
Beau-R vs. BeauR-T16A-3.4	ns	0.9900
Beau-R vs. BeauR-T16A-3.6	ns	0.9677
Beau-R vs. BeauR-T16A-4.7	ns	0.9998
Beau-R vs. BeauR-T16A-4.9	ns	>0.9999
Beau-R vs. BeauR-A26F-11.2	ns	0.9989
Beau-R vs. BeauR-A26F-11.3	ns	>0.9999
Beau-R vs. BeauR-A26F-12.3	ns	0.9998
BeauR-T16A-3.4 vs. BeauR-T16A-3.6	ns	0.6233
BeauR-T16A-3.4 vs. BeauR-T16A-4.7	ns	0.9071
BeauR-T16A-3.4 vs. BeauR-T16A-4.9	ns	0.9955
BeauR-T16A-3.4 vs. BeauR-A26F-11.2	ns	0.8575
BeauR-T16A-3.4 vs. BeauR-A26F-11.3	ns	0.9595

BeauR-T16A-3.4 vs. BeauR-A26F-12.3	ns	>0.9999
BeauR-T16A-3.6 vs. BeauR-T16A-4.7	ns	0.9989
BeauR-T16A-3.6 vs. BeauR-T16A-4.9	ns	0.9472
BeauR-T16A-3.6 vs. BeauR-A26F-11.2	ns	0.9998
BeauR-T16A-3.6 vs. BeauR-A26F-11.3	ns	0.9929
BeauR-T16A-3.6 vs. BeauR-A26F-12.3	ns	0.8361
BeauR-T16A-4.7 vs. BeauR-T16A-4.9	ns	0.9992
BeauR-T16A-4.7 vs. BeauR-A26F-11.2	ns	>0.9999
BeauR-T16A-4.7 vs. BeauR-A26F-11.3	ns	>0.9999
BeauR-T16A-4.7 vs. BeauR-A26F-12.3	ns	0.9866
BeauR-T16A-4.9 vs. BeauR-A26F-11.2	ns	0.9969
BeauR-T16A-4.9 vs. BeauR-A26F-11.3	ns	>0.9999
BeauR-T16A-4.9 vs. BeauR-A26F-12.3	ns	>0.9999
BeauR-A26F-11.2 vs. BeauR-A26F-11.3	ns	>0.9999
BeauR-A26F-11.2 vs. BeauR-A26F-12.3	ns	0.9710
BeauR-A26F-11.3 vs. BeauR-A26F-12.3	ns	0.9972

Table 8.58: Figure 5.15.B, S2 expression relative to S

Tukey's multiple comparisons test	Summary	Adjusted P Value
Beau-R vs. BeauR-T16A-3.4	ns	>0.9999
Beau-R vs. BeauR-T16A-3.6	ns	0.7581
Beau-R vs. BeauR-T16A-4.7	ns	0.6624
Beau-R vs. BeauR-T16A-4.9	ns	>0.9999
Beau-R vs. BeauR-A26F-11.2	ns	0.9337
Beau-R vs. BeauR-A26F-11.3	ns	0.4286
Beau-R vs. BeauR-A26F-12.3	ns	0.9814
BeauR-T16A-3.4 vs. BeauR-T16A-3.6	ns	0.8193
BeauR-T16A-3.4 vs. BeauR-T16A-4.7	ns	0.7311
BeauR-T16A-3.4 vs. BeauR-T16A-4.9	ns	>0.9999
BeauR-T16A-3.4 vs. BeauR-A26F-11.2	ns	0.9615
BeauR-T16A-3.4 vs. BeauR-A26F-11.3	ns	0.4951
BeauR-T16A-3.4 vs. BeauR-A26F-12.3	ns	0.9917
BeauR-T16A-3.6 vs. BeauR-T16A-4.7	ns	>0.9999
BeauR-T16A-3.6 vs. BeauR-T16A-4.9	ns	0.7910
BeauR-T16A-3.6 vs. BeauR-A26F-11.2	ns	0.9998
BeauR-T16A-3.6 vs. BeauR-A26F-11.3	ns	0.9988
BeauR-T16A-3.6 vs. BeauR-A26F-12.3	ns	0.9967
BeauR-T16A-4.7 vs. BeauR-T16A-4.9	ns	0.6988
BeauR-T16A-4.7 vs. BeauR-A26F-11.2	ns	0.9986
BeauR-T16A-4.7 vs. BeauR-A26F-11.3	ns	0.9999
BeauR-T16A-4.7 vs. BeauR-A26F-12.3	ns	0.9876
BeauR-T16A-4.9 vs. BeauR-A26F-11.2	ns	0.9495
BeauR-T16A-4.9 vs. BeauR-A26F-11.3	ns	0.4629
BeauR-T16A-4.9 vs. BeauR-A26F-12.3	ns	0.9876
BeauR-A26F-11.2 vs. BeauR-A26F-11.3	ns	0.9691
BeauR-A26F-11.2 vs. BeauR-A26F-12.3	ns	>0.9999
BeauR-A26F-11.3 vs. BeauR-A26F-12.3	ns	0.9065

Table 8.59: Figure 5.19, Preliminary Inhibitor Screen

Tukey's multiple comparisons test	Summary	Adjusted P Value
Beau-R Cell Lysate		
Mock vs. DMSO	ns	0.9807
Mock vs. IMP-1088	ns	0.9618
Mock vs. BFA	****	<0.0001
Mock vs. Exo1	ns	0.9950
Mock vs. ES2	ns	>0.9999
Mock vs. Fli-06	****	<0.0001
Mock vs. Blebbistatin	ns	0.9107
Mock vs. Paprotrain	ns	>0.9999
Mock vs. Monensin	ns	0.9204
DMSO vs. IMP-1088	ns	>0.9999
DMSO vs. BFA	****	<0.0001
DMSO vs. Exo1	ns	>0.9999
DMSO vs. ES2	ns	0.9815
DMSO vs. Fli-06	****	<0.0001
DMSO vs. Blebbistatin	ns	>0.9999
DMSO vs. Paprotrain	ns	0.9452
DMSO vs. Monensin	ns	>0.9999
IMP-1088 vs. BFA	****	<0.0001
IMP-1088 vs. Exo1	ns	>0.9999
IMP-1088 vs. ES2	ns	0.9632
IMP-1088 vs. Fli-06	***	0.0001
IMP-1088 vs. Blebbistatin	ns	>0.9999
IMP-1088 vs. Paprotrain	ns	0.9084
IMP-1088 vs. Monensin	ns	>0.9999
BFA vs. Exo1	****	<0.0001
BFA vs. ES2	****	<0.0001
BFA vs. Fli-06	ns	0.5872
BFA vs. Blebbistatin	****	<0.0001
BFA vs. Paprotrain	****	<0.0001
BFA vs. Monensin	****	<0.0001
Exo1 vs. ES2	ns	0.9952
Exo1 vs. Fli-06	****	<0.0001
Exo1 vs. Blebbistatin	ns	>0.9999
Exo1 vs. Paprotrain	ns	0.9798
Exo1 vs. Monensin	ns	>0.9999
ES2 vs. Fli-06	****	<0.0001
ES2 vs. Blebbistatin	ns	0.9132
ES2 vs. Paprotrain	ns	>0.9999
ES2 vs. Monensin	ns	0.9227
Fli-06 vs. Blebbistatin	***	0.0002
Fli-06 vs. Paprotrain	****	<0.0001
Fli-06 vs. Monensin	***	0.0002
Blebbistatin vs. Paprotrain	ns	0.8263
Blebbistatin vs. Monensin	ns	>0.9999
Paprotrain vs. Monensin	ns	0.8407

BeauR-T16A Cell Lysate		
Mock vs. DMSO	ns	>0.9999
Mock vs. IMP-1088	ns	0.9756
Mock vs. BFA	****	<0.0001
Mock vs. Exo1	ns	0.9773
Mock vs. ES2	ns	>0.9999
Mock vs. Fli-06	***	0.0004
Mock vs. Blebbistatin	ns	0.9812
Mock vs. Paprotrain	ns	0.9926
Mock vs. Monensin	ns	>0.9999
DMSO vs. IMP-1088	ns	0.9269
DMSO vs. BFA	****	<0.0001
DMSO vs. Exo1	ns	0.9952
DMSO vs. ES2	ns	>0.9999
DMSO vs. Fli-06	***	0.0008
DMSO vs. Blebbistatin	ns	0.9963
DMSO vs. Paprotrain	ns	0.9689
DMSO vs. Monensin	ns	>0.9999
IMP-1088 vs. BFA	****	<0.0001
IMP-1088 vs. Exo1	ns	0.4234
IMP-1088 vs. ES2	ns	0.9959
IMP-1088 vs. Fli-06	****	<0.0001
IMP-1088 vs. Blebbistatin	ns	0.4432
IMP-1088 vs. Paprotrain	ns	>0.9999
IMP-1088 vs. Monensin	ns	0.8595
BFA vs. Exo1	****	<0.0001
BFA vs. ES2	****	<0.0001
BFA vs. Fli-06	ns	0.4724
BFA vs. Blebbistatin	****	<0.0001
BFA vs. Paprotrain	****	<0.0001
BFA vs. Monensin	****	<0.0001
Exo1 vs. ES2	ns	0.9214
Exo1 vs. Fli-06	*	0.0105
Exo1 vs. Blebbistatin	ns	>0.9999
Exo1 vs. Paprotrain	ns	0.5392
Exo1 vs. Monensin	ns	0.9991
ES2 vs. Fli-06	***	0.0002
ES2 vs. Blebbistatin	ns	0.9311
ES2 vs. Paprotrain	ns	0.9993
ES2 vs. Monensin	ns	0.9996
Fli-06 vs. Blebbistatin	**	0.0096
Fli-06 vs. Paprotrain	****	<0.0001
Fli-06 vs. Monensin	**	0.0014
Blebbistatin vs. Paprotrain	ns	0.5603
Blebbistatin vs. Monensin	ns	0.9994
Paprotrain vs. Monensin	ns	0.9275

Table 8.60: Figure 5.20.B, BFA Dose Response Supernatant

Tukey's multiple comparisons test	Summary	Adjusted P Value

BeauR		
DMSO vs. 0	ns	0.7717
DMSO vs. 0.1	*	0.0343
DMSO vs. 0.5	*	0.0343
DMSO vs. 1	*	0.0343
DMSO vs. 5	*	0.0343
DMSO vs. 10	*	0.0343
0 vs. 0.1	***	0.0006
0 vs. 0.5	***	0.0006
0 vs. 1	***	0.0006
0 vs. 5	***	0.0006
0 vs. 10	***	0.0006
0.1 vs. 0.5	ns	>0.9999
0.1 vs. 1	ns	>0.9999
0.1 vs. 5	ns	>0.9999
0.1 vs. 10	ns	>0.9999
0.5 vs. 1	ns	>0.9999
0.5 vs. 5	ns	>0.9999
0.5 vs. 10	ns	>0.9999
1 vs. 5	ns	>0.9999
1 vs. 10	ns	>0.9999
5 vs. 10	ns	>0.9999
BeauR-T16A		
DMSO vs. 0	***	0.0009
DMSO vs. 0.1	**	0.0048
DMSO vs. 0.5	**	0.0048
DMSO vs. 1	**	0.0048
DMSO vs. 5	**	0.0048
DMSO vs. 10	**	0.0048
0 vs. 0.1	****	<0.0001
0 vs. 0.5	****	<0.0001
0 vs. 1	****	<0.0001
0 vs. 5	****	<0.0001
0 vs. 10	****	<0.0001
0.1 vs. 0.5	ns	>0.9999
0.1 vs. 1	ns	>0.9999
0.1 vs. 5	ns	>0.9999
0.1 vs. 10	ns	>0.9999
0.5 vs. 1	ns	>0.9999
0.5 vs. 5	ns	>0.9999
0.5 vs. 10	ns	>0.9999
1 vs. 5	ns	>0.9999
1 vs. 10	ns	>0.9999
5 vs. 10	ns	>0.9999
BeauR-A26F		
DMSO vs. 0	ns	0.4910
DMSO vs. 0.1	ns	0.1409
DMSO vs. 0.5	ns	0.1406
DMSO vs. 1	ns	0.1406
DMSO vs. 5	ns	0.1406
DMSO vs. 10	ns	0.1406

0 vs. 0.1	**	0.0010
0 vs. 0.5	**	0.0010
0 vs. 1	**	0.0010
0 vs. 5	**	0.0010
0 vs. 10	**	0.0010
0.1 vs. 0.5	ns	>0.9999
0.1 vs. 1	ns	>0.9999
0.1 vs. 5	ns	>0.9999
0.1 vs. 10	ns	>0.9999
0.5 vs. 1	ns	>0.9999
0.5 vs. 5	ns	>0.9999
0.5 vs. 10	ns	>0.9999
1 vs. 5	ns	>0.9999
1 vs. 10	ns	>0.9999
5 vs. 10	ns	>0.9999

Table 8.61: Figure 5.20.B, BFA Dose Response Cell Lysate

Tukey's multiple comparisons test	Summary	Adjusted P Value
BeauR		
DMSO vs. 0	ns	0.9997
DMSO vs. 0.1	****	<0.0001
DMSO vs. 0.5	****	<0.0001
DMSO vs. 1	****	<0.0001
DMSO vs. 5	****	<0.0001
DMSO vs. 10	****	<0.0001
0 vs. 0.1	****	<0.0001
0 vs. 0.5	****	<0.0001
0 vs. 1	****	<0.0001
0 vs. 5	****	<0.0001
0 vs. 10	****	<0.0001
0.1 vs. 0.5	ns	0.9889
0.1 vs. 1	ns	0.9556
0.1 vs. 5	ns	0.9998
0.1 vs. 10	ns	0.8827
0.5 vs. 1	ns	>0.9999
0.5 vs. 5	ns	0.9997
0.5 vs. 10	ns	0.9990
1 vs. 5	ns	0.9956
1 vs. 10	ns	>0.9999
5 vs. 10	ns	0.9757
BeauR-T16A		
DMSO vs. 0	ns	>0.9999
DMSO vs. 0.1	****	<0.0001
DMSO vs. 0.5	****	<0.0001
DMSO vs. 1	****	<0.0001
DMSO vs. 5	****	<0.0001
DMSO vs. 10	****	<0.0001
0 vs. 0.1	****	<0.0001
0 vs. 0.5	****	<0.0001

0 vs. 1	****	<0.0001
0 vs. 5	****	<0.0001
0 vs. 10	****	<0.0001
0.1 vs. 0.5	ns	0.9049
0.1 vs. 1	ns	0.3736
0.1 vs. 5	ns	0.5911
0.1 vs. 10	ns	0.6712
0.5 vs. 1	ns	0.9626
0.5 vs. 5	ns	0.9968
0.5 vs. 10	ns	0.9992
1 vs. 5	ns	0.9998
1 vs. 10	ns	0.9989
5 vs. 10	ns	>0.9999
BeauR-A26F		
DMSO vs. 0	ns	0.7613
DMSO vs. 0.1	****	<0.0001
DMSO vs. 0.5	****	<0.0001
DMSO vs. 1	****	<0.0001
DMSO vs. 5	****	<0.0001
DMSO vs. 10	****	<0.0001
0 vs. 0.1	****	<0.0001
0 vs. 0.5	****	<0.0001
0 vs. 1	****	<0.0001
0 vs. 5	****	<0.0001
0 vs. 10	****	<0.0001
0.1 vs. 0.5	ns	0.9980
0.1 vs. 1	ns	0.9963
0.1 vs. 5	ns	0.6412
0.1 vs. 10	ns	0.9100
0.5 vs. 1	ns	>0.9999
0.5 vs. 5	ns	0.9157
0.5 vs. 10	ns	0.9963
1 vs. 5	ns	0.9342
1 vs. 10	ns	0.9980
5 vs. 10	ns	0.9983

Table 8.62: Figure 5.20.C, BFA Dose Response Beau-R

Šídák's multiple comparisons test	Summary	Adjusted P Value
Supernatant - Cell Lysate		
DMSO	ns	0.4186
0	ns	0.9208
0.1	ns	0.6034
0.5	***	0.0006
1	**	0.0014
5	****	<0.0001
10	***	0.0002

Table 8.63: Figure 5.20.C, BFA Dose Response BeauR-T16A

Šídák's multiple comparisons test	Summary	Adjusted P Value
BeauR-T16A Supernatant - Cell Lysate		
DMSO	ns	0.9423
0	ns	>0.9999
0.1	ns	0.0685
0.5	***	0.0002
1	**	0.0016
5	****	<0.0001
10	****	<0.0001

Table 8.64: Figure 5.20.C, BFA Dose Response BeauR-A26F

Šídák's multiple comparisons test	Summary	Adjusted P Value
Supernatant - Cell Lysate		
DMSO	ns	0.4405
0	ns	>0.9999
0.1	*	0.0420
0.5	****	<0.0001
1	****	<0.0001
5	****	<0.0001
10	****	<0.0001

Table 8.65: Figure 5.21.B, BFA Time-course Supernatant

Tukey's multiple comparisons test	Summary	Adjusted P Value
M41-CK		
No BFA vs. 1	****	<0.0001
No BFA vs. 4	****	<0.0001
No BFA vs. 6	****	<0.0001
No BFA vs. 8	****	<0.0001
No BFA vs. 10	****	<0.0001
1 vs. 4	ns	>0.9999
1 vs. 6	ns	0.9972
1 vs. 8	ns	0.9969
1 vs. 10	ns	0.4527
4 vs. 6	ns	0.9990
4 vs. 8	ns	0.9931
4 vs. 10	ns	0.4002
6 vs. 8	ns	0.9360
6 vs. 10	ns	0.2173
8 vs. 10	ns	0.7438
Beau-R		
No BFA vs. 1	****	<0.0001
No BFA vs. 4	****	<0.0001

No BFA vs. 6	****	<0.0001
No BFA vs. 8	****	<0.0001
No BFA vs. 10	****	<0.0001
1 vs. 4	ns	0.9799
1 vs. 6	ns	>0.9999
1 vs. 8	ns	>0.9999
1 vs. 10	**	0.0073
4 vs. 6	ns	0.9655
4 vs. 8	ns	0.9653
4 vs. 10	*	0.0465
6 vs. 8	ns	>0.9999
6 vs. 10	**	0.0056
8 vs. 10	**	0.0056
BeauR-T16A		
No BFA vs. 1	****	<0.0001
No BFA vs. 4	****	<0.0001
No BFA vs. 6	****	<0.0001
No BFA vs. 8	****	<0.0001
No BFA vs. 10	****	<0.0001
1 vs. 4	ns	0.8738
1 vs. 6	ns	0.9995
1 vs. 8	ns	0.4111
1 vs. 10	**	0.0071
4 vs. 6	ns	0.7036
4 vs. 8	ns	0.9661
4 vs. 10	ns	0.1137
6 vs. 8	ns	0.2438
6 vs. 10	**	0.0028
8 vs. 10	ns	0.4588
BeauR-A26F		
No BFA vs. 1	****	<0.0001
No BFA vs. 4	****	<0.0001
No BFA vs. 6	****	<0.0001
No BFA vs. 8	****	<0.0001
No BFA vs. 10	****	<0.0001
1 vs. 4	ns	0.7676
1 vs. 6	ns	0.9124
1 vs. 8	ns	0.9843
1 vs. 10	**	0.0076
4 vs. 6	ns	0.9995
4 vs. 8	ns	0.9854
4 vs. 10	***	0.0001
6 vs. 8	ns	0.9994
6 vs. 10	***	0.0004
8 vs. 10	**	0.0011

Table 8.66: Figure 5.21.B, BFA Time-course Cell Lysate

Tukey's multiple comparisons test	Summary	Adjusted P Value
M41-CK		
No BFA vs. 1	****	<0.0001
No BFA vs. 4	****	<0.0001
No BFA vs. 6	****	<0.0001

No BFA vs. 8	****	<0.0001
No BFA vs. 10	****	<0.0001
1 vs. 4	ns	>0.9999
1 vs. 6	ns	0.7617
1 vs. 8	ns	0.3699
1 vs. 10	***	0.0010
4 vs. 6	ns	0.6882
4 vs. 8	ns	0.3040
4 vs. 10	***	0.0007
6 vs. 8	ns	0.9869
6 vs. 10	*	0.0408
8 vs. 10	ns	0.1696
Beau-R		
No BFA vs. 1	****	<0.0001
No BFA vs. 4	****	<0.0001
No BFA vs. 6	****	<0.0001
No BFA vs. 8	****	<0.0001
No BFA vs. 10	****	<0.0001
1 vs. 4	ns	0.9989
1 vs. 6	ns	0.9991
1 vs. 8	ns	0.7981
1 vs. 10	****	<0.0001
4 vs. 6	ns	>0.9999
4 vs. 8	ns	0.9452
4 vs. 10	***	0.0001
6 vs. 8	ns	0.9430
6 vs. 10	***	0.0001
8 vs. 10	**	0.0023
BeauR-T16A		
No BFA vs. 1	****	<0.0001
No BFA vs. 4	****	<0.0001
No BFA vs. 6	****	<0.0001
No BFA vs. 8	****	<0.0001
No BFA vs. 10	****	<0.0001
1 vs. 4	ns	0.9895
1 vs. 6	ns	0.7390
1 vs. 8	ns	0.3803
1 vs. 10	***	0.0001
4 vs. 6	ns	0.9715
4 vs. 8	ns	0.7545
4 vs. 10	***	0.0008
6 vs. 8	ns	0.9915
6 vs. 10	**	0.0075
8 vs. 10	*	0.0353
BeauR-A26F		
No BFA vs. 1	****	<0.0001
No BFA vs. 4	****	<0.0001
No BFA vs. 6	****	<0.0001
No BFA vs. 8	****	<0.0001
No BFA vs. 10	**	0.0087
1 vs. 4	ns	0.9998
1 vs. 6	ns	0.4193

1 vs. 8	ns	0.0806
1 vs. 10	****	<0.0001
4 vs. 6	ns	0.2806
4 vs. 8	*	0.0439
4 vs. 10	****	<0.0001
6 vs. 8	ns	0.9466
6 vs. 10	**	0.0010
8 vs. 10	*	0.0131

M41-CK

Supernatant - Cell Lysate		
No BFA	ns	>0.9999
1	ns	0.6212
4	ns	0.6321
6	ns	0.1371
8	ns	0.1931
10	ns	0.0689

Table 8.67: Figure 5.21.C, BFA Time-course Beau-R

Šídák's multiple comparisons test	Summary	Adjusted P Value
Supernatant - Cell Lysate		
No BFA	ns	0.9244
1	**	0.0017
4	**	0.0036
6	***	0.0007
8	***	0.0001
10	****	<0.0001

Table 8.68: Figure 5.21.C, BFA Time-course BeauR-T16A

Šídák's multiple comparisons test	Summary	Adjusted P Value
Supernatant - Cell Lysate		
No BFA	ns	0.8950
1	**	0.0077
4	*	0.0181
6	***	0.0005
8	**	0.0084
10	**	0.0013

Table 8.69: Figure 5.21.C, BFA Time-course BeauR-A26F

Šídák's multiple comparisons test	Summary	Adjusted P Value

Supernatant - Cell Lysate		
No BFA	ns	0.9990
1	ns	0.0592
4	*	0.0146
6	**	0.0014
8	***	0.0007
10	**	0.0030

Table 8.70: Figure 5.22.B, Fli-06 Dose Response Supernatant

Tukey's multiple comparisons test	Summary	Adjusted P Value
Beau-R		
DMSO vs. 0	ns	0.9969
DMSO vs. 1	ns	0.8815
DMSO vs. 5	***	0.0005
DMSO vs. 10	****	<0.0001
DMSO vs. 50	****	<0.0001
DMSO vs. 100	****	<0.0001
0 vs. 1	ns	0.9950
0 vs. 5	****	<0.0001
0 vs. 10	****	<0.0001
0 vs. 50	****	<0.0001
0 vs. 100	****	<0.0001
1 vs. 5	****	<0.0001
1 vs. 10	****	<0.0001
1 vs. 50	****	<0.0001
1 vs. 100	****	<0.0001
5 vs. 10	**	0.0011
5 vs. 50	****	<0.0001
5 vs. 100	****	<0.0001
10 vs. 50	ns	0.1334
10 vs. 100	ns	0.2565
50 vs. 100	ns	0.9998
BeauR-T16A		
DMSO vs. 0	ns	0.8539
DMSO vs. 1	ns	>0.9999
DMSO vs. 5	****	<0.0001
DMSO vs. 10	****	<0.0001
DMSO vs. 50	****	<0.0001
DMSO vs. 100	****	<0.0001
0 vs. 1	ns	0.8106
0 vs. 5	****	<0.0001
0 vs. 10	****	<0.0001
0 vs. 50	****	<0.0001
0 vs. 100	****	<0.0001
1 vs. 5	****	<0.0001
1 vs. 10	****	<0.0001
1 vs. 50	****	<0.0001
1 vs. 100	****	<0.0001
5 vs. 10	ns	0.1704

5 vs. 50	****	<0.0001
5 vs. 100	****	<0.0001
10 vs. 50	**	0.0034
10 vs. 100	**	0.0070
50 vs. 100	ns	>0.9999
BeauR-A26F		
DMSO vs. 0	ns	0.9989
DMSO vs. 1	ns	>0.9999
DMSO vs. 5	***	0.0006
DMSO vs. 10	****	<0.0001
DMSO vs. 50	****	<0.0001
DMSO vs. 100	****	<0.0001
0 vs. 1	ns	0.9952
0 vs. 5	***	0.0001
0 vs. 10	****	<0.0001
0 vs. 50	****	<0.0001
0 vs. 100	****	<0.0001
1 vs. 5	***	0.0009
1 vs. 10	****	<0.0001
1 vs. 50	****	<0.0001
1 vs. 100	****	<0.0001
5 vs. 10	*	0.0227
5 vs. 50	****	<0.0001
5 vs. 100	****	<0.0001
10 vs. 50	ns	0.1219
10 vs. 100	*	0.0455
50 vs. 100	ns	0.9994

Table 8.71: Figure 5.22.B, Fli-06 Dose Response Cell Lysate

Tukey's multiple comparisons test	Summary	Adjusted P Value
Beau-R		
DMSO vs. 0	ns	0.9997
DMSO vs. 1	ns	0.9791
DMSO vs. 5	****	<0.0001
DMSO vs. 10	****	<0.0001
DMSO vs. 50	****	<0.0001
DMSO vs. 100	****	<0.0001
0 vs. 1	ns	0.9993
0 vs. 5	****	<0.0001
0 vs. 10	****	<0.0001
0 vs. 50	****	<0.0001
0 vs. 100	****	<0.0001
1 vs. 5	***	0.0001
1 vs. 10	****	<0.0001
1 vs. 50	****	<0.0001
1 vs. 100	****	<0.0001
5 vs. 10	*	0.0259
5 vs. 50	****	<0.0001
5 vs. 100	****	<0.0001

10 vs. 50	**	0.0080
10 vs. 100	**	0.0020
50 vs. 100	ns	0.9988
BeauR-T16A		
DMSO vs. 0	ns	>0.9999
DMSO vs. 1	ns	0.9991
DMSO vs. 5	****	<0.0001
DMSO vs. 10	****	<0.0001
DMSO vs. 50	****	<0.0001
DMSO vs. 100	****	<0.0001
0 vs. 1	ns	0.9976
0 vs. 5	****	<0.0001
0 vs. 10	****	<0.0001
0 vs. 50	****	<0.0001
0 vs. 100	****	<0.0001
1 vs. 5	****	<0.0001
1 vs. 10	****	<0.0001
1 vs. 50	****	<0.0001
1 vs. 100	****	<0.0001
5 vs. 10	ns	0.1538
5 vs. 50	****	<0.0001
5 vs. 100	****	<0.0001
10 vs. 50	*	0.0118
10 vs. 100	*	0.0127
50 vs. 100	ns	>0.9999
BeauR-A26F		
DMSO vs. 0	ns	0.7414
DMSO vs. 1	ns	0.9999
DMSO vs. 5	***	0.0003
DMSO vs. 10	****	<0.0001
DMSO vs. 50	****	<0.0001
DMSO vs. 100	****	<0.0001
0 vs. 1	ns	0.9038
0 vs. 5	*	0.0184
0 vs. 10	****	<0.0001
0 vs. 50	****	<0.0001
0 vs. 100	****	<0.0001
1 vs. 5	***	0.0007
1 vs. 10	****	<0.0001
1 vs. 50	****	<0.0001
1 vs. 100	****	<0.0001
5 vs. 10	ns	0.3082
5 vs. 50	****	<0.0001
5 vs. 100	****	<0.0001
10 vs. 50	**	0.0017
10 vs. 100	**	0.0012
50 vs. 100	ns	>0.9999

Table 8.72: Figure 5.22.C, Fli-06 Dose Response Beau-R

Šídák's multiple comparisons test	Summary	Adjusted P Value
Supernatant - Cell Lysate		
DMSO	ns	0.1697
0	ns	0.7813
1	ns	>0.9999
5	ns	0.9094
10	ns	0.1802
50	ns	0.8894
100	ns	>0.9999

Table 8.73: Figure 5.22.C, Fli-06 Dose Response BeauR-T16A

Šídák's multiple comparisons test	Summary	Adjusted P Value
Supernatant - Cell Lysate		
DMSO	ns	0.9540
0	ns	>0.9999
1	ns	0.7854
5	ns	0.4623
10	ns	0.4756
50	ns	0.2729
100	ns	0.3627

Table 8.74: Figure 5.22.C, Fli-06 Dose Response BeauR-A26F

Šídák's multiple comparisons test	Summary	Adjusted P Value
Supernatant - Cell Lysate		
DMSO	ns	0.5810
0	ns	>0.9999
1	ns	0.7056
5	ns	0.7225
10	ns	0.1107
50	ns	0.9131
100	ns	0.7598

Table 8.75: Figure 5.23, Exo1

Tukey's multiple comparisons test	Summary	Adjusted P Value
BeauR		
0 vs. DMSO	ns	0.9991
0 vs. 10	ns	0.4847
0 vs. 50	ns	0.9026
0 vs. 100	ns	0.8812
0 vs. 500	ns	0.8307

0 vs. 1000	ns	0.6569
DMSO vs. 10	ns	0.2629
DMSO vs. 50	ns	0.4087
DMSO vs. 100	ns	0.2154
DMSO vs. 500	ns	0.1189
DMSO vs. 1000	ns	0.5211
10 vs. 50	ns	0.9990
10 vs. 100	ns	0.9980
10 vs. 500	ns	>0.9999
10 vs. 1000	ns	0.9953
50 vs. 100	ns	>0.9999
50 vs. 500	ns	0.9515
50 vs. 1000	ns	>0.9999
100 vs. 500	ns	0.9981
100 vs. 1000	ns	>0.9999
500 vs. 1000	ns	>0.9999
BeauR-T16A		
0 vs. DMSO	ns	0.8503
0 vs. 10	ns	0.4249
0 vs. 50	ns	0.9592
0 vs. 100	ns	0.9446
0 vs. 500	ns	0.9720
0 vs. 1000	ns	0.9993
DMSO vs. 10	ns	0.9996
DMSO vs. 50	ns	0.8783
DMSO vs. 100	ns	0.5285
DMSO vs. 500	ns	0.5064
DMSO vs. 1000	ns	0.0514
10 vs. 50	ns	0.9345
10 vs. 100	ns	0.9719
10 vs. 500	ns	0.8775
10 vs. 1000	ns	0.6246
50 vs. 100	ns	0.9974
50 vs. 500	ns	0.9923
50 vs. 1000	ns	0.6431
100 vs. 500	ns	0.6869
100 vs. 1000	**	0.0093
500 vs. 1000	ns	0.3297
BeauR-A26F		
0 vs. DMSO	ns	0.8831
0 vs. 10	ns	0.4542
0 vs. 50	ns	0.9374
0 vs. 100	ns	0.7179
0 vs. 500	ns	0.6106
0 vs. 1000	ns	0.8542
DMSO vs. 10	ns	>0.9999
DMSO vs. 50	ns	0.9912
DMSO vs. 100	ns	0.9999
DMSO vs. 500	ns	0.9997
DMSO vs. 1000	ns	>0.9999
10 vs. 50	ns	0.3123
10 vs. 100	ns	0.9974

10 vs. 500	ns	0.6522
10 vs. 1000	ns	0.9998
50 vs. 100	ns	0.7470
50 vs. 500	ns	0.4912
50 vs. 1000	ns	0.9716
100 vs. 500	ns	>0.9999
100 vs. 1000	ns	0.9996
500 vs. 1000	ns	0.9980

Table 8.76: Figure 5.24.B, Monensin Dose Response Supernatant

Tukey's multiple comparisons test	Summary	Adjusted P Value
Beau-R		
0 vs. 5	ns	0.6216
0 vs. 10	*	0.0241
0 vs. 50	***	0.0006
5 vs. 10	ns	0.2384
5 vs. 50	**	0.0085
10 vs. 50	ns	0.3455
BeauR-T16A		
0 vs. 5	ns	0.4771
0 vs. 10	ns	0.0529
0 vs. 50	***	0.0004
5 vs. 10	ns	0.5559
5 vs. 50	**	0.0085
10 vs. 50	ns	0.1241
BeauR-A26F		
0 vs. 5	ns	0.9988
0 vs. 10	ns	0.0505
0 vs. 50	***	0.0008
5 vs. 10	*	0.0376
5 vs. 50	***	0.0006
10 vs. 50	ns	0.2512

Table 8.77: Figure 5.24.B, Monensin Dose Response Cell Lysate

Tukey's multiple comparisons test	Summary	Adjusted P Value
Beau-R		
0 vs. 5	ns	0.4283
0 vs. 10	*	0.0150
0 vs. 50	****	<0.0001
5 vs. 10	ns	0.2802
5 vs. 50	****	<0.0001
10 vs. 50	**	0.0038
BeauR-T16A		
0 vs. 5	ns	0.5855

0 vs. 10	ns	0.1568
0 vs. 50	***	0.0002
5 vs. 10	ns	0.7876
5 vs. 50	**	0.0032
10 vs. 50	*	0.0236
BeauR-A26F		
0 vs. 5	ns	>0.9999
0 vs. 10	ns	0.8456
0 vs. 50	**	0.0058
5 vs. 10	ns	0.8668
5 vs. 50	**	0.0065
10 vs. 50	*	0.0328

Table 8.78: Figure 5.24.C, Monensin Dose Response Beau-R

Šídák's multiple comparisons test	Summary	Adjusted P Value
Supernatant - Cell Lysate		
0	ns	>0.9999
5	ns	0.9973
10	ns	0.8342
50	ns	0.8279

Table 8.79: Figure 5.24.C, Monensin Dose Response BeauR-T16A

Šídák's multiple comparisons test	Summary	Adjusted P Value
Supernatant - Cell Lysate		
0	ns	0.9989
5	ns	0.8541
10	ns	0.6993
50	ns	0.3137

Table 8.80: Figure 5.24.C, Monensin Dose Response BeauR-A26F

Sidak's multiple comparisons test	Summary	Adjusted P Value
Supernatant - Cell Lysate		
0	ns	>0.9999
5	ns	>0.9999
10	ns	0.1650
50	ns	0.1210

8.5.4. Chapter 6

Table 8.81: Figure 6.1.B, M41K-T16A E qPCR

Tukey's multiple comparisons test	Summary	Adjusted P Value
6		
Mock vs. M41K	ns	>0.9999
Mock vs. M41K-T16A-2.3	ns	>0.9999
Mock vs. M41K-T16A-2.6	ns	>0.9999
Mock vs. M41K-T16A-8.3	ns	0.9996
M41K vs. M41K-T16A-2.3	ns	>0.9999
M41K vs. M41K-T16A-2.6	ns	>0.9999
M41K vs. M41K-T16A-8.3	ns	>0.9999
M41K-T16A-2.3 vs. M41K-T16A-2.6	ns	>0.9999
M41K-T16A-2.3 vs. M41K-T16A-8.3	ns	>0.9999
M41K-T16A-2.6 vs. M41K-T16A-8.3	ns	0.9996
48		
Mock vs. M41K	****	<0.0001
Mock vs. M41K-T16A-2.3	****	<0.0001
Mock vs. M41K-T16A-2.6	****	<0.0001
Mock vs. M41K-T16A-8.3	****	<0.0001
M41K vs. M41K-T16A-2.3	ns	0.8705
M41K vs. M41K-T16A-2.6	ns	0.9938
M41K vs. M41K-T16A-8.3	ns	0.8630
M41K-T16A-2.3 vs. M41K-T16A-2.6	ns	0.9805
M41K-T16A-2.3 vs. M41K-T16A-8.3	ns	0.3329
M41K-T16A-2.6 vs. M41K-T16A-8.3	ns	0.6455

Table 8.82: Figure 6.2. Reference Gene Validation

Unpaired t test	
P value	<0.0001
P value summary	****
Significantly different (P < 0.05)?	Yes
One- or two-tailed P value?	Two-tailed
t, df	t=26.08, df=34

Table 8.83: Figure 6.3, M41K-T16A qPCR IFN-α

Tukey's multiple comparisons test	Summary	Adjusted P Value
6		
Mock vs. M41K	ns	>0.9999
Mock vs. M41K-T16A-2.3	ns	0.4839
Mock vs. M41K-T16A-2.6	ns	>0.9999
Mock vs. M41K-T16A-8.3	ns	0.9939
M41K vs. M41K-T16A-2.3	ns	0.5575
M41K vs. M41K-T16A-2.6	ns	>0.9999

M41K vs. M41K-T16A-8.3	ns	0.9977
M41K-T16A-2.3 vs. M41K-T16A-2.6	ns	0.4385
M41K-T16A-2.3 vs. M41K-T16A-8.3	ns	0.2778
M41K-T16A-2.6 vs. M41K-T16A-8.3	ns	0.9974
48		
Mock vs. M41K	****	<0.0001
Mock vs. M41K-T16A-2.3	**	0.0016
Mock vs. M41K-T16A-2.6	****	<0.0001
Mock vs. M41K-T16A-8.3	****	<0.0001
M41K vs. M41K-T16A-2.3	ns	0.6880
M41K vs. M41K-T16A-2.6	ns	0.7415
M41K vs. M41K-T16A-8.3	ns	0.3594
M41K-T16A-2.3 vs. M41K-T16A-2.6	ns	0.1257
M41K-T16A-2.3 vs. M41K-T16A-8.3	*	0.0342
M41K-T16A-2.6 vs. M41K-T16A-8.3	ns	0.9616

Table 8.84: Figure 6.3, M41K-T16A qPCR IL-6

Tukey's multiple comparisons test	Summary	Adjusted P Value
6		
Mock vs. M41K	ns	0.5950
Mock vs. M41K-T16A-2.3	ns	0.6347
Mock vs. M41K-T16A-2.6	ns	0.7094
Mock vs. M41K-T16A-8.3	ns	0.9590
M41K vs. M41K-T16A-2.3	ns	>0.9999
M41K vs. M41K-T16A-2.6	ns	0.9997
M41K vs. M41K-T16A-8.3	ns	0.9306
M41K-T16A-2.3 vs. M41K-T16A-2.6	ns	>0.9999
M41K-T16A-2.3 vs. M41K-T16A-8.3	ns	0.9485
M41K-T16A-2.6 vs. M41K-T16A-8.3	ns	0.9739
48		
Mock vs. M41K	**	0.0011
Mock vs. M41K-T16A-2.3	*	0.0323
Mock vs. M41K-T16A-2.6	****	<0.0001
Mock vs. M41K-T16A-8.3	****	<0.0001
M41K vs. M41K-T16A-2.3	ns	0.4510
M41K vs. M41K-T16A-2.6	ns	0.7240
M41K vs. M41K-T16A-8.3	ns	0.4601
M41K-T16A-2.3 vs. M41K-T16A-2.6	ns	0.0550
M41K-T16A-2.3 vs. M41K-T16A-8.3	*	0.0219
M41K-T16A-2.6 vs. M41K-T16A-8.3	ns	0.9911

Table 8.85: Figure 6.3, M41K-T16A qPCR IFN-β

Tukey's multiple comparisons test	Summary	Adjusted P Value
6		
Mock vs. M41K	ns	0.9266
Mock vs. M41K-T16A-2.3	ns	0.7734

Mock vs. M41K-T16A-2.6	ns	0.5277
Mock vs. M41K-T16A-8.3	ns	0.9076
M41K vs. M41K-T16A-2.3	ns	0.9962
M41K vs. M41K-T16A-2.6	ns	0.9351
M41K vs. M41K-T16A-8.3	ns	>0.9999
M41K-T16A-2.3 vs. M41K-T16A-2.6	ns	0.9931
M41K-T16A-2.3 vs. M41K-T16A-8.3	ns	0.9981
M41K-T16A-2.6 vs. M41K-T16A-8.3	ns	0.9504
48		
Mock vs. M41K	****	<0.0001
Mock vs. M41K-T16A-2.3	****	<0.0001
Mock vs. M41K-T16A-2.6	****	<0.0001
Mock vs. M41K-T16A-8.3	****	<0.0001
M41K vs. M41K-T16A-2.3	ns	0.9914
M41K vs. M41K-T16A-2.6	ns	0.9998
M41K vs. M41K-T16A-8.3	ns	0.4869
M41K-T16A-2.3 vs. M41K-T16A-2.6	ns	0.9984
M41K-T16A-2.3 vs. M41K-T16A-8.3	ns	0.2629
M41K-T16A-2.6 vs. M41K-T16A-8.3	ns	0.3982

Table 8.86: Figure 6.3, M41K-T16A qPCR IL-1β

Tukey's multiple comparisons test	Summary	Adjusted P Value
6		
Mock vs. M41K	ns	0.6390
Mock vs. M41K-T16A-2.3	ns	0.3121
Mock vs. M41K-T16A-2.6	ns	0.6293
Mock vs. M41K-T16A-8.3	ns	0.7228
M41K vs. M41K-T16A-2.3	ns	0.9936
M41K vs. M41K-T16A-2.6	ns	>0.9999
M41K vs. M41K-T16A-8.3	ns	0.9990
M41K-T16A-2.3 vs. M41K-T16A-2.6	ns	0.9777
M41K-T16A-2.3 vs. M41K-T16A-8.3	ns	0.9468
M41K-T16A-2.6 vs. M41K-T16A-8.3	ns	0.9998
48		
Mock vs. M41K	ns	0.0885
Mock vs. M41K-T16A-2.3	ns	0.2733
Mock vs. M41K-T16A-2.6	***	0.0008
Mock vs. M41K-T16A-8.3	**	0.0063
M41K vs. M41K-T16A-2.3	ns	0.9650
M41K vs. M41K-T16A-2.6	ns	0.2216
M41K vs. M41K-T16A-8.3	ns	0.7148
M41K-T16A-2.3 vs. M41K-T16A-2.6	ns	0.0686
M41K-T16A-2.3 vs. M41K-T16A-8.3	ns	0.3446
M41K-T16A-2.6 vs. M41K-T16A-8.3	ns	0.8793

Table 8.87: Figure 6.4, M41K-T16A Ciliary Activity *ex vivo*

Dunn's multiple comparisons test	Summary	Adjusted P Value
Mock vs. M41-K (Control)	****	<0.0001
Mock vs. 2.3	ns	0.7728
Mock vs. 2.6	*	0.0373
Mock vs. 8.3	****	<0.0001
M41-K (Control) vs. 2.3	***	0.0010
M41-K (Control) vs. 2.6	ns	0.0566
M41-K (Control) vs. 8.3	ns	>0.9999
2.3 vs. 2.6	ns	>0.9999
2.3 vs. 8.3	*	0.0122
2.6 vs. 8.3	ns	0.3573

Table 8.88: Figure 6.7, M41K-T16A Ciliary Activity *in vivo*

Tukey's multiple comparisons test	Summary	Adjusted P Value
4		
Mock vs. M41K-T16A	ns	0.9953
Mock vs. M41-K	ns	0.2488
M41K-T16A vs. M41-K	ns	0.2139
6		
Mock vs. M41K-T16A	*	0.0176
Mock vs. M41-K	ns	0.0558
M41K-T16A vs. M41-K	ns	0.8594

Chapter 9: Bibliography

1. Ogando NS, Ferron F, Decroly E, Canard B, Posthuma CC, Snijder EJ. The Curious Case of the Nidovirus Exoribonuclease: Its Role in RNA Synthesis and Replication Fidelity. Front Microbiol. 2019 Aug 7;10:1813. doi: 10.3389/fmicb.2019.01813.

2. Saberi A, Gulyaeva AA, Brubacher JL, Newmark PA, Gorbalenya AE. A planarian nidovirus expands the limits of RNA genome size. PLoS Pathog. 2018 Nov 1;14(11):e1007314. doi: 10.1371/journal.ppat.1007314

3. Woo PC, Huang Y, Lau SK, Yuen KY. Coronavirus genomics and bioinformatics analysis. Viruses. 2010 Aug;2(8):1804-20. doi: 10.3390/v2081803.

4. Woo PC, Lau SK, Lam CS, Lai KK, Huang Y, Lee P, Luk GS, Dyrting KC, Chan KH, Yuen KY. Comparative analysis of complete genome sequences of three avian coronaviruses reveals a novel group 3c coronavirus. J Virol. 2009 Jan;83(2):908-17. doi: 10.1128/JVI.01977-08

5. Schalk AF, Hawn MC. An apparently new respiratory disease of baby chicks. J Am Vet Med Assoc 1931; 78: 413-23.

6. Cook JK, Jackwood M, Jones RC. The long view: 40 years of infectious bronchitis research. Avian Pathol. 2012;41(3):239-50. doi: 10.1080/03079457.2012.680432.

7. De Wit JJ. Detection of infectious bronchitis virus. Avian Pathol. 2000 Apr;29(2):71-93. doi: 10.1080/03079450094108.

8. Valastro V, Holmes EC, Britton P, Fusaro A, Jackwood MW, Cattoli G, Monne I. S1 gene-based phylogeny of infectious bronchitis virus: An attempt to harmonize

virus classification. Infect Genet Evol. 2016 Apr;39:349-364. doi: 10.1016/j.meegid.2016.02.015

9. Jackwood, M.W. and de Wit, S. Infectious Bronchitis. In Diseases of Poultry, D.E. Swayne (Ed.). 2013 doi: 10.1002/9781119421481.ch4

10. Bennett, R. and Ijpelaar, J. Updated Estimates of the Costs Associated with Thirty Four Endemic Livestock Diseases in Great Britain: A Note. Journal of Agricultural Economics, 2005 56: 135-144. doi: 10.1111/j.1477-9552.2005.tb00126.x

11. Hudson CB, Beaudette FR. INFECTION OF THE CLOACA WITH THE VIRUS OF INFECTIOUS BRONCHITIS. Science. 1932 Jul 8;76(1958):34. doi: 10.1126/science.76.1958.34-a

12. Darbyshire JH, Rowell JG, Cook JK, Peters RW. Taxonomic studies on strains of avian infectious bronchitis virus using neutralisation tests in tracheal organ cultures. Arch Virol. 1979;61(3):227-38. doi: 10.1007/BF01318057.

13. Cavanagh D. Coronavirus avian infectious bronchitis virus. Vet Res. 2007 Mar-Apr;38(2):281-97. doi: 10.1051/vetres:2006055.

14. Meir R, Rosenblut E, Perl S, Kass N, Ayali G, Perk S, Hemsani E. Identification of a novel nephropathogenic infectious bronchitis virus in Israel. Avian Dis. 2004 Sep;48(3):635-41. doi: 10.1637/7107

15. Zhang X, Liao K, Chen S, Yan K, Du X, Zhang C, Guo M, Wu Y. Evaluation of the reproductive system development and egg-laying performance of hens infected with TW I-type infectious bronchitis virus. Vet Res. 2020 Jul 31;51(1):95. doi: 10.1186/s13567-020-00819-4.

16. Matthijs MG, van Eck JH, Landman WJ, Stegeman JA. Ability of Massachusetts-type infectious bronchitis virus to increase colibacillosis susceptibility

in commercial broilers: a comparison between vaccine and virulent field virus. Avian Pathol. 2003 Oct;32(5):473-81. doi: 10.1080/0307945031000154062.

17. Geerligs HJ, Boelm GJ, Meinders CA, Stuurman BG, Symons J, Tarres-Call J, Bru T, Vila R, Mombarg M, Karaca K, Wijmenga W, Kumar M. Efficacy and safety of an attenuated live QX-like infectious bronchitis virus strain as a vaccine for chickens. Avian Pathol. 2011 Feb;40(1):93-102. doi: 10.1080/03079457.2010.542742.

18. Britton P, Armesto M, Cavanagh D, Keep S. Modification of the avian coronavirus infectious bronchitis virus for vaccine development. Bioeng Bugs. 2012 Mar-Apr;3(2):114-9. doi: 10.4161/bbug.18983.

19. Jordan B. Vaccination against infectious bronchitis virus: A continuous challenge. Vet Microbiol. 2017 Jul;206:137-143. doi: 10.1016/j.vetmic.2017.01.002

20. To J, Surya W, Fung TS, Li Y, Verdià-Bàguena C, Queralt-Martin M, Aguilella VM, Liu DX, Torres J. Channel-Inactivating Mutations and Their Revertant Mutants in the Envelope Protein of Infectious Bronchitis Virus. J Virol. 2017 Feb 14;91(5):e02158-16. doi: 10.1128/JVI.02158-16.

21. Boltz DA, Zimmerman CR, Nakai M, Bunick D, Scherba G, Bahr JM. Epididymal stone formation and decreased sperm production in roosters vaccinated with a killed strain of avian infectious bronchitis virus. Avian Dis. 2006 Dec;50(4):594-8. doi: 10.1637/7654-052506R.1

22. Oade MS, Keep S, Freimanis GL, Orton RJ, Britton P, Hammond JA, Bickerton E. Attenuation of Infectious Bronchitis Virus in Eggs Results in Different Patterns of Genomic Variation across Multiple Replicates. J Virol. 2019 Jun 28;93(14):e00492-19. doi: 10.1128/JVI.00492-19

23. Hopkins SR, Yoder HW Jr. Reversion to virulence of chicken-passaged infectious bronchitis vaccine virus. Avian Dis. 1986 Jan-Mar;30(1):221-3.

24. Casais R, Thiel V, Siddell SG, Cavanagh D, Britton P. Reverse genetics system for the avian coronavirus infectious bronchitis virus. J Virol. 2001 Dec;75(24):12359-69. doi: 10.1128/JVI.75.24.12359-12369.2001.

25. Keep S, Stevenson-Leggett P, Steyn A, Oade MS, Webb I, Stuart J, Vervelde L, Britton P, Maier HJ, Bickerton E. Temperature Sensitivity: A Potential Method for the Generation of Vaccines against the Avian Coronavirus Infectious Bronchitis Virus. Viruses. 2020 Jul 14;12(7):754. doi: 10.3390/v12070754.

26. Luytjes W, Bredenbeek PJ, Noten AF, Horzinek MC, Spaan WJ. Sequence of mouse hepatitis virus A59 mRNA 2: indications for RNA recombination between coronaviruses and influenza C virus. Virology. 1988 Oct;166(2):415-22. doi: 10.1016/0042-6822(88)90512-0.

27. Brierley I, Jenner AJ, Inglis SC. Mutational analysis of the "slippery-sequence" component of a coronavirus ribosomal frameshifting signal. J Mol Biol. 1992 Sep 20;227(2):463-79. doi: 10.1016/0022-2836(92)90901-u.

28. Keep S, Oade MS, Lidzbarski-Silvestre F, Bentley K, Stevenson-Leggett P, Freimanis GL, Tennakoon C, Sanderson N, Hammond JA, Jones RC, Britton P, Bickerton E. Multiple novel non-canonically transcribed sub-genomic mRNAs produced by avian coronavirus infectious bronchitis virus. J Gen Virol. 2020 Oct;101(10):1103-1118. doi: 10.1099/jgv.0.001474.

29. Bentley K, Keep SM, Armesto M, Britton P. Identification of a noncanonically transcribed subgenomic mRNA of infectious bronchitis virus and other gammacoronaviruses. J Virol. 2013 Feb;87(4):2128-36. doi: 10.1128/JVI.02967-12.

30. Dinan AM, Keep S, Bickerton E, Britton P, Firth AE, Brierley I. Comparative Analysis of Gene Expression in Virulent and Attenuated Strains of Infectious Bronchitis Virus at Subcodon Resolution. J Virol. 2019 Aug 28;93(18):e00714-19. doi: 10.1128/JVI.00714-19.

31. Cavanagh D NS. Infectious bronchitis. In: Calnek BW BH, Beard CW, McDougald LR, Saif YM, editor. Diseases of Poultry, 10th Edn. Iowa: Iowa State Univeristy Press; 1997. p. 511-26.

32. Ziebuhr J, Thiel V, Gorbalenya AE. The autocatalytic release of a putative RNA virus transcription factor from its polyprotein precursor involves two paralogous papain-like proteases that cleave the same peptide bond. J Biol Chem. 2001 Aug 31;276(35):33220-32. doi: 10.1074/jbc.M104097200.

33. Ziebuhr J, Snijder EJ, Gorbalenya AE. Virus-encoded proteinases and proteolytic processing in the Nidovirales. J Gen Virol. 2000 Apr;81(Pt 4):853-79. doi: 10.1099/0022-1317-81-4-853.

34. Fang SG, Shen H, Wang J, Tay FP, Liu DX. Proteolytic processing of polyproteins 1a and 1ab between non-structural proteins 10 and 11/12 of Coronavirus infectious bronchitis virus is dispensable for viral replication in cultured cells. Virology. 2008 Sep 30;379(2):175-80. doi: 10.1016/j.virol.2008.06.038.

35. Peng S, Wang Y, Zhang Y, Song X, Zou Y, Li L, Zhao X, Yin Z. Current Knowledge on Infectious Bronchitis Virus Non-structural Proteins: The Bearer for Achieving Immune Evasion Function. Front Vet Sci. 2022 Apr 8;9:820625. doi: 10.3389/fvets.2022.820625.

36. van der Hoeven B, Oudshoorn D, Koster AJ, Snijder EJ, Kikkert M, Bárcena M. Biogenesis and architecture of arterivirus replication organelles. Virus Res. 2016 Jul 15;220:70-90. doi: 10.1016/j.virusres.2016.04.001.

37. Doyle N, Neuman BW, Simpson J, Hawes PC, Mantell J, Verkade P, Alrashedi H, Maier HJ. Infectious Bronchitis Virus Nonstructural Protein 4 Alone Induces Membrane Pairing. Viruses. 2018 Sep 6;10(9):477. doi: 10.3390/v10090477.

38. Maier HJ, Cottam EM, Stevenson-Leggett P, Wilkinson JA, Harte CJ, Wileman T, Britton P. Visualizing the autophagy pathway in avian cells and its application to studying infectious bronchitis virus. Autophagy. 2013 Apr;9(4):496-509. doi: 10.4161/auto.23465.

39. Subissi L, Imbert I, Ferron F, Collet A, Coutard B, Decroly E, Canard B. SARS-CoV ORF1b-encoded nonstructural proteins 12-16: replicative enzymes as antiviral targets. Antiviral Res. 2014 Jan;101:122-30. doi: 10.1016/j.antiviral.2013.11.006.

40. Xu LH, Huang M, Fang SG, Liu DX. Coronavirus infection induces DNA replication stress partly through interaction of its nonstructural protein 13 with the p125 subunit of DNA polymerase δ. J Biol Chem. 2011 Nov 11;286(45):39546-59. doi: 10.1074/jbc.M111.242206.

41. Minskaia E, Hertzig T, Gorbalenya AE, Campanacci V, Cambillau C, Canard B, Ziebuhr J. Discovery of an RNA virus 3'->5' exoribonuclease that is critically involved in coronavirus RNA synthesis. Proc Natl Acad Sci U S A. 2006 Mar 28;103(13):5108-13. doi: 10.1073/pnas.0508200103.

42. Chen Y, Cai H, Pan J, Xiang N, Tien P, Ahola T, Guo D. Functional screen reveals SARS coronavirus nonstructural protein nsp14 as a novel cap N7 methyltransferase. Proc Natl Acad Sci U S A. 2009 Mar 3;106(9):3484-9. doi: 10.1073/pnas.0808790106.

43. Bouvet M, Debarnot C, Imbert I, Selisko B, Snijder EJ, Canard B, Decroly E. In vitro reconstitution of SARS-coronavirus mRNA cap methylation. PLoS Pathog. 2010 Apr 22;6(4):e1000863. doi: 10.1371/journal.ppat.1000863.

44. Egloff MP, Ferron F, Campanacci V, Longhi S, Rancurel C, Dutartre H, Snijder EJ, Gorbalenya AE, Cambillau C, Canard B. The severe acute respiratory syndrome-coronavirus replicative protein nsp9 is a single-stranded RNA-binding subunit unique in the RNA virus world. Proc Natl Acad Sci U S A. 2004 Mar 16;101(11):3792-6. doi: 10.1073/pnas.0307877101.

45. Hartenian E, Nandakumar D, Lari A, Ly M, Tucker JM, Glaunsinger BA. The molecular virology of coronaviruses. J Biol Chem. 2020 Sep 11;295(37):12910-12934. doi: 10.1074/jbc.REV120.013930.

46. Wang X, Liao Y, Yap PL, Png KJ, Tam JP, Liu DX. Inhibition of protein kinase R activation and upregulation of GADD34 expression play a synergistic role in facilitating coronavirus replication by maintaining de novo protein synthesis in virus-infected cells. J Virol. 2009 Dec;83(23):12462-72. doi: 10.1128/JVI.01546-09.

47. Ojha NK, Liu J, Yu T, Fang C, Zhou J, Liao M. Interplay of the ubiquitin proteasome system and the innate immune response is essential for the replication of infectious bronchitis virus. Arch Virol. 2021 Aug;166(8):2173-2185. doi: 10.1007/s00705-021-05073-3.

48. Eriksson KK, Cervantes-Barragán L, Ludewig B, Thiel V. Mouse hepatitis virus liver pathology is dependent on ADP-ribose-1''-phosphatase, a viral function conserved in the alpha-like supergroup. J Virol. 2008 Dec;82(24):12325-34. doi: 10.1128/JVI.02082-08.

49. Keep S, Bickerton E, Armesto M, Britton P. The ADRP domain from a virulent strain of infectious bronchitis virus is not sufficient to confer a pathogenic phenotype to the attenuated Beaudette strain. J Gen Virol. 2018 Aug;99(8):1097-1102. doi: 10.1099/jgv.0.001098.

50. Gao B, Gong X, Fang S, Weng W, Wang H, Chu H, Sun Y, Meng C, Tan L, Song C, Qiu X, Liu W, Forlenza M, Ding C, Liao Y. Inhibition of anti-viral stress

granule formation by coronavirus endoribonuclease nsp15 ensures efficient virus replication. PLoS Pathog. 2021 Feb 26;17(2):e1008690. doi: 10.1371/journal.ppat.1008690.

51. Zhao J, Sun L, Zhao Y, Feng D, Cheng J, Zhang G. Coronavirus Endoribonuclease Ensures Efficient Viral Replication and Prevents Protein Kinase R Activation. J Virol. 2020 Dec 23;95(7):e02103-20. doi: 10.1128/JVI.02103-20.

52. Zuo J, Cao Y, Wang Z, Shah AU, Wang W, Dai C, Chen M, Lin J, Yang Q. The mechanism of antigen-presentation of avian bone marrowed dendritic cells suppressed by infectious bronchitis virus. Genomics. 2021 Jul;113(4):1719-1732. doi: 10.1016/j.ygeno.2021.04.027.

53. Cottam EM, Maier HJ, Manifava M, Vaux LC, Chandra-Schoenfelder P, Gerner W, Britton P, Ktistakis NT, Wileman T. Coronavirus nsp6 proteins generate autophagosomes from the endoplasmic reticulum via an omegasome intermediate. Autophagy. 2011 Nov;7(11):1335-47. doi: 10.4161/auto.7.11.16642.

54. Miguel B, Pharr GT, Wang C. The role of feline aminopeptidase N as a receptor for infectious bronchitis virus. Brief review. Arch Virol. 2002 Nov;147(11):2047-56. doi: 10.1007/s00705-002-0888-1.

55. Chu VC, McElroy LJ, Aronson JM, Oura TJ, Harbison CE, Bauman BE, Whittaker GR. Feline aminopeptidase N is not a functional receptor for avian infectious bronchitis virus. Virol J. 2007 Feb 26;4:20. doi: 10.1186/1743-422X-4-20.

56. Tresnan DB, Holmes KV. Feline aminopeptidase N is a receptor for all group I coronaviruses. Adv Exp Med Biol. 1998;440:69-75. doi: 10.1007/978-1-4615-5331-1_9.

57. Winter C, Schwegmann-Weßels C, Cavanagh D, Neumann U, Herrler G. Sialic acid is a receptor determinant for infection of cells by avian Infectious bronchitis virus. J Gen Virol. 2006 May;87(Pt 5):1209-1216. doi: 10.1099/vir.0.81651-0.

58. Winter C, Herrler G, Neumann U. Infection of the tracheal epithelium by infectious bronchitis virus is sialic acid dependent. Microbes Infect. 2008 Apr;10(4):367-73. doi: 10.1016/j.micinf.2007.12.009.

59. Madu IG, Chu VC, Lee H, Regan AD, Bauman BE, Whittaker GR. Heparan sulfate is a selective attachment factor for the avian coronavirus infectious bronchitis virus Beaudette. Avian Dis. 2007 Mar;51(1):45-51. doi: 10.1637/0005-2086(2007)051[0045:HSIASA]2.0.CO;2.

60. Zhang Z, Yang X, Xu P, Wu X, Zhou L, Wang H. Heat shock protein 70 in lung and kidney of specific-pathogen-free chickens is a receptor-associated protein that interacts with the binding domain of the spike protein of infectious bronchitis virus. Arch Virol. 2017 Jun;162(6):1625-1631. doi: 10.1007/s00705-017-3280-x.

61. Everest H, Stevenson-Leggett P, Bailey D, Bickerton E, Keep S. Known Cellular and Receptor Interactions of Animal and Human Coronaviruses: A Review. Viruses. 2022 Feb 8;14(2):351. doi: 10.3390/v14020351.

62. Sainz B Jr, Rausch JM, Gallaher WR, Garry RF, Wimley WC. The aromatic domain of the coronavirus class I viral fusion protein induces membrane permeabilization: putative role during viral entry. Biochemistry. 2005 Jan 25;44(3):947-58. doi: 10.1021/bi048515g.

63. de Groot RJ. Structure, function and evolution of the hemagglutinin-esterase proteins of corona- and toroviruses. Glycoconj J. 2006 Feb;23(1-2):59-72. doi: 10.1007/s10719-006-5438-8.

64. Burkard C, Verheije MH, Wicht O, van Kasteren SI, van Kuppeveld FJ, Haagmans BL, Pelkmans L, Rottier PJ, Bosch BJ, de Haan CA. Coronavirus cell entry occurs through the endo-/lysosomal pathway in a proteolysis-dependent manner. PLoS Pathog. 2014 Nov 6;10(11):e1004502. doi: 10.1371/journal.ppat.1004502.

65. Maier HJ, Hawes PC, Cottam EM, Mantell J, Verkade P, Monaghan P, Wileman T, Britton P. Infectious bronchitis virus generates spherules from zippered endoplasmic reticulum membranes. mBio. 2013 Oct 22;4(5):e00801-13. doi: 10.1128/mBio.00801-13.

66. Snijder EJ, Limpens RWAL, de Wilde AH, de Jong AWM, Zevenhoven-Dobbe JC, Maier HJ, Faas FFGA, Koster AJ, Bárcena M. A unifying structural and functional model of the coronavirus replication organelle: Tracking down RNA synthesis. PLoS Biol. 2020 Jun 8;18(6):e3000715. doi: 10.1371/journal.pbio.3000715.

67. Doyle N, Simpson J, Hawes PC, Maier HJ. Coronavirus RNA Synthesis Takes Place within Membrane-Bound Sites. Viruses. 2021 Dec 17;13(12):2540. doi: 10.3390/v13122540.

68. Sawicki SG, Sawicki DL. Coronaviruses use discontinuous extension for synthesis of subgenome-length negative strands. Adv Exp Med Biol. 1995;380:499-506. doi: 10.1007/978-1-4615-1899-0_79.

69. Perlman S, Netland J. Coronaviruses post-SARS: update on replication and pathogenesis. Nat Rev Microbiol. 2009 Jun;7(6):439-50. doi: 10.1038/nrmicro2147.

70. Rajah MM, Bernier A, Buchrieser J, Schwartz O. The Mechanism and Consequences of SARS-CoV-2 Spike-Mediated Fusion and Syncytia Formation. J Mol Biol. 2022 Mar 30;434(6):167280. doi: 10.1016/j.jmb.2021.167280.

71. de Haan CA, Stadler K, Godeke GJ, Bosch BJ, Rottier PJ. Cleavage inhibition of the murine coronavirus spike protein by a furin-like enzyme affects cell-cell but not virus-cell fusion. J Virol. 2004 Jun;78(11):6048-54. doi: 10.1128/JVI.78.11.6048-6054.2004.

72. Corse E, Machamer CE. The cytoplasmic tail of infectious bronchitis virus E protein directs Golgi targeting. J Virol. 2002 Feb;76(3):1273-84. doi: 10.1128/jvi.76.3.1273-1284.2002.

73. Swift AM, Machamer CE. A Golgi retention signal in a membrane-spanning domain of coronavirus E1 protein. J Cell Biol. 1991 Oct;115(1):19-30. doi: 10.1083/jcb.115.1.19.

74. Lontok E, Corse E, Machamer CE. Intracellular targeting signals contribute to localization of coronavirus spike proteins near the virus assembly site. J Virol. 2004 Jun;78(11):5913-22. doi: 10.1128/JVI.78.11.5913-5922.2004.

75. Corse E, Machamer CE. The cytoplasmic tails of infectious bronchitis virus E and M proteins mediate their interaction. Virology. 2003 Jul 20;312(1):25-34. doi: 10.1016/s0042-6822(03)00175-2.

76. Kuo L, Masters PS. Genetic evidence for a structural interaction between the carboxy termini of the membrane and nucleocapsid proteins of mouse hepatitis virus. J Virol. 2002 May;76(10):4987-99. doi: 10.1128/jvi.76.10.4987-4999.2002.

77. de Haan CA, Smeets M, Vernooij F, Vennema H, Rottier PJ. Mapping of the coronavirus membrane protein domains involved in interaction with the spike protein. J Virol. 1999 Sep;73(9):7441-52. doi: 10.1128/JVI.73.9.7441-7452.1999.

78. Klumperman J, Locker JK, Meijer A, Horzinek MC, Geuze HJ, Rottier PJ. Coronavirus M proteins accumulate in the Golgi complex beyond the site of virion budding. J Virol. 1994 Oct;68(10):6523-34. doi: 10.1128/JVI.68.10.6523-6534.1994.

79. Saraste J, Prydz K. Assembly and Cellular Exit of Coronaviruses: Hijacking an Unconventional Secretory Pathway from the Pre-Golgi Intermediate Compartment via the Golgi Ribbon to the Extracellular Space. Cells. 2021 Feb 26;10(3):503. doi: 10.3390/cells10030503.

80. Glick BS, Luini A. Models for Golgi traffic: a critical assessment. Cold Spring Harb Perspect Biol. 2011 Nov 1;3(11):a005215. doi: 10.1101/cshperspect.a005215.

81. Tartakoff AM, Vassalli P. Plasma cell immunoglobulin secretion: arrest is accompanied by alterations of the golgi complex. J Exp Med. 1977 Nov 1;146(5):1332-45. doi: 10.1084/jem.146.5.1332.

82. Salanueva IJ, Carrascosa JL, Risco C. Structural maturation of the transmissible gastroenteritis coronavirus. J Virol. 1999 Oct;73(10):7952-64. doi: 10.1128/JVI.73.10.7952-7964.1999.

83. Alonso-Caplen FV, Matsuoka Y, Wilcox GE, Compans RW. Replication and morphogenesis of avian coronavirus in Vero cells and their inhibition by monensin. Virus Res. 1984;1(2):153-67. doi: 10.1016/0168-1702(84)90070-4.

84. Westerbeck JW, Machamer CE. The Infectious Bronchitis Coronavirus Envelope Protein Alters Golgi pH To Protect the Spike Protein and Promote the Release of Infectious Virus. J Virol. 2019 May 15;93(11):e00015-19. doi: 10.1128/JVI.00015-19.

85. Ghosh S, Dellibovi-Ragheb TA, Kerviel A, Pak E, Qiu Q, Fisher M, Takvorian PM, Bleck C, Hsu VW, Fehr AR, Perlman S, Achar SR, Straus MR, Whittaker GR, de Haan CAM, Kehrl J, Altan-Bonnet G, Altan-Bonnet N. β-Coronaviruses Use Lysosomes for Egress Instead of the Biosynthetic Secretory Pathway. Cell. 2020 Dec 10;183(6):1520-1535.e14. doi: 10.1016/j.cell.2020.10.039.

86. Saraste J, Enyioko M, Dale H, Prydz K, Machamer C. Evidence for the role of Rab11-positive recycling endosomes as intermediates in coronavirus egress from epithelial cells. Histochem Cell Biol. 2022 Sep;158(3):241-251. doi: 10.1007/s00418-022-02115-y.

87. Luini A, Mironov AA, Polishchuk EV, Polishchuk RS. Morphogenesis of post-Golgi transport carriers. Histochem Cell Biol. 2008 Feb;129(2):153-61. doi: 10.1007/s00418-007-0365-8.

88. Bosch BJ, van der Zee R, de Haan CA, Rottier PJ. The coronavirus spike protein is a class I virus fusion protein: structural and functional characterization of the fusion core complex. J Virol. 2003 Aug;77(16):8801-11. doi: 10.1128/jvi.77.16.8801-8811.2003.

89. Gallagher TM, Buchmeier MJ. Coronavirus spike proteins in viral entry and pathogenesis. Virology. 2001 Jan 20;279(2):371-4. doi: 10.1006/viro.2000.0757.

90. Parsons LM, Bouwman KM, Azurmendi H, de Vries RP, Cipollo JF, Verheije MH. Glycosylation of the viral attachment protein of avian coronavirus is essential for host cell and receptor binding. J Biol Chem. 2019 May 10;294(19):7797-7809. doi: 10.1074/jbc.RA119.007532.

91. Stevenson-Leggett P, Armstrong S, Keep S, Britton P, Bickerton E. Analysis of the avian coronavirus spike protein reveals heterogeneity in the glycans present. J Gen Virol. 2021 Aug;102(8):001642. doi: 10.1099/jgv.0.001642.

92. Millet JK, Goldstein ME, Labitt RN, Hsu HL, Daniel S, Whittaker GR. A camel-derived MERS-CoV with a variant spike protein cleavage site and distinct fusion activation properties. Emerg Microbes Infect. 2016 Dec 21;5(12):e126. doi: 10.1038/emi.2016.125.

93. Yamada Y, Liu DX. Proteolytic activation of the spike protein at a novel RRRR/S motif is implicated in furin-dependent entry, syncytium formation, and infectivity of coronavirus infectious bronchitis virus in cultured cells. J Virol. 2009 Sep;83(17):8744-58. doi: 10.1128/JVI.00613-09.

94. Kubo H, Yamada YK, Taguchi F. Localization of neutralizing epitopes and the receptor-binding site within the amino-terminal 330 amino acids of the murine coronavirus spike protein. J Virol. 1994 Sep;68(9):5403-10. doi: 10.1128/JVI.68.9.5403-5410.1994.

95. Matsuyama S, Taguchi F. Two-step conformational changes in a coronavirus envelope glycoprotein mediated by receptor binding and proteolysis. J Virol. 2009 Nov;83(21):11133-41. doi: 10.1128/JVI.00959-09.

96. Shang J, Zheng Y, Yang Y, Liu C, Geng Q, Luo C, Zhang W, Li F. Cryo-EM structure of infectious bronchitis coronavirus spike protein reveals structural and functional evolution of coronavirus spike proteins. PLoS Pathog. 2018 Apr 23;14(4):e1007009. doi: 10.1371/journal.ppat.1007009.

97. Bickerton E, Maier HJ, Stevenson-Leggett P, Armesto M, Britton P. The S2 Subunit of Infectious Bronchitis Virus Beaudette Is a Determinant of Cellular Tropism. J Virol. 2018 Sep 12;92(19):e01044-18. doi: 10.1128/JVI.01044-18.

98. de Groot RJ, Luytjes W, Horzinek MC, van der Zeijst BA, Spaan WJ, Lenstra JA. Evidence for a coiled-coil structure in the spike proteins of coronaviruses. J Mol Biol. 1987 Aug 20;196(4):963-6. doi: 10.1016/0022-2836(87)90422-0

99. Saikatendu KS, Joseph JS, Subramanian V, Neuman BW, Buchmeier MJ, Stevens RC, Kuhn P. Ribonucleocapsid formation of severe acute respiratory syndrome coronavirus through molecular action of the N-terminal domain of N protein. J Virol. 2007 Apr;81(8):3913-21. doi: 10.1128/JVI.02236-06.

100. Fan H, Ooi A, Tan YW, Wang S, Fang S, Liu DX, Lescar J. The nucleocapsid protein of coronavirus infectious bronchitis virus: crystal structure of its N-terminal domain and multimerization properties. Structure. 2005 Dec;13(12):1859-68. doi: 10.1016/j.str.2005.08.021.

101. Zúñiga S, Sola I, Moreno JL, Sabella P, Plana-Durán J, Enjuanes L. Coronavirus nucleocapsid protein is an RNA chaperone. Virology. 2007 Jan 20;357(2):215-27. doi: 10.1016/j.virol.2006.07.046.

102. Zúñiga S, Cruz JL, Sola I, Mateos-Gómez PA, Palacio L, Enjuanes L. Coronavirus nucleocapsid protein facilitates template switching and is required for efficient transcription. J Virol. 2010 Feb;84(4):2169-75. doi: 10.1128/JVI.02011-09.

103. Jayaram H, Fan H, Bowman BR, Ooi A, Jayaram J, Collisson EW, Lescar J, Prasad BV. X-ray structures of the N- and C-terminal domains of a coronavirus nucleocapsid protein: implications for nucleocapsid formation. J Virol. 2006 Jul;80(13):6612-20. doi: 10.1128/JVI.00157-06.

104. Keane SC, Giedroc DP. Solution structure of mouse hepatitis virus (MHV) nsp3a and determinants of the interaction with MHV nucleocapsid (N) protein. J Virol. 2013 Mar;87(6):3502-15. doi: 10.1128/JVI.03112-12.

105. Ruch TR, Machamer CE. The hydrophobic domain of infectious bronchitis virus E protein alters the host secretory pathway and is important for release of infectious virus. J Virol. 2011 Jan;85(2):675-85. doi: 10.1128/JVI.01570-10.

106. Binns MM, Boursnell ME, Tomley FM, Brown TD. Nucleotide sequence encoding the membrane protein of the IBV strain 6/82. Nucleic Acids Res. 1986 Jul 11;14(13):5558.

107. Wang J, Fang S, Xiao H, Chen B, Tam JP, Liu DX. Interaction of the coronavirus infectious bronchitis virus membrane protein with beta-actin and its

implication in virion assembly and budding. PLoS One. 2009;4(3):e4908. doi: 10.1371/journal.pone.0004908.

108. Masters PS. The molecular biology of coronaviruses. Adv Virus Res. 2006;66:193-292. doi: 10.1016/S0065-3527(06)66005-3

109. Stern DF, Sefton BM. Coronavirus proteins: structure and function of the oligosaccharides of the avian infectious bronchitis virus glycoproteins. J Virol. 1982 Dec;44(3):804-12. doi: 10.1128/JVI.44.3.804-812.1982

110. Liang JQ, Fang S, Yuan Q, Huang M, Chen RA, Fung TS, Liu DX. N-Linked glycosylation of the membrane protein ectodomain regulates infectious bronchitis virus-induced ER stress response, apoptosis and pathogenesis. Virology. 2019 May;531:48-56. doi: 10.1016/j.virol.2019.02.017.

111. Jimenez-Guardeño JM, Regla-Nava JA, Nieto-Torres JL, DeDiego ML, Castaño-Rodriguez C, Fernandez-Delgado R, Perlman S, Enjuanes L. Identification of the Mechanisms Causing Reversion to Virulence in an Attenuated SARS-CoV for the Design of a Genetically Stable Vaccine. PLoS Pathog. 2015 Oct 29;11(10):e1005215. doi: 10.1371/journal.ppat.1005215.

112. Kuo L, Hurst-Hess KR, Koetzner CA, Masters PS. Analyses of Coronavirus Assembly Interactions with Interspecies Membrane and Nucleocapsid Protein Chimeras. J Virol. 2016 Apr 14;90(9):4357-4368. doi: 10.1128/JVI.03212-15.

113. Westerbeck JW, Machamer CE. A Coronavirus E Protein Is Present in Two Distinct Pools with Different Effects on Assembly and the Secretory Pathway. J Virol. 2015 Sep;89(18):9313-23. doi: 10.1128/JVI.01237-15.

114. Schoeman D, Fielding BC. Coronavirus envelope protein: current knowledge. Virol J. 2019 May 27;16(1):69. doi: 10.1186/s12985-019-1182-0.

115. Liu DX, Inglis SC. Internal entry of ribosomes on a tricistronic mRNA encoded by infectious bronchitis virus. J Virol. 1992 Oct;66(10):6143-54. doi: 10.1128/JVI.66.10.6143-6154.1992.

116. Boscarino JA, Logan HL, Lacny JJ, Gallagher TM. Envelope protein palmitoylations are crucial for murine coronavirus assembly. J Virol. 2008 Mar;82(6):2989-99. doi: 10.1128/JVI.01906-07.

117. Lopez LA, Riffle AJ, Pike SL, Gardner D, Hogue BG. Importance of conserved cysteine residues in the coronavirus envelope protein. J Virol. 2008 Mar;82(6):3000-10. doi: 10.1128/JVI.01914-07.

118. Yuan Q, Liao Y, Torres J, Tam JP, Liu DX. Biochemical evidence for the presence of mixed membrane topologies of the severe acute respiratory syndrome coronavirus envelope protein expressed in mammalian cells. FEBS Lett. 2006 May 29;580(13):3192-200. doi: 10.1016/j.febslet.2006.04.076.

119. Alvarez E, DeDiego ML, Nieto-Torres JL, Jiménez-Guardeño JM, Marcos-Villar L, Enjuanes L. The envelope protein of severe acute respiratory syndrome coronavirus interacts with the non-structural protein 3 and is ubiquitinated. Virology. 2010 Jul 5;402(2):281-91. doi: 10.1016/j.virol.2010.03.015.

120. Maeda J, Repass JF, Maeda A, Makino S. Membrane topology of coronavirus E protein. Virology. 2001 Mar 15;281(2):163-9. doi: 10.1006/viro.2001.0818.

121. Cohen JR, Lin LD, Machamer CE. Identification of a Golgi complex-targeting signal in the cytoplasmic tail of the severe acute respiratory syndrome coronavirus envelope protein. J Virol. 2011 Jun;85(12):5794-803. doi: 10.1128/JVI.00060-11.

122. Carrasco L. Modification of membrane permeability induced by animal viruses early in infection. Virology. 1981 Sep;113(2):623-9. doi: 10.1016/0042-6822(81)90190-2.

123. Pinto LH, Holsinger LJ, Lamb RA. Influenza virus M2 protein has ion channel activity. Cell. 1992 May 1;69(3):517-28. doi: 10.1016/0092-8674(92)90452-i

124. Liao Y, Lescar J, Tam JP, Liu DX. Expression of SARS-coronavirus envelope protein in Escherichia coli cells alters membrane permeability. Biochem Biophys Res Commun. 2004 Dec 3;325(1):374-80. doi: 10.1016/j.bbrc.2004.10.050

125. Wilson L, Gage P, Ewart G. Hexamethylene amiloride blocks E protein ion channels and inhibits coronavirus replication. Virology. 2006 Sep 30;353(2):294-306. doi: 10.1016/j.virol.2006.05.028.

126. Wang K, Xie S, Sun B. Viral proteins function as ion channels. Biochim Biophys Acta. 2011 Feb;1808(2):510-5. doi: 10.1016/j.bbamem.2010.05.006.

127. Mould JA, Drury JE, Frings SM, Kaupp UB, Pekosz A, Lamb RA, Pinto LH. Permeation and activation of the M2 ion channel of influenza A virus. J Biol Chem. 2000 Oct 6;275(40):31038-50. doi: 10.1074/jbc.M003663200.

128. Henkel JR, Weisz OA. Influenza virus M2 protein slows traffic along the secretory pathway. pH perturbation of acidified compartments affects early Golgi transport steps. J Biol Chem. 1998 Mar 13;273(11):6518-24. doi: 10.1074/jbc.273.11.6518.

129. Gannagé M, Dormann D, Albrecht R, Dengjel J, Torossi T, Rämer PC, Lee M, Strowig T, Arrey F, Conenello G, Pypaert M, Andersen J, García-Sastre A, Münz C. Matrix protein 2 of influenza A virus blocks autophagosome fusion with lysosomes. Cell Host Microbe. 2009 Oct 22;6(4):367-80. doi: 10.1016/j.chom.2009.09.005.

130. Schubert U, Ferrer-Montiel AV, Oblatt-Montal M, Henklein P, Strebel K, Montal M. Identification of an ion channel activity of the Vpu transmembrane domain and its involvement in the regulation of virus release from HIV-1-infected cells. FEBS Lett. 1996 Nov 25;398(1):12-8. doi: 10.1016/s0014-5793(96)01146-5

131. McClenaghan C, Hanson A, Lee SJ, Nichols CG. Coronavirus Proteins as Ion Channels: Current and Potential Research. Front Immunol. 2020 Oct 9;11:573339. doi: 10.3389/fimmu.2020.573339.

132. Chan CM, Tsoi H, Chan WM, Zhai S, Wong CO, Yao X, Chan WY, Tsui SK, Chan HY. The ion channel activity of the SARS-coronavirus 3a protein is linked to its pro-apoptotic function. Int J Biochem Cell Biol. 2009 Nov;41(11):2232-9. doi: 10.1016/j.biocel.2009.04.019.

133. Chen CC, Krüger J, Sramala I, Hsu HJ, Henklein P, Chen YM, Fischer WB. ORF8a of SARS-CoV forms an ion channel: experiments and molecular dynamics simulations. Biochim Biophys Acta. 2011 Feb;1808(2):572-9. doi: 10.1016/j.bbamem.2010.08.004.

134. Castaño-Rodriguez C, Honrubia JM, Gutiérrez-Álvarez J, DeDiego ML, Nieto-Torres JL, Jimenez-Guardeño JM, Regla-Nava JA, Fernandez-Delgado R, Verdia-Báguena C, Queralt-Martín M, Kochan G, Perlman S, Aguilella VM, Sola I, Enjuanes L. Role of Severe Acute Respiratory Syndrome Coronavirus Viroporins E, 3a, and 8a in Replication and Pathogenesis. mBio. 2018 May 22;9(3):e02325-17. doi: 10.1128/mBio.02325-17.

135. Wilson L, McKinlay C, Gage P, Ewart G. SARS coronavirus E protein forms cation-selective ion channels. Virology. 2004 Dec 5;330(1):322-31. doi: 10.1016/j.virol.2004.09.033.

136. Torres J, Parthasarathy K, Lin X, Saravanan R, Kukol A, Liu DX. Model of a putative pore: the pentameric alpha-helical bundle of SARS coronavirus E protein in lipid bilayers. Biophys J. 2006 Aug 1;91(3):938-47. doi: 10.1529/biophysj.105.080119.

137. Kuzmin A, Orekhov P, Astashkin R, Gordeliy V, Gushchin I. Structure and dynamics of the SARS-CoV-2 envelope protein monomer. Proteins. 2022 May;90(5):1102-1114. doi: 10.1002/prot.26317.

138. Nieto-Torres JL, DeDiego ML, Verdiá-Báguena C, Jimenez-Guardeño JM, Regla-Nava JA, Fernandez-Delgado R, Castaño-Rodriguez C, Alcaraz A, Torres J, Aguilella VM, Enjuanes L. Severe acute respiratory syndrome coronavirus envelope protein ion channel activity promotes virus fitness and pathogenesis. PLoS Pathog. 2014 May 1;10(5):e1004077. doi: 10.1371/journal.ppat.1004077.

139. Parthasarathy K, Lu H, Surya W, Vararattanavech A, Pervushin K, Torres J. Expression and purification of coronavirus envelope proteins using a modified β-barrel construct. Protein Expr Purif. 2012 Sep;85(1):133-41. doi: 10.1016/j.pep.2012.07.005.

140. Torres J, Wang J, Parthasarathy K, Liu DX. The transmembrane oligomers of coronavirus protein E. Biophys J. 2005 Feb;88(2):1283-90. doi: 10.1529/biophysj.104.051730.

141. Torres J, Maheswari U, Parthasarathy K, Ng L, Liu DX, Gong X. Conductance and amantadine binding of a pore formed by a lysine-flanked transmembrane domain of SARS coronavirus envelope protein. Protein Sci. 2007 Sep;16(9):2065-71. doi: 10.1110/ps.062730007

142. Ruch TR, Machamer CE. A single polar residue and distinct membrane topologies impact the function of the infectious bronchitis coronavirus E protein. PLoS Pathog. 2012;8(5):e1002674. doi: 10.1371/journal.ppat.1002674.

143. Surya W, Li Y, Torres J. Structural model of the SARS coronavirus E channel in LMPG micelles. Biochim Biophys Acta Biomembr. 2018 Jun;1860(6):1309-1317. doi: 10.1016/j.bbamem.2018.02.017.

144. Hogue, B.G. and Machamer, C.E. Coronavirus Structural Proteins and Virus Assembly. In Nidoviruses (eds S. Perlman, T. Gallagher and E.J. Snijder). 2007. doi: 10.1128/9781555815790.ch12

145. Stodola JK, Dubois G, Le Coupanec A, Desforges M, Talbot PJ. The OC43 human coronavirus envelope protein is critical for infectious virus production and propagation in neuronal cells and is a determinant of neurovirulence and CNS pathology. Virology. 2018 Feb;515:134-149. doi: 10.1016/j.virol.2017.12.023.

146. Raamsman MJ, Locker JK, de Hooge A, de Vries AA, Griffiths G, Vennema H, Rottier PJ. Characterization of the coronavirus mouse hepatitis virus strain A59 small membrane protein E. J Virol. 2000 Mar;74(5):2333-42. doi: 10.1128/jvi.74.5.2333-2342.2000.

147. Fischer F, Stegen CF, Masters PS, Samsonoff WA. Analysis of constructed E gene mutants of mouse hepatitis virus confirms a pivotal role for E protein in coronavirus assembly. J Virol. 1998 Oct;72(10):7885-94. doi: 10.1128/JVI.72.10.7885-7894.1998.

148. Regla-Nava JA, Nieto-Torres JL, Jimenez-Guardeño JM, Fernandez-Delgado R, Fett C, Castaño-Rodríguez C, Perlman S, Enjuanes L, DeDiego ML. Severe acute respiratory syndrome coronaviruses with mutations in the E protein are attenuated and promising vaccine candidates. J Virol. 2015 Apr;89(7):3870-87. doi: 10.1128/JVI.03566-14.

149. DeDiego ML, Alvarez E, Almazán F, Rejas MT, Lamirande E, Roberts A, Shieh WJ, Zaki SR, Subbarao K, Enjuanes L. A severe acute respiratory syndrome coronavirus that lacks the E gene is attenuated in vitro and in vivo. J Virol. 2007 Feb;81(4):1701-13. doi: 10.1128/JVI.01467-06.

150. Castaño-Rodriguez C, Honrubia JM, Gutiérrez-Álvarez J, DeDiego ML, Nieto-Torres JL, Jimenez-Guardeño JM, Regla-Nava JA, Fernandez-Delgado R, Verdia-

Báguena C, Queralt-Martín M, Kochan G, Perlman S, Aguilella VM, Sola I, Enjuanes L. Role of Severe Acute Respiratory Syndrome Coronavirus Viroporins E, 3a, and 8a in Replication and Pathogenesis. mBio. 2018 May 22;9(3):e02325-17. doi: 10.1128/mBio.02325-17.

151. Fett C, DeDiego ML, Regla-Nava JA, Enjuanes L, Perlman S. Complete protection against severe acute respiratory syndrome coronavirus-mediated lethal respiratory disease in aged mice by immunization with a mouse-adapted virus lacking E protein. J Virol. 2013 Jun;87(12):6551-9. doi: 10.1128/JVI.00087-13

152. Li S, Yuan L, Dai G, Chen RA, Liu DX, Fung TS. Regulation of the ER Stress Response by the Ion Channel Activity of the Infectious Bronchitis Coronavirus Envelope Protein Modulates Virion Release, Apoptosis, Viral Fitness, and Pathogenesis. Front Microbiol. 2020 Jan 24;10:3022. doi: 10.3389/fmicb.2019.03022.

153. Laconi A, van Beurden SJ, Berends AJ, Krämer-Kühl A, Jansen CA, Spekreijse D, Chénard G, Philipp HC, Mundt E, Rottier PJM, Hélène Verheije M. Deletion of accessory genes 3a, 3b, 5a or 5b from avian coronavirus infectious bronchitis virus induces an attenuated phenotype both in vitro and in vivo. J Gen Virol. 2018 Aug 1;99(10):1381–90. doi: 10.1099/jgv.0.001130.

154. van Beurden SJ, Berends AJ, Krämer-Kühl A, Spekreijse D, Chenard G, Philipp HC, Mundt E, Rottier PJM, Verheije MH. Recombinant live attenuated avian coronavirus vaccines with deletions in the accessory genes 3ab and/or 5ab protect against infectious bronchitis in chickens. Vaccine. 2018 Feb 14;36(8):1085-1092. doi: 10.1016/j.vaccine.2018.01.017.

155. Gutiérrez-Álvarez J, Honrubia JM, Sanz-Bravo A, González-Miranda E, Fernández-Delgado R, Rejas MT, Zúñiga S, Sola I, Enjuanes L. Middle East respiratory syndrome coronavirus vaccine based on a propagation-defective RNA

replicon elicited sterilizing immunity in mice. Proc Natl Acad Sci U S A. 2021 Oct 26;118(43):e2111075118. doi: 10.1073/pnas.2111075118.

156. Casais R, Davies M, Cavanagh D, Britton P. Gene 5 of the avian coronavirus infectious bronchitis virus is not essential for replication. J Virol. 2005 Jul;79(13):8065-78. doi: 10.1128/JVI.79.13.8065-8078.2005.

157. Hodgson T, Britton P, Cavanagh D. Neither the RNA nor the proteins of open reading frames 3a and 3b of the coronavirus infectious bronchitis virus are essential for replication. J Virol. 2006 Jan;80(1):296-305. doi: 10.1128/JVI.80.1.296-305.2006.

158. Zhang Y, Xu Z, Cao Y. Host Antiviral Responses against Avian Infectious Bronchitis Virus (IBV): Focus on Innate Immunity. Viruses. 2021 Aug 26;13(9):1698. doi: 10.3390/v13091698.

159. Eifart P, Ludwig K, Böttcher C, de Haan CA, Rottier PJ, Korte T, Herrmann A. Role of endocytosis and low pH in murine hepatitis virus strain A59 cell entry. J Virol. 2007 Oct;81(19):10758-68. doi: 10.1128/JVI.00725-07.

160. Chen S, Cheng A, Wang M. Innate sensing of viruses by pattern recognition receptors in birds. Vet Res. 2013 Sep 9;44(1):82. doi: 10.1186/1297-9716-44-82.

161. Yu L, Zhang X, Wu T, Su J, Wang Y, Wang Y, Ruan B, Niu X, Wu Y. Avian infectious bronchitis virus disrupts the melanoma differentiation associated gene 5 (MDA5) signaling pathway by cleavage of the adaptor protein MAVS. BMC Vet Res. 2017 Nov 13;13(1):332. doi: 10.1186/s12917-017-1253-7.

162. Khan S, Roberts J, Wu SB. Regulation of Immunity-Related Genes by Infectious Bronchitis Virus Challenge in Spleen of Laying Chickens. Viral Immunol. 2020 Jun;33(5):413-420. doi: 10.1089/vim.2019.0139.

163. Gürtler C, Bowie AG. Innate immune detection of microbial nucleic acids. Trends Microbiol. 2013 Aug;21(8):413-20. doi: 10.1016/j.tim.2013.04.004.

164. Amarasinghe A, Abdul-Cader MS, Almatrouk Z, van der Meer F, Cork SC, Gomis S, Abdul-Careem MF. Induction of innate host responses characterized by production of interleukin (IL)-1β and recruitment of macrophages to the respiratory tract of chickens following infection with infectious bronchitis virus (IBV). Vet Microbiol. 2018 Feb;215:1-10. doi: 10.1016/j.vetmic.2018.01.001.

165. Asif M, Lowenthal JW, Ford ME, Schat KA, Kimpton WG, Bean AG. Interleukin-6 expression after infectious bronchitis virus infection in chickens. Viral Immunol. 2007 Sep;20(3):479-86. doi: 10.1089/vim.2006.0109.

166. Kint J, Fernandez-Gutierrez M, Maier HJ, Britton P, Langereis MA, Koumans J, Wiegertjes GF, Forlenza M. Activation of the chicken type I interferon response by infectious bronchitis coronavirus. J Virol. 2015 Jan 15;89(2):1156-67. doi: 10.1128/JVI.02671-14.

167. Li J, Liu Y, Zhang X. Murine coronavirus induces type I interferon in oligodendrocytes through recognition by RIG-I and MDA5. J Virol. 2010 Jul;84(13):6472-82. doi: 10.1128/JVI.00016-10.

168. Pei J, Sekellick MJ, Marcus PI, Choi IS, Collisson EW. Chicken interferon type I inhibits infectious bronchitis virus replication and associated respiratory illness. J Interferon Cytokine Res. 2001 Dec;21(12):1071-7. doi: 10.1089/107999001317205204.

169. Kovacsovics-Bankowski M, Rock KL. A phagosome-to-cytosol pathway for exogenous antigens presented on MHC class I molecules. Science. 1995 Jan 13;267(5195):243-6. doi: 10.1126/science.7809629.

170. Koepke L, Hirschenberger M, Hayn M, Kirchhoff F, Sparrer KM. Manipulation of autophagy by SARS-CoV-2 proteins. Autophagy. 2021 Sep;17(9):2659-2661. doi: 10.1080/15548627.2021.1953847.

171. de Wit JJ, Nieuwenhuisen-van Wilgen J, Hoogkamer A, van de Sande H, Zuidam GJ, Fabri TH. Induction of cystic oviducts and protection against early challenge with infectious bronchitis virus serotype D388 (genotype QX) by maternally derived antibodies and by early vaccination. Avian Pathol. 2011 Oct;40(5):463-71. doi: 10.1080/03079457.2011.599060.

172. Hennion RM, Hill G. The preparation of chicken kidney cell cultures for virus propagation. Methods Mol Biol. 2015;1282:57-62. doi: 10.1007/978-1-4939-2438-7_6

173. Himly M, Foster DN, Bottoli I, Iacovoni JS, Vogt PK. The DF-1 chicken fibroblast cell line: transformation induced by diverse oncogenes and cell death resulting from infection by avian leukosis viruses. Virology. 1998 Sep 1;248(2):295-304. doi: 10.1006/viro.1998.9290.

174. Hennion RM. The preparation of chicken tracheal organ cultures for virus isolation, propagation, and titration. Methods Mol Biol. 2015;1282:51-6. doi: 10.1007/978-1-4939-2438-7_5.

175. Hodgson T, Casais R, Dove B, Britton P, Cavanagh D. Recombinant infectious bronchitis coronavirus Beaudette with the spike protein gene of the pathogenic M41 strain remains attenuated but induces protective immunity. J Virol. 2004 Dec;78(24):13804-11. doi: 10.1128/JVI.78.24.13804-13811.2004.

176. Casais R, Dove B, Cavanagh D, Britton P. Recombinant avian infectious bronchitis virus expressing a heterologous spike gene demonstrates that the spike protein is a determinant of cell tropism. J Virol. 2003 Aug;77(16):9084-9. doi: 10.1128/jvi.77.16.9084-9089.2003

177. Keep S, Stevenson-Leggett P, Dowgier G, Everest H, Freimanis G, Oade M, Hammond JA, Armesto M, Vila R, Bru T, Geerligs H, Britton P, Bickerton E. Identification of Amino Acids within Nonstructural Proteins 10 and 14 of the Avian

Coronavirus Infectious Bronchitis Virus That Result in Attenuation In Vivo and In Ovo. J Virol. 2022 Mar 23;96(6):e0205921. doi: 10.1128/jvi.02059-21

178. Britton P, Green P, Kottier S, Mawditt KL, Penzes Z, Cavanagh D, Skinner MA. Expression of bacteriophage T7 RNA polymerase in avian and mammalian cells by a recombinant fowlpox virus. J Gen Virol. 1996 May;77 (Pt 5):963-7. doi: 10.1099/0022-1317-77-5-963.

179. Keep SM, Bickerton E, Britton P. Transient dominant selection for the modification and generation of recombinant infectious bronchitis coronaviruses. Methods Mol Biol. 2015;1282:115-33. doi: 10.1007/978-1-4939-2438-7_12

180. Britton P, Evans S, Dove B, Davies M, Casais R, Cavanagh D. Generation of a recombinant avian coronavirus infectious bronchitis virus using transient dominant selection. J Virol Methods. 2005 Feb;123(2):203-11. doi: 10.1016/j.jviromet.2004.09.017.

181. Armesto M, Bentley, K, Bickerton, E, Keep, S. and Britton, P. Coronavirus reverse genetics. Reverse Genetics of RNA Viruses: Applications and Perspectives: Wiley Blackwell; 2013.

182. Keep SM, Bickerton E, Britton P. Transient dominant selection for the modification and generation of recombinant infectious bronchitis coronaviruses. Methods Mol Biol. 2015;1282:115-33. doi: 10.1007/978-1-4939-2438-7_12.

183. Batra A, Maier HJ, Fife MS. Selection of reference genes for gene expression analysis by real-time qPCR in avian cells infected with infectious bronchitis virus. Avian Pathol. 2017 Apr;46(2):173-180. doi: 10.1080/03079457.2016.1235258.

184. Vandesompele J, De Preter K, Pattyn F, Poppe B, Van Roy N, De Paepe A, Speleman F. Accurate normalization of real-time quantitative RT-PCR data by

geometric averaging of multiple internal control genes. Genome Biol. 2002 Jun 18;3(7). doi: 10.1186/gb-2002-3-7-research0034.

185. Keep SM, Bickerton E, Britton P. Partial purification of IBV and subsequent isolation of viral RNA for next-generation sequencing. Methods Mol Biol. 2015;1282:109-12. doi: 10.1007/978-1-4939-2438-7_11

186. Freimanis GL, Oade MS. Whole-Genome Sequencing Protocols for IBV and Other Coronaviruses Using High-Throughput Sequencing. Methods Mol Biol. 2020;2203:67-74. doi: 10.1007/978-1-0716-0900-2_5.

187. Schwede T, Kopp J, Guex N, Peitsch MC. SWISS-MODEL: An automated protein homology-modeling server. Nucleic Acids Res. 2003 Jul 1;31(13):3381-5. doi: 10.1093/nar/gkg520.

188. Jumper J, Evans R, Pritzel A, Green T, Figurnov M, Ronneberger O, Tunyasuvunakool K, Bates R, Žídek A, Potapenko A, Bridgland A, Meyer C, Kohl SAA, Ballard AJ, Cowie A, Romera-Paredes B, Nikolov S, Jain R, Adler J, Back T, Petersen S, Reiman D, Clancy E, Zielinski M, Steinegger M, Pacholska M, Berghammer T, Bodenstein S, Silver D, Vinyals O, Senior AW, Kavukcuoglu K, Kohli P, Hassabis D. Highly accurate protein structure prediction with AlphaFold. Nature. 2021 Aug;596(7873):583-589. doi: 10.1038/s41586-021-03819-2.

189. Mirdita M, Schütze K, Moriwaki Y, Heo L, Ovchinnikov S, Steinegger M. ColabFold: making protein folding accessible to all. Nat Methods. 2022 Jun;19(6):679-682. doi: 10.1038/s41592-022-01488-1.

190. Doyle N, Hawes PC, Simpson J, Adams LH, Maier HJ. The Porcine Deltacoronavirus Replication Organelle Comprises Double-Membrane Vesicles and Zippered Endoplasmic Reticulum with Double-Membrane Spherules. Viruses. 2019 Nov 5;11(11):1030. doi: 10.3390/v11111030

191. Webb I, Keep S, Littolff K, Stuart J, Freimanis G, Britton P, Davidson AD, Maier HJ, Bickerton E. The Genetic Stability, Replication Kinetics and Cytopathogenicity of Recombinant Avian Coronaviruses with a T16A or an A26F Mutation within the E Protein Is Cell-Type Dependent. Viruses. 2022 Aug 15;14(8):1784. doi: 10.3390/v14081784.

192. Bickerton E, Maier HJ, Stevenson-Leggett P, Armesto M, Britton P. The S2 Subunit of Infectious Bronchitis Virus Beaudette Is a Determinant of Cellular Tropism. J Virol. 2018 Sep 12;92(19):e01044-18. doi: 10.1128/JVI.01044-18.

193. Desmyter J, Melnick JL, Rawls WE. Defectiveness of interferon production and of rubella virus interference in a line of African green monkey kidney cells (Vero). J Virol. 1968 Oct;2(10):955-61. doi: 10.1128/JVI.2.10.955-961.1968.

194. Giotis ES, Ross CS, Robey RC, Nohturfft A, Goodbourn S, Skinner MA. Constitutively elevated levels of SOCS1 suppress innate responses in DF-1 immortalised chicken fibroblast cells. Sci Rep. 2017 Dec 13;7(1):17485. doi: 10.1038/s41598-017-17730-2.

195. Schilling MA, Katani R, Memari S, Cavanaugh M, Buza J, Radzio-Basu J, Mpenda FN, Deist MS, Lamont SJ, Kapur V. Transcriptional Innate Immune Response of the Developing Chicken Embryo to Newcastle Disease Virus Infection. Front Genet. 2018 Feb 27;9:61. doi: 10.3389/fgene.2018.00061.

196. Davison TF. The immunologists' debt to the chicken. Br Poult Sci. 2003 Mar;44(1):6-21. doi: 10.1080/0007166031000085364.

197. Netland J, DeDiego ML, Zhao J, Fett C, Álvarez E, Nieto-Torres JL, Enjuanes L, Perlman S. Immunization with an attenuated severe acute respiratory syndrome coronavirus deleted in E protein protects against lethal respiratory disease. Virology. 2010 Mar 30;399(1):120-128. doi: 10.1016/j.virol.2010.01.004.

198. Fung TS, Torres J, Liu DX. The Emerging Roles of Viroporins in ER Stress Response and Autophagy Induction during Virus Infection. Viruses. 2015 Jun 4;7(6):2834-57. doi: 10.3390/v7062749

199. Kuzmin A, Orekhov P, Astashkin R, Gordeliy V, Gushchin I. Structure and dynamics of the SARS-CoV-2 envelope protein monomer. Proteins. 2022 May;90(5):1102-1114. doi: 10.1002/prot.26317.

200. Moratorio G, Henningsson R, Barbezange C, Carrau L, Bordería AV, Blanc H, Beaucourt S, Poirier EZ, Vallet T, Boussier J, Mounce BC, Fontes M, Vignuzzi M. Attenuation of RNA viruses by redirecting their evolution in sequence space. Nat Microbiol. 2017 Jun 5;2(8):17088. doi: 10.1038/nmicrobiol.2017.88.

201. Bordería AV, Isakov O, Moratorio G, Henningsson R, Agüera-González S, Organtini L, Gnädig NF, Blanc H, Alcover A, Hafenstein S, Fontes M, Shomron N, Vignuzzi M. Group Selection and Contribution of Minority Variants during Virus Adaptation Determines Virus Fitness and Phenotype. PLoS Pathog. 2015 May 5;11(5):e1004838. doi: 10.1371/journal.ppat.1004838.

202. Oade MS, Keep S, Freimanis GL, Orton RJ, Britton P, Hammond JA, Bickerton E. Attenuation of Infectious Bronchitis Virus in Eggs Results in Different Patterns of Genomic Variation across Multiple Replicates. J Virol. 2019 Jun 28;93(14):e00492-19. doi: 10.1128/JVI.00492-19

203. Oade MS. Characterising the process of attenuation by serial egg passaging of Infectious bronchitis virus (IBV) using genomic and phenotypic methods. University of Glasgow; 2019.

204. Promkuntod N, van Eijndhoven RE, de Vrieze G, Gröne A, Verheije MH. Mapping of the receptor-binding domain and amino acids critical for attachment in the spike protein of avian coronavirus infectious bronchitis virus. Virology. 2014 Jan 5;448:26-32. doi: 10.1016/j.virol.2013.09.018.

205. Ou X, Zheng W, Shan Y, Mu Z, Dominguez SR, Holmes KV, Qian Z. Identification of the Fusion Peptide-Containing Region in Betacoronavirus Spike Glycoproteins. J Virol. 2016 May 27;90(12):5586-5600. doi: 10.1128/JVI.00015-16.

206. Churchill AE. The Use of Chicken Kidney Tissue Culture in the Study of the Avian Viruses of Newcastle Disease, Infectious Laryngo Tracheitis and Infectious Bronchitis. Res Vet Sci. 1965 Apr;6:162-9.

207. Riss T, Niles A, Moravec R, Karassina N, Vidugiriene J. Cytotoxicity Assays: In Vitro Methods to Measure Dead Cells. 2019, May 1. In: Markossian S, Grossman A, Brimacombe K, Arkin M, Auld D, Austin C, Baell J, Chung TDY, Coussens NP, Dahlin JL, Devanarayan V, Foley TL, Glicksman M, Haas JV, Hall MD, Hoare S, Inglese J, Iversen PW, Kales SC, Lal-Nag M, Li Z, McGee J, McManus O, Riss T, Saradjian P, Sittampalam GS, Tarselli M, Trask OJ Jr, Wang Y, Weidner JR, Wildey MJ, Wilson K, Xia M, Xu X, editors. Assay Guidance Manual. Bethesda (MD): Eli Lilly & Company and the National Center for Advancing Translational Sciences

208. Das S, Meinel MK, Wu Z, Müller-Plathe F. The role of the envelope protein in the stability of a coronavirus model membrane against an ethanolic disinfectant. J Chem Phys. 2021 Jun 28;154(24):245101. doi: 10.1063/5.0055331.

209. Dingle, J.G. Module 4: Gas exchange and thermoregulation. In Study Book: Poultry Husbandry 1; University of Southern Queensland: Toowoomba, Australia, 1990.

210. Hofstad MS. Stability of avian infectious bronchitis virus at 56 C. Cornell Vet. 1956 Jan;46(1):122-8.

211. Kuo L, Masters PS. The small envelope protein E is not essential for murine coronavirus replication. J Virol. 2003 Apr;77(8):4597-608. doi: 10.1128/jvi.77.8.4597-4608.2003.

212. Ortego J, Ceriani JE, Patiño C, Plana J, Enjuanes L. Absence of E protein arrests transmissible gastroenteritis coronavirus maturation in the secretory pathway. Virology. 2007 Nov 25;368(2):296-308. doi: 10.1016/j.virol.2007.05.032.

213. Almazán F, DeDiego ML, Sola I, Zuñiga S, Nieto-Torres JL, Marquez-Jurado S, Andrés G, Enjuanes L. Engineering a replication-competent, propagation-defective Middle East respiratory syndrome coronavirus as a vaccine candidate. mBio. 2013 Sep 10;4(5):e00650-13. doi: 10.1128/mBio.00650-13.

214. Nishimura K, Fukagawa T, Takisawa H, Kakimoto T, Kanemaki M. An auxin-based degron system for the rapid depletion of proteins in nonplant cells. Nat Methods. 2009 Dec;6(12):917-22. doi: 10.1038/nmeth.1401.

215. Ruch TR, Machamer CE. The coronavirus E protein: assembly and beyond. Viruses. 2012 Mar;4(3):363-82. doi: 10.3390/v4030363.

216. Nelson C, Froes P, Dyck AM, Chavarría J, Boda E, Coca A, Crespo G, Lima H. Monitoring temperatures in the vaccine cold chain in Bolivia. Vaccine. 2007 Jan 5;25(3):433-7. doi: 10.1016/j.vaccine.2006.08.017.

217. Fanelli A, Mantegazza L, Hendrickx S, Capua I. Thermostable Vaccines in Veterinary Medicine: State of the Art and Opportunities to Be Seized. Vaccines (Basel). 2022 Feb 5;10(2):245. doi: 10.3390/vaccines10020245.

218. Corse E, Machamer CE. Infectious bronchitis virus E protein is targeted to the Golgi complex and directs release of virus-like particles. J Virol. 2000 May;74(9):4319-26. doi: 10.1128/jvi.74.9.4319-4326.2000.

219. Lim KP, Liu DX. The missing link in coronavirus assembly. Retention of the avian coronavirus infectious bronchitis virus envelope protein in the pre-Golgi compartments and physical interaction between the envelope and membrane

proteins. J Biol Chem. 2001 May 18;276(20):17515-23. doi: 10.1074/jbc.M009731200

220. Venkatagopalan P, Daskalova SM, Lopez LA, Dolezal KA, Hogue BG. Coronavirus envelope (E) protein remains at the site of assembly. Virology. 2015 Apr;478:75-85. doi: 10.1016/j.virol.2015.02.005

221. Liu DX, Inglis SC. Association of the infectious bronchitis virus 3c protein with the virion envelope. Virology. 1991 Dec;185(2):911-7. doi: 10.1016/0042-6822(91)90572-s.

222. Sakaguchi T, Leser GP, Lamb RA. The ion channel activity of the influenza virus M2 protein affects transport through the Golgi apparatus. J Cell Biol. 1996 May;133(4):733-47. doi: 10.1083/jcb.133.4.733

223. Champliaud MF, Burgeson RE, Jin W, Baden HP, Olson PF. cDNA cloning and characterization of sciellin, a LIM domain protein of the keratinocyte cornified envelope. J Biol Chem. 1998 Nov 20;273(47):31547-54. doi: 10.1074/jbc.273.47.31547.

224. Mühleisen TW, Leber M, Schulze TG, Strohmaier J, Degenhardt F, Treutlein J, Mattheisen M, Forstner AJ, Schumacher J, Breuer R, Meier S, Herms S, Hoffmann P, Lacour A, Witt SH, Reif A, Müller-Myhsok B, Lucae S, Maier W, Schwarz M, Vedder H, Kammerer-Ciernioch J, Pfennig A, Bauer M, Hautzinger M, Moebus S, Priebe L, Czerski PM, Hauser J, Lissowska J, Szeszenia-Dabrowska N, Brennan P, McKay JD, Wright A, Mitchell PB, Fullerton JM, Schofield PR, Montgomery GW, Medland SE, Gordon SD, Martin NG, Krasnow V, Chuchalin A, Babadjanova G, Pantelejeva G, Abramova LI, Tiganov AS, Polonikov A, Khusnutdinova E, Alda M, Grof P, Rouleau GA, Turecki G, Laprise C, Rivas F, Mayoral F, Kogevinas M, Grigoroiu-Serbanescu M, Propping P, Becker T, Rietschel M, Nöthen MM, Cichon S.

Genome-wide association study reveals two new risk loci for bipolar disorder. Nat Commun. 2014 Mar 11;5:3339. doi: 10.1038/ncomms4339.

225. Zhang H, Li Y, Wang HB, Zhang A, Chen ML, Fang ZX, Dong XD, Li SB, Du Y, Xiong D, He JY, Li MZ, Liu YM, Zhou AJ, Zhong Q, Zeng YX, Kieff E, Zhang Z, Gewurz BE, Zhao B, Zeng MS. Ephrin receptor A2 is an epithelial cell receptor for Epstein-Barr virus entry. Nat Microbiol. 2018 Feb;3(2):1-8. doi: 10.1038/s41564-017-0080-8.

226. Nakamura N, Rabouille C, Watson R, Nilsson T, Hui N, Slusarewicz P, Kreis TE, Warren G. Characterization of a cis-Golgi matrix protein, GM130. J Cell Biol. 1995 Dec;131(6 Pt 2):1715-26. doi: 10.1083/jcb.131.6.1715.

227. Appenzeller C, Andersson H, Kappeler F, Hauri HP. The lectin ERGIC-53 is a cargo transport receptor for glycoproteins. Nat Cell Biol. 1999 Oct;1(6):330-4. doi: 10.1038/14020.

228. Lippincott-Schwartz J, Yuan LC, Bonifacino JS, Klausner RD. Rapid redistribution of Golgi proteins into the ER in cells treated with brefeldin A: evidence for membrane cycling from Golgi to ER. Cell. 1989 Mar 10;56(5):801-13. doi: 10.1016/0092-8674(89)90685-5.

229. Scheel J, Pepperkok R, Lowe M, Griffiths G, Kreis TE. Dissociation of coatomer from membranes is required for brefeldin A-induced transfer of Golgi enzymes to the endoplasmic reticulum. J Cell Biol. 1997 Apr 21;137(2):319-33. doi: 10.1083/jcb.137.2.319.

230. Feng Y, Yu S, Lasell TK, Jadhav AP, Macia E, Chardin P, Melancon P, Roth M, Mitchison T, Kirchhausen T. Exo1: a new chemical inhibitor of the exocytic pathway. Proc Natl Acad Sci U S A. 2003 May 27;100(11):6469-74. doi: 10.1073/pnas.0631766100.

231. Plutner H, Cox AD, Pind S, Khosravi-Far R, Bourne JR, Schwaninger R, Der CJ, Balch WE. Rab1b regulates vesicular transport between the endoplasmic reticulum and successive Golgi compartments. J Cell Biol. 1991 Oct;115(1):31-43. doi: 10.1083/jcb.115.1.31.

232. Monetta P, Slavin I, Romero N, Alvarez C. Rab1b interacts with GBF1 and modulates both ARF1 dynamics and COPI association. Mol Biol Cell. 2007 Jul;18(7):2400-10. doi: 10.1091/mbc.e06-11-1005.

233. Alvarez C, Garcia-Mata R, Brandon E, Sztul E. COPI recruitment is modulated by a Rab1b-dependent mechanism. Mol Biol Cell. 2003 May;14(5):2116-27. doi: 10.1091/mbc.e02-09-0625.

234. Romero N, Dumur CI, Martinez H, García IA, Monetta P, Slavin I, Sampieri L, Koritschoner N, Mironov AA, De Matteis MA, Alvarez C. Rab1b overexpression modifies Golgi size and gene expression in HeLa cells and modulates the thyrotrophin response in thyroid cells in culture. Mol Biol Cell. 2013 Mar;24(5):617-32. doi: 10.1091/mbc.E12-07-0530.

235. Yamayoshi S, Neumann G, Kawaoka Y. Role of the GTPase Rab1b in ebolavirus particle formation. J Virol. 2010 May;84(9):4816-20. doi: 10.1128/JVI.00010-10.

236. Lippincott-Schwartz J, Yuan L, Tipper C, Amherdt M, Orci L, Klausner RD. Brefeldin A's effects on endosomes, lysosomes, and the TGN suggest a general mechanism for regulating organelle structure and membrane traffic. Cell. 1991 Nov 1;67(3):601-16. doi: 10.1016/0092-8674(91)90534-6.

237. Yonemura Y, Li X, Müller K, Krämer A, Atigbire P, Mentrup T, Feuerhake T, Kroll T, Shomron O, Nohl R, Arndt HD, Hoischen C, Hemmerich P, Hirschberg K, Kaether C. Inhibition of cargo export at ER exit sites and the trans-Golgi network by

the secretion inhibitor FLI-06. J Cell Sci. 2016 Oct 15;129(20):3868-3877. doi: 10.1242/jcs.186163.

238. Krämer A, Mentrup T, Kleizen B, Rivera-Milla E, Reichenbach D, Enzensperger C, Nohl R, Täuscher E, Görls H, Ploubidou A, Englert C, Werz O, Arndt HD, Kaether C. Small molecules intercept Notch signaling and the early secretory pathway. Nat Chem Biol. 2013 Nov;9(11):731-8. doi: 10.1038/nchembio.1356.

239. Zhang Y, Liu J, Peng X, Zhu CC, Han J, Luo J, Rui R. KIF20A regulates porcine oocyte maturation and early embryo development. PLoS One. 2014 Jul 18;9(7):e102898. doi: 10.1371/journal.pone.0102898.

240. Echard A, Jollivet F, Martinez O, Lacapère JJ, Rousselet A, Janoueix-Lerosey I, Goud B. Interaction of a Golgi-associated kinesin-like protein with Rab6. Science. 1998 Jan 23;279(5350):580-5. doi: 10.1126/science.279.5350.580.

241. Goud B, Zahraoui A, Tavitian A, Saraste J. Small GTP-binding protein associated with Golgi cisternae. Nature. 1990 Jun 7;345(6275):553-6. doi: 10.1038/345553a0.

242. Zhang C, Brown MQ, van de Ven W, Zhang ZM, Wu B, Young MC, Synek L, Borchardt D, Harrison R, Pan S, Luo N, Huang YM, Ghang YJ, Ung N, Li R, Isley J, Morikis D, Song J, Guo W, Hooley RJ, Chang CE, Yang Z, Zarsky V, Muday GK, Hicks GR, Raikhel NV. Endosidin2 targets conserved exocyst complex subunit EXO70 to inhibit exocytosis. Proc Natl Acad Sci U S A. 2016 Jan 5;113(1):E41-50. doi: 10.1073/pnas.1521248112.

243. Salanueva IJ, Carrascosa JL, Risco C. Structural maturation of the transmissible gastroenteritis coronavirus. J Virol. 1999 Oct;73(10):7952-64. doi: 10.1128/JVI.73.10.7952-7964.1999.

244. Limouze J, Straight AF, Mitchison T, Sellers JR. Specificity of blebbistatin, an inhibitor of myosin II. J Muscle Res Cell Motil. 2004;25(4-5):337-41. doi: 10.1007/s10974-004-6060-7

245. Torgerson RR, McNiven MA. The actin-myosin cytoskeleton mediates reversible agonist-induced membrane blebbing. J Cell Sci. 1998 Oct;111 (Pt 19):2911-22. doi: 10.1242/jcs.111.19.2911.

246. Mousnier A, Bell AS, Swieboda DP, Morales-Sanfrutos J, Pérez-Dorado I, Brannigan JA, Newman J, Ritzefeld M, Hutton JA, Guedán A, Asfor AS, Robinson SW, Hopkins-Navratilova I, Wilkinson AJ, Johnston SL, Leatherbarrow RJ, Tuthill TJ, Solari R, Tate EW. Fragment-derived inhibitors of human N-myristoyltransferase block capsid assembly and replication of the common cold virus. Nat Chem. 2018 Jun;10(6):599-606. doi: 10.1038/s41557-018-0039-2.

247. Agoni C, Salifu EY, Enslin G, Kwofie SK, Soliman ME. Dual-Inhibition of Human N-Myristoyltransferase Subtypes Halts Common Cold Pathogenesis: Atomistic Perspectives from the Case of IMP-1088. Chem Biodivers. 2022 Feb;19(2):e202100748. doi: 10.1002/cbdv.202100748.

248. Burkard C, Verheije MH, Wicht O, van Kasteren SI, van Kuppeveld FJ, Haagmans BL, Pelkmans L, Rottier PJ, Bosch BJ, de Haan CA. Coronavirus cell entry occurs through the endo-/lysosomal pathway in a proteolysis-dependent manner. PLoS Pathog. 2014 Nov 6;10(11):e1004502. doi: 10.1371/journal.ppat.1004502.

249. Bartolák-Suki E, Imsirovic J, Parameswaran H, Wellman TJ, Martinez N, Allen PG, Frey U, Suki B. Fluctuation-driven mechanotransduction regulates mitochondrial-network structure and function. Nat Mater. 2015 Oct;14(10):1049-57. doi: 10.1038/nmat4358.

250. Morita H, Matsuoka A, Kida JI, Tabata H, Tohyama K, Tohyama Y. KIF20A, highly expressed in immature hematopoietic cells, supports the growth of HL60 cell line. Int J Hematol. 2018 Dec;108(6):607-614. doi: 10.1007/s12185-018-2527-y.

251. Shen L, Niu J, Wang C, Huang B, Wang W, Zhu N, Deng Y, Wang H, Ye F, Cen S, Tan W. High-Throughput Screening and Identification of Potent Broad-Spectrum Inhibitors of Coronaviruses. J Virol. 2019 May 29;93(12):e00023-19. doi: 10.1128/JVI.00023-19.

252. Kumakura M, Kawaguchi A, Nagata K. Actin-myosin network is required for proper assembly of influenza virus particles. Virology. 2015 Feb;476:141-150. doi: 10.1016/j.virol.2014.12.016.

253. Niemann H, Boschek B, Evans D, Rosing M, Tamura T, Klenk HD. Post-translational glycosylation of coronavirus glycoprotein E1: inhibition by monensin. EMBO J. 1982;1(12):1499-504. doi: 10.1002/j.1460-2075.1982.tb01346.x

254. Gack MU, Shin YC, Joo CH, Urano T, Liang C, Sun L, Takeuchi O, Akira S, Chen Z, Inoue S, Jung JU. TRIM25 RING-finger E3 ubiquitin ligase is essential for RIG-I-mediated antiviral activity. Nature. 2007 Apr 19;446(7138):916-920. doi: 10.1038/nature05732.

255. Liuyu T, Yu K, Ye L, Zhang Z, Zhang M, Ren Y, Cai Z, Zhu Q, Lin D, Zhong B. Induction of OTUD4 by viral infection promotes antiviral responses through deubiquitinating and stabilizing MAVS. Cell Res. 2019 Jan;29(1):67-79. doi: 10.1038/s41422-018-0107-6.

256. Grunewald ME, Chen Y, Kuny C, Maejima T, Lease R, Ferraris D, Aikawa M, Sullivan CS, Perlman S, Fehr AR. The coronavirus macrodomain is required to prevent PARP-mediated inhibition of virus replication and enhancement of IFN expression. PLoS Pathog. 2019 May 16;15(5):e1007756. doi: 10.1371/journal.ppat.1007756.

257. Bonaparte MI, Dimitrov AS, Bossart KN, Crameri G, Mungall BA, Bishop KA, Choudhry V, Dimitrov DS, Wang LF, Eaton BT, Broder CC. Ephrin-B2 ligand is a functional receptor for Hendra virus and Nipah virus. Proc Natl Acad Sci U S A. 2005 Jul 26;102(30):10652-7. doi: 10.1073/pnas.0504887102.

258. Darling TK, Lamb TJ. Emerging Roles for Eph Receptors and Ephrin Ligands in Immunity. Front Immunol. 2019 Jul 4;10:1473. doi: 10.3389/fimmu.2019.01473.

259. Wu J dHC, Liu Q, Bouchet BP, Noordstra I, Jiang K, Hua S, Martin M, Yang C, Grigoriev I, Katrukha EA, Altelaar AFM, Hoogenraad CC, Qi RZ, Klumperman J, Akhmanova A. Molecular Pathway of Microtubule Organization at the Golgi Apparatus. Dev Cell. 2016;39(1):44-60.

260. Wu J, de Heus C, Liu Q, Bouchet BP, Noordstra I, Jiang K, Hua S, Martin M, Yang C, Grigoriev I, Katrukha EA, Altelaar AFM, Hoogenraad CC, Qi RZ, Klumperman J, Akhmanova A. Molecular Pathway of Microtubule Organization at the Golgi Apparatus. Dev Cell. 2016 Oct 10;39(1):44-60. doi: 10.1016/j.devcel.2016.08.009.

261. An Y, Rininger JA, Jarvis DL, Jing X, Ye Z, Aumiller JJ, Eichelberger M, Cipollo JF. Comparative glycomics analysis of influenza Hemagglutinin (H5N1) produced in vaccine relevant cell platforms. J Proteome Res. 2013 Aug 2;12(8):3707-20. doi: 10.1021/pr400329k.

262. Saraste J, Enyioko M, Dale H, Prydz K, Machamer C. Evidence for the role of Rab11-positive recycling endosomes as intermediates in coronavirus egress from epithelial cells. Histochem Cell Biol. 2022 Sep;158(3):241-251. doi: 10.1007/s00418-022-02115-y.

263. Yang X, Li J, Liu H, Zhang P, Chen D, Men S, Li X, Wang H. Induction of innate immune response following introduction of infectious bronchitis virus (IBV) in

the trachea and renal tissues of chickens. Microb Pathog. 2018 Mar;116:54-61. doi: 10.1016/j.micpath.2018.01.008.

264. Jang H, Koo BS, Jeon EO, Lee HR, Lee SM, Mo IP. Altered pro-inflammatory cytokine mRNA levels in chickens infected with infectious bronchitis virus. Poult Sci. 2013 Sep;92(9):2290-8. doi: 10.3382/ps.2013-03116.

265. Whitsett JA. Airway Epithelial Differentiation and Mucociliary Clearance. Ann Am Thorac Soc. 2018 Nov;15 (Suppl3):S143-S148. doi: 10.1513/AnnalsATS.201802-128AW.

266. Cook JK, Darbyshire JH, Peters RW. The use of chicken tracheal organ cultures for the isolation and assay of avian infectious bronchitis virus. Arch Virol. 1976;50(1-2):109-18. doi: 10.1007/BF01318005.

267. Cavanagh D, Elus MM, Cook JK. Relationship between sequence variation in the S1 spike protein of infectious bronchitis virus and the extent of cross-protection in vivo. Avian Pathol. 1997;26(1):63-74. doi: 10.1080/03079459708419194.

268. Stevenson-Leggett P. Investigation into infectious bronchitis virus (IBV) spike glycoprotein glycosylation, pathogenicity and tropism: University of Liverpool; 2018.

269. Zhao Y, Cheng J, Yan S, Jia W, Zhang K, Zhang G. S gene and 5a accessory gene are responsible for the attenuation of virulent infectious bronchitis coronavirus. Virology. 2019 Jul;533:12-20. doi: 10.1016/j.virol.2019.04.014.

270. Davidson AD, Williamson MK, Lewis S, Shoemark D, Carroll MW, Heesom KJ, Zambon M, Ellis J, Lewis PA, Hiscox JA, Matthews DA. Characterisation of the transcriptome and proteome of SARS-CoV-2 reveals a cell passage induced in-frame deletion of the furin-like cleavage site from the spike glycoprotein. Genome Med. 2020 Jul 28;12(1):68. doi: 10.1186/s13073-020-00763-0.

271. Sakaguchi T, Leser GP, Lamb RA. The ion channel activity of the influenza virus M2 protein affects transport through the Golgi apparatus. J Cell Biol. 1996 May;133(4):733-47. doi: 10.1083/jcb.133.4.733.